Probing the Origins of Directly Imaged Planets and Brown Dwarfs: From Atmospheric Compositions to Binarity

Thesis by
Wenhao Jerry Xuan

In Partial Fulfillment of the Requirements for the
Degree of
Doctor of Philosophy in Astrophysics

CALIFORNIA INSTITUTE OF TECHNOLOGY
Pasadena, California

2025
Defended February 24, 2025

Wenhao Jerry Xuan
ORCID: 0000-0002-6618-1137

ACKNOWLEDGEMENTS

First and foremost, I would like to thank Dimitri Mawet for his unwavering support and confidence in me over the years. From a cold email in 2016, he welcomed me to his group as a SURF student, and entrusted me with building an instrument prototype that would later evolve into KPIC. I had just finished my freshman year in college and had no experience in instrumentation. It was my summer internships at Caltech that consolidated my dream of pursuing a career in astronomy. Throughout my PhD, Dimitri's optimism, vision, and constructive feedback have been a source of constant energy that propelled me forward. His humor and easygoing style have also fostered an enjoyable and collaborative environment in the group, which I am honored to be a part of.

I would also like to thank Heather Knutson, who I view as my second PhD advisor. In our weekly atmosphere meetings, Heather has always provided me with invaluable advice, ideas, and encouragement. Her excellent courses on Planetary Atmospheres and Bayesian Statistics have also been foundational for my PhD research. My PhD would not be possible without her guidance and support.

My PhD would not have been the same without the guidance of Jason Wang and Jean-Baptiste Ruffio, former postdocs at Caltech, who taught me everything about KPIC data, modeling, and more. Thank you for answering my many questions on Slack, Zoom, and in person. Special thanks to Jason for sponsoring part of my visit to Keck Observatory in 2022, where I spent a memorable time working on the KPIC instrument full-time and enjoying Hawaii.

I'd like to thank my current and former group mates for keeping the research environment fun and cordial: Yinzi, Katelyn, Aniket, Dan, Elijah, Niyati, Yapeng, Arielle, Jason, J-B, Bin, Ashley, Jorge, Susan, Andrea – thank you for the many social activities after work, from the board game nights, Monday Settebello's and friendsgivings that we enjoyed together. I could not have asked for a better group to be a part of.

I am also grateful to members of our mini-atmosphere group for four years of wonderful scientific discussions and mutual support: Julie Inglis, Nicole Wallack, and Yapeng Zhang. When the retrievals became too hairy, I always knew who to turn to. Yapeng Zhang, thank you for being a patient and kind mentor to me in several projects, and for brainstorming ideas together that led to several successful

proposals.

I have benefited from interactions with many other faculty members at Caltech. Special thanks to Konstantin Batygin, Geoff Blake, and Gregg Hallinan for serving on my committee and providing guidance in my research. I am grateful to Konstantin for illuminating discussions on three-body dynamics and exciting ideas about moons around brown dwarf binaries. I also benefited much from your two courses on Planet Formation and Planet Dynamics. Thank you Geoff Blake for providing excellent feedback in each of my KPIC papers, and for fruitful discussions on isotopologues and exoplanet atmospheres. Thank you Gregg, Shri, and Kareem for fun discussions in the context of the Gliese 229 B project. I want to thank Andrew Howard for his openness to collect new RV data for me, which directly contributed to my HIP 55507 AB paper. Lynne Hillenbrand, thank you for pushing me to excel and reach higher.

I am very grateful to Judy McClain for her rapid responses and help with travel logistics. You have helped me navigate tough and unusual situations with regards to the Hawaii trip. Thank you for making it possible. Special thanks to Shelly Pelfrey and Lani Kiyota at Keck for being so welcoming and for making sure everything was smooth for my visit at Keck. Thank you Lisa Christiansen for helping me navigate the world of budgets. Gita Patel, thank you for being there for the graduate students and for keeping weekly traditions like donuts alive.

To members of the KPIC team, thank you for being awesome and kind. It has been immensely rewarding to be part of this collaboration, and I have learned a lot from many of you. Just to name a few, Luke, Nem, Dan, Yinzi, Ben, Katelyn, Jacques, Tobias, Dino, Charlotte, Eduardo, Ashley, and Kent, thank you for all the support you provided in my KPIC endeavors.

I have spent many nights observing with Keck in my PhD. Thank you to all the Keck staff for your help with the calibrations and observations, especially Greg, Carlos, Rosalie, Arina, Peter, Avinash, Charlotte, Sam, and others.

Several external collaborators have played a key role in my PhD. Paul Mollière, thank you for showing me the ropes when it comes to retrievals, and for answering my several dozens of emails. Without you and petitRADTRANS, my PhD would likely have been quite different. Rebecca Oppenheimer, thank you for your unwavering support and contagious enthusiasm in the Gliese 229 Bab project. You pushed me to excel and write a paper in record time. For the binarity paper, I am also extremely grateful to William Thompson, Antoine Mérand, and Dori Blakely for surmounting

many challenges in modeling the GRAVITY data and orbit, Sylvestre Lacour for guiding me through the proposals and observations and bringing together the team. Thank you Dino Hsu, Jared Kolecki, Simon Grimm, Anne Peck for contributing crucial parts in my KPIC papers. I also want to thank Marshall Perrin, who provided expert guidance in the JWST/MIRI project.

During my undergrad years, several Caltech SURF mentors have played an important role in my development as a scientist. Thank you Gary and Henry for being incredible mentors for me during two SURF projects, where I learned so much about instrumentation, coding, and high-contrast imaging; key skills that were extremely helpful in my PhD. Your unwavering support during these projects gave me a first taste of how satisfying research can be. Thank you Kent Wallace for teaching me and Michael. You showed us the ropes of astronomical optics and helped us build the first prototype fiber injection unit. Thank you Marta for guiding me through a highly challenging project in my third SURF, and for introducing me to senior folks at conferences. You gave me a first taste of high-resolution spectroscopy, which became the focus of my PhD. During my SURFs, I have also benefited from discussions with former Caltech/JPL postdocs Ji, Elodie, Max, Vanessa, Ricky, Tiffany, and Rahul.

To my roommate Adolfo Carvalho, thank you for many fun memories in our apartment and beyond, for teaching me several cooking recipes, and for taking care of the cats when I was traveling. I will also miss the weekly tennis games with Aniket, James, and Hazel. Thank you Zhuyun, SamWu, and Yuhan for being excellent officemates in my third and fourth years. Thanks to former and current grads, Evan, Nik, Tony, Ivey, SamP, SamR, Kaustav, Dillon, Michael, Sarah, Ryan, Jakob, Dee, Emily, Jess, Yash, Kathryn, Natsuko, Delina, Harshda, Soumyadeep, Hazel, Luke and others for making Cahill a friendly environment.

To my cats, Zodi, Bambam, and Pebble, who have filled our home with warmth, your presence has greatly heightened my happiness in grad school. Thank you for sharing a home with me.

To my parents and my sister, thank you for your endless love and support. Finally, to my partner Dr. Jingwen Zhang, thank you for being there at every step of the way, for your love and companionship, and for all the fond memories we shared across oceans.

ABSTRACT

High-contrast imaging has revealed a population of substellar companions, generally classified as giant planets ($\sim 2-13\ M_{\rm Jup}$) or brown dwarfs ($\sim 13-75\ M_{\rm Jup}$), orbiting at large separations ($\sim 3-1000$ au) from their host stars. Past studies have mostly relied on low-resolution spectroscopy ($R \sim 20-100$) to study their atmospheres, but encountered hurdles in measuring reliable atmospheric abundances. In my thesis, I work to overcome these challenges by studying these objects using high-resolution spectroscopy from Keck/KPIC, a unique single-mode fiber feed into NIRSPEC that provides $R \sim 35,000$ spectra in the near-infrared. Besides studying substellar atmospheres with KPIC, I contributed significantly to its data reduction pipeline and calibration procedure.

With KPIC, I used atmospheric retrievals to characterize a large sample of planetary-mass companions and brown dwarfs to shed light on their formation history. First, I measured the carbon and oxygen abundances of high-mass brown dwarfs and low-mass M dwarfs ($m \approx 60-90\ M_{\rm Jup}$) and showed they are chemically homogeneous to their host stars (Chapters 2 and 3). I also made one of the first estimates of the vertical mixing rate in a L/T transition brown dwarf companion from its relative H_2O, CO, and CH_4 abundances (Chapter 2). Next, I carried out a survey of eight planetary-mass companions with estimated masses between $10-30\ M_{\rm Jup}$ (Chapter 4). I found that these companions also have C and O abundances clustered around the solar value, similar to abundances of stars in the same star-forming regions. In these studies, I made several isotopologue ratio measurements including $^{12}CO/^{13}CO$ and showed that a late-M dwarf companion has the same $^{12}C/^{13}C$ and $^{16}O/^{18}O$ as its K6V host star. Overall, my KPIC studies show that companions with $m \gtrsim 10\ M_{\rm Jup}$ likely form as the tail-end of star formation, consistent with the conclusions from demographic and orbital architecture studies of substellar companions.

Next, I worked on addressing the over-massive brown dwarf problem, an emerging phenomenon where several brown dwarf companions have dynamical masses higher than predictions from evolutionary models given their luminosities. This problem can be solved if these objects are not single entities. Using VLTI/GRAVITY and VLT/CRIRES+, I resolved the first brown dwarf companion, Gliese 229B, into two nearly-equal mass brown dwarfs, Gliese 229 Ba and Bb, on a 12 day orbit (Chapter 5). Gliese 229Bab is the tightest substellar binary orbiting a star, and indicates that other over-massive brown dwarfs might also be unresolved, tight binaries. As a

follow-up study, I analyzed JWST/MIRI spectrum ($5 - 14$ μm) of Gliese 229 Bab to show that both brown dwarfs have similar C/O and metallicities as their host star, as expected for a star-like formation scenario (Chapter 6).

PUBLISHED CONTENT AND CONTRIBUTIONS

Xuan, J. W. et al. (July 2024a). "Are These Planets or Brown Dwarfs? Broadly Solar Compositions from High-resolution Atmospheric Retrievals of ~10–30 M_{Jup} Companions". In: *The Astrophysical Journal* 970.1, 71, p. 71. DOI: 10.3847/1538-4357/ad4796.

J.W.X. developed the target list for the survey, observed with Keck/KPIC to acquire the data, carried out literature research on each system, performed the atmospheric retrieval analyses, and wrote the paper.

Xuan, J. W. et al. (Dec. 2024b). "Atmospheric Abundances and Bulk Properties of the Binary Brown Dwarf Gliese 229Bab from JWST/MIRI Spectroscopy". In: *The Astrophysical Journal Letters* 977.2, L32, p. L32. DOI: 10.3847/2041-8213/ad92f9.

J.W.X. conceived of the project and wrote the JWST Cycle 2 proposal, extracted the MIRI spectrum, performed the spectral fits with Sonora models, and wrote the paper. M.P. developed the forward model method to remove the stellar contamination in the data as part of data reduction.

Xuan, J. W. et al. (Oct. 2024c). "The cool brown dwarf Gliese 229 B is a close binary". In: *Nature* 634.8036, pp. 1070–1074. DOI: 10.1038/s41586-024-08064-x.

J.W.X. conceived of the project, wrote the ESO proposals to acquire the VLTI/GRAVITY and VLT/CRIRES+ data, performed the CRIRES+ spectral fitting to obtain radial velocities, and wrote the paper. A.M., W.T. and D.B. led the GRAVITY closure phase modelling and orbital analysis. Y.Z. reduced the raw CRIRES+ data. S.L. reduced the raw GRAVITY data.

Xuan, J. W. et al. (Feb. 2024d). "Validation of Elemental and Isotopic Abundances in Late-M Spectral Types with the Benchmark HIP 55507 AB System". In: *The Astrophysical Journal* 962.1, 10, p. 10. DOI: 10.3847/1538-4357/ad1243.

J.W.X. conceived of the project and validated the bound nature of the companion HIP 55507 B from Keck/NIRC2 observations. J.W.X. collected KPIC spectra of HIP 55507 A and B, performed atmospheric retrieval and orbital analyses for the system, and wrote the paper.

Xuan, J. W. et al. (Oct. 2022). "A Clear View of a Cloudy Brown Dwarf Companion from High-resolution Spectroscopy". In: *The Astrophysical Journal* 937.2, 54, p. 54. DOI: 10.3847/1538-4357/ac8673.

J.W.X. extracted the KPIC and archival spectra of HD 4747 B, built an atmospheric retrieval framework based on petitRADTRANS, performed the spectral and orbital analysis, and wrote the paper. J.K. measured the abundances of the host star HD 4747 A from optical spectroscopy.

TABLE OF CONTENTS

LIST OF ILLUSTRATIONS

LIST OF TABLES

NOMENCLATURE

ADI. angular differential imaging.

AO. adaptive optics.

AU. astronomical units.

Gyr. giga years.

HDC. high dispersion coronagraphy.

HRS. high-resolution spectroscopy.

HWO. Habitable Worlds Observatory (NASA Mission).

IWA. inner working angle.

JWST. James Webb Space Telescope.

K band. Astronomical band spanning 1.9 to 2.5 μm.

KPIC. Keck Planet Imager and Characterizer.

LRS. low-resolution spectroscopy.

MMR. mass-mixing ratio.

Myr. mega years.

NIRSPEC. Near Infrared Spectrograph (Keck II Telescope).

P-T profile. pressure-temperature profile.

PSF. point spread function.

R. resolving power.

RDI. reference differential imaging.

RV. radial velocity.

S/N. signal-to-noise ratio.

VLT(I). Very Large Telescope (Interferometer).

VMR. volume-mixing ratio.

Chapter 1

INTRODUCTION

To an extraterrestrial astronomer, the most obvious feature of the solar system besides the Sun is likely Jupiter. A patient radial velocity expert will readily recover the 12 m/s motion that Jupiter induces on the Sun after carefully removing stellar activity. An astrometry aficionado 10 parsecs from us will see the Sun make loops in their night sky with a size of 0.5 milliarcseconds – small but measurable by their equivalent mission to *Gaia*. A direct imaging specialist, after battling atmospheric turbulence for years, will detect Jupiter as the first planet in our system after the launch of a dedicated space telescope. These astronomers will likely ponder about the formation of Jupiter, and compare it with the planets in their home system. They will find it remarkable how diverse the structure of different stellar neighborhoods can be, and become enthusiastic about the possibility of life elsewhere. For Earth-based astronomers today, Jupiter-like gas giant planets remain the most accessible exoplanets to study. Brown dwarf companions to stars, close cousins of gas giant planets, are also excellent laboratories to study the various physical and chemical processes governing both classes of objects.

1.1 Exoplanet detection techniques

Radial velocity

The first detection of an exoplanet around a main-sequence star was achieved using the radial velocity (RV) technique back in 1995 (Mayor et al., 1995). The planet 51 Pegasi b, a gas giant with a mass of 0.5 $M_{\rm Jup}$, was found to orbit its host star every 4.2 days. This exceedingly short orbital period meant that the star exhibited radial velocity shifts with a semi-amplitude of $\approx$ 60 m s^{-1}. The radial velocity semi-amplitude is given by (Lovis et al., 2010)

$$K = \frac{28.4329 \text{ m s}^{-1}}{\sqrt{1-e^2}} \frac{m_p \sin i}{M_J} \left(\frac{M_* + m_p}{M_\odot}\right)^{-2/3} \left(\frac{P}{1 \text{ yr}}\right)^{-1/3} \tag{1.1}$$

where e, i and P are the orbital eccentricity, sky-projected inclination and orbital period, respectively, and m_p and M_* are the masses of the planet and host star. Traditionally, only the radial velocity of the star could be measured, since even giant planets are generally thousands to millions of times fainter than their stars.

More recently, advances in infrared high-resolution spectroscopy have enabled RV measurements of giant planets and brown dwarf companions § 1.3, which has provided useful orbital and dynamical mass constraints for the companions, and enabled searches for exomoons and brown dwarf binaries (Ruffio et al. 2023a; Do Ó et al. 2023; Horstman et al. 2024, Chapters 3 and 5).

By measuring the host star's RV at all orbital phases, we can measure the semi-amplitude K and the minimum mass of the planet ($m_p \sin i$). Strictly speaking, this is only possible when the total mass ($M_* + m_p$) is known. In the exoplanet case, $m_p \ll M_*$, so given an estimate of the host star's mass, $m_p \sin i$ can readily obtained. For a random distribution of orbits, the inclination along the line of sight (i) is uniform in $\sin i$, meaning that it is statistically more likely to observe edge-on orbits than face-on ones. In general, additional information from astrometry or transits is required to measure i and the true planet mass.

Long-term radial velocity campaigns have obtained decade-long baselines, and are now sensitive to giant planets on Jupiter-like scales. Recent studies have shown that gas giants are most commonly found between 1 – 10 AU of their stars, with the peak in occurrence rate roughly corresponding to the location of the water snowlines in the protoplanetary disk (Fulton et al., 2021), which is the radial location where water starts to condense around young stars.

Transits

The transit technique relies on a special geometry between the observer and the observed planetary system, where the exoplanet's orbit has i close to 90°. In this configuration, the planet would periodically transit in front (and eclipse behind) its star, which then exhibits variations in brightness. The transit depth can be used to measure planetary radii, as it is proportional to $(R_p/R_*)^2$, where R_p is the planet's radius and R_* is the stellar radius. Stellar radii can be measured by modeling spectroscopy, photometry, or interferometry observations. When combined with precise parallax measurements from the *Gaia* mission, our knowledge of stellar radii is now accurate to the few percent level for many planet-host stars (e.g. Fulton et al., 2018; Berger et al., 2020).

The first transiting exoplanet detection was announced by Charbonneau et al. (2000), and featured the gas giant HD 209458 b, which orbited its star every 3.5 days. Thanks to the success of space observatories like *Kepler* (Borucki et al., 2010) and the Transiting Exoplanet Survey Satellite (*TESS*, Ricker et al. 2015), the transit technique

has yielded by far the most exoplanets known to date (Fig. 1.1), revolutionizing our understanding of exoplanet demographics. While giant planets on short orbits are the easiest to detect from the transit and radial velocity techniques, we now know that such planets, dubbed hot Jupiters, are rare, with an occurrence rate of $\approx 0.6 - 1.2\%$ (e.g. Wright et al., 2012; Petigura et al., 2018). On the other hand, transit detections have shown that planets with sizes between Earth and Neptune, with radii $\sim 1-4R_{\oplus}$, are the most common type of planets in the galaxy and exist around at least a third of Sun-like stars at orbital distances < 1 AU (Winn et al., 2024). It is remarkable that there is no equivalent planet in our solar system.

As the transit light curve is sensitive to the line of sight inclination, combining transit and radial velocity measurements directly constrains the planet's mass. This is extremely useful, both as a way to confirm transiting planet candidates, and as input for detailed characterization. For example, knowledge of the mass, radius, and by extension surface gravity is crucial to interpreting transmission spectroscopy measurements, whose signal strength inversely is proportional to the planet's surface gravity (Kreidberg, 2018).

Absolute astrometry

Astrometry measures the precise positions and motions of stars and other celestial objects in the sky. In contrast to radial velocity, which probes motion in the line of sight direction, astrometry measures these positions in sky plane, or the tangential directions (right ascension and declination). Absolute astrometry is the measurement of positions relative to a fixed reference frame, such as the The International Celestial Reference System (ICRS, Charlot et al. 2020). By monitoring the absolute astrometry of stars over time, one can detect companions around them by searching for periodic wobbles in the star's trajectory. A star's trajectory is also shaped by parallax and proper motion, two main observables of absolute astrometry. The angular displacement on the sky is the relevant quantity in astrometric detections (Perryman et al., 2014)

$$\alpha = \left(\frac{m_p}{M_*}\right)\left(\frac{a}{1\ \mathrm{AU}}\right)\left(\frac{d}{1\mathrm{p}c}\right)\mathrm{arcsec} \tag{1.2}$$

where α is known as the astrometric signature, a is the semi-major axis of the planetary orbit with respect to the barycenter, and d is the distance to the system. Provided sufficient time baseline (and orbital phase coverage), absolute astrometry is most sensitive to massive, long-period planets around nearby stars.

The *Gaia* spacecraft, which started operations in July 2014 and collected its last photons in January 2025, measured absolute astrometry and photometry for billions of stars and celestial objects. *Gaia* builds on the success of the *Hipparcos* spacecraft, which operated from from 1989 to 1993 and provided a catalog of high precision astrometry and parallax measurements for over 100,000 stars. Epoch astrometry from *Hipparcos* has yielded detections, orbital solutions, and dynamical masses for binary stars as well as dozens of brown dwarfs and giant planets, often in combination with complementary RV observations (e.g. Lindegren et al., 1997; Sozzetti et al., 2010; Sahlmann et al., 2011; Snellen et al., 2018). Epoch astrometry from *Gaia* has not yet been released, but is expected in 2026, and predicted to uncover hundreds or even thousands of new giant planets (e.g. Perryman et al., 2014; Holl et al., 2022). In the meantime, the non-single star catalog was released by the *Gaia* team in 2022 based on processing a subset of stars. This catalog, and *Gaia* astrometry in general, have already yielded several candidate and confirmed exoplanets (e.g. Holl et al., 2023; Stefansson et al., 2024; Winn, 2022; Marcussen et al., 2023), dormant stellar-mass black holes around nearby stars (El-Badry et al., 2023b; El-Badry et al., 2023a; Gaia Collaboration et al., 2024), and numerous new binary star systems, introducing something of a binary star renaissance (El-Badry, 2024).

A powerful advancement over the past years is the combination of *Gaia* and *Hipparcos* astrometry (T. D. Brandt, 2018; T. D. Brandt, 2021a; Snellen et al., 2018; Kervella et al., 2019). A single star exhibits a nearly linear motion as it orbits in the galaxy, whereas non-single stars could show differences in proper motions at different epochs. This is the basis of the proper motion anomaly technique, which is also known as astrometric accelerations. Specifically, one constructs a baseline proper motion vector by differencing the positions between the *Hipparcos* and *Gaia* epochs (either DR2 or DR3), which approximates the long-term velocity of the star in the galaxy. Significant differences between the proper motions measured in epoch 2016/1991.25 (for *Gaia* DR3/*Hipparcos*) and the baseline proper motion vector indicate that the star is undergoing orbital motion, thereby providing evidence for companions. This technique has been hugely successful in the exoplanet and brown dwarf fields. The PMa has increased the success rate of direct imaging observations, yielding several new exoplanets and brown dwarfs (e.g. Currie et al., 2020; Kuzuhara et al., 2022; Franson et al., 2023c; Franson et al., 2023b; De Rosa et al., 2023; Currie et al., 2023b) in the span of years. When combined with radial velocities for instance, the PMa technique has provided rare but valuable 3-D orbits for gas giants (e.g. Li et al., 2023; Venner et al., 2021). In multi-planet systems,

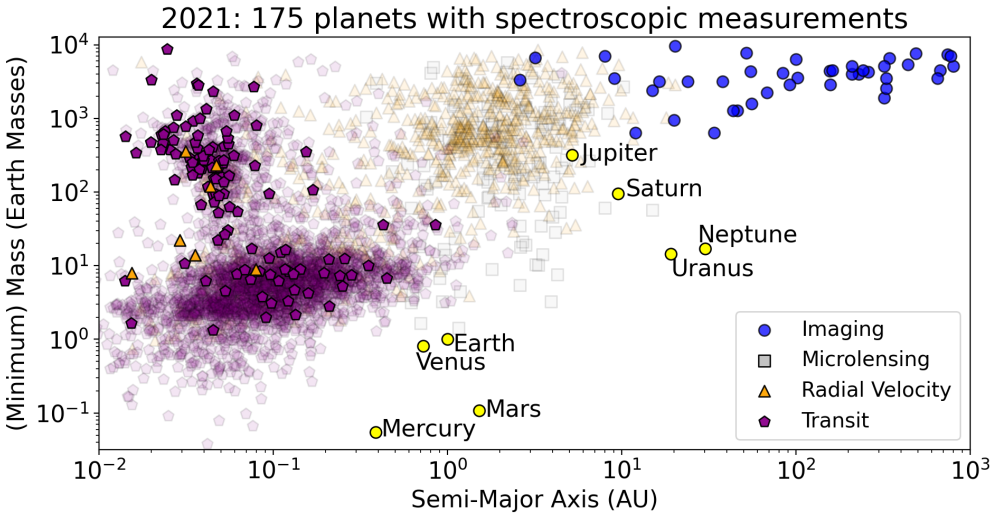

Figure 1.1: Exoplanets detected from the various detection techniques as of 2021. Bold symbols indicate the 175 planets with spectroscopic measurements: directly imaged companions represent a substantial fraction of this population. Reproduced from Currie et al. (2023a) using data from the NASA Exoplanet Archive.

this has resulted in mutual inclination measurements between short-period planets ($P < 100$ days) and outer giant planets (J. W. Xuan et al., 2020a; De Rosa et al., 2020; J. Zhang et al., 2024), as well as giant planets and their debris disks (J. W. Xuan et al., 2020c), widening our knowledge of planetary system architectures.

Direct imaging

The previously described exoplanet detection techniques rely on measuring light from the host star to infer the presence of planets. Direct imaging, on the other hand, is designed to directly capture photons from exoplanets. This is done by suppressing and removing the starlight with dedicated instruments, observational, and post-processing techniques to achieve high-contrast. Recent reviews on direct imaging include Bowler (2016) and Currie et al. (2023a). A typical direct imaging instrument uses adaptive optics to reach a nearly diffraction limited point-spread function (PSF) and coronagraphs to remove the diffraction pattern of the star. Planet light, which is slightly off-axis compared to the star, is allowed to transit through mostly unhindered and imaged on the science detector. Techniques such as angular differential imaging (Marois et al., 2006) and reference star differential imaging (Lafrenière et al., 2009) are used to isolate the planet signal from the quasi-static speckle field. At small separations, direct imaging is generally limited by photon noise from the residual starlight and the lower throughput of the coronagraph, whereas at larger angular

separations, thermal background from the sky and instrumental background tends to limits detectability.

Because planets cool down as they age, direct imaging has been most successful for young gas giants that are still bright from the release of internal energy from formation. The planet-to-star flux ratios of the current sample of directly imaged planets ranges from about 10^{-4} to 10^{-6} in the near-infrared wavelengths. In the past two decades, direct imaging has revealed a population of widely-separated (> 1 AU), substellar companions ($1 - 75\ M_{\rm Jup}$) to stars. Traditionally, these objects are classified into giant planets ($m < 13\ M_{\rm Jup}$) and brown dwarfs ($13 < m < 75\ M_{\rm Jup}$) based on the deuterium burning limit (Oppenheimer et al., 2000). These directly imaged companions, which span the boundary between our own Jupiter and low-mass M dwarfs, are the subject of this thesis.

Direct imaging naturally enables the spectroscopic studies of exoplanets (see Fig. 1.1), which provide a wealth of information on their atmospheric makeup and dynamics, internal structure, and evolution. In fact, among the nearly 6000 exoplanets discovered so far, less than 200 have measured spectra (see Fig 1). Directly imaged planets account for $\sim$ 50 of these, whereas the remaining are from transmission and/or emission spectroscopy of close-in planets.

1.2 Giant planet and brown dwarf formation

Together, the detection techniques outlined above have revealed a stunning diversity of exoplanets in our galaxy. These planets range from Mars-sized bodied on day-long periods to massive gas giants orbiting hundreds of AU from their stars. From transits and RVs, the myriad super-Earths, sub-Neptunes, and hot Jupiters have revealed large gaps in our knowledge of planet formation, since the canonical theories were developed to explain the origin of the solar system. The population of directly imaged companions, sometimes referred to as super-Jupiters, represent the other extreme in terms of mass and semi-major axis. Many of the directly imaged companions blur the line between giant planets and brown dwarfs and challenge our understanding of both planet and star formation processes.

While it is very challenging to know a priori how a given companion formed, three main mechanisms are typically invoked to explain the population of directly imaged companions. These are core accretion, disk fragmentation, and molecular cloud fragmentation (in two morphological variants, filament or core). The disk and cloud fragmentation mechanisms are illustrated in Fig. 1.2. Beyond these, dynamical

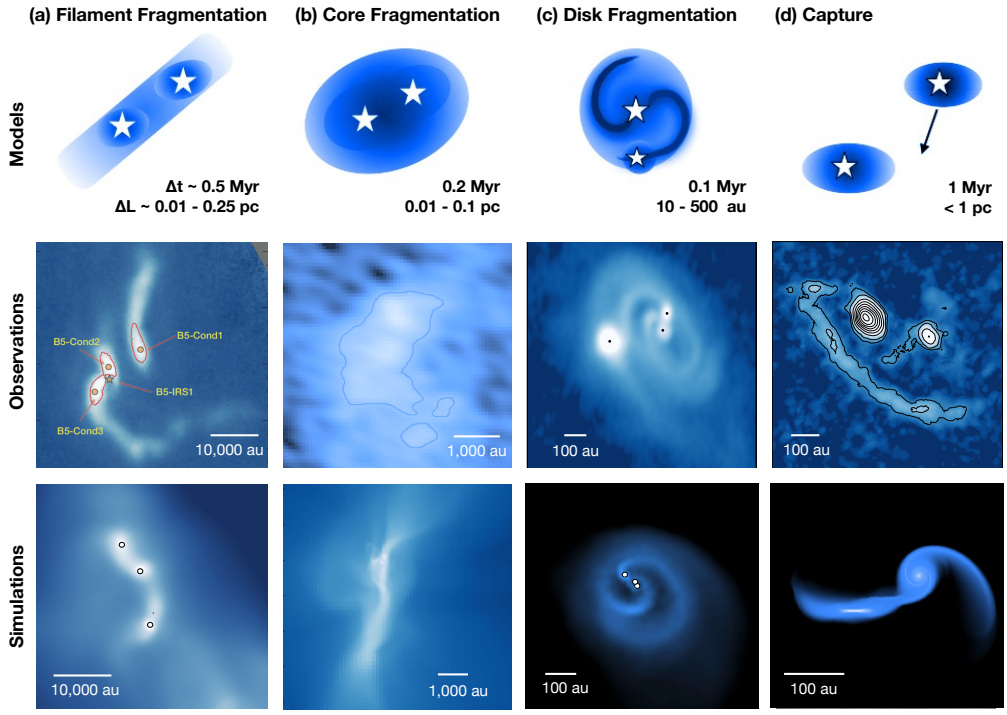

Figure 1.2: Summary of mechanisms for multiple formation. Top: Model and approximate range of time and length scales for each process. Middle: Proposed observational examples. From left to right: B5 in Perseus (Pineda et al. 2015), SM1N in Ophiuchus (Kirk et al. 2017), L1448 IRS3B in Perseus (Reynolds et al. 2021) and RW Aur (Rodriguez et al. 2018). Bottom: Examples from numerical simulations. From left to right: Guszejnov et al. (2021) Offner et al. (2016), Bate (2018), and Munoz et al. (2015). Figure reproduced from Offner et al. (2023).

capture could also be responsible for the widest separation companions ($a \gtrsim 1000$ AU), though even these objects would still originally be formed through one of the three mechanisms above.

Giant planets are generally thought to form via bottom-up core accretion (Pollack et al., 1996). In the classic picture, this is a three-part process, where a solid core first coalesces from solids in the protoplanetary disk. These solids could either come from large kilometer-sized planetesimals, or millimeter-to-centimeter sized pebbles. Because planetesimal accretion is increasingly inefficient at large orbital distances, pebble accretion is usually theorized to be responsible for forming the cores of directly imaged planets with $a > 10$ AU (Johansen et al., 2017). In the second stage, gas is slowly accreted onto the core along with remaining planetesimals, and the growth rate is limited by the ability of the protoplanet to cool. Finally, after

the envelope has grown to be more massive than the core, runaway gas accretion ensures and the planet becomes a gas giant. Core accretion models require a large solid budget to rapidly form the massive cores of giant planets, and therefore prefer more massive and/or metal-rich stars (Fischer et al., 2005).

An alternative method to explain at least some giant planets is top-down disk fragmentation (Boss, 1997). Whereas core accretion is a slow process operating on million-year timescales, disk instability occurs early and fast ($\ll 1$ Myr) and is more likely to occur in the most massive disks (K. Kratter et al., 2016; Speedie et al., 2024). The standard reference for quantifying whether a disk undergoes instability due to its self-gravity is the Toomre Q parameter (Toomre, 1964)

$$Q = \frac{c_s \Omega}{\pi G \Sigma} \tag{1.3}$$

where c_s is the sound speed, Ω is the Keplerian orbital frequency, and Σ is the disk surface density. As Q drops below unity, the disk becomes unstable to collapse under its own gravity. Because c_s is proportional to temperature for an ideal gas, and Σ is proportional to the disk mass, colder and more massive disks are more prone to fragment. In typical conditions, $M_{\rm disk}/M_* > 0.1$ is required for disk instability.

Overall, disk fragmentation is thought to be give rise preferentially to brown dwarf and stellar companions rather than planets (e.g. Adams et al., 1989; Stamatellos et al., 2009; K. M. Kratter et al., 2010a; K. Kratter et al., 2016). This is because disk fragmentation should typically produce massive objects with masses $\approx 10\ M_{\rm Jup}$ Rafikov, 2005, which are expected to further accrete from the gaseous disk and grow into the brown dwarf or stellar regime. To stay in the planetary regime, atypically cool disks are required and one needs to somehow limit further accretion (K. M. Kratter et al., 2010a).

Brown dwarf companions are thought to be products of either disk fragmentation or molecular cloud fragmentation. The latter mechanism certainly gives rise to a wealth of isolated brown dwarfs. Recent observations suggest that cloud fragmentation operates down to only a few Jupiter masses (e.g. Luhman et al., 2024; Langeveld et al., 2024). Within the larger star-forming complex, objects can dynamically interact and become captured or ejected from their original configurations. Within a few AU of stars, there is a so-called brown dwarf desert, where brown dwarfs are found to be rarer ($< 1\%$) than even hot Jupiters (e.g. Halbwachs et al., 2000; Ma et al., 2014). The existence of the brown dwarf desert likely points to the inefficiency of

core accretion to form objects with $> 10\ M_{\rm Jup}$ (or at least their ability to survive disk-driven inward migration, Armitage et al. 2002), and is consistent with a picture where most brown dwarf companions form at wider separations from disk or cloud fragmentation.

The complexity of these various formation processes means that we observe a diverse range of substellar companions with different properties, from Jupiter-like planets within 10 AU of their stars (Macintosh et al., 2014; Franson et al., 2023b) to objects with a few Jupiter masses at thousands of AU from their star (Z. Zhang et al., 2021a). By studying directly imaged substellar companions on a statistical level, previous studies have uncovered evidence for diverging trends in semi-major axis, eccentricity, and stellar obliquity around a mass of $\sim 10 - 15\ M_{\rm Jup}$ (Nielsen et al., 2019; Bowler et al., 2020; Bowler et al., 2023; Nagpal et al., 2023). In particular, companions with $m < 10\ M_{\rm Jup}$ tend to orbit more massive stars and have more circular orbits that are aligned with the stellar spin axis. On the other hand, objects above this mass threshold tend to orbit a variety of stars from low-mass M dwarfs to massive B stars, and have a more uniform distribution of orbital eccentricities and stellar obliquities. However, as noted by Do Ó et al. (2023), the exact boundary is unclear between planets and brown dwarfs and limited by the small number of companions with $m < 10\ M_{\rm Jup}$. There is also evidence that transiting giant planets show different preferences for host star metallicity above and below $10\ M_{\rm Jup}$ (Schlaufman, 2018). While these studies hint at different formation mechanisms at play, they provide limited information on what those mechanisms are.

The atmospheric compositions of giant planets provide a complementary diagnostic of formation history. Specifically, carbon and oxygen are usually the most easy elements to measure, and the carbon-to-oxygen ratio (C/O) and metallicity have become popular diagnostics of planet formation (Öberg et al., 2011; Madhusudhan, 2012; P. Mollière et al., 2022). Here, metallicity is usually measured as C/H, the relative abundance of carbon compared to hydrogen. To first order, gas giants formed via core accretion should have varied atmospheric compositions depending on where they formed and what material they accreted, as solid and gas compositions vary radially in the protoplanetary disk due to processes such as condensation. Such planets are also predicted to follow a mass-metallicity relationship, with lower mass planets having higher atmospheric metallicity (Thorngren et al., 2016). On the other hand, companions that formed via disk instability or cloud fragmentation should resemble their stars in terms of atmospheric composition, as found for wide stellar

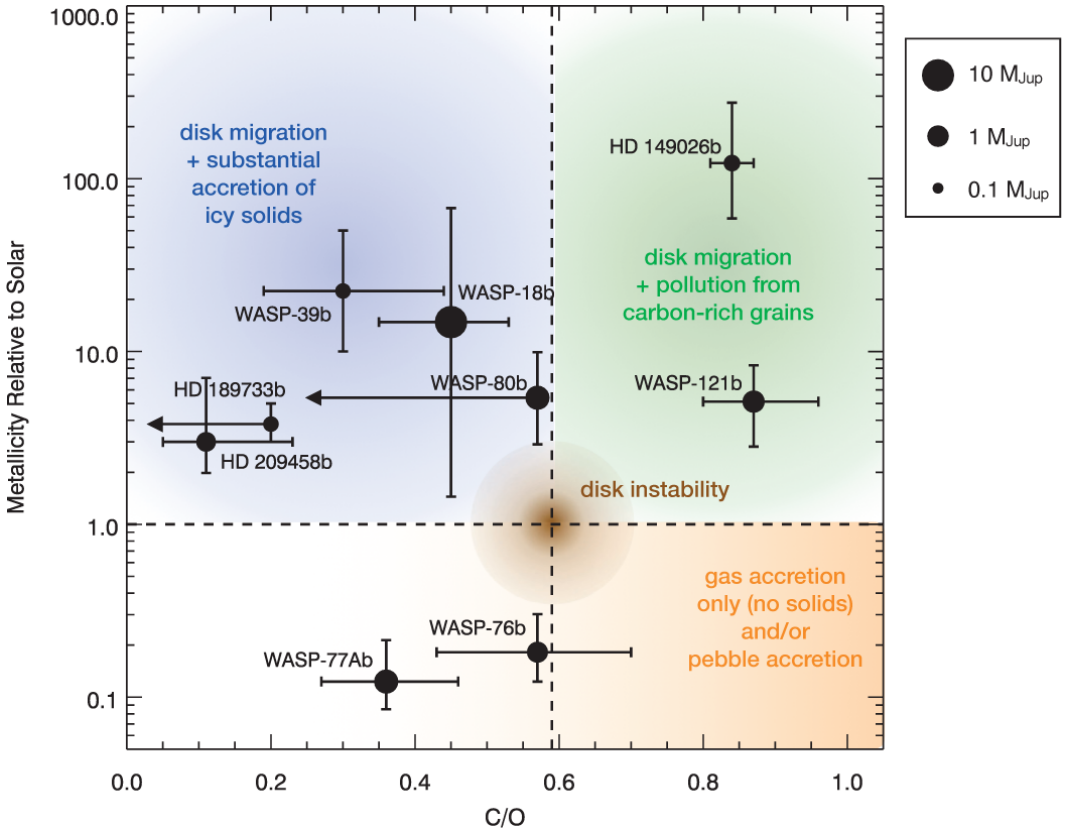

Figure 1.3: Metallicity vs. C/O ratio for exoplanets with measurements of both carbon- and oxygen-bearing species from JWST or high-resolution ground-based spectrographs as of the writing of this article. Planets formed via core accretion have varied compositions, whereas disk instability planets should mimic their stellar compositions (intersection of dashed lines). Figure and caption reproduced from Kempton et al. (2024).

binaries (Hawkins et al., 2020).

Consistent with this picture, atmospheric surveys have shown that $\lesssim 10\ M_{\rm Jup}$ gas giants orbiting close to their stars (hot Jupiters, $a \lesssim 0.1$ AU) tend to have metal-enriched and varied compositions (Kempton et al. 2024, see Fig. 1.3). What does the picture look like for higher mass companions (with $m > 10-75\ M_{\rm Jup}$)? Is there a compositional boundary that can be identified as a function of mass or semi-major axis? In other words, what is the smallest and closest-in planet that can form via gravitational instability, and what is the most distant and massive planet that can form via core accretion? This thesis seeks to answer some of these questions from the lens of spectroscopic observations.

1.3 Spectroscopy of directly imaged companions

History and overview

Previous atmospheric characterization of substellar companions have mainly relied on low-resolution spectroscopy (LRS) with resolving powers of $R \approx 20 - 100$. The workhorse instruments for low-resolution spectroscopy include the Gemini Planet Imager (Macintosh et al., 2014) formerly at the Gemini South telescope, SPHERE IFS (Claudi et al., 2008) at the Very Large Telescope (VLT), and CHARIS (Groff et al., 2017) at the Subaru telescope. These instruments all utilize integral field spectrographs (IFS), which collect spectra in a two-dimensional area. After subtracting stellar contamination using techniques such as angular differential imaging or spectral differential imaging, the companion spectra can be extracted. Details on the procedure for extracting low-resolution spectroscopy for high-contrast companions can be found in Pueyo (2016) and Greenbaum et al. (2018).

LRS is sensitive to continuum emission from the deepest observable layer of the atmosphere and modified by opacity sources further up. Some highlights from LRS studies of directly imaged planets and brown dwarfs include systematic characterizations of HR 8799 planets which find significant differences in their spectra (Greenbaum et al., 2018; J. J. Wang et al., 2022), measurements of C/O and metallicity from atmospheric retrievals (see § 1.4 (Gravity Collaboration et al., 2020; P. Mollière et al., 2020), and the detection of CH_4 in 51 Eri b (Macintosh et al., 2015). Previous studies have found several challenges with analyzing low-resolution spectroscopy. For instance, an important but poorly understood opacity source comes from clouds, which significantly modify the spectra of many observed exoplanet and brown dwarf (Gao et al., 2021). Due to our limited knowledge in cloud physics, a reliable assessment of atmospheric conditions from LRS is often fraught with complex degeneracies between clouds, the atmospheric thermal structure, and chemical abundances (e.g. Burningham et al., 2017; P. Mollière et al., 2020).

Increasingly, directly imaged companions have been observed with medium-resolution spectroscopy (MRS; $R \sim 4000$), where molecular bands (i.e. groups of lines) start to be resolved (e.g. Konopacky et al., 2013; Barman et al., 2015; Hoeijmakers et al., 2018; Hoch et al., 2020; Hoch et al., 2022; Ruffio et al., 2021). Major instruments include OSIRIS (Larkin et al., 2006) at the W.M. Keck Observatory, and SINFONI (Eisenhauer et al., 2003) at the Very Large Telescope. At medium-resolution, molecular detections of CO and H_2O have been made for several directly imaged companions, while the non-detection or weak detections of CH_4 have suggested

strong vertical mixing (Barman et al., 2015). At medium-resolution, cross-talk between different molecules can sometimes result in ambiguous detections, for instance the validity of the CH_4 detection from Keck/OSIRIS remains unclear for HR 8799 b (Petit dit de la Roche et al., 2018; Ruffio et al., 2021).

Towards high-contrast, high-resolution spectroscopy

The next upgrade in spectral resolution brings us to the regime of high resolution spectroscopy (HRS; $R > 25,000$), where molecular bands are resolved into individual absorption lines. An excellent review of HRS for exoplanets is provided by Birkby (2018). The first successful demonstration of HRS in exoplanets was published in 2010 by Snellen et al. (2010), who used VLT/CRIRES to detect CO in the first transiting hot Jupiter HD 209458 b. Since then, HRS has become a powerful tool for the study of hot Jupiters, whose rapid orbital motion induce significant RV shifts (typically hundreds of m/s) over the course of a few hours. This allows their spectra to be disentangled in velocity space from the relatively static stellar and telluric spectra. For hot Jupiters, detections are generally made from a cross-correlation technique (Brogi et al., 2019), which boosts signal strength by co-adding multiple spectral lines in the planetary atmosphere. For directly imaged planets, the first demonstration of HRS was by Snellen et al. (2014), who also used CRIRES to measure the projected spin rate of β Pictoris b from the rotational broadening of its CO and H_2O lines.

Compared to LRS, HRS can provide more robust molecular signatures compared to medium- or low-resolution spectroscopy. The relative line depths between different molecules such as CO, H_2O, and CH_4 are directly sensitive to abundance ratios. The line core-to-continuum ratio provides information on the metallicity. This makes HRS an ideal tool for measuring atmospheric compositions. Furthermore, for a given object, the cores of absorption lines form higher up in the atmosphere compared to the continuum probed by LRS. Specifically, the line cores generally form above the common cloud decks and provide a window into the atmosphere that is relatively unaffected by clouds (see Gandhi et al. 2020, Chapter 2). Because clouds are a major source of confusion in atmospheric studies, the ability of HRS to probe above clouds can be quite powerful.

High-resolution observations also uniquely enable the measurement of the planet's projected rotation rate ($v \sin i$) and radial velocity (RV), which manifest as broadening and shifts in the spectral lines (see Fig. 1.4). Rotation rates of substellar com-

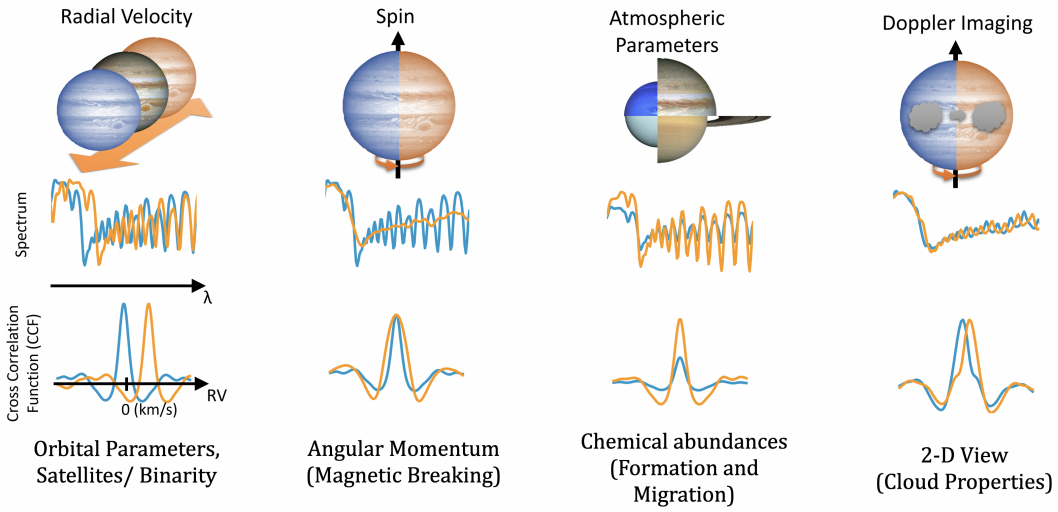

Figure 1.4: High-resolution spectroscopy enables a variety of science cases. Figure adapted from presentation by Jean-Baptiste Ruffio.

panions provide important constraints on their angular momentum history (Snellen et al., 2014; Bryan et al., 2020a; J. W. Xuan et al., 2020b; Hsu et al., 2024a), which relates to their accretion process and magnetic breaking (Batygin, 2018). Radial velocity measurements can be used to search for exo-moons around the companions themselves (Ruffio et al., 2023a; Horstman et al., 2024), or resolve companions that were apparently single into binary brown dwarfs or binary planets (Triaud et al., 2020). The binarity fraction, mass ratio and separation distributions of binary brown dwarfs provide complementary anchors for formation models of substellar companions (see Chapter 5).

Workhorse instruments suited to high-contrast spectroscopy of directly imaged planets include CRIRES+ (formerly CRIRES) at the VLT (Kaeufl et al., 2004; Dorn et al., 2014; Dorn et al., 2023), NIRSPEC (specifically in AO mode, known as NIRSPAO) and at Keck (McLean et al., 1998; Martin et al., 2018). Upgrades and additions to the adaptive optics systems at various instruments have also brought new capabilities, including KPIC, which will be detailed below, HiRISE at the VLT (Vigan et al., 2024), and REACH at Subaru (Kotani et al., 2020). These latter instruments combine high-contrast capabilities with high-resolution spectroscopy, aiming at detailed characterization of planets and brown dwarfs at small angular separations.

Keck Planet Imager and Characterizer

My thesis heavily features the Keck Planet Imager and Characterizer (KPIC; Mawet et al. 2017; Delorme et al. 2021), an instrument that I helped commission and de-

velop throughout my PhD (e.g. Xin et al., 2023; Echeverri et al., 2023; Echeverri et al., 2024). At its core, KPIC uses single-mode fibers to direct planet light into a high-resolution spectrograph (see Fig. 1.5), which provides a resolving power of $R \approx 35,000$ in K band (1.9-2.5 μm). The coupling between high-contrast imaging and high-resolution spectroscopy (HRS) allows KPIC to acquire high fidelity planet spectra. At high-resolution, molecular lines from planets can be more easily distinguished from the residual stellar flux (i.e. speckles), which is the dominant noise source for high-contrast planets at small separations. This is because of the vastly different temperatures between stars and planets (e.g. $T_{\rm eff} \approx 1100$ K for HR 8799 c, d, e while $T_{\rm eff} \approx 7400$ K for HR 8799 A), and the relative RV shift (typically on the order of several km/s) between planet and stellar lines due to orbital motion. Due to these advantages, KPIC is well-suited for measuring atmospheric compositions for directly imaged planets and brown dwarfs. In contrast, at low spectral resolutions, modulations of the residual stellar spectrum occur at similar frequencies as molecular bands from the planet, complicating abundance measurements. In Chapters 2-4, I measure and compare the atmospheric compositions of a sample of substellar companions using KPIC to identify the dominant formation pathways among the population.

1.4 Atmospheric modeling and retrievals

To interpret spectroscopic observations, the exoplanet and brown dwarf field uses two main methods. The first method fits the data with grids of self-consistent models, which are one-dimensional atmosphere models that calculate the pressure–temperature profile of an atmosphere in radiative-convective equilibrium. These models are often parametrized by the effective temperature ($T_{\rm eff}$), surface gravity ($\log g$), and sometimes, the metallicity and carbon-to-oxygen ratio (C/O). A variety of models are available in the literature, such as the Sonora models (M. S. Marley et al., 2021; Mukherjee et al., 2024; Morley et al., 2024), ATMO2020 and variants (Phillips et al., 2020; Chabrier et al., 2023; Leggett et al., 2021), and BT-Settl (Allard et al., 2012). Different models contain different assumptions and use different line lists for their opacities, which can complicate spectral analysis. However, the latest models such as Sonora Elf Owl (Mukherjee et al., 2024) have updated to use the most accurate line lists.

Over the last few years, the alternative retrieval approach has been gaining popularity. In an atmospheric retrieval, one computes the emergent spectrum on the fly using a radiative transfer or spectral synthesis code that accepts a set of input pa-

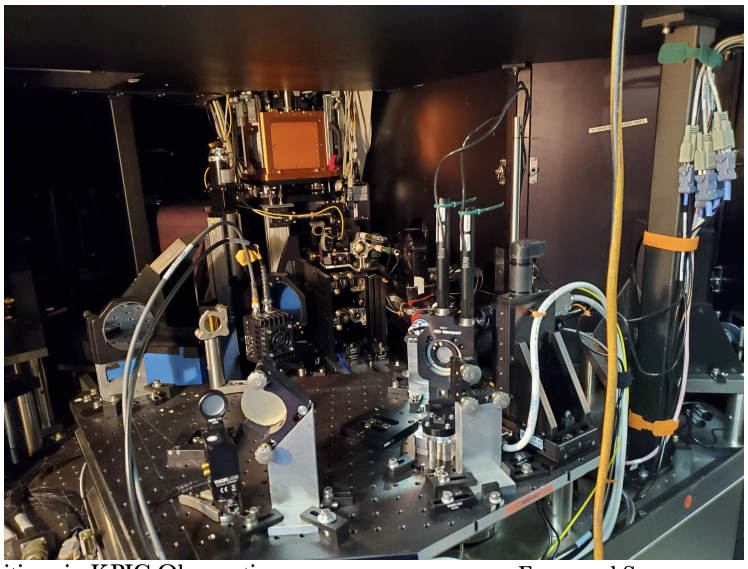

Fiber Positions in KPIC Observation

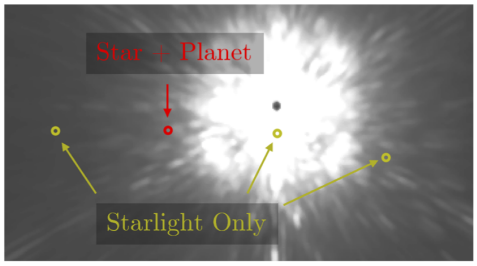

Extracted Spectrum

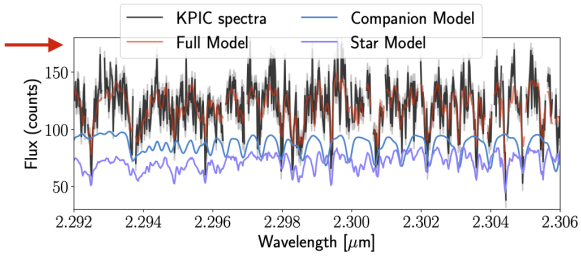

Figure 1.5: Top: photo of the KPIC instrument in the Keck II AO room. Bottom: KPIC uses single-mode fibers to feed companion light into the high-resolution spectrograph NIRSPEC ($R \approx 35,000$ in K band). The left panel shows locations of fibers relative to the stellar point-spread function for an example observing sequence. The red circle is the fiber centered on the companion (left panel is from J. J. Wang et al. 2021c). The right panel shows a schematic what the extracted spectrum would look like in black, which is a combination of companion light (blue), diffracted starlight (purple), as well as telluric and instrument transmission. The spectral difference between the star and companion is only visible at high-resolution; in LRS they are indistinguishable, which biases atmospheric analyses.

rameters. Instead of solving the pressure-temperature profile (P-T) self-consistently, retrievals parametrize the P-T profile using functions that do not necessarily contain physical constraints on the atmosphere. Below, we briefly summarize the different components of an atmospheric retrieval.

Atmospheric retrieval code

In this thesis, I use `petitRADTRANS`, a spectral synthesis code designed for exoplanet retrievals. For details on the code, I refer the reader to P. Mollière et al. (2019b) and P. M. Mollière (2017). For directly imaged companions, we observe the emission

spectrum. In `petitRADTRANS`, the model emission spectrum is calculated using the intensity along rays of different directions. Furthermore, a plane-parallel atmosphere in local thermodynamic equilibrium is assumed. For cloudy atmospheres, scattering can be included. The scattering prescription is described in P. Mollière et al. (2020) and P. M. Mollière (2017). Below, I detail the different components that go into a spectral synthesis code like `petitRADTRANS`.

Radiative transfer

For this section, I follow Section 6.3.1 of P. M. Mollière (2017). To calculate the emission spectrum of a planet or brown dwarf, one needs to solve the radiative equation

$$\frac{dI(\tau)}{d\tau} = S(\tau) - I(\tau) \tag{1.4}$$

where τ is the optical depth, $S(\tau)$ is the source function, and $I(\tau)$ is the intensity. The source function is the ratio of the emission coefficient to the extinction coefficient (ϵ / κ). Extinction includes two components, absorption and scattering. The optical depth along a one-dimensional path s is

$$d\tau(s) = -\kappa(s)ds \tag{1.5}$$

Note that all these quantities are frequency dependent, but the frequency dependence has been dropped for clarity. The solution to the radiative transfer equation can be written as

$$I(\tau) = I(0)e^{-\tau} + \int_0^\tau S(\tau')e^{\tau'-\tau}\, d\tau', \tag{1.6}$$

where $I(0)$ is the initial intensity. Based on this, the outgoing intensity at the top of the atmosphere can be expressed as

$$I^{\text{top}} = I^{\text{bot}}\mathcal{T}_{\text{atmo}} + \int_{\mathcal{T}_{\text{atmo}}}^1 S(\mathcal{T})\, d\mathcal{T}, \tag{1.7}$$

where $\mathcal{T}(\tau) = e^{-\tau}$ is the transmission from a given point in the atmosphere to the top, and I^{bot} is the upward intensity from the bottom of the atmosphere. Given the assumption of local thermal equilibrium, one can use Kirchhoff's Law to substitute

$S = B$, where B is Planck function at the frequency and temperature of interest. In practice, in codes such as `petitRADTRANS`, this equation is discretized into n plane-parallel layers, and the emergent intensity is calculated by summing the contributions from each layer to the next layer. In typical retrieval studies, n is generally chosen to be ≈ 100 (see e.g. Chapters 2, 3).

In the atmosphere of directly imaged planets and brown dwarfs, temperature generally decreases with decreasing pressure towards the top of the atmosphere. In this case, one expects to observe absorption lines rather than emission lines. This can be understood by approximating the deep interior as a blackbody emitter that sends photons upwards towards cooler and less dense regions of gas. Photons of certain wavelengths will be absorbed by molecules and atoms in the gas, and re-emitted isotropically. In the observer's point of view, only a small fraction of absorbed radiation is re-emitted, so we observe dips in the blackbody spectra, or absorption lines. Conversely, emission lines are formed when the atmosphere exhibits a temperature inversion, where temperature increases with decreasing pressure. Recently, Faherty et al. (2024) presented evidence for a temperature inversion in an isolated brown dwarf, which showed methane emission rather than absorption. However, the vast majority of directly imaged companions show absorption lines.

Opacities

Here, we refer to the mass-independent opacity, which is simply κ/ρ, where κ is the extinction coefficient and ρ is the mass density of the gas. Opacity is usually expressed in units of cm^2/g. To setup a retrieval, one needs to specify the line opacities and continuum opacity sources under consideration. Line opacities arise from molecular or atomic transitions, which get excited by photons in narrow frequency range, whose energy match given molecular rotational or vibrational states, or atomic electronic quantum states. Due to the temperature conditions in exoplanets and brown dwarfs, molecular line opacity is generally more important than atomic line opacity at the infrared wavelengths. For atmospheres with effective temperatures > 1500 K, CO and H_2O lines are prominent across several near-infrared bands. For colder atmospheres, CH_4 becomes a major line opacity source, and at effective temperatures $< 1000\ K$, NH_3 also becomes important. The strength of any molecular lines also depend on the abundance of that molecule in the observable atmosphere. This is regulated by chemical reactions as well as vertical mixing processes, which could result in departures from chemical equilibrium (see **Chemistry**).

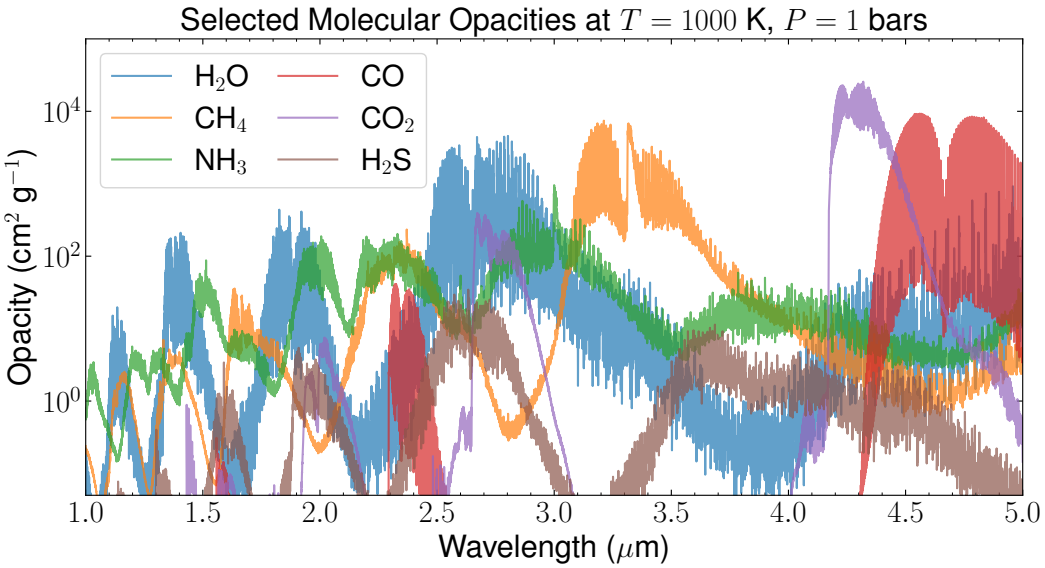

Figure 1.6: Opacities of major molecules in giant planets and brown dwarf atmospheres. The opacities are shown for a temperature of 1000 K and a pressure of 1 bar. The opacities are plotted at R = 5000 for clarity. I use the following line lists: H_2O (Polyansky et al., 2018), CO (Rothman et al., 2010), CH_4 (Hargreaves et al., 2020), H_2S (Azzam et al., 2016), NH_3 (Coles et al., 2019), CO_2 (Rothman et al., 2010).

Besides the major molecular opacities (e.g. Fig. 1.6), trace species also provide important constraints on the atmospheric physics and formation histories. Trace species generally have much lower relative abundance compared to major absorbers, making them difficult to detect. However, in certain opacity windows, where other opacity contributions are low, trace species can be detected especially with high-resolution spectroscopy. For example, the ^{13}CO isotopologue has recently been detected in exoplanets and brown dwarfs (Y. Zhang et al., 2021b; Y. Zhang et al., 2021a). Due to its slightly different molar mass, the absorption lines of ^{13}CO occur at different wavelengths compared to ^{12}CO, making them detectable at medium to high-resolution (Gandhi et al., 2023) despite the $\approx$ 90 times lower relative abundance of ^{13}C compared to ^{12}C.

For gas giant atmospheres, collision induced absorption (CIA) from H_2 and He are major sources of continuum opacity. CIA in these atmospheres arises from the close encounters of molecules in high pressure conditions, which alter the charge distribution of molecules and temporarily form complex molecular groups. The result is the production of new energy transitions that depend on the temperature, pressure, and number density of particles. The resulting opacity from CIA is smooth

as a function of wavelength or frequency, unlike line opacities which produce narrow features.

The accuracy of line lists, which are used to compute opacity tables, could limit the accuracy of retrievals. Molecular line lists are especially important for exoplanets, but are also difficult to theoretically derive or empirically measure for more complex molecules. Recently, the HITEMP team released a significantly updated CH_4 line list (Hargreaves et al., 2020). In Chapter 2, I generate new CH_4 opacity tables for use in `petitRADTRANS` using this line list. Our use of this new line list boosted the detection of CH_4 in brown dwarf companion HD 4747 B, which is one of the first detections of CH_4 in any directly imaged companion. In Chapter 3, to study M dwarf companions with $T_{\rm eff} > 2000$ K, I upgraded several opacity tables in `petitRADTRANS` to $T = 4500$ K using the open source database DACE (Grimm et al., 2021). Therefore, while line lists and opacities can be a limiting factor, it is also more straightforward to upgrade these components in the retrieval context, compared to the grid model.

Clouds

Cloud particles absorb and scatter photons in atmospheres, and are another source of opacity. In semi-physical cloud models, the cloud particle size and shapes and optical properties (real and imaginary refractive indices) need to be prescribed in order to calculate the cloud opacity.

This is the case for the EddySed cloud model (Ackerman et al., 2001) implemented in `petitRADTRANS`. In EddySed, the mean particle size is determined by balancing sedimentation and vertical mixing, which are respectively parameterized by the f_{sed} and K_{zz}. A size distribution is also required, and popular choices are a lognormal distribution, or a Hansen distribution (Hansen, 1971). In the EddySed model in `petitRADTRANS`, the free parameters are therefore f_{sed}, K_{zz}, the width of the size distribution, and the cloud mass fraction at the cloud base. By default, the cloud base is set at the intersection of the cloud condensation curve and the temperature pressure profile. In a retrieval, one can modify any of these aspects. For example, it has been shown that cloud particle sizes in brown dwarfs appear to be much smaller than predicted by EddySed (e.g. Luna et al., 2021). In this case, it might be more appropriate to directly fit for the mean cloud particle size, allowing for more flexibility (Nasedkin et al., 2024). Even the cloud base pressure could be a free parameter in the retrieval. When making such changes, it is important to understand

the physical consequences.

For the cloud particle shape, the most common assumption is a spherical, homogeneous particle. The Mie scattering theory is used to compute the absorption and scattering cross-sections in this case. Alternatively, `petitRADTRANS` allows the use of a slightly more complex particle shape, known as the Distribution of Hollow Spheres (Min et al., 2005). Here, the particles are still spherical but contain a cavity in the middle, which has been found to better describe the properties of solid grains in other astronomical contexts, such as for disks around young stars (e.g. Juhász et al., 2010)

Simpler cloud models are also available in retrieval codes like `petitRADTRANS`. For example, in a gray cloud or gray opacity model, one can add a constant opacity across wavelengths to the model. This can be appropriate for narrow wavelength ranges, where the slope of the cloud absorption or scattering cross sections are nearly constant. For data with wider wavelength ranges, another commonly used cloud model is the power law clouds, which set the cloud opacity as a function of wavelength. The index of the power law, and the opacity at a specific wavelength are free parameters in such models.

Chemistry

To calculate the total opacity of a given atmospheric layer one also needs to know the composition, i.e., the molecular and atomic abundances. In retrievals, abundances are typically specified in units of mass-mixing ratio, or volume-mixing ratio. One can convert between these if the mean molecular mass is known. In a retrieval, there are two main ways to specify the abundances. The first is to freely retrieve the abundances of each molecular and atomic species, while assuming that the abundances are vertically constant. In this approach, each relevant species requies a free parameter.

In the second method, the chemical equilibrium abundances of different species are solved for at given temperature, pressure, and global abundance values. The most common global abundance knobs are the overall metallicity and C/O (Lei et al., 2024), which together set the elemental abundances of each element under consideration. From the elemental abundances, a chemical network is constructed, and the solution is found by minimizing the Gibbs free energy. These retrievals are sometimes known as ‘chemically-consistent retrievals,’ and in practice one usually computes the chemical table beforehand. At each retrieval step, interpolation of the

chemical table then provides the abundances of each species. It is common to include the effect of disequilibrium chemistry in these retrievals using a quench prescription (Zahnle et al., 2014), which fits for a quench pressure above which the abundances of certain molecules are held constant. Evidence for carbon disequilibrium chemistry has been found for several brown dwarfs and exoplanets (see e.g. Chapter 2).

Pressure-temperature profile

To compute the emergent spectrum, the last required piece is the pressure-temperature profile of the atmosphere. There are dozens of different prescriptions for the P-T profile in the literature. These range from free profiles that simply fit the temperature at different pressure points (e.g. Pelletier et al., 2021), interpolating in betwen points, to physically motivated profiles based on radiative equilibrium (Guillot, 2010), and hybrid profiles that impose constraints in certain parts of the atmosphere (P. Mollière et al., 2020). For emission spectroscopy of brown dwarfs and giant planets, Rowland et al. (2023) explored the effect of different P-T prescriptions on the results using mock retrievals, and found that more flexible profiles produce more reliable results for the atmospheric composition. In reality, the choice of P-T profile is usually decided on a case by case basis depending on the nature and quality of the data. In recent years, a common choice in retrievals of directly imaged planets has been to use free P-T profiles, but adopt priors based on self-consistent models (Z. Zhang et al., 2023). This is also the approach used in Chapters 3 and 4 of this thesis.

Summary

Both retrievals and self-consistent models are valuable in the study of substellar atmospheres and complementary in many ways. For example, recent retrieval studies have started imposing constraints in the freely fitted P-T profile based on self-consistent atmospheric models (Z. Zhang et al. 2023, see also Chapters 3-4). In retrieval studies, it is crucial to validate the physicality of the results by referencing self-consistent models. This thesis uses both approaches to spectral analysis, with the goal of obtaining reliable atmospheric composition measurements of substellar companions.

In this thesis, the key goal of atmospheric analysis is measuring the chemical composition. For the objects and the wavelengths studied here, the major absorbers are CO, H_2O, CH_4, NH_3, and the isotopologues ^{13}CO and $H_2^{18}O$. Isotopic measurements of exoplanets were recently demonstrated (Y. Zhang et al., 2021b), and could provide a new probe into formation history. The key test of that the atmospheric papers

perform is whether the companions share consistent carbon, oxygen, and isotopic abundances as their host stars. This theme is common to Chapters 2, 3, 4, and 6.

1.5 Dynamical masses and evolutionary models

Mass is a fundamental quantity for in both the stellar and substellar regimes. Substellar objects cool down as they age. Even when the age and luminosity are known, one usually needs to use evolutionary models to infer a model-dependent mass. For directly imaged companions, dynamical mass has traditionally been difficult to measure as it requires long baseline measurements of the stellar orbit either from radial velocities or astrometry. The prohibitively long orbital periods (hundreds to thousands of years) of many companions render this task challenging. Recently, the combination of *Gaia* and *Hipparcos* astrometry has provided a new avenue of measuring dynamical masses of giant planets and brown dwarf companions (T. D. Brandt, 2018; T. D. Brandt, 2021b; Kervella et al., 2019; J. W. Xuan et al., 2020a).

Dynamical masses are important for many reasons. First, they could provide valuable priors for atmospheric studies, which usually have little constraining power on mass. Such priors are used in the atmospheric analyses presented in Chapters 2, 3, and 6 of this thesis. Second, dynamical masses provide strong tests of substellar evolutionary models, which compute the expected luminosities, temperatures, and radii of substellar objects at different ages. When age constraints are available, for example from the host star's age, we can test whether these models predict the correct luminosities for the substellar companions. If they do not, we could be missing key physics in the models, which are critical since they are used to estimate masses for the majority of directly imaged companions that lack dynamical masses. Alternatively, the companions might not be single entities. In Chapter 5, I explore this topic in the context of the over-massive brown dwarf problem, whereby the masses of several faint brown dwarfs, as calculated from their orbits, are greater than theory predicts from their luminosities. A natural explanation is that these are binary brown dwarfs, unresolved by previous observations (G. M. Brandt et al., 2021b; Cheetham et al., 2018). With new observational capabilities, we are now starting to resolve brown dwarf companions that were previously thought to be single into tight brown dwarf binaries.

Remaining chapters

This thesis starts with three papers on high-resolution atmospheric retrievals of low-mass companions from $10 - 90\ M_{\rm Jup}$. I develop the retrieval and forward modeling

framework in Chapter 2, which is used in Chapters 3 and 4. With the survey of eight substellar companions in Chapter 4, this part of the thesis establishes the trend that objects with $m > 10\ M_{\rm Jup}$ share similar carbon and oxygen compositions as their host stars. This result delineates a formation boundary, where by companions with high masses or mass ratios represent the tail end of star formation. In these studies, I made several novel measurements of the $^{12}C/^{13}C$ ratios in substellar companions. I also demonstrated the power of relative radial velocity measurements in improving dynamical mass constraints.

In Chapters 5 and 6, I focus on the iconic Gliese 229 system, which consists of the first discovered brown dwarf companion, Gliese 229 B. The dynamical mass and low luminosity of this companion has defied evolutionary models, which predict an object of 71 $M_{\rm Jup}$ would be much brighter than observed. From independent observations using high-resolution spectroscopy and optical interferometry, I led a study that resolved Gliese 229 B into two brown dwarfs, Ba and Bb, on a tight 12-day orbit. Gliese 229 Bab becomes the tightest known substellar binary orbiting another star, and suggests that other anomalous brown dwarf companions could be binary as well. In Chapter 6, I use the James Webb Space Telescope Mid-infrared Instrument to study the $5 - 14\mu$m spectrum of Gliese 229 Bab, and constrain its bulk properties and atmospheric composition. I found that the two brown dwarfs share the same composition as their primary star, indicative of formation from direct gravitational collapse.

Chapter 2

A CLEAR VIEW OF A CLOUDY BROWN DWARF COMPANION FROM HIGH-RESOLUTION SPECTROSCOPY

This chapter is a reproduction of my first atmospheric retrieval paper, where I studied the brown dwarf companion HD 4747 B using both high-resolution KPIC spectrum, and low-resolution spectrum from GPI and SPHERE that I re-analyzed. I also carried out orbit fits to refine the dynamical mass of the brown dwarf, which served as a prior for the retrievals. This paper contained several highlights, including one of the first detections of CH_4 in a high-contrast substellar companion, which was bolstered by upgrading the CH_4 opacity tables with the improved HITEMP CH_4 line list from Hargreaves et al. 2020. The joint constraints on CO and CH_4 also allowed us to estimate the vertical diffusion coefficient in this brown dwarf's atmosphere. It was through this project that I developed my tools for carrying out retrievals, which I use and improve upon in the next two chapters.

Xuan, J. W. et al. (Oct. 2022). "A Clear View of a Cloudy Brown Dwarf Companion from High-resolution Spectroscopy". In: *The Astrophysical Journal* 937.2, 54, p. 54. DOI: 10.3847/1538-4357/ac8673.

Abstract

Direct imaging studies have mainly used low-resolution spectroscopy ($R \sim 20-100$) to study the atmospheres of giant exoplanets and brown dwarf companions, but the presence of clouds has often led to degeneracies in the retrieved atmospheric abundances (e.g. C/O, metallicity). This precludes clear insights into the formation mechanisms of these companions. The Keck Planet Imager and Characterizer (KPIC) uses adaptive optics and single-mode fibers to transport light into NIRSPEC ($R \sim 35,000$ in K band), and aims to address these challenges with high-resolution spectroscopy. Using an atmospheric retrieval framework based on `petitRADTRANS`, we analyze KPIC high-resolution spectrum ($2.29 - 2.49$ μm) and archival low-resolution spectrum ($1 - 2.2$ μm) of the benchmark brown dwarf HD 4747 B ($m = 67.2 \pm 1.8$ $M_{\rm Jup}$, $a = 10.0 \pm 0.2$ au, $T_{\rm eff} \approx 1400$ K). We find that our measured

C/O and metallicity for the companion from the KPIC high-resolution spectrum agree with that of its host star within $1-2\sigma$. The retrieved parameters from the K band high-resolution spectrum are also independent of our choice of cloud model. In contrast, the retrieved parameters from the low-resolution spectrum are highly sensitive to our chosen cloud model. Finally, we detect CO, H_2O, and CH_4 (volume mixing ratio of $\log(CH_4)=-4.82 \pm 0.23$) in this L/T transition companion with the KPIC data. The relative molecular abundances allow us to constrain the degree of chemical disequilibrium in the atmosphere of HD 4747 B, and infer a vertical diffusion coefficient that is at the upper limit predicted from mixing length theory.

2.1 Introduction

The Keck Planet Imager and Characterizer (KPIC) is a new suite of instrument upgrades at Keck II, including a single-mode fiber injection unit (Mawet et al., 2017; Delorme et al., 2021) that feeds light into the upgraded NIRSPEC (Martin et al., 2018; López et al., 2020), enabling high-resolution spectroscopy (HRS[1]) at $R \sim 35,000$ in K band. By using single-mode fibers to inject light from planets and brown dwarfs at high-contrast, KPIC provides suppression of the stellar point-spread function at the fiber input and a stable line spread function that is independent of incoming wavefront aberrations (Mawet et al., 2017; J. J. Wang et al., 2021c). By observing at high-resolution, we can further distinguish between star and planet light from their spectral differences (J. Wang et al., 2017; Mawet et al., 2017). Recently, J. J. Wang et al. (2021c) published the KPIC detections of HR 8799 c, d, e, demonstrating the ability of KPIC to detect molecular lines and measure the rotational line broadening of planets at high contrast ($\Delta K \approx 11$) and small separations (≈ 0.4") from their host star.

The atmospheric composition of a substellar object holds a wealth of information about its formation, accretion, and evolutionary history, as well as fundamental physical processes that shape its atmosphere. It is therefore important to assess how well KPIC and other fiber-fed, high-resolution spectrographs (e.g. Subaru/REACH Kotani et al. 2020 and VLT/HiRISE Otten et al. 2021) can measure the atmospheric compositions of directly imaged planets and brown dwarfs. Specifically, previous studies of gas giant planet formation have highlighted the carbon-to-oxygen ratio (C/O) and metallicity (e.g. [C/H]) of the atmosphere as informative probes of

[1]We will use HRS to abbreviate both high-resolution spectroscopy (the technique) and high-resolution spectra (the data) in this paper. The same is true for LRS: low-resolution spectra or spectroscopy.

formation history (e.g. Öberg et al., 2011; Madhusudhan, 2012; Piso et al., 2015). To first order, a companion with a C/O and metallicity similar to that of its host star is consistent with formation via gravitational instability in a protostellar disk or fragmentation in a molecular cloud, akin to binary star formation (Bate et al., 2002). On the other hand, differences between the companion and stellar C/O are suggestive of core accretion (Pollack et al., 1996) as the likely formation mechanism, and in that scenario, could be used to constrain where the companion formed in the disk relative to ice lines of major C- and O-bearing molecules (e.g. H_2O, CO_2, and CO). This picture can be complicated by a variety of effects such as the relative amount of solids incorporated into the planet's atmosphere (e.g. Madhusudhan et al., 2014; Öberg et al., 2016; Mordasini et al., 2016; Gravity Collaboration et al., 2020; Pelletier et al., 2021).

So far, atmospheric characterization of directly imaged companions has mostly relied on low-resolution spectroscopy (LRS) with resolving powers of $R \approx 20 - 100$. LRS is sensitive to continuum emission originating from the deepest observable layer of the atmosphere and modified by opacity sources further up. Many of these companions have temperatures warm enough for silicate clouds to condense in their atmospheres (M. Marley et al., 2015), and there is much evidence that cloud opacity plays an important role in the LRS of directly imaged companions and brown dwarfs with L or L/T transition spectral types (e.g. Skemer et al., 2014; Burningham et al., 2017; Gravity Collaboration et al., 2020). However, due to our limited knowledge of cloud physics, a reliable assessment of atmospheric abundances from LRS could be fraught with degeneracies between clouds, the pressure-temperature profile, and chemical abundances (e.g. Burningham et al., 2017). In addition, the retrieval results can also be highly sensitive to systematics in different data sets that are combined to obtain a wider wavelength coverage (J. Wang et al., 2020). More encouragingly, P. Mollière et al. (2020) report atmospheric abundances that are relatively robust to clouds and model choices, though Burningham et al. (2021) show that issues such as an unphysically small radius could persist despite improvements in cloud modeling and extensive wavelength coverage ($1 - 15\mu$m).

Recently, J. Wang et al. (2022) presented the first atmospheric free retrievals at high-resolution for a directly imaged companion. They studied the L-type brown dwarf HR 7672 B ($T_{\rm eff} \approx 1800$ K) using KPIC HRS and near-infrared photometry, and measured carbon and oxygen abundances that are consistent within $< 1.5\sigma$ to that of its host star. In this paper, we present a detailed atmospheric study of

HD 4747 B using both KPIC HRS (K band) and archival low-resolution spectra (LRS) from 1-2.2 μm that we re-extract in a uniform manner. While the KPIC HRS resolves individual molecular lines and conains direct information about a companion's atmospheric abundances, LRS provides spectral shape and luminosity measurements, which has the potential to complement the HRS.

Compared to HR 7672 B, HD 4747 B is a colder L/T transition object ($T_{\rm eff} \approx 1400$ K) with strong evidence for clouds and a similar color to directly imaged planets such as HR 8799 c,d,e (Crepp et al., 2018; Peretti et al., 2019). Like HR 7672 B, the wealth of prior knowledge available for HD 4747 B makes it a valuable benchmark object to test whether we can make robust inferences with spectroscopic data. First, we are able to precisely measure the dynamical mass of HD 4747 B (§ 2.2). Mass is a fundamental quantity that is poorly constrained for most directly imaged companions (Bowler, 2016). Furthermore, given its high mass, HD 4747 B is expected to have formed via direct gravitational collapse in the same cloud or disk as its host star, which means that we can assume chemical homogeneity: the brown dwarf and primary star should share the same chemical composition. Finally, with the companion mass, observed luminosity, and stellar age, we can independently estimate the brown dwarf's radius from evolutionary models.

In this paper, we use the open-source radiative transfer code `petitRADTRANS` (P. Mollière et al., 2019b; P. Mollière et al., 2020) to fit the HRS and LRS for HD 4747 B in a retrieval framework. The main goals of our study are to measure the atmospheric composition of this brown dwarf companion using both the HRS and LRS, and to present a detailed characterization of its atmosphere, including constraints on clouds, chemical equilibrium or disequilibrium, and the detection of CH_4. In this process, we also explore the relative advantages and disadvantages of HRS versus LRS.

This paper is organized as follows: in § 2.2, we summarize the system properties including our mass measurement for HD 4747 B. Our spectroscopic data and data reduction procedure is described in § 2.3. We then discuss our spectral analysis framework in § 2.4. We present individual and joint retrievals of the HRS and LRS in § 2.5, § 2.6 and § 2.7, respectively. We summarize the lessons learned in § 2.8, and conclude in § 2.9.

2.2 System properties

Host star

In this section, we summarize relevant properties of the host star. HD 4747 is a main-sequence, solar-type star located $\approx$ 19 parsec away based on its Gaia eDR3 parallax (Brown et al., 2021). Chromospheric emission in the Ca II H&K lines are visible in the stellar spectrum ($\log R_{HK} = -4.72 \pm 0.02$), which Peretti et al. (2019) used to derive an age of 2.3 ± 1.4 Gyr from the age-$\log R_{HK}$ calibration of Mamajek et al. (2008). This agrees with the gyro-chronological age estimate of $3.3^{+2.3}_{-1.9}$ Gyr from Crepp et al. (2018). These studies also converged on T_{eff} around 5300–5400 K, and a surface gravity $\log(g)$ of 4.5–4.65. Of particular relevance to this study are the C/O ratio and metallicity of the host star, since we expect these to be roughly similar to those of the brown dwarf. HD 4747 is found to have a sub-solar metallicity, with [Fe/H]=-0.23 ± 0.05 from Peretti et al. (2019) and [Fe/H]=-0.22 ± 0.04 from Crepp et al. (2018). Previous studies including Brewer et al. (2016) and Peretti et al. (2019) also measured the elemental abundances for the star, but either did not take into account non-local thermodynamic equilibrium (LTE) effects on their oxygen abundances (Amarsi et al., 2019) or do not quote error bars. We instead carry out a new analysis using the method described in Kolecki et al. (2021) to derive the abundances for different elements, and correct the results to account for 3D non-LTE effects (Amarsi et al., 2019) on the results. For this analysis, we used an archival spectrum from FEROS (Kaufer et al., 1997) which covers 350-920 nm at $R = 48,000$. Using this spectrum, we measure the equivalent widths of absorption lines and compare them to model stellar atmospheres in an iterative approach using the MOOG code (Sneden, 1973). From our derived carbon and oxygen abundances, we find C/O=0.48 ± 0.08. The iron abundance is [Fe/H]=-0.30 ± 0.5, in agreement with previous studies.

Since Fe condenses out for temperatures below $\approx$ 1800 K (M. Marley et al., 2015), it is not a relevant gaseous absorber in the photosphere of HD 4747 B. Therefore, the more useful metrics for comparison are C and O. From our analysis above, we find [C/H]= -0.08 ± 0.06 and [O/H]= -0.02 ± 0.04 for the host star. [C/H] is defined as $\log_{10}(N_C/N_H)_{star}$ - $\log_{10}(N_C/N_H)_{sun}$, where N_C and N_H are the number fraction of C and H respectively. [O/H] is defined similarly. We adopt Asplund et al. (2009) as our solar reference in order to be consistent with `petitRADTRANS`, which we use to model the atmosphere of HD 4747 B.

Table 2.1: Selected parameters from orbit fit for HD 4747 AB

Parameter	Value
M ($M_\odot$)	0.85 ± 0.04
m ($M_{\rm Jup}$)	67.2 ± 1.8
a (AU)	10.0 ± 0.2
Inclination (deg)	48.0 ± 0.9
Ascending Node (deg)	89.4 ± 1.1
Period (yr)	33.2 ± 0.4
Argument of Periastron (deg)	267.2 ± 0.5
Eccentricity	0.7317 ± 0.0014
Epoch of Periastron (JD)	2462615 ± 155

Note: The dynamical mass of the host star, which is fit as a free parameter, agrees well with isochrone-derived masses from Peretti et al. (2019) and Crepp et al. (2018).

Orbit and Dynamical Mass

The orbit and mass of HD 4747 B have been measured by several studies using relative astrometry from Keck/NIRC2, host star radial velocities (RV) from Keck/HIRES, and Gaia-Hipparcos absolute astrometry (T. D. Brandt et al., 2019a; J. W. Xuan et al., 2020a). Here, we take advantage of 23 yr of RV observations published in Rosenthal et al. (2021) and the improved precision of the Hipparcos-Gaia Catalog of Accelerations (HGCA) (T. D. Brandt, 2021a) based on Gaia eDR3 (Brown et al., 2021) to update the orbit and mass of HD 4747 B. HD 4747 B shows significant proper motion anomalies (PMa) in both the Gaia and Hipparcos epochs, with S/N of 77.2 and 9.1, and the position angle and amplitude of the PMa is consistent with being induced by the brown dwarf companion. For the relative astrometry, we use data points tabulated in T. D. Brandt et al. (2019a), except for the two GPI epochs measured by Crepp et al. (2018), which we replaced with our new measurements from § 2.3. We choose not to use the companion RV as measured by KPIC for this fit, because it does not appreciably improve our already well-constrained orbital solution.

To fit the relative astrometry, radial velocity, and absolute astrometry from Gaia and Hipparcos together, we use the `orvara` package (T. D. Brandt et al., 2021), which is designed to jointly fit these types of data and takes into account the Gaia and Hipparcos astrometry at the epoch astrometry level using `htof` (G. M. Brandt

et al., 2021a). We use the priors listed in Table 4 of T. D. Brandt et al. (2021) for the fitted parameters. The posterior is sampled using the parallel-tempering MCMC sampler (Vousden et al., 2016), a fork of emcee (Foreman-Mackey et al., 2013) over 50000 steps with 10 temperatures and 100 walkers. The fits converged as determined by visual inspection of the chains, and we discarded the first ten percent as burn-in. In `orvara`, the system parallax and other linear parameters are analytically marginalized out to speed up the fits.

The resulting orbit and mass measurements are tabulated in Table 2.1, while the model fits are shown in Appendix A. We find a companion mass of $m = 67.2 \pm 1.8\ M_{\rm Jup}$, which is consistent with previous values, but more precise. We checked the `orvara` results with a second fit where we model the Gaia and Hipparcos astrometry using the methodology in J. W. Xuan et al. (2020a). This gives $m = 67.1 \pm 2.0\ M_{\rm Jup}$, consistent with the `orvara` result. Furthermore, the companion mass and orbital parameters we find are also consistent with results from orbit fits that only use RV and imaging data (no Gaia-Hipparcos astrometry) from Peretti et al. (2019) and Crepp et al. (2018). We adopt the companion mass from our `orvara` fit for the spectral analysis in this paper.

2.3 Spectroscopic data

High-resolution spectroscopy

KPIC observations

We observed HD 4747 B on UT 2020 September 28 with Keck/NIRSPEC. The data were collected using the first version of the KPIC fiber injection unit (FIU) (Delorme et al., 2021). The FIU is located downstream of the Keck II adaptive optics system and is used to inject light from a selected object into one of the single mode fibers connected to NIRSPEC. We obtain spectrum in K band, which is broken up into nine echelle orders from 1.94-2.49 μm. The observing strategy is identical to that of J. J. Wang et al. (2021c). In short, we placed the companion on the fiber with the highest throughput and acquired six exposures of 600 seconds each, for a total integration time of 1 hour. The relative astrometry of the companion was computed using whereistheplanet.com (J. J. Wang et al., 2021b), based on data in Peretti et al. (2019). For calibration purposes, we acquired a pair of 60 second exposures of the host star before observing the companion, and a pair of 60 second exposures of a telluric standard star (HIP 6960) after the companion exposures so as to share nearly the same airmass. Using exposures on the host star, we calculated an end-to-end throughput from the top of the atmosphere to the detector of 1.8 – 2.0% during the

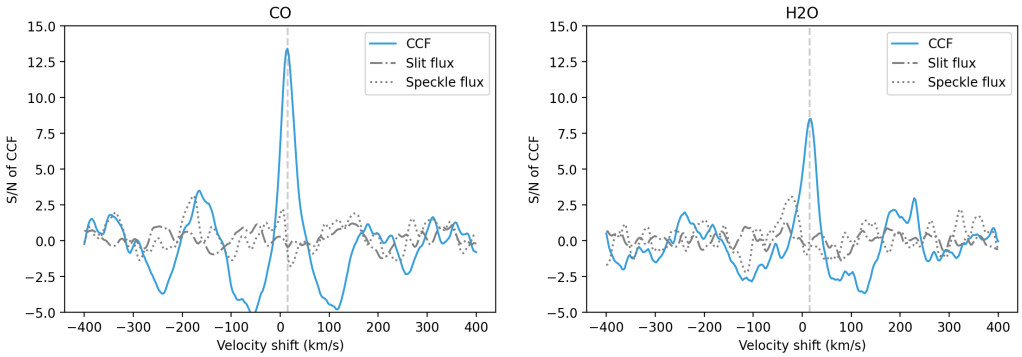

Figure 2.1: Cross-correlation functions (CCFs) in blue show detections of CO and H_2O using 3 spectral orders of the KPIC HRS. Gray lines represent CCFs of the background flux (from the slit) and speckle flux, whose standard deviations are used as estimates of the CCF noise. The vertical dashed lines at 15 km/s show the expected RV of the companion from its known orbit. The strong structure in the blue CCFs outside the peaks arise because we only fit single molecules here.

observations.

Data reduction

To extract the spectra from the raw data, we follow the procedure outlined in J. J. Wang et al. (2021c), which the KPIC team has implemented in a public Python pipeline.[2] The images for all objects were reduced in the same way. First, we removed the thermal background from the images using combined instrument background frames taken during daytime. As shown in J. J. Wang et al. (2021c), the thermal background of our data is dominated by the warm optics rather than the sky background. We also remove persistent bad pixels identified using the background frames. Then, we use data from the telluric standard star to fit the trace of each column in the four fibers and nine spectral orders, which give us the position and standard deviation of the PSF (in spatial direction) at each column. The trace positions and widths were additionally smoothed using a cubic spline in order to mitigate random noise. We adopt the trace locations and widths as the line spread function (LSF) positions and widths in the dispersion dimension.

For every frame, we then extracted the 1D spectra in each column of each order. To remove residual background light, we subtracted the median of pixels that are at least 5 pixels away from every pixel in each column. Finally, we used optimal extraction to sum the flux using weights defined by the 1D Gaussian LSF profiles

[2] `https://github.com/kpicteam/kpic_pipeline`

calculated from spectra of the telluric star.

The extracted spectra have a median signal-to-noise ratio (S/N) of $\approx$ 8 per pixel element, which has a typical width of 0.2 Å, and consists of a mixture of light from the brown dwarf companion and stellar speckles. The S/N of KPIC is optimized for wavelengths around 2.3 μm, where CO has a series of strong absorption lines. For our analysis, we use three spectral orders from 2.29-2.49 μm, which contain the strongest absorption lines from the companion and have relatively few telluric absorption lines. Note that the three spectral orders have gaps in between them, so we have data over $\approx$ 0.13 μm (instead of 0.2 μm; see Fig. 2.3).

As a preliminary analysis, we cross-correlate our KPIC spectra with single-molecule templates assuming $T_{\rm eff}$ = 1400 K and log(g)=5.5 from the Sonora model grid (M. S. Marley et al., 2021). In short, we estimate the maximum likelihood value for both the single-molecule companion flux and speckle flux in the data as a function of RV (radial velocity) shift using the method described in J. J. Wang et al. (2021c), which is based on Ruffio (2019). We find that H_2O and CO are detected with S/N of 8.5 and 13.5 respectively (Fig. 2.1). CH_4 is not detected with statistical confidence in this crude analysis, but we present evidence for a weak CH_4 detection in § 2.5.

Low-resolution spectroscopy

Gemini Planet Imager IFS

The Gemini Planet Imager (GPI) observed HD 4747 B on UT 2015 December 24 and 25, in the K_1 (1.90-2.19 μm, R = 66) and H (1.50-1.80 μm, R = 46.5) bands, respectively, and the data were published in Crepp et al. (2018). After doing some fits to the published spectrum, we found that the average flux levels of the K_1 and H bands are inconsistent, and the error bars appear to be significantly over-estimated.

We therefore re-extracted the GPI spectrum using the `pyKLIP` package (J. J. Wang et al., 2015), which models a stellar point spread function (PSF) with Karhunen-Loève Image Processing (KLIP, also known as Principal Component Analysis) following the framework in Soummer et al. (2012) and Pueyo (2016). We tested various model choices to minimize the residuals after stellar PSF subtraction while preserving the companion signal. A key parameter we tuned was the number of Karhunen-Loève (KL) modes. KL modes represent an orthogonal basis for patterns in the images that are used to model the stellar PSF. We chose 5 and 12 KL modes to subtract the stellar PSF in the H and K_1 band data, respectively. After subtracting the stellar PSF, we first extracted the companion's relative astrometry in terms of separation and

position angle, which are reported in Appendix B (Table 2.5). Then, we extracted the flux at the companion's determined location as a function of wavelength, which gave us the raw spectrum. Note that rather than using spectral differential imaging (SDI) to subtract the stellar PSF, we only used angular differential imaging (ADI). For a bright companion like HD 4747 B, ADI is more than sufficient to properly remove the PSF of the star given sufficient parallactic angle rotation.

To flux-calibrate the raw spectrum, we used the satellite spot flux ratios[3] to find the companion-to-star flux ratio. To obtain the observed flux density of the companion, we empirically determined the flux scaling factor R^2/d^2 by fitting a PHOENIX model (Husser et al., 2013) of the star ($T_{\rm eff}$ = 5400, log(g)=4.5, and [Fe/H] = -0.5) using the star's 2MASS J, H, K (Cutri et al., 2003) and the Gaia G band magnitudes (Riello et al., 2021). The zeropoint fluxes and filter transmission of the photometric bands are downloaded from the SVO Filter Service[4] and the Gaia website.[5] To obtain measurement uncertainties, we injected 20 fake companions at the same separation and equally spaced position angles in the data, and repeated the same spectral extraction process. We avoided using the fake injections that were within 20° of the real companion to avoid biasing the fluxes. We inflated the uncertainties on the extracted spectra by 2.5% to account for errors in the stellar flux calibration. The value of 2.5% is estimated by comparing our empirically computed flux scaling factor with the value of R^2/d^2 of the star (using the radius from Peretti et al. 2019 and the Gaia parallax).

SPHERE IFS

HD 4747 B was observed on UT 2016 December 12 and 2017 September 28 with the Spectro-Polarimetric High-contrast Exoplanet Research (SPHERE; Beuzit et al. 2019). The SPHERE Integral Field Spectrograph (IFS) (Claudi et al., 2008) collects data in the YH band from 0.95-1.6 μm (R = 29). The extracted spectra was published in Peretti et al. (2019), but is not available. We therefore reduced the raw data using the SPHERE pipeline (Vigan, 2020), and performed a similar post-processing procedure with pyKLIP as described above for the GPI spectra. The only difference is that we needed to use ADI+SDI to perform PSF-subtraction for the SPHERE IFS data, which did not have enough parallactic angle rotation (only $\approx$ 0.2°). For the SPHERE IFS data, flux calibration is based on unocculted

[3]https://www.gemini.edu/instrumentation/gpi/capability

[4]http://svo2.cab.inta-csic.es/theory/fps/

[5]https://www.cosmos.esa.int/web/gaia/edr3-passbands

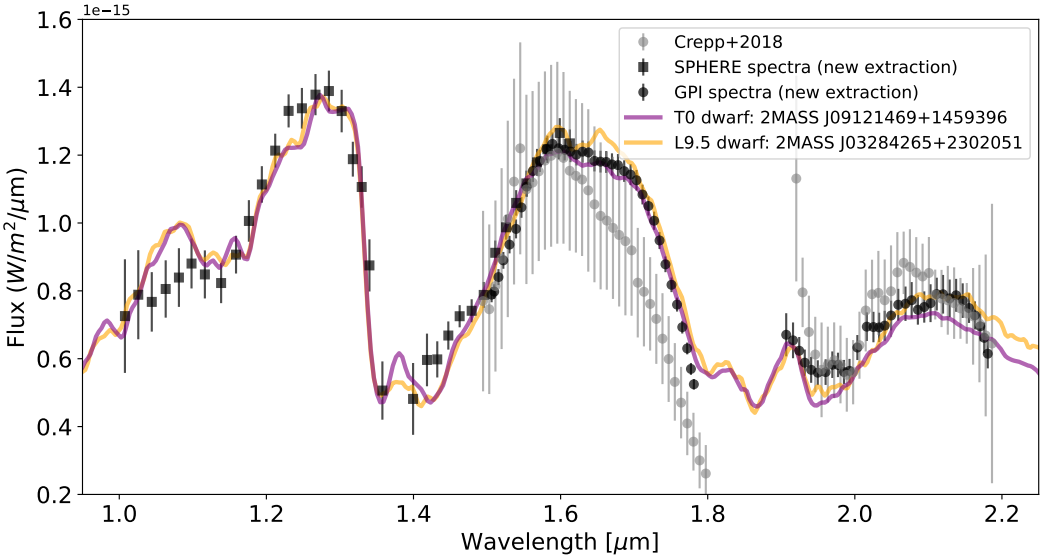

Figure 2.2: Our extracted LRS of HD 4747 B from GPI and SPHERE are plotted in black circles and squares, respectively, and the published spectra for GPI is shown in gray dots from Crepp et al. (2018). Overplotted in color are spectra of a L9.5 dwarf and T0 dwarf from SPEX (Burgasser, 2014), which show good agreement with our extracted spectra, demonstrating that HD 4747 B is consistent with a spectral type near the L/T transition.

observations of the host star. We chose to use the 2017 data for our analysis since it was taken under much better observing conditions and yields slightly higher spectral S/N than the 2016 data, despite shorter integration times.

Results and comparison with previous LRS

Our newly extracted GPI and SPHERE spectra are plotted in black circles and squares respectively in Fig. 2.2, and available in Appendix B (Table 2.4). The absolute flux scaling of our GPI spectrum agrees well with the published spectrum in gray from Crepp et al. (2018), but the uncertainties are much smaller. The shape of our new SPHERE spectrum also agrees well with that in Peretti et al. (2019). From the PSF-subtracted images, the brown dwarf companion is detected with a median S/N per wavelength bin of ≈ 61 and ≈ 26 in the GPI H and K_1 bands, and ≈ 20 in the SPHERE data. When comparing the extracted spectrum to that of field brown dwarfs from the SPEX library (Burgasser, 2014) in Fig. 2.2, we find that the newly extracted GPI spectrum is in better agreement compared to the previously published spectrum. As in Crepp et al. (2018) and Peretti et al. (2019), we find a spectral type near the L/T transition (the best matching spectra were from a L9.5 and T0 dwarf). The SPHERE IFS spectrum increases our wavelength coverage

by a factor of ~ 2, which we find is important for constraining model atmosphere parameters in our fits to the LRS.

2.4 Spectral analysis

Forward modeling the KPIC high-resolution spectrum

Here, we briefly describe the framework to forward model and fit the HRS from KPIC, which follows J. J. Wang et al. (2021c). When a companion of interest is aligned with one of the KPIC fibers, the companion light and a fraction of light from the host star's speckle field are injected into the fiber. At the projected separation of HD 4747 B (≈ 0.6 arcsec), we find the speckles are roughly the same brightness as our companion ($K_s \approx 14.4$ from Crepp et al. 2016). Furthermore, the light is transmitted through Earth's atmosphere and modulated by the instrument optics. Thus, we build two forward models (one for the companion, one for speckles) and jointly fit them as a linear combination. Below we detail how we generate each of the model components.

The companion spectral templates are generated with `petitRADTRANS`. We shift the templates in wavelength space to fit for the radial velocity. Then, we rotationally broaden the templates by a projected rotation rate $v \sin i$ using the `fastRotBroad` function in `PyAstronomy` (Czesla et al., 2019), and convolve the templates with the instrumental LSF. The effect of limb darkening is included in `petitRADTRANS` by integrating intensities along multiple angles between the ray and atmospheric normal.

Next, we multiply the companion model by the telluric response function, which characterizes the atmospheric transmission as a function of wavelength and includes telluric absorption lines. The telluric model is calculated by dividing the spectrum of the standard star (HIP 6960) by a PHOENIX stellar model with matching properties ($T_{\rm eff} = 9200$ and $\log(g)$=4.0).

To model the speckle contribution to the data, we use on-axis observations of the host star taken before the companion exposures. These observations are reduced in the same way as the companion spectra, but have much higher S/N. Unlike the companion models, the host star observations are already modulated by telluric transmission.

The last step is to remove continuum variations. The KPIC spectra are not flux-calibrated and contain a smoothly varying continuum due to stellar speckles and wavelength-dependent atmospheric refraction. Therefore, we apply high-pass fil-

tering with a median filter of 100 pixels (~ 0.002 μm) on both the data and models to subtract the continuum following J. J. Wang et al. (2021c). To determine the optimal filter size, we carried out a series of injection-recovery tests, and found that $\sim$ 100 pixels is best at recovering weak molecular signals for our data set. Larger filter sizes (e.g. 200 pixels or more) do not remove the continuum sufficiently, and smaller filter sizes (50 pixels or less) tend to be overly aggressive at removing weak molecular signals.

Finally, we flux-normalize both the companion and stellar models and multiply them by different flux scaling factors, which are fitted parameters. The flux scales are in units of counts as measured by the NIRSPEC detector. After scaling, the companion and speckle models are added and the same high-pass filter is applied on the final model before fitting it to the data.

Atmospheric retrieval setup

We implement a 'retrieval' framework based on `petitRADTRANS` to model the data, which means that we freely retrieve the chemical abundances, vertical temperature structure, and cloud properties from the data. Previous studies have used retrievals to model HRS of self-luminous exoplanets and brown dwarfs (e.g. Burningham et al., 2017; P. Mollière et al., 2020), and show that it can be a powerful alternative to fitting self-consistent grid models, which solve for the abundances and temperature profiles with physical assumptions such as chemical equilibrium. The retrieval approach allows more flexibility to fit the data and can potentially provide much more detailed information about the atmospheric properties, with the caveat that it is important to check for physical plausibility of the models since retrievals need not be self-consistent.

In our main set of retrievals, we fit for the chemical abundances in terms of C/O and atmospheric metallicity [C/H][6] along with a quench pressure (where the chemical timescale of a certain reaction is equal to the mixing timescale) to allow for disequilibrium chemistry, the temperature profile (§ 2.4), the cloud structure (§ 2.4), and other parameters such as the radius. We denote these quenched chemistry retrievals to distinguish from free retrievals where the abundances of each gas species is fit independently. Each component of the model is described in the subsections below. We use the correlated-k and line-by-line opacity sampling methods in `petitRADTRANS` for the low-resolution and high-resolution retrievals respectively.

[6]We denote the atmospheric metallicity as [C/H] because we are only sensitive to C- and O-bearing molecules in this brown dwarf's atmosphere.

For high-resolution, we include opacities for CO, H_2O, CH_4, NH_3, and CO_2, and for low-resolution we additionally include Na and K. This is because the alkali lines have wings which affect the $\sim$ 1 μm portion of the LRS, while their opacities are negligible over the portion of K band covered by our HRS. We repeated our baseline HRS retrieval with Na and K included and found that the addition of these two species did not influence the results or improve the fit.

Because the native high-resolution opacities are at $R = 10^6$, much higher than the resolution of our HRS resolution ($R \approx 35,000$), we down-sampled the opacity tables by a factor of six in order to speed up the retrievals (by roughly the same factor) and reduce the corresponding computational cost. We checked that the maximum deviation in synthetic spectra obtained by using the down-sampled opacities relative to the full-resolution opacity model is $< 5\%$ of the minimum HRS error bars. In addition, we repeated our fiducial HRS retrieval with the native opacities ($R = 10^6$) and found that it yielded the same results. We re-binned the correlated-k opacities to $R = 200$ for our fits to the LRS, which has a maximum resolution of 66. We also repeated our fiducial LRS retrieval at the native $R = 1000$ opacities and found the results are fully consistent.

Temperature structure and chemistry

We retrieve the pressure-temperature (PT) profile of the brown dwarf between $P = 10^{-4} - 10^3$ bars, which sets the vertical extent of the atmosphere. We use the P-T profile parametrization from P. Mollière et al. (2020) which has six free parameters. The spatial coordinate is an optical depth $\tau = \delta P^{\alpha}$, where δ and α are the first two parameters. The atmosphere then consists of a high altitude region (top of atmosphere to $\tau = 0.1$) fitted with three temperature points equi-distant in log pressure, a middle radiative region ($\tau = 0.1$ to radiative-convective boundary) which uses the Eddington approximation with T_0 as the 'internal temperature', and a lower region (radiative-convective boundary to bottom of atmosphere), which is set to follow the moist adiabatic temperature gradient once the atmosphere becomes unstable to convection (P. Mollière et al., 2020). We ignore stellar irradiation as a source of heat because the total incident energy on HD 4747 B at periastron ($\approx$ 2.7 au) is approximately four orders of magnitude less than its luminosity, which is dominated by the brown dwarf's internal energy.

In our quenched chemistry retrievals, the C/O, [C/H], and P-T profile determine the equilibrium chemical abundances (mass fractions of molecules) as a function of pres-

sure, by interpolating the chemical equilibrium table from P. Mollière et al. (2020). The opacities we include in the models are listed in § 2.4. In `petitRADTRANS`, the abundances of all metals except oxygen are assumed to scale together such that [C/H] = [Si/H] = [N/H], etc. Then, C/O and [C/H] are combined to set the oxygen abundance (P. Mollière et al., 2020). We use Asplund et al. (2009) as our reference for the solar metallicity in these models.

Finally, we include a quench pressure P_{quench} which fixes the abundances of H_2O, CO, and CH_4 where $P < P_{quench}$ using the equilibrium values found at P_{quench} (Zahnle et al., 2014; P. Mollière et al., 2020). The inclusion of P_{quench} allows for the possibility of disequilibrium chemistry, which occurs where the atmospheric mixing timescale is shorter than the chemical reaction timescale. We only include a quench pressure for the net reaction between H_2O, CO, and CH_4 because these molecules are the only ones detectable in our KPIC HRS (see § 2.5 for the CH_4 detection), and chemical kinetics modeling indicates that the abundances of these three molecules are closely linked to each other by a series of reactions (e.g. Moses et al., 2013). In summary, our quenched chemistry retrievals use C/O, [C/H] and P_{quench} to set the abundances of each gas species for a given P-T profile.

Clouds

Crepp et al. (2018) and Peretti et al. (2019) analyzed LRS for HD 4747 B and found evidence for a cloudy atmosphere. We summarize their results in Table 2.2 along with our new measurements. In this study, we consider both clear and cloudy models in order to explore the sensitivity of our retrieved abundances to the assumed cloud properties. For our cloudy model, we use the EddySed model from Ackerman et al. (2001) as implemented in `petitRADTRANS` (P. Mollière et al., 2020). In this model, the cloud particles both absorb and scatter the outgoing photons from the atmosphere according to measured optical properties (P. Mollière et al., 2019b). The cloud particles can be either crystalline or amorphous, and the opacities of the clouds are computed assuming either homogeneous and spherical particles, modeled with Mie theory, or irregularly-shaped cloud particles, modeled with the Distribution of Hollow Spheres (DHS) (Min et al., 2005; P. Mollière et al., 2019b).

For HD 4747 B, we consider models with two different cloud species ($MgSiO_3$ and Fe) and properties (amorphous or crystalline particles). We choose to focus on $MgSiO_3$ and Fe for several reasons. First, the condensation curves of these two species intersect the thermal profile of a $T_{\rm eff}$ = 1400 K, log(g)=5.5 object from the

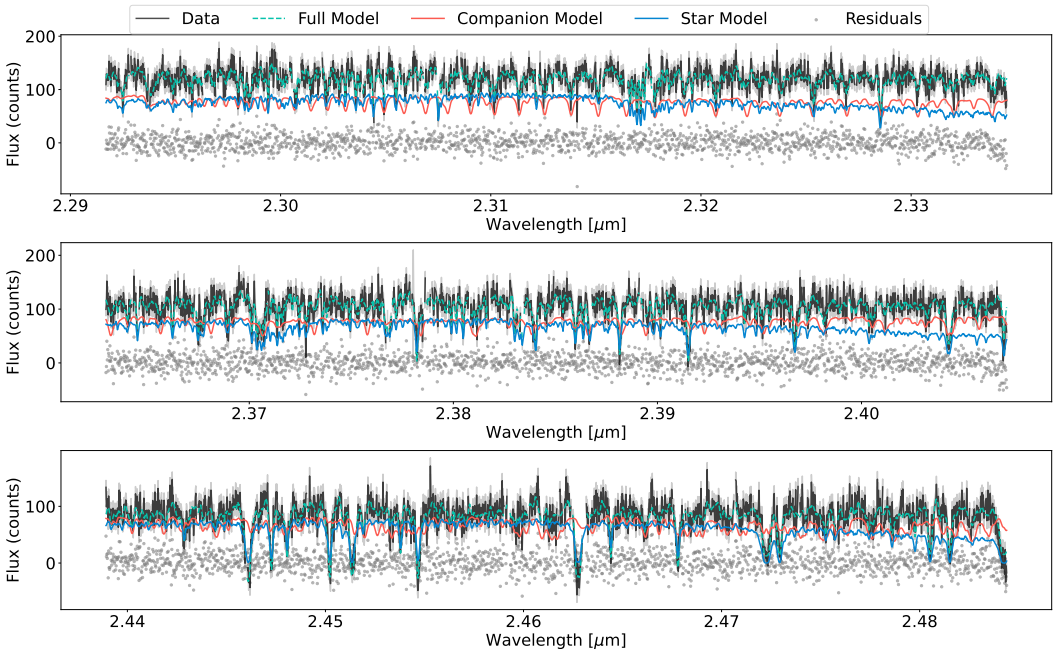

Figure 2.3: The KPIC HRS used in this study are plotted in black, with error bars inflated to the best fit value in gray. A sample full model is shown in teal (dashed), and consists of the companion model in orange (which has been RV shifted and broadened), and the stellar model in blue to model the speckle contribution. The companion model shown does not include tellurics to focus on molecular features, but tellurics are included in our fits. The residuals are shown as gray points.

Sonora atmospheric model (M. S. Marley et al., 2021) at $\sim 10-50$ bars. While the Sonora model is cloudless, it provides a rough estimate of which cloud species are relevant. Second, recent theoretical work has shown that $MgSiO_3$ is expected to be the most important cloud species for substellar objects with $T_{\rm eff} > 950$ K due to its low nucleation energy barriers and the relatively high elemental abundances of Mg, Si, and O (Gao et al., 2020). Finally, studies using mid-IR spectroscopy from Spitzer have found direct evidence for a $MgSiO_3$ absorption feature at ~ 10 μm in field brown dwarfs (Cushing et al., 2006; Luna et al., 2021), and specifically amorphous $MgSiO_3$ (Burningham et al., 2021). Although $MgSiO_3$ and Fe clouds do not have distinct features in the near-IR, they still impact the near-IR spectrum by contributing a wavelength-dependent opacity. Our baseline model uses amorphous $MgSiO_3$ modeled with Mie theory (abbreviated $MgSiO_3$, 'am') for the clouds. In addition, we also consider models with $MgSiO_3$, 'cd', which assumes crystalline cloud particles modeled with DHS, as well as models with two cloud species ($MgSiO_3$ + Fe) for the LRS.

Methane opacities

Given that HD 4747 B is located near the L/T transition for brown dwarfs, we might expect to observe methane in its atmosphere. Previous L band studies have detected methane in field brown dwarfs with spectral types as early as mid-L, or up to $T_{\rm eff} \approx 1800$ K (K. S. Noll et al., 2000; Johnston et al., 2019). In this study, we adopted the HITEMP CH_4 line list from Hargreaves et al. (2020), which we convert into opacities following the `petitRADTRANS` documentation. When cross-correlating a model generated with the HITEMP CH_4 opacities with a late T dwarf, we obtained a CCF S/N of ≈ 15, in comparison to ≈ 5 when cross-correlating with a model generated from the default CH_4 opacities from ExoMol (Yurchenko et al., 2014) in `petitRADTRANS`.

Additional fit parameters

`petitRADTRANS` computes the flux density as emitted at the surface of the object. For the LRS, we scale the model by the distance and companion radius, where the radius is another free parameter, and the distance is taken from the Gaia eDR3 parallax (Brown et al., 2021). For the HRS, we also fit the companion's radial velocity and $v \sin i$, as well as an error multiple term to account for any underestimation in the data uncertainties.

Due to imperfect starlight subtraction in the spectral extraction process, we found that our LRS likely still contains correlated noise from the wavelength-dependence of speckles, as has been noted by several previous studies on high-contrast companions (e.g. De Rosa et al., 2016; Samland et al., 2017; Currie et al., 2018; J. J. Wang et al., 2020; J. J. Wang et al., 2021a). This is evident in the residual frames, where we can see speckles at 5-20% of the companion intensity in the PSF-subtracted images. We therefore adopt a Gaussian process with a squared exponential kernel to empirically estimate the correlated noise in the GPI H, K and SPHERE YJH bands when fitting models to the data. Following J. J. Wang et al. (2020), we assume that our extracted error bars contain a fraction f_{amp} of correlated noise, and $1 - f_{amp}$ of white noise, and fit for f_{amp} and the scale of correlation l. This adds $2 \times 3 = 6$ additional parameters to the retrievals.

As an alternative model, we also tried fitting the LRS with error inflation terms and flux scaling factors for the SPHERE and GPI spectra along the lines of P. Mollière et al. (2020), but found that our results were very sensitive to our choice of prior for the flux scaling factor. We conclude that our GP model is better suited to account

for correlated noise from speckles, and use it in all LRS fits presented in this work.

Priors

We adopt uniform or log-uniform priors for all model parameters except for the mass, for which we use a Gaussian prior of $67.2 \pm 1.8\ M_{\rm Jup}$ from the dynamical mass measurement (§ 2.2). For the parametric P-T profile parameters, we exclude profiles that contain temperature inversions, as the heat budgets of widely separated companions are dominated by their internal luminosities. For the companion's radius, we use a uniform prior between 0.6 - 1.2 $R_{\rm Jup}$. When including a quench pressure, we use a log-uniform prior from 10^{-4} - 10^{3}, which is the full pressure range of our models. The priors for all retrieval parameters are tabulated in Appendix C.

Model fitting with nested sampling

We use nested sampling as implemented by `dynesty` (Speagle, 2020) to find the posterior distributions for the model parameters. Specifically, we use 200 live points and adopt the stopping criterion that the estimated contribution of the remaining prior volume to the total evidence is less than 1%. We repeated a few retrievals using 1000 live points and found the evidence remains roughly the same, implying the fits have converged when using 200 live points.

One advantage of adopting nested sampling is that we can use the Bayesian evidence from each fit to calculate the Bayes factor B, which assesses the relative probability of model M_2 compared to M_1. We will use the Bayes factor to compare different models throughout this paper to determine whether a given M_2 is justified over M_1. In Table 2.2, we take a baseline model ($MgSiO_3$, am) to be M_1 and compare other models to it. Based on Jeffreys (1983), a model with 100 times lower B than the model with the highest B can be 'decisively' rejected. B of $\lesssim 10$ is considered weak evidence for preferring one model over the other. We first run retrievals with only the HRS (§ 2.5), only the LRS (§ 2.6), as well as joint retrievals with both HRS and LRS (§ 2.7).

Table 2.2: Spectral retrievals carried out on HD 4747 B. The rightmost column lists the Bayes factor (B) for each retrieval, with the EddySed ($MgSiO_3$, am) model as the baseline model with $B = 1$. We adopt the first row (in bold) as our final results for this paper.

Data/Reference	Cloud Model	C/O	[C/H]	Radius ($R_{\rm Jup}$)	$\log(g)$	$T_{\rm eff}$ (K)	B
HRS (KPIC)	**EddySed ($MgSiO_3$, am)**	$\mathbf{0.66 \pm 0.04}$	$\mathbf{-0.10^{+0.18}_{-0.15}}$	$\mathbf{0.82^{+0.19}_{-0.13}}$	$\mathbf{5.39^{+0.15}_{-0.18}}$	$\mathbf{1652^{+128}_{-218}}$	1.0
HRS	EddySed ($MgSiO_3$, cd)	0.67 ± 0.04	$-0.06^{+0.23}_{-0.18}$	0.90 ± 0.19	$5.32^{+0.20}_{-0.17}$	1577^{+167}_{-253}	1.15
HRS	Clear	$0.67^{+0.05}_{-0.04}$	$-0.09^{+0.24}_{-0.16}$	$0.87^{+0.19}_{-0.17}$	$5.34^{+0.19}_{-0.17}$	1677^{+132}_{-142}	0.61
HRS	Clear (chemical equilibrium)	0.60 ± 0.02	$0.73^{+0.40}_{-0.31}$	$0.69^{+0.12}_{-0.06}$	$5.27^{+0.20}_{-0.14}$	1402^{+143}_{-110}	1.6×10^{-3}
LRS (GPI+SPHERE)	EddySed ($MgSiO_3$, am)	$0.55^{+0.06}_{-0.14}$	$0.22^{+0.25}_{-0.47}$	$0.70^{+0.05}_{-0.03}$	$5.53^{+0.04}_{-0.05}$	1473^{+17}_{-20}	1.0
LRS	EddySed ($MgSiO_3$, cd)	$0.45^{+0.08}_{-0.09}$	$-0.27^{+0.17}_{-0.19}$	0.77 ± 0.04	$5.45^{+0.04}_{-0.05}$	1443 ± 28	0.69
LRS	EddySed ($MgSiO_3$ + Fe, am)	$0.66^{+0.07}_{-0.10}$	$0.21^{+0.18}_{-0.24}$	0.73 ± 0.03	$5.50^{+0.03}_{-0.04}$	1458^{+21}_{-19}	1.54
LRS	EddySed ($MgSiO_3$ + Fe, cd)	$0.29^{+0.06}_{-0.07}$	$-0.51^{+0.17}_{-0.19}$	0.75 ± 0.03	$5.47^{+0.04}_{-0.03}$	1453^{+24}_{-21}	2.65
LRS	Clear	$0.12^{+0.02}_{-0.01}$	$-1.37^{+0.07}_{-0.05}$	1.10 ± 0.04	5.12 ± 0.03	1262 ± 16	7.0×10^{-26}
Peretti et al. (2019)	Cloudy retrieval	$0.13^{+0.14}_{-0.08}$	$-1.15^{+0.47}_{-0.39}$	0.85 ± 0.03	5.40 ± 0.03	1350 ± 50	...
Crepp et al. (2018)	Cloudy grid	...	...	...	$5.2^{+0.5}_{-0.6}$	1410^{+130}_{-140}	...

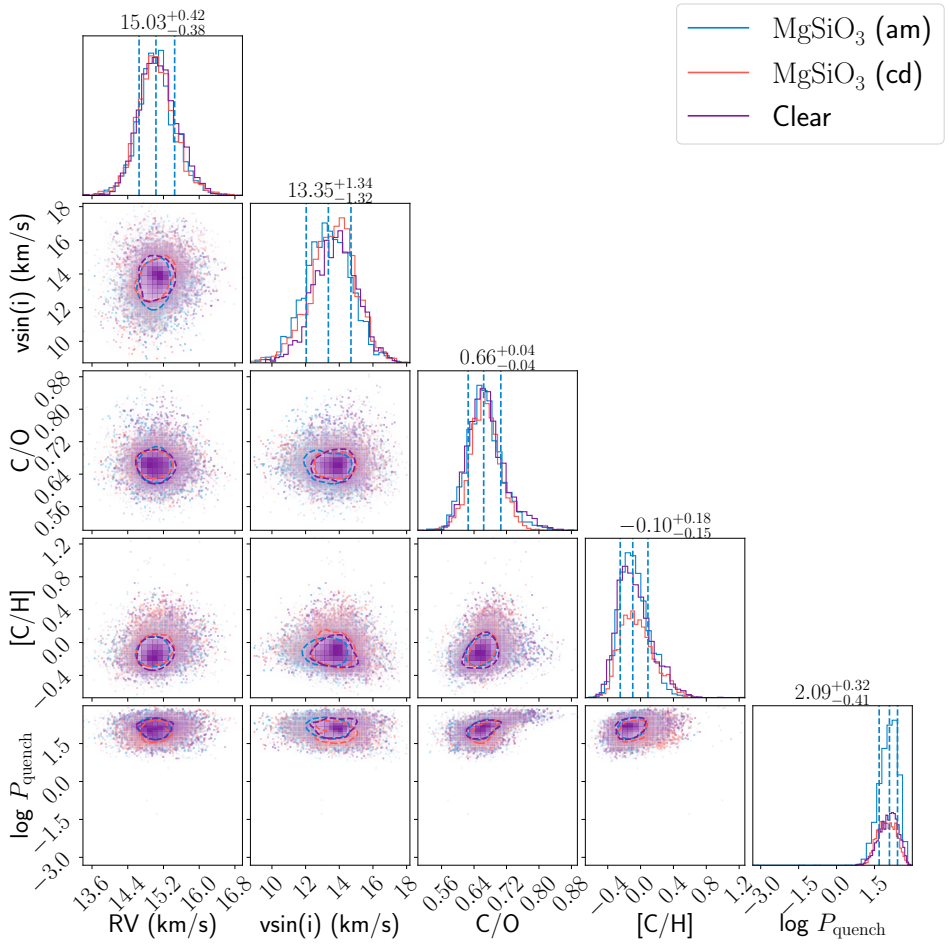

Figure 2.4: Posterior distributions for five key parameters from HRS retrievals of HD 4747 B, using the EddySed cloud model ($MgSiO_3$, 'am' and 'cd' in blue and red), and the clear model in purple. The titles on each histogram show the median and 68% credible interval for the baseline retrieval ($MgSiO_3$, am). Regardless of the cloud model used, the results agree well between different fits for the RV, $v \sin i$, C/O, [C/H] (discussed in § 2.5), and quench pressure (discussed in § 2.5).

2.5 High-resolution retrievals (KPIC)

Overview

From our HRS retrievals of HD 4747 B, we find that both clear and cloudy models yield consistent results for the atmospheric parameters (abundances, temperature structure, quenching) and bulk properties (radius, radial velocity, spin). A few selected parameters are plotted in Fig. 2.4 and tabulated in Table 2.2. The insensitivity of the HRS retrieval results to clouds, a major finding of this paper, is discussed in § 2.5. In Fig. 2.3, we plot the data, a best fit model, and residuals for the baseline HRS retrieval. We report values from this retrieval as the final results of this paper, with selected parameters shown in the first row of Table 2.2 and joint posterior

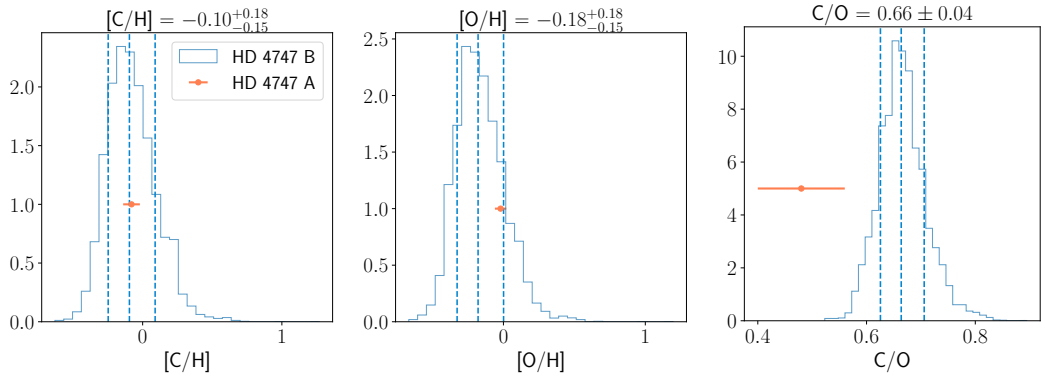

Figure 2.5: Retrieved C and O abundances (relative to solar) and C/O for HD 4747 B in blue. The titles on each histogram showing the median and 68% credible interval. The red points show the stellar values from § 2.2. The [C/H] agrees well, [O/H] is consistent within 1σ between the companion and star, and C/O is consistent at the 2σ level.

distributions in Appendix C. We also plot the contribution from the planet and star separately at their best-fit flux levels. We compute the auto-correlation function of the residuals and find that there is no evidence for correlated noise or strong systematics. Unless otherwise specified, we quote results from the baseline EddySed cloud model ($MgSiO_3$, am). See Appendix C for the posterior distributions of other parameters from our baseline model.

To make sure that we are fitting the correct signal, we check the RV and flux level of the companion. From our orbital posteriors for HD 4747 B, the expected RV shift on the night of our HRS observation is 15.0 ± 0.1 km/s in the Earth's reference frame, which is a combination of the system barycenter velocity, the Earth's relative velocity with respect to HD 4747, and the companion's orbital velocity. The fitted RV of 15.0 ± 0.4 km/s agrees perfectly with this value (see Fig. 2.4). In addition, the companion flux level in the spectral orders from 2.29 to 2.49 μm is 85 ± 10 counts, comparable to the speckle flux levels in these orders. Taking into account the difference in wavelengths and the difference in integration time (600 s for the companion, 60 s for the on-axis star), we estimate that our measured companion flux corresponds to $\Delta K_s = 8.3 \pm 0.3$ mag, which is within 3σ of the photometric $\Delta K_s = 9.05 \pm 0.14$ mag reported by Crepp et al. (2018). The agreement between these contrast values are reasonably good given the time-varying throughput of KPIC (Delorme et al., 2021), and the fact that we subtract out the continuum with high-pass filtering, effects which complicate a direct flux comparison.

Fig. 2.4 also shows the projected spin rate $v \sin i = 13.2^{+1.4}_{-1.5}$ km/s, which is compa-

rable to the rotation rates observed for field brown dwarfs with similar spectral types (e.g. Konopacky et al., 2012). We also plot the retrieved quench pressure P_{quench} in Fig. 2.4, which indicates that the chemical reaction timescale becomes longer than the vertical mixing timescale at pressures lower than P_{quench}. Thus, disequilibrium chemistry is clearly affecting the atmosphere (see § 2.5 for details).

We compute T_{eff} by sampling from our posterior to generate low-resolution models over a large wavelength range (0.5 to 30 μm) and calculating the integrated flux. We then solve for T_{eff} using the Stefan-Boltzmann law. When computing T_{eff}, we include opacities from Na and K, which are important sources of opacity near visible wavelengths. As shown in Table 2.2, the retrieved radius and T_{eff} from HRS have broad distributions, which reflect the relatively weak luminosity constraints from the HRS ($\log(L_{bol}/L_{\odot})$=$-4.33^{+0.23}_{-0.25}$). This is because the HRS is not flux-calibrated and we remove the continuum in our fits. Comparing to values of radius and T_{eff} from previous work based on LRS (Crepp et al., 2018; Peretti et al., 2019), our retrieved values from the HRS retrievals are consistent at the $1-2\sigma$ level (see Table 2.2). We discuss the constraints on these parameters from the LRS in § 2.6.

We compare our retrieved [C/H], [O/H], and C/O with that of the host star (see § 2.2) in Fig. 2.5. Our retrieved C abundance agrees well with the host star value, while the O abundance is lower by about 1σ. This results in our retrieved C/O for the companion being higher by about 2σ compared to the stellar value. Here and elsewhere in the paper, we compute the 'σ difference' between two measurements by dividing the difference in the two median values by the quadrature sum of the uncertainties from both measurements. We discuss the implications of our measured abundances for HD 4747 B in § 2.8.

Why are our KPIC HRS insensitive to clouds in HD 4747 B?

Clouds represent a significant source of uncertainty in many published models of substellar atmospheres (e.g. Burningham et al., 2017; J. Wang et al., 2020). However, we find that the retrieved parameters from our KPIC HRS are insensitive to the choice of cloud model for HD 4747 B. As shown in Fig 2.4, the posteriors for radius, RV, $v \sin i$, C/O, [C/H], and quench pressure are nearly identical across the various models. The same is true for other parameters.

Table 2.2 shows that the different cloud models are indistinguishable for the KPIC HRS; the clear model fits as well as the cloudy models, with $B = 0.61$, which does not pass the threshold of $B = 10/0.1$ to be considered statistically favored/disfavored.

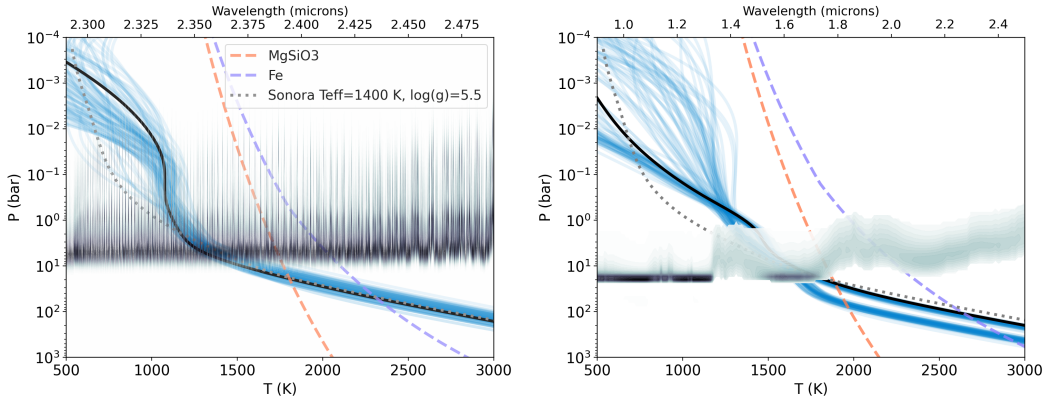

Figure 2.6: The P-T profiles from our HRS retrieval (left panel) and LRS retrieval (right panel) with the baseline cloud model ($MgSiO_3$, am). In each panel, black lines show the best-fit profile and blue lines are 100 random draws from the posterior. We also show a cloudless Sonora P-T profile (M. S. Marley et al., 2021) with similar bulk properties as HD 4747 B in dotted gray. The condensation curves for $MgSiO_3$ and Fe clouds are plotted in dashed lines. We also overplot the emission contribution function as contours, which show the fraction of flux (darker indicates higher fraction) a given pressure layer contributes to the total flux at a given wavelength (P. Mollière et al., 2019b). Thus, these use the wavelength axes, and not the temperature axes. The HRS is sensitive to the continuum forming around a few bars and line cores which form up to 10^{-2} bars. Over the same wavelength range of 2.29-2.49 μm, the LRS shows the continuum arises from $\approx 1-10$ bars, consistent with the HRS.

This indicates that the data can be fitted adequately without clouds; indeed the cloud parameters for the EddySed models span their respective prior ranges almost uniformly as shown in Appendix C. As we will discuss in § 2.6, the LRS show that the atmosphere of HD 4747 B is cloudy. This implies that cloud opacity must be minimal at the pressures probed by our HRS.

To understand this, we plot in Fig. 2.6 the retrieved P-T profiles (black and blue lines), cloud condensation curves (dashed lines), and emission contribution functions. The left and right panels show results from the HRS and LRS retrievals, respectively. The emission contribution function for HRS shows that we are sensitive to pressures ranging from a few bars, where the continuum forms, up to $\approx 10^{-2}$ bars in the cores of individuals lines. Note that the contribution functions use the wavelength axes on the top. In the EddySed model, the cloud base is set at the intersection of the P-T profile and a given cloud condensation curve (dashed lines). For $MgSiO_3$, this corresponds to a pressure of $\approx 10-20$ bars when using our HRS-retrieved P-T profile. As the cloud mass fraction drops exponentially above the cloud base

in the EddySed model (controlled by K_{zz} and f_{sed}), we find that the cloud opacity decreases to negligible levels by the time we reach pressures of a few bars where the continuum forms. For this reason, we do not consider models with Fe clouds in our HRS retrievals, since the Fe cloud base forms even deeper than that of $MgSiO_3$.

Therefore, our KPIC HRS are insensitive to clouds because we cover both a relatively small wavelength range (2.29-2.49 μm) and a range where molecular opacities from H_2O, CO, and CH_4 are significant. The small wavelength range means that the cloud opacity is effectively constant in wavelength. The strong molecular opacity in HRS allows us to resolve many individual absorption lines and obtain good constraints on the atmospheric composition for molecules present in this region of the spectrum. The opacity of these molecules decrease at shorter wavelength due to decreasing excitation cross sections, so the continuum shifts to higher pressures (deeper down) at shorter wavelengths. This effect is visible in the LRS contribution function, where close to 1 μm, the emission originates from roughly the same pressure as the $MgSiO_3$ cloud base, making the y and J bands particularly sensitive to clouds (see Fig. 2.10).

Could the KPIC HRS be affected by clouds at lower pressures (higher altitudes) than predicted by the EddySed model? Several studies have found that including clouds at lower pressures than predicted by EddySed produces better fits to mid-IR spectra of isolated brown dwarfs (e.g. Burningham et al., 2021; Luna et al., 2021). As shown in Fig. 2.6, our HRS P-T profiles show a nearly isothermal region between about 0.1-1 bars, which could suggest a degeneracy with clouds (Burningham et al., 2017). To check whether the P-T parameterization affects our results, we run a retrieval with a fixed P-T, namely the self-consistent profile over-plotted in gray. We find that all posteriors from this fixed P-T fit overlap within 1σ with those from our baseline retrieval. Thus, we conclude that the isothermal part of the P-T we retrieve is not biasing our conclusions. To further examine the possibility of clouds at lower pressures, we also run an opaque cloud model with infinite opacity below a retrieved pressure, and a gray cloud model that adds a constant cloud opacity at each pressure layer. When fitting the HRS with these more flexible cloud models, we also find consistent results with the baseline model. In the second model, the gray opacity is bounded to lie below $\sim 0.03\ g/\mathrm{cm}^{-3}$, and the pressure of the infinitely opaque cloud is required to be deeper than $\sim$ 1 bar. Therefore, even with these less constraining cloud parameterizations, we find that our HRS still prefers solutions with minimal cloud opacity.

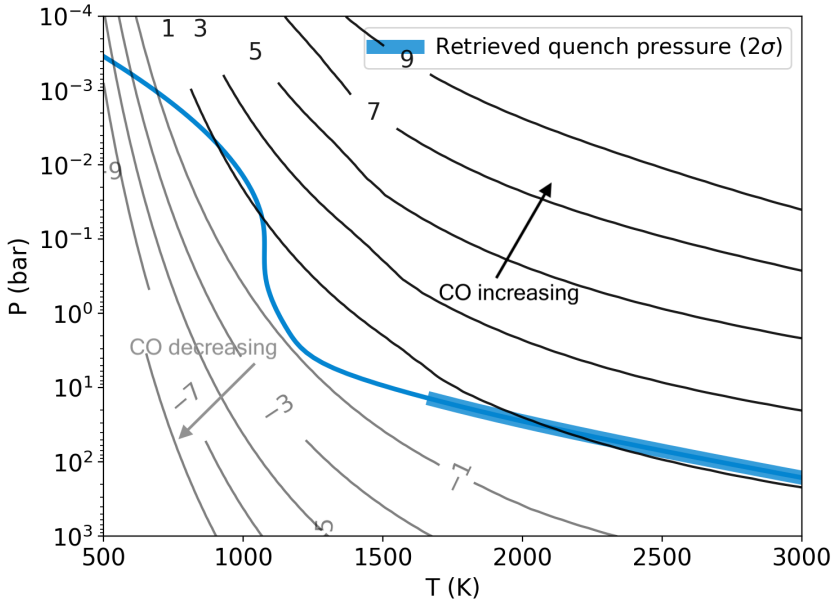

Figure 2.7: The best-fit P-T profile from our baseline HRS retrieval in blue, with the thicker region indicating the retrieved quench pressure (2σ interval of 14-836 bars). Lines of constant log(CO/CH_4) volume mixing ratios are shown, with black lines (gray lines) indicating the region where CO (CH_4) is more abundant. The P-T profile nearly overlaps with the log(CO/CH_4) = +1 line below $\sim$ 20 bars, which is where we retrieve the quench pressure to be from the HRS.

Disequilibrium chemistry with deep quenching pressure

In our retrievals, we include a simple model for disequilibrium chemistry using the quench pressure prescription in `petitRADTRANS`, which is motivated by Zahnle et al. (2014). Specifically, the abundances of CH_4, CO, and H_2O are held constant at atmospheric pressures lower than the retrieved P_{quench} parameter. We find that when including quenching, the goodness of fit increases drastically compared to fits with full chemical equilibrium. For example, between two clear retrievals with and without quenching, we find that $B \approx 380$ in favor of the quenched retrieval. From the Bayes factor interpretation of Benneke et al. (2013), this represents a detection of quenching at $\approx 3.9\sigma$ significance. The quench pressure retrieved is also highly consistent between retrievals with different cloud models, with 1 and 2σ intervals of 50 – 260 and 14 – 836 bars (Fig. 2.4). In this section, we explore reasons why the data prefer disequilibrium chemistry in the atmosphere of HD 4747 B. The physical implications of our retrieved quench pressure, including an estimate of the vertical diffusion coefficient (K_{zz}), are discussed in § 2.8.

To understand why the data prefer a deep quench pressure, we plot lines of constant

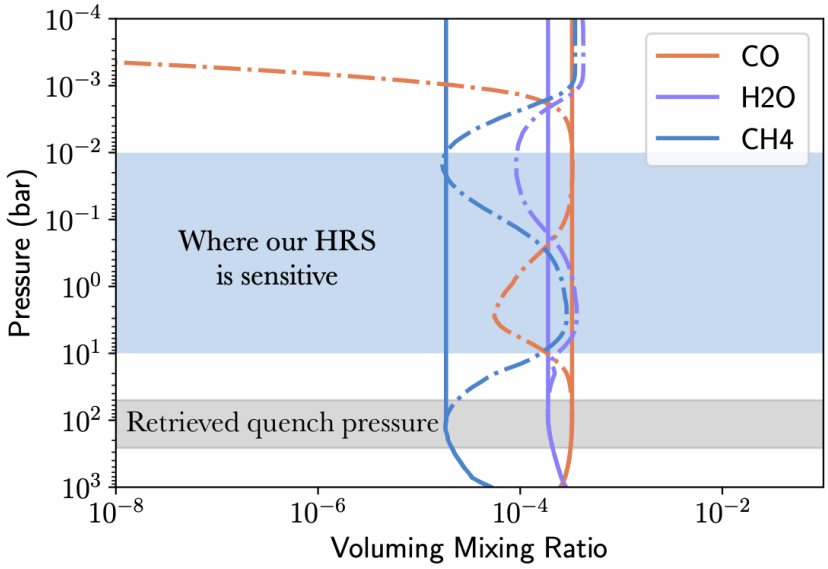

Figure 2.8: Solid lines: best fit volume mixing ratios (VMRs) of CO, H_2O, and CH_4 from our baseline HRS retrieval with chemical quenching. Dashed lines: the corresponding VMRs when quenching is turned off (i.e. equilibrium abundances) for the same retrieval. The 1σ quench pressure is indicated by the gray region, and the blue region shows schematically the pressures where our HRS is sensitive. Within the blue region, the relative CO/CH_4 ratio can differ by orders of magnitude between the quenched abundances and the equilibrium abundances.

$\log(CO/CH_4)$ volume mixing ratios (VMR) along with the best-fit P-T profile from our baseline HRS retrieval in Fig. 2.7. We calculate CO/CH_4 from this quenched chemistry retrieval by finding the abundances of each molecule in the chemical grid, iterating over our posterior distribution of C/O, [C/H], and P-T profile. We find that $CO/CH_4=13.6^{+5.8}_{-4.6}$. If the atmosphere was in chemical equilibrium, we repeat our calculation and find that we would expect $CO/CH_4=1.35^{+0.21}_{-0.17}$, which is ten times smaller than our retrieved value in the quenched chemistry model. Thus, the relative under-abundance of CH_4 relative to CO in our HRS leads our models to prefer a deep quench pressure. The value of CO/CH_4 also determines our retrieved the quench pressure, whose 2σ interval is indicated by the thick blue region in Fig. 2.7. Because the P-T profile nearly overlaps the curve of $CO/CH_4 = 10$ at $\sim$ 20 bars and deeper, a broad range of quench pressures deeper than $\sim$ 20 bars are consistent with the data.

As another way to visualize the detection of disequilibrium chemistry, we plot the molecular abundances in VMR as a function of pressure in Fig. 2.8. The solid lines show the VMRs for the HRS quenched chemistry retrieval, while dashed lines show

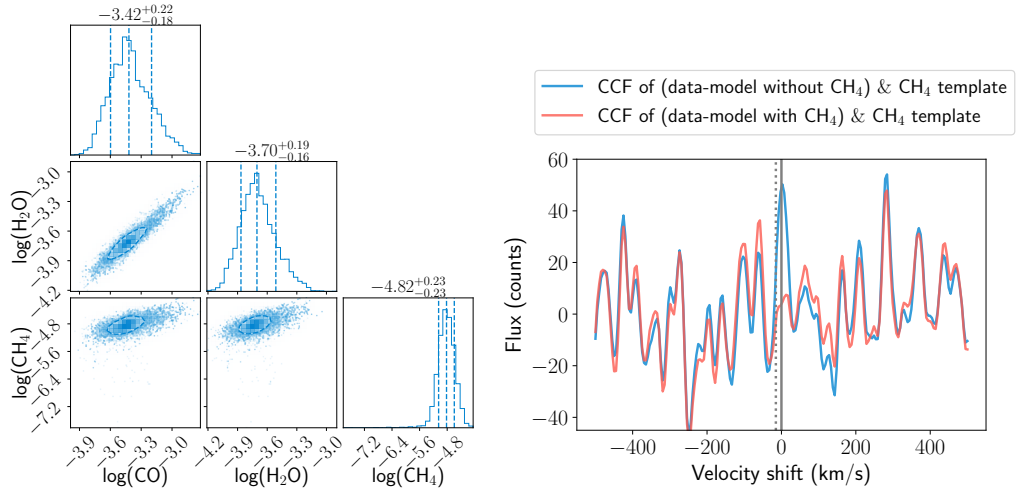

Figure 2.9: Left panel: Joint posterior distributions of the log(VMR) of CO, H_2O, and CH_4 from a KPIC HRS retrieval where we directly fit the molecular abundances and assume they are constant across pressure. Right panel: Cross-correlation functions of a pure CH_4 template with (KPIC data - model without CH_4) in blue, and the CCF of the CH_4 template with (data - model with CH_4) in red. The CH_4 template is generated with best fit parameters of the full model with CH_4, CO, and H_2O and manually setting opacities of CO and H_2O to zero. The gray solid line indicates the companion rest frame and the gray dotted line is the telluric rest frame. The residuals are taken from two spectral orders (2.29-2.41 μm) with stronger CH_4 detection.

the VMRs for the same model with quenching turned off manually. By comparing the solid and dashed lines, we see that at the pressures probed by our observations, the relative abundances of CO, CH_4, and H_2O differ by several orders of magnitude between the quenched model and expectations from chemical equilibrium.

Detection of methane in the HRS

Table 2.3: Free retrievals carried out on HD 4747 B for validating the CH_4 detection in the KPIC HRS (Sec 2.5). We list the log volume-mixing ratios of molecules included, and the Bayes factor between the model with and without CH_4.

Molecules	log(CO)	log(H_2O)	log(CH_4)	B
CO, H_2O	$-3.51^{+0.21}_{-0.17}$	$-3.77^{+0.19}_{-0.16}$	...	1
CO, H_2O, CH_4	$-3.42^{+0.22}_{-0.18}$	$-3.70^{+0.19}_{-0.16}$	-4.82 ± 0.23	84

In this section, we take a closer look at the relatively weak methane absorption signal in our HRS, which leads us to prefer quenched models where the CO/CH4 ratio is a factor of ten higher than predicted in models assuming chemical equilibrium. We

confirm the presence of detectable levels of methane in the HRS by running a pair of free retrievals, one with only H_2O and CO, and one with H_2O, CO, and CH_4. The results of these retrievals are listed in Table 2.3. In these free retrievals, we fit the abundances of each absorbing species independently and assume a constant abundance as a function of pressure. Although we also considered models that included NH_3 and CO_2, we only obtained upper limits on their abundances, and therefore excluded them from our fits in this section. Finally, given the insensitivity of the HRS to clouds, we carry out these tests with the clear model to save computation time.

We find that the data strongly prefer the model with CH_4, with a Bayes factor of 84 (3.4σ significance; Benneke et al. 2013). As shown in Table 2.3, we obtain $\log(CH_4) = -4.82 \pm 0.23$ from the free retrieval, and the CH_4 posterior in Fig. 2.9 shows no strong covariance with the abundances of either CO or H_2O. If the atmosphere was in chemical equilibrium, we would expect a CH_4 VMR that is ten times higher than what we retrieve, according to the same calculation described in § 2.5. We note that the abundances from the free retrieval with CH_4 also agree well with the corresponding VMRs from our quenched chemistry retrievals. This is not surprising given the deep quench pressure we retrieve, which makes the molecules abundances constant in the regions where our HRS is sensitive (see Fig. 2.8).

We separately visualize the CH_4 detection in cross-correlation space by carrying out an analysis similar to that described in Y. Zhang et al. (2021a). First, we make a 'pure CH_4 template' from the best-fit companion model with CH_4, H_2O, and CO by manually setting the abundances of H_2O and CO to zero. If the model without CH_4 is fitting poorly due to its inability to fit CH_4 lines in the data, we would expect the residuals of this model, which we denote R = (data - model without CH_4), to contain CH_4 lines. Therefore, we cross-correlate R with the pure CH_4 template, plotted as the blue CCF in Fig. 2.9. In addition, we plot the CCF of R' = (data - model with CH_4) with the pure CH_4 template in red for comparison. The blue CCF shows a peak at 0 km/s (solid gray line), where we expect a real signal to be since the models have been shifted by the best fit companion RV. If the residuals were dominated by telluric CH_4 for example, the CCF peak would appear at the dotted gray line (negative of the RV, or -15 km/s). Thus, even though the height of the CH_4 peak in the blue CCF is small compared to the surrounding structure, the fact that it is located at the companion RV is evidence of a real signal from CH_4.

In our CCF framework, the y-axis is the estimated flux level (in counts) of the

companion signal from a least-squares minimization. As shown in Fig. 2.9, we find a flux level of ≈ 50 counts for CH_4, which is an estimate of the companion flux in the residuals. Importantly, this value is consistent with the flux value found when we repeat the same CCF analysis with H_2O (i.e. comparing a model with only CO and CH_4 and the baseline model of CO, H_2O, and CH_4). For a molecule such as NH_3, which we see no evidence of in the KPIC HRS, the flux value from the CCF becomes unbounded as the least-squares routine used for computing the CCF fails to converge.

Finally, we check for cross-talk between H_2O and CH_4 by cross-correlating R with the pure water template and detect no CCF peaks. Furthermore, we note that in a retrieval with only CO and CH_4 (no H_2O), the retrieved CH_4 abundance is consistent with the value from the full model including CO, H_2O and CH_4.

We therefore conclude that the data strongly favor the presence of detectable levels of methane in the HRS, with an abundance significantly lower than that predicted by equilibrium chemistry models. The detection of methane at $\log(CH_4) = -4.82 \pm 0.23$ demonstrates the ability of KPIC to retrieve species that are more than an order of magnitude lower in VMR than the dominant molecular constituents in the data, in only 1 hour of integration time.

2.6 Low-resolution retrievals (GPI + SPHERE)

Overview

In this section, we present the results from our fits to the LRS and compare our retrieved parameters to those from the HRS fits. We fit the LRS using the same models as before. These include one clear model and four different implementations of the EddySed cloud model where we vary our assumptions about the unknown cloud properties. The cloudy models consist of two $MgSiO_3$ retrievals with am and cd particles (explained in § 2.4), and two retrievals with $MgSiO_3$ and Fe clouds (again, am and cd). In Fig. 2.10, we plot the data, best-fit cloudy and clear models, the residuals, and the GP models of the residuals. The posteriors for a few key parameters from these retrievals are plotted in Fig. 2.11 and tabulated in Table 2.2. See Appendix C for the posterior distributions of other parameters in the baseline model.

When comparing the clear and cloudy models in Fig. 2.10, we see that the data shortward of ~ 1.2 μm is poorly fit by models without clouds. This causes the clear model to have $B \approx 7 \times 10^{-26}$; it is overwhelmingly ruled out compared to

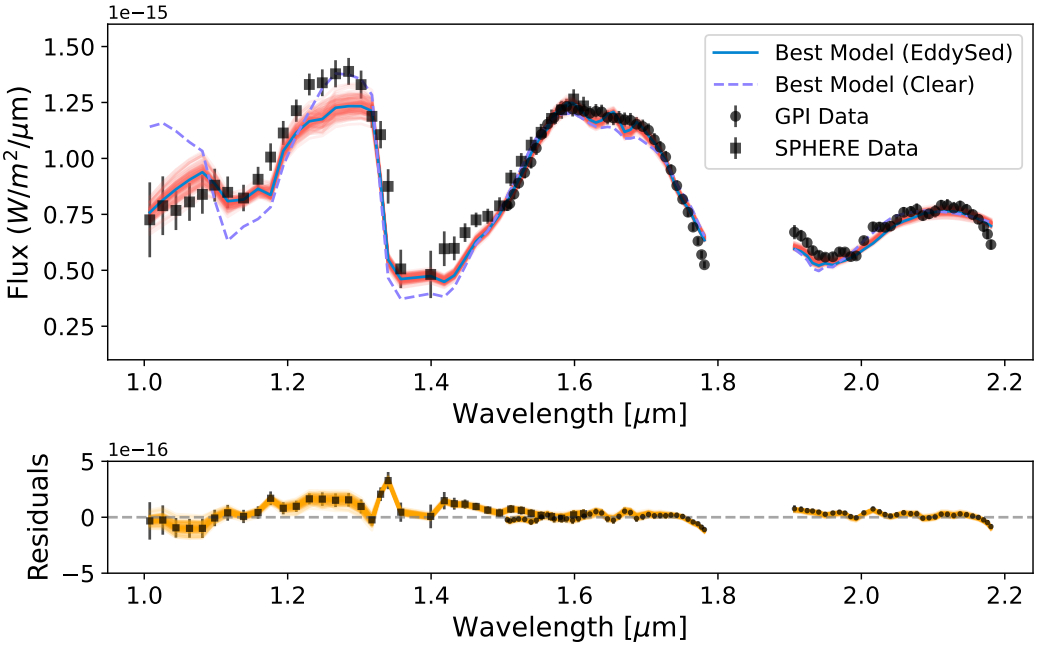

Figure 2.10: Top panel: best-fit cloudy model (EddySed + $MgSiO_3$, am) in blue and random models drawn from the posterior in light orange for a LRS retrieval of HD 4747 B. The best-fit clear model is overplotted in dashed purple, which fits visibly worse from $\approx 1.0-1.2$ μm. Bottom panel: the residuals of the cloudy model shown in error bars, along with random draws of the GP models for the residuals in orange.

the baseline EddySed model. In addition, when we plot the models over a larger wavelength range in Fig. 2.12, we find that the cloudy models agree with the NIRC2 L band photometry from Crepp et al. (2016), while the clear model over-predicts the L band flux by $\approx 2\sigma$. We did not include these photometric points in our retrievals.

Fig. 2.10 shows that the SPHERE J band data from $\approx 1.2-1.35$ μm is not well fit by even the cloudy model, which could either be caused by model mismatch or speckle contamination that artificially raises the flux. The GP model finds that $\sim 60\%$ of the SPHERE error bars and $\sim 90\%$ of the GPI error bars are from correlated noise, with correlation length scales of ~ 6 and ~ 2 wavelength channels, respectively. This confirms our initial intuition that the noise in the SPHERE and GPI images is likely dominated by correlated speckle noise based on visual inspection of the images. For the SPHERE data set, we estimate that the retrieved length scale is roughly equal to the number of steps that a speckle would move across the PSF for our brown dwarf's separation; indeed, we see speckles moving across the companion PSF in the reduced images. Overall, the SPHERE spectrum is less reliable than that from

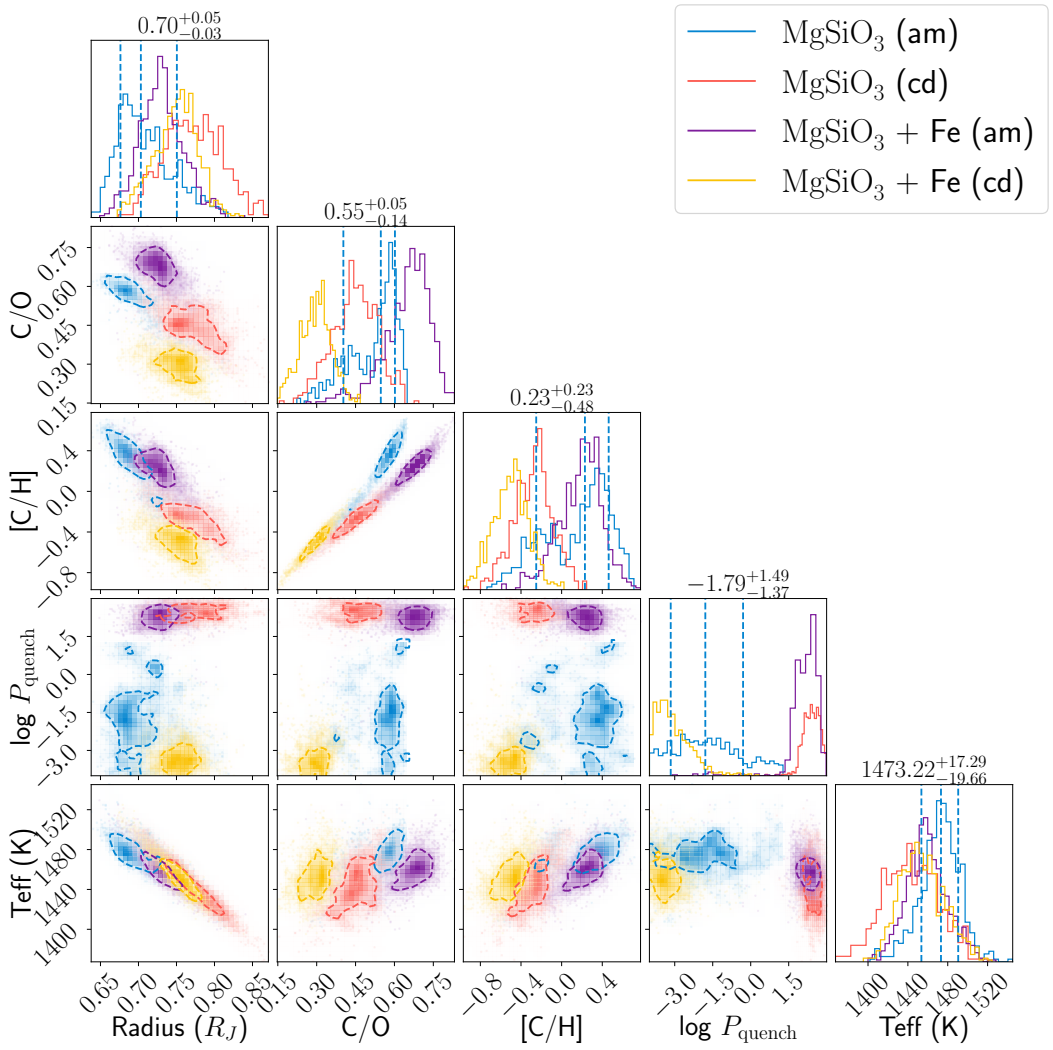

Figure 2.11: Posterior distributions for a few key parameters from LRS retrievals of HD 4747 B, using the EddySed model with $MgSiO_3$ clouds (blue: amorphous; red: crystalline), and $MgSiO_3$ + Fe clouds (purple: amorphous, yellow: crystalline). The titles on each histogram show the median and 68% credible interval for the $MgSiO_3$, am model. The results disagree by as much as 3σ, especially in 2-D space, and display strong covariance between C/O and [C/H]. The radius retrieved is also generally smaller than predicted by evolutionary models.

GPI because only 4 exposures are available, compared to the $\sim$ 40 exposures from GPI.

Finally, the P-T profile retrieved from our baseline LRS retrieval shows a bi-modal distribution (see Fig. 2.6). The degeneracy seen here may be related to issues with the LRS (see § 2.6).

Comparison with prior knowledge

Because the LRS is flux-calibrated, we can check whether our retrieved radii and effective temperatures are physical and consistent with prior knowledge for this benchmark companion. Using the known age and mass of HD 4747 B (3 ± 2 Gyr and m = 67.2 ± 1.8 $M_{\rm Jup}$), we interpolate the COND evolutionary models (Baraffe et al., 2003) to find a model-predicted radius of $0.8^{+0.07}_{-0.03} R_{\rm Jup}$, and a predicted T_{eff} = 1450^{+350}_{-180} K. Peretti et al. (2019) compared the SPHERE spectrum of HD 4747B to those of field brown dwarfs to derive a more tightly constrained T_{eff} = 1350 ± 50 K (see Table 2.2), which we adopt in the subsequent discussion.

We calculate the effective temperatures of the models in our retrievals by integrating the flux over 0.5-30 μm. For the baseline EddySed model, we find T_{eff} = 1473^{+17}_{-20} K, and a radius of $0.70^{+0.05}_{-0.03}$ $R_{\rm Jup}$. Compared to prior expectations however, the radius retrieved is too small by $\approx 1.5\sigma$ while T_{eff} is too high by $\approx 2\sigma$. From substellar evolutionary models, the minimum possible radius of a brown dwarf should be $\approx 0.74 R_{\rm Jup}$, which is imposed by electron degeneracy pressure (Chabrier et al., 2009). We find that T_{eff} and radius are correlated in the LRS retrievals, as shown in Fig. 2.11, which is expected as different combinations of these two parameters can produce the same total luminosity. However, our total luminosity agrees well with the luminosity predicted by evolutionary models.

Several previous retrieval studies have also found smaller than expected radius for L dwarfs, which may be attributed to the presence of heterogeneous surface features, such as patchy clouds, that are not captured in current 1-D retrieval frameworks (e.g. Kitzmann et al., 2020; E. C. Gonzales et al., 2020a; Burningham et al., 2021). On the other hand, E. C. Gonzales et al. (2021) retrieved a radius consistent with evolutionary models for a seemingly cloudless L dwarf. Whether the radii from evolutionary models are correct is an assumption that is now being tested by a growing sample of transiting brown dwarfs from TESS (e.g. Carmichael et al., 2020).

In our retrievals with both $MgSiO_3$ and Fe clouds, we retrieve slightly larger radii that are more consistent with the evolutionary model prediction. This could indicate that a single cloud model ($MgSiO_3$) may be inadequate in attenuating the flux from the deep atmosphere. However, models with two cloud species do not improve the fit significantly (B = 1.5-3 compared to the baseline model with $MgSiO_3$ only). Furthermore, the MgSiO3, cd model actually has the largest retrieved radius, but our data cannot distinguish between crystalline and amorphous particles. We conclude

that our retrieved radius is sensitive to aspects of the cloud models that are poorly constrained by the existing data for this object.

LRS at longer wavelengths could improve abundance and cloud constraints

While the LRS can provide tighter constraints on the cloud parameters and radius compared to the HRS, we find that many retrieved parameters, including the atmospheric abundances, are very sensitive to model choices. In Fig. 2.11, we overplot the posteriors distributions of a few parameters from our four EddySed models. The retrieved C/O and [C/H] have large uncertainties and can disagree at the 3σ level between models. The values also span a significant portion of the parameter space (>1 dex in metallicity), and show much stronger covariance compared those measured from the HRS (see Fig. 2.4). However, all cloudy models fit the LRS well, with Bayes factors within a factor of ~ 3 (see Table 2.2), so we cannot distinguish between them.

We note that P. Mollière et al. (2020) were able to obtain much better constraints on the composition of HR 8799e, which also has a cloudy atmosphere, using LRS data sets from 0.95-2.5 μm. Their LRS had SNR between 4-11 per wavelength bin, much lower than the SNR of our LRS (between 20-60 per wavelength bin). Unlike P. Mollière et al. (2020), however, our study does not have LRS in the second half of K band ($2.2 - 2.5$ μm), which contains a strong CO bandhead as well as significant H_2O and CH_4 opacities. When we compute the CO abundances from our LRS retrievals, we find that they are not well constrained, with 1σ intervals that are $\gtrsim 3$ wider than the CO constraint from HRS. In Fig. 2.12, we plot random draws of our baseline model color-coded by metallicity out to 5 μm. As shown, the models diverge quickly in the $2.2 - 2.5$ μm range. The fact that we miss this crucial wavelength region could explain why P. Mollière et al. (2020) obtain more robust constraints on atmospheric abundances, and P-T profiles that agree better with self-consistent models than we do, despite using data with a lower SNR.

Fig. 2.12 also shows a clear gradient in metallicity beyond 2.5 μm. In some of our cloudy LRS retrievals, we see a covariance between metallicity and cloud mass fraction, where lower metallicities correspond to higher cloud mass fractions, as well as larger, more physically consistent radii (see Fig. 2.11). The degeneracy between metallicity and cloud mass fraction might arise because both molecular opacities and clouds contribute opacity, and our data has insufficient wavelength coverage to probe more regions where the gas and cloud opacities are sufficiently

different. From the LRS retrievals, we consistently find a factor of $\sim 2-3$ more CH_4 and H_2O than observed in the HRS, implying that the LRS retrievals could be compensating for our imperfect cloud models by increasing the gas opacities.

Using a more flexible cloud model might alleviate some of these issues. For example, Burningham et al. (2021) retrieved the 1-15 μm LRS of a field L dwarf and found the data preferred silicate clouds much higher up than the predicted cloud base locations from condensation curves. In addition, their retrieved cloud particles also have smaller sizes (sub-micron) than predicted by the EddySed model (a few microns). Similarly, Luna et al. (2021) found that sub-micron cloud particles at lower pressures than predicted by EddySed are required to fit the mid-IR silicate feature ($\approx 8-10$ μm) of many L dwarfs. They found that the microphysical cloud model CARMA (Turco et al., 1979; Toon et al., 1988; Gao et al., 2018) allows them to fit their data much better and even place constraints on which cloud species are producing the observed absorption feature.

Both the above-mentioned studies benefited from data at ~ 10 μm that significantly help with constraining cloud properties. Thus, to obtain better abundance measurements with LRS, it is not only important to obtain full coverage in the near-IR (which we lack), but also to acquire data in the mid-IR. JWST can obtain low- and medium-resolution spectroscopy of brown dwarfs spanning the near- to mid-IR wavelengths using the NIRSpec and MIRI instruments. Future ground-based instruments such as SCALES at Keck (Stelter et al., 2020) will also provide LRS in the mid-IR.

2.7 Joint retrievals

In this section, we describe the results of joint retrievals to both the HRS and LRS for HD 4747 B. In practice, we set up two radiative transfer routines with `petitRADTRANS` using line-by-line (for HRS) and correlated-k (for LRS) opacity sampling respectively. The HRS and LRS models share the same atmospheric parameters and priors, but each has some unique parameters (e.g. RV and $v \sin i$ for HRS, GP kernel parameters for LRS). Within one nested sampling retrieval, we add the log likelihoods from the HRS and LRS components at each step of sampling to get the total log likelihood. We consider both clear and cloudy EddySed models for our joint retrievals.

Because the LRS prefer clouds, the cloudy model ($MgSiO_3$, am) is overwhelmingly preferred in our joint retrieval, with a Bayes factor in excess of 10^{34} compared to the clear model. From the cloudy model, we retrieve C/O= 0.70 ± 0.03 and

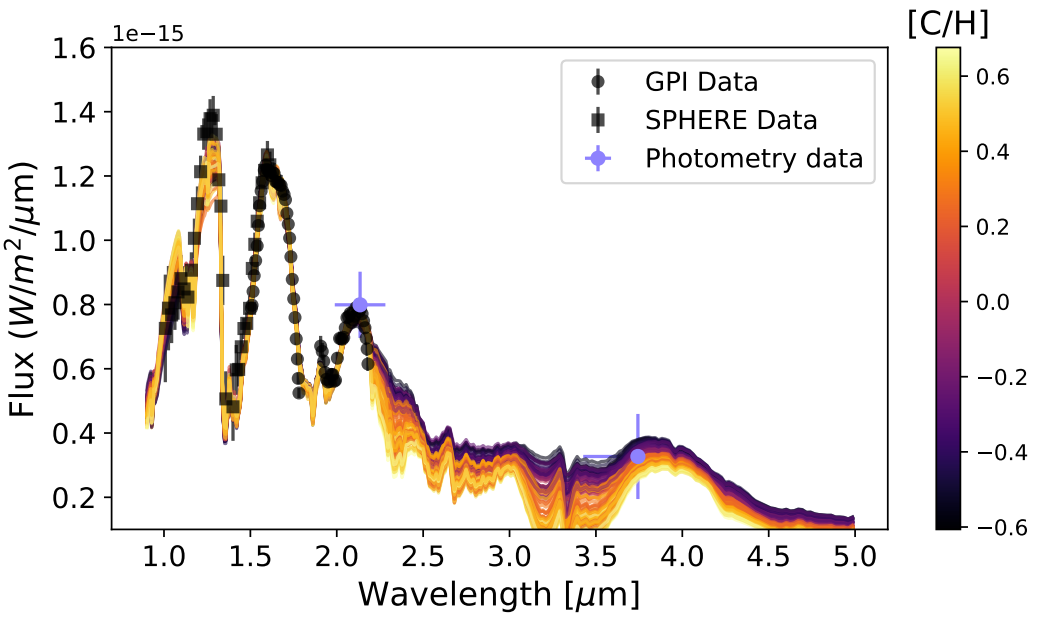

Figure 2.12: Random models drawn from the posterior of the baseline LRS retrieval ($MgSiO_3$, am), plotted over a larger wavelength range and color-coded by [C/H], the metallicity. There is a gradient in [C/H] in the L ($\approx 3.4 - 4.2$ μm) and M ($\approx 4.55 - 4.8$ μm) bands, which can be distinguished with comparable S/N LRS in these bands. The GPI and SPHERE data are shown in black, and we also overplot the photometric data points from Crepp et al. (2016), which are not included in the retrievals but nonetheless agree with our models.

[C/H]$= 0.34 \pm 0.07$. The retrieved uncertainties on these parameters are lower than in the HRS-only retrieval (which had C/O$= 0.66 \pm 0.04$ and [C/H]$= -0.10^{+0.18}_{-0.15}$). In addition, the C/O from our joint fit is consistent with the C/O from our HRS fit. This is not surprising, because the HRS places tight constraints on the relative line depths (and hence the relative abundance ratios) of CH_4, H_2O, and CO. However, the joint fit pushes the metallicity to higher values, which corresponds to increased gas abundances as shown in Fig. 2.13. The joint fit results translate to a $> 4\sigma$ discrepancy in [C/H] between HD 4747 A&B, while there is no discrepancy if we take the results from the HRS fit. This implies that the joint fit might be compensating for inadequacies in modeling clouds by increasing the gas opacities, as discussed in § 2.6 for the LRS-only case. We ran additional joint retrievals where we varied the cloud parameters (e.g. adding Fe clouds) and found similar results.

If we compare the log likelihoods of the HRS part of the joint fit to that from the HRS-only fit, we find that the HRS is fit less well by $\approx e^{10}$ (which translates to $\approx 4\sigma$) in the joint fit, implying a trade-off between fitting the LRS and HRS. We

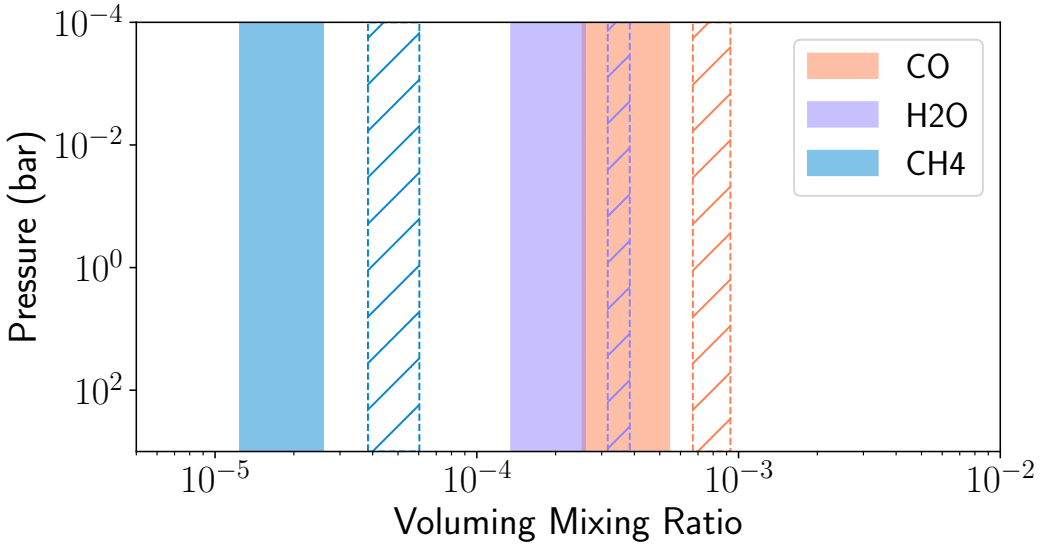

Figure 2.13: Filled areas: 1σ intervals for the CO, H_2O, and CH_4 abundances from our KPIC HRS retrieval. Hatched areas: the same for a joint retrieval (HRS + LRS). The retrieved abundances are 2-3 times higher in the joint retrieval, while the relative abundance ratios between species stays roughly the same (which produces a similar C/O). This highlights the fact that HRS is better at constraining relative abundances than absolute abundances.

can qualitatively compare the LRS S/N per wavelength bin to the CCF S/N of the HRS, which approximates the total constraining power of the HRS. When including all molecules in our model, we find a CCF S/N of $\approx$ 15 for the HRS. For the LRS, the average S/N per wavelength bin is $\approx$ 20 for the SPHERE YJH data and $\approx 60/30$ between the GPI H/K_1 data. This explains why the joint fits prioritize fitting the LRS at the expense of the HRS.

As discussed in § 2.6, the LRS are very model-sensitive and additionally contaminated by correlated noise. For this reason, we adopt the HRS-only results as the best estimate of HD 4747 B's atmospheric properties in this paper (see first row of Table 2.2). We leave it to future work, preferably aided by longer wavelength coverage in LRS, to achieve a more satisfactory joint retrieval.

2.8 Discussion

Next steps for high-resolution spectroscopy

Our KPIC HRS provide a better handle on the atmospheric abundances of HD 4747 B, and are less sensitive to model choices than our LRS. In fact, our K band HRS are essentially agnostic to clouds in the brown dwarf's atmosphere; all retrieved parameters are consistent independent of our chosen cloud model (Fig. 2.4). As discussed

in § 2.5, this is because our HRS covers a wavelength region (2.29 – 2.49 μm) of high molecular opacity, and probes emission across a wide range of atmospheric pressures where cloud opacity is negligible (up to 10^{-2} bars in line cores). While clouds affect the continuum near 1 μm in the LRS, they have little effect on the line depths across the wavelength range of our HRS. The relative lines depths are sensitive to relative molecular abundances, which directly constrains C/O. These results advocate for using HRS to measure atmospheric abundances.

In the future, it is important to explore whether these findings hold true for other substellar objects. In upcoming papers, we will present KPIC HRS retrievals of brown dwarf companions and giant planets spanning a range of effective temperatures and surface gravities. Ultimately, it would also be useful to constrain cloud properties with HRS. For transmission spectroscopy, Gandhi et al. (2020) found that their simulated near-IR HRS for warm Neptunes are more sensitive to molecular abundances than LRS for the same reasons highlighted in this study. While both clouds and metallicity affect the line depths in HRS, Gandhi et al. (2020) show that increasing the wavelength coverage (e.g. going from 0.9-1.7 μm to 0.9-2.5 μm) helps distinguish between clouds and metallicity and provide better constraints on both. Thus, if we wish to obtain constraints on clouds and abundances at the same time, it would be important to extend our current HRS to a broader range of wavelengths. KPIC Phase II will allow us to obtain L band data ($\approx$ 3.4 – 4.1 μm) to complement existing K band data (Delorme et al., 2021), and future upgrades could benefit from including H and J bands as well.

In this study, we have assumed that the atmosphere of HD 4747 B is globally uniform. However, it would be important to examine the impact of 3-D effects, including non-uniform cloud coverage. Past studies with photometry or LRS show that many brown dwarfs exhibit clear rotational variability signals (e.g. Apai et al., 2013; Zhou et al., 2018; Biller et al., 2018; Manjavacas et al., 2021; Vos et al., 2022), which appear to be caused by inhomogeneities in their cloud properties. Therefore, time-resolved observations are important to understanding clouds and 3-D effects.

With HRS, we can use the time-varying line depth and shape to map the 2-D brightness distributions of these objects (e.g. Crossfield et al., 2014). In this paper, we used 1 hour of KPIC data for HD 4747 B. Given our measured $v \sin i$ and assuming a radius of $0.8 R_{\rm Jup}$, we would expect a 5 or 7 hour rotation period if i is equal to the orbital inclination or $i = 90°$. Thus, it may be possible to sample a full rotation period within a single observing night, with the caveat that measurements of

the true rotation period remain difficult for high-contrast companions (Biller et al., 2021).

Methane and the presence of disequilibrium chemistry

Our HRS retrievals indicate that the ratio of CO/CH4 (VMR) is ≈ 10 times higher than expected by equilibrium chemistry (see § 2.5). To gain more physical intuition, we convert the quench pressure from our HRS retrievals to an estimate of the vertical diffusion coefficient, K_{zz}. To do this, we match the chemical timescale of the CO-CH_4 reaction from Zahnle et al. (2014) with the mixing timescale $\tau_{mix} = L^2/K_{zz}$. While the length scale L is typically taken to be the pressure scale height H for lack of a better estimate, Smith (1998) show that this assumption is not valid across several reactions in the atmospheres of Jupiter and Neptune. In fact, Smith (1998) find that $L \approx 0.1H$, which changes the inferred K_{zz} by two orders of magnitude. Similarly, Ackerman et al. (2001) also note that the mixing length is generally shorter than the pressure scale height H in stable atmospheric regions. Due to the uncertainty in L, we adopt $L = \alpha H$, where α is a scaling factor, and $H = \frac{k_B T}{\mu m g}$ (μ: mean molecular weight, g: surface gravity, T: the local temperature). For each value of quench pressure from our posteriors, we compute the necessary quantities to derive a posterior for K_{zz}. For instance, if $\alpha = 0.1$, we find $K_{zz} = 5 \times 10^8 - 1 \times 10^{12}$ cm^{2}s^{-1} (1σ). On the other hand, if $\alpha = 1$, we obtain $K_{zz} = 5 \times 10^{10} - 1 \times 10^{14}$ cm^{2}s^{-1}.

There have been few quantitative measurements of K_{zz} for substellar companions. Miles et al. (2020) used M-band LRS to constrain the CO abundance and estimate the vertical diffusion coefficient, K_{zz}, for seven field brown dwarfs. However, their objects have T_{eff} between 250-750 K, much colder than HD 4747 B. In terms of objects with $T_{eff} \gtrsim 1000$ K, Barman et al. (2015) reported a detection of CH_4 in HR 8799b ($T_{eff} \sim 1000$ K) with Keck/OSIRIS data, which they used to estimate K_{zz} between $10^6 - 10^8$ cm^{2}s^{-1}. However, this CH_4 detection was not confirmed by an independent study (Petit dit de la Roche et al., 2018), and recently Ruffio et al. (2021) concluded that future higher-resolution follow up is needed to resolve the discrepant CH_4 signal strengths found by different analyzes. Ruffio et al. (2021) point out that if the CH_4 abundance was over-estimated by Barman et al. (2015), that would imply a larger K_{zz}. Using LRS, P. Mollière et al. (2020) found a well-constrained quench pressure for HR 8799e ($T_{eff} \sim 1100$ K) from `petitRADTRANS` retrievals, which could similarly be converted to a K_{zz} constraint. In summary, our finding HD 4747 B, which is $\sim 300 - 400$ K hotter than HR 8799b&e and much older (a few Gyr from § 2.2) than most directly imaged planets, represents an important new

data point because hotter objects are expected to be closer to equilibrium, making chemical disequilibrium processes harder to detect (e.g. Moses et al., 2013).

Zahnle et al. (2014) provide an upper limit for K_{zz} from mixing length theory (Gierasch et al., 1985) assuming full convection. For HD 4747 B, their Equation 4 translates to an upper limit of $\approx 10^9$ cm^{2}s^{-1}. Depending on α, our retrieved K_{zz} either exceeds this upper limit by $\gtrsim 2\sigma$ (if $L = H$), or is very close to this limit (if $L = 0.1H$). Together, this suggests that convection is driving the vertical mixing in HD 4747 B, and that the mixing efficiency is likely close to its predicted maximum. We check whether our inferred K_{zz} makes sense by comparing them to those predicted by self-consistent atmospheric models with disequilibrium chemistry from Karalidi et al. (2021) and (Mukherjee et al., 2024). For an object with properties similar to HD 4747 B, our measured CH_4 VMR is consistent with $K_{zz} \sim 10^8 - 10^{12}$ in these models (with the assumption that $L = H$). These values of K_{zz} are roughly consistent with our estimate based on P_{quench}, and also near the upper limit from Zahnle et al. (2014). On the modeling front, it would be valuable to carry out 3-D hydrodynamical simulations (e.g. X. Zhang et al., 2018; Tan et al., 2021a) of brown dwarf interiors to independently estimate K_{zz} (Tan, 2022) and compare the results to that inferred by our data. Such simulations could also reveal what physical processes might cause a discrepancy between mixing length theory and our observations.

Dynamical versus Spectroscopic Mass Constraints

For a majority of substellar companions observed by direct imaging, there are no dynamical mass constraints. To assess whether our mass prior plays an important role in the results, we repeat our HRS and LRS retrievals with the baseline cloud model but use uniform priors in mass from 10 to 100 M_{Jup} ('free-mass'). For the HRS free-mass retrieval, we find that all parameters change by less than 1σ compared to the mass-prior retrieval. The mass itself shows a broad distribution (33-76 M_{Jup} at 1σ) that encompasses the dynamical mass. Because our KPIC HRS are not flux calibrated, the radius is not well constrained. In this case, we get large uncertainties in the spectroscopic mass because mass is inferred from the retrieved surface gravity, which depends on the poorly-constrained radius.

Our LRS free-mass retrieval also yields posteriors for all parameters that are consistent between 1-2 σ with the mass-prior retrieval. Furthermore, the mass retrieved by the LRS is 59^{+7}_{-8} M_{Jup}, which agrees within about 1σ with the dynamical mass. This provides confidence that reasonable mass constraints can be placed on sub-

stellar objects from LRS. The radius retrieved is $0.77 \pm 0.03\ R_{\rm Jup}$, consistent with evolutionary model predictions and close to the radius from the mass-prior retrieval, suggesting the two retrievals find a similar surface gravity.

Atmospheric abundances of HD 4747 AB

We retrieve [C/H] and [O/H] values that are 1σ consistent with those of the host star, as discussed in § 2.5. Both companion and the star are mildly sub-solar in terms of their metal content. However, our retrieved C/O=0.66 ± 0.04 is higher by approximately 2σ than the stellar C/O=0.48 ± 0.08.

The question is whether the marginal discrepancy in C/O is from astrophysical or systematic reasons. For example, J. Wang et al. (2022) carried out retrieval experiments on simulated HRS ($2.2 - 2.35\ \mu$m, $R = 35,000$) and found that their formal error bars are likely under-estimated due to systematic errors at the ~ 0.15 level in C/O. Using KPIC HRS from 2.23-2.33 μm, they found $\approx 1 - 1.5\sigma$ discrepancies between the [C/H] and [O/H] abundances of HR 7672 A and B, another benchmark brown dwarf system. On an earlier study of benchmark brown dwarfs, Line et al. (2015) quoted 1σ uncertainties of $0.2 - 0.3$ in their brown dwarf C/O (much larger than our formal C/O uncertainty of 0.04), and concluded that a 2σ agreement between the stellar and companion C/O is sufficiently good given the caveats. It is also possible that the uncertainties on stellar abundances are under-estimated given non-LTE effects (Line et al., 2015).

Another factor that might contribute to the 2σ discrepancy in C/O is uncertainties in the chemistry of condensates. The chemical model of `petitRADTRANS` we use accounts for the equilibrium condensation of various species and reports the global (rather than gas phase) C and O abundances (P. Mollière et al., 2019b). In particular, species such as $MgSiO_3$ and Mg_2SiO_4 contain 3 or 4 oxygen atoms per molecule, and are expected to hold a significant portion of O (Line et al., 2015). From our HRS retrievals, we find that $\approx 18\%$ of O is condensed into solids such as $MgSiO_3$. In order to decrease the global C/O of the brown dwarf by ≈ 0.1 (therefore making the companion and stellar C/O agree at the 1σ level), we require a $\sim 20\%$ increase in the net O abundance. Keeping everything else unchanged, this means the $MgSiO_3$ mass fraction, which is predicted by the chemical model to be $\sim 2 \times 10^{-3}$ in our retrievals, needs to be doubled to $\sim 4 \times 10^{-3}$. From the LRS retrievals, the cloud base MgSiO3 fraction can be as high as 10^{-2}. Therefore, a factor of ~ 2 uncertainty in the abundance of $MgSiO_3$ could make our C/O consistent at the 1σ level with the

stellar value.

Given these caveats, we conclude that the 2σ difference between our retrieved C/O for HD 4747 B and the stellar value is not significant, and HD 4747 AB are consistent with being chemically homogeneous. Chemical homogeneity is expected by models where brown dwarf companions form via gravitational fragmentation in molecular clouds (e.g. Padoan et al., 2004) or massive protostellar disks (e.g. Stamatellos et al., 2007). Simulations suggest that brown dwarfs typically form as part of unstable, high-order multiple systems, which undergo chaotic interactions that reduce the multiplicity over time (e.g. Bate et al., 2002; Thies et al., 2010; Bate, 2012). With a semi-major axis of 10 au, HD 4747 B is unlikely to have been directly affected by such encounters, but its relatively high orbital eccentricity (≈ 0.73) could encode such a dynamically 'hot' past.

2.9 Conclusions

Using high-resolution spectra ($R \sim 35,000$) obtained by Keck/KPIC, we retrieve [C/H]=$-0.10^{+0.18}_{-0.15}$, [O/H]=$-0.18^{+0.18}_{-0.15}$, and C/O=0.66±0.04 for the benchmark brown dwarf companion HD 4747 B (formal error bars). The C and O abundances are consistent with the stellar values to $\lesssim 1\sigma$, while the C/O ratio is consistent at the 2σ level, as expected for a binary-star like formation scenario. This shows that we can measure the atmospheric abundances for high contrast substellar companions to the 20% level with KPIC and our current modeling framework, which J. Wang et al. (2022) also show for another benchmark brown dwarf. We outline some other key findings from our study below.

We measure precise abundances from the KPIC HRS (2.29 – 2.49 μm), which are insensitive to our choice of cloud model. Our abundance measurements suggest that HD 4747 B has a CO/CH_4 ratio that is 10 times higher than predicted by equilibrium chemistry, corresponding to a quench pressure of $50-260$ bars (1σ). This translates to a high vertical diffusion coefficient K_{zz} which depends on the assumed length scale L. However, even if L is ten times smaller than the pressure scale height, we get $K_{zz} = 5 \times 10^8 - 1 \times 10^{12}$ cm^{2}s^{-1}, which implies a mixing strength that is at or above the upper limit predicted by mixing length theory.

The composition retrieved from our LRS (1-2.2 μm) is both sensitive to model choices, and can be biased by the presence of speckles. For this reason, HRS provides a more reliable picture of the atmospheric composition in the current data sets, although the LRS could be improved with additional observation at longer

wavelengths including the L and M bands. Despite these challenges, the current LRS does provide a spectroscopic mass estimate that is 1σ consistent with the dynamical mass for the brown dwarf.

Although our joint retrieval results are likely biased by the limited LRS wavelength coverage, joint analyzes of LRS and HRS remain a promising avenue to constrain cloud properties and abundances simultaneously and provide a more complete picture of substellar atmospheres. When extended wavelength coverage is available, it would also be important to consider possible 3-D effects, including patchy clouds. These might be constrained by obtaining multiple spectra sampling a rotation period. Additional modeling work on condensation, chemistry, and vertical mixing rates are also important to inform future observational results.

2.10 Acknowledgements

We thank the referee for helpful comments that improved the manuscript. J.X. thanks Michael Zhang for advice in computing the CH_4 opacities, Jonathan Fortney for discussions on chemical disequilibrium, and Konstantin Batygin for discussions on brown dwarf formation.

We wish to recognize and acknowledge the very significant cultural role and reverence that the summit of Maunakea has always had within the indigenous Hawaiian community. We are most fortunate to have the opportunity to conduct observations from this mountain. This research has benefitted from the SpeX Prism Library maintained by Adam Burgasser at http://www.browndwarfs.org/spexprism. Funding for KPIC has been provided by the California Institute of Technology, the Jet Propulsion Laboratory, the Heising-Simons Foundation, the Simons Foundation, and the United States National Science Foundation Grant No. AST-1611623. AV acknowledges funding from the European Research Council (ERC) under the European Union's Horizon 2020 research and innovation programme, grant agreements No. 757561 (HiRISE). HAK acknowledges support from the President's and Director's Research & Development Fund Program, which is jointly funded by the Jet Propulsion Laboratory and the California Institute of Technology under a contract with the National Aeronautics and Space Administration. The computations presented here were conducted in the Resnick High Performance Center, a facility supported by Resnick Sustainability Institute at the California Institute of Technology.

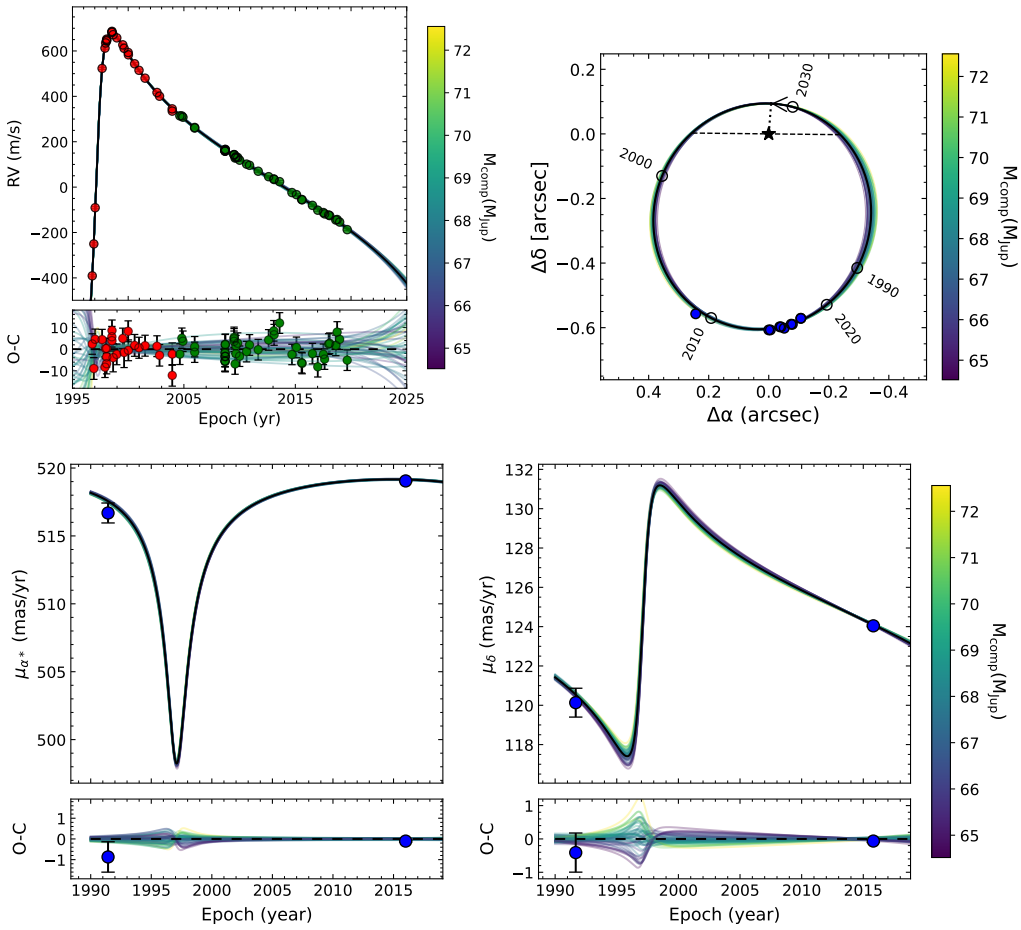

Figure 2.14: Results from a joint fit to host star radial velocity (top left), relative astrometry (top right), and absolute astrometry (bottom panel) for the HD 4747 system. The data together constrain the orbital parameters and mass of both the companion and host star well (Table 2.1).

2.11 Appendix

Orbit fits for HD 4747 B

Our orbit fit for the HD 4747 system is shown in Fig. 2.14.

Extracted Low-resolution spectrum and GPI astrometry

Our extracted spectrum for HD 4747 B based on observations with GPI (Crepp et al., 2018) and SPHERE (Peretti et al., 2019) are given in Table 2.4. Our relative astrometry measurements based on the GPI data are listed in Table 2.5.

Table 2.4: Extracted Low-Resolution Spectrum for HD 4747 B

Wavelength (μ**m**)	**Flux** ($10^{-15} \times W/\mathrm{m}^2/\mu$**m**)	**Flux Error** ($10^{-15} \times W/\mathrm{m}^2/\mu$**m**)
SPHERE (YJH)		
1.008	0.726	0.167
1.026	0.789	0.131
1.044	0.767	0.088
1.063	0.806	0.085
1.081	0.839	0.086
1.098	0.880	0.073
1.116	0.848	0.071
1.138	0.823	0.059
1.159	0.907	0.056
1.176	1.006	0.061
1.194	1.114	0.054
1.212	1.213	0.050
1.230	1.330	0.049
1.248	1.338	0.060
1.267	1.378	0.061
1.285	1.389	0.060
1.302	1.330	0.063
1.318	1.188	0.051
1.330	1.106	0.061
1.340	0.875	0.077
1.358	0.506	0.086
1.399	0.482	0.106
1.418	0.596	0.078
1.432	0.598	0.053
1.447	0.668	0.042
1.463	0.725	0.033
1.479	0.741	0.034
1.495	0.788	0.038
1.511	0.912	0.036
1.526	0.987	0.036
1.540	1.059	0.038
1.553	1.117	0.038

Wavelength (μ**m**)	**Flux** ($10^{-15} \times W/\mathrm{m}^2/\mu$**m**)	**Flux Error** ($10^{-15} \times W/\mathrm{m}^2/\mu$**m**)
1.568	1.179	0.040
1.582	1.217	0.040
1.599	1.266	0.044
1.613	1.235	0.041
GPI (*H*)		
1.506	0.789	0.022
1.510	0.798	0.022
1.516	0.841	0.024
1.522	0.890	0.025
1.531	0.936	0.026
1.539	0.983	0.028
1.547	1.046	0.031
1.554	1.107	0.031
1.562	1.153	0.032
1.572	1.183	0.033
1.581	1.218	0.033
1.589	1.233	0.034
1.597	1.220	0.033
1.605	1.216	0.032
1.613	1.210	0.031
1.621	1.201	0.032
1.630	1.210	0.033
1.638	1.208	0.032
1.646	1.183	0.031
1.654	1.181	0.032
1.662	1.180	0.032
1.670	1.172	0.033
1.678	1.171	0.033
1.686	1.153	0.032
1.695	1.143	0.031
1.703	1.126	0.030
1.711	1.084	0.029
1.719	1.050	0.028
1.727	1.007	0.027
1.735	0.949	0.025

Wavelength (μ**m**)	**Flux** ($10^{-15} \times W/\mathrm{m}^2/\mu$**m**)	**Flux Error** ($10^{-15} \times W/\mathrm{m}^2/\mu$**m**)
1.743	0.878	0.023
1.751	0.818	0.022
1.758	0.759	0.021
1.765	0.693	0.019
1.772	0.630	0.017
1.777	0.570	0.018
1.781	0.525	0.015
GPI (K_1)		
1.892	0.547	0.063
1.898	0.627	0.054
1.905	0.608	0.081
1.907	0.671	0.032
1.916	0.654	0.026
1.924	0.624	0.020
1.932	0.588	0.019
1.941	0.567	0.019
1.950	0.559	0.018
1.960	0.561	0.019
1.969	0.582	0.020
1.977	0.582	0.018
1.985	0.561	0.018
1.993	0.564	0.018
2.003	0.633	0.018
2.016	0.694	0.021
2.025	0.693	0.022
2.033	0.692	0.022
2.041	0.697	0.022
2.049	0.727	0.022
2.059	0.759	0.023
2.069	0.762	0.025
2.077	0.772	0.027
2.086	0.744	0.022
2.094	0.752	0.023
2.103	0.764	0.028
2.111	0.790	0.024

Wavelength (μm)	**Flux ($10^{-15} \times W/\mathrm{m}^2/\mu\mathrm{m}$)**	**Flux Error ($10^{-15} \times W/\mathrm{m}^2/\mu\mathrm{m}$)**
2.120	0.790	0.028
2.129	0.778	0.028
2.138	0.787	0.024
2.147	0.771	0.025
2.155	0.749	0.022
2.163	0.728	0.021
2.170	0.695	0.022
2.176	0.662	0.023
2.181	0.615	0.022
2.183	0.471	0.025

Table 2.5: Extracted GPI Astrometry for HD 4747 B

Time (BJD)	**Separation (arcsec)**	**Position angle (deg)**
2457380.5	0.5989 ± 0.002	183.9 ± 0.2
2457381.5	0.5984 ± 0.002	183.5 ± 0.2

2.12 Priors and posteriors for retrieval parameters

Here we list the priors on our retrieved parameters and include joint posterior distributions of selected parameters from our baseline HRS and LRS retrievals.

Table 2.6: Priors of the HD 4747 B retrieval. $\mathcal{U}$ stands for a uniform distribution, with two numbers representing the lower and upper boundaries. $\mathcal{G}$ stands for a Gaussian distribution, with numbers representing the median and standard deviation. (a) and (b): These priors follow P. Mollière et al. (2020). $P_{\rm phot}$ is the pressure where $\tau = 1$, and $T_{\rm connect}$ is the uppermost temperature of the 'photospheric' layer, and is computed by setting $\tau = 0.1$ in the Eddington Approximation (see eq. 1 and 2 in P. Mollière et al. 2020). This prior, along with those on T_1 and T_2 are used to prevent temperature inversions. (c) $\tilde{X}_{\rm MgSiO_3/Fe}$ represents the scaling factor for the cloud mass fraction, so that $\log(\tilde{X}_{\rm MgSiO_3/Fe}) = 0$ refers to a fraction equal to the equilibrium mass fraction. $f_{\rm sed}$, $K_{\rm zz}$, and $\sigma_{\rm g}$ are parameters in the EddySed cloud model (Ackerman et al., 2001). When fitting molecular abundances directly (e.g. in § 2.5), we use the same mass fraction prior on all molecules included.

Parameter	Prior	Parameter	Prior
Mass ($M_{\rm Jup}$)	$\mathcal{G}(67.2, 1.8)$	C/O	$\mathcal{U}(0.1, 1.6)$
Radius ($R_{\rm Jup}$)	$\mathcal{U}(0.6, 1.2)$	$[Fe/H]$	$\mathcal{U}(-1.5, 1.5)$
T_1 (K)	$\mathcal{U}(0, T_2)$	$\log(P_{\rm quench}/{\rm bar})$	$\mathcal{U}(-4, 3)$
T_2 (K)	$\mathcal{U}(0, T_3)$	$f_{\rm sed}$	$\mathcal{U}(0, 10)$
T_3 (K)	$\mathcal{U}(0, T_{\rm connect})^{(a)}$	$\log(K_{\rm zz}/{\rm cm^2 s^{-1}})$	$\mathcal{U}(5, 13)$
$T_{\rm int}$ (K)	$\mathcal{U}(700, 2500)$	$\sigma_{\rm g}$	$\mathcal{U}(1.05, 3)$
α	$\mathcal{U}(1, 2)$	$\log(\tilde{X}_{\rm MgSiO_3})^{(c)}$	$\mathcal{U}(-2.3, 1)$
$\log(\delta)$	$P_{\rm phot} \in [10^{-3}, 100]^{(b)}$	$\log(\tilde{X}_{\rm Fe})$	$\mathcal{U}(-2.3, 1)$
Additional parameters for HRS			
RV (km/s)	$\mathcal{U}(-30, 30)$	$v \sin i$ (km/s)	$\mathcal{U}(0, 50)$
Error multiple	$\mathcal{U}(1, 4)$	Flux scale (counts)	$\mathcal{U}(0, 200)$
Gaussian process parameters for LRS			
$\log(f_{\rm amp})$	$\mathcal{U}(10^{-4}, 1)$	$\log(l)$ $(\mu{\rm m})$	$\mathcal{U}(10^{-3}, 0.5)$
Mass fraction of molecules			
log(MMR)	$\mathcal{U}(10^{-1}, 10^{-7})$		

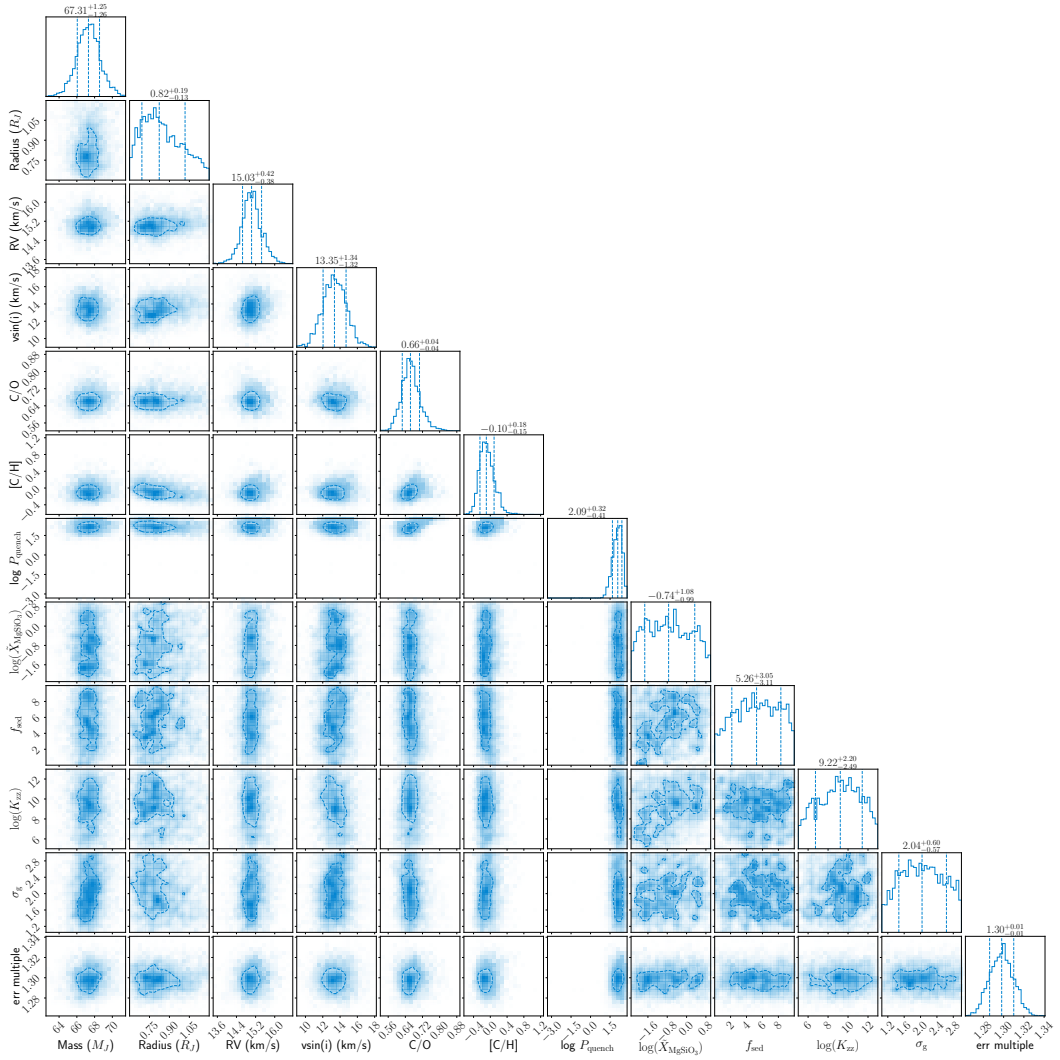

Figure 2.15: Joint posterior distributions for the HRS retrieval of HD 4747 B. We omit the P-T profile parameters, which are better visualized by the P-T plot in Fig. 2.6.

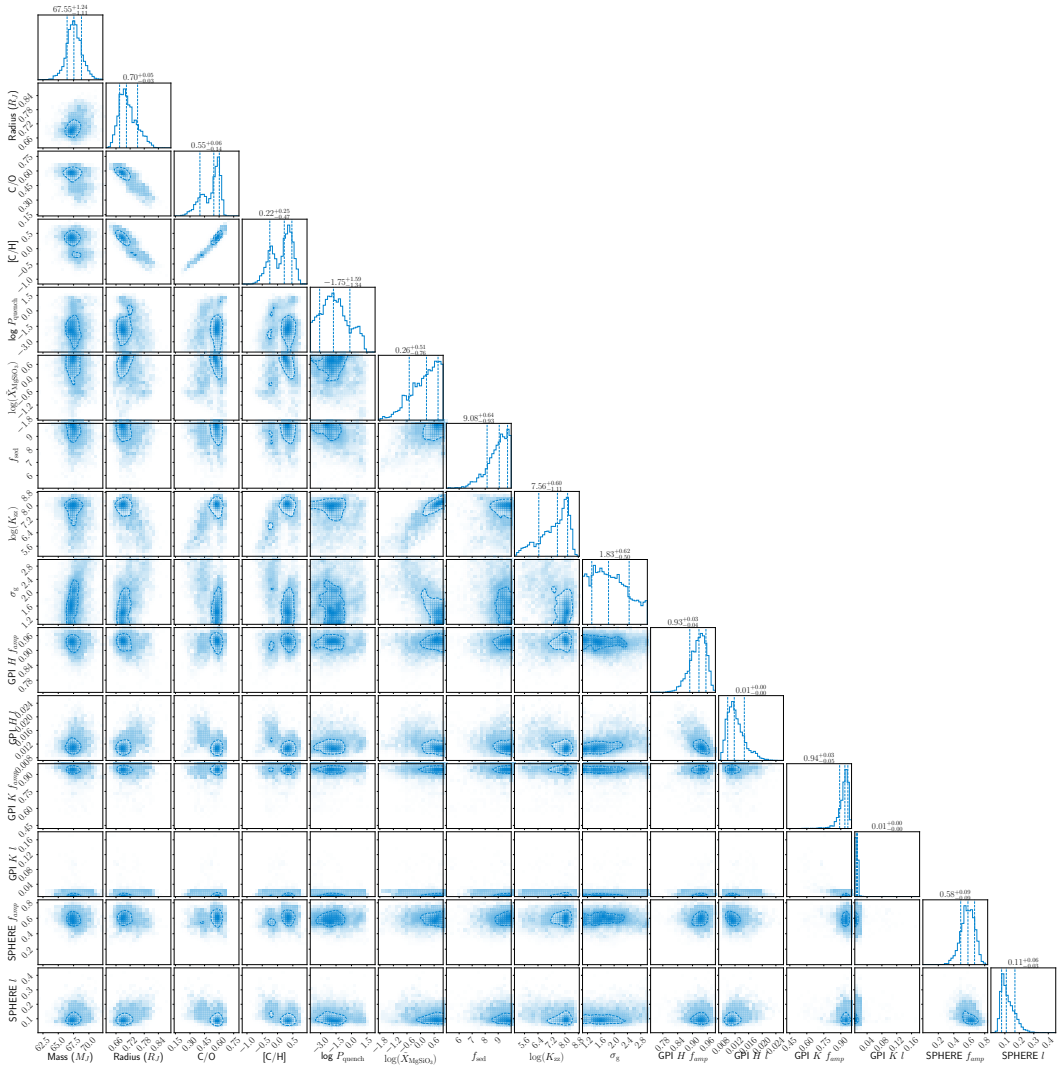

Figure 2.16: Joint posterior distributions for the LRS retrieval of HD 4747 B. We omit the P-T profile parameters, which are better visualized by the P-T plot in Fig. 2.6. The distribution for a few parameters are bi-modal.

Chapter 3

VALIDATION OF ELEMENTAL AND ISOTOPIC ABUNDANCES IN LATE-M SPECTRAL TYPES WITH THE BENCHMARK HIP 55507 AB SYSTEM

This chapter reproduces my second KPIC paper, where I study the HIP 55507 AB system. This paper grew out of my interest in searching for new planets and brown dwarfs using the Hipparcos-Gaia Catalog of Accelerations (HGCA) by Brandt et al. I first identified HIP 55507 B as a potential substellar companion from analyzing Keck/HIRES radial velocity data, the HGCA, and an archival Keck/NIRC2 observation from 2012. I subsequently imaged the companion myself with NIRC2 in 2022 and 2023 to extend the astrometric baseline. I identified a mistake in the archival astrometry, which led me to re-analyze the archival NIRC2 data. When combining all the data, I found that the companion is in fact a low-mass star, right above the hydrogen-burning limit. To accomodate the higher temperature of this star in my retrieval framework, I upgraded the molecular opacities to reach 4500 K or higher. I also analyzed the primary star spectrum from KPIC. Given the high S/N of the data (due to the companion's brightness), I focused the paper on isotopic ratio comparisons between the primary star and the companion.

Xuan, J. W. et al. (Feb. 2024). "Validation of Elemental and Isotopic Abundances in Late-M Spectral Types with the Benchmark HIP 55507 AB System". In: *The Astrophysical Journal* 962.1, 10, p. 10. DOI: 10.3847/1538-4357/ad1243.

Abstract

M dwarfs are common host stars to exoplanets but often lack atmospheric abundance measurements. Late-M dwarfs are also good analogs to the youngest substellar companions, which share similar $T_{\rm eff} \sim 2300 - 2800$ K. We present atmospheric analyses for the M7.5 companion HIP 55507 B and its K6V primary star with Keck/KPIC high-resolution ($R \sim 35,000$) K band spectroscopy. First, by including KPIC relative radial velocities between the primary and secondary in the orbit fit, we improve the dynamical mass precision by 60% and find $M_B = 88.0^{+3.4}_{-3.2}\ M_{\rm Jup}$, putting

HIP 55507 B above the stellar-substellar boundary. We also find that HIP 55507 B orbits its K6V primary star with $a = 38^{+4}_{-3}$ AU and $e = 0.40 \pm 0.04$. From atmospheric retrievals of HIP 55507 B, we measure $[C/H] = 0.24 \pm 0.13$, $[O/H] = 0.15 \pm 0.13$, and C/O=0.67 ± 0.04. Moreover, we strongly detect ^{13}CO (7.8σ significance) and tentatively detect $H_2^{18}O$ (3.7σ significance) in companion's atmosphere, and measure $^{12}CO/^{13}CO = 98^{+28}_{-22}$ and $H_2^{16}O/H_2^{18}O = 240^{+145}_{-80}$ after accounting for systematic errors. From a simplified retrieval analysis of HIP 55507 A, we measure $^{12}CO/^{13}CO = 79^{+21}_{-16}$ and $C^{16}O/C^{18}O = 288^{+125}_{-70}$ for the primary star. These results demonstrate that HIP 55507 A and B have consistent $^{12}C/^{13}C$ and $^{16}O/^{18}O$ to the $< 1\sigma$ level, as expected for a chemically homogeneous binary system. Given the similar flux ratios and separations between HIP 55507 AB and systems with young, substellar companions, our results open the door to systematically measuring ^{13}CO and $H_2^{18}O$ abundances in the atmospheres of substellar or even planetary-mass companions with similar spectral types.

3.1 Introduction

The elemental abundances of exoplanets and substellar companions encode their accretion history, providing valuable insights into planet and star formation mechanisms. It is now well-recognized that measuring abundance ratios besides C/O are crucial for breaking degeneracies and providing a more complete picture of substellar atmospheres (e.g. Cridland et al., 2020; Turrini et al., 2021; P. Mollière et al., 2022; Chachan et al., 2023) when compared to abundance measurements of their host stars. Recently, isotopologue ratios have also emerged as an observable in substellar atmospheres (Morley et al., 2019; P. Mollière et al., 2019a). Y. Zhang et al. (2021b) measured $^{12}CO/^{13}CO = 31^{+17}_{-10}$ for the young super Jupiter TYC 8998-760-1 b, while Line et al. (2021) reported $^{12}CO/^{13}CO = 10.2\tilde{}42.6$ for the hot Jupiter WASP-77 Ab. Finnerty et al. (2023) also reported a tentative ^{13}CO enrichment for WASP-33 b, although higher signal-to-noise (S/N) data is needed to confirm this result. On the other hand, Y. Zhang et al. (2021a) reported $^{12}CO/^{13}CO = 97^{+25}_{-17}$ for an isolated brown dwarf. These results potentially indicate that the varying $^{12}C/^{13}C$ of these objects can be used to constrain their formation histories. However, more analysis and measurements are required to bolster our confidence in these results (Line et al., 2021).

There are abundant measurements of isotopologues in the stellar literature, especially for giant stars. More recently, studies have measured isotopologue ratios in dwarf stars (e.g. Crossfield et al., 2019; Botelho et al., 2020; Coria et al., 2023), which

are thought to better preserve the initial isotopic abundances in their envelopes compared to giant stars, and therefore useful for constraining galactic chemical evolution (Romano et al., 2017). For context, the Sun has $^{12}C/^{13}C = 93.5 \pm 3.1$ and $^{16}O/^{18}O = 525 \pm 21$ (Lyons et al., 2018), while the average local interstellar medium values are $^{12}C/^{13}C = 69 \pm 6$ and $^{16}O/^{18}O = 557 \pm 30$ (Wilson, 1999). In circumstellar disks, the relative isotopic abundances can differ from the inherited interstellar medium values due to processes such as self-shielding. For example, Calahan et al. (2022) showed that in certain regions of the inner disk, self-shielding of CO, $C^{18}O$ and UV-shielding of H_2O can result in an enhanced $H_2^{18}O$ abundance at the expense of $C^{18}O$. In Y. Zhang et al. (2021b), the authors proposed that ices beyond the CO snow line may be ^{13}CO-rich, so if a planet accreted a significant amount of ice beyond the CO snow line it may exhibit a lower $^{12}CO/^{13}CO$ value compared to its host star. However, more detailed modeling work is needed to understand the details of isotopic composition and fractionation chemistry in circumstellar disks (Öberg et al., 2023).

In this work, we study the HIP 55507 AB system, which consists of a M7.5 companion that orbits at ~40 AU from its K6V primary star. The M dwarf companion was initially identified from a radial velocity (RV) trend and later confirmed by adaptive optics imaging (E. J. Gonzales et al., 2020). Using K-band high-resolution ($R \sim 35,000$) spectra from Keck/KPIC, we carry out an atmospheric retrieval analysis of HIP 55507 B to measure the C/O, $[C/H]$, $^{12}CO/^{13}CO$, and $H_2^{16}O/H_2^{18}O$ in its atmosphere. In addition, we analyze the KPIC spectra of the primary star, HIP 55507 A, to measure its $^{12}CO/^{13}CO$ and $C^{16}O/C^{18}O$ using a simplified version of the same framework.

From the high-resolution spectra, we also measure the radial velocities (RV) of both stars to compute their relative RV. Relative RV data have been shown to improve orbital constraints for directly imaged companions especially when the other data only sparsely cover the orbital period (Schwarz et al., 2016; Ruffio et al., 2019; Do Ó et al., 2023). We include the KPIC relative RVs in orbit fits to measure the companion's orbital parameters and dynamical mass.

This paper is organized as follows. In § 3.2, we describe the properties of HIP 55507 A, including an estimate of its age. The Keck/HIRES, Keck/NIRC2, and Keck/KPIC observations and data reduction are detailed in § 3.3. In § 3.4, we summarize the orbit fits for HIP 55507 B. § 3.5 lays out our spectral analysis framework for both HIP 55507 A and B, including the retrieval setup. § 3.6 de-

scribes the lessons from our of injection-recovery tests for atmospheric retrievals of HIP 55507 B. The main results of our spectral analysis are described in § 3.7, with our conclusions in § 3.8.

3.2 Primary star properties

HIP 55507 A is a K6V star located at 25.41 pc with $M = 0.67 \pm 0.02\ M_{\odot}$ and $T_{\rm eff} = 4250 \pm 90$ K (Yee et al., 2017; Sebastian et al., 2021; Stassun et al., 2019; Anders et al., 2022). By comparing the star's Keck/HIRES optical spectra with an empirical spectral library using the `SpecMatch-Emp` tool (Yee et al., 2017), we obtain $[Fe/H] = -0.02 \pm 0.09$ for the star.[1] We tabulate the literature properties of HIP 55507 A in Table 3.1. HIP 55507 A hosts a low-mass companion first detected from RV and direct imaging as part of the TRENDS survey (E. J. Gonzales et al., 2020).

We estimated the age of HIP 55507 A in two ways. First, we searched for lithium with the ARC Echelle Spectrograph (S.-i. Wang et al., 2003) at the Apache Point Observatory 3.5 m on 2023/04/30. The spectrum was reduced with `pyvista`.[2] The spectrum is placed at rest wavelengths by applying a barycentric correction and removing the radial velocity measured by Gaia DR2 (Gaia Collaboration et al., 2018). No Li absorption is visible at 6707.79 Å above the noise and we determine an upper limit of 20 mÅ on the lithium equivalent width (EW) by constructing a series of Li lines with Gaussian profiles of varying EWs. With this EW upper limit, we place a lower limit on the stellar age using BAFFLES (Stanford-Moore et al., 2020), which uses a Bayesian framework to calculate probability distributions on stellar age for single stars based on Li EW measurements of stars in stellar associations with robust ages. BAFFLES can derive a probability distribution function for a field star given an upper limit on Li EW by using fits to the median Li EW as a function of B-V for each cluster and the scatter about those relations. Given a Li EW upper limit of 20 mÅ and B-V=1.24 for HIP 55507 A, we find 2σ and 3σ lower age limits of 838 and 286 Myr, respectively (see Fig 3.1).

We also searched TESS light curves for rotational modulation using the `lightkurve` package (Lightkurve Collaboration et al., 2018). HIP 55507 A was observed over two consecutive TESS sectors covering a baseline of 57 days. From the light

[1] The error bar of 0.09 dex comes from the root-mean-square difference between the measured [Fe/H] of stars in the spectral library and their derived [Fe/H] from `SpecMatch-Emp`. It is the recommended uncertainty to adopt when using `SpecMatch-Emp` (Yee et al., 2017).

[2] https://pyvista.readthedocs.io/en/latest/index.html

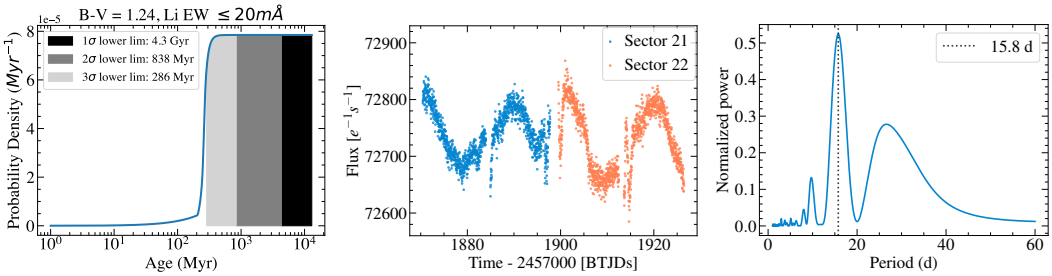

Figure 3.1: Left: The posterior probability distribution function for the age of HIP 55507 A from BAFFLES (solid blue line), given a lithium equivalent width upper limit of 20 mÅ and B-V=1.24. The different shaded regions are 1, 2, and 3σ lower limits for the age. Middle: TESS light curves from Sectors 21 and 22 extracted from the lightkurve package showing periodic modulation. Right: Interpreting this as rotational modulation, a Lomb-Scargle periodogram shows a rotation period of 15.8 ± 1.8 days. The uncertainties on the rotation period were determined from the full-width half maximum of the peak. These two lines of evidence both point towards an age of $\approx 1-2$ Gyr for the star.

curves, we found a clear periodic signal of 15.8 days (see Fig 3.1). Nearby stars within 15 arcmin do not exhibit similar modulation, suggesting the modulation likely originates from HIP 55507 A. If we attribute the periodic signal to the stellar rotation period, a Lomb-Scargle analysis of the two TESS sectors yields a period of 15.8 ± 1.8 days. Given $T_{\rm eff}$ = 4250 ± 90 K, we use the gyrochronology tool from Bouma et al. (2023) to derive an age of $1.7^{+0.4}_{-0.7}$ Gyr. Therefore, both the lack of Li and relatively slow rotation point to an age of $\sim 1-2$ Gyr for HIP 55507 A.

Table 3.1: Properties of HIP 55507 AB

Property	**Value**	**References**
HIP 55507 A		
$\alpha_{2000.0}$	11:22:05.75	1
$\delta_{2000.0}$	+46:54:30.2	1
π^a (mas)	39.35 ± 0.015	1
Distance (pc)	25.41 ± 0.02	1
$\mu_\alpha \cos\delta$ (mas yr^{-1})	−197.49 ± 0.01	1
μ_δ (mas yr^{-1})	−134.78 ± 0.01	1
SpT	K6V	4
Gaia G (mag)	9.271 ± 0.003	1
J (mag)	7.367 ± 0.021	6
H (mag)	6.760 ± 0.042	6

Property	Value	References
K_s (mag)	6.613 ± 0.021	6
$W1$ (mag)	6.544 ± 0.075	7
$W2$ (mag)	6.553 ± 0.023	7
Age (Gyr)	$1.7^{+0.4}_{-0.7}$	This paper
Mass[a] ($M_\odot$)	0.67 ± 0.02	2,3,4,5
Literature $T_{\rm eff}$ (K)	4250 ± 90	2,3,5
Literature $\log g$ (dex)	4.58 ± 0.06	3,4,5,8
Literature $v \sin i$ (km s^{-1})	3.0 ± 1.0	5
$T_{\rm eff}$ (K)	4200 ± 50	This paper
$\log g$ (dex)	4.40 ± 0.25	This paper
$P_{\rm rot}$ (days)	15.8 ± 1.8	This paper
[Fe/H]	-0.02 ± 0.09	This paper
^{12}CO/^{13}CO	79^{+21}_{-16}	This paper
C^{16}O/C^{18}O	288^{+125}_{-70}	This paper
HIP 55507 B		
SpT	M7.5	This paper
Mass ($M_{\rm Jup}$)	$88.0^{+3.4}_{-3.2}$	This paper
$v \sin i$ (km s^{-1})	5.50 ± 0.25	This paper
[C/H]	0.24 ± 0.13	This paper
[O/H]	0.15 ± 0.13	This paper
C/O	0.67 ± 0.04	This paper
^{12}CO/^{13}CO	98^{+28}_{-22}	This paper
$H_2^{16}O/H_2^{18}O$	240^{+145}_{-80}	This paper

Notes: (a) We correct for the DR3 parallax zeropoint following the guidelines in Lindegren et al. (2021). (b) The literature values for the stellar mass, $T_{\rm eff}$, and $\log g$ agree reasonably, so we take the weighted average from the more recent papers and adopt the standard deviation of the different values as the uncertainty for each parameter.

References: (1) Gaia Collaboration et al. (2023), (2) Sebastian et al. (2021), (3) Stassun et al. (2019), (4) Petigura (2015), (5) Anders et al. (2022), (6) Cutri et al. (2003), (7) Cutri et al. (2021), (8) Fouesneau et al. (2022), (9) Yee et al. (2017).

3.3 Observations and data reduction

Keck/HIRES

We collected spectra of HIP 55507 A from April 2009 to June 2023 using the High Resolution Echelle Spectrometer (HIRES, $R \approx 60,000$; Vogt et al. 1994) at the W.M. Keck Observatory. The data from 2009 to 2015 were collected as part of the M2K program (Gaidos et al., 2013). The observation setup is the same as that used by the California Planet Search (Howard et al., 2010). The wavelength calibration was computed using an iodine gas cell in the light path. A iodine-free template spectrum bracketed by observations of rapidly rotating B-type stars was used to deconvolve the stellar spectrum from the spectrograph point-spread function. We then forward model the spectra taken with the iodine cell using the deconvolved template spectra, the point-spread function model and the iodine cell line atlas (Butler et al., 1996). The Keck/HIRES RVs are presented in Appendix 3.10, and show a long-term trend with curvature, which is induced by HIP 55507 B (Appendix 3.10).

Keck/NIRC2

We observed HIP 55507 B in L' band on UT 2021 May 19 and K and M_s bands on UT 2022 June 9 using Keck/NIRC2. We did not use a focal plane mask but observed in pupil tracking mode to exploit sky rotation for angular differential imaging (ADI, Liu 2004; Marois et al. 2006). HIP 55507 B was also imaged with Keck/NIRC2 on UT 2012 Jan 7 and 2015 May 29 (PI: Justin Crepp) as part of the TRENDS survey (E. J. Gonzales et al., 2020). The astrometry from E. J. Gonzales et al. (2020) shows a $\sim 100°$ discrepancy in position angle (PA) compared to calibrated images on the Keck Observatory Archive (KOA).[3], which could be caused by a mismatch between pupil tracking and field tracking modes used in each observation (E. Gonzales, priv. commun.). Therefore, we re-analyzed the archival NIRC2 data from E. J. Gonzales et al. (2020) to update the astrometry. Finally, we include a single astrometric epoch from UT 2021 Dec 21 reported in Franson et al. (2023c).

We first pre-process the data using the Vortex Imaging Processing (VIP) software package (Gomez Gonzalez et al., 2017; Christiaens et al., 2023). We perform flat-fielding, bad-pixel removal, and correct for geometric distortions by applying the solution in Service et al. (2016) for observations after the NIRC2 camera and adaptive optics system were realigned on UT 2015 April 13 and the solution from Yelda et al. (2010) for the archival 2012 observation. Then, we perform sky-subtraction following the procedure described in W. J. Xuan et al. (2018). To

[3] `https://koa.ipac.caltech.edu/cgi-bin/KOA/nph-KOAlogin`

register the HIP 55507 B frames, we identify the star's position by fitting a 2D Gaussian to the stellar point spread function (PSF) in each frame.

After obtaining the pre-processed cubes, we extracted the astrometry and photometry of the companion using `pyKLIP` (J. J. Wang et al., 2015), which models a stellar PSF with Karhunen-Loève Image Processing (KLIP) following the framework in Soummer et al. (2012) and Pueyo (2016). We used ADI to subtract the stellar PSF and tested various model choices to minimize the residuals after stellar PSF subtraction while preserving the companion signal, following guidelines in Redai et al. (2023). The 2015 observations for HIP 55507 used field tracking mode, so we used a least-squares minimization code to compute the astrometry. We note that our measured astrometry from the archival E. J. Gonzales et al. (2020) data agree at the $< 1\sigma$ level with those reported in Franson et al. (2023c), who also re-analyzed these data.

Table 3.2: NIRC2 Astrometry and Photometry for HIP 55507 B

Time (JD-2400,000)	UT Date	Filter	Sep. (mas)	PA (deg)	Δm	m	$M_{\rm abs}$	Ref.
55934.1	2012-01-07[a]	H	475.6 ± 3.0	292.33 ± 0.36	N/A	N/A	N/A	1
55934.1	2012-01-07[a]	K'	475.6 ± 3.0	292.50 ± 0.36	N/A	N/A	N/A	1
57171.7	2015-05-29[a]	$K_{\rm cont}$	550.7 ± 3.0	274.93 ± 0.40	N/A	N/A	N/A	1
59353.7	2021-05-19	L'	732.0 ± 3.0	254.75 ± 0.24	4.75 ± 0.01	11.29 ± 0.08	9.27 ± 0.08	2
59569.7	2021-12-21[b]	$K_{\rm s}$	748 ± 5	254.04 ± 0.20	N/A	N/A	N/A	3
59739.7	2022-06-09	$M_{\rm s}$	773.1 ± 5.0	252.04 ± 0.40	4.99 ± 0.05	11.54 ± 0.06	9.52 ± 0.06	2
59739.7	2022-06-09	K	767.0 ± 3.1	252.30 ± 0.23	5.07 ± 0.03	11.66 ± 0.04	9.63 ± 0.04	2
60034.96	2023-03-31	K	789.9 ± 3.0	250.96 ± 0.40	5.05 ± 0.05	11.64 ± 0.04	9.61 ± 0.05	2

Notes: (a) We re-analyzed the data from these epochs to revise the astrometry. Photometry from these epochs is unreliable due to occultation of the central star by the Lyot Coronagraph. (b) This epoch is from Franson et al. (2023c), who did not quote photometry.
References: (1) E. J. Gonzales et al. (2020), (2) This paper, (3) Franson et al. (2023c).

Table 3.3: KPIC Observations of HIP 55507 AB

UT Date	Target	Exposure Time [min]	Airmass	Throughput	Median S/N per pixel	Science Fibers
2021 July 4	HIP 55507 A	2	1.4	1.1%	150	2,3
2021 July 4	HIP 55507 B	40	1.4	1.1%	10.6	2,3
2023 May 2	HIP 55507 A	4	1.1	4.6%	225	2,3
2023 May 2	HIP 55507 B	30	1.1	4.6%	22.3	2,3

Notes: The throughput is the end-to-end throughput measured from the top of the atmosphere, varying with wavelength due to differential atmospheric refraction and the instrumental blaze function. The throughput is computed using the HIP 55507 A spectra and its 2MASS K_s = 6.613 (Cutri et al., 2003). We report the 95% percentile throughput over the K band, averaged over all frames. The median spectral S/N per pixel from 2.29-2.49 μm is also reported.

From pyKLIP forward modeling (J. J. Wang et al., 2016), we obtain the flux ratio between the star and companion for each photometric band, which we convert to apparent and absolute magnitudes. For L' and M_s bands, we scale the flux ratios to the primary star's $W1$ and $W2$ mag respectively.[4] We convert the 2MASS K into MKO K for HIP 55507 A using color relations in Leggett et al. (2006), before calculating the MKO K for HIP 55507 B. The measured astrometry and photometry are provided in Table 3.2, and an example of the pyKLIP forward modeling is shown in Appendix 3.10.

Keck/KPIC

We observed the HIP 55507 AB system with the upgraded Keck/NIRSPEC (Martin et al., 2018) using the KPIC fiber injection unit (FIU; Mawet et al. 2017; Delorme et al. 2021; Echeverri et al. 2022) on UT 2021 July 4 and 2023 May 2 (see Table 3.3). The FIU is located downstream of the Keck II adaptive optics system and is used to inject light from a selected target into one of the single-mode fibers connected to NIRSPEC. We obtained $R \sim 35,000$ spectra in K band, which is broken up into nine echelle orders from 1.94-2.49 μm. The observing strategy is similar to that of J. J. Wang et al. (2021c), except we 'nodded' between two fibers to enable background subtraction between adjacent frames. We also acquire short exposures of HIP 55507 A before observing the companion, and spectra of a nearby A0 standard star (HIP 56147) at similar airmass.

We briefly summarize the KPIC data reduction procedure with the public Python pipeline.[5] For details, see J. J. Wang et al. (2021c). First, we apply nod-subtraction between adjacent frames as the spectral traces of each fiber lands on a different location in the detector. We also remove persistent bad pixels identified from the background frames. Then, we use data from the telluric standard star to fit the trace of each column in the four fibers (two of which contain science data) and nine spectral orders, which give the position and standard deviation of the PSF in the spatial direction at each column. The trace positions and widths are additionally smoothed using a cubic spline to mitigate random noise.

For every frame, we extracted the 1D spectra in each column of each spectral order. To remove residual background light, we subtracted the median of pixels that are at least 5 pixels away from every pixel in each column. Finally, we used optimal

[4] We assume the stars have L'-$W1$ = 0 and M_s'-$W2$ = 0 as these photometric bands are in the Rayleigh–Jeans tail of the spectral energy distribution for HIP 55507 A.

[5] https://github.com/kpicteam/kpic_pipeline

extraction (Horne, 1986) to sum the flux using weights defined by the 1D Gaussian line-spread function (LSF) profiles calculated from spectra of the telluric star.

For our analysis, we use three spectral orders from 2.29-2.49 μm, which contain strong absorption lines of CO and H_2O from the companion, and CO from the primary star. These orders also have relatively few telluric absorption lines. Note that the three spectral orders have gaps in between them, so the KPIC data effectively cover a range of ≈ 0.13 μm after accounting for the gaps.

Table 3.4: Selected parameters from orbit fit

Parameter	**Value**
M ($M_\odot$)	0.675 ± 0.037
m (M_J)	$88.0^{+3.4}_{-3.2}$
a (AU)	$37.8^{+3.5}_{-2.7}$
Inclination (deg)	119.3 ± 0.7
Ascending node (deg)	219.9 ± 0.7
Period (yr)	266^{+44}_{-33}
Argument of periastron (deg)	$243.9^{+5.3}_{-5.8}$
Eccentricity	0.40 ± 0.04
Epoch of periastron (JD)	$2549330^{+16644}_{-12418}$

Notes: A Gaussian prior of 0.67 ± 0.04 $M_\odot$ was imposed on the primary star mass.

3.4 Basic properties of HIP 55507 B

Orbit fits with relative RVs

The relative radial velocity (RV) between HIP 55507 A and B can be directly measured from our KPIC data. From the two KPIC epochs, we extract two relative RV points (listed in Appendix 3.10) from fitting the KPIC spectra of both HIP 55507 A and B (see § 3.5).

In the Hipparcos-Gaia Catalog of Accelerations (T. D. Brandt, 2021a), HIP 55507 A shows a significant proper motion anomaly with S/N of $\approx$ 28 in the Gaia epoch, with an amplitude that is consistent with being induced by HIP 55507 B. We perform orbit fits using RVs of HIP 55507 A from HIRES, relative astrometry from NIRC2 imaging, Gaia and Hipparcos absolute astrometry, and two relative RV points between HIP 55507 A and B from KPIC. We use the `orvara` package (T. D. Brandt et al., 2021) for these fits, which is able to jointly fit the aforementioned data. For the primary mass, we use a Gaussian prior of 0.67 ± 0.04 $M_\odot$, doubling the standard

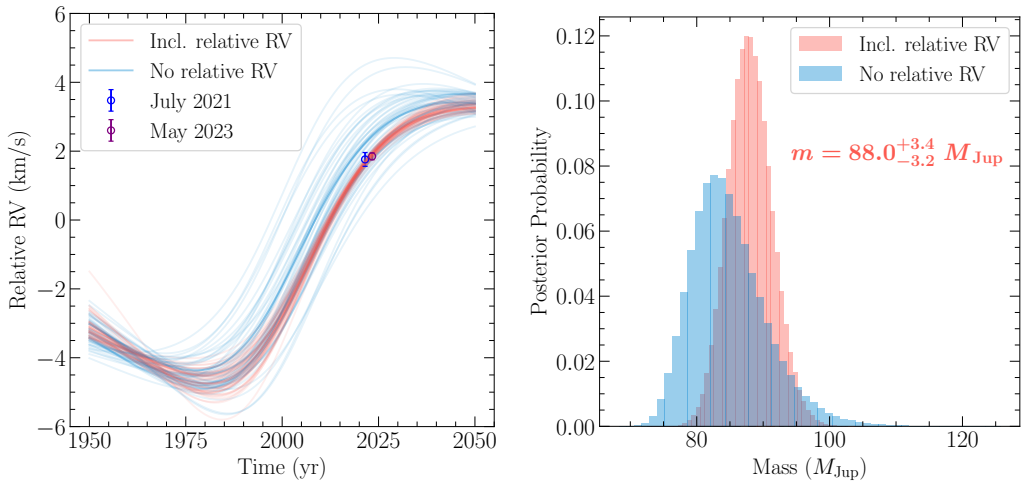

Figure 3.2: Left: model relative RV of the HIP 55507 AB system over time from random draws to the posterior distributions of the orbit fits. The red and blue curves are from the fit with and without the relative RVs, respectively. The data points show the observed relative RVs from KPIC. Right: The companion mass posteriors with (red) and without (blue) using the relative RVs, which show a reduction in the mass uncertainty and a slight shift of the median value when the relative RV is incorporated.

deviation of 0.02 $M_\odot$ between literature mass measurements (Table 3.1). We use log-uniform or uniform priors on the other parameters following T. D. Brandt et al. (2021). We tested orbit fits where we further increase the width of the primary mass prior to $0.67 \pm 0.08\ M_\odot$ (or 12% of the mass), and find the resulting posterior for companion mass shifts by $< 1\%$, while the uncertainties on all parameters are consistent to the $< 15\%$ level.

Our orbit and mass measurements are summarized in Table 3.4. We find a dynamical mass of $88.0^{+3.4}_{-3.2}\ M_{\rm Jup}$ from this baseline fit. We run a second orbit fit that excluded the KPIC relative RVs to assess their effect on the results. We find that the addition of the two relative RV points from KPIC reduces the companion's mass uncertainty by $\approx 60\%$ and shifts the median of the mass posterior to slightly higher values, as shown in Fig. 3.2. The uncertainty on the orbital eccentricity also reduces by $\approx 50\%$ when including the relative RVs, and we find a moderate eccentricity of 0.40 ± 0.04. In Fig. 3.2, we visualize the effect of the relative RVs by plotting random draws from the posteriors of the relative RV (red) and no relative RV fit (blue). While the overall orbital trend is constrained by the other data, the KPIC relative RVs help narrow down the spread in relative RV space, thereby reducing the companion mass uncertainty.

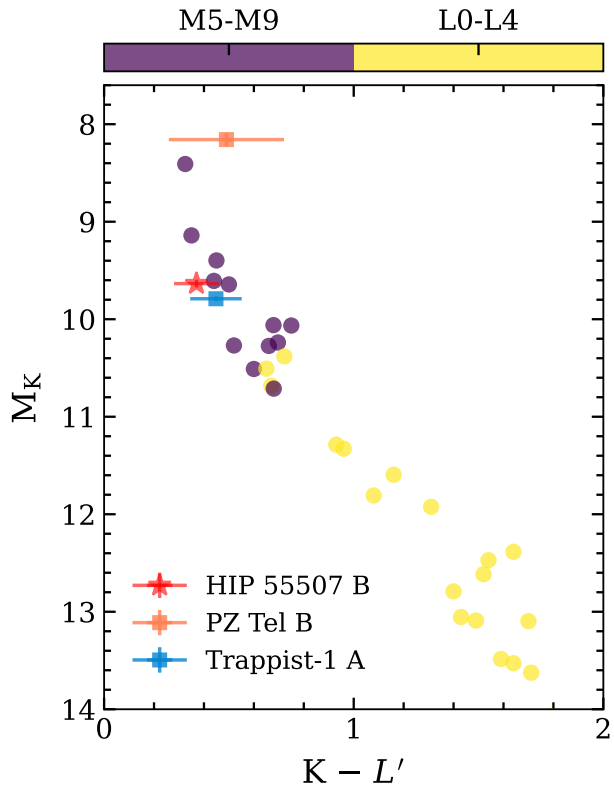

Figure 3.3: A color-magnitude diagram with M_K and $K - L'$. HIP 55507 B is shown as the red star, whereas purple and yellow points in the background are field brown dwarfs with late-M and early-L spectral types, respectively. We also label PZ Tel B, a late-M type substellar companion (Biller et al., 2010; Maire et al., 2016; Stolker et al., 2020), and Trappist-1 A (Cutri et al., 2003; Cutri et al., 2021), which have properties similar to HIP 55507 B.

Bulk properties and evolutionary state

We place HIP 55507 B on a color-magnitude diagram (CMD) in Fig. 3.3. As shown, HIP 55507 B is consistent with a late-M spectral type, and is located very close to Trappist-1 A (an M8.0 star; Gillon et al. 2016) on the CMD. Indeed, Trappist-1 A has an inferred mass of $93 \pm 6\ M_{\rm Jup}$ from model fitting (Grootel et al., 2018), very similar to the dynamical mass we measure for HIP 55507 B. Using relations in Dupuy et al. (2012) and our measured absolute $K_{\rm MKO}$ of 9.63 ± 0.04, we estimate a spectral type of M7.5 ± 0.5 for HIP 55507 B.

From our spectral retrievals on the KPIC K band spectra ($R \sim 35,000$) and K, L', M_s photometry, we estimate $\log(L_{\rm bol}/L_\odot) = -3.29 \pm 0.02$ for HIP 55507 B (see details in § 3.7).[6] In Fig. 3.4, we place HIP 55507 B's $L_{\rm bol}$ on isochrone tracks from Baraffe

[6]As a second estimate of $L_{\rm bol}$, we use the empirical relation from Sanghi et al. (2023) between

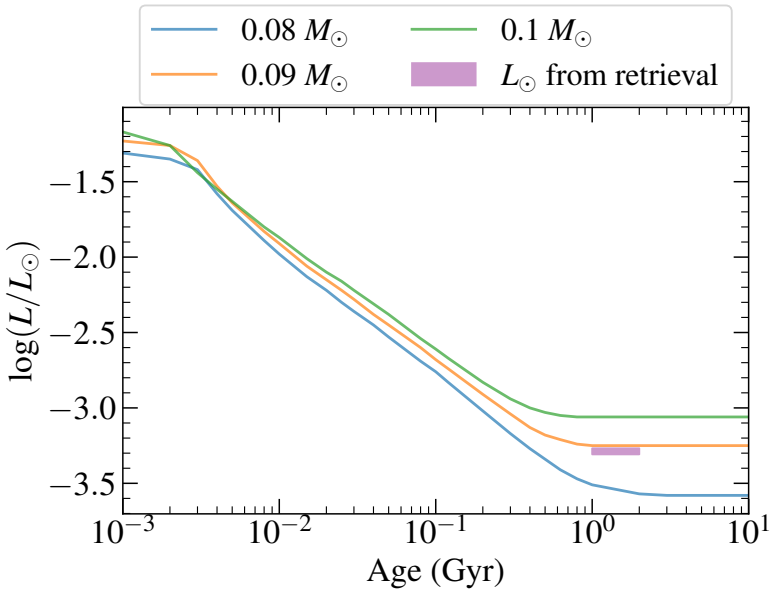

Figure 3.4: Isochrones from Baraffe et al. (2015) for three different masses. We show the measured $L_{\rm bol}$ for HIP 55507 B from spectral retrievals and the estimated age of 1-2 Gyr for the system as the purple shaded region. Both this region and the dynamical mass ($0.084 \pm 0.003 M_\odot$) lie in between the $0.08 M_\odot$ and $0.09 M_\odot$ isochrones, suggesting that HIP 55507 B's measured properties are consistent with the evolutionary model, and that it is likely on the hydrogen-burning main sequence.

et al. (2015), and find that the companion falls between the $0.08 M_\odot$ and $0.09 M_\odot$ isochrones. Therefore, the dynamical mass and $L_{\rm bol}$ for HIP 55507 B are consistent with the Baraffe et al. (2015) substellar model for an age of $\sim 1-2$ Gyr, suggesting that the companion has likely reached the hydrogen-burning main-sequence.

3.5 Spectral analysis framework

In this section, we describe the framework to analyze KPIC spectroscopy of both HIP 55507 A and B. First, we describe the forward model for KPIC (§ 3.5), including the model we use to fit fringing modulations (§ 3.5). Then, we describe the PHOENIX-ACES grid model fits to HIP 55507 A spectra (§ 3.5). Lastly, we layout the atmospheric retrieval setup (§ 3.5), which is applied to both HIP 55507 A and B to measure their molecular and/or isotopic abundances.

K_{MKO} and L_{bol} to obtain $\log(L_{\rm bol}/L_\odot) = -3.21 \pm 0.08$, where the rms scatter of the empirical relation is folded into our luminosity uncertainty. This is consistent with our spectrally-derived $L_{\rm bol}$.

Forward model of the KPIC spectrum

Our forward model for KPIC spectra largely follows the framework in J. W. Xuan et al. (2022), with a few updates. In summary, we generate atmospheric templates with `petitRADTRANS` (P. Mollière et al., 2019b; P. Mollière et al., 2020). These templates are shifted in RV and rotational broadening is performed using the open-source function from Carvalho et al. (2023).[7]

Next, we convolve the RV-shifted and rotationally-broadened templates with the instrumental LSF, which we determine from the spectral trace widths in the spatial direction (§ 3.3). As noted by J. J. Wang et al. (2021c), NIRSPEC was designed with a difference in focal lengths in the spatial and dispersion directions by a factor of 1.13 (Robichaud et al., 1998). Following J. J. Wang et al. (2021c), we conservatively allow the LSF width to vary between 1.0 and 1.2 times the width measured in the spatial direction when generating the instrument-convolved companion templates. This uncertainty propagates to our $v \sin i$ uncertainty.

Next, the atmospheric template is multiplied by the telluric and instrumental response, which we determine from spectra of the standard star HIP 56147. For the primary star, HIP 55507 A, that completes the forward model. For the companion, HIP 55507 B, the above procedures constitute a portion of its forward model. The other portion we need to consider for the companion is speckle contribution from the primary star, which we find to account for $\sim 1 - 10\%$ of the total flux in HIP 55507 B's spectra given the relatively small separation of $\approx 0.75 - 0.8''$ between HIP 55507 A and B. To model the speckle contribution in the companion data, we use observations of HIP 55507 A taken immediately before the companion exposures.

Finally, we flux-normalize the companion and stellar models and multiply them by different flux scale factors, which are in units of counts as measured by NIRSPEC. After scaling, the companion and speckle models are added in the case of HIP 55507 B. To remove the smoothly varying continuum in the KPIC spectra, we apply high-pass filtering with a median filter of 100 pixels (~ 0.002 μm) on the data and forward models for both HIP 55507 A and B. The choice of 100 pixels was found to be optimal for KPIC data from J. W. Xuan et al. (2022) for accurately

[7] We note that the commonly used `fastRotBroad` function from `PyAstronomy` (Czesla et al., 2019) is only valid for small wavelength arrays, and the question of how small depends on spectral resolution. At $R \sim 35,000$, our injection-recovery tests (§ 3.6) show `fastRotBroad` can lead to $v \sin i$ biases at the $\sim 10\%$ level for $v \sin i \sim 5$ km/s. In contrast, the Carvalho et al. (2023) method is accurate over arbitrarily large wavelength grids.

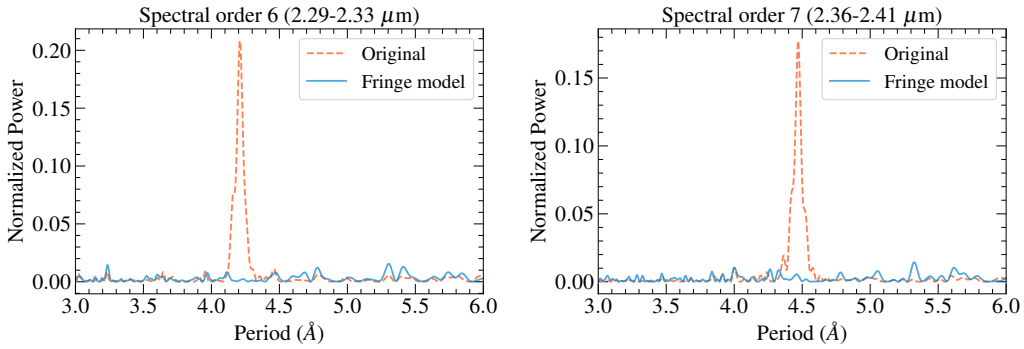

Figure 3.5: Lomb-Scargle periodograms of the residuals from fitting the KPIC spectra of HIP 55507 A. The blue and red periodograms are generated from the residuals of fits with and without the fringing model, respectively. The power between $\approx 4 - 4.5$Å, which is the characteristic frequency of fringing from the KPIC dichroic, is greatly diminished. The two panels are for different spectral orders.

retrieving molecular abundances in KPIC data. To summarize, the forward model for HIP 55507 B is:

$$FM_B = \alpha_c T M_c + \alpha_s D_s \tag{3.1}$$

where FM_B denotes the forward model for HIP 55507 B, α_c and α_s are the flux scales of the companion and speckle, T is the telluric and instrumental response, M_c is the companion template from `petitRADTRANS`, and D_s is the observed KPIC spectra of HIP 55507 A, which already has T factored in. In contrast, the forward model for HIP 55507 A is:

$$FM_A = \alpha_A T M_A \tag{3.2}$$

where α_A is the flux scale of the primary star in its on-axis observations, M_A is the primary star template from `petitRADTRANS`, and T is the same transmission function as above. The median filter is applied to both sides of these equations. In reality, we find additional modulation in the HIP 55507 AB data from fringing, which we also account for in our models.

Fringing model for KPIC data

KPIC data are affected by a time-varying fringing effect that produces quasi-periodic wiggles in the spectra that can imitate spectral absorption features (Finnerty et al., 2022). Given the high S/N of the HIP 55507 A and B spectra, we noticed the dominant component in the residuals is due to fringing. We describe the details of our fringing model in Appendix 3.10. Here, we simply point out that one optic in KPIC (a dichroic) causes the fringing signal to change between the HIP 55507 A

spectra and the off-axis HIP 55507 B spectra. The characteristic fringe period induced by this dichroic is ∼4 Å at 2.3 μm (see Fig. 3.5). We note that the fringe model effectively modifies the T component of Eq. 3.1 and Eq. 3.2 with an additional transmission term, and therefore applies to all our spectral fits for HIP 55507 A and B.

To incorporate fringing in our spectral fits, we adopt a three-step approach. First, we fit the spectra without the fringe model. The residuals from this first fit are characterized by fringing modulations. Second, we perform a least-squares optimization in the residuals of the first fit to find the best-fit fringing parameters that minimize the fringing signal. Third, in the final spectral fit, we fit the atmospheric parameters and fringe parameters jointly, while adopting the best-fit fringe parameters from the second step as initial guesses. The motivation for this is to avoid the excessively large and complex likelihood space from the fringe model, while also incorporating uncertainties from the fringe model into our atmospheric parameters.

As described in Appendix 3.10, our fringe model adds three parameters for each spectral order. In Fig. 3.5, we plot the periodogram of the residuals with and without including the fringing model when fitting HIP 55507 A spectra. The power between ≈4-4.5 Å is noticeably attenuated by the fringe model.

PHOENIX-ACES model fits to HIP 55507 A

To derive the primary star's bulk properties, we first fit its KPIC spectra with the PHOENIX-ACES model (Husser et al., 2013), which here constitutes M_A in Eq. 3.2. Specifically, we use two spectral orders spanning 2.29-2.41 μm, with a gap in between. Our model grid assumes solar metallicity, and we vary the $T_{\rm eff}$, log(g), RV, $v \sin i$, and stellar flux scale (α_A in Eq. 3.2). The parameters for the PHOENIX-ACES model fits are summarized in Table 3.6. We note that for HIP 55507 A, $v \sin i$ acts as a stand-in for the combined effects of rotational broadening and macroturbulence.[8] The results of the PHOENIX-ACES fits are presented in Appendix 3.10. Next, we fit the HIP 55507 A spectra using a retrieval framework (see below).

[8]The effects from macroturbulent broadening and rotation are similar and difficult to distinguish at low velocities. Microturbulent broadening is taken into account by the PHOENIX-ACES models, which adopts a microturbulent velocity of 0.48 km/s (Husser et al., 2013) for an atmosphere with properties similar to our K6V star ($T_{\rm eff}$ = 4300 K, $\log g$ = 4.5, see Table 3.1).

Atmospheric retrieval setup

Here, we describe the atmospheric retrieval setup for HIP 55507 B and A to generate M_c and M_A in Eq. 3.1 and Eq. 3.2, respectively. Retrievals allow us to measure the isotopologue abundances in both stars. Specifically, we setup radiative transfer routines with `petitRADTRANS` using the line-by-line opacity sampling method, and down-sample the native $R = 10^6$ opacity tables by a factor of 3 to speed up the retrievals. In the following, we describe the opacities, chemistry, temperature profile, and cloud models used in the retrievals. The fitted parameters for HIP 55507 B are summarized in Table 3.5.

We note that compared to the retrieval analysis of HIP 55507 B, our retrievals for HIP 55507 A contain several simplifications, which we highlight throughout this section. Carrying out a retrieval with a free temperature profile and chemical abundances, as we do for HIP 55507 B, is not realistic at this stage for HIP 55507 A. Our K band spectrum for this K6V star is dominated by CO lines with minor contributions from a few atomic lines. H_2O is mostly dissociated in the K6V star's photosphere such that we cannot constrain the relative ratios of C and O. With more wavelength coverage (e.g. H+K bands to probe OH, CO, CN), a spectral synthesis approach could be a way to measure elemental abundances and C/O for HIP 55507 A, as achieved for a K7V dwarf by Hejazi et al. (2023).

Opacity sources

We require high temperature opacities for our stars. For HIP 55507 B, our preliminary retrievals show that there is contribution to the emission spectrum from regimes with $T > 3000$ K (see Fig. 3.6), which exceeds the 3000 K upper limit of default `petitRADTRANS` opacity tables for molecules (P. Mollière et al., 2019b). Therefore, whenever possible, we update our opacity tables to go to $T_{\rm max} = 4500$ K or higher using the DACE opacity database generated with the HELIOS-K opacity calculator (Grimm et al., 2015; Grimm et al., 2021).[9] In particular, we upgrade the line opacities of $H_2^{16}O$ (Polyansky et al., 2018), OH (Brooke et al., 2016), FeH (Dulick et al., 2003; Bernath, 2020), TiO (McKemmish et al., 2019), AlH (Yurchenko et al., 2018), and VO (McKemmish et al., 2016) to reach 4500 K. For $H_2^{18}O$, we adopt the line list from Polyansky et al. (2017) which is valid up to 3000 K. For H_2S, we use the line list from Azzam et al. (2016), valid up to 2000 K. Finally, we include the atomic line species Na, K, Mg, Ca, Ti, Fe, and Al (Kurucz, 2011).

[9] `https://dace.unige.ch/opacityDatabase/`

For HIP 55507 A, the photosphere is at even higher temperatures, but the K band spectra of this star is dominated by mostly CO and the aforementioned atomic lines. Therefore, we only include these opacities for the HIP 55507 A retrievals. We generate opacities for $C^{16}O$, ^{13}CO, $C^{18}O$ that are valid up to 9000 K from Rothman et al. (2010).

For the continuum opacities in both stars, we include the collision induced absorption (CIA) from H_2-H_2 and H_2-He, as well as the H- bound-free and free-free opacity.

Table 3.5: Fitted parameters and priors in HIP 55507 B retrievals

Parameter	**Prior**	**Parameter**	**Prior**
Mass (M_J)	$\mathcal{N}(88.0, 3.4)$	Radius (R_J)	$\mathcal{U}(0.6, 2.5)$
$T_{\rm anchor}$ (K)	$\mathcal{U}(1900, 2700)$	RV (km/s)	$\mathcal{U}(-30, 30)$
ΔT_1 (K)	$\mathcal{U}(400, 1000)$	$v \sin i$ (km/s)	$\mathcal{U}(0, 30)$
ΔT_2 (K)	$\mathcal{U}(50, 700)$	C/O	$\mathcal{U}(0.1, 1.0)$
ΔT_3 (K)	$\mathcal{U}(50, 600)$	[C/H]	$\mathcal{U}(-1.5, 1.5)$
ΔT_4 (K)	$\mathcal{U}(50, 600)$	log(CO)	$\mathcal{U}(0, 6)$
ΔT_5 (K)	$\mathcal{U}(50, 600)$	log(H_2O)	$\mathcal{U}(0, 6)$
ΔT_6 (K)	$\mathcal{U}(50, 600)$	log(CO_2)	$\mathcal{U}(0, 6)$
ΔT_7 (K)	$\mathcal{U}(50, 600)$	log(gray opacity/cm^{2}g^{-1})[a]	$\mathcal{U}(-6, 6)$
$f_{\rm sed}$[b]	$\mathcal{U}(0, 10)$	log(K_{zz}/cm^{2}s^{-1})[b]	$\mathcal{U}(5, 13)$
σ_g[b]	$\mathcal{U}(1.05, 3)$	log($\tilde{X}_{Al_2O_3}$)[b]	$\mathcal{U}(-2.3, 1)$
Fringe and other parameters			
Optical path length, d (mm)	$\mathcal{U}(4, 5)$	Comp. flux, α_c (counts)	$\mathcal{U}(0, 300)$
Fractional amplitude, F	$\mathcal{U}(10^{-6}, 1)$	Speckle flux, α_s (counts)	$\mathcal{U}(0, 200)$
Dichroic temperature, T_d (K)	$\mathcal{U}(150, 330)$	Error multiple[c]	$\mathcal{U}(1, 5)$

Notes: $\mathcal{U}$ stands for a uniform distribution, with two numbers representing the lower and upper boundaries. $\mathcal{N}$ stands for a Gaussian distribution, with numbers representing the median and standard deviation. The fringe parameters d, F, and T_d are described in Appendix 3.10.
(a) Parameter for the gray cloud model (constant gray opacity).
(b) Parameters for the EddySed cloud model. $\tilde{X}_{Al_2O_3}$ is the scaling factor for the cloud mass fraction, so that $\log(\tilde{X}_{Al_2O_3}) = 0$ refers to a fraction equal to the equilibrium mass fraction. $f_{\rm sed}$, K_{zz}, and σ_g together set the cloud mass fraction as a function of pressure and the cloud particle size distribution (P. Mollière et al., 2020).
(c) The error multiple term is fitted for KPIC data to account for any underestimation in the uncertainties.

Table 3.6: Fitted parameters and priors in HIP 55507 A retrieval and PHOENIX-ACES fit

Parameter (retrieval)	**Prior**	**Parameter (PHOENIX-ACES)**	**Prior**
Mass ($M_\odot$)	$\mathcal{U}(0.63, 0.71)$	$T_{\rm eff}$ (K)	$\mathcal{U}(3000, 5500)$
Radius ($R_\odot$)	$\mathcal{U}(0.64, 0.72)$	$\log g$ (dex)	$\mathcal{U}(3.5, 5.5)$
$v \sin i$ (km/s)	$\mathcal{U}(0, 30)$	$v \sin i$ (km/s)	$\mathcal{U}(0, 30)$
RV (km/s)	$\mathcal{U}(-30, 30)$	RV (km/s)	$\mathcal{U}(-30, 30)$
C/O	$\mathcal{N}(B_\mu, B_\sigma)$		
[C/H]	$\mathcal{N}(B_\mu, B_\sigma)$		
log(CO)	$\mathcal{U}(0, 6)$		
$\log(CO_2)$	$\mathcal{U}(0, 6)$		
Fringe and other parameters (common)			
Optical path length, d (mm)	$\mathcal{U}(4, 5)$	Star flux, α_A (counts)	$\mathcal{U}(0, 10000)$
Fractional amplitude, F	$\mathcal{U}(10^{-6}, 1)$	Error multiple	$\mathcal{U}(1, 5)$
Dichroic temperature, T_d (K)	$\mathcal{U}(150, 330)$		

Notes: Symbols for priors are the same as in Table 3.5. The parameters for the HIP 55507 A retrieval and PHOENIX-ACES fits are in the left and right columns, respectively. 'Fringe and other parameters' are common to both. For C/O and [C/H], B_μ and B_σ represent the median and 1σ interval measured for the companion, HIP 55507 B, which are used as Gaussian priors in the HIP 55507 A retrieval.

Chemistry and isotopologue ratios

The default chemical equilibrium grid in `petitRADTRANS` does not save the abundances of all the species we include as opacity sources. Therefore, we generate a custom chemical equilibrium grid using `easyCHEM`,[10] which is the same code used by P. Mollière et al. (2020). We validated our new grid against the `petitRADTRANS` chemical grid for overlapping species and find excellent agreement (fractional differences of $< 1\%$). The abundances of species are set by two parameters in our grid: the carbon abundance [C/H], and the carbon-to-oxygen ratio C/O, which determines the oxygen abundance along with [C/H]. We are only sensitive to the abundances of C and O in this work, and therefore assume that the other metals scale with C. Our grid goes up to 8000 K, more than hot enough for the K6V primary star. For the solar elemental abundances, we adopt Asplund et al. (2009).

In our retrievals, the abundances of the main isotopologues are obtained from interpolating the chemical equilibrium grid for each value of C/O and [C/H]. Then, for each minor isotopologue included, we fit for an isotopologue ratio parameter akin to Y. Zhang et al. (2021b). In our baseline retrievals, we fit for three ratios: $^{12}C^{16}O/^{13}C^{16}O$, $^{12}C^{16}O/^{12}C^{18}O$, and $H_2^{16}O/H_2^{18}O$. This allows us to explore

[10] `https://easychem.readthedocs.io/en/latest/content/installation.html`

whether the $^{16}O/^{18}O$ ratio differs between CO and H_2O, which may arise from isotopic fractionation processes such as self-shielding of CO and UV shielding of H_2O (Calahan et al., 2022). In addition, fitting two ratios allows us to examine whether the data show evidence for $H_2^{18}O$, $^{12}C^{18}O$, or both.

Temperature structure

For HIP 55507 B, we adopt a modified version of the pressure-temperature (P-T) profile from Piette et al. (2020). Our profile is parameterized by seven $\Delta T/\Delta P$ values between eight pressure points and the temperature at one of these pressures. Instead of having the pressure points equally spaced in log pressure, we preferentially concentrate pressure points around the peak of the weighted emission contribution, as this is where the data are most informative. The selected pressure points are labeled in Fig. 3.6, and the modeled pressure extent is between log(bar) = -4.0 to 1.4. For the radiative transfer, the eight P-T points from our profile are interpolated onto a finer grid of 100 P-T points using a monotonic cubic interpolation as recommended by Piette et al. (2020). Unlike Piette et al. (2020), we do not apply smoothing to our profiles as smoothing has been shown to bias retrieval results (Rowland et al., 2023).

For HIP 55507 A, we fix its P-T profile to a Phoenix P-T profile (Husser et al., 2013) matching properties of the star ($T_{\rm eff}$ = 4300 K and log(g)=4.5) for simplicity.

Clouds

Clouds are expected to play a minimal role for late-M objects like HIP 55507 B, and no role for a K6V star like HIP 55507 A, as temperatures are too hot for cloud condensates to remain stable. For completeness in our HIP 55507 B retrievals, we consider both clear and cloudy models to explore the sensitivity of our retrieved abundances to assumed cloud properties. For the cloudy models, we use a gray cloud model where a constant opacity is added to the atmosphere, and the EddySed model (Ackerman et al., 2001) as implemented in `petitRADTRANS` (P. Mollière et al., 2020). We used Al_2O_3 clouds in the EddySed model, as Al_2O_3 is expected to be more important at higher $T_{\rm eff}$ (Wakeford et al., 2015).

Summary of retrieval setup for both stars

As noted earlier, we make simplifications in retrieving the spectra of HIP 55507 A. To summarize the retrieval setup for A: 1) we adopt priors on C/O and [C/H] for HIP 55507 A using measured values from HIP 55507 B, 2) fix the P-T profile to a

Phoenix P-T profile (Husser et al., 2013), and, 3) allow the stellar mass and radius to vary within 1σ intervals given in Table 3.1.

In contrast, we freely fit for all these parameters in the HIP 55507 B retrievals, with the exception of mass. For the companion's mass, we adopt a dynamical mass prior determined from § 3.4. The fitted parameters and adopted priors in HIP 55507 B and A retrievals are listed in Table 3.5 and Table 3.6, respectively.

Jointly fitting photometry for HIP 55507 B

For HIP 55507 B, we jointly fit the KPIC high-resolution spectra with the K, L', and M_s photometric points in Table 3.2 to better constrain the bulk properties of the companion. The apparent magnitudes were converted into flux density units by computing the zeropoint for each photometric filter using the `species` package (Stolker et al., 2020). For the photometry model, we use the correlated-k opacities in `petitRADTRANS` (re-binned to $R = 50$). The photometry model does not add any new parameters, as it is fully described by the atmospheric parameters introduced earlier. In joint KPIC+photometry retrievals, we add the log likelihoods from the photometry and KPIC components.

Model fitting with nested sampling

We use nested sampling as implemented by `dynesty` (Speagle, 2020) to find the posterior distributions for all model parameters listed in Table 3.5 for HIP 55507 B, and Table 3.6 for HIP 55507 A. We use 600 live points and adopt the stopping criterion that the estimated contribution of the remaining prior volume to the total evidence is less than 1%. We confirmed that increasing the number of live points to 1000 does not meaningfully change the posteriors of our retrieved parameters.

Table 3.7: Input and retrieved parameters from injection-recovery tests

Parameter	**RV (km/s)**	$v \sin i$ **(km/s)**	**C/O**	[C/H]	**log(CO)**	**log(H_2O)**	**log(CO_2)**
Input values	10.0; -10.0	5.00	0.70	0.0	2.00	2.30	2.78
RV = 10 km/s	9.96 ± 0.03	5.02 ± 0.09	0.706 ± 0.005	0.02 ± 0.03	2.05 ± 0.04	2.27 ± 0.05	...
RV = -10 km/s	−10.05 ± 0.02	4.99 ± 0.09	0.693 ± 0.005	0.01 ± 0.03	1.90 ± 0.03	$2.33^{+0.14}_{-0.11}$	...

Notes: The injections were performed on a non-illuminated KPIC fiber to sample realistic thermal noise properties. We place a Gaussian prior on the mass, so do not report this value.

3.6 Injection-recovery tests

To validate our retrieval framework, we perform a series of injection-recovery retrievals on simulated data for HIP 55507 B. We inject model spectrum from `petitRADTRANS` in the extracted spectrum of a non-illuminated fiber. Such a fiber still measures the thermal background of the instrument, and serves as a realistic 'noise spectrum' since thermal noise is the dominant source of noise for our data. Specifically, we use the extracted fiber 4 trace at the time of observations. We took the fiber 4 trace on exposures where HIP 55507 B was aligned to fiber 2, at which time fiber 4 was located $\sim 2''$ away from the companion and $\sim 2.5''$ away from HIP 55507 A. Examination of the extracted spectra from fiber 4 shows that there is negligible leaked light: the median of the flux is ≈ 0 counts. We multiply the companion model by the telluric response function (T) for fiber 4, add a speckle flux contribution using the primary star spectra, and high-pass filter the simulated data in the same way as for the real data.

For the input companion model, we use a P-T profile from the SPHINX model grid (Iyer et al., 2023) with $T_{\rm eff}$ = 2500 K, log(g)=5.25, solar metallicity, and C/O=0.7. We set the mass (87 $M_{\rm Jup}$) and radius (1.1 $R_{\rm Jup}$) of our injected companion to be consistent with this $\log g$, and the chemical abundances to C/O=0.7 and [C/H] = 0, consistent with that assumed in the P-T profile. To achieve a similar S/N as the real data, we inject similar companion and speckle flux values as the data. We carry out two injections at different RV shifts (-10 and 10 km/s) to sample various parts of the background trace. In addition to simulating a KPIC model, we also simulate three photometry points using the same input values. The parameters of the simulated models are given in Table 3.7.

In our simulated model we inject ^{12}CO/^{13}CO = 100 ($\log(^{12}\mathrm{CO}/^{13}\mathrm{CO}) = 2.0$) and $\mathrm{H_2^{16}O}/\mathrm{H_2^{18}O}$ = 200 ($\log(\mathrm{H_2^{16}O}/\mathrm{H_2^{18}O}) \approx 2.301$), similar to what we find in the real data. Since we do not detect $\mathrm{C^{16}O}/\mathrm{C^{18}O}$ in the data, we inject a lower value of $\mathrm{C^{16}O}/\mathrm{C^{18}O}$ = 600 ($\log(\mathrm{C^{16}O}/\mathrm{C^{18}O}) \approx 2.778$) to see whether this can be recovered in our tests. Note that our isotopologue ratios are fitted in log scale in the retrieval.

As shown in Table 3.7, $\log(^{12}\mathrm{CO}/^{13}\mathrm{CO})$ and $\log(\mathrm{H_2^{16}O}/\mathrm{H_2^{18}O})$ are recovered, though systematic offsets of $0.05-0.1$ dex can be present in the retrieved $\log(^{12}\mathrm{CO}/^{13}\mathrm{CO})$. On the other hand, the systematic bias is only ~ 0.03 dex for $\log(\mathrm{H_2^{16}O}/\mathrm{H_2^{18}O})$. To be conservative, we adopt 0.1 dex as the systematic error for both of these isotopologue ratios in our retrievals of the real data. The $\log(\mathrm{C^{16}O}/\mathrm{C^{18}O})$ posterior is not well-bounded, though the 3σ lower limit for $\log(\mathrm{C^{16}O}/\mathrm{C^{18}O})$ does contain

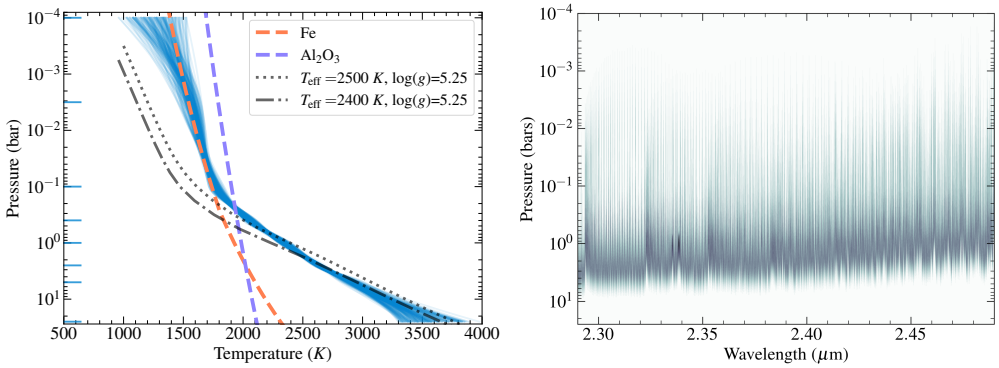

Figure 3.6: Left: blue: random draws from the posterior of the retrieved P-T profiles from the baseline retrieval. The gray lines show SPHINX models (Iyer et al., 2023) with similar bulk properties as HIP 55507 B. The condensation curves for Fe and Al_2O_3 clouds are plotted in colored dashed lines. The horizontal ticks on the y-axis are pressure points between which we fit ΔT values in our P-T parameterization. Right: The emission contribution function of the best-fit baseline model. There is non-zero contribution at $\sim$ 5 bars, where the temperature profile (left panel) exceeds 3000 K.

the injected value. Further tests show that we cannot reliably retrieve values of $C^{16}O/C^{18}O = 200 - 300$, suggesting it is harder to detect $C^{18}O$ compared to $H_2^{18}O$ with our KPIC spectra. From examining the $C^{18}O$ opacities, we find that this is may be due to the fact that many $C^{18}O$ lines overlap in wavelength with ^{13}CO lines, thereby masking the weaker signal from $C^{18}O$.

From the injection-recovery tests, we find that C/O and [C/H] are well-recovered, with only $\sim$ 0.01 deviations in C/O between the injected and recovered values, and $<$ 0.02 dex deviations in the [C/H] values. We attribute the slight offsets between the injected and retrieved values to random noise in the background trace.

As mentioned in § 3.5, the choice of rotational broadening kernel can have an impact on the retrieved $v \sin i$. Even when using the direct integration method from Carvalho et al. (2023), we note that the retrieved $v \sin i$ can still be biased by the down-sampling factor for the line-by-line opacities. At the KPIC resolution of $R \sim 35,000$ and for a $v \sin i$ of 5.0 km/s (technically below our resolution limit of $\sim$ 7.5 km/s), we find that down-sampling the native $R = 10^6$ opacities by a factor of 3 or less allows us to accurately recover the input $v \sin i$ of 5.0 km/s.

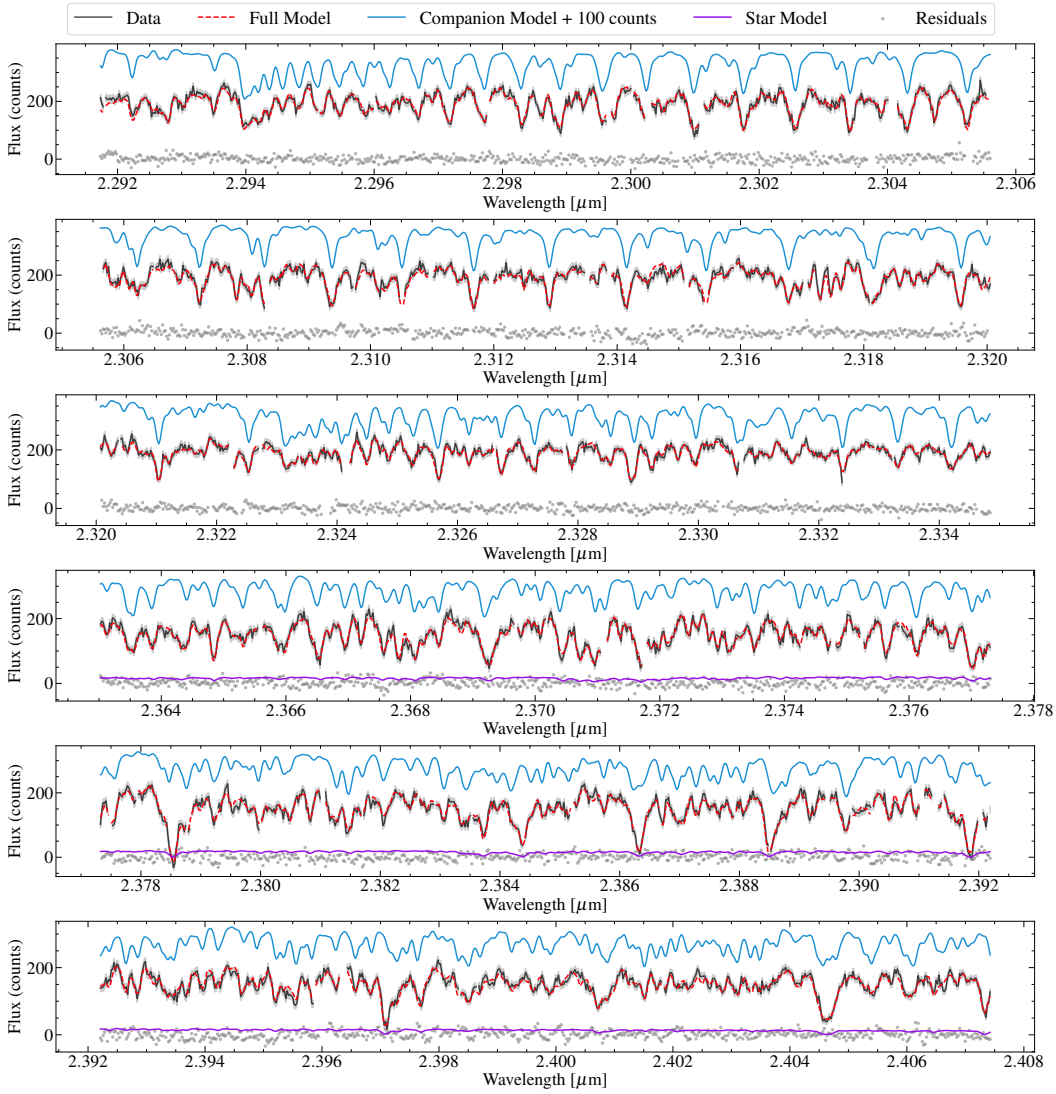

Figure 3.7: KPIC data (2023, fiber 2) for HIP 55507 B are plotted in black, with error bars in gray. We plot two out of three spectral orders (2.29 – 2.41 μm), and each order is broken into three panels. The full model (FM_B in Eq. 3.1) is in red, and consists of the companion model (M_c) in blue, which has been RV shifted and broadened, the stellar spectra (D_s) in purple to model the speckle contribution, and the telluric and instrumental response (T). The fringing model is also incorporated in the full model. The residuals are shown as gray points. For clarity, an offset of +100 counts was added to the companion model. The speckle contribution is small, and consistent with zero for the first spectral order (top three panels), where we omitted the purple line.

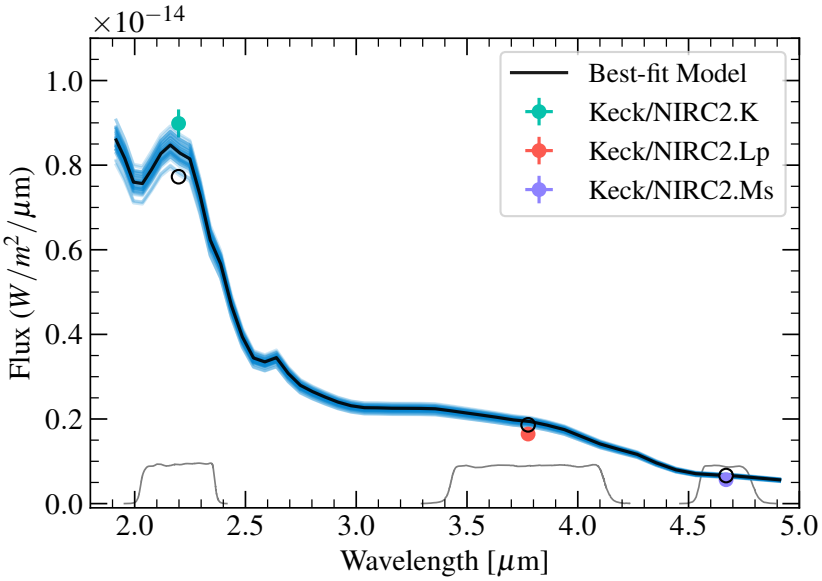

Figure 3.8: The photometry part of the retrieval for HIP 55507 B. The data are plotted in colored points, with filter transmission functions shown below. The best-fit model photometry points are shown in black open circles. The black curve is the best-fit spectra underlying the model photometry, while blue curves are random draws from the posterior.

3.7 Retrieval results

HIP 55507 B

We run three sets of retrievals for HIP 55507 B: two sets for the 2021 and 2023 KPIC datasets separately, and one set that combines the 2021 and 2023 KPIC data. By default, we include the K, L', and M_s photometric data in the retrievals, but we also tested fits where we excluded the photometry. Retrieved parameters from each set of retrievals are presented in Table 3.8, and the baseline retrieval (2021+2023+photometry) is in bold. We plot the KPIC spectra and best-fit models in Fig. 3.7, while the photometry fit is shown in Fig. 3.8. The joint posterior distributions of a few parameters from the baseline retrieval are shown in Fig. 3.9.

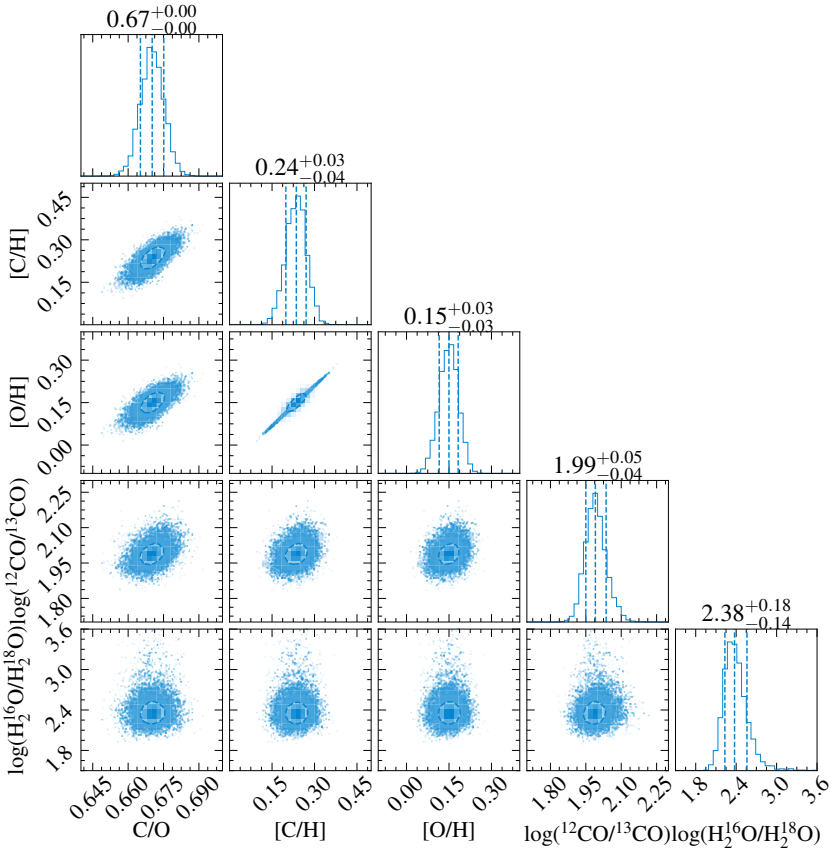

Figure 3.9: Posterior distributions for five key parameters from the baseline retrieval for HIP 55507 B. The titles on each histogram show the median and 68% credible interval. These represent the statistical errors, and we account for systematic errors in our reported values in Table 3.8. Note that [O/H] is not fitted in the retrievals, but calculated from the C/O and [C/H] posteriors. The tight correlation between [C/H] and [O/H] indicates that KPIC high-resolution spectra can constrain relative abundances to much higher precision than absolute abundances, as found by previous high-resolution studies (J. W. Xuan et al., 2022; Finnerty et al., 2023).

Table 3.8: Spectral Retrievals and Results

Data/Observing Date	**Isotopologues Included**	**C/O**	[C/H]	**CO**	**H_2O**	**Radius (R_J)**	**T_{eff} (K)**	**ln(B)**
2023/05/02								
KPIC + Phot.	^{13}CO, $H_2^{18}O$, $C^{18}O$	0.68 ± 0.01	0.26 ± 0.04	106^{+14}_{-11}	165^{+68}_{-44}	1.32 ± 0.02	2367 ± 20	0
KPIC + Phot.	$H_2^{18}O$, $C^{18}O$	0.68 ± 0.01	0.26 ± 0.04	...	150^{+87}_{-38}	1.32 ± 0.02	2355 ± 20	-28.0
KPIC + Phot.	^{13}CO, $C^{18}O$	0.68 ± 0.01	0.25 ± 0.05	103^{+12}_{-9}	...	1.32 ± 0.02	2372 ± 20	-4.9
KPIC + Phot. (Gray)	^{13}CO, $H_2^{18}O$, $C^{18}O$	0.68 ± 0.01	0.25 ± 0.04	106^{+13}_{-11}	163^{+67}_{-42}	1.32 ± 0.02	2366 ± 20	2.5
KPIC + Phot. (Al_2O_3)	^{13}CO, $H_2^{18}O$, $C^{18}O$	0.68 ± 0.01	0.25 ± 0.05	103^{+13}_{-9}	167^{+72}_{-46}	1.32 ± 0.02	2368 ± 20	2.3
KPIC	^{13}CO, $H_2^{18}O$, $C^{18}O$	0.69 ± 0.01	0.00 ± 0.12	114^{+15}_{-12}	172^{+63}_{-43}	1.92 ± 0.27	2348 ± 20	...
2021/07/04								
KPIC + Phot.	^{13}CO, $H_2^{18}O$, $C^{18}O$	0.64 ± 0.01	0.14 ± 0.05	63^{+13}_{-8}	> 120 (3σ)	1.35 ± 0.02	2343 ± 25	0
KPIC + Phot.	$H_2^{18}O$, $C^{18}O$	0.64 ± 0.01	0.12 ± 0.05	...	> 96 (3σ)	1.35 ± 0.02	2351 ± 25	-14.8
2021/07/04 + 2023/05/02								
Adopted: KPIC + Phot.	^{13}CO, $H_2^{18}O$, $C^{18}O$	0.67 ± 0.04	0.24 ± 0.13	98^{+28}_{-22}	240^{+145}_{-80}	1.33 ± 0.02	2350 ± 50	...

Notes: A few atmospheric parameters and their central 68% credible interval with equal probability above and below the median are listed. These values only account for statistical error. In the final row, we list the adopted values accounting for systematic errors from the retrieval. The rightmost column lists the log Bayes factor ln(B) for each retrieval. We compute ln(B) with respect to the baseline model for each dataset, i.e., the models with ln(B)=0. Unless specified in parentheses, we use a clear model. 'Gray' refers to the gray opacity cloud model, and 'Al_2O_3' refers to the EddySed model with Al_2O_3 clouds.

P-T profile and clouds

The P-T profile from the baseline retrieval (clear model) is shown in Fig. 3.6. The cloudy models give almost identical P-T shapes as the clear model. We find that the lower atmosphere is fairly consistent with the self-consistent SPHINX models from Iyer et al. (2023), but the upper atmosphere is hotter and more isothermal. This could be due to a trade-off between clouds and an isothermal P-T profile, which is seen in most retrieval studies (e.g. Burningham et al., 2017; J. W. Xuan et al., 2022; Brown-Sevilla et al., 2023; Whiteford et al., 2023). As demonstrated by J. W. Xuan et al. (2022), narrow-band high-resolution spectra can be largely insensitive to clouds but still sensitive to gas-phase molecular abundances. To check if the isothermal upper P-T profile affects our results, we ran a retrieval for HIP 55507 B with the P-T profile fixed to the $T_{\rm eff}$ = 2400 K, $\log g$ = 5.25 SPHINX profile in Fig. 3.6. The resulting posteriors from this retrieval are consistent with the those from our baseline retrieval within 1σ, so we conclude that the isothermal upper atmosphere is not biasing our results.

For the 2023 KPIC dataset, we tested three clouds models: clear, gray opacity, and EddySed with Al_2O_3. To assess whether clouds are preferred by the data, we use the Bayesian evidence from each retrieval to calculate the Bayes factor B, which assesses the relative probability of an alternative model M_2 compared to M_1. Here, we take the clear model to be M_1. The data slightly prefer the gray opacity and EddySed models over the clear model, with ln(B)=2.5 and ln(B)=2.3, respectively, which correspond to $\sim 2.6\sigma$ preferences for the cloudy models using the Trotta (2008) scale. However, the cloud parameters are largely unconstrained, with a 3σ upper limit of 0.009 cm$^2/g$ for the gray opacity. The retrieved abundances are also identical between the cloudy and clear models (see Table 3.8), so we adopt the clear model as the baseline model.

Isotopologue abundances of ^{13}CO and $H_2^{18}O$

In the KPIC dataset from 2023, we strongly detect ^{13}CO and tentatively detect $H_2^{18}O$ in the atmosphere of HIP 55507 B, with $\log(^{12}CO/^{13}CO) = 2.03 \pm 0.05$ and $\log(H_2^{16}O/H_2^{18}O) = 2.22 \pm 0.15$. The 2021 epoch gives $\log(^{12}CO/^{13}CO) = 1.80 \pm 0.08$, which is 0.23 dex or $\approx 2.4\sigma$ lower than the 2023 value. $H_2^{16}O/H_2^{18}O$ is unconstrained from the 2021 epoch due to its lower S/N. The discrepancy in $\log(^{12}CO/^{13}CO)$ between datasets is somewhat higher than the 0.05 – 0.1 dex systematic bias we identify in our injection-recovery tests. In our reported values, which are based on a joint fit to both 2021 and 2023 datasets, we add a 0.1 dex

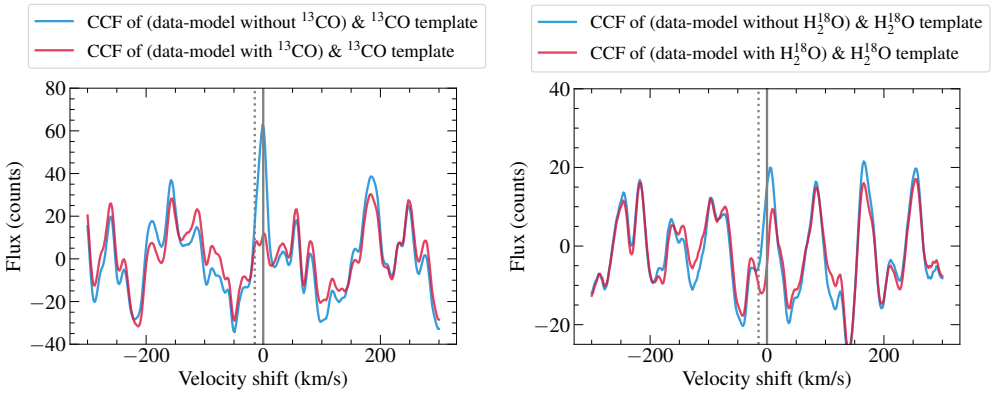

Figure 3.10: Left panel: The CCF between the ^{13}CO-only template and (data - best-fit model without ^{13}CO) in blue. The CCF between the ^{13}CO-only template and (data - best-fit model with ^{13}CO) is shown in red. The fact that the blue CCF shows a peak at the companion's rest frame (gray solid line) indicates a real ^{13}CO detection. For comparison, the gray dotted line is the telluric rest frame. In the red CCF, we do not expect a peak since ^{13}CO is fitted for in this model, so the residuals should be free of ^{13}CO. Right panel: same but for $H_2^{18}O$. The ^{13}CO signal is much clearer than the $H_2^{18}O$ signal, which remains tentative at this stage.

systematic error in quadrature to the measurement errors. In summary, we report $^{12}CO/^{13}CO = 98^{+28}_{-22}$ and $H_2^{16}O/H_2^{18}O = 240^{+145}_{-80}$ for HIP 55507 B. $C^{16}O/C^{18}O$ is unconstrained, with a formal 3σ lower limit of $\approx$ 440. However, as discussed in § 3.6, we often cannot recover $C^{16}O/C^{18}O$ values of 200-300 from injection-recovery tests, so the true $C^{16}O/C^{18}O$ value could in fact be lower than 440 and consistent with our $H_2^{16}O/H_2^{18}O$ value.

To assess whether the ^{13}CO and $H_2^{18}O$ isotopologues are needed to fit the data or whether we can adjust other parameters to improve the fits, we perform two retrievals with one of these isotopologues removed in each. These constitute the 'reduced models'. We then calculate the Bayes factor between these reduced models and the full model with all isotopologues included, which are tabulated in Table 3.8. The $\ln(B)$ values correspond to a 7.8σ detection of ^{13}CO and 3.7σ detection of $H_2^{18}O$.

We can obtain a complementary perspective on the robustness of these detections using the cross-correlation method, following the approach in Y. Zhang et al. (2021a) and J. W. Xuan et al. (2022). The goal of this analysis is to assess whether the full models prefer ^{13}CO and $H_2^{18}O$ independent of the Bayes factor calculation from our retrievals. To compute the cross-correlation function (CCF), we follow the framework from Ruffio et al. (2019), so the y-axis of our CCFs is the estimated flux

level (in counts) of the isotopologue signal from a least-squares minimization.

First, we compute the CCF between a ^{13}CO-only model and the (data - model without ^{13}CO). The latter is equivalent to the residuals of the reduced model, and will contain residual ^{13}CO lines if the data contains ^{13}CO. Then, we compute the CCF between the ^{13}CO-only model and the (data - model with ^{13}CO). This second CCF should not show a detection, as ^{13}CO is already fitted for in the model with ^{13}CO (i.e. the full model). We generate the isotopologue-only models by manually zeroing the opacities of all other line species except the isotopologue when computing the full model. The same process is repeated for $H_2^{18}O$, whose CCFs are shown in the right panel of Fig. 3.10.

We find that the ^{13}CO signal is cleaner compared to the $H_2^{18}O$ signal, as the CCF for $H_2^{18}O$ shows stronger residual structure in the wings, although there is a peak around 0 km/s (companion's rest frame) consistent with a real signal. However, because the remaining systematics are on a scale similar to that of the peak, we consider the $H_2^{18}O$ detection to be tentative in these data. It is possible that this detection is produced by remnant fringing features that our fringe model did not perfectly remove and/or residual telluric features, which are especially strong in the $2.45-2.49$ wavelength region where the $H_2^{18}O$ lines are strongest. A future upgrade to KPIC should greatly reduce the fringing from the dichroics, allowing us to re-visit $H_2^{18}O$ in HIP 55507 B's atmosphere with more confidence.

C/O and atmospheric metallicity

We retrieve C/O=0.68±0.01, [C/H] = 0.26±0.04 for the 2023 epoch and C/O=0.64± 0.01, [C/H] = 0.14 ± 0.05 for the 2021 epoch. These values are broadly consistent, with a $\sim$ 6% difference in C/O and 0.12 dex difference in [C/H]. Notably, the $\sim$ 6% difference in C/O between the two epochs is lower than the $\sim$ 15 – 20% error estimated by J. W. Xuan et al. (2022) and J. Wang et al. (2022) for benchmark BD companions, where it was assumed that the BD companions have the same compositions as their host stars.

We adopt a systematic error of 0.04 in C/O and 0.12 dex in [C/H] for our baseline retrieval, and report [C/H] = 0.24 ± 0.13, [O/H] = 0.15 ± 0.13, and C/O=0.67 ± 0.04 for HIP 55507 B. The primary star HIP 55507 A has [Fe/H] = -0.02 ± 0.09 from Keck/HIRES spectra in the optical (Table 3.1), consistent with a solar metallicity. If we assume [Fe/H]=[C/H] for the primary star, this implies the [C/H] between HIP 55507 A and B are consistent to within 1.6σ.

Effective temperature, luminosity, and radius

The addition of the photometry data in K, L', and M_s bands helps constrain the bulk parameters of HIP 55507 B. For example, when we omitted the photometry for the May 2023 retrieval, the retrieved radius is $R = 1.92 \pm 0.27\ R_{\rm Jup}$, while retrievals with the the photometry yield $R = 1.32 \pm 0.02\ R_{\rm Jup}$ (Table 3.8). We integrate model spectra with parameters drawn from the posteriors of our baseline retrieval to compute $\log(L_{\rm bol}/L_\odot) = -3.29 \pm 0.02$ and $T_{\rm eff} = 2350 \pm 50$ K. While the statistical uncertainties on these parameters are small, we note that the model uncertainties are likely larger since the flux information is derived from three photometric points covering a small portion of the $L_{\rm bol}$ budget.

Given measurements of the dynamical mass and $L_{\rm bol}$, we can compare the spectrally-inferred radius and $T_{\rm eff}$ to the predictions from evolutionary models. To do so, we interpolate the BHAC15, AMES-COND, and AMES-Dusty models (Baraffe et al., 2015; Allard et al., 2001) with Gaussian distributions of $m = 88.0 \pm 3.4\ M_{\rm Jup}$ and $\log(L_{\rm bol}/L_\odot) = -3.29 \pm 0.02$. We find that the evolutionary models favor $R \approx 1.08 \pm 0.02\ R_{\rm Jup}$ and $T_{\rm eff} = 2530 \pm 80\ K$, i.e. a smaller radius and larger $T_{\rm eff}$ than the spectral retrievals. A similar radius-$T_{\rm eff}$ degeneracy has been noted by several retrieval studies, although the discrepancy is usually in the opposite direction for colder brown dwarfs, with retrievals finding a smaller radius than evolutionary models (e.g. Lueber et al., 2022; E. C. Gonzales et al., 2022; Hood et al., 2023). Sanghi et al. (2023) compared radii inferred by evolutionary models and atmospheric models for a large sample of brown dwarfs and found significant discrepancies in $T_{\rm eff}$ and radius for late-M/early-L spectral types in both directions, which highlights ongoing challenges in measuring bulk properties from substellar atmospheric models and retrievals (see also Dupuy et al. 2010 for late-M dwarfs).

Projected rotation rate

We measure a relatively slow $v \sin i = 5.4 \pm 0.2$ km/s for HIP 55507 B, which is below the KPIC resolution limit of ~ 7.5 km/s at $R \sim 35,000$. The high S/N of the data allow us to tightly constrain $v \sin i$ values below the resolution limit, as we demonstrated using injection-recovery tests (Table 3.7).

HIP 55507 A

Using the higher S/N spectra from 2023, we carry out retrievals with the sole goal of measuring isotopic abundances in HIP 55507 A. The best-fit model and stellar spectra are shown in Appendix 3.10. We are able to measure ^{12}CO/^{13}CO and

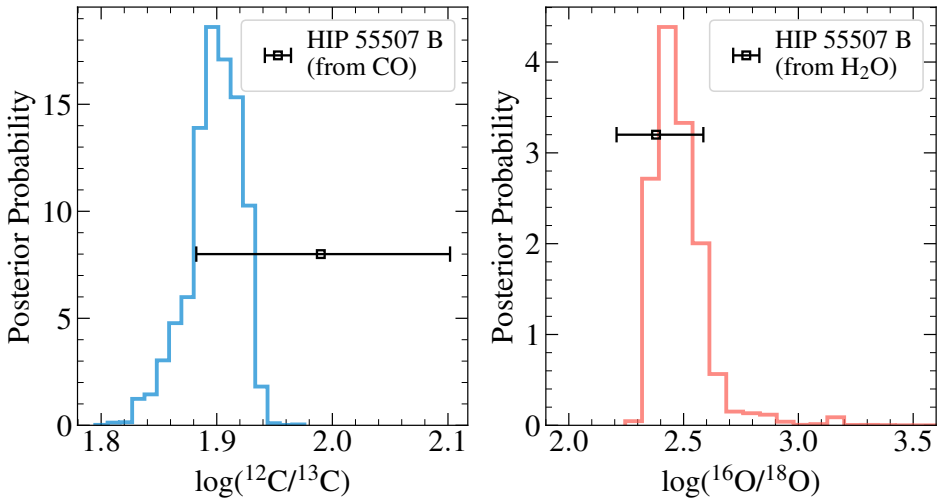

Figure 3.11: The posteriors for $\log(^{12}CO/^{13}CO)$ and $\log(C^{16}O/C^{18}O)$ measured from KPIC spectra of HIP 55507 A. We overplot the corresponding isotopic values measured for HIP 55507 B as error bars. Note that the $^{16}O/^{18}O$ constraint for HIP 55507 B is from $\log(H_2^{16}O/H_2^{18}O)$.

$C^{16}O/C^{18}O$ in the photosphere of the primary star. We add the same 0.1 dex systematic error as we did for HIP 55507 B, resulting in $^{12}CO/^{13}CO = 79^{+21}_{-16}$ and $C^{16}O/C^{18}O = 288^{+125}_{-70}$.

In these HIP 55507 A retrievals, we assumed a fixed P-T profile ($T_{\rm eff}$ = 4300 K, $\log g$ = 4.5). To assess the impact of this assumption on the resulting isotopic abundances, we repeated the fits with $T_{\rm eff}$ = 4200 K and $T_{\rm eff}$ = 4400 K P-T profiles (same $\log g$). We find that varying the P-T profile has little effect on the results; the posteriors shift by $< 1\sigma$.

Relative RVs between HIP 55507 AB

By combining the retrievals for HIP 55507 A and B, we compute the relative RV between the stars at the time of observation. The RV values corrected for barycentric motion are provided in Appendix 3.10. In both the 2021 and 2023 epochs, the stellar and companion RVs measured from fiber 3 are higher compared to those measured from fiber 2. This may be due to different RV zeropoints for each fiber. To compute the relative RV, we subtract the stellar RV from the companion RV for each fiber separately, and then take the average. For the 2023 epoch, the relative RV is consistent at the $<$ 0.05 km/s level between fibers. We conservatively adopt 0.1 km/s as the uncertainty. For the 2021 epoch, we adopt a larger uncertainty of 0.2 km/s as the relative RV values disagree by $\sim$ 0.15 km/s between fibers.

3.8 Discussion and conclusions

Relative radial velocities and dynamical mass

In this paper, we demonstrate the value of relative RV data in orbit fits, which are uniquely enabled by direct measurements of the companion RV (Ruffio et al., 2019; Ruffio et al., 2023a). When the primary star has sufficient absorption lines in the K band, as is the case for HIP 55507 A, we can directly measure the relative RV between the primary star and companion at the same epoch with Keck/KPIC. This measurement is powerful since it is insensitive to potential systematics from zeropoint offsets between different instruments used to acquire the spectra. By including two epochs of KPIC relative RVs in our orbit fit for HIP 55507 AB, we find a 60% improvement in the dynamical mass measurement for HIP 55507 B ($88.0^{+3.4}_{-3.2}\ M_{\rm Jup}$). Dynamical masses of low-mass companions are key measurements that allow us to test evolutionary and atmospheric models. Future work should explore whether relative RVs can also improve constraints on companion mass in systems with longer orbital separations (and therefore less orbital coverage), as many directly imaged companions have orbital separations $\gtrsim$ 100 AU.

We note that our orbit solution for HIP 55507 AB also represents a significant improvement compared to those presented in Feng et al. (2022), who did not use relative astrometry data from imaging and only had access to the first 6.3 years of HIRES RVs. Their derived orbital period of 14.0 ± 1.4 years and companion mass of $5.0 \pm 0.6\ M_{\rm Jup}$ for HIP 55507 B is significantly discrepant from our results. Furthermore, the observed luminosity of the companion from our NIRC2 data is consistent with a low-mass star and not a 5.0 $M_{\rm Jup}$ planet (see Fig. 3.4). In addition, we cannot re-produce their results even if we used the same data as Feng et al. (2022), namely the first 6.3 years of HIRES RVs and Gaia-Hipparcos absolute astrometry. In this case, our fits result in unbounded posteriors for mass and other orbital parameters (e.g. with a 1σ interval for semi-major axis from 13-840 AU). We conclude that the choice of prior ranges in the orbit fit may be biasing the Feng et al. (2022) results for HIP 55507 B.

Isotopologue ratios

Isotopologue ratios are thought to have implications for the formation pathway of planets and substellar companions, but our knowledge of how carbon and oxygen isotopic ratios relate to formation is still limited. We can benchmark the value of isotopologue measurements by using higher-mass brown dwarf and stellar companions which form via gravitational instability from a protostellar disk or molecular

cloud. Because these systems are dominated by gas accretion, they should exhibit the same isotopic ratios between the primary and secondary components, which we can test observationally. To our knowledge, for main-sequence stellar binaries, this test has only been demonstrated once with a M dwarf binary system (Crossfield et al., 2019).

Using high-resolution spectra from Keck/KPIC ($R \sim 35,000$), we perform atmospheric retrievals for the M7.5 companion HIP 55507 B ($T_{\rm eff} \sim 2400\ K$) and its K6V primary star ($T_{\rm eff} \sim 4300\ K$). For HIP 55507 B, we retrieve $[C/H] = 0.24 \pm 0.13$ and $C/O = 0.67 \pm 0.04$. As shown in Fig. 3.11, our measured $^{12}CO/^{13}CO = 98^{+28}_{-22}$ for HIP 55507 B is consistent to within 1σ with our measured $^{12}CO/^{13}CO = 79^{+21}_{-16}$ for the primary star under the assumption that HIP 55507 A and B share the same C/O and $[C/H]$. Furthermore, the $^{16}O/^{18}O$ measured from H_2O in HIP 55507 B is 240^{+145}_{-80}, consistent with $^{16}O/^{18}O = 288^{+125}_{-70}$ measured from CO in HIP 55507 A. The agreement between $^{12}C/^{13}C$ and $^{16}O/^{18}O$ in the HIP 55507 AB system represents is a rare test of chemical homogeneity for stellar binaries using isotopic ratios.

We note that our value of $H_2^{16}O/H_2^{18}O = 240^{+145}_{-80}$ for HIP 55507 B is lower by a factor of ~ 2 compared to the solar value of 525 ± 21 (Lyons et al., 2018). A large difference between the $^{16}O/^{18}O$ in HIP 55507 AB and the Sun is not unexpected, as measurements of $^{16}O/^{18}O$ in molecular clouds at the solar galactocentric distance show a factor of ~ 3 scatter (Nittler et al., 2012). Furthermore, studies of solar twins also reveal a wide range in $^{16}O/^{18}O$, with values as low as $50 - 100$ (Coria et al., 2023). Given the tentative nature of the $H_2^{18}O$ detection in HIP 55507 B however, follow-up observations would be needed to confirm this measurement. In addition, our KPIC spectra for HIP 55507 B does not have sufficient S/N to constrain $C^{16}O/C^{18}O$ even if $C^{16}O/C^{18}O$=$H_2^{16}O/H_2^{18}O$ (see § 3.6). Measuring $C^{16}O/C^{18}O$ in HIP 55507 B consistent with $C^{16}O/C^{18}O$ in the primary star would be a valuable test of our retrieval method and another piece of evidence supporting isotopic homogeneity between HIP 55507 A and B.

With a case study of the M7.5 companion HIP 55507 B using Keck/KPIC spectroscopy, we demonstrate the ability to measure carbon and oxygen elemental and isotopic abundances for late-M spectral types. In addition, we use KPIC to measure $^{12}C/^{13}C$ and $^{16}O/^{18}O$ for its K6V primary star and confirm that the companion and primary share the same isotopic abundances. While we made simplifications in our analysis of HIP 55507 A, future work with more extensive wavelength coverage (e.g.

H + K bands) could explore more sophisticated retrievals for late-K and early-M dwarf stars. Finally, the projected separation and flux ratio between HIP 55507 A and B are comparable to systems with young ($\sim 1-50$ Myr) substellar companions of similar spectral types as HIP 55507 B ($T_{\rm eff} \sim 2000-2800\ K$), which opens the door to systematically measuring the elemental and isotopic abundances of these companions with KPIC.

3.9 Acknowledgements

J.X. thanks Paul Mollière for help with generating new opacities in `petitRADTRANS` and using `easyCHEM`. J.X. is supported by the NASA Future Investigators in NASA Earth and Space Science and Technology (FINESST) award #80NSSC23K1434. J.X. also acknowledges support from the Keck Visiting Scholars Program (KVSP) to commission KPIC Phase II capabilities. D.E. is supported by the NASA FINESST award #80NSSC19K1423. D.E. also acknowledges support from the Keck Visiting Scholars Program (KVSP) to install the Phase II upgrades. Funding for KPIC has been provided by the California Institute of Technology, the Jet Propulsion Laboratory, the Heising-Simons Foundation (grants #2015-129, #2017-318, #2019-1312, #2023-4598), the Simons Foundation, and the NSF under grant AST-1611623. The computations presented here were conducted in the Resnick High Performance Center, a facility supported by Resnick Sustainability Institute at the California Institute of Technology. W. M. Keck Observatory access was supported by Northwestern University and the Center for Interdisciplinary Exploration and Research in Astrophysics (CIERA). This research has made use of the Keck Observatory Archive (KOA), which is operated by the W. M. Keck Observatory and the NASA Exoplanet Science Institute (NExScI), under contract with the National Aeronautics and Space Administration. The data presented herein were obtained at the W. M. Keck Observatory, which is operated as a scientific partnership among the California Institute of Technology, the University of California and the National Aeronautics and Space Administration. The Observatory was made possible by the generous financial support of the W. M. Keck Foundation. The authors wish to recognize and acknowledge the very significant cultural role and reverence that the summit of Mauna Kea has always had within the indigenous Hawaiian community. We are most fortunate to have the opportunity to conduct observations from this mountain.

3.10 Appendix

HIRES RVs for HIP 55507 A

Table 3.9: HIRES RV measurements for HIP 55507 A

Epoch [JD]	RV [m/s]	RV Error [m/s]
2454928.956275	−85.29	1.31
2455164.14972	−68.77	1.48
2455188.145761	−66.67	1.43
2455191.15537	−75.05	1.25
2455232.042467	−62.68	1.54
2455255.95588	−72.16	1.35
2455260.916671	−54.86	1.46
2455285.96214	−59.83	1.39
2455342.836003	−53.21	1.31
2455343.8461	−57.58	1.34
2455344.865259	−48.99	1.59
2455373.79232	−62.91	1.31
2455376.787806	−63.21	1.29
2455395.813169	−50.72	1.47
2455399.805149	−54.89	1.60
2455557.052607	−52.35	1.38
2455614.102829	−43.36	1.49
2455635.058738	−34.55	1.82
2455663.95977	−44.87	1.26
2455668.877009	−40.99	1.30
2455670.931216	−42.33	1.37
2456320.142426	16.08	1.54
2456327.067151	7.77	1.61
2456450.81181	0.54	1.28
2457201.75372	49.01	1.34
2459373.76488	159.65	1.27
2459541.113394	168.07	1.44
2459546.067624	180.16	1.30
2459592.990193	189.87	1.37
2460094.770983	199.76	1.58
2460104.749802	200.89	1.36

NIRC2 imaging and orbit fits for HIP 55507 AB

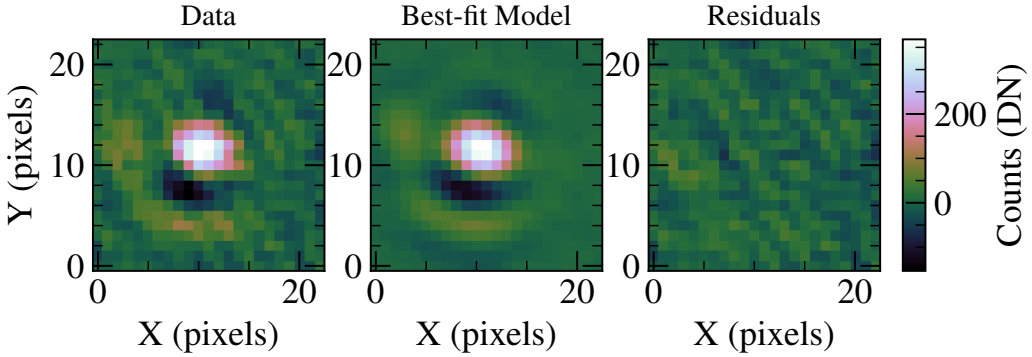

Figure 3.12: An example `pyklip` fit for the NIRC2 imaging data from UT 2022 June 9 with the *K* filter. The companion PSF after ADI is shown on the left panel, the forward model in the middle panel, and residuals in the right panel.

KPIC RVs for HIP 55507 AB

Table 3.10: Radial Velocity Measurements for HIP 55507 A and B from KPIC. We have applied the barycentric correction to the individual RVs for A and B, so their reference is the solar system barycenter. The relative RV is defined as $RV_B - RV_A$. For the relative RV values, we inflated the errors to account for systematics between fibers.

UT Date	Object	BJD-2400,000	SF2 RV (km/s)	SF3 RV (km/s)
2021 July 4	HIP 55507 A	59399.73	-5.48 ± 0.03	-5.38 ± 0.03
2021 July 4	HIP 55507 B	59399.73	-7.33 ± 0.06	-7.08 ± 0.07
Relative RV = -1.78 ± 0.20 km/s				
2023 May 2	HIP 55507 A	60066.78	-5.47 ± 0.02	-5.15 ± 0.02
2023 May 2	HIP 55507 B	60066.78	-7.31 ± 0.05	-7.03 ± 0.06
Relative RV = -1.86 ± 0.10 km/s				

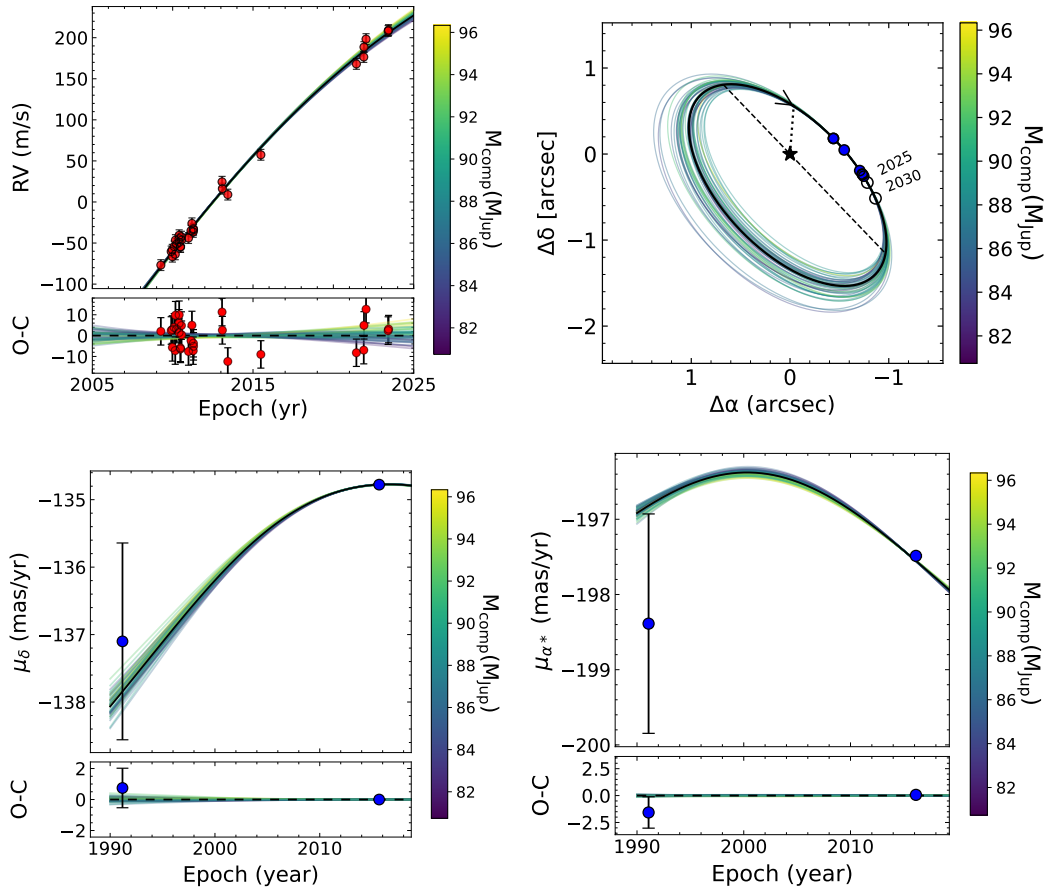

Figure 3.13: Results from the orbit fit using host star radial velocity (top left), relative astrometry (top right), absolute astrometry from Gaia and Hipparcos (bottom panels), and relative RVs from KPIC (shown in Fig. 3.2). The orbit fit is performed with the `orvara` package (T. D. Brandt et al., 2021). The random draws from the posterior are color-coded by the companion mass.

Fringing model for KPIC

We identified three sources of fringing in KPIC data, (two dichroics in KPIC, and optics in the NIRSPEC entrance window Finnerty et al., 2022. One of the two dichroics in particular causes the fringing signal to change when we switch from observing the primary star to observing an off-axis companion, as this dichroic is directly downstream of our fiber injection unit tip-tilt mirror which steers the light of either the star or companion in the fiber. When the tip-tilt mirror switches from the on-axis star to the off-axis companion, the angle of incidence of light into the dichroic changes, which causes the fringing signal to change. The change in modulation, t, as light passes through a transmissive optic is described by the well

known formula:

$$t = \left[1 + F \sin^2\left(\frac{2\pi n l \cos(\theta)}{\lambda}\right)\right]^{-1}. \tag{3.3}$$

Here, $F = 4R/(1-R)^2$ where R is the reflectivity of the material, n is the index of refraction of the material which depends on temperature and wavelength, l is the thickness of the material, θ is the angle of incidence into the material, and λ is the wavelength of light. All KPIC observations to date have spectra affected by three fringing modulation terms multiplied in series, but two of them are expected to be relatively static when going from star observations to companion observations.

We fit the fringing signal in these spectra with a simplified approximation where the companion observations experience an additional modulation term as compared to the star observations. We also simplify the above equation to:

$$t' = \left[1 + F \sin^2\left(\frac{2\pi n(T_d, \lambda) \times d}{\lambda}\right)\right]^{-1}. \tag{3.4}$$

We multiply t' onto the spectral response (i.e. T in Eq. 3.1 and Eq. 3.2) to match the fringing in the observed spectra for both HIP 55507 A and B. We fit for three parameters per spectral order: an optical path length (d) term that combines both the thickness of the glass and the angle of incidence, the fractional amplitude of the ghost from the dichroics (F), and the temperature of the dichroics (T_d) that governs the index of refraction. To model the CaF_2 dichroic we used the Sellmeier coefficients reported by Leviton et al., 2007 to determine how the index of refraction changes with wavelength and temperature. Each science fiber is treated separately, as the fringing is different in each due to different angles of incidence.

Fitting HIP 55507 A spectra with PHOENIX-ACES models

We fit the HIP 55507 A spectra using PHOENIX-ACES models (Husser et al., 2013) to measure RV, $T_{\rm eff}$, and $\log g$. Our grid of PHOENIX-ACES models assumes solar metallicity and has 100 K spacing in $T_{\rm eff}$ and 0.5 dex spacing in $\log g$. The forward model and fringing model used for this fit are described in § 3.5.

From these fits, we obtain a fairly consistent picture of $T_{\rm eff}$ and log(g) between the different observation epochs. Our statistical errors on each measured $T_{\rm eff}$ and log(g) are very small: $\sim$ 15 K for $T_{\rm eff}$ and 0.01 dex for log(g). In reality, model uncertainties are expected to be larger so we report the weighted averages and adopt half a grid step as the error bars. In summary, we find $T_{\rm eff} = 4200 \pm 50$ K and log(g)= 4.40 ± 0.25, which agree within 1σ with literature values listed in Table 3.1.

Fitting HIP 55507 A spectra with `petitRADTRANS`

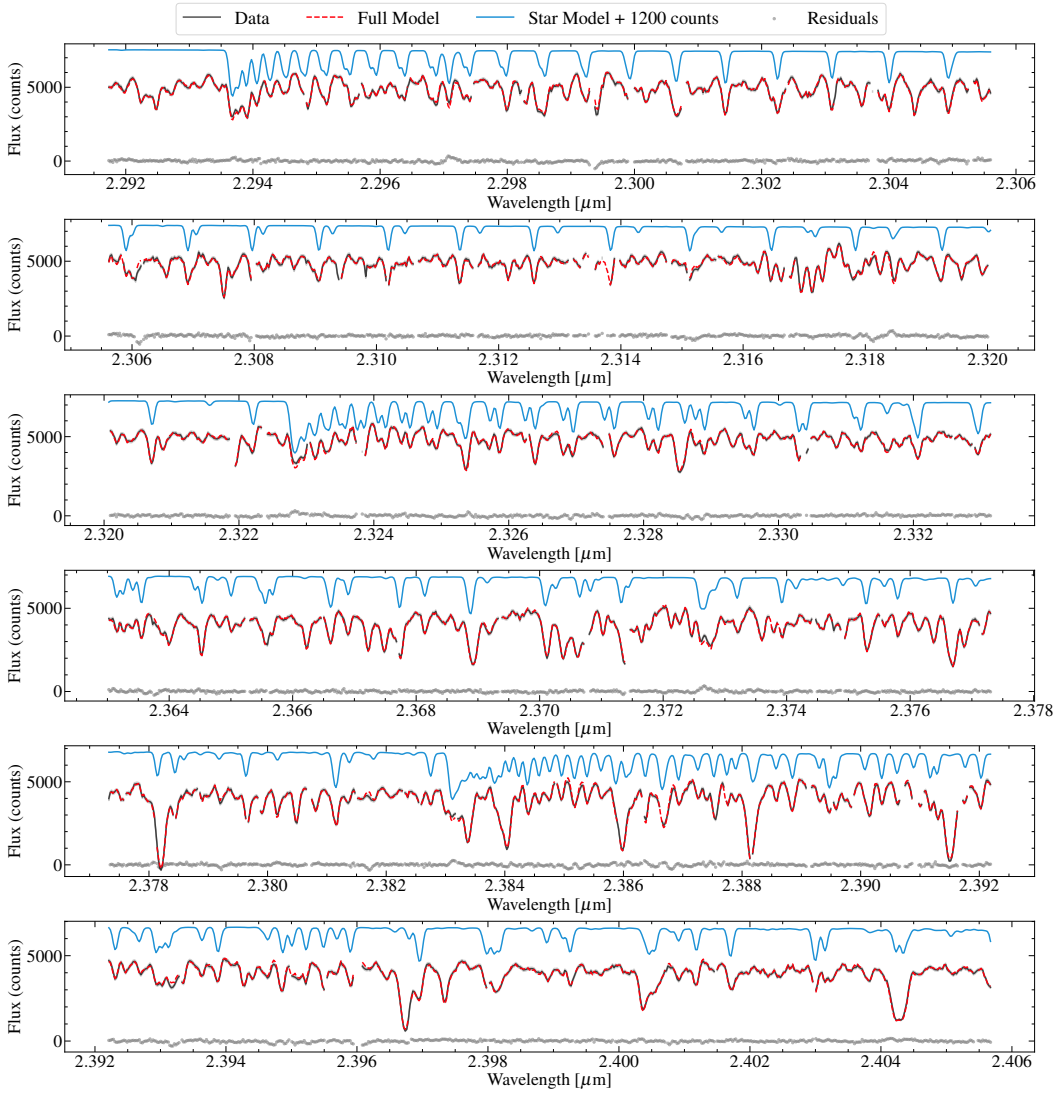

Figure 3.14: KPIC spectra for HIP 55507 A are plotted in black. We break up each spectral order into three panels. The full model (FM_A in Eq. 3.2) is in red, and includes the stellar model (M_A) from `petitRADTRANS` in blue and the telluric and instrumental response (T). The fringing model is also incorporated in the full model. The stellar model is offset by +1200 counts for clarity. The residuals are shown as gray points. CO lines dominate at these wavelengths for HIP 55507 A. We measure ^{12}CO/^{13}CO and C^{16}O/C^{18}O from the spectrum.

Chapter 4

ARE THESE PLANETS OR BROWN DWARFS? BROADLY SOLAR COMPOSITIONS FROM HIGH-RESOLUTION ATMOSPHERIC RETRIEVALS OF ~10–30 $M_{\rm Jup}$ COMPANIONS

This chapter reproduces my KPIC survey paper, where I uniformly measure the C and O abundances of eight substellar companions with masses of $\sim 10-30\ M_{\rm Jup}$. For two of the companions ($T_{\rm eff} \approx 1700-2000$ K), I find that cloudy atmospheric models fit better compared to clear models, which represents an update to the findings of Chapter 2. Specifically, I found that clouds could still modify the K-band high-resolution spectrum when the cloud base locations intersect with the emission contribution function. In contrast, for HD 4747 B, a colder companion with $T_{\rm eff} \approx 1400$ K and higher surface gravity, the major cloud bases are predicted to lie entirely below the emission contribution function in the K band. Overall, this paper extends the trend of chemical homogeneity found in my previous work to lower masses, demonstrating that companions with masses down to $\approx 10\ M_{\rm Jup}$ at wide separations (> 50 AU) are still chemically consistent with their host stars.

Xuan, J. W. et al. (July 2024). "Are These Planets or Brown Dwarfs? Broadly Solar Compositions from High-resolution Atmospheric Retrievals of ~10–30 M $_{Jup}$ Companions". In: *The Astrophysical Journal* 970.1, 71, p. 71. DOI: 10.3847/1538-4357/ad4796.

Abstract

Using Keck Planet Imager and Characterizer (KPIC) high-resolution (R~35000) spectroscopy from 2.29 – 2.49 μm, we present uniform atmospheric retrievals for eight young substellar companions with masses of ~10–30 $M_{\rm Jup}$, orbital separations spanning ~50–360 au, and $T_{\rm eff}$ between ~1500–2600 K. We find that all companions have solar C/O ratios, and metallicities, to within the 1-2σ level, with the measurements clustered around solar composition. Stars in the same stellar associations as our systems have near-solar abundances, so these results indicate that this population of companions is consistent with formation via direct gravitational collapse.

Alternatively, core accretion outside the CO snowline would be compatible with our measurements, though the high mass ratios of most systems would require rapid core assembly and gas accretion in massive disks. On a population level, our findings can be contrasted with abundance measurements for directly imaged planets with $m < 10\ M_{\rm Jup}$, which show tentative atmospheric metal enrichment compared to their host stars. In addition, the atmospheric compositions of our sample of companions are distinct from those of hot Jupiters, which most likely form via core accretion. For two companions with $T_{\rm eff}$~1700–2000 K (κ And b and GSC 6214-210 b), our best-fit models prefer a non-gray cloud model with $> 3\sigma$ significance. The cloudy models yield $2-3\sigma$ lower $T_{\rm eff}$ for these companions, though the C/O and [C/H] still agree between cloudy and clear models at the 1σ level. Finally, we constrain ^{12}CO/^{13}CO for three companions with the highest S/N data (GQ Lup b, HIP 79098 b, and DH Tau b), and report $v \sin i$ and radial velocities for all companions.

4.1 Introduction

High-contrast imaging surveys have revealed a population of substellar companions, generally classified as giant planets ($\sim 2-13\ M_{\rm Jup}$) or brown dwarfs ($\sim 13-75\ M_{\rm Jup}$), orbiting at large separations ($\sim 3-1000$ au) from their host stars (see reviews by Bowler, 2016; Currie et al., 2023a). Between giant planets and brown dwarfs, there are also dozens of low-mass substellar companions (m ~10–30 $M_{\rm Jup}$) at wide orbital separations (dozens to hundreds of au). These objects have often been termed 'planetary-mass companions' (e.g. Ireland et al., 2010; Kraus et al., 2013), though there is no conclusive evidence as to whether they form like planets. Insights into their formation processes would help provide more physically-based definitions for giant planets and brown dwarfs (Schlaufman, 2018), with giant planets being the product of bottom-up core accretion (Pollack et al., 1996), and brown dwarfs the product of top-down gravitational collapse either in a disk or molecular cloud (e.g. Offner et al., 2010; Bate, 2012; K. Kratter et al., 2016).

These widely-separated 10–30 $M_{\rm Jup}$ companions have occurrence rates of only a few percent (e.g. Nielsen et al., 2019). The rarity of these companions aligns with the difficulties that they pose to both planet-like and star-like formation processes. The current orbital locations of many of these companions are too far for either core accretion or disk instability to operate efficiently given low surface densities at large distances (> 100 au) in the disk (e.g. Dodson-Robinson et al., 2009). On the other hand, cloud fragmentation has issues explaining the extreme mass ratios (a few percent) of these systems (e.g. Bate, 2012). If these companions form via

core accretion at closer distances followed by outward scattering, there should be close-in companions that served as the scatters, which have not yet been detected (Bryan et al., 2016; Pearce et al., 2019).

To understand the nature of directly imaged companions, the field has focused on two complementary approaches. The first examines their orbital architectures as a function of companion mass. Such studies have found evidence for distinct distributions of semi-major axis, orbital eccentricity, and stellar obliquity around a dividing mass of $\sim 10-20\ M_{\rm Jup}$ (Nielsen et al., 2019; Bowler et al., 2020; Bowler et al., 2023; Nagpal et al., 2023), though the exact results can be sensitive to the specific dividing mass (Do Ó et al., 2023). This suggests a fuzzy boundary between giant planets and brown dwarfs and highlights the importance of further understanding the intermediate-mass companions with ~10–30 $M_{\rm Jup}$. The second approach relies on the analysis of spectro-photometry, which contains information about the physical processes and chemical inventory of their atmospheres. Indeed, the atmospheric abundances of substellar companions encode fossil information about their accretion histories, and could potentially inform different formation scenarios (e.g. Gravity Collaboration et al., 2020; P. Mollière et al., 2022).

Early studies highlighted the carbon and oxygen abundances of the atmosphere as informative observables (e.g. Öberg et al., 2011; Madhusudhan, 2012). To first order, the C/O ratios of solids in the disk are predicted to vary as a function of disk radius. Planets that form via core accretion in a protoplanetary disk, which is a relatively slow process occurring on Myr timescales, can incorporate varying quantities of gas and solids into their atmospheres, potentially resulting in a wide range of atmospheric metallicities and C/O ratios. On the other hand, companions that form rapidly on dynamical timescales via direct gravitational collapse are expected to inherit C/O and metallicities similar to those of their host stars, analogous to the case of binary star systems (Hawkins et al., 2020).

However, these predictions can be complicated by a range of effects. In particular, if widely-separated ($\gtrsim$ 100 au), ~10–30 $M_{\rm Jup}$ companions can form via core accretion outside the CO snowline, they are expected to have stellar C/O and metallicities as the solids at these locations are of stellar composition and the bulk of the metals is in the solid phase (Chachan et al., 2023). We may also see systematically lower atmospheric metallicities for objects that form via core accretion in the outer disk, as small grains could rapidly drain inward to the star in the absence of pressure gaps. On the other hand, if these companions form via disk instability, pressure

bumps and spiral structures can lead to local enhancements or reductions in the disk metallicity that can be inherited by the companions (e.g. Boley et al., 2011). Therefore, mapping the measured composition of a single planet/companion to a specific formation pathway is far from a simple one-to-one process and requires sophisticated disk models to fully disentangle the intricacies (P. Mollière et al., 2022).

While there could be significant uncertainty in interpreting the composition for a single object, a dominant process would be more apparent as a trend in the population. In this regard, J. Wang (2023a) noted that several imaged planets with $m \approx 3-13\ M_{\rm Jup}$ have metallicities higher than their star's by ≈0.1–0.7 dex, with typical errors of 0.2 dex (Gravity Collaboration et al., 2020; Petrus et al., 2021; Brown-Sevilla et al., 2023; J. Wang et al., 2023; P. Mollière et al., 2020; J. Wang, 2023a), suggesting that they may have formed via core accretion. Recently, Z. Zhang et al. (2023) also reported a potential ∼30–170× metal enrichment for AF Lep b ($\approx 3M_{\rm Jup}$) relative to its star. These measurements are not without caveats. For example, Z. Zhang et al. (2023) could not reliably constrain the C/O of AF Lep b from their low-resolution data and Landman et al. (2023b) showed that high-resolution retrievals of β Pic b lead to sub-stellar metallicity that disagree with the super-stellar metallicity found by Gravity Collaboration et al. (2020) using low-resolution data. Despite these caveats, there is a possible trend of super-stellar metallicities for at least some directly imaged planets. In contrast, higher mass ($m \sim 50-70\ M_{\rm Jup}$) brown dwarf companions generally exhibit both C/O and bulk metallicities consistent with their stellar values (e.g. Line et al., 2015; J. W. Xuan et al., 2022; J. Wang et al., 2022; Phillips et al., 2024), which is expected given their presumed binary-star like formation pathways. A few exceptions to this trend of chemical homogeneity between high mass BDs and their stars have been attributed to missing physics in the modeling, rather than real differences (e.g. Calamari et al., 2022; Balmer et al., 2023).

Systematically measuring the atmospheric compositions of ∼10–30 $M_{\rm Jup}$ companions could help determine their nature. To date, only a few of these companions have reported abundance measurements (Hoch et al., 2020; Y. Zhang et al., 2021b; Hoch et al., 2022; Palma-Bifani et al., 2023; Demars et al., 2023; Inglis et al., 2024), with a trend of approximately solar C/O values (Hoch et al., 2023). With the exception of Inglis et al. (2024) however, all these studies employed medium-resolution spectroscopy (R∼4000) and used self-consistent grid models to estimate

the companion's abundances. Grid models with low dimensionality can provide poor fits to data but yield unrealistically tight constraints on the model parameters (e.g. Ruffio et al., 2021), though this could be accounted for by inflating the uncertainties (Hoch et al., 2020). In addition, older grid models may contain outdated line lists, while the retrieval approach enables the incorporation of new line lists more easily. Retrievals also allow more flexibility in defining the cloud models and fitting for isotopic abundances. However, retrievals are not without caveats either. For example, retrieval studies often produce unphysically small radii (e.g. E. C. Gonzales et al., 2020b; Burningham et al., 2021; Lueber et al., 2022; Hood et al., 2023), and overly isothermal profiles which might suggest inadequacies in the cloud models (e.g. Burningham et al., 2017; Brown-Sevilla et al., 2023). Ultimately, it is important to compare both approaches, for example, by using the information from self-consistent thermal profiles as informed priors in retrievals (Z. Zhang et al., 2023; J. W. Xuan et al., 2024c).

In this paper, we present systematic atmospheric retrievals for a sample of eight young ($\sim 1-100$ Myr) companions with $m\sim$10–30 $M_{\rm Jup}$ using Keck Planet Imager and Characterizer (KPIC) high-resolution spectroscopy ($R\sim$35,000, K band). To ensure physical solutions, our retrievals are informed by mass and radius priors from evolutionary models, and self-consistent thermal profiles following J. W. Xuan et al. (2024c). We measure the C and O abundances of all companions and constrain the ^{12}C/^{13}C for three companions with the highest signal-to-noise (S/N) data. With the statistical leverage of our sample and uniform analysis framework, we aim to understand whether this population of objects is more akin to high-mass giant planets or low-mass brown dwarfs.

This paper is organized as follows: § 4.2 overviews the known properties of our eight systems and uniformly estimates the stellar ages and companion bulk properties from evolutionary models. In § 4.3, we describe the KPIC observations and data reduction. § 4.4 lays out our spectral analysis framework, including the atmospheric retrieval setup. The results of our retrievals are summarized in § 4.5, and we discuss the implications of our measurements and analysis in § 4.6. Finally, we present our conclusions in § 4.7.

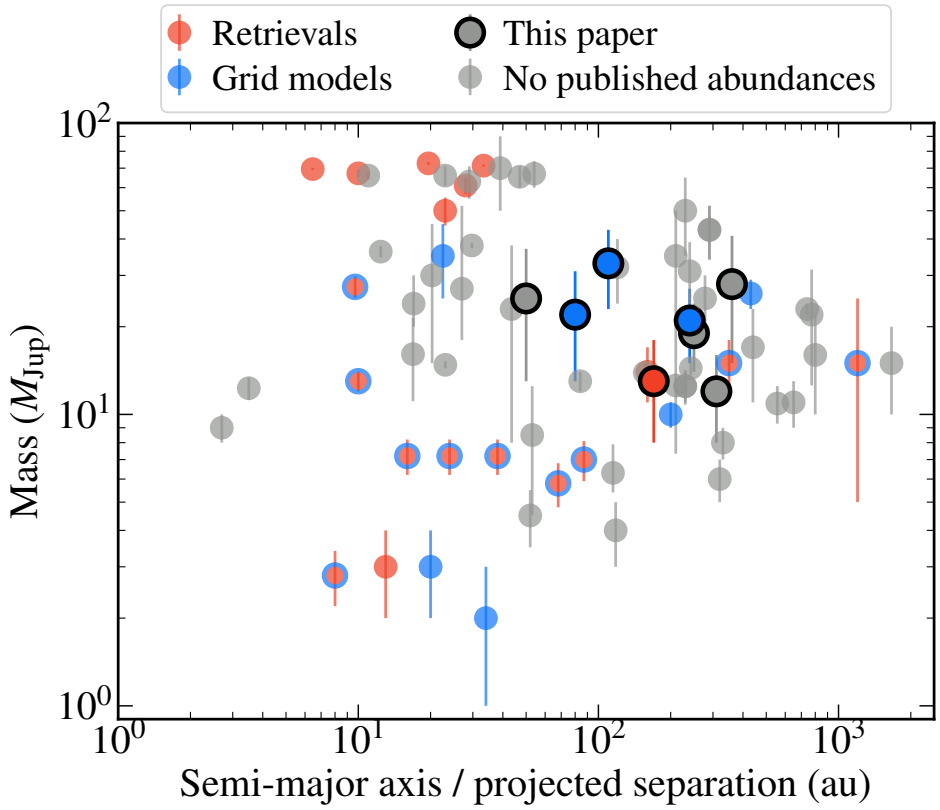

Figure 4.1: Confirmed directly imaged substellar companions that have published C/O and metallicity values from retrievals (red) and/or grid model fits (blue). Objects that have abundance measurements from both grid models and retrievals are shown as red points with a blue outline. The eight companions studied in this paper are denoted with a black outline. As shown, some of our objects have previous abundance measurements, which we summarize in § 4.2.

4.2 System properties

In Fig. 4.1, we place our sample in the context of directly imaged companions with both C/O and metallicity measurements.[1] Our sample consists of six late K to early

[1]Before this work, directly imaged companions with measured abundances from both retrievals and grid model fits are: AF Lep b (Z. Zhang et al., 2023; Palma-Bifani et al., 2024), HR 8799 b, c, d, e (Lavie et al., 2017; J. Wang et al., 2020; P. Mollière et al., 2020; J. Wang et al., 2023; Konopacky et al., 2013; Barman et al., 2015; Ruffio et al., 2021), β Pic b (Gravity Collaboration et al., 2020; Landman et al., 2023b), HIP 62426 b (J. Wang, 2023b; Petrus et al., 2021), HD 206893 B (Kammerer et al., 2021), VHS J1256–1257 b (Gandhi et al., 2023; Petrus et al., 2023; Petrus et al., 2024). The objects with abundances from retrievals are 51 Eri b (Whiteford et al., 2023; Brown-Sevilla et al., 2023), YSES 1 b (Y. Zhang et al., 2021b), HD 4747 B (J. W. Xuan et al., 2022), HR 7276 B (J. Wang et al., 2022), Gl 229 B (Calamari et al., 2022; Howe et al., 2022), HD 72426 B (Balmer et al., 2023), HD 33632 B (Hsu et al., 2024a), HD 984 B (Costes et al., 2024). Finally, objects with abundances from grid models are PDS 70 b and c (J. J. Wang et al., 2021a), κ And b (Hoch et al., 2020), HD 284149 b (Hoch et al., 2022), AB Pic b (Palma-Bifani et al., 2023), GQ Lup b and GSC 6214-210 b (Demars et al., 2023).

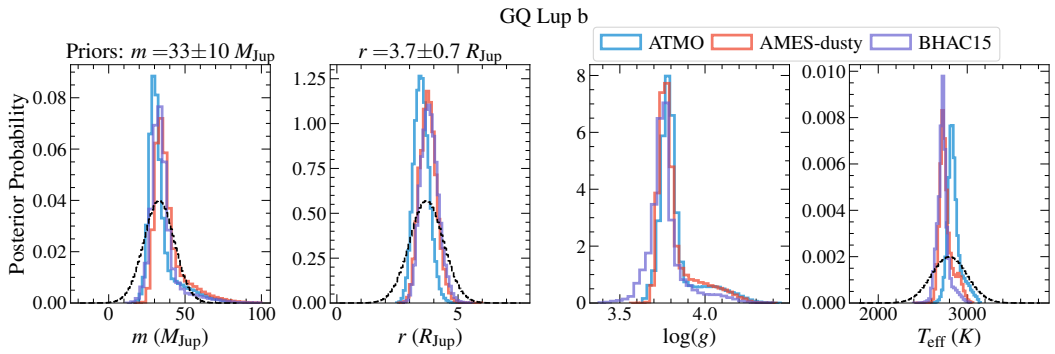

Figure 4.2: The interpolated mass, radius, $\log g$, and $T_{\rm eff}$ from three different evolutionary models (ATMO 2020 in blue, Phillips et al. 2020; AMES-Dusty in red, Allard et al. 2001; BHAC15 in purple, Baraffe et al. 2015) for GQ Lup b. The dashed black lines indicate the adopted priors for mass and radius in the retrievals. Plots for the other companions are shown in Appendix 4.10.

M type stars (GQ Lup, DH Tau, ROXs 12, ROXs 42B, 2M0122, GSC 6214-610) and two B stars (HIP 79098, κ And), and are either confirmed or likely members of various nearby star-forming regions and/or young moving groups. Indeed, five of the systems are located in the Scorpius–Centaurus association. Below, we summarize the properties of the systems, with a focus on parameters relevant to our retrieval study.

Stellar ages

The stellar, and by extension, system ages can inform the evolutionary states of substellar companions, including their radius and mass. To estimate ages of our stars, we either perform isochrone fitting or adopt a literature age when isochrone fitting is complicated by factors such as unresolved binarity. For isochrone fitting, we use the Baraffe et al. (2015) models (BHAC15) and fit using literature bolometric luminosity and $T_{\rm eff}$ measurements for the stars. We inflate the $T_{\rm eff}$ error bars to 150 K to be conservative, which is larger or equal to the reported $T_{\rm eff}$ uncertainties for our stars. For $L_{\rm bol}$, we apply a correction based on the stars' Gaia DR3 parallaxes, as several measurements were reported using a pre-Gaia distance. We implement a rejection-sampling method to interpolate the models in mass and age space following Dupuy et al. (2017). In short, for each mass-age pair, we compare the interpolated $T_{\rm eff}$ and $L_{\rm bol}$ to the measured values and accept values based on their probability. The median and 68% credible interval of the resulting age posteriors are listed in Table 4.1, and as we discuss in § 4.2, are all consistent with previous age estimates in the literature.

Companion mass and radius

Given the stellar ages and literature measurements of the companions' $L_{\rm bol}$, we can derive the expected companion mass and radius from substellar evolutionary models that have been shown to reasonably reproduce the bulk properties of benchmark substellar companions with dynamical masses (e.g. Dupuy et al., 2017) – although the models can differ from each other. To derive these priors while accounting for model uncertainty, we consider four different evolutionary models: ATMO 2020 (Phillips et al., 2020; Chabrier et al., 2023), SM08 (Saumon et al., 2008), AMES-Dusty (Allard et al., 2001), and BHAC15 (Baraffe et al., 2015).[2]

With the same rejection-sampling technique as described above, we use the stellar ages and companion $L_{\rm bol}$ to derive posteriors for mass, radius, $T_{\rm eff}$, and $\log g$. As described in § 4.4, we will use the evolutionary-model derived mass and radius as priors in our atmospheric retrievals. Since different models predict slightly different mass and radius, we visually determine mass and radius priors that encompass most of the posterior range for different models. These priors are listed in Table 4.1, and we show an example in Fig. 4.2. Plots for other companions are included in Appendix 4.10. We note that our derived masses and radii are consistent with previous estimates in the literature for each companion, and we rederive them for the sake of uniformity.

Overview of the systems

Below, we summarize the properties of each system, including our derived stellar ages and companion properties. Note that most of our companions show little orbital motion since their discovery, so we quote their projected orbital separations at the epoch of the KPIC observations. Statistically, the most likely orbital semi-major axis is similar to the observed projected separation (Yelverton et al., 2019).

ROXs 42B

ROXs 42B is a resolved binary with K-band flux ratio ∼3 (Ratzka et al., 2005) and a member of the ρ Ophiuchus cloud (ρ Oph). Our isochrone fits for the primary component yield an age of $2.2^{+1.8}_{-1.0}$ Myr, consistent with the ρ Oph age from Miret-Roig et al. (2022), who confirmed the star's ρ Oph membership from Gaia DR3 kinematics. A candidate companion was identified around the binary by

[2]Specifically, we use the chemical equilibrium models in ATMO 2020 and the hybrid cloud models in SM08. We note that the BHAC15 and SM08 grids do not cover the necessary parameter space for some of our companions, so we only use them when possible.

Ratzka et al. (2005) and later confirmed by Kraus et al., 2013. The companion is located at a projected separation $\rho \approx 1.2''$ from the central binary, or about 170 au.[3] The companion has a spectral type of $L1 \pm 1$ (Bowler et al., 2014b). Using the companion's $L_{\rm bol}$ from Currie et al. (2014), we estimate $m = 13 \pm 5\ M_{\rm Jup}$ and $r = 2.10 \pm 0.35\ R_{\rm Jup}$ for ROXs 42B b, consistent with previous studies (e.g. Kraus et al., 2013; Currie et al., 2014). An early retrieval study was performed by Daemgen et al. (2017), who used only $1 - 5\ \mu$m photometry and did not provide constraints on the companion's chemical abundances. Recently, Inglis et al. (2024) performed retrievals on pre-upgrade Keck/NIRSPEC spectra ($R \sim 25,000$) of the companion, finding $C/O = 0.50 \pm 0.05$, [Fe/H] $= -0.67 \pm 0.35$, and $v \sin i = 10.5 \pm 0.9$ km s^{-1}. ROXs 42 b has a mid IR excess from Spitzer indicative of a circumsubstellar disk (Martinez et al., 2021), although the companion does not show any accretion features.

ROXs 12

ROXs 12 is likely a member of ρ Oph (Miret-Roig et al., 2022). However, Luhman (2022) assign the star memberships of either ρ Oph or Upper Scorpius (Upper Sco). For consistency, we perform isochrone fitting to obtain $6.5^{+3.8}_{-2.6}$ Myr, consistent with the age estimate from Kraus et al. (2013). A candidate companion to ROXs 12 was first noted by Ratzka et al. (2005) and later confirmed by Kraus et al. (2013). The companion (ROXs 12 b) is located at a projected separation of $\approx 1.8''$ or about 250 au. Based on the companion's $L_{\rm bol}$ estimated by Bowler et al. (2017), we find m=19±5 $M_{\rm Jup}$ and r=2.2±0.35 $R_{\rm Jup}$. Bowler et al. (2017) perform a detailed characterization of the system, and we summarize the results. They determine a spectral type of $L0 \pm 2$ for the companion and find that the companion is likely on a misaligned orbit relative to the host star's spin axis. These authors also find evidence of an outer tertiary component in the system at 5000 au, which shares common proper motion and radial velocity as ROXs 12. A lack of Paβ emission indicates there is no evidence of a disk around ROXs 12 b. Bryan et al. (2020a) use pre-upgrade Keck/NIRSPEC to measure $v \sin i = 8.4^{+2.1}_{-1.4}$ km s^{-1} for ROXs 12 b.

DH Tau

DH Tau is a member of Taurus. Given the large age scatter in Taurus (e.g. Luhman, 2023), we perform isochrone fits to derive $0.7^{+0.3}_{-0.1}$ Myr. The companion to DH

[3]We report the projected separation at time of the KPIC observation for all companions, which is between 2020 to 2023.

Tau was discovered by Itoh et al. (2005) and Luhman et al. (2006), and orbits at a projected separation of $\approx$ 2.3″ or ≈310 au from DH Tau, which is part of an ultra-wide binary system (2210 au) with DI Tau (Kraus et al., 2009). Bonnefoy et al. (2014) determine a spectral type of M9−9.5 for DH Tau b. Based on the companion's $L_{\rm bol}$ from Luhman et al. (2006), we estimate m=12±4 $M_{\rm Jup}$ and r=2.6±0.6 $R_{\rm Jup}$ for the companion. J. W. Xuan et al. (2020b) measured $v \sin i$ = 9.6 ± 0.7 km s^{-1} for DH Tau b using pre-upgrade Keck/NIRSPEC data and detected CO and H_2O in its spectrum. DH Tau b is likely accreting via a circumsubstellar disk, as evidenced by the presence of the $H\alpha$ line, excess optical continuum emission (Zhou et al., 2014), the Paβ line (Bonnefoy et al., 2014), detection of linear polarization (Holstein et al., 2021), and mid-IR excess emission seen in Spitzer (Martinez et al., 2021).

GQ Lup

GQ Lup is an on-cloud member of Lupus 1. Galli et al. (2020) estimate an age of 1.2 − 1.8 Myr for Lupus 1. For consistency, we carry out isochrone fits and obtain $2.5^{+1.5}_{-0.9}$ Myr. The companion GQ Lup b was discovered by Neuhäuser et al. (2005) and has a projected separation of $\approx$ 0.7″ or $\approx$ 110 au. Alcalá et al. (2020) found a wide $\sim 0.15 M_\odot$ component at 2400 au, which they conclude to be most likely bound to GQ Lup A, making this a likely triple system. Like DH Tau b, GQ Lup b likely hosts a circumsubstellar disk, as indicated by $H\alpha$ and Paβ emission lines and an elevated optical continuum (Seifahrt et al., 2007; Zhou et al., 2014; Demars et al., 2023). Stolker et al. (2021) fitted 0.6–5 μm spectro-photometry of the companion and determined a spectral type of M9. They also found excess emission at 4–5 μm that can be explained from a blackbody with $T \approx 460$ K, which they attribute to a disk around GQ Lup b. Demars et al. (2023) used VLT/SINFONI medium-resolution data and grid models based on ATMO to estimate C/O and metallicity for GQ Lup b. Their values are broadly consistent with a solar composition, but discrepant between different observing epochs at the $\sim$ 60% level in C/O and > 0.4 dex in metallicity. From VLT/CRIRES spectroscopy of GQ Lup b, Schwarz et al. (2016) measured $v \sin i = 5.3^{+0.9}_{-1.0}$ km s^{-1} and made detections of CO and H_2O in the companion's atmosphere. Based on the companion's $L_{\rm bol}$ from Stolker et al. (2021), we estimate m = 33 ± 10 $M_{\rm Jup}$ and r = 3.7 ± 0.7 $R_{\rm Jup}$ for GQ Lup b.

GSC 06214-00210

GSC 06214-00210 (hereafter GSC 6214-210) is an Upper Sco member according to Miret-Roig et al. (2022), who determine the star to be in the slightly older "π

Sco" sub-group. Our isochrone fits yield $22.2^{+10.7}_{-8.0}$ Myr, consistent with the results from Pearce et al. (2019) who found $16.9^{+1.9}_{-2.9}$ Myr. The companion was discovered by Ireland et al. (2010) and is separated by 2.2″ on the sky or ≈ 240 au. Bowler et al. (2014a) determine a spectral type of M9.5 ± 1, and Bowler et al. (2011) detect Paβ line emission, indicating GSC 6214-210 b possesses a circumsubstellar disk. Demars et al. (2023) used VLT/SINFONI data and ATMO grid models to estimate C/O and [M/H] for GSC 6214-210 b. Their values are broadly consistent with solar, but discrepant between different epochs at the ∼ 70% level in C/O and ∼ 0.3 dex in metallicity. Bryan et al. (2018) use pre-upgrade Keck/NIRSPEC to measure $v \sin i = 6.1^{+4.9}_{-3.8}$ km s^{-1} for this companion. Using the companion's $L_{\rm bol}$ from Pearce et al. (2019), we estimate $m = 21 \pm 6\ M_{\rm Jup}$ and $r = 1.55 \pm 0.25\ R_{\rm Jup}$ for GSC 6214-210 b.

2MASS J01225093-2439505

2MASS J01225093-2439505 (hereafter 2M0122) is a member of AB Dor (Malo et al., 2013). Our isochrone fitting yields 144^{+105}_{-82} Myr, where the large error bars are due to the grid spacing. This age is consistent with the AB Dor age of 149^{+51}_{-19} Myr from C. P. M. Bell et al. (2015). The companion 2M0122 b was detected by Bowler et al. (2013) at a projected separation of ≈ 1.4″ or ≈ 50 au, who determine a spectral type of $L5 \pm 1$. Using the companion's $L_{\rm bol}$ from Hinkley et al. (2015), we estimate $m = 25 \pm 12\ M_{\rm Jup}$ and $r = 1.2 \pm 0.2\ R_{\rm Jup}$ for 2M0122 b.[4] Bryan et al. (2020b) use pre-upgrade Keck/NIRSPEC to measure $v \sin i = 13.4^{+1.4}_{-1.2}$ km s^{-1} for 2M0122 b, which enabled a measurement of the companion's obliquity when combined with its photometric rotation period of $6.0^{+2.6}_{-1.0}$ hr from Hubble Space Telescope (Zhou et al., 2019).

κ And

κ And is a probable member of Columba (Zuckerman et al., 2011), and has a range of previous age measurements as summarized by Hoch et al. (2020). Most recently, isochrone fitting from J. Jones et al. (2016) aided by an interferometric radius measurement of the star yields an age of 47^{+27}_{-40} Myr, broadly consistent with a Columba age. The BHAC15 grid does not go to high enough $T_{\rm eff}$ for κ And ($T_{\rm eff} \approx 11000$ K), so we adopt a uniform age prior between 5-100 Myr for this star based on the J. Jones et al. (2016) result to estimate the companion mass

[4]The large mass error incorporates a bi-modal distribution in the inferred masses for this companion, which is located at an age-luminosity space where degeneracies in mass exist due to deuterium burning (Bowler et al., 2013).

and radius. The companion κ And b was discovered by Carson et al. (2013), has spectral type of $L0-1$ Currie et al. (2018), and was at a projected separation of $\approx 0.8''$ at time of KPIC observations. Hoch et al. (2020) present a spectral analysis with $R \sim 4000$ K band Keck/OSIRIS spectra and report C/O= $0.70^{+0.09}_{-0.24}$ and a metallicity of $-0.2-0.0$. They also carry out orbit fits to estimate $a = 80^{+50}_{-20}$ au. With the companion's $L_{\rm bol}$ from Currie et al. (2018), we estimate $m = 22 \pm 9$ $M_{\rm Jup}$ and $r = 1.35 \pm 0.25$ $R_{\rm Jup}$.

HIP 79098

HIP 79098 is likely an unresolved binary in Upper Sco (Janson et al., 2019; Luhman et al., 2020). Miret-Roig et al. (2022) find HIP 79098 to be in the "σ Sco" sub-group of Upper Sco. Because the binary properties are unknown and the star exceeds the BHAC15 grid limits, we adopt the Upper Sco age of 10 ± 3 Myr for this system from Pecaut et al. (2016). The companion HIP 79098 b was discovered by Janson et al. (2019) at a projected separation of $\approx 2.4''$ or ≈ 360 au. This is the least studied companion in our sample, with only J, H, and K band photometry. Unlike for previous companions, we use HIP 79098 b's absolute K magnitude to estimate its $L_{\rm bol}$ with the empirical K-$L_{\rm bol}$ relation for young brown dwarfs from Sanghi et al. (2023). From this, we estimate $m = 28 \pm 13$ $M_{\rm Jup}$ and $r = 2.6 \pm 0.6$ $R_{\rm Jup}$ for the companion.

4.3 Observations and data reduction

KPIC observations

We observed the companions in this study using the upgraded Keck/NIRSPEC (Martin et al., 2018; López et al., 2020). The data were collected using both the first version of the KPIC fiber injection unit (FIU) (2019-2021; Delorme et al., 2021), and the upgraded phase 2 system (2022-2023; Echeverri et al., 2022). The FIU is located downstream of the Keck II adaptive optics system and is used to inject light from a selected target into one of the single-mode fibers connected to NIRSPEC. For all targets, we obtained $R \sim 35,000$ spectra in K band, which is broken up into nine echelle orders from 1.94-2.49 μm. The observing strategy is similar to that of J. J. Wang et al. (2021c), although in some datasets we 'nod' between two fibers to enable background subtraction between adjacent frames. The relative astrometry of each companion was computed using whereistheplanet.com (J. J. Wang et al., 2021b), based on literature orbital solutions and unpublished data for κ And b (J. Wang, private communication). For calibration purposes, we also acquire spectra

Table 4.1: System Properties for Young Companion Sample

Target Name	Host SpT	Host L_{bol}[b] ($L_{bol,\odot}$)	Host T_{eff} (K)	Age (Myr)	Comp. L_{bol}[b] ($L_{bol,\odot}$)	Comp. Mass (M_J)	Comp. Radius (R_J)	References
ROXs 42B[a] b	M0	-0.23 ± 0.10	3850 ± 150	$2.2^{+1.8}_{-1.0}$	-3.00 ± 0.10	13 ± 5	2.1 ± 0.35	3,8,11
ROXs 12 b	M0	-0.51 ± 0.06	3900 ± 150	$6.5^{+3.8}_{-2.6}$	-2.81 ± 0.10	19 ± 5	2.2 ± 0.35	3,13,18
DH Tau b	M2.3	-0.11 ± 0.02	3600 ± 150	$0.7^{+0.3}_{-0.2}$	-2.76 ± 0.12	12 ± 4	2.6 ± 0.6	1,15,17
GSC 6214-210 b	K5	0.66 ± 0.05	4200 ± 150	$22.2^{+10.7}_{-8.0}$	-3.35 ± 0.10	21 ± 6	1.55 ± 0.25	4,10,21,22
2M0122-2439 b	M3.5	-1.78 ± 0.11	3400 ± 150	144^{+105}_{-82}	-4.22 ± 0.10	25 ± 12	1.2 ± 0.2	2,12,19
GQ Lup b	K7	0.02 ± 0.10	4300 ± 150	$2.8^{+1.8}_{-1.1}$	-2.15 ± 0.10	33 ± 10	3.7 ± 0.7	6,9,14
κ And b	B9	1.88 ± 0.03	11100 ± 150	$5 - 100$	-3.78 ± 0.10	22 ± 9	1.35 ± 0.25	7,8,16,23
HIP 79098 b	B9	2.33 ± 0.03	11650 ± 150	10 ± 3	-2.60 ± 0.20	28 ± 13	2.6 ± 0.6	5,20,23

[a] ROXs 42B is a resolved binary (Ratzka et al., 2005). The "B" symbol here indicates it is the second brightest optical counterpart in the circle of the X-ray source ROXs 42; i.e., ROXs 42B is not physically associated with ROXs 42A. The L_{bol} and T_{eff} refer to those of the primary star, as calculated by Kraus et al. (2013) after accounting for the binary flux ratio.
[b] Bolometric luminosities have been updated with Gaia DR3 parallaxes. Some of the literature companion L_{bol} measurements have very small error bars (< 0.05 dex) despite the limited wavelength coverage from which they are derived. To be conservative, we adopt 0.1 dex uncertainties on the L_{bol} when the quoted uncertainty is smaller than this.
References: (1) Itoh et al. (2005), (2) Bowler et al. (2013), (3) Kraus et al. (2013), (4) Ireland et al. (2010), (5) Janson et al. (2019), (6) Neuhäuser et al. (2005), (7) Carson et al. (2013), (8) Currie et al. (2018), (9) Stolker et al. (2021), (10) Pearce et al. (2019), (11) Bowler et al. (2014b), (12) Hinkley et al. (2015), (13) Bowler et al. (2017), (14) Donati et al. (2012), (15) Luhman et al. (2006), (16) J. Jones et al. (2016), (17) Yu et al. (2023), (18) Ratzka et al. (2005), (19) Sebastian et al. (2021), (20) Pecaut et al. (2016), (21) Bowler et al. (2014a), (22) Bowler et al. (2011), (23) Gaia Collaboration (2022).

of the host stars before observing the companions, and spectra of a nearby telluric standard star (A0 or B9 spectral type) at similar airmass as the science target. The standard star is observed right before or after the associated science observations. Table 4.2 summarizes the observations reported in this paper.

Data reduction

We only briefly summarize the data reduction procedure in this paper and refer to J. W. Xuan et al. (2024c) for additional details. For datasets using a single science fiber, we remove the thermal background from the raw images using combined instrument background frames taken before or after the night of observation. For datasets where we perform fiber-nodding, we apply nod-subtraction between adjacent frames, as the spectral traces of each fiber land on a different location in the detector. We also remove persistent bad pixels identified from the background frames. Then, we use data from a telluric standard star to fit the trace of each column in the four fibers and nine spectral orders, which gives us the position and standard deviation of the point spread function (PSF) in the spatial direction at each column. The trace positions and widths are smoothed using a cubic spline to mitigate random

Table 4.2: KPIC observations presented in this work. The throughput is end-to-end throughput measured from the top of the atmosphere and varies with wavelength due to differential atmospheric refraction and the instrumental blaze function. We report the 95% percentile throughput over the K band, averaged over all frames. We also report the median spectral SNR per pixel from 2.29 – 2.49 μm.

Target	UT Date	Exposure Time [min]	Airmass	Throughput	Median SNR/pixel	Proj. Sep. [arcsec][b]	Kmag
GQ Lup b	2023 June 23	99	1.8-2.4	~ 2.8%	~ 12[a]	0.71	13.5
GSC 6214-210 b	2023 June 20	105	1.3-1.7	~ 3.4%	~ 2	2.19	15.0
HIP 79098 b	2022 July 18	70	1.4-1.5	~ 3.7%	~ 6	2.36	14.2
DH Tau b	2022 Oct 12	50	1.2-1.5	~ 1.9%	~ 4	2.34	14.2
ROXs 12 b	2020 July 3	110	1.4-1.6	~ 2.3%	~ 4	1.79	14.1
ROXs 42 Bb	2020 July 2	160	1.4-1.6	~ 2.1%	~ 2	1.17	15.0
2M0122-2439 b	2021 Nov 19	80	1.4-1.5	~ 1.1%	~ 1	1.45	14.5
κ And b	2022 Nov 12	180	1.1-1.4	~ 1.8%	~ 5[a]	0.77	14.6

[a] For these two companions, we quote the SNR from the companion light only; the SNR values are determined after fitting for the speckle contribution in the data.
[b] For each companion, we quote the separation at the time of KPIC observations presented in this paper.

noise. We adopt the trace locations and widths as the line spread function (LSF) positions and widths in the spectral dispersion dimension.

For every frame, we then extracted the 1D spectra in each column of each order. To remove residual background light, we subtracted the median of pixels that are at least 5 pixels away from every pixel in each column. Finally, we used optimal extraction to sum the fluxes using weights defined by the 1D Gaussian LSF profiles calculated from spectra of the telluric star.

For our analysis, we use three spectral orders from 2.29-2.49 μm, which contain strong CO and H_2O absorption lines from the companions. The three spectral orders have gaps in between, and cover wavelengths of 2.29 – 2.34 μm (order 33), 2.36 – 2.41 μm (order 32), and 2.44 – 2.49 μm (order 31), respectively.

4.4 Spectral analysis

Forward model of KPIC high-resolution spectra

Our forward model for KPIC data follows the framework of previous KPIC papers (e.g. J. J. Wang et al., 2021c; J. W. Xuan et al., 2024c). Here, we present a brief summary. First, we generate atmospheric templates with `petitRADTRANS` (P. Mollière et al., 2019b; P. Mollière et al., 2020), which are shifted in RV and rotationally broadened using the function from Carvalho et al. (2023). Then, we convolve the RV-shifted and rotationally-broadened templates with the instrumental

LSF determined from spectral trace widths in the spatial direction.[5]

Next, the atmospheric template is multiplied by the telluric and instrumental response (T in Eq. 4.1), which is determined by dividing the standard star spectra by a PHOENIX-ACES model (Husser et al., 2013) matching the standard star's $T_{\rm eff}$ and $\log g$. Since our standard stars have A0 or B9 spectral types, they have nearly no spectral lines in the wavelength region we use in our analysis (2.29-2.49 μm), mitigating errors due to an imperfect stellar spectrum. For six of our companions, which have projected separations ∼1.2–2.5″ and generally low companion-star contrasts, we find that the speckle intensity is negligible from preliminary analysis; when allowing for a speckle contribution the fit quality does not improve. The two exceptions are GQ Lup b and κ And b, which are separated by <0.8″ from their host stars (see Table 4.2). For these two datasets, we account for the significant speckle flux in the companion spectra using the on-axis observations of their host stars, taken immediately before the companion exposures.

The last step is to flux-normalize the companion and/or stellar models and multiply them by flux scale factors, which are in units of NIRSPEC counts. After scaling, the companion and speckle models are added in the case of GQ Lup b and κ And b, while for the other companions, we only consider the companion flux. To summarize, the forward model is:

$$\mathrm{FM}_b = \alpha_b T M_b + \alpha_s D_s \tag{4.1}$$

where FM_b denotes the forward model fitted to the data, α_b and α_s are the flux scaling factors of the companion and speckle, T is the combined telluric and instrumental response, M_b is the companion template from `petitRADTRANS`, and D_s is the observed KPIC spectra of the host star, which already has T factored in. Note that for the six other companions besides GQ Lup b and κ And b, α_s is taken to be zero.

Lastly, to remove the smoothly varying continuum in the KPIC spectra, we apply high-pass filtering with a median filter of 100 pixels (∼ 0.002 μm) on the data and forward model (FM_b) before computing the residuals. The choice of 100 pixels was determined from a series of injection-recovery tests by J. W. Xuan et al. (2022) as the optimal size for accurately retrieving molecular abundances in KPIC data. In Appendix 4.11, we also show results from an alternative continuum treatment with a spline model (Ruffio et al., 2023a; Agrawal et al., 2023).

[5]Following J. W. Xuan et al. (2024c), we allow the LSF width to vary between 1.0 and 1.2 times the width measured in the spatial direction when generating the instrument-convolved companion templates.

Preliminary analysis for molecular detection

To confirm detection of the companion signal in our data, we fit the KPIC spectra of each companion using atmospheric models from the cloudless `Sonora` grid (M. S. Marley et al., 2021). We select `Sonora` models with $T_{\rm eff}$ and $\log g$ that best match each companion's bulk properties, as estimated from the evolutionary models in § 4.2. Using the forward model framework described above, we estimate the maximum likelihood value for both the companion flux and speckle flux in the data as a function of RV shift, following Ruffio (2019) and J. J. Wang et al. (2021c). This forward model framework allows us to estimate the companion flux (in data counts) as a function of RV, which can be interpreted as a cross-correlation function (CCF). In this paper, we refer to this as the CCF for simplicity, but note that it is not the same as the traditional CCF (e.g. as in eq.1 of J. W. Xuan et al. 2020b). To estimate the CCF S/N, we perform the same fitting procedure using a spectral trace that contains only background flux, and take the standard deviation of this background CCF as noise. We calculate CCFs for templates with CO, H_2O, and CO + H_2O, as shown in Fig. 4.3. The companions are detected with CCF S/N between 7 to 80 when using the combined CO+H_2O template, and both CO and H_2O are individually detected with S/N > 3 for all companions. By detecting the major carbon and oxygen-bearing species in their atmospheres, we can constrain their atmospheric compositions with retrievals.

Atmospheric retrieval setup and inputs

We use the radiative-transfer code `petitRADTRANS` to generate synthetic companion templates for use in atmospheric retrievals. These synthetic templates represent M_b in Eq. 4.1 of the forward model. We use the line-by-line opacity sampling mode, and down-sample the native $R = 10^6$ opacities by a factor of 3 to speed up the retrievals. In our retrievals, we fit for the chemical abundances (§ 4.4), cloud structure (§ 4.4), and temperature profile (§ 4.4). We impose mass and radius priors motivated by evolutionary models in the retrievals (§ 4.4). Other parameters such as RV, $v \sin i$, and flux scales (α_b, α_s) are also fitted for in our forward model. As an example, we summarize the fitted parameters in Table 4.3 for κ And b.

Opacities

For the hottest companions in our sample, we find that there is contribution to the emission spectrum from regimes with $T > 3000$ K (see Fig. 4.4), which exceeds $T_{\rm max} = 3000$ K of default `petitRADTRANS` opacity tables. Therefore, we adopt the

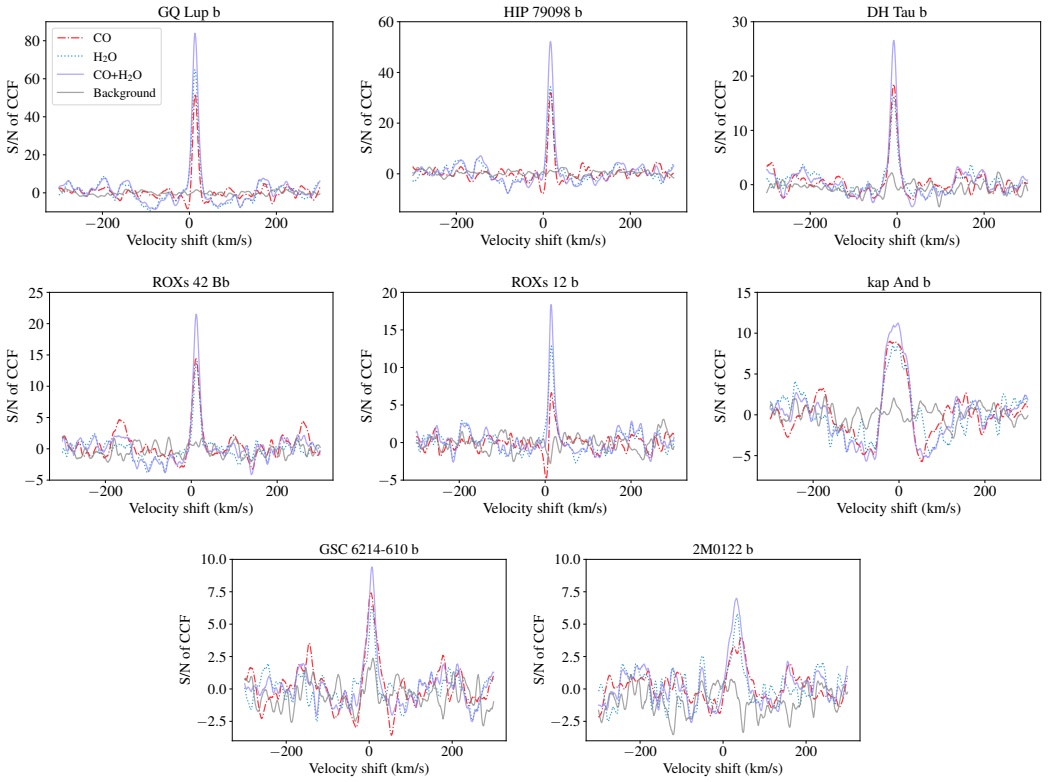

Figure 4.3: Cross-correlation functions (CCFs) with CO (red, dashdot lines), H_2O (blue, dotted lines), and CO+H_2O (purple, solid lines) molecular templates from M. S. Marley et al. (2021). Each panel is for a different companion, but shares the same legend. These CCFs are computed using 3 spectral orders from $2.29-2.49\,\mu$m. The gray lines are CCFs of the CO+H_2O templates with background flux in the slit, and we use the standard deviations of the gray lines to estimate the CCF noise. The effect of rotational broadening is clearly visible in the κ And b CCF.

opacities generated by J. W. Xuan et al. (2024c), which go up to 4500 K. We include the line opacities of $H_2^{16}O$ (Polyansky et al., 2018), $C^{16}O$, ^{13}CO (Rothman et al., 2010), OH (Brooke et al., 2016), FeH (Dulick et al., 2003; Bernath, 2020), TiO (McKemmish et al., 2019), AlH (Yurchenko et al., 2018), VO (McKemmish et al., 2016), H_2S (Azzam et al., 2016), and CH_4 (Hargreaves et al., 2020). In addition, we include atomic opacities from Na, K, Mg, Ca, Ti, Fe, Al, and Si (Kurucz, 2011). For continuum opacities, we include the collision induced absorption (CIA) from H_2-H_2 and H_2-He, as well as the H- bound-free and free-free opacity.

Chemistry

We parameterize the chemical abundances with C/O and [C/H], where [C/H] is equivalent to the bulk metallicity. In other words, we assume [C/H]=[Fe/H]=[N/H]

Table 4.3: Fitted Parameters and Priors for κ And b Retrievals

Parameter	Prior	Parameter	Prior
Mass (M_J)	$\mathcal{N}(22.0, 9.0)$	Radius (R_J)	$\mathcal{N}(1.35, 0.25)$
$T_{\rm anchor}$ [log(P) = -0.1][a] (K)	$\mathcal{U}(1600, 2800)$	RV (km s^{-1})	$\mathcal{U}(-50, 50)$
ΔT_1 [1.0 to 0.5] (K)	$\mathcal{U}(200, 700)$	$v \sin i$ (km s^{-1})	$\mathcal{U}(0, 80)$
ΔT_2 [0.5 to 0.3] (K)	$\mathcal{U}(50, 400)$	C/O	$\mathcal{U}(0.1, 1.0)$
ΔT_3 [0.3 to -0.1] (K)	$\mathcal{U}(50, 600)$	[C/H]	$\mathcal{U}(-1.5, 1.5)$
ΔT_4 [-0.1 to -0.4] (K)	$\mathcal{U}(0, 500)$	log CO	$\mathcal{U}(0, 6)$
ΔT_5 [-0.4 to -1.0] (K)	$\mathcal{U}(100, 750)$	$f_{\rm sed}$[d] (one for each cloud)	$\mathcal{U}(0, 10)$
ΔT_6 [-1.0 to -2.0] (K)	$\mathcal{U}(150, 650)$	log(K_{zz}/cm^2 s^{-1})[d]	$\mathcal{U}(5, 13)$
ΔT_7 [-2.0 to -4.0] (K)	$\mathcal{U}(50, 700)$	σ_g[d]	$\mathcal{U}(1.05, 3)$
log(gray opacity/cm^2 g^{-1})[b]	$\mathcal{U}(-6, 6)$	log($\tilde{X}_{\rm MgSiO_3}$)[d]	$\mathcal{U}(-2.3, 1)$
Error multiple[c]	$\mathcal{U}(1, 5)$	log($\tilde{X}_{\rm Fe}$)[d]	$\mathcal{U}(-2.3, 1)$
Comp. flux, α_c (counts)	$\mathcal{U}(0, 300)$	Speckle flux, α_s (counts)	$\mathcal{U}(0, 300)$

Notes: $\mathcal{U}$ stands for a uniform distribution, with two numbers representing the lower and upper boundaries. $\mathcal{N}$ stands for a Gaussian distribution, with numbers representing the mean and standard deviation. The P–T parameters are described in § 4.4 and the cloud parameters are described in § 4.4.

[a] The pressure at $T_{\rm anchor}$ and pressure points between which we fit ΔT values in our P–T profile are given in square brackets. They are in log(bar) units.

[b] Parameter for the gray opacity cloud model.

[c] An error multiple term is fitted for KPIC data to account for any underestimation of the uncertainties.

[d] Parameters for the EddySed cloud model.

and so on,[6] while the oxygen abundance is determined by [C/H] and C/O. We denote the bulk metallicity as [C/H] since we are only sensitive to C-, O-bearing species (i.e. CO, H_2O) in the companion atmospheres.

As in J. W. Xuan et al. (2022), we use an equilibrium chemistry grid in our retrievals computed with `easyCHEM`, a Gibbs free energy minimizer described in P. Mollière et al. (2017). In this paper, we update the chemical grid to use the updated solar elemental abundances from Asplund et al. (2021). Our chemical grid stores the mass-mixing ratios of both gas-phase species and condensates (which we use for the cloud model in the next section). We tested the option of including a quench pressure ($P_{\rm quench}$) to allow for carbon disequilibrium chemistry, which fixes the abundances of H_2O, CO, and CH_4 where $P < P_{\rm quench}$ using the equilibrium values

[6] We note that the assumption that [C/H]=[Fe/H] is only valid for companions that form outside the CO snowline (Chachan et al., 2023). Our companions are found at projected separations between $\sim 50-360$ au from their stars. Therefore, assuming no significant orbital migration took place, these companions are generally outside the inferred CO snowline locations of $\sim 30-80$ au for T Tauri stars with K spectral types and $\gtrsim 80$ au for Herbig Ae stars (e.g. Qi et al., 2013; Qi et al., 2015; Qi et al., 2019; K. Zhang et al., 2019).

found at $P_{\rm quench}$ (Zahnle et al., 2014). However, most of our companions are too hot ($T_{\rm eff} \gtrsim 1800\ K$) for CH_4 to be detectable, and simultaneous detection of CO and CH_4 is necessary to constrain carbon quenching (J. W. Xuan et al., 2022). Since we find that $P_{\rm quench}$ is unconstrained for all companions from preliminary tests, we do not include it in the reported retrievals.

Clouds

Condensate cloud opacity is expected to gradually decrease with increasing temperature from L to M spectral types, as important cloud particles such as $MgSiO_3$, Fe, and Al_2O_3 start to evaporate between ~1600–1900 K at a pressure of 0.1 bars (P. Mollière et al., 2022). Since our companions have spectral types ranging from L to early M spectral types, we consider both clear and cloudy models in order to explore the sensitivity of our retrieved abundances to the assumed cloud models.

For the cloudy models, we use 1) a simple gray opacity model which adds a constant opacity to the atmosphere, and the 2) EddySed model (Ackerman et al., 2001) as implemented in `petitRADTRANS`, which includes the effect of scattering from clouds (P. Mollière et al., 2020). We now describe fitted parameters of the EddySed model. First, $\log(\tilde{X}_{\rm MgSiO_3})$ is the scaling factor for the cloud mass fraction, so that $\log(\tilde{X}_{\rm MgSiO_3}) = 0$ is equal to the equilibrium mass fraction. The equilibrium mass fraction is determined by the chemical grid (see § 4.4). For each cloud condensate, this scaling factor along with $f_{\rm sed}$, $K_{\rm zz}$, and $\sigma_{\rm g}$ set the cloud mass fraction as a function of pressure and the cloud particle sizes (for details, see Ackerman et al., 2001; P. Mollière et al., 2020). Here, $f_{\rm sed}$ is the sedimentation efficiency, $K_{\rm zz}$ is the eddy diffusion coefficient, and $\sigma_{\rm g}$ is the width of the lognormal cloud particle size distribution. Following Z. Zhang et al. (2023), we fit a different $f_{\rm sed}$ for each cloud species but a global $K_{\rm zz}$ and $\sigma_{\rm g}$. Therefore, when including two different cloud species, there are a total of six cloud parameters.

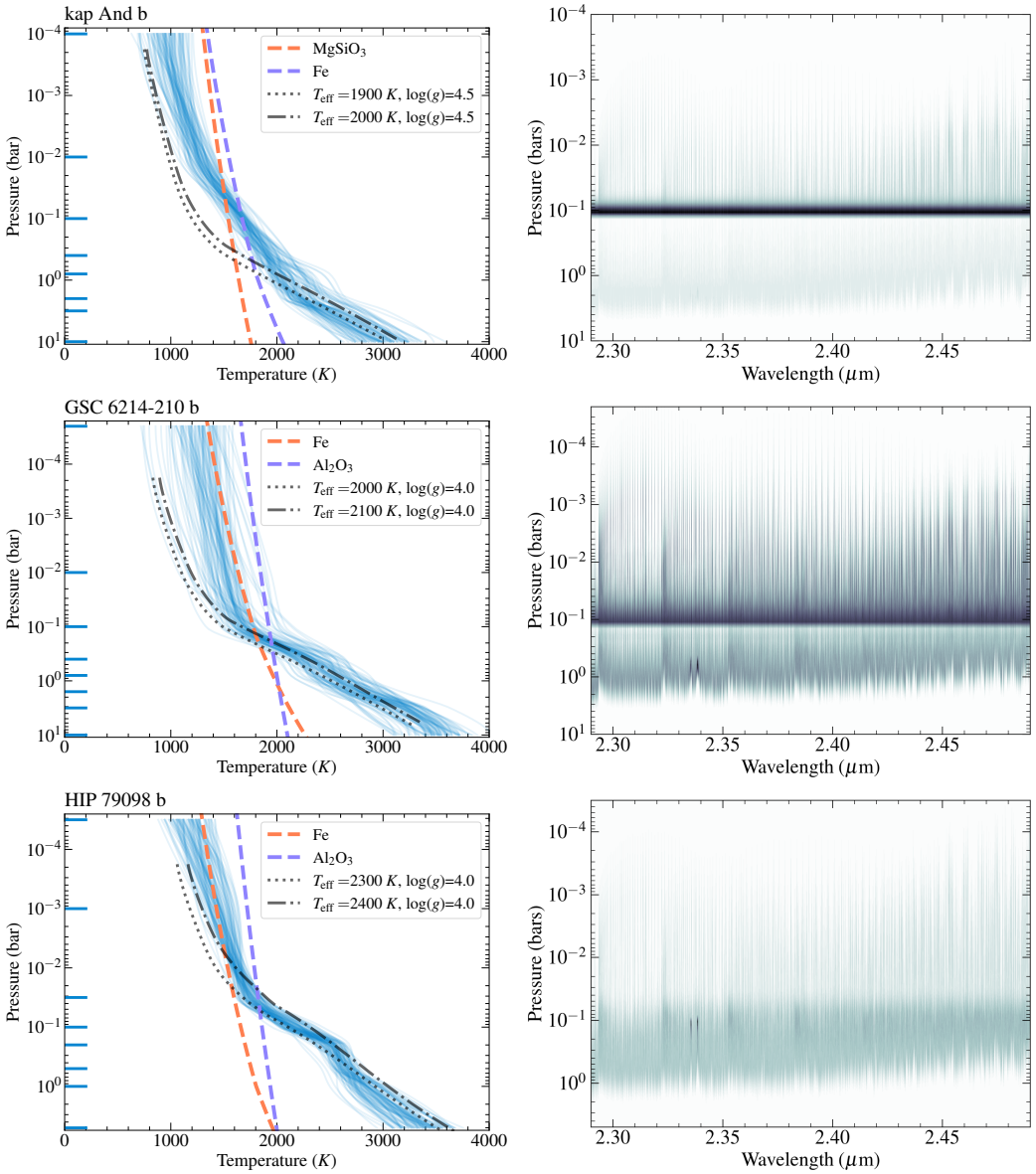

Figure 4.4: Retrieved P–T profiles and emission contribution functions for three example companions (one per row). Left panels: We plot random draws of the retrieved P–T profiles in blue. The gray lines show Sonora cloudless models (M. S. Marley et al., 2021) with similar bulk properties as the companions. Different cloud condensation curves are plotted as colored dashed lines. The horizontal blue lines mark pressure points between which we fit ΔT values in our P–T parameterization. Right panels: The emission contribution functions of the best-fit models. For a given wavelength, darker colors mean that a larger fraction of emission originates from that pressure level. The darker, bar-like structures seen for κ And b and GSC 6214-210 b coincide with the cloud base locations. In our best-fit EddySed models, we find that the total cloud optical depth (τ) is about 1.4/0.6 for κ And b/GSC 6214-210 b at their retrieved cloud bases, so a non-negligible part of the flux beneath the clouds can propagate through the cloud base. These two companions prefer the EddySed cloud model over the clear model to $> 3\sigma$ significance (see § 4.5). Plots for the other companions are included in Appendix 4.14.

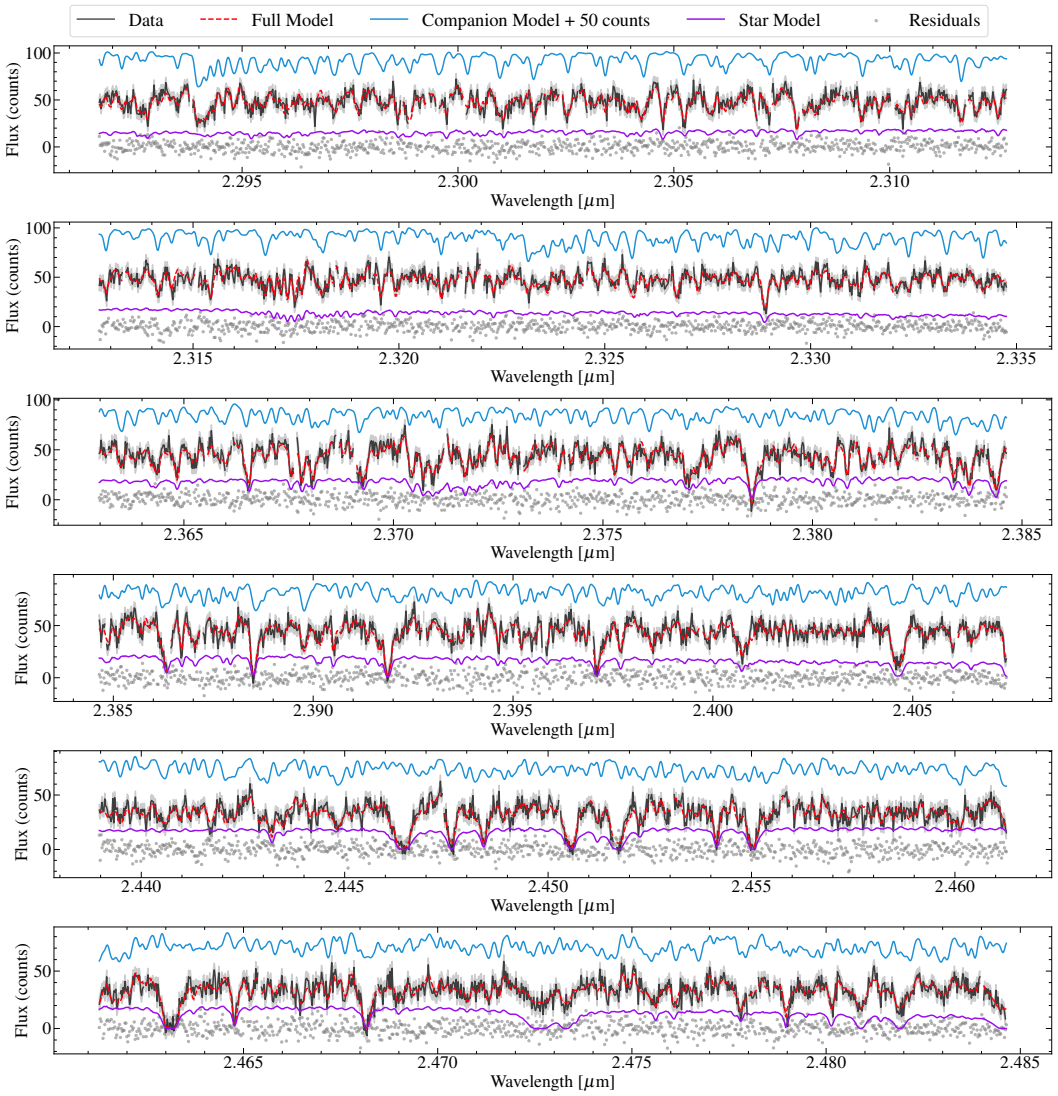

Figure 4.5: KPIC data of for GQ Lup b from one science fiber are shown in black, with error bars in gray. This represents half the data, since we nodded between two fibers. Each spectral order used in the retrieval is broken into two panels. The full model is shown in red dashed lines and consists of the RV-shifted and broadened companion model in blue (M_b in Eq. 4.1), the stellar model in purple (M_s) to model the speckle contribution, and the telluric and instrumental response (T). The residuals are shown as gray points. For clarity, an offset of +50 counts was added to the companion model. Plots for the other companions can be found in Appendix 4.13.

Given the range in $T_{\rm eff}$ of our objects, we consider models with $MgSiO_3$ + Fe for the colder objects ($T_{\rm eff} \lesssim 2000$ K) and Fe + Al_2O_3 for the hotter objects. Since the cross sections of these cloud species have similar slopes over the small wavelength range (2.29 – 2.49 μm) we are modeling (Wakeford et al., 2015), our choice of the cloud

species primarily serves to set the cloud base locations in the EddySed model. For each companion, we choose two cloud species which intersect their P–T profile at the deepest pressures (i.e. closer to the photosphere), as these clouds would more meaningfully impact the emission spectra.

Temperature structure

We adopt the pressure-temperature (P–T) parameterization from J. W. Xuan et al. (2024c), which is motivated by Piette et al. (2020). Our profile is parameterized by seven $\Delta T/\Delta P$ values between eight pressure points and the temperature at one of these pressures, $T_{\rm anchor}$. Because the photosphere for each companion is located at slightly different locations, we manually customize the pressure extent for each companion's retrieval to optimally encompass the companion's emission contribution. Specifically, we set at least four pressure points in the region where 90% of the flux originates, which we determine by computing the wavelength-weighted emission contribution function. We choose the other points to be approximately equally spaced in log pressure. The selected pressure points are labeled in Fig. 4.4 for a few companions, and listed in Table 4.3 and Appendix 4.12 for all companions. For the radiative transfer, the eight P–T points from our profile are interpolated onto a finer grid of 100 P–T points using a monotonic cubic interpolation as recommended by Piette et al. (2020). We do not apply smoothing to our profiles as Rowland et al. (2023) showed that smoothing can bias retrieval results.

Using this P–T prescription, we are able to set meaningful priors on the fitted $\Delta T/\Delta P$ values by considering atmospheric profiles from self-consistent models. After defining the pressure extent and pressure points used for a given companion, we fit SPHINX (Iyer et al., 2023) and Sonora (M. S. Marley et al., 2021) profiles with $T_{\rm eff}$ and $\log g$ similar to the companion's $T_{\rm eff}$ and $\log g$ using our P–T function. The expected $T_{\rm eff}$ and $\log g$ for each companion are determined from evolutionary models (§ 4.2). We save the best-fit P–T values of each self-consistent profile, noting that the $\Delta T/\Delta P$ values are very similar between profiles with different $T_{\rm eff}$ and $\log g$ as the slope is set by radiative-convective equilibrium. In the retrieval, we then set uniform P–T priors that bracket the mean of the best-fit values with a wide prior range of $\pm$ 50 – 100% of the mean value. While the self-consistent models we considered are cloudless, the wide uniform priors we impose allow sufficient flexibility in the profile shapes, as we discuss in § 4.5. We note that our method of setting physically-motivated priors on the P–T profile is similar in spirit to the approach from Z. Zhang et al., 2023, who imposed Gaussian priors on

the temperature gradient $d \ln T / d \ln P$ informed by self-consistent models in their retrievals. Both approaches leverage information from self-consistent P–T profiles to prevent the retrievals from returning overly isothermal or unphysical profiles.

Mass and radius priors from evolutionary models

The KPIC spectra are not flux-calibrated and cover a very small wavelength range. Hence, these data provide little information on a companion's radius and mass. We find that preliminary retrievals occasionally yield unphysical radii and $\log g$ for our companions (e.g. $\log g > 5$ for a young, low-gravity companion). Therefore, we adopt mass and radius priors from evolutionary models in our retrievals. These priors are described in § 4.2 and listed in Table 4.1.

Model fitting with nested sampling

We use nested sampling as implemented by `dynesty` (Speagle, 2020) to find the posterior distributions for the model parameters. Specifically, we use between 500-800 live points and adopt the stopping criterion that the estimated contribution of the remaining prior volume to the total evidence is less than 1%.

One advantage of adopting nested sampling is that we can use the Bayesian evidence from each fit to calculate the Bayes factor B, which quantifies the relative probability of model M_2 compared to M_1. We use the Bayes factor to compare different models throughout this paper to determine whether a given M_2 is justified over M_1.

4.5 Atmospheric retrieval results

We summarize the retrieval results in this section. Given the large number of objects, we focus on representative examples here. In Fig. 4.5, we plot the data and best-fit model for GQ Lup b, our highest S/N dataset. Plots for other companions are shown in Appendix 4.13. Key parameters from the retrievals for all companions are listed in Table 2.2. In § 4.5, we show the insensitivity of our results to the mass and radius priors used in the retrievals. We discuss the retrieved P–T profiles and compare the retrieved $T_{\rm eff}$ with predicted $T_{\rm eff}$ from evolutionary models in § 4.5. In § 4.5, we discuss whether cloudy models are preferred over clear models for our companions, and whether clouds impact the retrieved abundances. Finally, we discuss our C/O, [C/H] measurements in § 4.5 and ^{12}C/^{13}C constraints for three companions in § 4.5.

Effect of mass and radius priors

We adopt mass and radius priors in our retrievals to prevent the fits from yielding unphysical radii and $\log g$. In principle, jointly fitting photometry or low-resolution data with the KPIC HRS could provide the flux information needed to anchor the $L_{\rm bol}$ and radius. For example, Stolker et al. (2021) fit the 0.6-5 μm spectro-photometry for GQ Lup b accounting for dust extinction and emission from a circumplanetary disk and find 3.77 ± 0.10 $R_{\rm Jup}$, which is consistent with our priors derived from evolutionary models. However, as Stolker et al. (2021) illustrates, for broadband spectro-photometry it is necessary to model both extinction from dust and potential circumplanetary disk emission for the youngest companions. Several companions in our study likely possess circumplanetary disks as well (e.g. Bowler et al., 2011; Holstein et al., 2021; Stolker et al., 2021). Doing such modeling for all the companions in our sample is beyond the scope of this paper, which is focused on measuring atmospheric abundances from high-resolution spectra. Hence, we

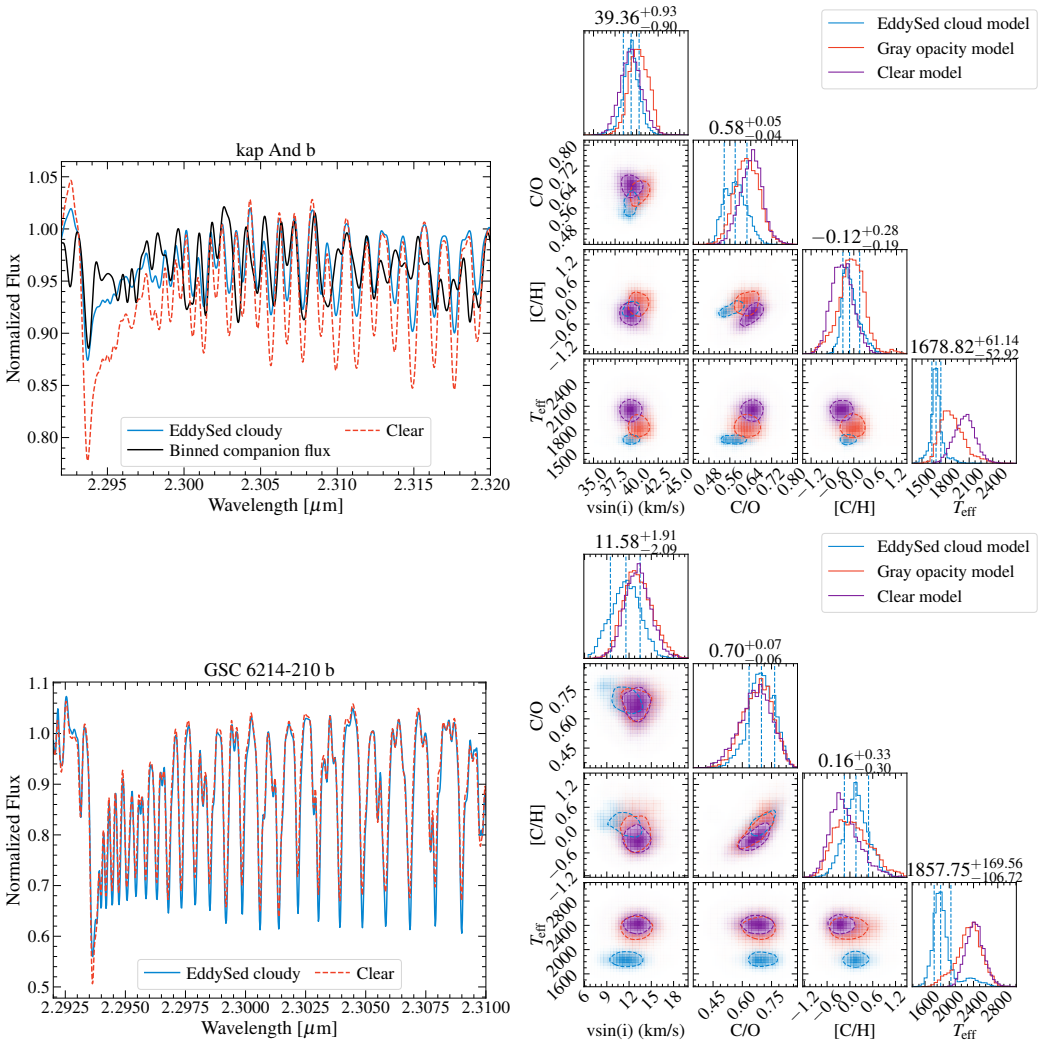

Figure 4.6: Top left: The best-fit Eddysed cloud model (blue) and clear model (red dashdot) for κ And b. These models are normalized companion templates from `petitRADTRANS`, and show non-gray variations in line depths and continuum location. We also overplot the normalized companion spectra (data - best-fit speckle model), which has been binned down to $R = 5000$ to better visualize the companion lines. Top right: the joint posterior distributions of $v \sin i$, C/O, [C/H], and $T_{\rm eff}$ from the different cloud models. There are $\approx 1\sigma$ variations in the abundances and $v \sin i$, while the $T_{\rm eff}$ is ≈ 350 K lower for the EddySed model compared to the clear model. Bottom panel: same but for GSC 6214-210 b. Note the different x-axis scales for the spectral plots, which are chosen for visualization purposes. The retrieved $T_{\rm eff}$ for GSC 6214-210 b is ≈ 500 K lower in the EddySed model compared to the clear model. Since the continuum-to-line contrast increases for lower $T_{\rm eff}$ atmospheres, this could cause absorption lines in the cloudy model to be deeper than those in the clear model despite the added cloud opacity, which is evident in the case of GSC 6214-210 b.

choose to adopt mass and radius priors to achieve the same purpose. We verified that these mass and radius priors do not affect the retrieved abundances by comparing against retrievals without the mass and radius priors, and found that the measured abundances vary by much less than 1σ when the priors are imposed.

P–T profile and effective temperature

Our retrieved P–T profiles mostly follow self-consistent (cloudless) profiles in the deeper atmosphere (see Fig. 4.4 and Appendix 4.14), but they can be hotter and more isothermal than the corresponding self-consistent models above the cloud bases. This could be due to several reasons. First, the cloudless model P–T profiles do not provide the best point of comparison for cloudy atmospheres, and cloud formation is expected to heat up the atmosphere above the cloud base resulting in a detached radiative zone (Tsuji, 2002; Burrows et al., 2006). This effect can be seen as a kink the P–T profile, which is most obvious for κ And b at pressures lower than $\sim$ 1 bar (see Fig. 4.4). Upcoming self-consistent models that include cloud radiative feedback (Morley et al. submitted) would provide a better comparison. Second, our retrievals could be showing evidence of the well-known cloud and isothermal P–T correlation (e.g. Burningham et al., 2017; P. Mollière et al., 2020), whereby a cloudier atmosphere can be re-produced by one with a more isothermal temperature gradient. While we attempt to address this behavior with our informed P–T profile priors, our priors are uniform and wide enough that isothermal behavior is still allowed. A stricter, Gaussian prior such as implemented by Z. Zhang et al. (2023) could prevent this behavior at the expense of limiting the parameter space for the retrieval to explore.

To assess whether our priors on the P–T profile affect the retrieved parameters, we repeat the baseline HIP 79098 b retrieval with wide priors from $0 - 2000$ K for each ΔT value. This second retrieval yielded the same median value and error bars for the abundances, RV, and $v \sin i$ as our baseline retrieval, indicating that our default P–T priors are conservative enough and not biasing the results.

From our retrievals, we compute $T_{\rm eff}$ by sampling the posteriors to generate low-resolution models from 0.1 to 30 μm, calculating the integrated flux, and applying the Stefan-Boltzmann law with the retrieved radii. To see how our results compare with evolutionary models, we compare our retrieved $T_{\rm eff}$ posteriors with the evolutionary-model predicted $T_{\rm eff}$ that were estimated in § 4.2. As with the mass and radius priors, we estimate a range of evolutionary $T_{\rm eff}$ that encompass all the models, which are

listed in Table 2.2.

For the two companions that showed $> 3\sigma$ preference for the EddySed cloud model, GSC 6214-210 b and κ And b, our retrieved $T_{\rm eff}$ from the EddySed model is lower compared to those from the clear and gray opacity models (see Fig. 4.6). In addition, the AMES-Dusty and SM08 models which include clouds generally predict lower $T_{\rm eff}$ for the same object compared to the cloudless ATMO 2020 and AMES-COND models (Appendix 4.10). The EddySed-retrieved $T_{\rm eff}$ for these two companions are closer to the predictions of the cloudy evolutionary models. For example, the EddySed-retrieved $T_{\rm eff}$ is 1680^{+60}_{-50} K for κ And b. For this companion, the cloudy SM08 evolutionary model predicts $T_{\rm eff} \approx 1760$ K while the cloudless ATMO 2020 evolutionary model predicts $T_{\rm eff} \approx 1860$ K (see Fig. 4.11). Thus, the overlap between the EddySed-retrieved $T_{\rm eff}$ and predicted $T_{\rm eff}$ from cloudy evolutionary models for GSC 6214-210 b and κ And bis consistent with the fact that we find evidence of clouds in these objects (discussed further in § 4.6).

Next, we discuss the six companions that did not show strong preference for cloudy models; these companions have similar retrieved $T_{\rm eff}$ posteriors between different cloud models. First, for ROXs 12 b, ROXs 42 Bb, and 2M0122 b, we find good agreement ($< 1\sigma$) between their retrieved and evolutionary $T_{\rm eff}$. For the remaining three, GQ Lup b, DH Tau b, and HIP 79098 b, which are among our hottest companions with late M spectral types, the retrieved $T_{\rm eff}$ from each cloud model is lower by $\sim 300 - 400$ K compared to the evolutionary model predictions (a $\sim 2\sigma$ discrepancy). We find that the retrieved $\log(L_{\rm bol}/L_{\odot})$ of these companions are also slightly lower than those predicted from the models by $\sim 0.1 - 0.2$ dex (or by $1 - 2\sigma$). On the other hand, the median-retrieved radius is slightly higher by $\sim 5 - 10\%$ compared to the median of the radius prior used in the retrieval.

J. W. Xuan et al. (2024c) also noted $T_{\rm eff}$ and radius discrepancies from retrievals of a M7.5 stellar companion with similar $T_{\rm eff}$, where the $T_{\rm eff}$/radius was slightly lower/higher than evolutionary models. One potential explanation is that high-resolution spectra after high-pass filtering are more sensitive to the slope of the P–T profile than the absolute temperature value (Landman et al., 2023b), and therefore may not provide accurate $T_{\rm eff}$. In our case, the retrieved $T_{\rm eff}$ is also influenced by the mass and radius priors we placed. However, this alone does not explain why only these companions show disagreement with the evolutionary models. Another reason for the $T_{\rm eff}$ discrepancy could be shortcomings in the treatment of clouds in evolutionary models, especially at the M to L transition. As shown by a systematic

study of brown dwarfs in Sanghi et al. (2023), clouds may be highly inaccurate at the M to L transition. This means that the evolutionary $T_{\rm eff}$ are not necessarily correct for late M objects.

For purposes of this paper, we simply check that our retrieved abundances are not affected by the retrieved $T_{\rm eff}$ by repeating retrievals with the P–T profile fixed to a self-consistent profile that has higher $T_{\rm eff}$. Specifically, for HIP 79098 b, we tried fixing the P–T profile to a SPHINX model profile (Iyer et al., 2023) with $T_{\rm eff} = 2600\ K$ and $\log g = 4.0$ (overplotted in Fig. 4.4) and repeated the retrieval. We find that all retrieved parameters shift by $< 1\sigma$ compared to the baseline retrieval. Therefore, we conclude that discrepancies in $T_{\rm eff}$ and radius have negligible impact on the retrieved abundances from our high-resolution data.

Impact of clouds

For most of our companions, the posteriors from our clear and cloudy retrievals overlap significantly; the median or best-fit retrieved abundance parameters are identical within $\ll 1\sigma$. We compare the cloudy models and clear models statistically with the log Bayes factor, or $\ln(B)$, which are listed in Table 2.2. The cloudy models are compared against the clear model, so a positive $\ln(B)$ for a cloudy model means it is preferred over the clear model. While all companions prefer cloudy models, the preference is only significant for κ And b and GSC 6214-210 b, which show 3.7σ and 3.4σ preferences for the EddySed cloud model. For these two companions, our median retrieved abundances from the EddySed models can differ by $\approx 1\sigma$ compared to the clear model, as we show in Fig. 4.6. For all other companions, the cloudy models are preferred by $0 - 2.6\sigma$, and the addition of clouds negligibly impact their retrieved abundances and other parameters.

We illustrate the impact of clouds on the retrieved spectra of κ And b and GSC 6214-210 b in Fig 4.6, which shows that both the continuum and line depths are varying in a distinctly non-gray behavior. This explains why the spectra could not be fit as well with the gray opacity model. As the data have relatively low S/N ($\sim$ 5 and $\sim$ 2 per pixel for κ And b and GSC 6214-210 b, respectively), the residual noise makes it difficult to clearly see the companion lines. Thus, we try to visualize the effect of clouds in the data after binning down the companion flux contribution of in data. Since the κ And b spectra have a non-zero speckle component (see Eq. 4.1), we subtract the best-fit speckle model from its KPIC spectra and then bin them down to $R = 5000$. As shown in Fig 4.6, we see that the companion line depths

do match better with the cloudy, EddySed model compared to the clear model for κ And b. However, the same effect is not as clear when we plot the GSC 6214-210 b companion flux, which is more noisy due to its lower S/N. In addition, the relative difference between the clear and cloudy model is smaller for this object. Thus, we conclude that a clear confirmation of the effect of clouds in high-resolution spectra would require higher S/N data. This could be achieved with longer integration times on our targets, or existing high S/N spectra of isolated brown dwarfs.

Why do only κ And b and GSC 6214-210 b prefer EddySed cloud models in our retrievals? Based on Table 2.2, we see that they are among the colder companions. Except for 2M0122 b, all other companions are predicted to be hotter. For κ And b, we retrieve $T_{\rm eff} = 1680^{+60}_{-50}$ K from the EddySed model and $T_{\rm eff} = 2050^{+130}_{-140}$ K for a clear atmosphere. For GSC 6214-210 b, we retrieve $T_{\rm eff} = 1860^{+170}_{-110}$ K and $T_{\rm eff} = 2420 \pm 150$ K from the EddySed and clear retrievals, respectively. As noted in § 4.5, the EddySed-retrieved $T_{\rm eff}$ for these two companions matches predictions from cloudy substellar evolutionary models (SM08, AMES-dusty) better than the $T_{\rm eff}$ retrieved from the clear model, which are overly high. The fact that we see evidence of clouds for only κ And b and GSC 6214-210 b suggests that the impact of clouds on the spectra is smaller for hotter companions and therefore harder to detect despite their higher S/N data (e.g. GQ Lup b has S/N per pixel 12 v.s. 5 for κ And b). When examining the P–T profiles for κ And b and GSC 6214-210 b, we see that their cloud bases are predicted to be closer to the K band continuum due to their lower $T_{\rm eff}$ (see Fig. 4.4). In contrast, for hotter companions, the cloud bases are at much lower pressures than the continuum. Physically, this means that there is more condensable cloud material for κ And b and GSC 6214-210 b at pressures closer to their photospheres, thereby causing them to appear cloudier.

Therefore, our results match the trend of decreasing cloud opacity with rising temperature that is observed across the L to M transition, for instance from the decreasing silicate cloud absorption strength at ≈8–11 μm seen in mid-IR Spitzer/IRS spectra of brown dwarfs (e.g. Cushing et al., 2006; Suárez et al., 2022). We note that the coldest of our companions, 2M0122 b, shows a weak preference (2σ) for the EddySed model, but its S/N is the lowest among the sample ($\sim$ 1 per pixel), which may prevent a stronger constraint of its clouds properties. Alternatively, viewing geometry also affects the strength of the silicate cloud feature of brown dwarfs, whose equators tend to be cloudier than their poles (Vos et al., 2017; Suárez et al., 2023). Given the measured companion spin axis inclination of 33^{+17}_{-9} deg (Bryan

et al., 2020b), 2M0122 b is close to a pole-on geometry, which may reduce the effect of clouds on its measured emission spectrum relative to companions with more equatorial viewing geometries. Finally, because spectral features become deeper compared to the continuum at lower $T_{\rm eff}$ for brown dwarfs (e.g. Ruffio et al., 2023b), this causes CO lines to be deeper in the EddySed model for GSC 6214-210 b, despite the impact of clouds (Fig. 4.6). This suggests a potential trade-off between $T_{\rm eff}$ (set by the P-T profile) and clouds. Future work using broader wavelength coverage or flux-calibrated data should be able to constrain $T_{\rm eff}$ better in order to confirm our findings. We further discuss the effect of clouds on high-resolution spectroscopy in § 4.6.

Carbon and oxygen abundances

Our retrieved C/O and [C/H] values for the companions are listed in Table 2.2. As with previous high-resolution studies (e.g. Finnerty et al., 2023; J. W. Xuan et al., 2024c), our constraints on the relative abundances of different molecular species as indicated by the ratio of their relative line depths, which are used to calculate C/O, are tighter than our constraints on the absolute abundances of individual molecular species, which are used to determine the overall atmospheric [C/H]. Specifically, our uncertainties range between 0.02 – 0.08 for C/O and 0.2 – 0.5 dex for [C/H] depending on the object and S/N. Both the C/O and [C/H] of our companions are consistent at the 1–2σ level with the solar composition from Asplund et al. (2021). The implications of our measured abundances for formation pathways are discussed in § 4.6.

^{12}CO/^{13}CO measurements

We obtain bounded constraints on ^{12}CO/^{13}CO for GQ Lup b, HIP 79098 b, and DH Tau b, which are the three companions with the highest S/N detections as shown by the CCFs (Fig. 4.3). To quantify the detection significance of ^{13}CO, we run additional retrievals where we leave out ^{13}CO opacities, and compute the Bayes factor between these 'reduced models' without ^{13}CO and the 'full model' that includes ^{13}CO and fits for ^{12}CO/^{13}CO. The resulting log Bayes factors are listed in Table 2.2, and correspond to 5.7σ, 4.3σ, and 3.4σ detections of the ^{13}CO isotopologue for GQ Lup b, HIP 79098 b, and DH Tau b, respectively. We note that ROXs 12 b also has a ^{12}CO/^{13}CO posterior which peaks at $\sim$ 100, but the corresponding detection significance is $< 3\sigma$ so we do not consider it in the following discussion. The other four companions show unbounded ^{12}CO/^{13}CO posteriors

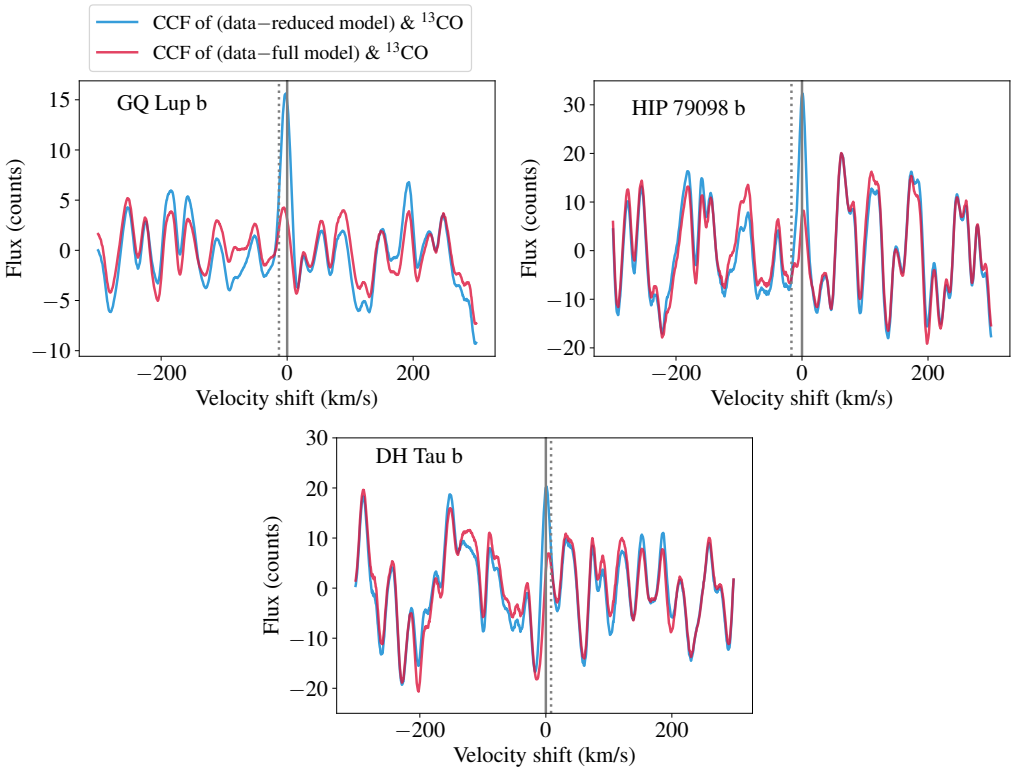

Figure 4.7: Left panel: The CCF between the ^{13}CO-only template and (data - best-fit reduced model) in blue for GQ Lup b. The reduced model retrieval does not include ^{13}CO opacities. The CCF between the ^{13}CO-only template and (data - best-fit full model) is shown in red. The full model retrieval includes ^{13}CO opacities. The fact that the blue CCF shows a peak at the companion's rest frame (gray solid line) indicates a real ^{13}CO detection. For comparison, the gray dotted line is the telluric rest frame. In the red CCF, we do not expect a peak since ^{13}CO is fitted for in this model, so the residuals should be free of ^{13}CO. Middle and right panels: same but for HIP 79098 b and DH Tau b. The ^{13}CO detection for DH Tau b is tentative.

from our tests, so their baseline models do not include ^{12}CO/^{13}CO.

Following J. W. Xuan et al. (2022), we perform a cross-correlation analysis to obtain a complementary perspective on the robustness of these ^{13}CO detections. The goal of this analysis is to assess whether the full models prefer ^{13}CO independent of the Bayes factor calculation. First, we compute the CCF between a ^{13}CO-only model and the (data - model without ^{13}CO). The latter is equivalent to the residuals of the reduced model, and will contain residual ^{13}CO lines if the data contain ^{13}CO. Then, we compute the CCF between the ^{13}CO-only model and the (data - model with ^{13}CO). This second CCF should not show a detection, as ^{13}CO is already fitted for in the full model. We generate ^{13}CO-only models by manually zeroing the opacities of all other line species except ^{13}CO when computing the full model. The

CCF calculations follow the framework described in § 4.4.

Table 4.4: Comparison of Our Measurements with Previous Work

Target Name	**C/O**	**Metallicity (× solar)**	$v \sin i$ **(km s^{-1})**	**Source**
GQ Lup b	$0.70^{+0.01}_{-0.02}$	$2.5^{+1.5}_{-1.0}$	$6.4^{+0.3}_{-0.4}$	TP
	$0.44^{+0.13}_{-0.11}$	1.7 ± 0.3	$5.3^{+0.9}_{-1.0}$	1, 7
κ And b	$0.58^{+0.05}_{-0.04}$	$0.8^{+0.8}_{-0.3}$	39.4 ± 0.9	TP
	$0.70^{+0.09}_{-0.24}$	1.0–1.6	38.4 ± 1.0	6, 9
GSC 6214-210 b	$0.70^{+0.07}_{-0.06}$	$1.4^{+1.6}_{-0.7}$	$11.6^{+1.9}_{-2.1}$	TP
	$0.48^{+0.16}_{-0.12}$	$0.7^{+0.3}_{-0.2}$	$6.1^{+4.9}_{-3.8}$	2, 7
2M0122 b	0.37 ± 0.08	$0.5^{+0.6}_{-0.2}$	$19.6^{+3.0}_{-2.5}$	TP
	...	...	$13.4^{+1.4}_{-1.2}$	3
ROXs 42B b	0.48 ± 0.08	$1.0^{+2.8}_{-0.7}$	$4.4^{+1.6\,7}_{-2.1}$	TP
	0.50 ± 0.05	$0.2^{+0.3}_{-0.1}$	10.5 ± 0.9	8
DH Tau b	$0.54^{+0.06}_{-0.05}$	$0.5^{+0.6}_{-0.2}$	$5.7^{+0.8}_{-1.0}$	TP
	...	...	9.6 ± 0.7	5
ROXs 12 b	0.54 ± 0.05	$0.5^{+0.4}_{-0.2}$	$3.6^{+1.2\,1}_{-1.6}$	TP
	...	...	$8.4^{+2.1}_{-1.4}$	4

Notes: TP refers to this paper.
References: (1) Schwarz et al. (2016), (2) Bryan et al. (2018), (3) Bryan et al. (2020b), (4) Bryan et al. (2020a), (5) J. W. Xuan et al. (2020b), (6) Hoch et al. (2020), (7) Demars et al. (2023), (8) Inglis et al. (2024), (9) Morris et al. (2024).

From the CCF analysis, we find that the CCFs for GQ Lup b and HIP 79098 b show convincing peaks at the companion's rest frame that indicate a strong ^{13}CO detection (see Fig. 4.7). However, the ^{13}CO CCF for DH Tau b is much noisier, showing residual structure comparable to the peak. Therefore, we consider the ^{13}CO detection in DH Tau b to be tentative, since it is possible that ^{13}CO is being used to fit for systematics that are unaccounted for in the model. This is consistent with the larger uncertainties in the ^{12}C/^{13}C of DH Tau b, and is expected given the lower S/N of the DH Tau b data compared to the data for the other two companions. We further discuss our ^{12}C/^{13}C measurements in the context of previous results in § 4.6.

4.6 Discussion

Comparison with previous work

As noted in § 4.2, many our companions have previous medium- or high-resolution studies which reported on their $v \sin i$ and/or atmospheric abundances. Table 4.4 compares our baseline KPIC measurements with previous results.

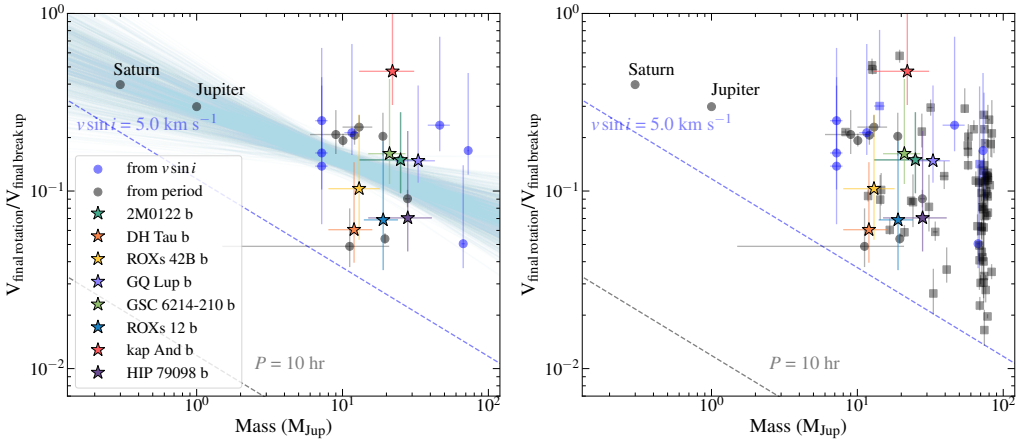

Figure 4.8: Top: The fractional final rotational velocities versus companion masses for sources in our sample (labeled) compared to companions with spin measurements from the literature, as well as Jupiter and Saturn. The literature values from $v \sin i$ and rotational periods are shown in blue and gray circles, respectively. The best-fit rotational trends from J. J. Wang et al., 2021c are plotted as light blue lines. The blue and gray dashed lines indicate typical measurement limits of $v \sin i$ (5.0 km s^{-1}) and period (10 hr) from the instruments used (Hsu et al., 2024a). Bottom: Same as the top panel but with the addition of field brown dwarfs as squares.

Hoch et al. (2020) used Keck/OSIRIS medium-resolution spectra ($R \sim 4000$, 2.22 – 2.4 μm) to measure the abundances of κ And b using a custom grid of PHOENIX models (Barman et al., 2011; Barman et al., 2015) that vary in metallicity and C/O. They report C/O = $0.70^{+0.09}_{-0.24}$ and [M/H] = 0.0 – 0.2, which are consistent with our measured C/O = $0.58^{+0.05}_{-0.04}$ and [C/H] = $-0.12^{+0.28}_{-0.19}$. Our measured $v \sin i$ = 39.4 ± 0.9 km s^{-1} for κ And b also agrees with the recent study by Morris et al. (submitted), who find 38.4 ± 0.1 km s^{-1} using KPIC data from a different observing night.

Schwarz et al. (2016) used VLT/CRIRES spectra ($R \sim 100,000$, 2.30 – 2.33 μm) to measure $v \sin i = 5.3^{+0.9}_{-1.0}$ km s^{-1} for GQ Lup b, which is consistent with our $v \sin i = 6.4^{+0.3}_{-0.4}$ km s^{-1} to within $\approx 1.1\sigma$. This agreement is reassuring given the $\sim 3\times$ lower spectral resolution of Keck/KPIC compared to VLT/CRIRES, and confirms the ability of KPIC to measure $v \sin i$ values below the resolution limit of ~ 7.5 km s^{-1}, as demonstrated by J. W. Xuan et al. (2024c) as well.

Demars et al. (2023) used VLT/SINFONI medium-resolution spectra and the self-consistent model ATMO (Tremblin et al., 2015; Tremblin et al., 2016) to fit the abundances of GQ Lup b and GSC 6214-210 b. They adopted C/O = $0.44^{+0.13}_{-0.11}$ and [M/H] = 0.23 ± 0.06 for GQ Lup b and C/O = $0.48^{+0.16}_{-0.12}$ and [M/H] = −0.16 ± 0.17

for GSC 6214-210 b. Overall, our measured abundances agree with their results at the $1-2\ \sigma$ level. However, we note that the Demars et al. (2023) results are discrepant between different observing epochs at the $\sim 60\%$ level in C/O and > 0.4 dex in [M/H], and sometimes hit the limits of their grid. In contrast, as we show in Appendix 4.11, our KPIC results between different observing epochs of GQ Lup b are consistent at the $< 3\%$ level in C/O and ~ 0.1 dex in [C/H]. This demonstrates the reliability of high-resolution spectra and our forward model + retrieval approach in measuring atmospheric abundances.

Five of our targets (ROXs 42 Bb, ROXs 12 b, DH Tau b, 2M0122 b, GSC 6214–210 b) have reported $v \sin i$ measurements with pre-upgrade Keck/NIRSPEC spectra ($R \sim 25,000$) as part of a spin survey for low-mass substellar companions (Bryan et al., 2018; J. W. Xuan et al., 2020b; Bryan et al., 2020a). We list the literature values along with our new values in Table 4.4, and discuss them below.

For the faster rotators GSC-6214-610 b and 2M0122 b, our measured $v \sin i$ are consistent with the pre-upgrade NIRSPEC values from Bryan et al. (2018) and Bryan et al. (2020b) at the 1σ and 2σ levels, respectively. For the slower rotators (ROXs 12 b, ROXs 42 Bb, and DH Tau b), we find $\gtrsim 3\sigma$ discrepancies in $v \sin i$, with a trend that KPIC measured $v \sin i$ values are lower than those from pre-upgrade NIRSPEC studies. However, we note that for ROXs 12 b and ROXs 42 Bb our KPIC data only prefer a non-zero spin with $\approx 1\sigma$ significance, so future data is required to definitively measure their $v \sin i$. For ROXs 42 Bb, Inglis et al. (2024) perform atmospheric retrievals with pre-upgrade NIRSPEC data and report $v \sin i = 10.5 \pm 0.9$ km s^{-1}, which agrees with the $v \sin i = 9.5^{+2.1}_{-2.3}$ km s^{-1} found by Bryan et al., 2018 for the same data. However, we find $v \sin i = 4.2^{+1.8}_{-2.2}$ km s^{-1} for ROXs 42 Bb. Despite these differences in $v \sin i$, our retrieved abundances for ROXs 42 Bb agree with those from Inglis et al. (2024). Finally, in J. W. Xuan et al. (2020b) we found $v \sin i = 9.6 \pm 0.7$ km s^{-1} for DH Tau b using pre-upgrade NIRSPEC data, while we measure $v \sin i = 5.7^{+0.8}_{-1.0}$ km s^{-1} with KPIC.

Low S/N spectra can preclude confident spin measurements, especially for very slow rotators. However, in all three cases above, the KPIC data have higher CCF S/N compared to the pre-upgrade NIRSPEC data. For ROXs 12 b, ROXs 42 Bb, and DH Tau b, we obtain $\sim 25\sigma$, $\sim 15\sigma$, and $\sim 20\sigma$ detections (Fig. 4.3), respectively, while the previous NIRSPEC detections have CCF S/N $\sim 10\sigma$ (J. W. Xuan et al., 2020b; Inglis et al., 2024). If the companions are in fact rotating faster, our KPIC data should have been able to reveal this.

Despite the higher CCF S/N of the KPIC data, the uncertainties of our new $v \sin i$ measurements are comparable with the older measurements. This suggests that there may be additional sources of uncertainty that the older NIRSPEC studies did not consider. For example, the retrieval approach allows us to vary the P-T profile and therefore adjust the pressure-broadened line shapes in each iteration. In contrast, J. W. Xuan et al. (2020b) and Bryan et al. (2020a) used fixed atmospheric templates to compute $v \sin i$, and may under-estimate the uncertainty introduced by the uncertain atmospheric properties of the companion.

We note that for a high S/N dataset of the isolated brown dwarf 2M0355, Y. Zhang et al. (2021a) found similar discrepancies in $v \sin i$ compared to Bryan et al. (2018). Using the same NIRSPEC data for the brown dwarf, Y. Zhang et al. (2021a) found an upper limit of 4 km s^{-1} for $v \sin i$, consistent with a non-detection of spin, but Bryan et al. (2018) reported $v \sin i = 14.7 \pm 1$ km s^{-1}. Using earlier $R \sim 25,000$ NIRSPEC data, Blake et al. (2010) also found a similarly large spin for this brown dwarf which agrees with the Bryan et al. (2018) value. Recently, however, Y. Zhang et al. (2022) used much higher resolution VLT/CRIRES+ spectra (R~80,000) to confirm the slow spin of 2M0355, finding $v \sin i = 2.5 - 3.0$ km s^{-1}. The fact that Y. Zhang et al. (2021a) and Bryan et al. (2018) used the same NIRSPEC data and found different $v \sin i$ for 2M0355 point to details in the data reduction and spectral extraction process as possible sources of discrepancy.

For example, the higher spin values from older NIRSPEC data may be the result of systematic underestimation of the instrumental line spread function, which is degenerate with $v \sin i$. For KPIC, the LSF is estimated using the spectral trace widths in the spatial direction, and conservatively allowed to vary between 1.0 to 1.2 times this width following J. J. Wang et al. (2021c), who found that the LSF is ≈ 1.1 times broader in the spectral direction than the spatial direction (see § 4.4). A major advantage of the single-mode fiber injection used by KPIC is the stability of the LSF, whose shape does not vary with the adaptive optics (AO) correction quality (only the intensity varies). Furthermore, we confirm that the KPIC LSF is constant over the course of an observing night by re-fitting the LSF every 20 minutes over a 3.5-hour period. The LSF weights in each refitting vary by $< 5\%$, with most of the variation in the line wings, suggesting we are limited by the signal-to-noise of each substack and that the flux-weighted LSF is even more stable. In addition, the LSF in KPIC is measured to vary as a function of wavelength by $\sim 10 - 20\%$ within and across different spectral orders. In regular NIRSPEC, the resolution should also

vary with wavelength at a similar level, but this wavelength-dependence is neglected in pre-upgrade NIRSPEC spin studies since it is hard to measure (J. W. Xuan et al., 2020b).

In contrast, for the pre-upgrade NIRSPEC analysis, the LSF was determined by fitting telluric lines in the host star spectra. For example, J. W. Xuan et al. (2020b) found $R = 24,800 \pm 1000$ from the DH Tau dataset, which was adopted as a Gaussian instrumental broadening kernel and assumed to be constant with wavelength. We note that NIRSPAO (NIRSPEC in AO mode) was used for these observations, and the size of the PSF was comparable or smaller than the slit width of $0.041''$ (J. W. Xuan et al., 2020b). In this case, variations in the AO correction quality cause varying PSF sizes, and when the PSF becomes smaller than the slit this would cause a narrower LSF. However, the effect of a varying LSF should be captured by measuring the instrumental resolution from telluric lines in the data, which are varying in the same way. However, as shown in J. W. Xuan et al. (2020b), the approach of determining the LSF width from telluric lines can sometimes produce poor fits and discrepant results between different spectral orders, which may bias the adopted LSF estimate.

We conclude that future work is required to explain the $v \sin i$ discrepancies in more detail. Given the higher spectral resolution, higher S/N, and more stable LSF of KPIC, and the fact that our KPIC-measured spin of GQ Lup b agrees with $R \sim 100{,}000$ CRIRES data (Schwarz et al., 2016), we conclude that our measurements are likely more reliable than pre-upgrade NIRSPEC observations of the same objects. Despite some differences, our new $v \sin i$ results are in good agreement with the findings from Bryan et al. (2020a) that low-mass substellar companions rotate much slower than their breakup velocities, pointing to mechanisms such as magnetic breaking that can efficiently reduce the companion's angular momentum on short timescales (Bryan et al., 2018; Batygin, 2018). Finally, our measured abundances for κ And b and ROXs 42B b both agree with previous work using medium- and high-resolution spectra (Hoch et al., 2020; Inglis et al., 2024), which is a validation of the power of these data to constrain chemical abundances in substellar companions and exoplanets. Except for ROXs 42B b, our KPIC measurements of the other seven companions are the first high-resolution retrievals of these objects.

Rotation rates and RVs

Here, we place our measured $v \sin i$ into context with literature spin measurements for low-mass companions and exoplanets. Given the discussion above, we update the $v \sin i$'s for DH Tau b, ROXs 42B b, ROXs 12 b, 2M0122 b, and GSC 6214-210 b. For bound companions, we compile literature measurements from Bryan et al., 2020c, and recent KPIC studies from J. J. Wang et al., 2021c; J. W. Xuan et al., 2022; J. Wang et al., 2022; J. W. Xuan et al., 2024c; Hsu et al., 2024a. For field brown dwarfs, we compile results from Crossfield et al., 2014; Tannock et al., 2021; Hsu et al., 2021; Hsu et al., 2024b; Vos et al., 2022. The spin measurements come from both $v \sin i$ and rotational period measurements. For the $v \sin i$ values, we assume isotropically distributed inclinations to remove the unknown i.

We compute how close the objects' final rotation speeds compare to their final break-up velocities by evolving their ages, radii, and spin velocities to 5 Gyr assuming constant angular momentum evolution, following the methodology detailed in J. Wang et al., 2022 and Hsu et al., 2024a. We adopt the evolutionary model from Baraffe et al., 2003 for this. Evolving the rotation to the same age allows us to remove age-dependent effects from literature measurements of $v \sin i$ or photometric rotational periods. Fig. 4.8 shows that the spin measurements in our sample fall within the overall trend compared to the literature measurements, and the best-fit rotational trend from J. J. Wang et al., 2021c, who identified a tentative anti-correlation between fractional rotation speed and object mass. Five companions in our sample have ages $\lesssim$ 10 Myr (ROXs 12 b, ROXs 42 Bb, DH Tau b, GQ Lup b, HIP 79098 b). These companions also have slower $v \sin i$ values below 10 km s^{-1} and are likely still undergoing gravitational contraction and gradually spinning-up. This fits the findings of Bryan et al. (2020a), who showed that younger substellar objects generally have lower rotation speeds than older objects, and that their rotation speeds increase as their radii contract with age following constant angular momentum evolution. On the other hand, the fractional rotation velocities of isolated brown dwarfs (squares) are much more scattered, and these field objects do not exhibit a clear trend for rotation. However, we note that field brown dwarfs with masses $\lesssim$30 $M_{\rm Jup}$ fall into the Y dwarf regime, for which rotation rates are extremely challenging to measure due to their faintness. To confirm the tentative trend between rotation rate and mass, it would be useful to extend $v \sin i$ or rotational period measurements to young, directly imaged planets with masses $\sim 1 - 10\ M_{\rm Jup}$. A detailed analysis of all KPIC rotation measurements will be presented in a future study.

In addition to measuring $v \sin i$, we also measure the RV of the companions at the observed epochs. We provide the companion RVs in Appendix 4.15, which could be used to refine their orbits (Ruffio et al., 2019; Do Ó et al., 2023; J. W. Xuan et al., 2024c).

The effect of clouds on narrowband high-resolution spectroscopy

A rather unexpected finding of this paper that narrow-band high-resolution spectra can be sensitive to clouds for $T_{\rm eff} \sim 1700 - 2000$ K objects, even after high-pass filtering the data and models. We illustrate the impact of clouds in Fig. 4.6 for κ And b and GSC 6214-210 b, the two companions which show $> 3\sigma$ preferences for the EddySed cloud model (Ackerman et al., 2001). In our retrievals with `petitRADTRANS`, the EddySed model accounts for both absorption and scattering from clouds, whose opacities are computed from optical constants of real condensates (P. Mollière et al., 2019b). We find that a simple, gray opacity cloud model is not sufficient to explain their spectra. The sensitivity to clouds appears to arise from line depth variations with wavelength, which we can visualize in the κ And b spectra after binning it down to average out the residual noise. While our data does not contain absolute flux information, the line depth variations are preserved after the HPF continuum removal procedure.

Despite their preference for clouds, we note that the retrieved C/O and metallicity for κ And b and GSC 6214-210 b are only weakly affected by clouds ($\lesssim 1\sigma$ level shifts). However, compared to the clear models, the EddySed cloudy models retrieve a much lower $T_{\rm eff}$. Specifically, the $T_{\rm eff}$ from the EddySed models are more consistent with cloudy evolutionary models (see § 4.5). The fact that κ And b and GSC 6214-210 b prefer clouds is consistent with their $T_{\rm eff}$ of $1700-2000$ K and early L spectral types. Specifically, silicate clouds cause a broad absorption feature around $\approx 8 - 11$ μm which has been directly observed in L dwarfs using mid-IR spectra from Spitzer and JWST (e.g. Cushing et al., 2006; Suárez et al., 2022; Miles et al., 2023). For brown dwarfs with $T_{\rm eff} \gtrsim 2000$ K, the silicate absorption band starts to disappear (Suárez et al., 2022), which is consistent with the fact that the hotter $T_{\rm eff} > 2200$ K companions in our sample show zero or weak preference clouds ($0 - 2.6\sigma$).

2M0122 b, with $T_{\rm eff} \sim 1500 - 1700$ K, presents an exception to this pattern. This companion should also be cloudy, but its low S/N data or nearly pole-on viewing angle (see § 4.5) may prevent a stronger constraint on clouds. In addition, due to our limited S/N, it is difficult to directly visualize the effect of clouds in the GSC 6214-

210 b spectra. We emphasize that future work with flux-calibrated data and wider wavelength coverage is required to confirm our findings of clouds in κ And b and GSC 6214-210 b. Retrieval studies of high S/N, high-resolution spectra for cloudy L dwarfs would also provide a good test of our findings.

Finally, we note that our results represent an update to J. W. Xuan et al. (2022), who found that the K band spectrum of brown dwarf companion HD 4747 B ($T_{\rm eff}$≈1400 K and log g≈5.3) is insensitive to clouds because the $MgSiO_3$ and Fe cloud bases are expected to lie below its K band photosphere. Our new findings indicate that when the cloud bases do intersect with the P–T profile near the photosphere, as is the case for $T_{\rm eff}$∼1700-2000 K companions, K band high-resolution spectroscopy could be sensitive to cloud opacities despite continuum removal. There remain significant challenges in retrieving accurate abundances in the presence of clouds from low-resolution data (e.g. Burningham et al., 2017; J. W. Xuan et al., 2022; Lueber et al., 2022; Inglis et al., 2024), so high-resolution retrievals of L dwarfs may provide a complementary way forward.

Towards atmospheric abundance trends for directly imaged companions

Host star abundances

Knowledge of the host star abundances is important for formation inferences, since they represent proxies for the natal elemental abundances in the protoplanetary disk or molecular cloud. For the young stars ($\sim 1-100$ Myr) in our sample, however, it is difficult to measure their C and O abundances due to complicating factors such as rotation, magnetic fields, veiling, and stellar activity. Even for field stars, C and O abundance calibrations are only recently being worked out for M and K spectral types (e.g. Souto et al., 2022; Hejazi et al., 2023); six of the eight stars in our sample fall into this category. The remaining two B9 stars, HIP 79098 and κ And, have extremely rapid rotation ($v \sin i > 100$ km s^{-1}) that leads to significant spectral line broadening. This causes neighboring individual lines to blend with each other, most of which cannot then be distinguished even with high-resolution spectroscopy.

To circumvent these challenges, studies have focused on more favorable targets: early K to late F young stars with lower rotation rates and no apparent veiling. The C and O abundances of these more solar-like stars can be estimated from atomic C and O lines in the visible using established abundance calibrations (Reggiani et al., 2024). Alternatively, we can utilize abundance measurements for other species, including Ca, Mg, Si, and Fe, which also have strong, isolated lines in the visible

(e.g. Santos et al., 2008; Biazzo et al., 2012). Importantly, Ca, Mg, and Si are alpha elements along with C and O. Using the elemental abundances of $\approx$ 6000 stars from the Hypatia catalog (Hinkel et al., 2014), we confirm that the abundances of Ca, Mg, and Si scale together with those of C and O to the $\lesssim$ 0.2 dex level. Below, we summarize previous abundance measurements for stars in the same star-forming associations as our host stars. Since stars in open clusters are found to be chemically homogeneous at the $<$ 0.03 dex level (e.g. De Silva et al., 2006; Bovy, 2016; Ting et al., 2012; Poovelil et al., 2020), stars in the same star-forming associations should also be chemically homogeneous at a similar level (Reggiani et al., 2024).

In terms of C and O, Reggiani et al. (2024) showed that the F7 star HD 181327 in the β Pic moving group has [C/H]= -0.08 ± 0.06, [O/H]= -0.10 ± 0.06, and C/O= 0.62 ± 0.08, which is very close to solar. Kinematic studies have shown that the β Pic moving group likely originated from the Scorpius–Centaurus (Sco-Cen) association (Mamajek et al., 2001; Ortega et al., 2002). This means that to first order, stars in the Sco-Cen association should also have roughly solar C and O abundances. Five of our stars belong to sub-regions within Sco-Cen (HIP 79098, GSC 6214-610, GQ Lup, ROXS 12, and ROXs 42B). J. Wang et al. (2020) measured [C/H]= 0.04 ± 0.12, [O/H]= 0.08 ± 0.14, and C/O= $0.54^{+0.12}_{-0.09}$ for HR 8799, which is an early F λ Boo star. The kinematic association of HR 8799 is unclear, but a recent study posits that HR 8799 may have formed either alone or in a since-dispersed small stellar group within a larger star-forming complex that gave birth to the Columba and Carina groups (Faramaz et al., 2021). If κ And is a member of Columba as suggested by the age measurement from J. Jones et al. (2016), then it likely has a solar composition as well.

In terms of other elements, Santos et al. (2008) measured Fe and Si abundances for six star-forming regions including Lupus, ρ Oph, and Taurus and found solar [Fe/H] and [Si/H] values across their sample. Four of our stars belong to these regions (GQ Lup, ROXS 12, ROXs 42B, DH Tau). More recently, Biazzo et al. (2017) analyzed the spectra of six other stars in Lupus and also found [Fe/H] $\approx$ 0.03 on average. We note that the Lupus and ρ Oph regions are both embedded in the larger Sco-Cen association. In Taurus, D'Orazi et al. (2011) found an average [Fe/H] = -0.01 ± 0.05 and [Si/H] consistent with zero from seven stars. In the older AB Dor moving group, where 2M0122 is, Biazzo et al. (2012) find average values of [Fe/H] = 0.10 ± 0.03, [Mg/Fe] = -0.03 ± 0.03, and [Ca/Fe] = -0.01 ± 0.05, again consistent with solar abundances to within 0.1 dex. Together, these studies paint a broad picture of solar

abundances in young star-forming regions (e.g. see also Biazzo et al., 2011; Spina et al., 2014).

Therefore, to first order, all our host stars are expected to have nearly solar C and O abundances to the $\sim 0.1 - 0.2$ dex level. We therefore proceed under the assumption that our host stars have solar compositions, but emphasize that future work should attempt to perform precise C and O abundance measurements for young stars in various star-forming regions in order to provide context for abundance measurements of directly imaged planets and brown dwarfs, a majority of which are young. Specifically, high-resolution, near-infrared spectroscopy has proven vitally important in characterizing the fundamental parameters and measuring the abundances of lower-mass host stars with spectral types later than mid-K (e.g. López-Valdivia et al., 2021; Souto et al., 2022; Hejazi et al., 2023; Cristofari et al., 2023). In these latter type stars, the atomic lines of C and O in the optical are too weak for abundance measurements, but instead, C- and O-bearing molecules such as OH and CO can be utilized to infer the C and O abundances. As mentioned, performing abundance measurements for young, late-type stars will involve a detailed accounting of the effects of magnetic fields, line veiling, and rotation, which we are working on including in a follow-up study in order to directly determine the stellar abundances.

Formation pathways of widely-separated, 10–30 $M_{\rm Jup}$ companions

The C/O and [C/H] measurements for our eight companions are summarized in Fig. 4.9. The companions all have C/O consistent to solar within 1σ level with the exception of our lowest S/N target, 2M0122 b, which has a lower C/O of 0.37 ± 0.08 but is still consistent with solar at the 2σ level. Their [C/H] values are likewise all consistent with solar at the $\approx 1 - 2\sigma$ level. Since we established that their host stars most likely possess solar C and O abundances, our measurements suggest chemical homogeneity between these low-mass companions and their stars. The trend of solar C/O ratios for widely-separated companions with $m \approx 10 - 30\ M_{\rm Jup}$ was first noted by Hoch et al. (2023), who compiled literature measurements and their own Keck/OSIRIS results. Our only overlap with the Hoch et al. (2023) sample is κ And b, as discussed in § 4.6. While Hoch et al. (2023) only studied C/O, our measurements of solar [C/H] provides a complementary piece of information. High-resolution studies of high-mass ($m \approx 60 - 70\ M_{\rm Jup}$) brown dwarf companions indicate that their atmospheric abundances are consistent with those of their host stars at the $\lesssim 2\sigma$ level (J. Wang et al., 2022; J. W. Xuan et al., 2022). Therefore,

our results, along with Hoch et al. (2023), indicate that widely-separated ($\gtrsim$ 50 au) 10–30 $M_{\rm Jup}$ companions, which have masses in between those of directly imaged planets and high-mass brown dwarfs, have abundance pattern that more closely resemble those of brown dwarfs.

On a population level, we can also compare our abundance measurements with those made for close-in hot Jupiters (HJs; $m \sim 0.4 - 10\ M_{\rm Jup}$, $a \sim 0.01 - 0.1$ au), which are found to have a large scatter in C/O and generally super-stellar atmospheric metallicities (e.g. Brogi et al., 2023; Alderson et al., 2023; August et al., 2023; T. J. Bell et al., 2023; Bean et al., 2023; Finnerty et al., 2024; Xue et al., 2024). These hot Jupiters almost certainly form via core accretion (within the CO snowline), though a variety of post-formation evolution processes are possible (see review by Fortney et al., 2021). The strong correlation between total heavy element mass and the total planet mass suggests these planets have solid cores consistent with core accretion (Thorngren et al., 2016), and the correlation between host star metallicity and their occurrence (Petigura et al., 2018; Osborn et al., 2020) also indicates that metals are needed for their formation. As shown in Fig. 4.9, our widely separated, 10–30 $M_{\rm Jup}$ companions occupy a region of the C/O and metallicity space that is clustered around solar (and likely stellar) composition, which is distinct than the the HJs. We carry out a weighted two-sample t-test to quantify the statistical likelihood that the compositions of HJs and those of our sample are drawn from the same population. We find p-values of 4.2×10^{-4} for C/O (3.5σ) and 7.5×10^{-6} for [C/H] (4.5σ), indicating that our measurements are inconsistent with the null hypothesis that the atmospheric compositions of HJs and our sample belong to the same population. Therefore, this serves as empirical evidence that our companions likely did not form via core accretion inside the CO snowline.

Our $\sim$10–30 $M_{\rm Jup}$ companions orbit a diverse group of host stars, with stellar masses spanning an order of magnitude between $\approx 0.35 - 0.45\ M_\odot$ for DH Tau and 2M0122 (Sebastian et al., 2021; Yu et al., 2023) to $\approx 3 - 4\ M_\odot$ for kap And b and HIP 79098 (Janson et al., 2019; Gaia Collaboration, 2022). This translates to a range of mass ratios (q) from ≈ 0.007 to 0.07 (with $\sim 30 - 60\%$ uncertainties on q mostly due to the uncertain companion masses). Previous studies find that multiple star formation operates in a largely scale-invariant manner, with mass ratio being a more informative quantity than masses of either component (e.g. Goodwin, 2013; Duchêne et al., 2023). For example, Duchêne et al. (2023) found a dearth of low-mass stellar companions around intermediate-mass stars ($M = 1.75 - 4.5\ M_\odot$)

with $q \approx 0.05 - 0.10$, which matches the 'brown dwarf desert' around solar-mass stars (e.g. Grether et al., 2006; Metchev et al., 2009; Sahlmann et al., 2011). They postulate that this mass ratio desert delineates two distinct formation regimes with systems with $q \lesssim 0.02$ forming in disks (either disk instability or core accretion), and those with $q \gtrsim 0.07$ forming through cloud fragmentation. Seven of our companions have $q \lesssim 0.03$, while 2M0122 b has $q \approx 0.07$, so a mix of formation mechanisms are possible.

How do our results fare in terms of the different formation mechanisms? Perhaps most directly, our findings are consistent with birth via direct gravitational collapse in a massive protostellar disk or cloud fragmentation, which should produce broadly stellar compositions as is seen for stellar binaries (e.g. Hawkins et al., 2020). While some studies predict that low-mass objects which form via disk instability can be subsequently enriched by the accretion of solids post-formation (Boley et al., 2011), it would be difficult to significantly alter the metallicity of the 10–30 $M_{\rm Jup}$ objects studied here (see also Inglis et al., 2024). For example, a 10× increase in metallicity for a 20 $M_{\rm Jup}$ object would require the addition of ∼2 $M_{\rm Jup}$ of solids. Assuming a solid-to-gas mass ratio of 0.01 for the disk, accretion of ∼2 $M_{\rm Jup}$ of solids would require a disk-to-star ratio exceeding 0.2 for a solar-mass star and that all the solids in the disk accrete onto the companion. Therefore, significant metal enrichment for our companions is challenging, especially as most of our stars are less massive the Sun. By a similar logic, significantly sub-solar metallicities are also unexpected for 10–30 $M_{\rm Jup}$ companions that form via disk instability.

Alternatively, our composition measurements could also be compatible with core accretion outside the CO snowline (i.e. in situ). Outside the CO snowline, nearly all the metals are condensed into solids as there is very little gas. As a result, the solids inherit a stellar composition. This means that unless the planet accreted more gas than solids and became extremely metal poor, accretion of solids at these locations would typically produce stellar C/O and metallicities (e.g. Chachan et al., 2023). Since our companions have nearly solar and stellar metallicities, they are chemically consistent with forming via core accretion outside the CO snowline. We note that planetesimal accretion is less efficient at wider orbital distances, but pebble accretion may be able to produce a sufficiently massive core on a reasonable timescale (Lambrechts et al., 2012). For example, Gurrutxaga et al. (2023) demonstrated pebble accretion pathways to form the giant planets PDS 70 b ($m \approx 2 - 6$ $M_{\rm Jup}$, $a \approx 21$ au) and c ($m \approx 3 - 10$ $M_{\rm Jup}$, $a \approx 34$ au; planet values

from J. J. Wang et al. 2021a). However, it remains to be seen whether realistic pebble accretion scenarios can produce our higher mass and wider separation (up to 360 au) companions. For example, half of our companions have $q \gtrsim 0.03$, which means that companion formation must begin early in a disk with disk-to-star mass ratio > 0.03 and finish before the bulk of the gas reservoir accretes onto the star. By the protoplanetary disk phase, typical disk-to-star mass ratios of ~ 0.01 have insufficient mass to produce $> 10\ M_{\rm Jup}$ companions around solar-mass stars even if all the disk mass goes into the companion (let alone around the M dwarfs in our sample). Finally, early, massive circumstellar disks can be prone to gravitational instability (K. Kratter et al., 2016), so an additional challenge of forming companions via core accretion at large distances is the need to prevent disk fragmentation from occurring.

The ^{12}C/^{13}C isotopic ratio

Minor isotopologues of carbon, oxygen, and nitrogen have recently been detected in exoplanets and brown dwarfs (Y. Zhang et al., 2021b; Y. Zhang et al., 2021a; Line et al., 2021; Barrado et al., 2023; Gandhi et al., 2023), allowing constraints on isotopic ratios such as ^{12}C/^{13}C, ^{12}O/^{18}O and ^{14}N/^{15}N. J. W. Xuan et al. (2024c) also demonstrated carbon and oxygen isotopic homogeneity between a late-M dwarf companion and its late-K primary star with Keck/KPIC spectroscopy. In this paper, we find bounded constraints on ^{12}CO/^{13}CO for three companions, GQ Lup b, HIP 79098 b, and DH Tau b, though the ^{13}CO detection for DH Tau b is tentative.

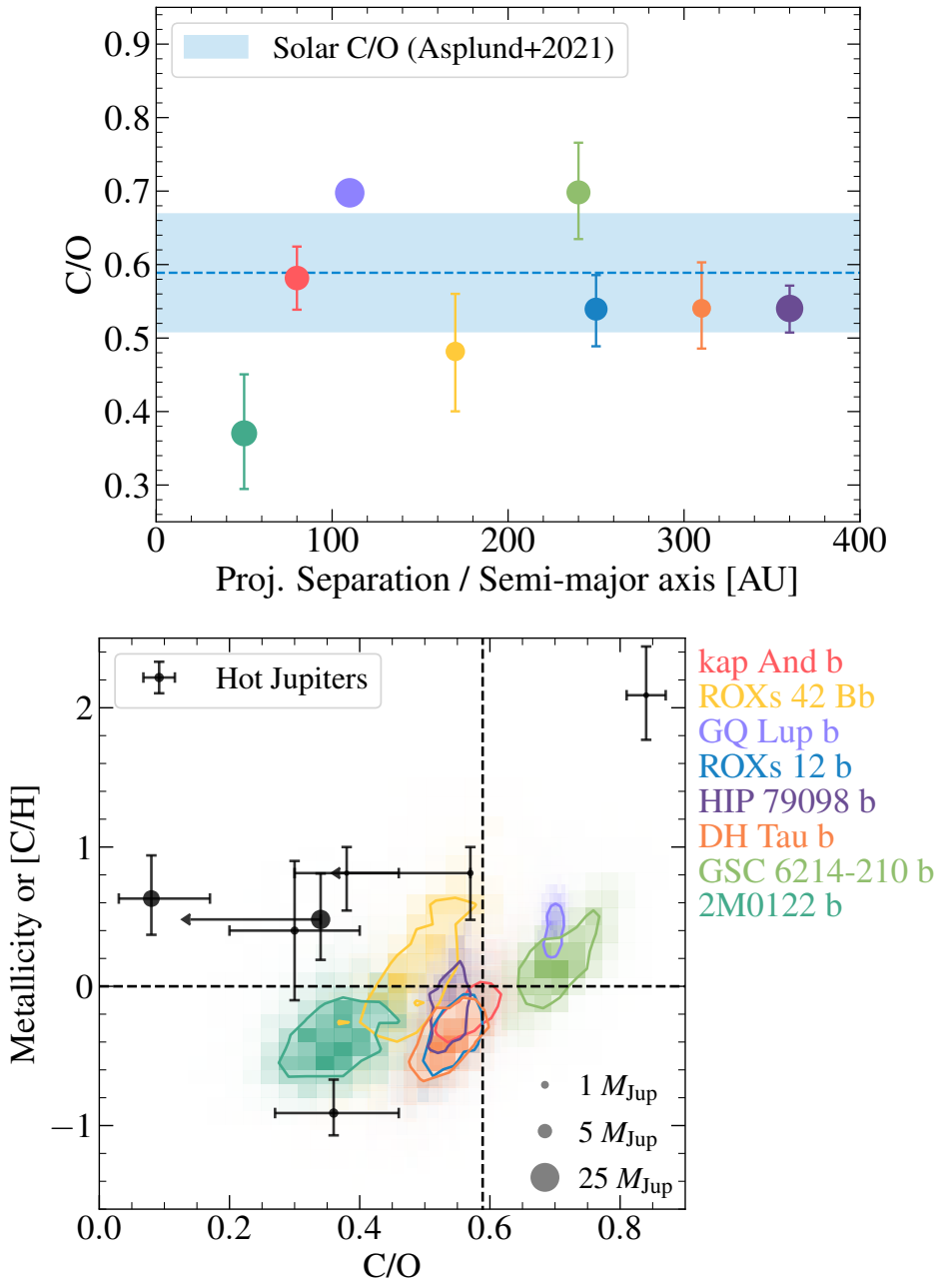

Figure 4.9: Left: C/O as a function of projected separation or semi-major axis for the eight companions in this study. The points are sized by companion mass, using the mass legend in the right panel. The blue line and region show the solar C/O value from Asplund et al. (2021). Right: In color: 1σ contours of C/O and [C/H] for the eight companions, which are all consistent with solar composition (intersection of dashed gray lines) to the 2σ level. In § 4.6, we justify that their host stars likely have solar composition as well. We overplot hot Jupiters which have abundance measurements for at least one oxygen-bearing and one carbon-bearing species from JWST or high-resolution spectroscopy as black points (Alderson et al., 2023; August et al., 2023; Bean et al., 2023; T. J. Bell et al., 2023; Brogi et al., 2023; Finnerty et al., 2024; Xue et al., 2024), which are also sized by mass. The hot Jupiters show considerable scatter and super-solar (and super-stellar) metallicities except for one planet, unlike our companions which cluster around solar (and stellar) composition.

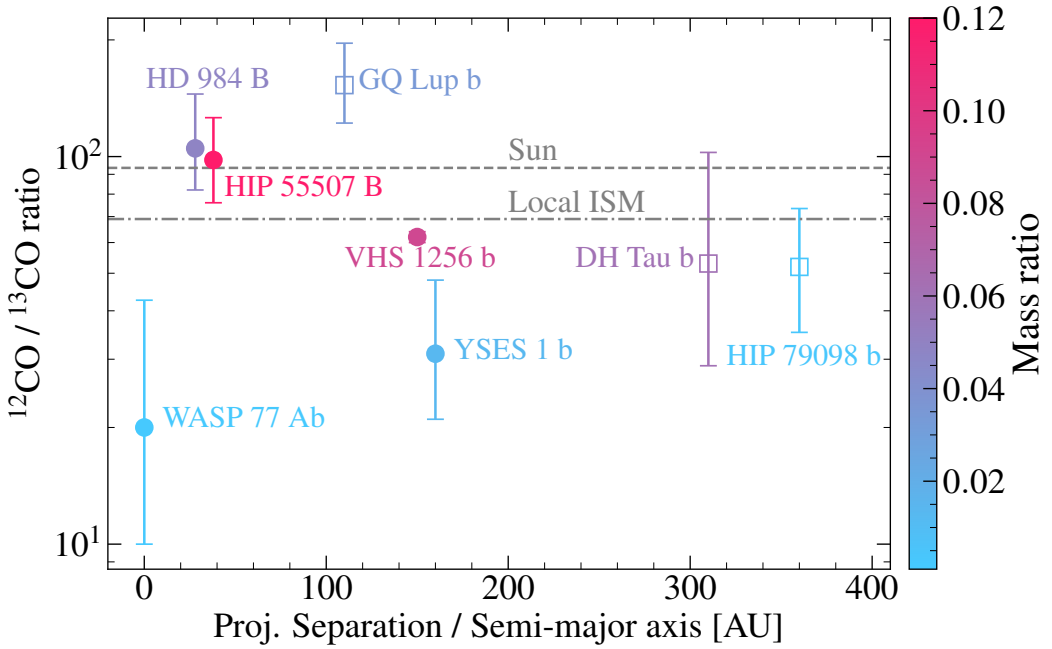

Figure 4.10: ^{12}C/^{13}C measured from CO as a function of projected separation or semi-major axis. The points are color-coded by companion-star mass ratio, and the three open squares are from this paper. The dashed and dashdot lines denote the solar value (Lyons et al., 2018) and ISM value (Wilson, 1999), respectively. The other points are from Line et al. (2021) for WASP-77 Ab, Y. Zhang et al. (2021b) for YSES 1 b, J. W. Xuan et al. (2024c) for HIP 55507 B, Costes et al. (2024) for HD 984 B, and Gandhi et al. (2023) for VHS 1256 b.

^{12}C/^{13}C is proposed to be a formation diagnostic as CO ice outside the CO snowline is expected to be enriched in ^{13}C due to isotopic selective fractionation processes such as CO self-shielding (Y. Zhang et al., 2021b). Planets forming via core/pebble accretion outside the CO snowline may therefore show a lower ^{12}C/^{13}C due to this effect. Our three companions show a range of ^{12}C/^{13}C values between ≈50–150. The values for DH Tau b (53^{+50}_{-24}) and HIP 79098 b (52^{+22}_{-17}) are broadly consistent with the local ISM value of ^{12}C/^{13}C = 69 ± 6 (Wilson, 1999), while GQ Lup b shows a higher ^{12}CO/^{13}CO of 153^{+43}_{-31}. In Appendix 4.11, we compare retrieval results from several different nights of KPIC data for GQ Lup b, and find ≈0.1 dex differences in the retrieved log(^{12}CO/^{13}CO) between different nights, which is consistent with the findings of J. W. Xuan et al. (2024c). When including the night-to-night scatter of 0.10 dex as a systematic error, GQ Lup b's measurement is consistent with the solar value of ^{12}C/^{13}C = 93.5 ± 3.1 (Lyons et al., 2018) at the 1σ level. Overall, these findings do not provide evidence that our companions accreted a significant amount of ice with low ^{12}C/^{13}C, consistent with their likely

star-like formation pathways.

In Fig. 4.10, we plot our new measurements along with previous constraints on the $^{12}C/^{13}C$ for exoplanets and low-mass companions. There is considerable scatter in the measurements, and no clear trend with orbital distance or mass ratio. Some of these results should be re-visited with better quality or higher-resolution data to reduce the error bars. For directly imaged companions, the exquisite S/N from JWST is poised to provide more precise measurements of isotopologue ratios, as demonstrated by Gandhi et al. (2023). Another direction is to obtain higher S/N data to detect additional isotopologues such as $C^{18}O$ and $H_2^{18}O$ (Y. Zhang et al., 2022; J. W. Xuan et al., 2024c) Finally, to better interpret isotopic ratio data, more work is required on the modeling side to understand the details of isotopic variability and fractionation chemistry in disks (Öberg et al., 2023).

System and orbital architectures

The formation of substellar companions should also be considered in the context of the host stellar system. As noted in § 4.2, five out of eight of our systems are either confirmed or likely multiple-star systems. ROXs 42B is a resolved binary with projected separation ∼12 au (Kraus et al., 2013) while HIP 79098 is a suspected binary (Janson et al., 2019), making the b components around them 'circumbinary.' One way to explain these configurations is via disk fragmentation, which generally produces multiple fragments that interact gravitationally (e.g. K. Kratter et al., 2016). For example, the protostellar disk around ROXs 42B could first fragment and form the secondary star, which continues to grow given high infall rates from the surrounding nebula. At a later stage when the disk mass is lower, but still gravitationally unstable, a second fragmentation could produce the ∼13 $M_{\rm Jup}$ companion. Dynamical interactions may cause the substellar companion to move away from the star while the secondary star moves inward.

On the other hand, DH Tau, ROXs 12, and GQ Lup have wide stellar companions at thousands of au (Kraus et al., 2009; Bowler et al., 2017; Alcalá et al., 2020). Alcalá et al. (2020) hypothesized that GQ Lup A and its wide (≈ 2400 au) stellar companion may have formed via turbulent fragmentation of a molecular cloud core, while GQ Lup b fragmented out of the circumprimary disk around GQ Lup A. Similar formation pathways may be responsible for the DH Tau and ROXs 12 systems as well. While disk fragmentation simulations do produce low-mass substellar companions (e.g. Stamatellos et al., 2009), it is challenging to prevent these companions from

further accretion to become low-mass stars or be tidally destroyed during a rapid inward migration phase powered by infall (Zhu et al., 2012; Forgan et al., 2013). Indeed, to produce the 10–30 $M_{\rm Jup}$ companions we observe today, fragmentation must occur in a narrow window after the period of high infall rates, but before the disk mass becomes too small for Toomre instability (K. M. Kratter et al., 2010b). Therefore, if disk fragmentation is a common formation mechanism, we should observe more low-mass stars around the same stellar types compared to substellar or planetary companions. Published observations are in qualitative agreement with this prediction. For example, Duchêne et al. (2023) find a significantly higher number of low-mass stellar companions around intermediate-mass stars compared to substellar companions.

Orbital architectures provide another piece of the puzzle. One informative probe is the relative alignment between different angular momentum vectors in the system. Recently, Bowler et al. (2023) presented a summary of stellar obliquity constraints for directly imaged substellar companions, finding that misalignment between the companion orbits and stellar spin axes are common. Specifically, GQ Lup b may be on a nearly perpendicular orbit with respect to the circumstellar disk around GQ Lup A, and is also misaligned with the star's spin axis (Stolker et al., 2021). Similarly, the orbit of ROXs 12 b is also likely misaligned compared to the stellar spin axis (Bowler et al., 2017; Bowler et al., 2023). Bryan et al. (2020b) provided the first measurement of companion obliquity for 2M0122 b, finding that the companion's spin axis is tentatively misaligned with respect to the stellar spin.[8] Since stellar binaries that form via turbulent fragmentation tend to have misaligned spin and orbital orientations (e.g. Jensen et al., 2014; Lee et al., 2016; Offner et al., 2016), random spin-orbit distributions should also be prevalent for systems with substellar companions if they form in this manner, which is consistent with current findings. Alternatively, wide, misaligned stellar companions in these systems could torque the disk around the primary, causing the companions that fragment in the disk to inherit such misalignments (e.g. Bowler et al., 2017). Finally, disk turbulence itself could result in random spin-orbit misalignments (Jennings et al., 2021). Regardless of the detailed mechanism, the system and orbital architectures of our systems are broadly consistent with star-like formation. This is consistent with the trend of chemical homogeneity we infer between these companions and their stars.

[8]We note that our higher KPIC $v \sin i$ measurement of $19.6^{+3.0}_{-2.5}$ km s^{-1} for 2M0122 b (see Table 4.4) would increase the line-of-sight inclination of the companion's spin axis, making it more aligned with the stellar spin axis. Due to the low S/N of our 2M0122 b spectra however, we emphasize that future data will be required to confirm the exact $v \sin i$ of this companion.

4.7 Conclusion

We have carried out a uniform atmospheric retrieval study of eight widely-separated substellar companions (~50–360 au, ~10–30 $M_{\rm Jup}$) with Keck/KPIC high-resolution K band spectroscopy. From these retrievals, we measure the companion's C/O, metallicity (denoted [C/H]), isotopic abundances, in addition to their cloud properties, spins, radial velocities, and temperature profiles. To complement the continuum-removed high-resolution data, we adopt mass and radius priors from evolutionary models in the retrievals.

First, we find that these companions have broadly solar composition (to within 2σ level), and likely stellar composition given the trend of solar abundances seen for stars in the same star-forming associations. Their abundance pattern is similar to systems with high-mass brown dwarf companions and stellar binaries, which show chemically homogeneity (e.g. Hawkins et al., 2020; J. Wang et al., 2022; J. W. Xuan et al., 2022). On the other hand, their abundances are distinct from hot Jupiters, which show a range in C/O and generally super-stellar metallicities (see Fig. 4.9), and directly imaged giant planets with $m \sim 3-10\ M_{\rm Jup}$, which show tentative metal enrichment (J. Wang, 2023a). Thus, the population of low-mass substellar companions from direct imaging likely traces the tail-end of star formation processes such as gravitational disk instability and cloud fragmentation, making them low-mass brown dwarfs instead of 'super-Jupiter' planets or 'planetary-mass companions.' Alternatively, we note that our composition measurements are also consistent with core accretion outside the CO snowline where these companions are observed today, since accretion at these locations would also yield stellar C/O and metallicities. However, such a scenario requires core accretion to proceed early and rapidly in a massive, protostellar disk in order to explain the accretion of 10–30 $M_{\rm Jup}$ of material, especially for the systems with lower mass host stars.

Second, we find evidence of clouds in two of the colder companions (Fig. 4.6), kap And b ($T_{\rm eff} = 1640^{+220}_{-170}\ K$) and GSC 6214-210 b ($T_{\rm eff} = 1860^{+170}_{-110}\ K$), with the EddySed cloud model being preferred by $\gtrsim 3\sigma$ compared to both the clear and gray cloud models. This indicates that narrow-band, high-resolution spectra can be sensitive to non-gray, scattering clouds when the cloud opacity is high near the photosphere, as is the case for these companions. This result highlights the potential of high-resolution spectroscopy in constraining both abundances and clouds for brown dwarfs and exoplanets.

Third, we present three new measurements of ^{12}CO/^{13}CO for GQ Lup b (153^{+43}_{-31}),

HIP 79098 b (52^{+22}_{-17}), and DH Tau b (53^{+50}_{-24}). A cross-correlation analysis shows solid detections for the first two companions, and a tentative detection of ^{13}CO for DH Tau b. From retrievals of six independent KPIC datasets of GQ Lup b data (Appendix 4.11), we find ≈ 0.1 dex systematic errors in ^{12}CO/^{13}CO, which is consistent with the findings of J. W. Xuan et al. (2024c). After accounting for systematics, our measurements agree with either the ISM or solar ^{12}C/^{13}C to within 1σ. We place these measurements in context of previous work and do not identify any clear trends between ^{12}C/^{13}C and mass, mass ratio, or orbital distance at this stage (Fig. 4.10). More precise and accurate measurements of ^{12}C/^{13}C and complementary measurements of the isotopic ratio in the host stars are necessary to further interpret these results.

Finally, we present radial velocity and spin measurements for the companions. We find some discrepancies between our $v \sin i$ values and previous studies using pre-upgrade Keck/NIRSPEC data (Bryan et al., 2020a), while our $v \sin i$ for GQ Lup b agrees with previous VLT/CRIRES measurements at a higher resolution of $R \sim 100,000$ (Schwarz et al., 2016). Due to the higher spectral resolution ($R \sim 35,000$), higher S/N, and more stable line spread function of KPIC (which uses post-upgrade NIRSPEC; Martin et al. 2018) compared to pre-upgrade NIRSPEC ($R \sim 25,000$), we adopt our new spin measurements in this paper. Seven out of eight of our companions have relatively slow $v \sin i \approx 4 - 20$ km s^{-1}, with kap And b being an outlier with $v \sin i = 39.4 \pm 0.9$ km s^{-1} (see also Morris et al. 2024). Our objects follow the overall trend of literature spin measurements, and display a large scatter in their fractional rotational velocities, v/v_{breakup}, as shown in Fig. 4.8.

Looking forward, it would be useful to obtain higher S/N spectra for some of the companions in order to obtain higher precision measurements. The results for 2M0122 b in particular should be re-visited, as this is our lowest S/N dataset and we also retrieve a much lower C/O for this companion than the rest of the sample. Higher S/N data would also help increase the quantity and quality of ^{12}CO/^{13}CO measurements. For example, Gandhi et al. (2023) showed that JWST/NIRSpec enables isotopologue measurements with unprecedented precision for widely-separated substellar companions. In addition, detailed forward modeling of the residual starlight could also open the door to studying close-in, high-contrast companions with the JWST/NIRSpec integral field unit (Ruffio et al., 2023a). The wide wavelength coverage of JWST would be useful for constraining cloud properties and measuring more elemental abundances besides C and O in order to break degeneracies in formation

inferences as well (e.g. Cridland et al., 2020; Turrini et al., 2021; Ohno et al., 2023; Chachan et al., 2023).

Many of the companions presented in this work have relatively large separations and low star-to-companion contrasts, making them accessible with traditional NIRSPEC in AO mode (Bryan et al., 2018). A natural next step would be to extend our measurements to companions with lower masses and smaller orbital distances. Keck/KPIC and similar instruments like VLT/HiRISE (Vigan et al., 2024) are ideal for these targets, as shown by J. J. Wang et al. (2021c). By targeting more directly imaged planets with high-resolution spectroscopy, we could further test the tentative trend of metal enrichment suggested by J. Wang (2023a) for these planets. Such measurements are especially important given literature discrepancies in the retrieved abundances for the same planet, either due to using data with different spectral resolution (e.g. β Pic b; Gravity Collaboration et al., 2020; Landman et al., 2023b), or using different retrieval methods on similar low-resolution data (e.g. 51 Eri b; Brown-Sevilla et al., 2023; Whiteford et al., 2023). As demonstrated by this paper and previous work, atmospheric abundance measurements from medium-to-high resolution spectroscopy are providing results that are reliable to uncertain assumptions about clouds (Y. Zhang et al., 2021a; J. W. Xuan et al., 2022; Inglis et al., 2024), and consistent across different observing nights (Ruffio et al., 2021; J. W. Xuan et al., 2024c; Landman et al., 2023a). Therefore, medium-to-high resolution spectroscopy is poised to improve our understanding of the nature and formation of directly imaged companions in the near future, bringing more clarity in the delineation between giant planets and their brown dwarf counterparts.

4.8 Acknowledgments

J.X. thanks Melanie Rowland, Yayaati Chachan, Michael Liu, Kazumasa Ohno, Douglas Lin, Ricardo López-Valdivia, Henrique Reggiani, and Jingwen Zhang for helpful discussions. J.X. is supported by the NASA Future Investigators in NASA Earth and Space Science and Technology (FINESST) award #80NSSC23K1434. J.X. also acknowledges support from the Keck Visiting Scholars Program (KVSP) to commission KPIC Phase II capabilities. D.E. is supported by the NASA FINESST award #80NSSC19K1423. D.E. also acknowledges support from the Keck Visiting Scholars Program (KVSP) to install the Phase II upgrades. Funding for KPIC has been provided by the California Institute of Technology, the Jet Propulsion Laboratory, the Heising-Simons Foundation (grants #2015-129, #2017-318, #2019-1312, #2023-4598), the Simons Foundation, and the NSF under grant AST-

1611623. The computations presented here were conducted in the Resnick High Performance Center, a facility supported by Resnick Sustainability Institute at the California Institute of Technology. W. M. Keck Observatory access was supported by Northwestern University and the Center for Interdisciplinary Exploration and Research in Astrophysics (CIERA). The data presented herein were obtained at the W. M. Keck Observatory, which is operated as a scientific partnership among the California Institute of Technology, the University of California and the National Aeronautics and Space Administration. The Observatory was made possible by the generous financial support of the W. M. Keck Foundation. The authors wish to recognize and acknowledge the very significant cultural role and reverence that the summit of Mauna Kea has always had within the indigenous Hawaiian community. We are most fortunate to have the opportunity to conduct observations from this mountain. This work benefited from the 2023 Exoplanet Summer Program in the Other Worlds Laboratory (OWL) at the University of California, Santa Cruz, a program funded by the Heising-Simons Foundation and NASA. The research here acknowledges use of the Hypatia Catalog Database, an online compilation of stellar abundance data as described in Hinkel et al. (2014), which was supported by NASA's Nexus for Exoplanet System Science (NExSS) research coordination network and the Vanderbilt Initiative in Data-Intensive Astrophysics (VIDA).

4.9 Appendix

4.10 Interpolated properties from evolutionary models

Here, we show the evolutionary-model predicted mass, radius, $\log g$, and $T_{\rm eff}$ distributions for the seven other companions. Different colors indicate different evolutionary models, with ATMO 2020 in blue (Phillips et al., 2020; Chabrier et al., 2023), AMES-Dusty in red (Allard et al., 2001), BHAC15 in purple (Baraffe et al., 2015), and SM08 in gray (Saumon et al., 2008). The distributions for GQ Lup b are shown in Fig. 4.2.

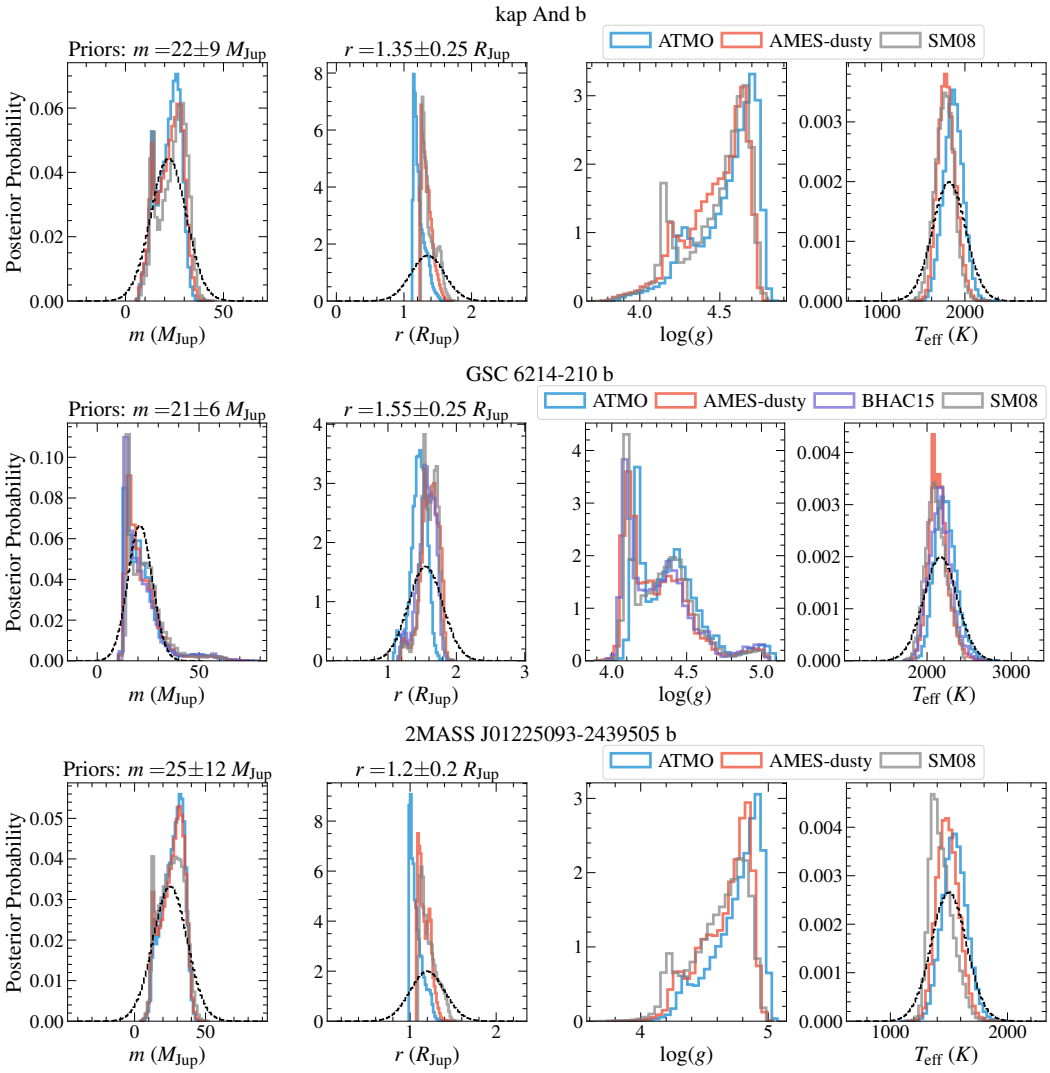
kap And b
Priors: m =22±9 M_{Jup}
r =1.35±0.25 R_{Jup}
ATMO
AMES-dusty
SM08
Posterior Probability
m (M_{Jup})
r (R_{Jup})
log(g)
T_{eff} (K)
GSC 6214-210 b
Priors: m =21±6 M_{Jup}
r =1.55±0.25 R_{Jup}
ATMO
AMES-dusty
BHAC15
SM08
Posterior Probability
m (M_{Jup})
r (R_{Jup})
log(g)
T_{eff} (K)
2MASS J01225093-2439505 b
Priors: m =25±12 M_{Jup}
r =1.2±0.2 R_{Jup}
ATMO
AMES-dusty
SM08
Posterior Probability
m (M_{Jup})
r (R_{Jup})
log(g)
T_{eff} (K)

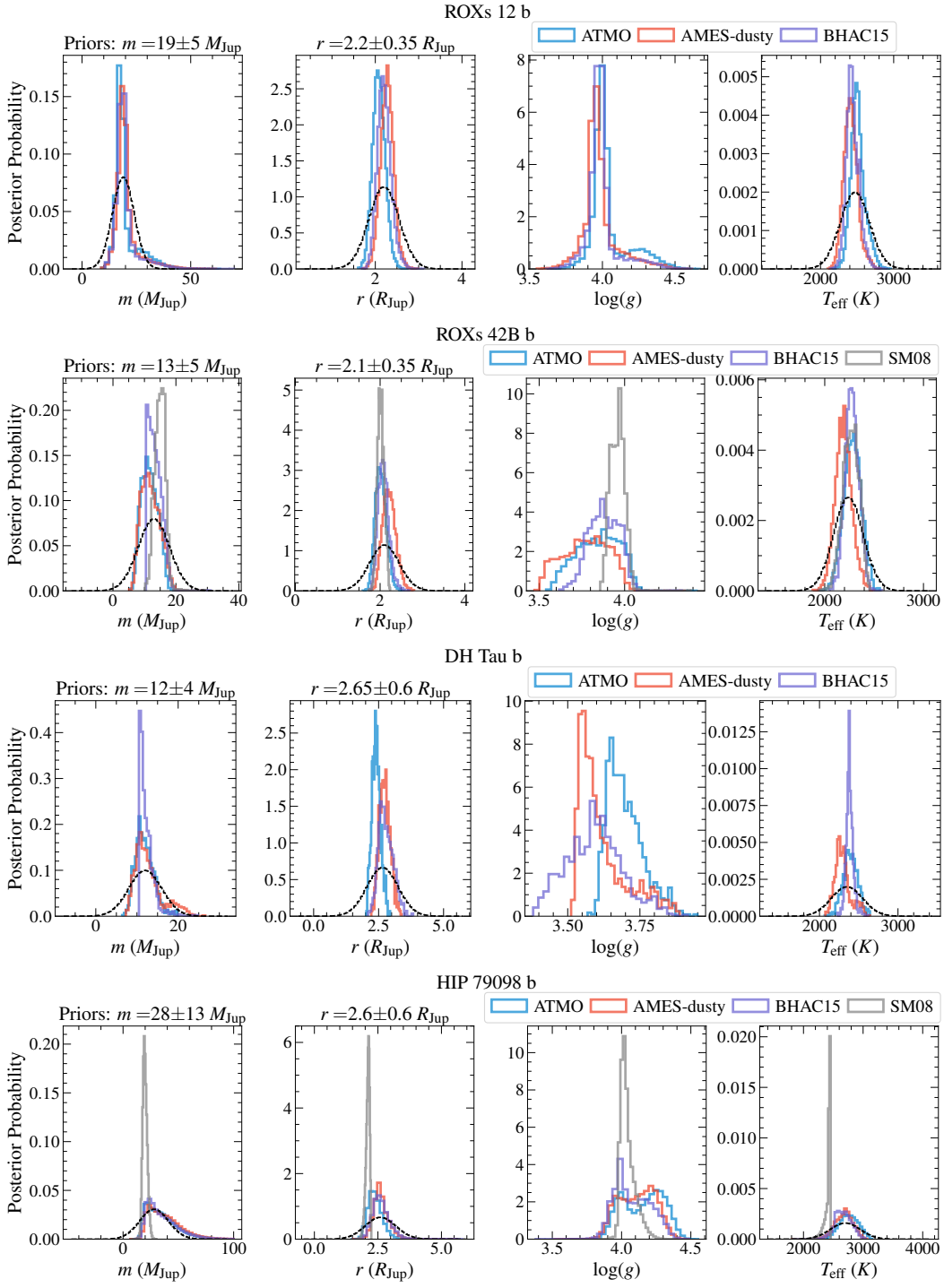

Figure 4.11: Same as Fig. 4.2, but for the other seven companions.

4.11 Comparing continuum removal methods with multiple datasets of GQ Lup b

We compare the retrieved abundances and $v \sin i$ between different observing epochs for GQ Lup b, our highest S/N target. In addition, we compare two methods of removing the continuum: the high-pass filter (HPF) method used in the paper and a spline model. As described in § 4.4, a median-filter with a size of 100 pixels (≈ 0.002 μm) is adopted as the HPF. The choice of the filter size is motivated by injection-recovery tests in J. W. Xuan et al. (2022), while the median-filter is found to perform better compared to Fourier-based filters or Gaussian filters (J. J. Wang et al., 2021c).

For the alternative, spline model, we follow the method in Ruffio et al. (2023a) using the open-source package `breads` (Agrawal et al., 2023).[9] Since the spline model allows us to modulate the companion continuum and the speckle continuum separately, we experimented with a few different choices. Our default spline model modulates the continuum of both speckle and companion with a third-order spline model. Specifically, we use three spline nodes per spectral order. We note that such a spline operates over a much larger scale ($\approx$ 1000 pixels) compared to our 100-pixel median filter, so is not an exact comparison to the HPF method. When we instead used 10 nodes per spectral order for the speckle continuum, the results were consistent with the 3-node model but the continuum oscillations appear more stochastic and less smooth, leading us to disfavor these higher number of nodes. Finally, we also experimented with a simpler model of not modulating the companion continuum and only modulating the speckle continuum. We find that this did not change the results significantly either.

To compare the two continuum removal methods, we perform retrievals on six independent datasets for GQ Lup b across three different nights (two fibers were used each night), UT 2023 June 23, June 24, and June 29. The same retrieval setup and priors are used. For the HPF, we jointly fit for flux scales for the companion and the speckle contribution, α_b and α_s (see Eq. 4.1). Similarly, the spline model performs a linear optimization to determine the spline parameters for each proposed model.

In Fig. 4.12, we compare the retrieved C/O, [C/H], and $\log(^{12}\mathrm{CO}/^{13}\mathrm{CO})$ between the different datasets for each continuum removal method. First, we note that the retrieved values between the two methods agree well; taking the median across the results from six datasets, we obtain C/O = 0.65, [C/H] = 0.17, $\log(^{12}\mathrm{CO}/^{13}\mathrm{CO})$ =

[9] `https://github.com/jruffio/breads`

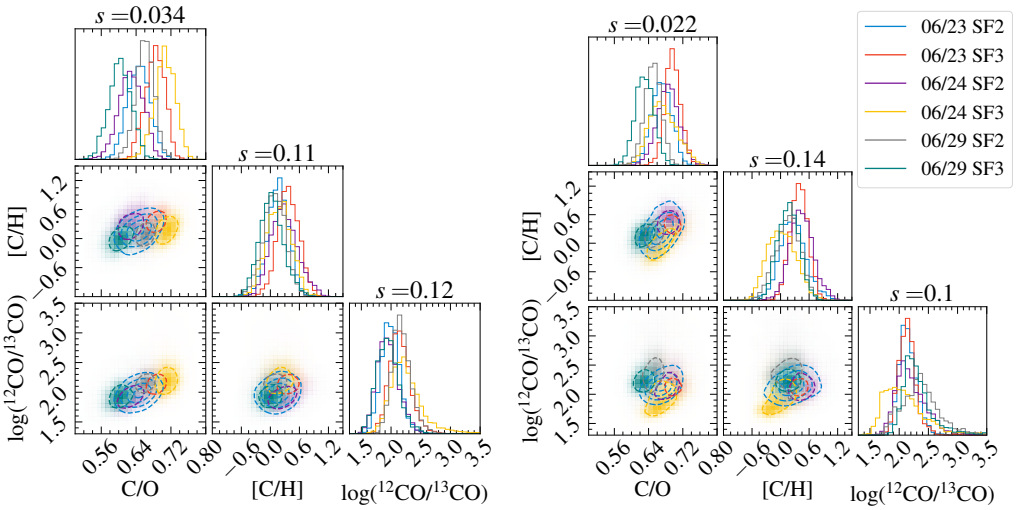

Figure 4.12: Left: posterior distributions of three key parameters from using the spline model. Six different datasets are compared (3 nights × 2 fibers per night). Right: the same but using the HPF (median-filter of 100 pixels). The titles on each histogram show the standard deviation (s) of the median between the six different posteriors. The legend is shared between both plots.

2.07 from the HPF method, and C/O = 0.67, [C/H] = 0.21, $\log(^{12}\mathrm{CO}/^{13}\mathrm{CO})$ = 2.15 from the spline method. Next, we quantify the relative agreement between different datasets with the standard deviation (s) of the median retrieved values. We find that the HPF yields a slightly lower spread in C/O by ≈ 35% compared to the spline method. The spread in [C/H] and $\log(^{12}\mathrm{CO}/^{13}\mathrm{CO})$ is comparable between the two methods. Therefore, we conclude that the performances of the two continuum removal methods are comparable for our data. We adopt the HPF as the continuum removal method in this paper to be consistent with previous KPIC retrieval papers (e.g. J. J. Wang et al., 2021c; J. W. Xuan et al., 2022; J. W. Xuan et al., 2024c), but note that our results will not be affected if we chose the spline model instead.

By comparing results from different datasets, we can also assess the level of systematic error in the retrieved parameters. Here, we focus on the HPF results. Approximating the standard deviation as the systematic error, we find night-to-night systematics of 0.022, 0.14 dex, and 0.10 dex for C/O, [C/H], and $\log(^{12}\mathrm{CO}/^{13}\mathrm{CO})$. These systematic errors are comparable in size to those found in J. W. Xuan et al. (2024c) by comparing two independent KPIC datasets for a M7.5 companion.

4.12 Priors for retrievals

Here, we list the fitted parameters and adopted priors for retrievals of the seven other companions. The corresponding information for κ And b is shown in Table 4.3.

Table 4.5: Fitted Parameters and Priors for GQ Lup b Retrievals

Parameter	**Prior**	**Parameter**	**Prior**
Mass ($M_{\rm Jup}$)	$\mathcal{N}(33.0, 10.0)$	Radius ($R_{\rm Jup}$)	$\mathcal{N}(3.7, 0.7)$
$T_{\rm anchor}$ [log(P)=-1.1] (K)	$\mathcal{U}(2000, 3000)$	RV (km s^{-1})	$\mathcal{U}(-50, 50)$
ΔT_1 (K)	$\mathcal{U}(400, 1100)$	$v \sin i$ (km s^{-1})	$\mathcal{U}(0, 80)$
ΔT_2 (K)	$\mathcal{U}(0, 400)$	C/O	$\mathcal{U}(0.1, 1.0)$
ΔT_3 (K)	$\mathcal{U}(0, 400)$	[C/H]	$\mathcal{U}(-1.5, 1.5)$
ΔT_4 (K)	$\mathcal{U}(100, 850)$	log(^{12}CO/^{13}CO)	$\mathcal{U}(0, 6)$
ΔT_5 (K)	$\mathcal{U}(50, 550)$	$f_{\rm sed}$	$\mathcal{U}(0, 10)$
ΔT_6 (K)	$\mathcal{U}(200, 750)$	log($K_{\rm zz}$/cm^2 s^{-1})	$\mathcal{U}(5, 13)$
ΔT_7 (K)	$\mathcal{U}(50, 600)$	$\sigma_{\rm g}$	$\mathcal{U}(1.05, 3)$
log(gray opacity/cm^2 g^{-1})	$\mathcal{U}(-6, 6)$	log($\tilde{X}_{\rm Al_2O_3}$)	$\mathcal{U}(-2.3, 1)$
Error multiple	$\mathcal{U}(1, 5)$	log($\tilde{X}_{\rm Fe}$)	$\mathcal{U}(-2.3, 1)$
Comp. flux, α_c (counts)	$\mathcal{U}(0, 100)$	Speckle flux, α_s (counts)	$\mathcal{U}(0, 100)$

Table 4.6: Fitted Parameters and Priors for HIP 79098 b Retrievals

Parameter	**Prior**	**Parameter**	**Prior**
ΔT_1 (K)	$\mathcal{U}(300, 800)$	$T_{\rm anchor}$ [log(P)=-0.7)] (K)	$\mathcal{U}(1900, 2800)$
ΔT_2 (K)	$\mathcal{U}(0, 400)$	Mass ($M_{\rm Jup}$)	$\mathcal{N}(28.0, 13.0)$
ΔT_3 (K)	$\mathcal{U}(50, 500)$	Radius ($R_{\rm Jup}$)	$\mathcal{N}(2.6, 0.6)$
ΔT_4 (K)	$\mathcal{U}(100, 500)$	Comp. flux, α_c (counts)	$\mathcal{U}(0, 100)$
ΔT_5 (K)	$\mathcal{U}(200, 650)$	log($\tilde{X}_{\rm Al_2O_3}$)	$\mathcal{U}(-2.3, 1)$
ΔT_6 (K)	$\mathcal{U}(50, 650)$	log($\tilde{X}_{\rm Fe}$)	$\mathcal{U}(-2.3, 1)$
ΔT_7 (K)	$\mathcal{U}(100, 450)$	log(^{12}CO/^{13}CO)	$\mathcal{U}(0, 6)$

Table 4.7: Fitted Parameters and Priors for DH Tau b Retrievals

Parameter	**Prior**	**Parameter**	**Prior**
ΔT_1 (K)	$\mathcal{U}(200, 900)$	$T_{\rm anchor}$ [log(P)=-0.7)] (K)	$\mathcal{U}(1800, 3000)$
ΔT_2 (K)	$\mathcal{U}(0, 450)$	Mass ($M_{\rm Jup}$)	$\mathcal{N}(12.0, 4.0)$
ΔT_3 (K)	$\mathcal{U}(50, 550)$	Radius ($R_{\rm Jup}$)	$\mathcal{N}(2.6, 0.6)$
ΔT_4 (K)	$\mathcal{U}(0, 450)$	Comp. flux, α_c (counts)	$\mathcal{U}(0, 100)$
ΔT_5 (K)	$\mathcal{U}(50, 650)$	log($\tilde{X}_{\rm Al_2O_3}$)	$\mathcal{U}(-2.3, 1)$
ΔT_6 (K)	$\mathcal{U}(200, 900)$	log($\tilde{X}_{\rm Fe}$)	$\mathcal{U}(-2.3, 1)$
ΔT_7 (K)	$\mathcal{U}(100, 700)$	log(^{12}CO/^{13}CO)	$\mathcal{U}(0, 6)$

Table 4.8: Fitted Parameters and Priors for ROX 12 b Retrievals

Parameter	**Prior**	**Parameter**	**Prior**
ΔT_1 (K)	$\mathcal{U}(150, 850)$	$T_{\rm anchor}$ [log(P)=-0.7)] (K)	$\mathcal{U}(2200, 3000)$
ΔT_2 (K)	$\mathcal{U}(0, 450)$	Mass ($M_{\rm Jup}$)	$\mathcal{N}(19.0, 5.0)$
ΔT_3 (K)	$\mathcal{U}(50, 550)$	Radius ($R_{\rm Jup}$)	$\mathcal{N}(2.2, 0.35)$
ΔT_4 (K)	$\mathcal{U}(0, 450)$	Comp. flux, α_c (counts)	$\mathcal{U}(0, 100)$
ΔT_5 (K)	$\mathcal{U}(50, 650)$	log($\tilde{X}_{\rm Al_2O_3}$)	$\mathcal{U}(-2.3, 1)$
ΔT_6 (K)	$\mathcal{U}(200, 900)$	log($\tilde{X}_{\rm Fe}$)	$\mathcal{U}(-2.3, 1)$
ΔT_7 (K)	$\mathcal{U}(100, 700)$	log(^{12}CO/^{13}CO)	$\mathcal{U}(0, 6)$

Table 4.9: Fitted Parameters and Priors for GSC 6214-210 b Retrievals

Parameter	Prior	Parameter	Prior
ΔT_1 (K)	$\mathcal{U}(200, 650)$	$T_{\rm anchor}$ [log(P)=-0.1)] (K)	$\mathcal{U}(1700, 3000)$
ΔT_2 (K)	$\mathcal{U}(100, 500)$	Mass ($M_{\rm Jup}$)	$\mathcal{N}(21.0, 6.0)$
ΔT_3 (K)	$\mathcal{U}(100, 450)$	Radius ($R_{\rm Jup}$)	$\mathcal{N}(1.55, 0.25)$
ΔT_4 (K)	$\mathcal{U}(0, 550)$	Comp. flux, α_c (counts)	$\mathcal{U}(0, 100)$
ΔT_5 (K)	$\mathcal{U}(400, 1000)$	$\log(\tilde{X}_{\rm Al_2O_3})$	$\mathcal{U}(-2.3, 1)$
ΔT_6 (K)	$\mathcal{U}(100, 750)$	$\log(\tilde{X}_{\rm Fe})$	$\mathcal{U}(-2.3, 1)$
ΔT_7 (K)	$\mathcal{U}(0, 500)$	$\log(^{12}{\rm CO}/^{13}{\rm CO})$	$\mathcal{U}(0, 6)$

Table 4.10: Fitted Parameters and Priors for 2M 0122 b Retrievals

Parameter	Prior	Parameter	Prior
ΔT_1 (K)	$\mathcal{U}(350, 800)$	$T_{\rm anchor}$ [log(P)=-0.3)] (K)	$\mathcal{U}(950, 1800)$
ΔT_2 (K)	$\mathcal{U}(100, 500)$	Mass ($M_{\rm Jup}$)	$\mathcal{N}(25.0, 12.0)$
ΔT_3 (K)	$\mathcal{U}(0, 500)$	Radius ($R_{\rm Jup}$)	$\mathcal{N}(1.2, 0.2)$
ΔT_4 (K)	$\mathcal{U}(0, 300)$	Comp. flux, α_c (counts)	$\mathcal{U}(0, 100)$
ΔT_5 (K)	$\mathcal{U}(0, 300)$	$\log(\tilde{X}_{\rm MgSiO_3})$	$\mathcal{U}(-2.3, 1)$
ΔT_6 (K)	$\mathcal{U}(0, 400)$	$\log(\tilde{X}_{\rm Fe})$	$\mathcal{U}(-2.3, 1)$
ΔT_7 (K)	$\mathcal{U}(0, 400)$		

Table 4.11: Fitted Parameters and Priors for ROXs 42 Bb Retrievals

Parameter	Prior	Parameter	Prior
ΔT_1 (K)	$\mathcal{U}(200, 1200)$	$T_{\rm anchor}$ [log(P)=-1.0)] (K)	$\mathcal{U}(1300, 3000)$
ΔT_2 (K)	$\mathcal{U}(50, 550)$	Mass ($M_{\rm Jup}$)	$\mathcal{N}(13.0, 5.0)$
ΔT_3 (K)	$\mathcal{U}(50, 550)$	Radius ($R_{\rm Jup}$	$\mathcal{N}(2.1, 0.35)$
ΔT_4 (K)	$\mathcal{U}(50, 550)$	Comp. flux, α_c (counts)	$\mathcal{U}(0, 100)$
ΔT_5 (K)	$\mathcal{U}(50, 750)$	$\log(\tilde{X}_{\rm Al_2O_3})$	$\mathcal{U}(-2.3, 1)$
ΔT_6 (K)	$\mathcal{U}(50, 750)$	$\log(\tilde{X}_{\rm Fe})$	$\mathcal{U}(-2.3, 1)$
ΔT_7 (K)	$\mathcal{U}(50, 650)$		

Notes: For definitions and table notes see Table 4.3. In the table entries for companions after GQ Lup b, we omit a few common parameters that use the same priors. The different cloud species considered for each companion are indicated. Note that we only fit for speckle flux in the GQ Lup b and kap And b data, as explained in § 4.4.

4.13 Best-fit models from retrievals

Here, we plot the KPIC spectra and best-fit models for the seven other companions. The corresponding plot for GQ Lup b is shown in Fig. 4.5.

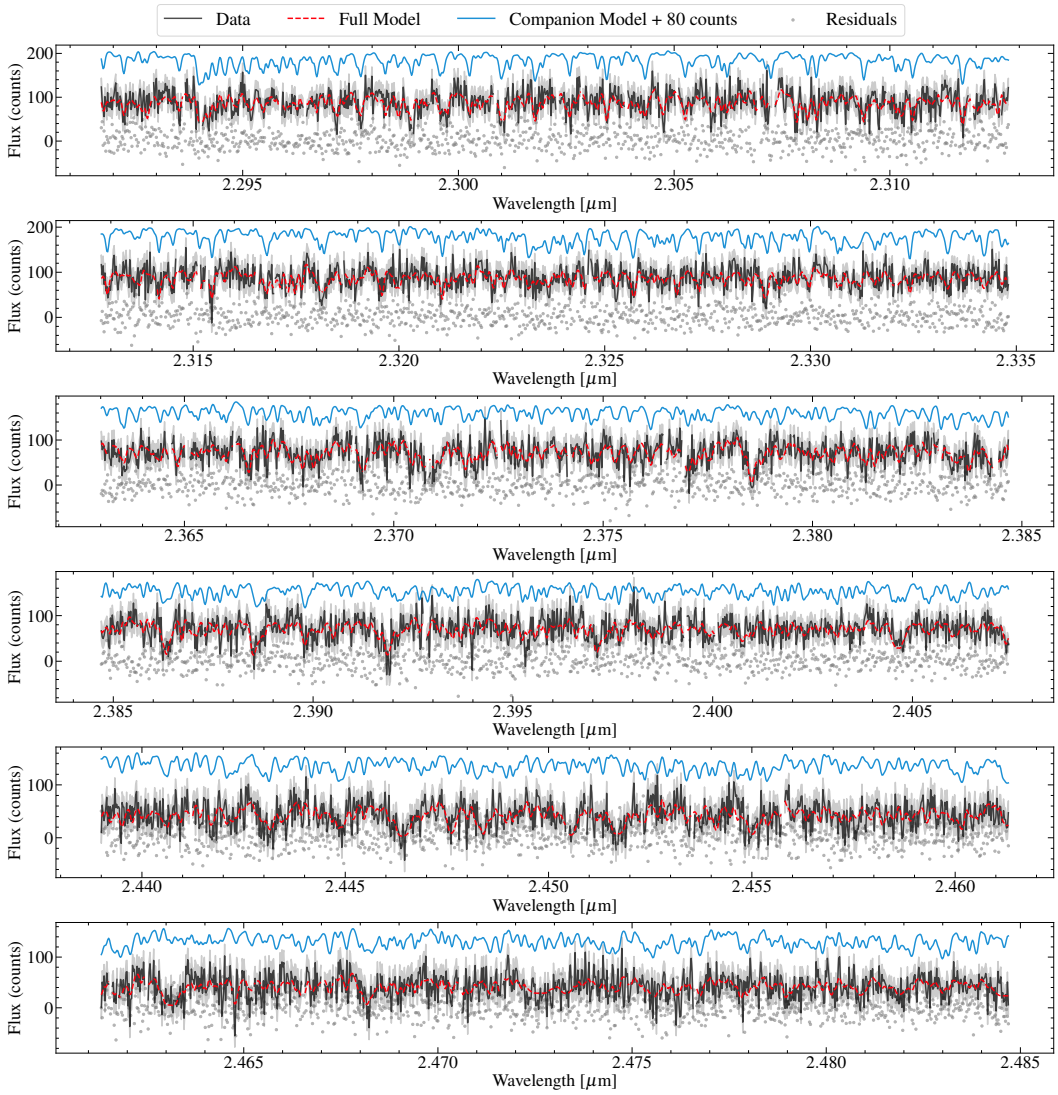

Figure 4.13: Same as Fig. 4.5, but for HIP 79098 b.

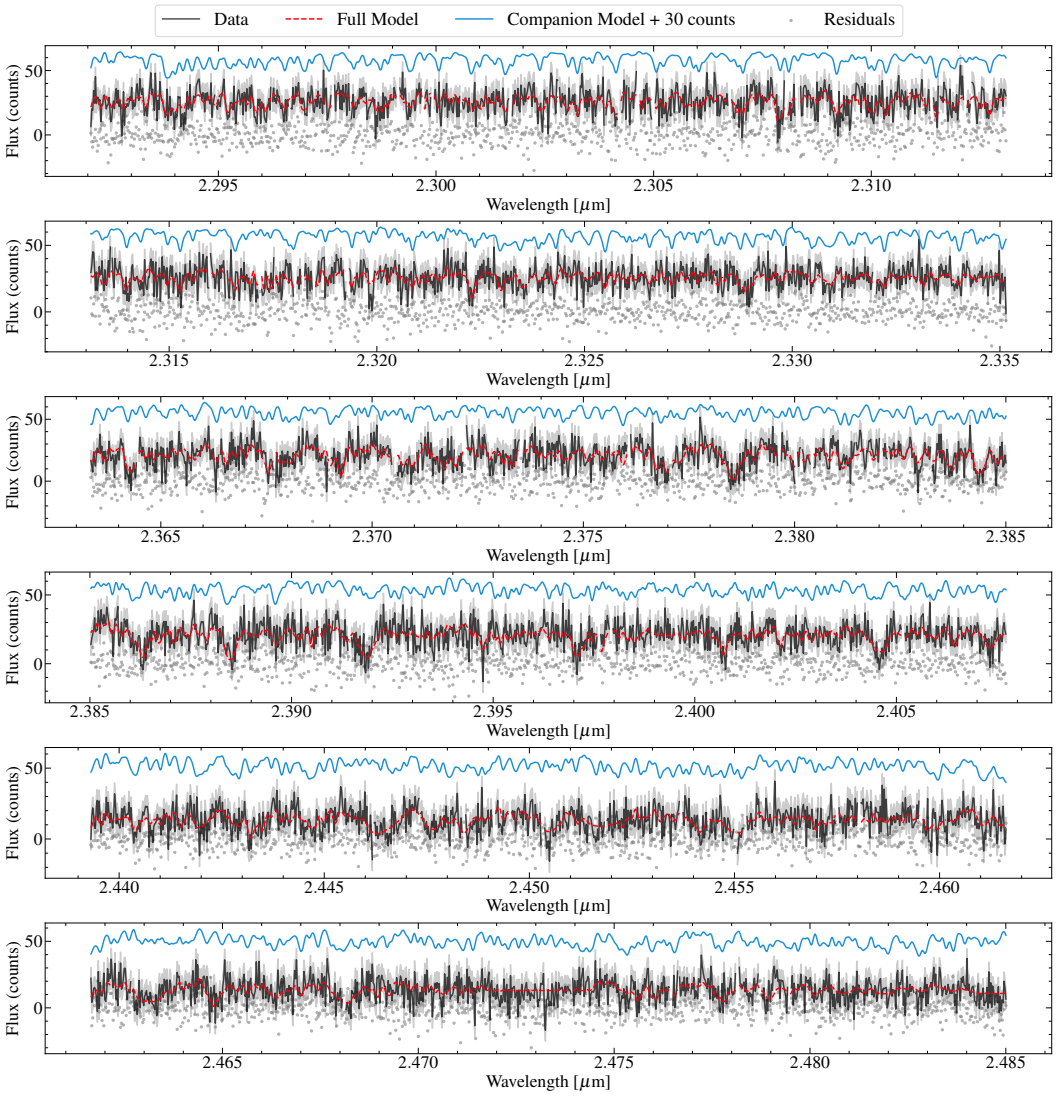

Figure 4.14: Same as Fig. 4.13, but for DH Tau b.

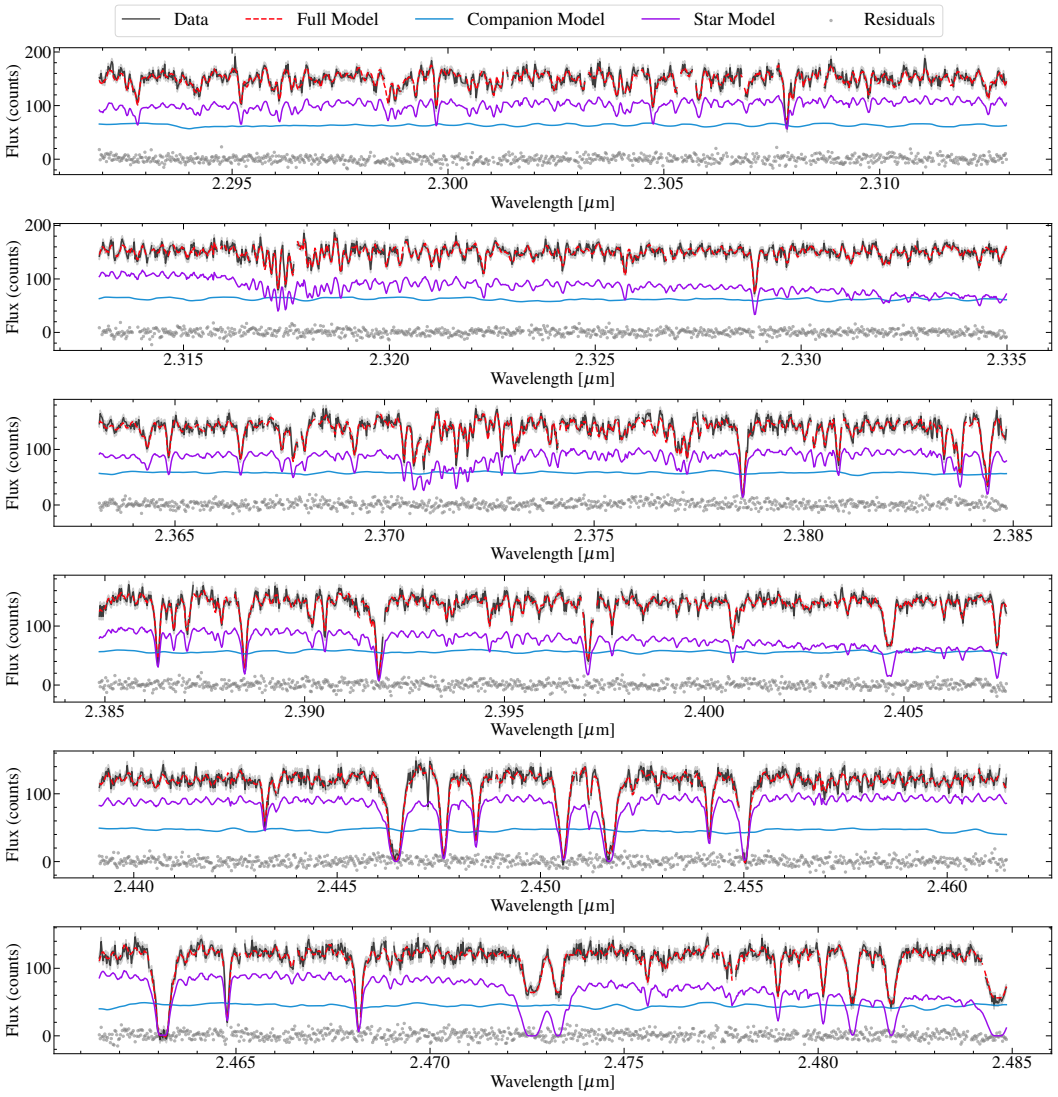

Figure 4.15: Same as Fig. 4.13, but for kap And b.

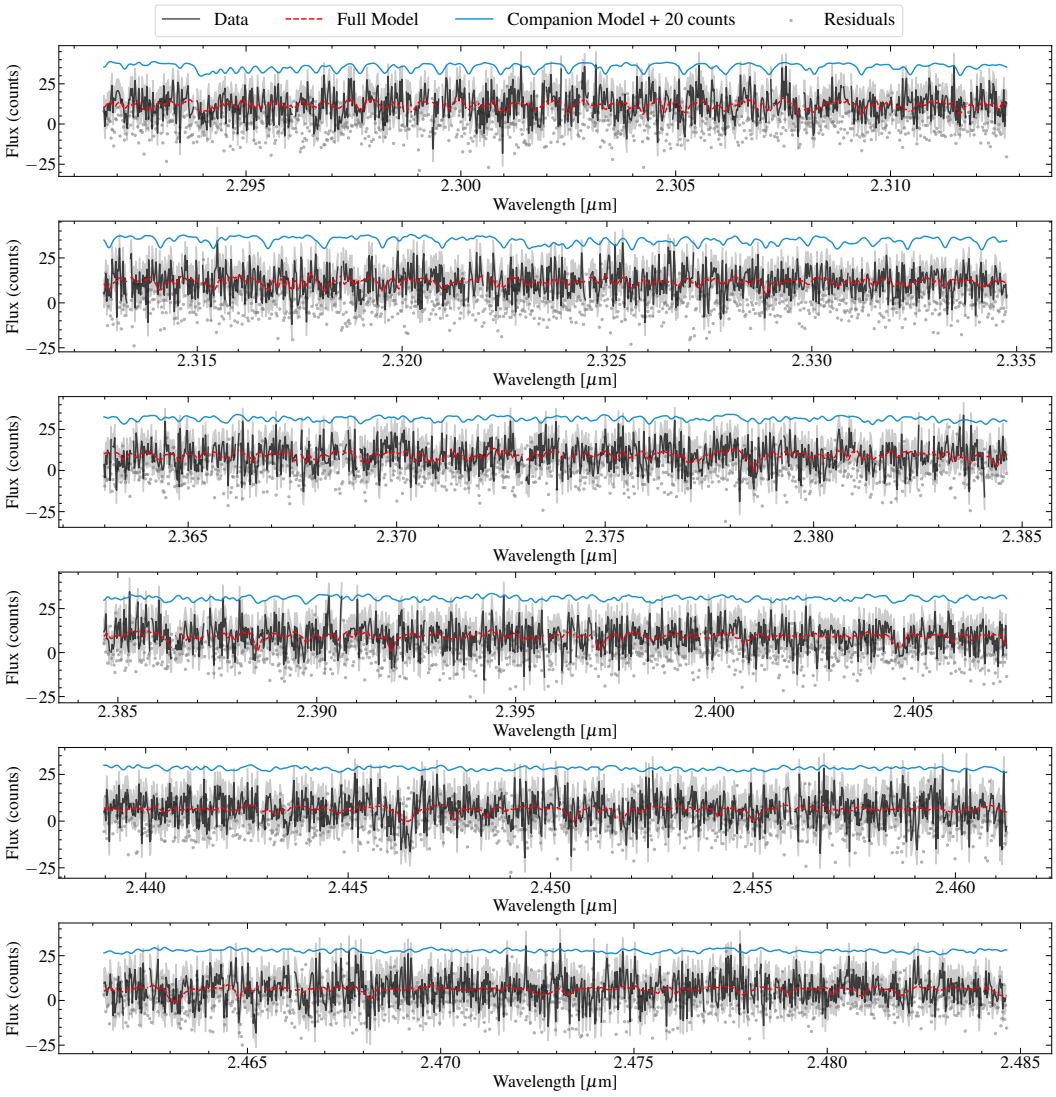

Figure 4.16: Same as Fig. 4.13, but for GSC 6214-210 b.

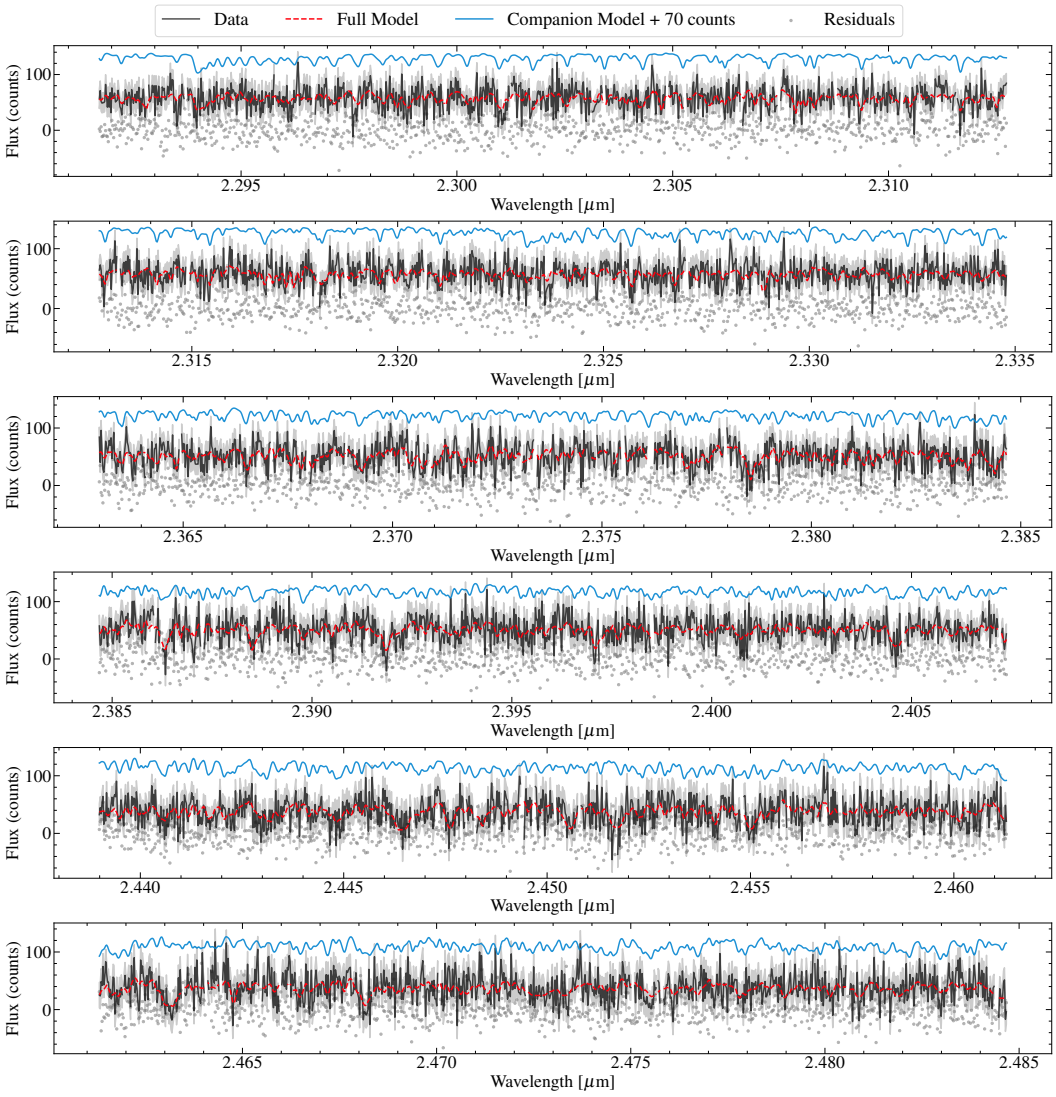

Figure 4.17: Same as Fig. 4.13, but for ROXs 12 b.

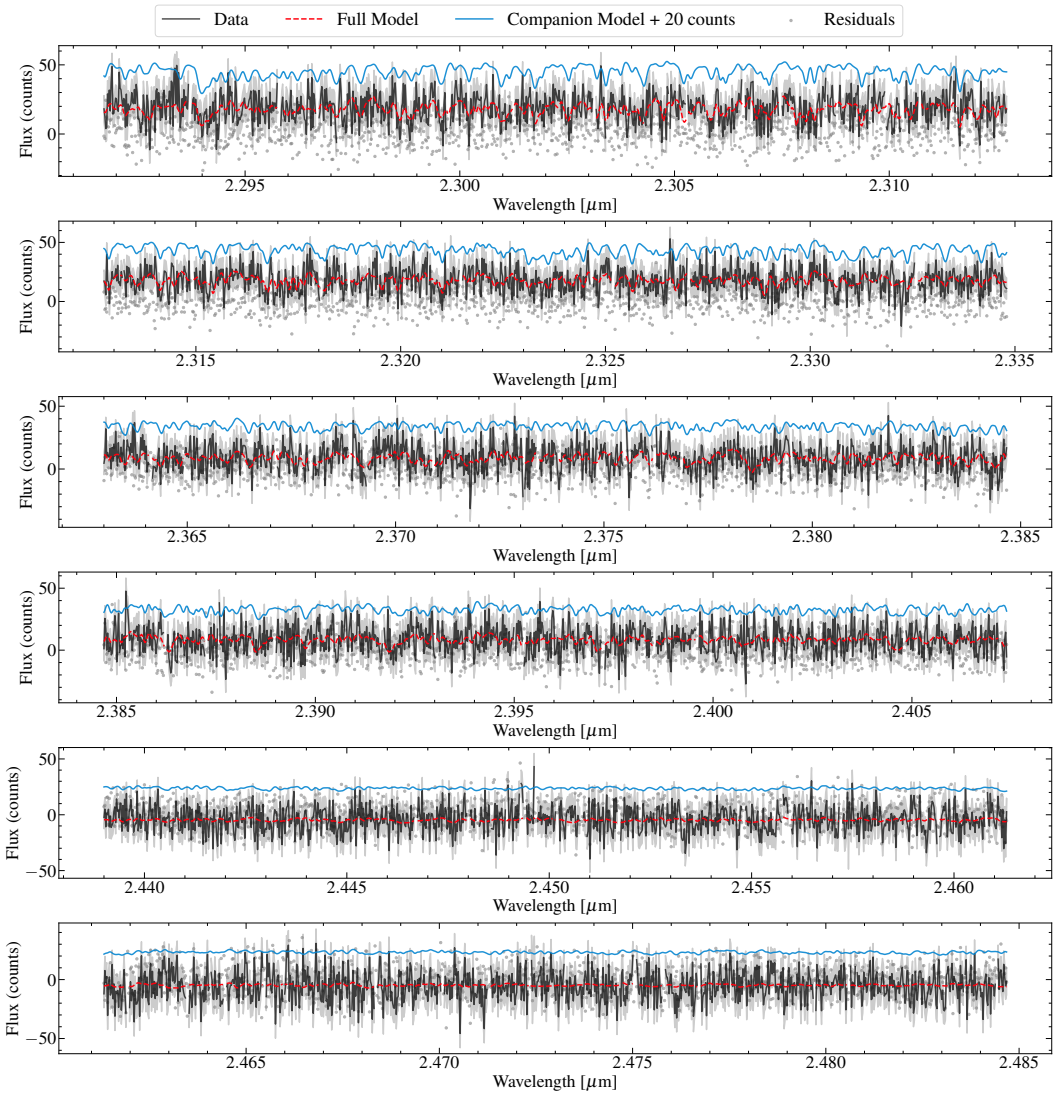

Figure 4.18: Same as Fig. 4.13, but for ROXs 42B b.

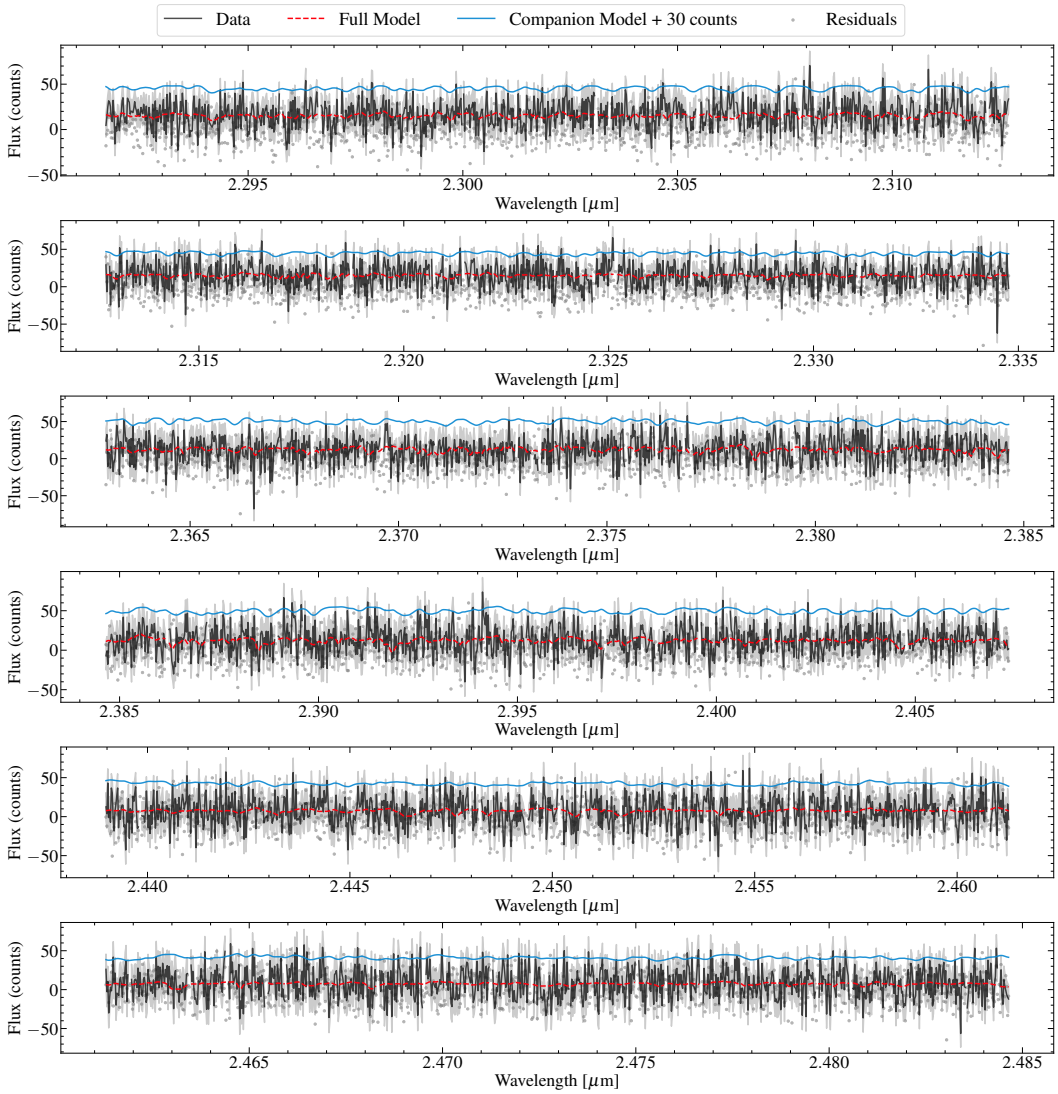

Figure 4.19: Same as Fig. 4.13, but for 2M0122 b. Visually, and from the CCF analysis (Fig. 4.3), this is our lowest S/N dataset. Retrievals for 2M0122 b should be re-visited with improved S/N data.

4.14 Pressure-temperature profiles and emission contribution functions

Here, we plot the retrieved temperature profiles and emission contribution functions for the five other companions. The corresponding plots for κ And b, GSC 6214-210 b, and HIP 79098 b are shown in Fig. 4.4. We note that a super-adiabatic region is visible in the P-T profile of GQ Lup b around 5×10^{-1} bars. Deviations from self-consistent 1D models such as SPHINX and Sonora are not unexpected due to 3D effects such as rotation-induced horizontal transport (Tan et al., 2021b). However, our data alone is insufficient to show that this super-adiabatic region is real. For purposes of this paper, we check that the retrieved P-T profile of GQ Lup b does not bias its retrieved parameters by running a separate retrieval with a fixed P-T profile matching the $T_{\rm eff} = 2600$ K, $\log g = 4.0$ SPHINX profile. The resulting posteriors are consistent to within 1σ for all parameters, demonstrating that the results are not sensitive to the exact shape of the P-T profile.

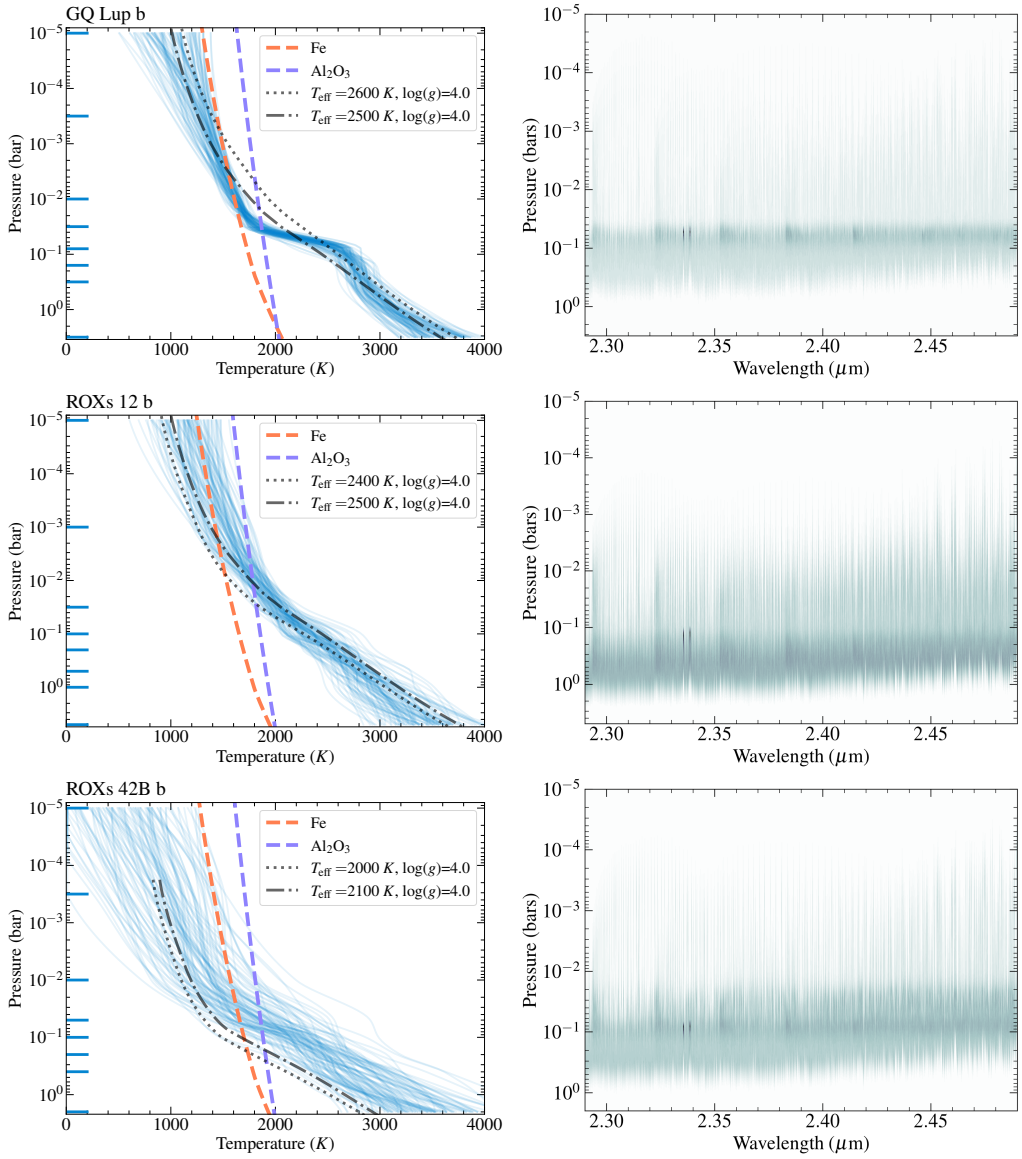
GQ Lup b
Fe
Al_2O_3
$T_{\rm eff}$ =2600 K, log(g)=4.0
$T_{\rm eff}$ =2500 K, log(g)=4.0
Pressure (bar)
Temperature (K)
Pressure (bars)
Wavelength (μm)
ROXs 12 b
Fe
Al_2O_3
$T_{\rm eff}$ =2400 K, log(g)=4.0
$T_{\rm eff}$ =2500 K, log(g)=4.0
Pressure (bar)
Temperature (K)
Pressure (bars)
Wavelength (μm)
ROXs 42B b
Fe
Al_2O_3
$T_{\rm eff}$ =2000 K, log(g)=4.0
$T_{\rm eff}$ =2100 K, log(g)=4.0
Pressure (bar)
Temperature (K)
Pressure (bars)
Wavelength (μm)

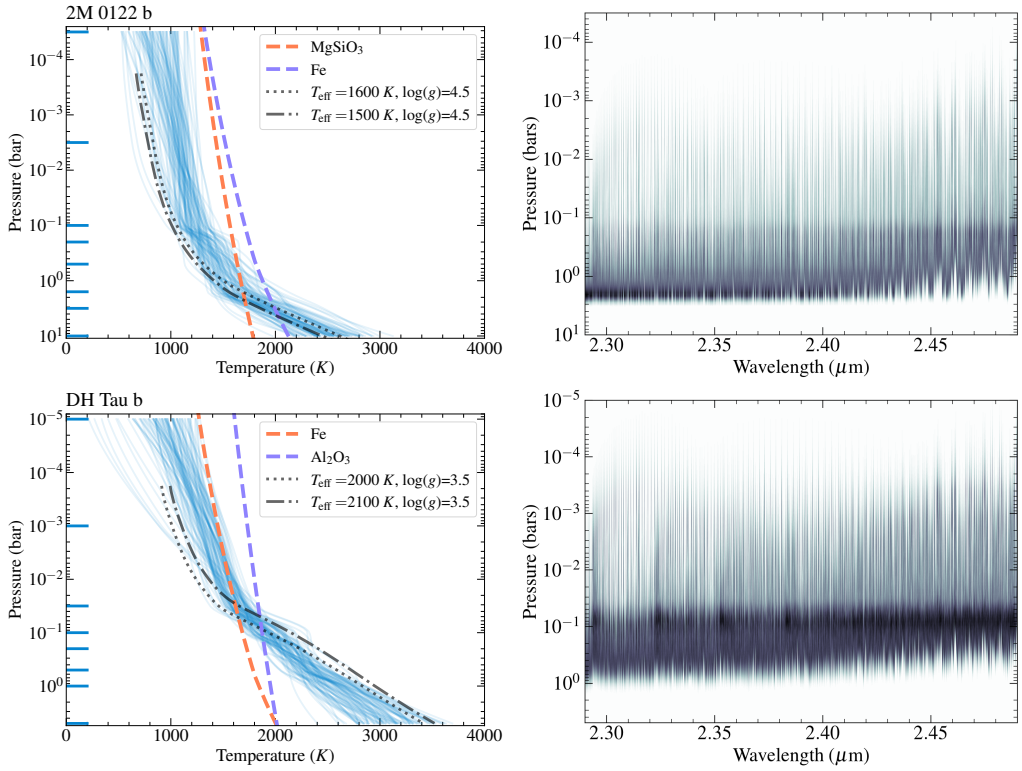

Figure 4.20: Same as Fig. 4.4, but for the other five companions.

4.15 Radial velocities for the substellar companions

Here, we list the measured RVs of the eight companions, which have been corrected for barycentric motion.

Table 4.12: KPIC Radial Velocity Measurements for Eight Substellar Companions Studied in This Work. We have applied the barycentric correction to the RVs, so their reference is the solar system barycenter.

Object	UT Date	BJD-2400,000	RV (km s^{-1})
κ And b	2022 Nov 12	59895.347	-17.7 ± 0.9
GSC 6214-210 b	2023 June 23	60118.407	-5.5 ± 0.7
GQ Lup b	2023 June 23	60118.296	0.0 ± 0.1
HIP 79098 b	2022 July 18	59778.331	-6.0 ± 0.1
2M0122 b	2021 Nov 19	59537.338	10.8 ± 1.5
ROXs 12 b	2020 July 3	59033.347	-2.4 ± 0.2
ROXs 42B b	2020 July 2	59032.347	-3.3 ± 0.4
DH Tau b	2022 Oct 12	59864.434	14.9 ± 0.3

Chapter 5

THE COOL BROWN DWARF GLIESE 229 B IS A CLOSE BINARY

This chapter is a reproduction of my paper on the resolving the first brown dwarf companion into a tight binary, now named Gliese 229 Bab. While I focused on atmospheric retrievals in the first few years of my PhD, I maintained an interest in Gaia astrometry, dynamical masses, and searching for new companions with direct imaging. In Dec 2022, while writing my JWST cycle 2 proposal for Gliese 229 B, I read up on the observed tension between its dynamical mass and luminosity. In a casual Slack message to Jason Wang, I asked about the feasibility of observing this companion with VLTI/GRAVITY to resolve the potential binarity. Jason introduced me to a few GRAVITY experts, and I ended up leading an ESO proposal to use both GRAVITY and CRIRES+ to resolve the companion into two. We did not have high expectations, since the prospect of resolving the first brown dwarf into a binary was almost too good to be true. So when the first GRAVITY data arrived in Dec 2023, it was incredible to see the strong signs of binarity. Some of the GRAVITY data were noisy, so Dimitri Mawet pushed me to analyze the CRIRES+ data, which I had been putting off. After extracting the CRIRES+ RV time series, we were very satisfied and excited to find that the RVs and GRAVITY data were in excellent agreement.

After the acceptance of the Nature paper, I had the opportunity to write a Research Briefings with Rebecca Oppenheimer, one of the original discovers of Gliese 229 B in 1994. The Research Briefing provides a more accessible version of the paper, and can be found here.

Xuan, J. W. et al. (Oct. 2024). "The cool brown dwarf Gliese 229 B is a close binary". In: *Nature* 634.8036, pp. 1070–1074. DOI: 10.1038/s41586-024-08064-x.

Abstract

Owing to their similarities with giant exoplanets, brown dwarf companions of stars provide insights into the fundamental processes of planet formation and evolution.

From their orbits, several brown dwarf companions are found to be more massive than theoretical predictions given their luminosities and the ages of their host stars (G. M. Brandt et al., 2021b; Cheetham et al., 2018; Li et al., 2023). Either the theory is incomplete or these objects are not single entities. For example, they could be two brown dwarfs each with a lower mass and intrinsic luminosity (G. M. Brandt et al., 2021b; Howe et al., 2023). The most problematic example is Gliese 229 B (Nakajima et al., 1995; Oppenheimer et al., 1995), which is at least 2–6 times less luminous than model predictions given its dynamical mass of 71.4 ± 0.6 Jupiter masses ($M_{\rm Jup}$) (G. M. Brandt et al., 2021b). We observed Gliese 229 B with the GRAVITY interferometer and, separately, the CRIRES+ spectrograph at the Very Large Telescope. Both sets of observations independently resolve Gliese 229 B into two components, Gliese 229 Ba and Bb, settling the conflict between theory and observations. The two objects have a flux ratio of 0.47 ± 0.03 at a wavelength of 2 μm and masses of 38.1 ± 1.0 and 34.4 ± 1.5 $M_{\rm Jup}$, respectively. They orbit each other every 12.1 days with a semimajor axis of 0.042 astronomical units (AU). The discovery of Gliese 229 BaBb, each only a few times more massive than the most massive planets, and separated by 16 times the Earth–moon distance, raises new questions about the formation and prevalence of tight binary brown dwarfs around stars.

5.1 Main

Gliese 229 B, the first brown dwarf with methane-absorption features (Nakajima et al., 1995; Oppenheimer et al., 1995), orbits the M1V star Gliese 229 A (0.58 ± 0.01$M_{\odot}$) with a semimajor axis of 33 AU (G. M. Brandt et al., 2021b). The powerful combination of Gaia DR3 and Hipparcos astrometry, as well as decades of imaging and radial velocity (RV) monitoring of the host star, enable a precise dynamical mass measurement of 71.4 ± 0.6 $M_{\rm Jup}$ for the companion (G. M. Brandt et al., 2021b). The high mass of Gliese 229 B has defied all existing substellar evolutionary models, which predict that a 71.4-$M_{\rm Jup}$ object with age from 1 to 10 Gyr would have a bolometric luminosity about 2–20 times higher than the measured value of $\log(L_{\rm bol}/L_{\odot}) = -5.21 \pm 0.05$ (G. M. Brandt et al., 2021b; Filippazzo et al., 2015; Saumon et al., 2008; Phillips et al., 2020) (see Figure 5.3 and Figure 5.4). In fact, for models that include clouds, 71.4 $M_{\rm Jup}$ is near the hydrogen-burning limit (at solar metallicity) that defines the substellar–stellar boundary (Oppenheimer et al., 2000) (Saumon et al. 2008: 73.3 $M_{\rm Jup}$; Morley et al. 2024: 70.2 $M_{\rm Jup}$). The mass–luminosity discrepancy for Gliese 229 B raises questions about the accuracy

of the models, which has serious implications, as these models are used to infer masses for most of the directly imaged giant planets and brown dwarf companions that lack dynamical masses.

Alternatively, the low luminosity of brown dwarf companions such as Gliese 229 B could be explained if they consist of a spatially unresolved pair of brown dwarfs instead of a single one (G. M. Brandt et al., 2021b; Cheetham et al., 2018; Li et al., 2023; Howe et al., 2023). Other indications of the unusual nature of Gliese 229 B include its near-infrared spectrum, which does not conform to spectral standards, prompting Burgasser et al. (2006) to assign it a spectral type of peculiar T7. Despite these anomalies, past observations have unsuccessfully attempted to resolve Gliese 229 B into a binary brown dwarf with adaptive optics imaging (T. D. Brandt et al., 2019b). The previous non-detections along with the proximity of the system (5.76 parsec from Gaia (Gaia Collaboration, 2022)) suggest that a putative binary would have a tight separation of < 0.2 AU or a small mass ratio (G. M. Brandt et al., 2021b). However, known binary brown dwarfs show a strong preference for equal mass ratios and a separation distribution peaking between approximately 1 and 3 AU (Burgasser et al., 2007; Fontanive et al., 2018).

We observed Gliese 229 B on five nights using the Very Large Telescope Interferometer (VLTI) in GRAVITY Wide mode (GRAVITY+ Collaboration et al., 2022) with the Unit Telescopes of the European Southern Observatory (ESO) at Cerro Paranal, Chile. The observations were performed in the K band (1.95–2.45 μm). We extracted closure phases from the GRAVITY data (see Methods), in which a non-zero closure phase indicates a departure from central symmetry, for example, a binary source. As part of the same programme, we observed Gliese 229 B with the CRyogenic InfraRed Echelle Spectrograph Upgrade Project (CRIRES+) (Dorn et al., 2023) on UT3 of the Very Large Telescope in the H band (1.50–1.75 μm) on seven different nights to monitor its RV. The CRIRES+ spectra have a resolving power ($\lambda/\Delta\lambda$) of about 100,000 and were extracted as described in Methods.

We find strongly non-zero closure phases in the first epoch of GRAVITY observations (Figure 5.5) that are consistent with a binary source. The subsequent GRAVITY epochs confirm the detection and provide evidence of orbital motion between the two components (Figure 5.1). With the first epoch alone, the null hypothesis that Gliese 229 B is a single source (i.e., all closure phases should be zero) leads to a reduced χ^2 of 55 (288 degrees of freedom). Carrying out a grid search for the companion as described in Gallenne et al. (2015), we find a secondary

brown dwarf located ≈ 5 mas south of the brighter, primary brown dwarf, with a secondary-to-primary flux ratio of ≈ 0.5. The binary fit has a much lower reduced χ^2 of 1.27. In the binary fit, we also account for linear motion of the companion over the 2.5-h observing window. We find that the companion moves in a direction nearly perpendicular to the vector between itself and the brighter brown dwarf at a rate of $4.6^{+1.5}_{-0.8}$ mas/day (Figure 5.1), consistent with the expected motion of ≈ 4.6 mas from a circular, face-on orbit for a total mass of 71 $M_{\rm Jup}$.

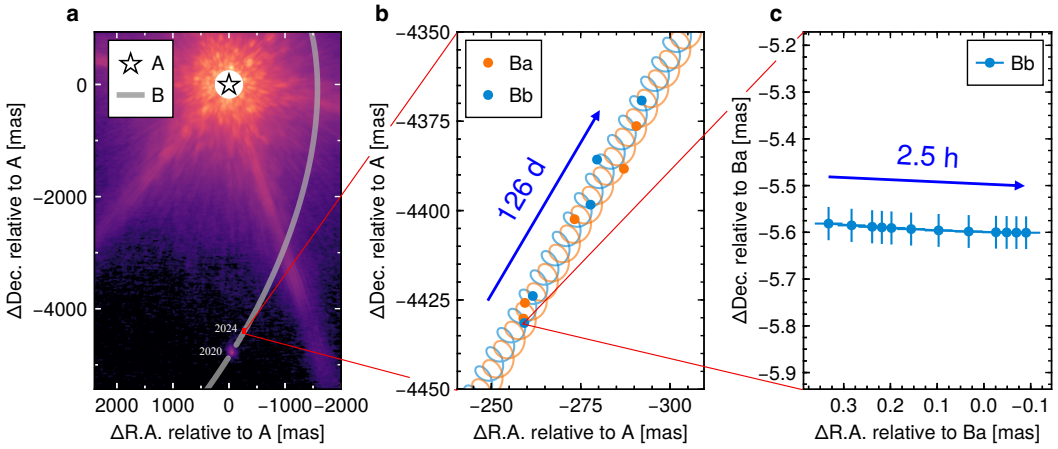

Figure 5.1: (a) A Keck/NIRC2 Ks band image of the Gliese 229 system taken on Oct 18, 2021. The binary brown dwarf is unresolved given Keck's resolution of 45 milliarcsecond. The gray line indicates the best estimate of the outer orbit of Gliese 229 BaBb around A (G. M. Brandt et al., 2021b). (b) A zoom-in for the maximum a-posteriori binary brown dwarf orbit from the GRAVITY and CRIRES+ joint fit, where measured positions of Gliese 229 Ba and Bb in each GRAVITY epoch are shown as orange and blue points, respectively. The average uncertainty on the derived relative position between Bb and Ba is between 0.01 and 0.05 milliarcseconds. Note that GRAVITY and CRIRES+ only measure the differential positions between Ba and Bb, so the length and direction of the spiral pattern are derived from the maximum a-posteriori draw of the outer orbit (gray line in panel a). (c) The motion of Gliese 229 Bb relative to Gliese 229 Ba during the 2.5 h observing window of the first night of GRAVITY observations.

Contemporaneous CRIRES+ monitoring independently confirms that Gliese 229 B is a binary brown dwarf. Initially, we cross-correlated the CRIRES+ spectra of Gliese 229 B with a Sonora Elf Owl atmospheric model (Mukherjee et al., 2024) assuming $T_{\rm eff}$ = 900 K, $\log g$ = 5.0 (Calamari et al., 2022). The cross-correlation functions (CCFs) displayed time-varying line locations and shapes consistent with the partially resolved spectra of two brown dwarfs orbiting each other (Figure 5.6, 5.7). Therefore, we fit the CRIRES+ spectra as emission from two brown dwarfs and account for a small amount of starlight leakage into the slit using observations

of Gliese 229 A (Figure 5.2, see Methods). Based on the GRAVITY measured flux ratio, we started with atmospheric models with $T_{\rm eff}$ = 850 K and $\log g$ = 5.0 for the primary brown dwarf and $T_{\rm eff}$ = 750 K and $\log g$ = 5.0 for the secondary (see Methods) to extract the RV of each brown dwarf. For each CRIRES+ epoch, alternative fits of the spectra with a single-component brown dwarf model are disfavored with statistical significance $\gtrsim 20\sigma$. The extracted RVs display unambiguous signs of a spectroscopic binary (Figure 5.2).

We combine the CRIRES+ and GRAVITY data to characterize the orbit of the binary brown dwarf. The orbit fits are performed with PMOIRED (Mérand, 2022) and Octofitter (Thompson et al., 2023), as described in Methods. The data are well fit by the model with a reduced χ^2 of 2.2 (513 degrees of freedom) and slightly broad but symmetrical closure phase residuals, with the model accounting for all closure phase features. The GRAVITY K band flux ratio is constrained by the joint fit to 0.47 ± 0.03. We derive an orbital period of 12.134±0.003 days, corresponding to a semi-major axis of 0.0424±0.0004 AU, or about 90 Jupiter radii. The ratio of the RV semi-amplitudes directly constrains the mass ratio (q) to $0.90^{+0.06}_{-0.02}$. From the binary brown dwarf's orbit, we independently measure a total mass of 72.5±1.3 $M_{\rm Jup}$, which is consistent with the mass derived by G. M. Brandt et al. (2021b) from the orbit of the unresolved Gliese 229 B around Gliese 229 A. We measure component masses of 38.1±1.0 $M_{\rm Jup}$ and 34.4±1.5 $M_{\rm Jup}$, an eccentricity of 0.234±0.004, and inclination of 31.4±0.3°. The eccentricity of Gliese 229 Bab is typical compared to the eccentricity distribution of field brown dwarf binaries (Dupuy et al., 2017). We note that the outer orbit of Gliese 229 Bab around Gliese 229 A is highly eccentric ($e \approx 0.85$) and viewed nearly face-on (G. M. Brandt et al., 2021b). The binary brown dwarf's orbit is moderately misaligned relative to the outer orbit by 37^{+7}_{-10} °. Additionally, the host star's spin orientation is viewed nearly edge-on (Bowler et al., 2023) and therefore misaligned relative to both inner and outer orbits.

To make the astrometric and spectroscopic observations fully self-consistent with the atmosphere models, we interpolate the ATMO 2020 substellar evolutionary model (Phillips et al., 2020; Chabrier et al., 2023) to search for component masses and ages that simultaneously reproduce the GRAVITY K band flux ratio and bolometric luminosity (see Methods). Adopting a prior on the total mass of 72.5±1.3 $M_{\rm Jup}$, we find that a binary brown dwarf with mass ratio of 0.87±0.03 and age of 2.45±0.20 Gyr matches the models well. This mass ratio is consistent at the 1σ level with the value derived from the orbit fit. From ATMO 2020, the primary component is estimated

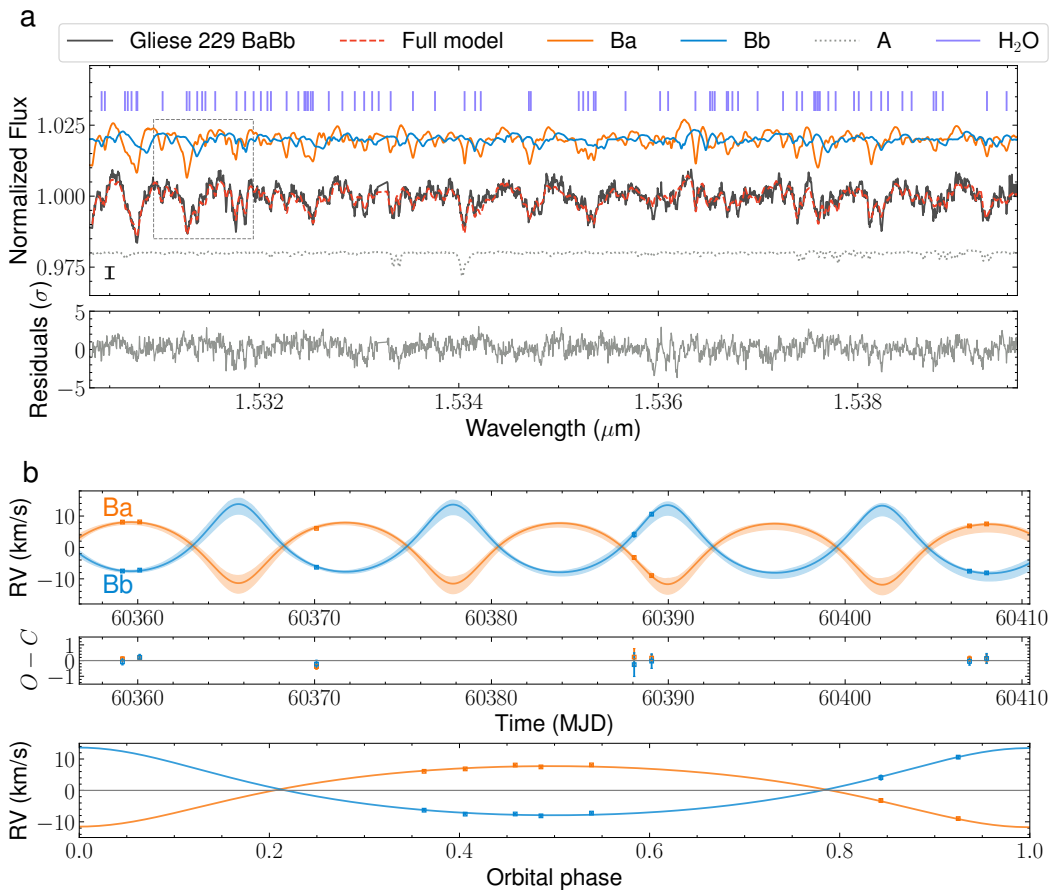

Figure 5.2: (a) A segment of the CRIRES+ spectrum from 2024-03-20 (black) used to compute radial velocities of Gliese 229 Ba and Bb. The region is dominated by water absorption lines from the brown dwarfs, whose positions are marked in purple. The orange and blue curves are spectral models for Ba and Bb, while the dashed gray curve is the CRIRES+ spectra of Gliese 229 A used to model stellar contamination. The three model components have been offset for clarity. The full model is shown in red. The median uncertainty of the spectrum is denoted by the 1σ error bar on the lower left. In the gray box, we highlight a region where distinct lines from Ba and Bb can be identified by eye. (b) The orange and blue points show the radial velocities of Gliese 229 Ba and Bb extracted from seven epochs of VLT/CRIRES+ spectra. Solid lines denote the joint CRIRES+ and GRAVITY orbit fit with 2σ uncertainty regions in shade. The middle panel shows the residuals of the best fit, and the bottom panel shows the phase-folded radial velocity orbit.

to have $T_{\rm eff} = 860 \pm 20$ K, $\log g = 5.11 \pm 0.01$ dex, and $\log(L_{\rm bol}/L_\odot) = -5.41 \pm 0.04$, while the secondary component has $T_{\rm eff} = 770 \pm 20$ K, $\log g = 5.03 \pm 0.01$ dex, and $\log(L_{\rm bol}/L_\odot) = -5.58 \pm 0.04$. Our inferred age agrees with the value of ≈2-6 Gyr estimated for the host star (T. D. Brandt et al., 2019b). Therefore, our detection of the binary and measurements of its properties bring the system into much better

alignment with substellar evolutionary models, as shown in Figure 5.3.

Although the near-unity mass ratio between Gliese 229 Ba and Bb fits with previous brown dwarf binaries (Fontanive et al., 2018), the semi-major axis of approximately 0.042 AU makes it the tightest brown dwarf binary in a triple system (Figure 5.8). Among brown dwarf binaries orbiting stars, the next closest binaries have semi-major axis values more than an order of magnitude larger at about 0.9 AU (for example, Gliese 569Bab Dupuy et al. 2017). A few isolated ultracool dwarf binaries with component masses between 0.08-0.09 $M_{\odot}$ have smaller separations (Hsu et al., 2023; Lodieu et al., 2015), but among unambiguous brown dwarf binaries, only 2MASS J0535–0546AB and SPEC J1510–2818AB have comparable separations of 0.04 and 0.06 AU, respectively (Stassun et al., 2006; Triaud et al., 2020). The formation mechanism of brown dwarf binaries around stars remains an open question, and both observations and simulations are highly incomplete for brown dwarf binaries with separations < 1 AU (Burgasser et al., 2006). Opacity-limited fragmentation restricts the primordial separations of objects to distances > 10 AU (Low et al., 1976), implying that significant dynamical and dissipative processes are required to form tight brown dwarf binary systems (Burgasser et al., 2012). Although the exact processes for dissipation is unclear, tidal interactions between the gaseous envelopes or accretion disks around the forming objects are likely important (Stamatellos et al., 2009; Lazzoni et al., 2024). For binary brown dwarfs orbiting stars, fragmentation of a massive circumstellar disk is another potential formation route, where two proto-brown dwarfs fragment in the disk and become bound in a close encounter (Stamatellos et al., 2009). Ultimately, any formation mechanism would need to account for the highly eccentric outer orbit of Gliese 229 A-Bab and the misalignments between the inner orbit, outer orbit, and host star spin axis.

Thirty years after its discovery, Gliese 229 B continues to teach us about substellar objects. The discovery of Gliese 229 BaBb provides a potential resolution to the mass-luminosity tension for brown dwarf companions and suggests that other unusually massive brown dwarfs, such as HD 4113 C (Cheetham et al., 2018), could be unresolved substellar binaries as well. Future efforts to resolve other anomalous brown dwarf companions into binaries are essential for rigorously testing substellar evolutionary models, which are routinely used to interpret observations of giant planets. Although known brown dwarf binaries have separations peaking between 1-3 AU (Fontanive et al., 2018), Gliese 229 Bab demonstrates the existence of binary substellar companions to stars with separations well below 1 AU. The 12

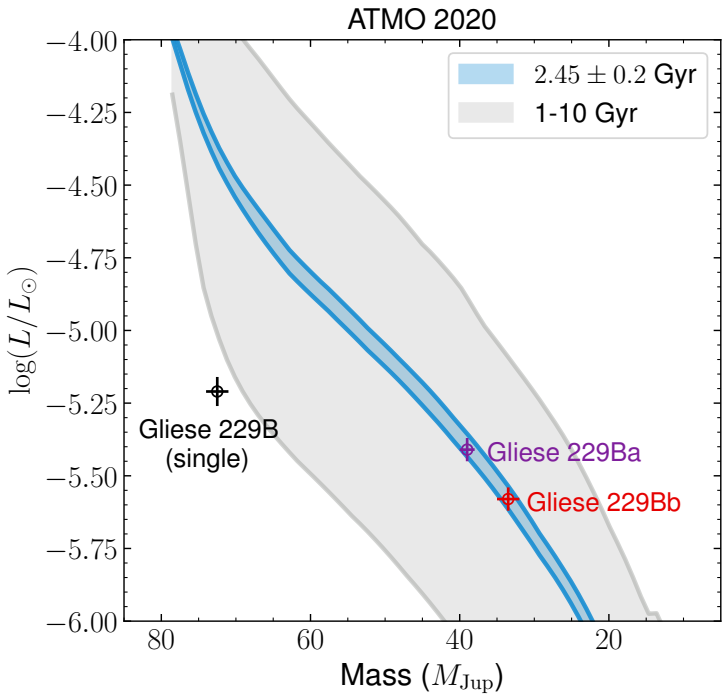

Figure 5.3: The dynamical masses from our orbit fit and inferred luminosities of Gliese 229 Ba (purple) and Bb (red) from the ATMO 2020 evolutionary model. As a single brown dwarf, Gliese 229 B is under-luminous compared to model predictions for all plausible ages of the system from Phillips et al. (2020). The mass-luminosity tension is also present for other models (see Figure 5.4). As a binary brown dwarf, the system is well-explained by the ATMO 2020 model for an age of 2.45±0.20 Gyr, resolving the mass-luminosity tension.

day orbital period of Gliese 229 Bab places the two brown dwarfs deep within the Hill sphere of each other, suggesting a formation pathway that involves significant energy dissipation. A major goal of exoplanet studies in the next decade is the search for exomoons and binary planets. Among isolated brown dwarf binaries, there are already examples of systems where both components have masses in the planetary regime (Best et al., 2017; Theissen et al., 2020) (below 13 $M_{\rm Jup}$), in addition to several systems with ≈4-13 $M_{\rm Jup}$ companions orbiting low-mass brown dwarfs (Chauvin et al., 2005; Calissendorff et al., 2023; Bowler et al., 2015). It is unclear how common binary planets or exomoons are around stars. With further improvements in sensitivity, the combination of interferometry, high-resolution spectroscopy, and transit photometry is poised to unveil new discoveries and provide insights into these questions.

Table 5.1: Orbital and physical parameters of Gliese 229 BaBb

Parameter	Confidence Interval (frequentist analysis)	Credible Interval (Bayesian analysis)
Orbital period (day)	12.134 ± 0.003	12.137 ± 0.001
Semimajor axis (au)	0.0424 ± 0.0004	0.0422 ± 0.0001
Eccentricity	0.234 ± 0.004	0.234 ± 0.002
Argument of periastron (°)	180.7 ± 1.2	182.8 ± 0.9
Inclination (°)	31.4 ± 0.3	31.1 ± 0.4
Longitude of ascending node (°)	213 ± 2	210.3 ± 1.2
Time of periastron (MJD)	60377.88 ± 0.04	60377.85 ± 0.02
Mass ratio (M_2/M_1)	$0.90^{+0.06}_{-0.02}$	$0.91^{+0.06}_{-0.05}$
Mass of Ba, M_1 (M_{Jup})	38.1 ± 1.0	37 ± 1
Mass of Bb, M_2 (M_{Jup})	34.4 ± 1.5	34 ± 1
Flux ratio, f_2/f_1 (2.0 μm)	0.47 ± 0.03	0.53 ± 0.02
γ_{RV} (km/s)	0.4 ± 0.2	0.46 ± 0.20
Total mass of B (M_{Jup})	72.5 ± 1.3	71.3 ± 0.5

The argument of periastron refers to the primary brown dwarf, Gliese 229 Ba.

5.2 Methods

VLTI/GRAVITY observations and data reduction

We observed Gliese 229 BaBb with GRAVITY (GRAVITY Collaboration et al., 2017) at the VLTI using the four Unit Telescopes of Paranal (program IDs: 0112.C-2369(A) and 2112.D-5036(A); PI: Xuan). We obtained data at five epochs: 26 and 30 December 2023, 28 February 2024, 29 March 2024, and 29 April 2024 (universal time). We used GRAVITY in the wide-angle dual-field mode (GRAVITY+ Collaboration et al., 2022), recently commissioned as part of the GRAVITY+ upgrade (Eisenhauer, 2019). In this mode, the field is divided into two at the telescope level and carried independently within the GRAVITY delay lines. One field, centered on the star Gliese 229 A, is used by the GRAVITY fringe tracker (Lacour et al., 2019; Nowak et al., 2024) to stabilize the fringes by compensating for the atmospheric piston and vibrations in the system. The other field, centered on the companion (now known to be binary), is observed by the GRAVITY spectrometer. The scientific observations were conducted with medium spectral resolution (R=500) in the unpolarized mode. A log of the observations is given in Table 5.2.

The reduction of the raw data was performed using the ESO GRAVITY pipeline v1.6.4 (Lapeyrere et al., 2014). This version of the pipeline can reduce the wide-angle data, but we had to disable the acquisition camera reduction to do so. In wide-angle mode, we could not use the fringe tracker to reference the phase (as is traditionally done for exoplanet observations; see Lacour et al. 2024), but we could use the closure phase to detect the companion. The closure phases are averaged for each exposure, yielding several values per night.

The best datasets were obtained during the first two nights (see Table 5.2). In

December 2023, the two epochs showed closure phase values on the order of 40 degrees between 2 and 2.2 μm, with an SNR above 10. At longer wavelengths, CH_4 absorption and lower instrumental throughout prevent us from recording a robust closure phase. The closure phase signal was clear enough to confirm the binary nature of Gliese 229 BaBb. Moreover, injection-recovery tests show that the first epoch GRAVITY data are sensitive to objects 2-3 magnitudes fainter than Gliese 229 Ba at separations from 3 to 19 milliarcsecond, largely ruling out a third brown dwarf in the field. While the binary detection was clear, the data were too sparse to determine the orbital parameters, so we requested ESO Director's Discretionary Time to continue monitoring the object from February to late April, after which the target was no longer observable. The data quality was poor in February due to seeing conditions, and in March due to an issue with the pointing of the GRAVITY fibers. Despite this, a few below-average quality datasets were salvageable. The last dataset, obtained on UT 2024 April 29, was of high quality, benefiting from a recent instrumental upgrade of the VLTI beam compressor differential delay lines. During this last run, an SNR close to 20 was achieved, providing a clear detection to finalize the astrometric orbit of the binary.

VLT/CRIRES+ observations and data reduction

We observed the Gliese 229 system with the upgraded CRIRES+ (Dorn et al., 2014; Dorn et al., 2023) mounted on VLT (program ID: 0112.C-2369(B); PI: Xuan). We obtained seven epochs of data on 19 and 20 February 2024, 1, 19, and 20 March 2024, 7 and 8 April 2024 (universal time, see log in Table 5.2). The wavelength setting H1567 and 0.2 arcsecond slit width were used to cover H_2O and CH_4 absorption lines from 1.47-1.78 μm and achieve a spectral resolution of R$\approx$100,000. The observations are taken in adaptive optics mode. For each epoch, we first observe the A0V telluric standard star 10 Lep (which is at a similar airmass as Gliese 229) and the primary star Gliese 229 A, before offsetting the slit to the companion's location $\approx$4.4 arcsec away. The relative astrometry of the companion is determined using the orbit from G. M. Brandt et al. (2021b). The CRIRES+ slit was set perpendicular to the position angle of the companion to minimize the leakage of starlight into the slit. We used the standard ABBA nodding scheme for background removal.

We reduced the data with a customized open-source pipeline excalibuhr (Y. Zhang et al., 2024). It follows the general calibration steps of the ESO's pipeline CR2RES, including dark and flat correction, spectral order tracing, slit curvature tracing and initial wavelength solution. We removed the sky background via nod subtraction and

combined individual exposures at each nodding position. The 1D spectra were then extracted using the optimal extraction method (Horne, 1986). We used the spectrum of the standard star 10 Lep as a proxy to remove the telluric transmission features. The wavelength regions contaminated by strong telluric lines (with transmission less than 70%) were masked in the following analyses. Using observations of the telluric standard star, we carried out an additional wavelength calibration against a telluric transmission model generated by ESO's sky model calculator SkyCalc (S. Noll et al., 2012; A. Jones et al., 2013). This was achieved by applying a third-order polynomial to the initial wavelength solution in each order and optimizing the correlation between the observed spectrum of the telluric standard star and the template spectrum.

On average, we achieved a S/N≈30 per wavelength channel per epoch at 1.57 μm for the extracted spectra of Gliese 229 BaBb, which includes emission from the companion and stellar contamination at the companion's location. To estimate the spectral resolution of our observations, we used the ESO sky software Molecfit (Smette et al., 2015) to fit the spectra of the telluric standard star. We find stable line spread functions across different nights with Gaussian profile widths of 3.05, 3.12, 3.28, 3.27. 3.05, 3.28, and 3.05 pixels, for seven epochs respectively. They correspond to an average resolving power of ≈100,000 as expected.

Extraction of radial velocities from CRIRES+

To calculate the RVs of Gliese 229 Ba and Bb, we fit the CRIRES+ spectrum from 1.510–1.583 μm, which covers two spectral orders. Each order is broken up into three chunks that are recorded on different detectors. The data from 1.45-1.50 μm are omitted due to significant telluric contamination. We also omit the data longward of 1.60 μm for two reasons. First, Gliese 229 Ba and Bb are extremely faint from 1.6 to 1.78 μm due to CH_4 absorption (see low-resolution spectrum in Geballe et al. 1996), which results in lower S/N data. Second, our preliminary fits show that the models provide a poorer match to the data beyond 1.6 μm. While we are using the most accurate CH_4 line list from Hargreaves et al. (2020), Tannock et al. (2022) showed that even this line list can produce discrepant $v \sin i$, radial velocity, and $T_{\rm eff}$ measurements by fitting the spectrum of an isolated T dwarf. To avoid biasing the RV measurements, we focus on the water-dominated region from 1.510–1.583 μm, where the H_2O line list from ref. 55 is shown to be accurate (Tannock et al., 2022).

In the spectrum of Gliese 229 BaBb, we noticed atomic lines from Gliese 229 A,

indicating a modest amount of stellar contamination from the bright host star (10 magnitudes brighter in H band). Therefore, we model the spectrum of Gliese 229 BaBb with three components: two brown dwarfs (Ba and Bb) and the primary star. The models for the brown dwarfs are generated using the temperature and abundances profiles from Sonora Elf Owl (Mukherjee et al., 2024). As the resolution limit of Elf Owl is R=5000, we re-compute the models at R=1,000,000 using the open-source radiative transfer code petitRADTRANS (P. Mollière et al., 2019b). We include the line opacities of CH_4, H_2O, CO, CO_2, H_2S, NH_3, PH_3, C_2H_2, HCN, Na, K, and FeH, in addition to H_2-H_2, and H_2-He continuum opacities. To account for stellar contamination, we use the CRIRES+ spectrum of the star taken right before the Gliese 229 B exposures. Before fitting, we continuum-normalize each order of the Gliese 229 BaBb spectrum with a median filter of width 100 pixels ($\approx$ 5Å).

We fit the RV shift of the brown dwarfs at each observing date, the $v \sin i$ for each brown dwarf, flux scaling factors, and multiplicative error inflation terms. A different flux scaling factor is used for Gliese 229 Ba, Bb, and the primary star. To reduce the dimensionality, we optimize the linear flux scaling terms and error inflation terms at each iteration following Ruffio et al. (2023a). In the fit, we rotationally broaden the atmospheric models using the code from Carvalho et al. (2023), apply the RV shifts, and convolve the models to R=100,000 with a Gaussian profile. Next, we apply the optimal scale factors to the respective models to construct the combined model (Figure 5.2) and apply the same median filter to the combined model. The posterior is sampled with the nested sampling code DYNESTY (Speagle, 2020), and we use 1000 live points. We find that on average, the host star contributes $\approx$20% of the total flux in the Gliese 229 BaBb spectrum. Because the lines from the M1V primary star are very distinct from T dwarf lines (e.g. Figure 5.2), they do not impact our RV measurements.

After obtaining the RV posteriors, we apply barycentric corrections for each night using tools in the Astropy package (Astropy Collaboration et al., 2022) and subtract the RV of the primary star taken from Fouqué et al. (2018). The resulting RV points of Gliese 229 Ba and Bb are shown in Figure 5.2, and included in Table 5.4. The statistical errors on the measured RVs are typically $\approx$0.1 km/s. We consider several sources of systematic uncertainties. First, we measure the stellar RVs over the same nights to assess the instrumental jitter. The procedure is described below, and adds a 0.1 km/s uncertainty. Second, we consider the impact that uncertain atmospheric

parameters have on the retrieved RVs by repeating the spectral fits with a range of different models. Besides the fiducial model (850 K + 750 K), we consider the following $T_{\rm eff}$ combinations: (900 K + 800 K), (900 K + 750 K), (850 K + 700 K), (850 K + 800 K), (800 K + 750 K). We set $\log g$=5.0, C/O=0.68, and [M/H]=0.0 for all models. The abundances are chosen to match those of the host star, which has a nearly solar metallicity (Neves et al., 2013; Kuznetsov et al., 2019) and C/O=0.68±0.12 (Nakajima et al., 2015). The $\log g$ is fixed because the evolutionary models predict a relatively small range of variation in $\log g$ (see Table 5.3). In addition, we fix the vertical eddy diffusion parameter $\log K_{\rm zz}$ to 2.0 as found by Mukherjee et al. (2024). We use the scatter in RV values derived from each fit as an independent source of systematic error. These add systematic uncertainties on the order of ≈0.2-0.7 km/s, depending on the epoch.

We compute cross-correlations functions (CCF) of the primary star spectra to verify the stability of the CRIRES+ wavelength solution and line spread function (Figure 5.6). We adopt a PHOENIX-ACES model (Husser et al., 2013) with $T_{\rm eff}$ = 3800 K and $\log g$ = 4.5 for the primary star. Over the 2.5 months observing period, the RV change caused by orbital motion of Gliese 229 A around the system barycenter is < 2 m/s, which we ignore. Approximating the stellar CCFs as Gaussian functions, we measure the stellar RVs as the center of the Gaussian. We find that the stellar RV is stable at the 0.1 km/s level across the seven observing epochs.

From the CRIRES+ fits, we find that the two brown dwarfs have projected rotation rates ($v \sin i$) below our measurement limit. The 3σ upper limits of $v \sin i$ for Gliese 229 Ba and Bb are < 0.6 km/s and <0.7 km/s, respectively. If the two brown dwarfs are tidally synchronized, their rotational velocities would be ≈0.4 km/s. Assuming their rotational axes are aligned with the orbital axis, this implies $v \sin i$ ≈0.2 km/s, which is well below the size of the line spread function (≈3 km/s) for CRIRES+. Thus, our non-detection of spin is consistent with the brown dwarfs being tidally locked, or nearly tidally locked, which is expected based on their tidal despinning time (see the 'Dynamics' section).

Bulk properties of Gliese 229 Ba and Bb

Using ATMO 2020 evolutionary models (Phillips et al., 2020), we estimate the component masses of Gliese 229 Ba and Bb that best reproduce the bolometric luminosity of $\log(L_{\rm bol}/L_{\odot}) = -5.21 \pm 0.05$ (Filippazzo et al., 2015) and GRAVITY K band flux ratio of 0.47±0.03. We additionally include J, H, K magnitudes of the

combined source (Leggett et al., 2002) as constraints in our fit. ATMO 2020 includes three separate models with differing amounts of non-equilibrium (NEQ) chemistry. We adopt the "NEQ weak" model but note that the results are similar if we used "NEQ strong" or "CEQ". We use ATMO 2020 tables with pre-computed Mauna Kea Observatories (MKO) magnitudes. While the GRAVITY K band transmission profile is not identical to that of MKO K, the flux ratio measurement effectively divides out the transmission function. Our fit is parameterized with three parameters: mass ratio, age, and total mass. We place a Gaussian prior of 72.5±1.3 MJup on total mass, as derived from our orbit fit. For a given set of masses and age, we interpolate to obtain the $\log(L_{\rm bol}/L_\odot)$, and J, H, K magnitude of each brown dwarf, requiring that their combined magnitudes and luminosities match the observed values. We sample the posterior using a Markov Chain Monte Carlo method (Foreman-Mackey et al., 2013) with 10000 steps and 30 walkers. The first 2000 steps are discarded as burn-in. Overall, the ATMO 2020 models match the observations well for an age of 2.45±0.2 Gyr (Figure 5.3). The inferred age is somewhat model-dependent, but we find that ages of 2-4 Gyr generally match the properties of the binary brown dwarf by considering alternative evolutionary models in Figure 5.4.

From the ATMO 2020 model, we also interpolate for the $T_{\rm eff}$, $\log g$, and $\log(L_{\rm bol}/L_\odot)$ of each brown dwarf, which we tabulate in Table 5.3. We adopt the closest grid points in Sonora Elf Owl to these values to compute high-resolution spectral models and fit the CRIRES+ spectra. We emphasize that these $T_{\rm eff}$ estimates are model-based. Upcoming JWST spectroscopy of Gliese 229 BaBb from 1-15 μm (GO3762; PI: Xuan) should enable robust two-component spectral fits and provide independent estimates of the bulk properties for each brown dwarf.

We perform a second estimate of the bulk properties of Gliese 229 Ba and Bb using calibrated empirical relations for field brown dwarfs from (Sanghi et al., 2023). First, we estimate individual absolute MKO M_K magnitudes of Gliese 229 Ba and Bb from their combined-light MKO K magnitude ($K_{\rm MKO}$ = 14.36 ± 0.05) (Leggett et al., 2002), the GRAVITY K band flux ratio (0.47 ± 0.03), and the system parallax (173.574 ± 0.017 mas) (Gaia Collaboration, 2022). This yields M_K,Ba = 15.98 ± 0.05 mag and M_K,Bb = 16.80 ± 0.05 mag. Next, using the MKO M_K-$L_{\rm bol}$ and MKO M_K-$T_{\rm eff}$ relations for field objects in Sanghi et al. (2023), we find $\log(L_{\rm bol,1}/L_\odot) = -5.36 \pm 0.07$ dex, $T_{\rm eff,1} = 810 \pm 55$ K, and $\log(L_{\rm bol,2}/L_\odot) = -5.56 \pm 0.07$ dex, $T_{\rm eff,1} = 694 \pm 55$ K. These values are consistent with those inferred from the ATMO 2020 evolutionary models at the $\approx 1\sigma$ level.

The closest matching spectral types are T7 for Gliese 229 Ba and T8 for Gliese 229 Bb.

Orbit fits

To derive orbital parameters, we jointly fit the GRAVITY closure phases and CRIRES+ RVs. Instead of computing positions from the closure phases for each epoch, we directly model them in the orbit fit. Not only does this take into account the multiple possible positions at each epoch, it also avoids intermediate products, preserving noise properties. We implemented this joint model in two different frameworks: a frequentist approach in PMOIRED (Mérand, 2022) and a Bayesian approach in Octofitter (Thompson et al., 2023). These methods independently arrive at consistent results. The methods were additionally validated using high quality GRAVITY data and high S/N radial velocities from VLT/UVES (Gallenne et al., 2023) for a binary star system, where we confirm that a close-phase orbital fit and an orbit fit using per-epoch separations and position angles yielded the same result. In both codes, we adopt a standard coordinate system for the orbit where +X points East, +Y points North, and +Z points away from the observer.

For the PMOIRED analysis, the best orbit is found by gradient descent, first on the radial velocity data and then on the joint model after adding the closure phase data. We only include the GRAVITY data from 2.05-2.18 μm as strong methane absorption results in extremely low S/N past 2.18 μm. In addition, the wavelength channels are binned to six points over the 2.05-2.18 μm range. In order to better estimate the final uncertainties, bootstrapping is used: 5000 random datasets are generated using sampling with replacement, and each time an orbital solution is fitted from a first guess drawn around the best values with four times the uncertainties. Bootstrapping has been shown to mitigate the correlations in interferometric data analysis (Lachaume et al., 2019). GRAVITY data are correlated, primarily because closure phases share baselines and baselines share telescopes (as formalized in Kammerer et al. (2020)). Moreover, data taken at the same time and with the same telescope triples have experienced the same biases from atmospheric turbulence and same calibration processes. To account for these correlations, all closure phases from the same date and baseline triangle are drawn together on the bootstrapping. First, we search for the best-fit orbit to the radial velocity data alone. This leads to an excellent solution with P=12.12±0.04 d, e=0.22±0.03, q=0.91±0.03 and a reduced χ^2 of 1.3. We allow for a RV offset term, γ_{RV} to account for possible inaccuracies in the systematic RV of the system. Next, we perform a joint fit to the GRAVITY

and CRIRES+ data. The results are shown in Table 5.1, and the relative orbit of the binary brown dwarf is plotted in Figure 5.9. We adopt the PMOIRED results as the baseline values in this paper.

For the Octofitter analysis, we completed joint Bayesian modeling of both the CRIRES+RVs and GRAVITY data. We used non-reversible parallel tempering (Syed et al., 2019; Syed et al., 2022; Surjanovic et al., 2022; Surjanovic et al., 2023) to search the entire multi-modal parameter space globally for the best-fitting parameter values. Rather than working with the closure phases directly, this analysis first converts the closure phases into a set of non-redundant kernel phases for each wavelength (Blackburn et al., 2020). This improves the accuracy of the model uncertainties compared to working directly with the closure phases, which share baselines (mitigated in the PMOIRED analysis after-the-fact using bootstrapping). Finally, we add an additional kernel-phase "jitter" term for each epoch of data (five in total). This term allows the model to absorb some amount of systematic calibration error in the GRAVITY data, again resulting in more realistic uncertainties in the final model parameters. For this model, we included data in the 2.025 - 2.15 μm range with no spectral binning. The orbital parameters from the joint model are listed in Table 5.1, and are consistent with PMOIRED results at the $\approx$1.5 sigma level. We find strong evidence that, when combining the GRAVITY data with the CRIRES+ RVs, the orbit solution is uniquely determined and no secondary modes in the posterior are significant.

We provide posterior predictions of the relative separation and position angle of Gliese 229 Ba-Bb in Table 5.5. We stress that these are inferred values and not statistically independent like traditional astrometry, as they are derived from a joint analysis of all epochs. They should not be used as inputs to an orbit fit, as they themselves are the outputs of such a fit. Instead, orbit fits should use the GRAVITY closure phases.

Dynamics

Given their small separation, Gliese 229 Ba and Bb are probably tidally locked with each other, with rotation periods equal to the orbital period of 12 days. We quantify the tidal locking timescale using Peale (1977). With an initial spin velocity of 20 km s^{-1} and initial radius of 1 $R_{\rm Jup}$, we find a despinning time of about 2 Gyr, which is shorter than or comparable with the estimated system age of approximately 2–6 Gyr (T. D. Brandt et al., 2019b). As noted earlier, our CRIRES+ analysis shows that

both brown dwarfs have $v \sin i < 0.7$ km s^{-1}, which is consistent with them being tidally locked.

In the current configuration of Gliese 229 A-BaBb, the highly eccentric and misaligned outer AB orbit ($e \approx 0.85$, G. M. Brandt et al. 2021b) could induce secular perturbations that pump up the eccentricity of the inner BaBb orbit by means of the eccentric von Zeipel–Lidov–Kozai mechanism (Naoz, 2016). Consequently, tidal interactions may shrink the BaBb orbit. We estimate that the Kozai secular precession timescale given by equation (3) in Batygin et al. (2009) is about 0.2 Myr for Gliese 229 Bb. The secondary brown dwarf also undergoes precession from the quadrupole potential from its tidal and rotational bulges and from the leading order effects of general relativity. If these effects operate on a shorter timescale, they could suppress Kozai oscillations. For our brown dwarfs, we adopt tidal parameters $Q = 3\times10^4$, $k_2 = 0.565$ based on Jupiter. The exact values of Q and k_2 are unknown for brown dwarfs but estimates from hot Jupiters generally produce values within one order of magnitude of Jupiter's values (Efroimsky et al., 2022). We estimate the precession rates using equations (6)–(8) in Batygin et al. (2009) and find that the precession rate owing to general relativity is the fastest, with a corresponding timescale of about 0.6 Myr, which is still longer than the Kozai timescale. In the absence of further perturbations or bodies, the triple system may therefore undergo Kozai oscillations. However, detailed N-body simulations and follow-up work are required to further evaluate the dynamical state of the system.

5.3 Data availability

The reduced CRIRES+ and GRAVITY data will be made public through Zenodo (J. Xuan et al., 2024a) at: https://doi.org/10.5281/zenodo.13851639.

5.4 Code availability

The CRIRES+ data reduction was performed with excalibuhr. (`https://github.com/yapenzhang/excalibuhr`). The orbit fits were performed with PMOIRED (`https://github.com/amerand/PMOIRED`) and Octofitter (`https://sefffal.github.io/Octofitter.jl/dev/`). The atmospheric models were generated using inputs from Sonora Elf Owl `https://zenodo.org/records/10385821` and the petitRADTRANS radiative transfer tool available at `https://petitradtrans.readthedocs.io/`. ATMO 2020 models are available for download at `http://opendata.erc-atmo.eu`.

5.5 Acknowledgements

J.W.X. thanks S. Mukherjee, T. Dupuy, B. Lacy, C. Morley, J. Fortney, Y. Zhou, C-C. Hsu, G. Hallinan, and S. Kulkarni for helpful discussions. J.W.X. acknowledges support for this work through the NASA FINESST Fellowship award 80NSSC23K1434. S.L. acknowledges the support of the French "Agence Nationale de la Recherche" (ANR), under grants ANR-21-CE31-0017 (project ExoVLTI) and ANR-22-EXOR-0005 (PEPR Origins). M.C. Liu acknowledges support from the Gordon and Betty Moore Foundation through grant GBMF8550. J.Wa. acknowledges support from NASA Grant 80NSSC23K0280. P.K. acknowledges funding from the European Research Council (ERC) under the European Union's Horizon 2020 research and innovation program (project UniverScale, grant agreement 951549). P.G. acknowledges the financial support provided by FCT/Portugal through grants PTDC/FIS-AST/7002/2020 and UIDB/00099/2020. This paper is based on observations collected at the European Southern Observatory under ESO programme 0112.C-2369(A), 0112.C-2369(B), and 2112.D-5036(A). This research has made use of the Jean-Marie Mariotti Center Aspro service available at `http://www.jmmc.fr/aspro`. This work has benefitted from The UltracoolSheet at `http://bit.ly/UltracoolSheet`, maintained by Will Best, Trent Dupuy, Michael Liu, Aniket Sanghi, Rob Siverd, and Zhoujian Zhang, and developed from compilations by Sanghi et al. (2023), Dupuy et al. (2012), Dupuy et al. (2013), Deacon et al. (2014), Liu et al. (2016), Best et al. (2018), Best et al. (2021), and Schneider et al. (2023).

5.6 Author Contributions

J.W.X. led the telescope proposals for Gliese 229, performed the CRIRES+ spectral fitting to obtain radial velocities, and wrote the manuscript. A.M., W.T., and D.B. led the closure phase modeling and orbital analysis. Y.Z. reduced the raw CRIRES+ data. S.L. reduced the raw GRAVITY data. D.M., R.O., M.L., and A.B. provided advice on the writing and figures. J.K. computed the GRAVITY sensitivity limits. K.B. provided guidance on the system dynamics. A.Sa. performed the analysis with empirical relations. H.K. provided advice on the CRIRES+ spectral fits. R.B.-R. and M.Sa. obtained confirmation Keck/NIRC2 images. The remaining authors constitute the GRAVITY team and commented on the manuscript.

5.7 Extended Data Figures

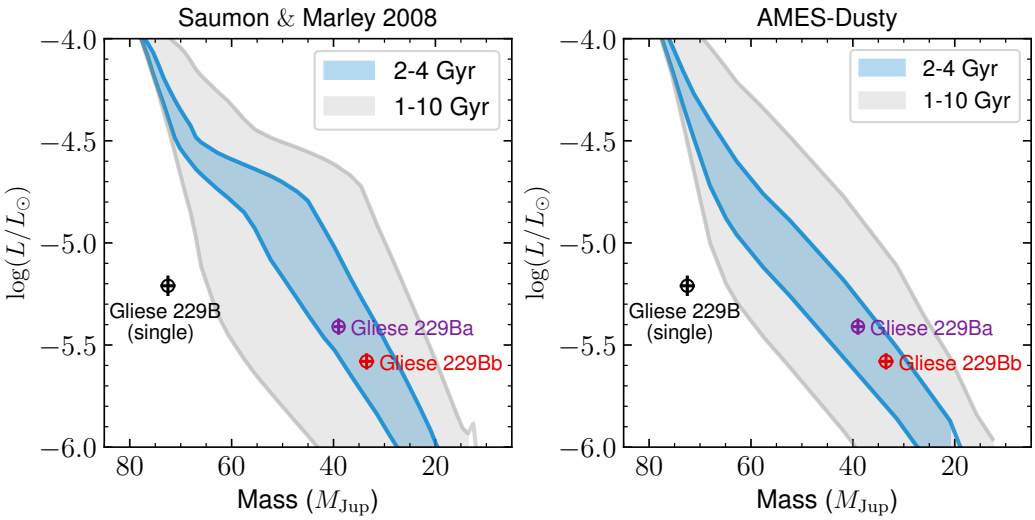

Figure 5.4: The dynamical masses and estimated luminosities of Gliese 229 Ba (purple) and Bb (red) from the ATMO 2020 evolutionary model fit. As a single brown dwarf, Gliese 229 B is under-luminous compared to model predictions even at 10 Gyr (leftmost gray line). As a binary brown dwarf, the system is consistent with the Saumon & Marley 2008 (Saumon et al., 2008) and AMES-Dusty (Allard et al., 2001) models for an age of $\approx 2 - 4$ Gyr.

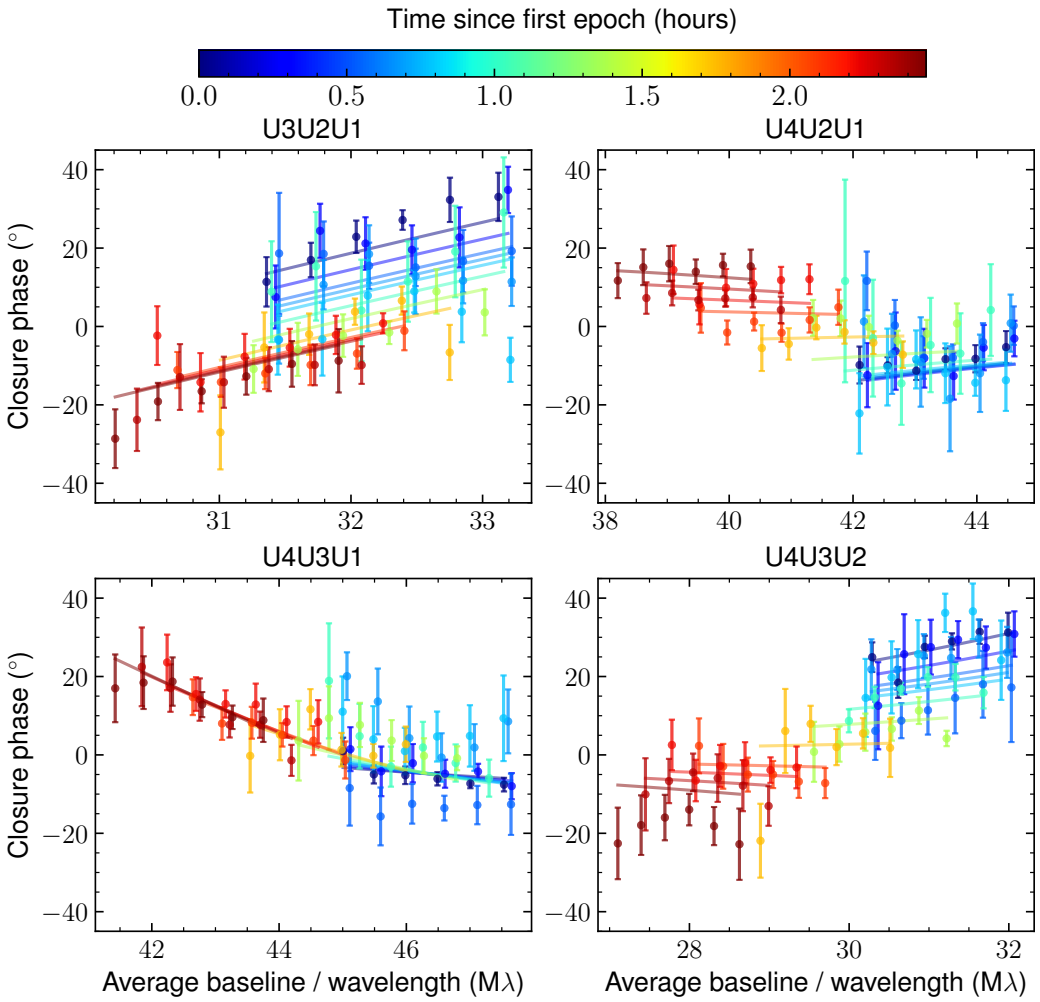

Figure 5.5: The GRAVITY closure phases measurements in the first epoch (2023-12-26). The data are in points, and the models are shown as lines. Each panel is for a different baseline triangle between the four unit telescopes at the Very Large Telescope (U1, U2, U3, U4). The color code indicates the time since the first data point (in hours). The data are well described by the model, with a majority of residuals at the $< 2\sigma$ level. A single source would have zero closure phases throughout.

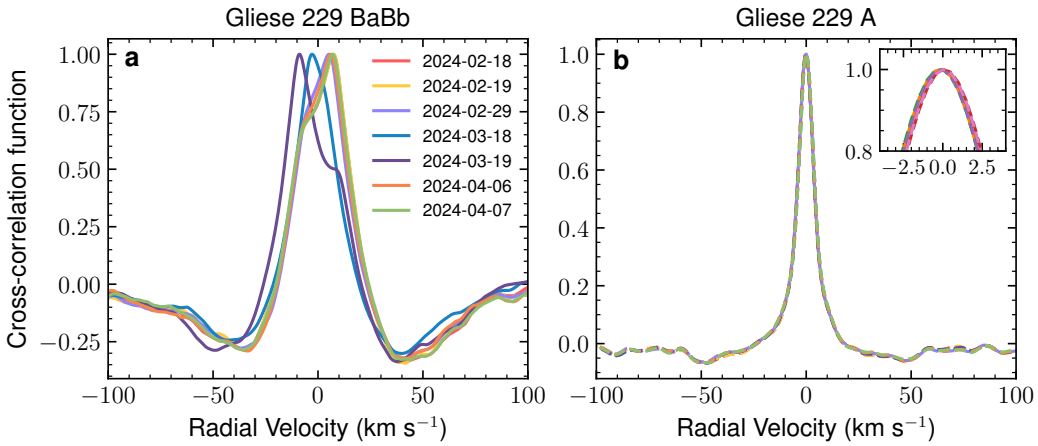

Figure 5.6: (a) Cross-correlation functions (CCFs) between CRIRES+ spectra of Gliese 229 B and an atmospheric model with $T_{\rm eff}$ = 900 K, $\log g$ = 5.0 computed using Sonora Elf Owl temperature and chemistry profiles. The CCF shapes are distorted and variable over time, characteristic of a double-lined spectroscopic binary. (b) CCFs between CRIRES+ spectra of Gliese 229 A and a PHOENIX-ACES model65 with $T_{\rm eff}$ = 3800 K and $\log g$ = 4.5. The inset shows a zoom-in of the CCF peak. The stellar RVs are stable at the 0.1 km/s level over the observing period, validating the wavelength solution of CRIRES+.

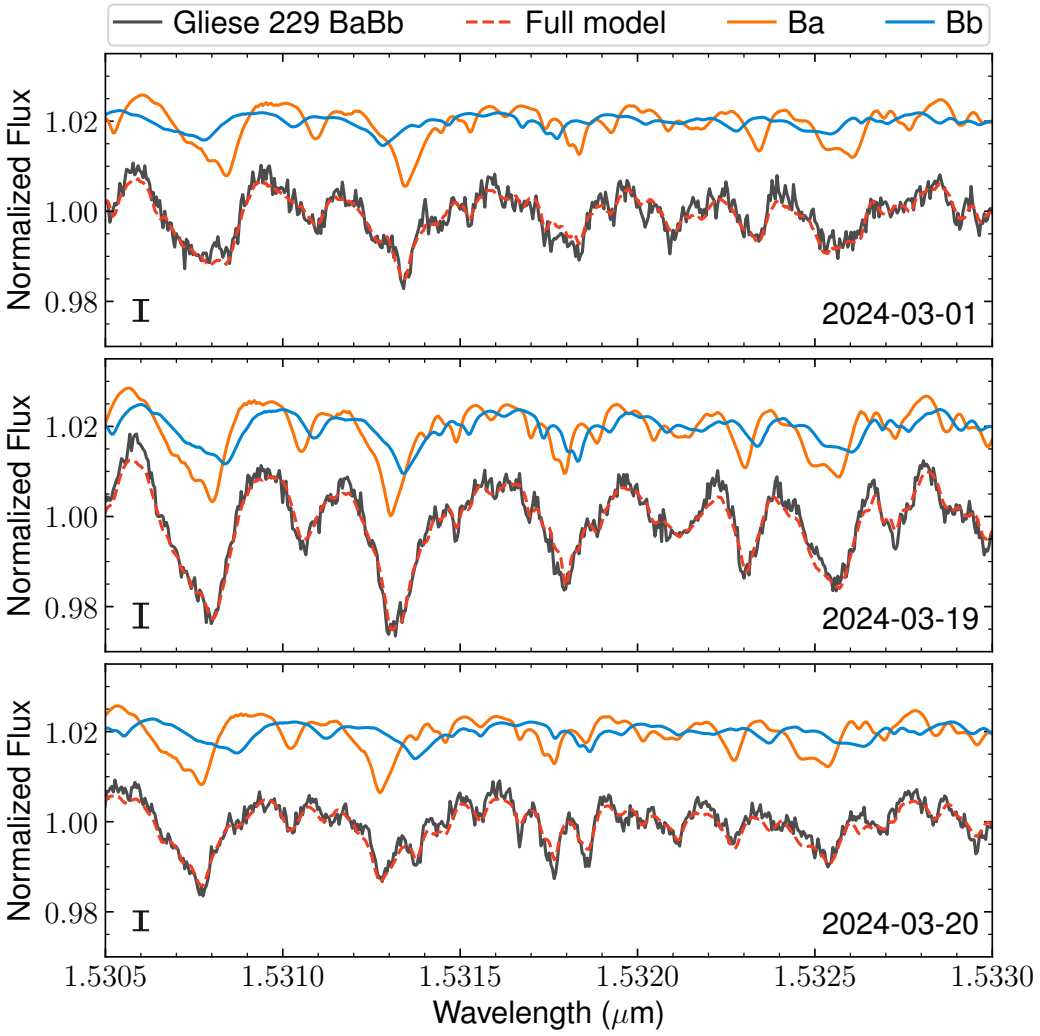

Figure 5.7: A small portion of the CRIRES+ spectra on three different nights where we achieve the highest S/N (black). The Ba and Bb models are shown in teal and purple, while the full model is in red. The median uncertainties for the spectra are denoted as error bars on the lower left (1σ). Absorption lines from the two brown dwarfs can be seen combining over the observing sequence. The data from 2024-03-19 were taken with the best seeing conditions and consequently contains the highest flux from the brown dwarfs and minimal stellar contamination from Gliese 229 A. Therefore, the lines appear deeper for this epoch.

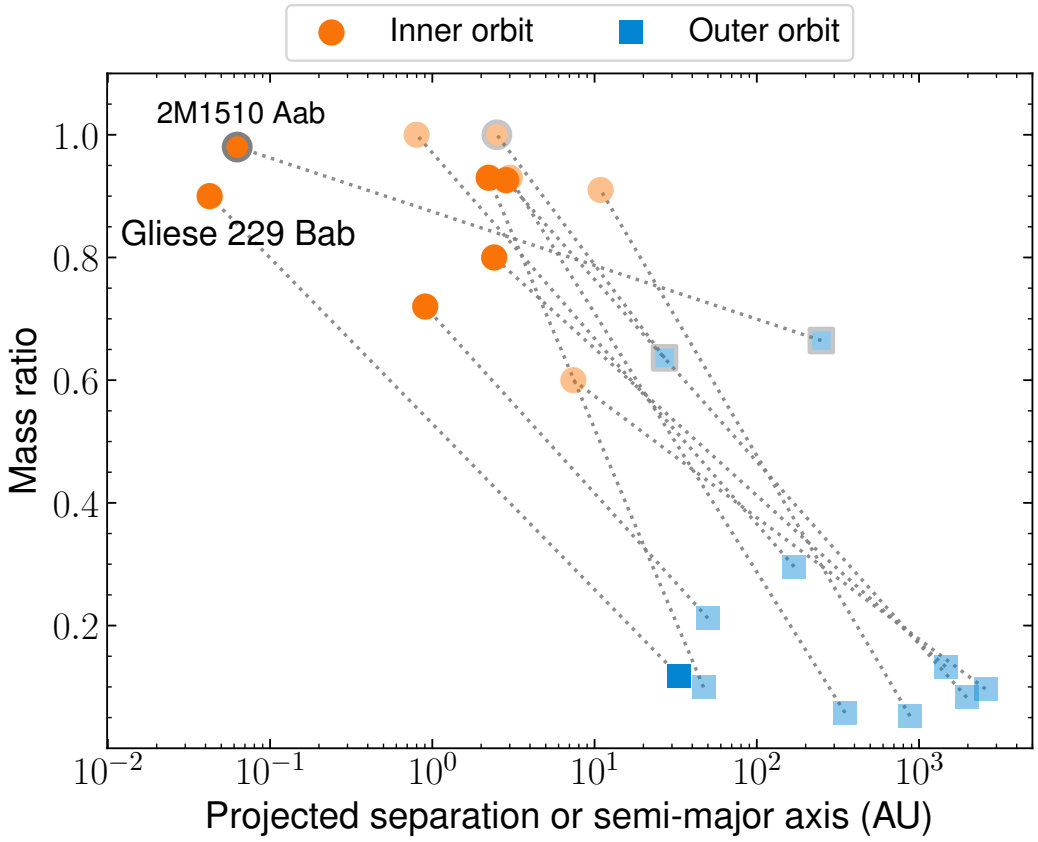

Figure 5.8: For each system, we show the orbital separation and mass ratio of the brown dwarf binary in orange. The separation of the outer orbit (i.e. that between the brown dwarfs and the third component) and mass ratio of the brown dwarf binary relative to the total system mass is in blue. Many systems have prohibitively long orbital periods or lack published orbit solutions; we use transparent points to denote projected separations, and opaque points for semi-major axes. Each system is connected with a gray dotted line. We label the similarly tight binary 2M1510 Aab from Triaud et al. (2020). The circles with gray outlines are triple brown dwarf systems, where all components are substellar. Among brown dwarf binaries orbiting stars, Gliese 229 Bab has an inner orbit more than an order of magnitude smaller than other systems. The parameters for other systems are taken from Deacon et al. (2014), Golimowski et al. (2004), Burgasser et al. (2005), Dupuy et al. (2014), Dupuy et al. (2009), Nielsen et al. (2013), Chen et al. (2022), and Radigan et al. (2013).

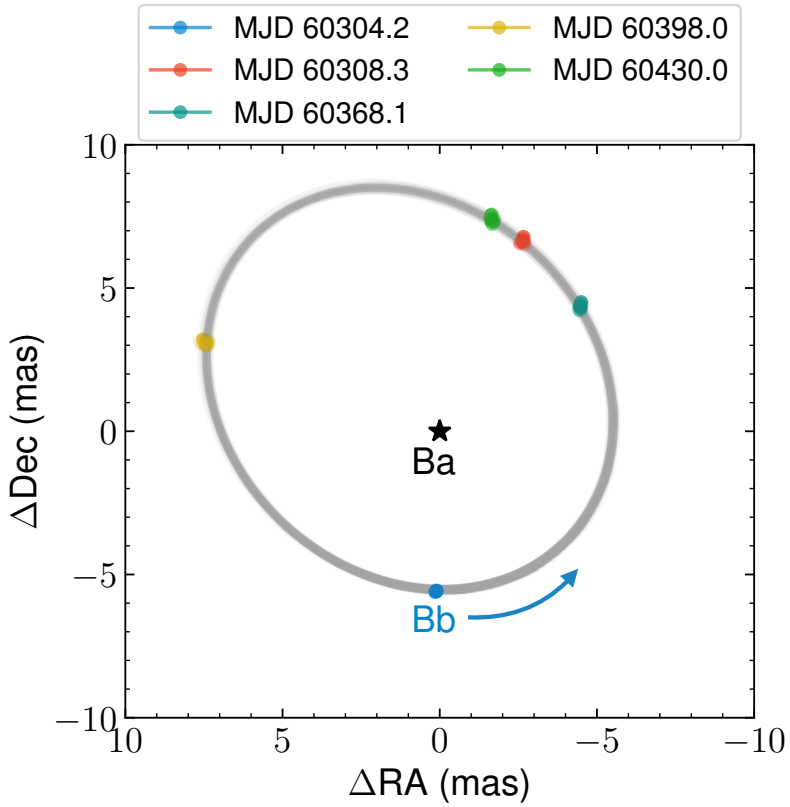

Figure 5.9: Random draws of the relative astrometric orbit of Gliese 229 Ba-Bb from the PMOIRED fit are shown as gray curves. The position of the primary brown dwarf Gliese 229 Ba is marked with a star at the origin. The colored points show random draws of the predicted astrometric positions of Bb with respect to Ba from the joint GRAVITY and CRIRES+ orbit fit over the five observing epochs.

5.8 Extended Data Tables

Table 5.2: GRAVITY wide and CRIRES+ observation log for Gliese 229 BaBb

Instrument	Start (UT)	End (UT)	NEXP/NDIT/DIT (s)	Airmass	TAU0 (ms)	Seeing (arcsec)
GRAVITY	2023-12-26T04:14:07	2023-12-26T06:48:36	13/4/100	1-1.16	5-20	0.5-1.1
GRAVITY	2023-12-30T05:47:25	2023-12-30T06:32:50	4/4/100	1.1-1.2	5-10	0.4-0.8
GRAVITY	2024-02-28T02:57:39	2024-02-28T03:36:49	3/4/100	1.2-1.4	5-6	0.7-0.9
GRAVITY	2024-03-29T00:31:24	2024-03-29T01:17:35	4/4/100	1.1-1.3	8-12	0.4-0.6
GRAVITY	2024-04-29T23:15:22	2024-04-29T23:29:21	2/4/100	1.3-1.4	4-10	0.7-0.8
CRIRES+	2024-02-19T02:27:37	2024-02-19T04:10:34	6/1/900	1.1-1.4	7-18	0.6-1.15
CRIRES+	2024-02-20T02:22:28	2024-02-20T03:00:26	2/1/900	1.1	5-7	0.8-1.5
CRIRES+	2024-03-01T01:45:04	2024-03-01T03:28:13	6/1/900	1.1-1.4	7-9	0.5-0.8
CRIRES+	2024-03-19T00:54:23	2024-03-19T02:37:11	6/1/900	1.1-1.5	6-8	0.4-0.7
CRIRES+	2024-03-20T00:36:04	2024-03-20T02:18:21	6/1/900	1.1-1.4	2-6	0.6-0.7
CRIRES+	2024-04-07T00:12:23	2024-04-07T01:12:00	4/1/600	1.2-1.4	4-6	0.6-0.9
CRIRES+	2024-04-08T23:31:31	2024-04-08T00:24:28	4/1/600	1.1-1.2	7-8	0.7-1.0

Table 5.3: Bulk properties of Gliese 229 BaBb inferred from the ATMO 2020 evolutionary model.

Parameter	ATMO 2020
Mass ratio	0.87 ± 0.03
Age (Gyr)	2.45 ± 0.20
$T_{\mathrm{eff},Ba}$ (K)	860 ± 20
$T_{\mathrm{eff},Bb}$ (K)	770 ± 20
$\log(g)_{Ba}$ (dex)	5.11 ± 0.01
$\log(g)_{Bb}$ (dex)	5.03 ± 0.01
$\log(L/L_{\odot})_{Ba}$	-5.41 ± 0.04
$\log(L/L_{\odot})_{Bb}$	-5.58 ± 0.04

Table 5.4: Radial velocities of Gliese 229 Ba and Bb from VLT/CRIRES+.

Time (MJD)	RV_{Ba} (km/s)	RV_{Bb} (km/s)
60359.14	8.07 ± 0.12	-7.51 ± 0.19
60360.11	8.13 ± 0.14	-7.22 ± 0.19
60370.11	6.07 ± 0.17	-6.31 ± 0.25
60388.07	-3.21 ± 0.54	4.09 ± 0.75
60389.058	-8.97 ± 0.23	10.60 ± 0.46
60407.03	6.85 ± 0.16	-7.55 ± 0.24
60408.00	7.49 ± 0.27	-8.10 ± 0.32

Table 5.5: Derived relative astrometry of Gliese 229 Ba-Bb from the Octofitter fit.

Date [UTC]	Projected separation [mas]	Position Angle [deg]	Separation [AU]
2023-12-26 05:15:42	5.58 ± 0.01	178.4 ± 0.9	0.0338 ± 0.0001
2023-12-30 06:11:23	7.10 ± 0.05	-22.0 ± 0.1	0.0453 ± 0.0002
2024-02-28 03:13:29	6.19 ± 0.04	-46.5 ± 0.3	0.0413 ± 0.0001
2024-03-29 00:31:14	7.95 ± 0.03	67.6 ± 0.5	0.0488 ± 0.0001
2024-04-29 23:15:12	7.49 ± 0.04	-13.5 ± 0.2	0.0468 ± 0.0002

As noted in Methods, these values should not be used directly in orbit fits.

Chapter 6

ATMOSPHERIC ABUNDANCES AND BULK PROPERTIES OF THE BINARY BROWN DWARF GLIESE 229 BAB FROM JWST/MIRI SPECTROSCOPY

This chapter reproduces my JWST/MIRI paper on Gliese 229 Bab, the newly resolved brown dwarf binary from the previous chapter. The JWST data are from a cycle 2 proposal that I led (GO 3762). I did not know this was a binary brown dwarf when writing the JWST proposal. One of the goals of the proposal was in fact to refine and validate the bolometric luminosity estimate of Gliese 229 B, which relied on $1-5$ μm spectro-photometry. From my analysis of the MIRI data, it turns out that the previous estimate of luminosity was accurate, so the mass-luminosity tension is indeed present if Gliese 229 B were a single object. In this chapter, I fitted the MIRI spectrum with Sonora Elf Owl models to determine the composition and bulk properties of the binary. We find that the two brown dwarfs share identical metallicity and C/O as their host star. I discuss potential reasons why previous studies might have overestimated the C/O of Gliese 229 B, and the broader trend of retrieval studies finding elevated C/O for T dwarfs.

Xuan, J. W. et al. (Dec. 2024). "Atmospheric Abundances and Bulk Properties of the Binary Brown Dwarf Gliese 229Bab from JWST/MIRI Spectroscopy". In: *The Astrophysical Journal Letters* 977.2, L32, p. L32. DOI: 10.3847/2041-8213/ad92f9.

Abstract

We present JWST/MIRI low-resolution spectroscopy ($4.75-14$ μm) of the first known substellar companion, Gliese 229Bab, which was recently resolved into a tight binary brown dwarf. Previous atmospheric retrieval studies modeling Gliese 229B as a single brown dwarf have reported anomalously high carbon-to-oxygen ratios (C/O) of ≈ 1.1 using $1-5$ μm ground-based spectra. Here, we fit the MIRI spectrum of Gliese 229Bab with a two-component binary model using the Sonora Elf Owl grid and additionally account for the observed K band flux ratio of the

binary brown dwarf. Assuming the two brown dwarfs share the same abundances, we obtain $C/O = 0.65 \pm 0.05$ and $[M/H] = 0.00^{+0.04}_{-0.03}$ as their abundances (2σ statistical errors), which are fully consistent with the host star abundances. We also recover the same abundances if we fit the MIRI spectrum with a single brown dwarf model, indicating that binarity does not strongly affect inferred abundances from mid-infrared data when the $T_{\rm eff}$ are similar between components of the binary. We measure $T_{\rm eff} = 900^{+78}_{-29}$ K and $T_{\rm eff} = 775^{+20}_{-33}$ K for the two brown dwarfs. We find that the vertical diffusion coefficients of $\log K_{\rm zz} \approx 4.0$ are identical between the two brown dwarfs and in line with $\log K_{\rm zz}$ values inferred for isolated brown dwarfs with similar $T_{\rm eff}$. Our results demonstrate the power of mid-infrared spectroscopy in providing robust atmospheric abundance measurements for brown dwarf companions and by extension, giant planets.

6.1 Introduction

Brown dwarf companions ($m \approx 13 - 72\ M_{\rm Jup}$) to stars provide excellent tests of substellar atmospheric and evolutionary models, and serve as a key bridge to understanding the population of directly imaged giant exoplanets. From the powerful combination of *Hipparcos-Gaia* astrometry (T. D. Brandt, 2018; Kervella et al., 2019; J. W. Xuan et al., 2020a) and long-term radial velocity and imaging observations, a growing subset of brown dwarf companions now have their dynamical masses measured (e.g. T. D. Brandt et al., 2019b; T. D. Brandt et al., 2019a; Franson et al., 2022; Franson et al., 2023c; Franson et al., 2023a; Rickman et al., 2024). The dynamical masses can be compared with bolometric luminosity and stellar age measurements to benchmark substellar evolutionary models (e.g. Zapatero Osorio et al., 2004; Stassun et al., 2006; Dupuy et al., 2014; Dupuy et al., 2017). Such studies have revealed a number of discrepancies between models and observations, including a sample of older brown dwarf companions that appear under-luminous given their measured masses (typically > 2 Gyr; Cheetham et al. 2018; T. D. Brandt et al. 2019b; Bowler et al. 2021), and a number of young companions that are over-luminous for their masses (e.g. Dupuy et al., 2009; Dupuy et al., 2014; G. M. Brandt et al., 2021b). It is crucial to investigate the reason behind these discrepancies, as the same models are used to estimate model-dependent masses for the vast majority of imaged planets and brown dwarf companions that lack direct mass measurements, for instance due to prohibitively long orbital periods.

Dynamical masses also provide crucial information to aid atmospheric studies, which are often under-constrained and display complex degeneracies between sur-

face gravity, clouds, and metallicity (e.g. Z. Zhang et al., 2021b; J. W. Xuan et al., 2022; Landman et al., 2023b; Balmer et al., 2024). The introduction of dynamical mass priors in atmospheric studies can help to exclude nonphysical parts of the parameter space, and have become widely adopted whenever available (e.g. Z. Zhang et al., 2023; Nasedkin et al., 2024; Hsu et al., 2024a). Brown dwarf companions that have both dynamical masses and precise spectroscopic observations sensitive to multiple molecular species provide the most stringent tests of substellar models. For example, numerous studies using high-resolution ground-based spectroscopy have shown that companions with $m \gtrsim 40\ M_{\rm Jup}$ are chemically homogeneous with their host stars, as expected for objects that formed via direct gravitational collapse from the same disk or cloud (e.g. J. W. Xuan et al., 2022; J. Wang et al., 2022; Hsu et al., 2024a; Costes et al., 2024; J. W. Xuan et al., 2024c). Recently, J. W. Xuan et al. (2024a) also showed that this trend extends to the $\sim 10-30\ M_{\rm Jup}$ regime, implying that gravitational instabilities can form systems with a broad range of masses and mass ratios (see also Hoch et al. 2023).

Gliese 229B is one of the closest brown dwarf systems (5.761 parsec; Gaia Collaboration 2022) (Nakajima et al., 1995; Oppenheimer et al., 1995), orbiting the M1V star Gliese 229A on a highly eccentric orbit ($e \approx 0.8$) with semi-major axis of 33 AU. G. M. Brandt et al. (2021b) measured a precise dynamical mass of $71.4 \pm 0.6\ M_{\rm Jup}$ for Gliese 229B, which is unusually high given the low luminosity of the source. While Gliese 229B has been studied as a benchmark single brown dwarf for nearly three decades, J. W. Xuan et al. (2024b) recently used VLTI/GRAVITY and VLT/CRIRES+ to show that Gliese 229B is in fact comprised of two brown dwarfs, Ba and Bb, orbiting each other on a tight orbit with $a \approx 0.042$ AU (or orbital period of 12.1 days).[1] The properties of Gliese 229BaBb resolve previous tensions between mass and luminosity and recast the system as a benchmark brown dwarf binary in a triple system.

There have been numerous atmospheric studies on Gliese 229B over the years using optical and near-infrared spectrum from $0.6-2.5\ \mu$m, and in some cases, $0.6-5\ \mu$m. The early studies mainly matched the spectrum with model grids or performed by-eye identification of absorption features (e.g. M. S. Marley et al., 1996; Geballe et al., 1996; K. S. Noll et al., 1997; Oppenheimer et al., 1998; Saumon et al., 2000; Leggett et al., 2002). To summarize, these studies constrain the $T_{\rm eff}$ between about 850 to 1100 K, find evidence of disequilibrium chemistry from the over-abundance

[1] See also the complementary evidence for binarity presented in Whitebook et al. (2024).

of CO, but disagree strongly on the surface gravity, which ranges from $\log g = 3.5$ to $\log g = 5.3$. Two of these studies attempted to measure the metallicity of Gliese 229 B, and find sub-solar values between -0.5 to -0.3 dex (Saumon et al., 2000; Leggett et al., 2002), but noted that the metallicity is degenerate with the poorly constrained surface gravity.

There have also been two atmospheric retrievals published using the same near-infrared spectra of Gliese 229B (Calamari et al., 2022; Howe et al., 2022). Both of these retrieval studies find a solar metallicity for Gliese 229B, unlike the earlier studies. However, both studies also found an elevated $C/O \approx 1.1$, which is unexpected given the nearly solar $C/O = 0.68 \pm 0.12$ of the primary star (Nakajima et al., 2015). C/O values exceeding 1 have been reported for a number of T dwarfs using low-resolution, near-infrared spectroscopy (e.g. Zalesky et al., 2019; Zalesky et al., 2022; Gaarn et al., 2023), and is usually thought to be an observational bias caused by either data systematics or model inaccuracies (or both), though the exact reason is unclear (Gaarn et al., 2023; Calamari et al., 2024). While there could be some T dwarfs with actual $=C/O > 1$, such objects should be quite rare given the paucity of FGK stars with $=C/O > 1$ in the solar neighborhood (e.g. Brewer et al., 2016). Finally, the discovery that Gliese 229B is a binary brown dwarf (J. W. Xuan et al., 2024b) naturally raises the question of what effect, if any, its binarity might have on atmospheric retrieval studies.

Although most previous atmospheric studies of Gliese 229B treated this companion as a single object, Howe et al. (2023) tried fitting a two-component grid model to its $1 - 5\mu$m spectra. However, due to limitations of the models and the limited quality and wavelength coverage of the data, their binary fits produced significant residuals and were not statistically preferred over the single-brown dwarf retrievals in Howe et al. (2022). The properties inferred for the brown dwarf binary from Howe et al. (2023) are also inconsistent with the mass ratio and flux ratio measured by J. W. Xuan et al. (2024b).

In this paper, we present JWST Mid Infrared Instrument (MIRI) low-resolution spectroscopy of Gliese 229B from $4.75 - 14$ μm. Informed by the results from J. W. Xuan et al. (2024b), we model the spectrum using a binary brown dwarf model and estimate the effective temperature, surface gravity, and vertical mixing rate for each component. In addition, we provide updated measurements of the binary's atmospheric metallicity and C/O ratio.

6.2 Observations and Data Reduction

We observed Gliese 229B using JWST's Mid Infrared Instrument (MIRI; Rieke et al. 2015) on UT 2023 December 13 (GO3762, PI: Xuan). The observations were carried out with the low-resolution spectrometer (LRS; Kendrew et al. 2015) in fixed slit mode ($0\farcs51 \times 4\farcs7$). We obtained spectroscopy from 5˘14 μm with an average resolving power of ~ 100.

At the start of the observation, a target acquisition exposure was taken on the star Gliese 229 to measure and correct for observatory pointing uncertainties, and an offset move was performed to position the companion Gliese 229B within the LRS slit. A target acquisition confirmation exposure was taken (F560W filter, 16.6 seconds) to allow precise confirmation measurement of the achieved position of Gliese 229B within the slit. Finally, two spectral exposures were taken with the LRS prism. We used the typical two-point "along slit nod" dither (Gordon et al., 2015), and observed for a total exposure time of 571.66 s in FASTR1 readout mode using 25 groups per integration. The MIRI data used in this paper can be found in MAST: http://dx.doi.org/10.17909/950e-3e83.

Data Reduction and Forward Modeling Host Star Contamination

We reduced the data using the JWST pipeline (version 1.14.0 and CRDS context jwst1255.pmap), plus additional custom steps to clean bad pixel outliers and to subtract the modest amount of contamination from host starlight within the slit.

Speckle contamination arises from the host star point spread function (PSF) diffraction pattern. Light from the star's PSF wings that enters the LRS slit accounts for approximately 10% of the flux at the companion location. To remove stellar contamination, we forward model the off-axis host star PSF with WebbPSF (Perrin et al., 2012; Perrin et al., 2014). The details of forward modeling and subtraction procedure are provided in Appendix 6.8.

After subtracting the stellar PSF, the two science observation nods are subtracted from one another to remove the observatory thermal background. We extracted independent sets of spectra from the two spectral traces. A key performance metric for the forward modeling process is the consistency of the spectra measured for each of the two nods. Without subtracting the host star PSF, the spectra from the two nods differ by $\approx 10\%$; after subtraction they agree to $\approx 2-3\%$.

Extracted Spectrum

After obtaining the nod-subtracted 2D spectrum, we proceed to extract the 1D spectrum using the JWST Level 3 pipeline. Specifically, we perform a box extraction centered on the spectral traces using the `extract_1d` function in the pipeline, with a box width of 8 pixels. The width is chosen to fully enclose the core of the spectral trace, while minimizing the included background area. Aperture correction is taken into account based on our box width, and the pipeline combines the two nods into a final spectrum. The extracted spectrum of Gliese 229Bab is shown in Fig. 6.1, along with opacities of the major relevant molecular sources.

The nominal wavelength range for MIRI LRS is $5-14$ μm. Our spectrum for Gliese 229Bab has an average S/N of ≈ 400 per point compared to the background noise, although systematics from subtracting the stellar speckles limit our effective S/N to $\approx 30-50$ given the $2-3\%$ difference between nods. While the $10-14$ μm region suffers more strongly from an inaccurate wavelength solution, this can be corrected with a second order polynomial (see § 6.3 and Fig. 6.10). Furthermore, after carrying out initial fits to the $5-14$ μm data, we find that our best-fit models can be extended blueward to 4.75 μm and still fit the data well. Extending to 4.75 μm allows us to capture the end of the mid-infrared CO absorption band. Therefore, we adopt a wavelength range of $4.75-14$ μm for the MIRI spectrum presented in this paper.

6.3 Spectral analysis

Resolving power and wavelength correction

First, we describe our treatment of two important aspects of the data, the variable resolving power, and the imperfect wavelength solution available at the time of analysis. We account for both these effects using additional nuisance parameters.

The resolving power ($R = \lambda/\Delta\lambda$) of MIRI LRS increases with wavelength in a nearly linear manner. In this work, we account for this by fitting a linear relation between R and the data wavelengths, λ

$$R_\lambda = r_0 + r\lambda \tag{6.1}$$

where r and r_0 are free parameters. In each iteration of the fit, the model spectrum is convolved with a variable Gaussian kernel whose standard deviation σ is given by

Table 6.1: Fitted Parameters and Priors

Parameter	**Prior**
Physical parameters	
Total Mass ($M_{\rm Jup}$)	$\mathcal{N}(71.3, 0.5)$
q	$\mathcal{N}(0.91, 0.05)$
$T_{\rm eff,1}$ (K)	$\mathcal{U}(575, 1200)$
$T_{\rm eff,2}$ (K)	$\mathcal{U}(575, T_{\rm eff,1})$
$\log g_{,1}$	$\mathcal{U}(4.2, 5.5)$
$\log g_{,2}$	$\mathcal{U}(\log g_{,1}, 5.5)$
C/O	$\mathcal{U}(0.23, 1.15)$
[M/H]	$\mathcal{U}(-1.0, 1.0)$
$\log(K_{\rm zz,1}/{\rm cm^2 s^{-1}})$	$\mathcal{U}(2.0, 9.0)$
$\log(K_{\rm zz,2}/{\rm cm^2 s^{-1}})$	$\mathcal{U}(2.0, 9.0)$
Nuisance parameters	
10^b	$\mathcal{U}(0.01 \times \min(\epsilon_{\rm i}^2), 100 \times \max(\epsilon_{\rm i}^2))$
w_0 $(\mu{\rm m})$	$\mathcal{U}(-0.15, 0.15)$
w_1	$\mathcal{U}(0.96, 1.04)$
w_2 $(\mu{\rm m}^{-1})$	$\mathcal{U}(-0.003, 0.003)$
r_0	$\mathcal{U}(-150, 0)$
r $(\mu{\rm m}^{-1})$	$\mathcal{U}(10, 35)$

We use $_1$ to denote Gliese 229Ba, the primary brown dwarf, and $_2$ to denote Gliese 229Bb, the secondary brown dwarf. In the single brown dwarf model, the priors adopted are the same as those for the $_1$ component. $\mathcal{U}$ stands for a uniform distribution, with two numbers representing the lower and upper boundaries. $\mathcal{N}$ stands for a Gaussian distribution, with numbers representing the mean and standard deviation. For the 10^b error inflation factor, ϵ_i refers to the data uncertainties (see Eq. 6.4).

$$\sigma = \frac{\lambda / R_\lambda}{2\sqrt{2 \log 2}} \tag{6.2}$$

Second, our initial fits show inaccuracies in the wavelength solution, especially at longer wavelengths. We include a quadratic wavelength correction to improve the wavelength solution. The corrected data wavelengths (λ') are given by

$$\lambda' = w_0 + w_1 \lambda + w_2 \lambda^2 \tag{6.3}$$

where λ is the wavelength from the pipeline, and w_0, w_1, and w_2 are coefficients of the polynomial that we fit for. In practice, we fit the parameters for R_λ and λ'

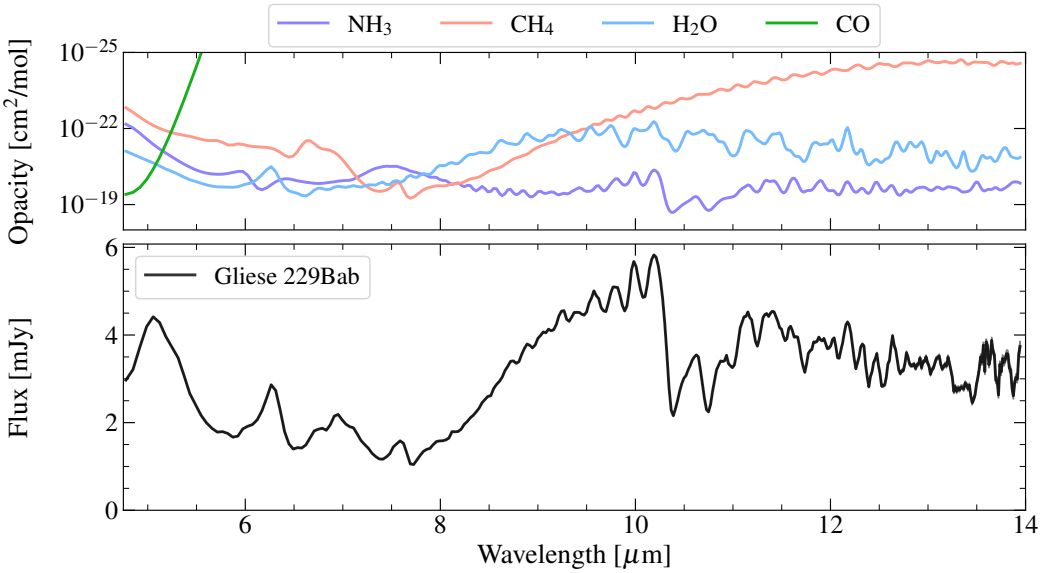

Figure 6.1: Top panel: Opacities of the major molecular absorbers in the mid-infrared spectrum of Gliese 229Bab. The units are cm^2 per molecule. Note that the y-axis is inverted. Bottom panel: MIRI LRS spectrum of Gliese 229Bab in black. The error bars are shown as shaded regions around the spectrum, but are not visible by eye except for the reddest wavelengths.

once using a single brown dwarf model and subsequently adopt the best-fit values for subsequent fits.

Model fitting with Elf Owl

We fit the MIRI LRS data of Gliese 229B using the Sonora Elf Owl models (Mukherjee et al., 2024). The Elf Owl grid includes five parameters: the effective temperature ($T_{\rm eff}$), surface gravity ($\log g$), vertical diffusion coefficient ($\log K_{zz}$), carbon-to-oxygen ratio (C/O), and bulk metallicity ([M/H]). While the models are cloudless, we do not expect cloud opacity to affect the near or mid infrared spectra of late T dwarfs (e.g. Line et al., 2017; Suárez et al., 2022; Mukherjee et al., 2024). We note that alternative cloudless models for brown dwarfs exist, and some recent ones include ATMO 2020, Sonora Bobcat, and Sonora Cholla (Phillips et al., 2020; M. S. Marley et al., 2021; Karalidi et al., 2021). However, ATMO 2020 assumes solar abundances, whereas Bobcat varies metallicity and C/O but does not account for disequilibrium chemistry. In addition, Cholla varies the $\log K_{zz}$ but fixes the abundances to solar. While we only use Elf Owl in this paper, it would be informative to compare how well different models fit the MIRI data of Gliese 229B in future studies.

Using JWST/NIRSpec spectroscopy, Beiler et al. (2024) showed that substellar models including Sonora Elf Owl under-estimate the CO_2 abundance in brown dwarf atmospheres due to inaccurate treatments of disequilbrium chemistry. On the other hand, the non-detection of PH_3 suggests an over-prediction of the PH_3 abundance. Our MIRI LRS data are not sensitive to the strongest features from CO_2 and PH_3 at approximately $4.2 - 4.4$ μm.

As Gliese 229B has been resolved into a binary brown dwarf (J. W. Xuan et al., 2024b), our fiducial model is a two-component binary model that allows different $T_{\rm eff}$, $\log g$, and $\log K_{zz}$ values for each brown dwarf. Given the limiting resolution of our MIRI LRS data, we assume the C/O and [M/H] to be identical between the two brown dwarfs in our fiducial model. However, we also fit models with two distinct sets of C/O and [M/H] for each brown dwarf to test this assumption. We parameterize the component masses using the mass ratio (q) and total mass. The component masses along with the individual $\log g$ are used to compute the radii, which scales the model flux along with the distance. The distance to the source is fixed at 5.761 parsec based on the Gaia DR3 parallax measurement (Gaia Collaboration, 2022).

For the total mass and mass ratio, we adopt Gaussian priors from J. W. Xuan et al. (2024b) (see Table 6.1). From physical considerations of energy conservation and degeneracy pressure, we always expect the more massive brown dwarf to be hotter and have a higher surface gravity than the less massive component. Thus, we put priors on the secondary brown dwarf such that its $T_{\rm eff}$ and $\log g$ are always lower than that of the primary component.

In addition to nuisance parameters for the resolving power and wavelength correction (§ 6.3), we fit an error inflation term b following Line et al. (2015), which scales the pipeline errors (ϵ) such that

$$\epsilon' = \sqrt{\epsilon + 10^b} \tag{6.4}$$

where ϵ' are the adopted errors for the log likelihood calculation. Fitting the error inflation term allows us to account for systematic uncertainties from the speckle subtraction (§ 6.2) and model uncertainties. In total, we have 10 physical parameters and 6 nuisance parameters for the binary model, which are summarized in Table 6.1. In addition to the binary model, we also consider a single brown dwarf model to assess whether ignoring binarity changes the atmospheric composition

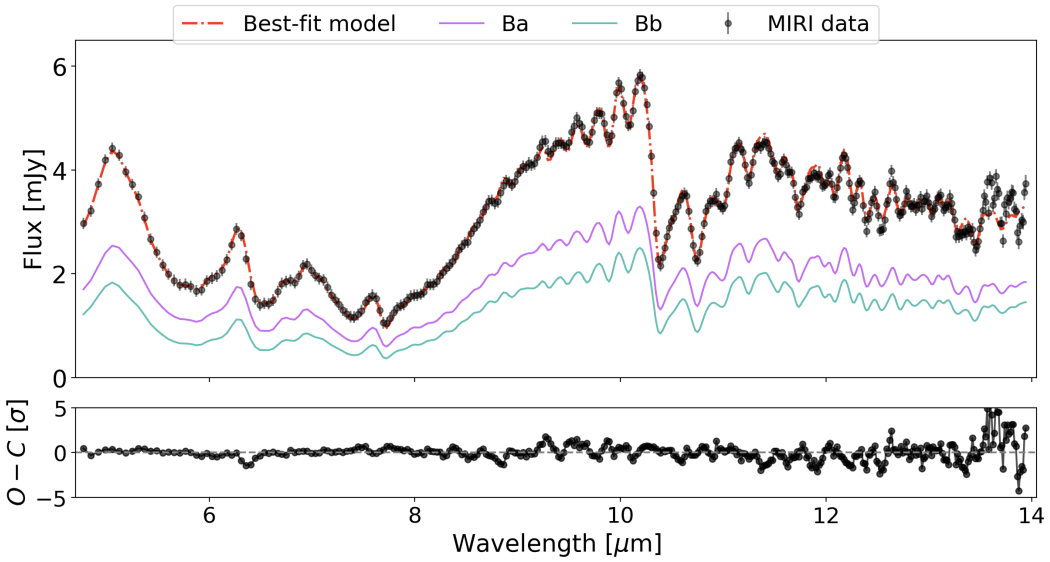

Figure 6.2: Top panel: MIRI LRS spectrum of Gliese 229Bab in black circles. The error bars shown have been inflated by the best-fit error inflation factor. The red dashdot curve shows the best-fit model spectrum, which is the addition of the individual component spectra, Ba (purple), and Bb (teal). Bottom panel: residuals of the fit (data-model) plotted in units of σ differences. Overall, the data are well-fit by the model ($< 2\sigma$ residuals), except for the wavelength region past 12μm where the pipeline calibration is still work in progress.

measurements from the MIRI data.

K band flux ratio from GRAVITY

To further constrain the atmospheric models, we fit the K band (2.025 – 2.15 μm) flux ratio ($K_{\mathrm{B}b}/K_{\mathrm{B}a}$) of 0.50 ± 0.03 between Gliese 229Ba and Bb measured by GRAVITY (J. W. Xuan et al., 2024b). To do so, we integrate the model spectra for each brown dwarf from 2.025 – 2.15 μm and compute the model flux ratio between Bb and Ba. In summary, the joint likelihood is

$$ln\mathcal{L} = -\frac{1}{2}(\chi^2_{MIRI} + \chi^2_{K_{\mathrm{B}b}/K_{\mathrm{B}a}}) \tag{6.5}$$

Nested sampling

To sample the posteriors, we use the nested sampling package `dynesty` (Speagle, 2020). We adopt 1000 live points and stop sampling when the estimated contribution of the remaining prior volume to the total evidence is $< 1\%$.

6.4 Results

Here, we discuss the key results of our spectral fits. We focus on the results of the fiducial model, i.e. the binary brown dwarf model that assumes the same abundances for Gliese 229 Ba and Bb. The best-fit fiducial model is shown in Fig. 6.2, and the retrieved parameters are listed in Table 6.2.

The exquisite spectro-photometric precision of MIRI spectrum produces very small uncertainties for most parameters, even after including the error inflation term in our fits. In all cases, the 68% confidence intervals of the posterior estimates are smaller than the grid spacing of the model parameters. To be conservative, we report the 95% confidence intervals for all parameters in this work. Grid model fits yielding small uncertainties have been observed in previous work (e.g. Z. Zhang et al., 2021b; Petrus et al., 2024), and half the grid spacing could be a more conservative estimate of the model fitting uncertainties. In the relevant parameter space of Elf Owl we are using, half the grid spacing would correspond to uncertainties of 25 K for $T_{\rm eff}$, 0.125 dex for $\log g$, 0.11 for C/O, 0.25 dex for [M/H], and 1 dex for $\log K_{zz}$.

In reality, other sources of uncertainties could also be important, such as those arising from model or data systematics. From inter-comparing substellar model grids, Lueber et al. (2023) showed that different models disagree strongly on the inferred surface gravity for the same brown dwarf, while Sanghi et al. (2023) highlight issues with the BT-Settl and ATMO 2020 atmospheric models (Allard et al., 2012; Phillips et al., 2020) in yielding accurate $T_{\rm eff}$ at the M/L transition and for L dwarfs. For Gliese 229 Bab, our precise knowledge of their dynamical masses significantly benefits the spectral fits in this regard. For high-contrast companions, other sources of error include correlated noise from the wavelength-dependence of the stellar PSF (e.g. Greco et al., 2016; J. W. Xuan et al., 2022; Nasedkin et al., 2023).

Resolving power and wavelength correction

We include the parameters for resolving power and wavelength correction (§ 6.3) in an initial single brown dwarf fit. The parameters are well-constrained, and we subsequently adopt the best-fit values for these parameters in our final binary fit. We tested that freely fitting for these nuisance parameters in the binary brown dwarf model does not affect the results of the binary model.

Our retrieved resolving power as a function of wavelength is shown in Fig. 6.9, and quantitatively agrees with an R that is set by the size of the diffraction-limited PSF

(Beiler et al., 2023). Accounting for the quadratic wavelength correction visually improves the fit for several absorption features (see Fig. 6.10) and is statistically favored at the 13σ level. This suggests that there is room for additional improvements to the default MIRI LRS wavelength solution from the JWST pipeline.

Bulk properties

We find $T_{\rm eff} = 900^{+78}_{-29}$ K, $\log g = 5.15^{+0.15}_{-0.04}$, $R = 0.81^{+0.05}_{-0.12}$ $R_{\rm Jup}$ for the primary brown dwarf, Ba, and $T_{\rm eff} = 775^{+20}_{-33}$ K, $\log g = 5.07^{+0.04}_{-0.11}$, $R = 0.85^{+0.12}_{-0.05}$ $R_{\rm Jup}$ for the secondary brown dwarf, Bb (2σ uncertainties, see Fig. 6.8). We note that these posteriors show long tails which result from covariances between the parameters. The radius and $T_{\rm eff}$ of Ba and Bb are correlated; for example, a larger radius of Ba correlates with a smaller radius for Bb to match the total flux. This correlation between radius also explains the correlation between $\log g$ of each brown dwarfs. Overall, our measured values for $T_{\rm eff}$, $\log g$, and radius are consistent at the 1σ level with values from J. W. Xuan et al. (2024b), who derived bulk properties using ATMO 2020 evolutionary tracks based on the total luminosity and K band flux ratio of the binary. Upcoming medium-resolution ($R \approx 2000 - 4000$) JWST/NIRSpec spectroscopy from $1 - 5$ μm (GO3762) should further improve constraints on the bulk properties for Gliese 229 Ba and Bb.

Bolometric luminosity and flux ratio

We estimate the bolometric luminosity of Gliese 229 Ba and Bb from our model fits using the measured $T_{\rm eff}$ and radii of each component. We find $\log(L_{\rm bol}/L_\odot) = -5.40 \pm 0.01$ for Ba, and $\log(L_{\rm bol}/L_\odot) = -5.60 \pm 0.03$ for Bb. By summing up the component $L_{\rm bol}$, we estimate the total luminosity of the combined source to be $\log(L_{\rm bol}/L_\odot) = -5.19 \pm 0.01$, consistent with the value of -5.21 ± 0.05 estimated using spectro-photometry < 5 μm by Filippazzo et al. (2015). Therefore, we confirm that the under-luminosity problem of Gliese 229B as a single source is resolved by the binary model.

C/O, metallicity, and vertical diffusion parameter

We provide updated abundance measurements for Gliese 229Bab. From our fiducial model which assumes the same abundances for the two brown dwarfs (Table 6.2), we find $\mathrm{C}/O = 0.65 \pm 0.05$ and $[M/H] = 0.00^{+0.04}_{-0.03}$ (2σ statistical errors). Alternatively, in our model with distinct C/O and [M/H] values for each brown dwarf, we find $\mathrm{C}/O_{Ba} = 0.54^{+0.23}_{-0.14}$ and $\mathrm{C}/O_{Bb} = 0.82^{+0.29}_{-0.31}$, $[M/H]_{Ba} = 0.07^{+0.35}_{-0.18}$ and $[M/H]_{Bb} =$

Table 6.2: Stellar abundances and results of Elf Owl fits

Parameter	Value
Gliese 229 A	
C/O[a]	0.68 ± 0.12
[M/H][a]	-0.02 ± 0.06
Binary brown dwarf model (same abundances)	
C/O	0.65 ± 0.05
[M/H]	$0.00^{+0.04}_{-0.03}$
$T_{\rm eff\,1}$ (K)	900^{+78}_{-29}
$T_{\rm eff\,2}$ (K)	775^{+20}_{-33}
$\log g_1$	$5.15^{+0.15}_{-0.04}$
$\log g_2$	$5.07^{+0.04}_{-0.11}$
$\log K_{zz,1}$	$3.7^{+1.3}_{-1.4}$
$\log K_{zz,2}$	$4.0^{+2.2}_{-1.4}$
R_1 (R_J)	$0.81^{+0.05}_{-0.12}$
R_2 (R_J)	$0.85^{+0.12}_{-0.05}$
$\log(L/L_\odot)$[b]	-5.19 ± 0.01
$\log(L/L_\odot)_1$	-5.40 ± 0.01
$\log(L/L_\odot)_2$	-5.60 ± 0.03
Single brown dwarf model	
C/O	0.65 ± 0.05
[M/H]	-0.02 ± 0.04
$T_{\rm eff}$ (K)	840 ± 9
$\log g$	4.92 ± 0.01
$\log K_{zz}$	3.8 ± 0.3
R (R_J)	1.165 ± 0.015
$\log(L/L_\odot)$	-5.19 ± 0.01

We list the median and 95% credible interval with equal probability above and below the median for parameters derived in this work. These uncertainties only account for statistical error. $_1$ refers to the primary brown dwarf, Ba, and $_2$ refers to the secondary brown dwarf, Bb. (a) The stellar metallicity is computed from references listed in § 6.4. The stellar C/O is from Nakajima et al. (2015), and its uncertainty is 1σ. (b) The luminosities are computed from the measured $T_{\rm eff}$ and radii from our spectral fits and the Stefan-Boltzmann Law.

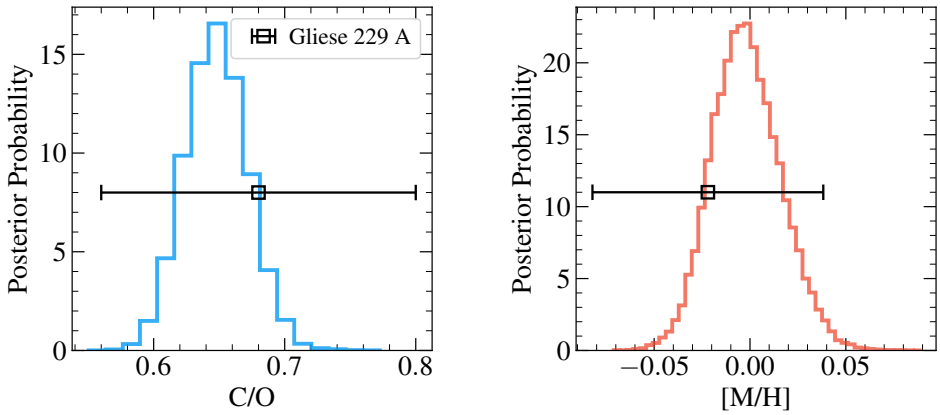

Figure 6.3: Histograms show the posteriors for C/O and [M/H] from our Sonora Elf Owl fits to Gliese 229Bab. The error bars show the measured abundances for Gliese 229A from the literature, whose sources in given in § 6.4. The abundances of Bab and A are consistent at the $< 1\sigma$ level, demonstrating the power of JWST/MIRI LRS in making robust abundance measurements.

$-0.07^{+0.23}_{-0.26}$ (2σ) for the two brown dwarfs (Table 6.3). These values are consistent at the 1.5σ and 1σ levels between Ba and Bb, justifying our assumption of fitting a single set of abundances for the two brown dwarfs. Furthermore, we note that the fiducial model is weakly favored over the model with distinct abundances for Ba and Bb, with log Bayes factor of 1.1 (or 2σ preference).

We note that our reported C/O represents the global or bulk C/O in the atmosphere, as Elf Owl models are parameterized by the global C/O. Therefore, no correction to account for oxygen that is lost to refractory cloud condensation (e.g. J. W. Xuan et al., 2022; Calamari et al., 2024) is needed. The M1V star Gliese 229 A has a C/O measurement from Nakajima et al. (2015), who used Gemini/IGRINS spectroscopy in H and K bands to derive $C/O = 0.68 \pm 0.12$ for the star, which is slightly higher, but within 1σ of the solar C/O of 0.59 ± 0.08 from Asplund et al. (2021). There are numerous metallicity measurements for Gliese 229 A that broadly agree on a near-solar metallicity. Synthesizing the more recent studies (Marfil et al., 2021; Rice et al., 2020; Gaidos et al., 2014; Hojjatpanah et al., 2019; Hojjatpanah et al., 2020; Maldonado et al., 2020; Schweitzer et al., 2019; Neves et al., 2013; Kuznetsov et al., 2019), we adopt [M/H] $= -0.02 \pm 0.06$ for the star.[2] Therefore, our values for C/O and [M/H] for Gliese 229Bab are fully consistent with those of its host star (Fig. 6.3). The chemical homogeneity between Gliese 229 A and Gliese 229Bab

[2]Specifically, we take the weighted average of measurements from these studies and use the standard deviation of the different values as the uncertainty.

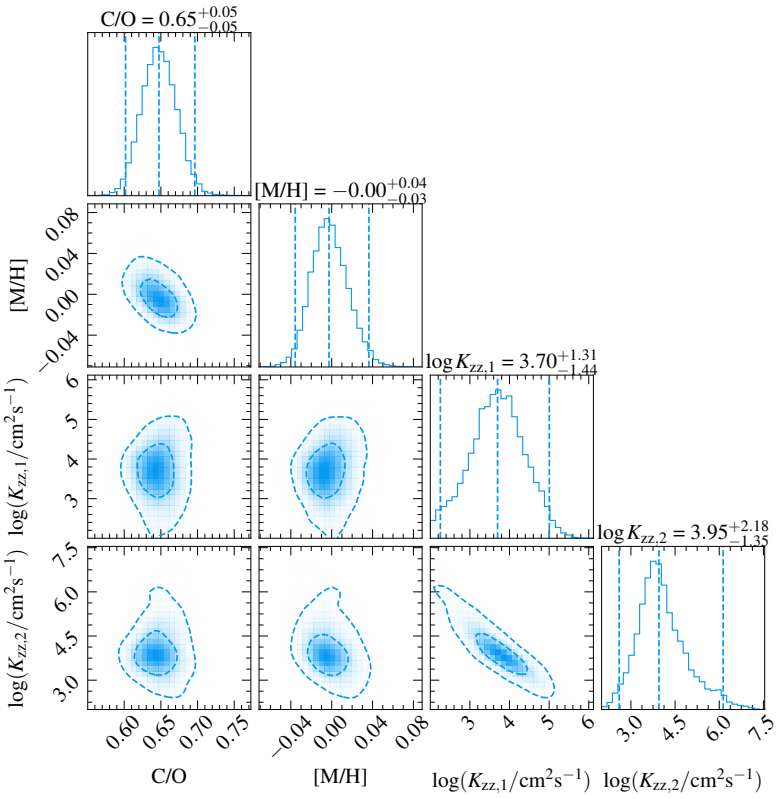

Figure 6.4: Joint posterior distributions for C/O, [M/H], and log K_{zz} for each brown dwarf from the binary model that assumes the same abundances for Ba and Bb. The dashed lines on the 1D histograms show 95% confidence intervals, while dashed lines on the 2D histograms represent 1σ and 2σ contours.

is consistent with expectations from formation via gravitational disk instability or molecular cloud fragmentation. We discuss our new abundance measurements in light of previous studies § 6.5.

The strong absorption features of NH_3, H_2O, and CH_4 in our data provide constraints on the vertical diffusion parameter K_{zz}. By changing the K_{zz} in otherwise identical models, we observe that higher K_{zz} values quench CO and NH_3 at deeper pressures where their abundances are higher, resulting in stronger absorption features for these molecules with higher K_{zz}. For the atmospheric conditions of Gliese 229 Ba and Bb, the CO volume-mixing ratio in particular changes strongly with different K_{zz} (a factor of $\approx 3-4$ increase from log K_{zz} = 2.0 to log K_{zz} = 4.0), which the bluest part (4.75 – 5.0 μm) of the MIRI LRS data are sensitive to.

From our fits, we find clear evidence of disequilibrium chemistry, and measure nearly identical values of K_{zz} for the two brown dwarfs, $\log(K_{zz,1}/\mathrm{cm^2s^{-1}}) = 3.7^{+1.3}_{-1.4}$ and $\log(K_{zz,2}/\mathrm{cm^2s^{-1}}) = 4.0^{+2.2}_{-1.4}$. These values are generally in line with those found

for isolated brown dwarfs of similar $T_{\rm eff}$ in Mukherjee et al. (2024).

Single brown dwarf fits

As a test, we additionally fit the MIRI LRS data using a single brown dwarf model, whose results are included in Table 6.2. Interestingly, we obtain nearly the same abundances from the single brown dwarf model as the binary model, which suggests the binarity of Gliese 229Bab is not confounding abundance measurements for our MIRI LRS data. This is likely caused by the low-resolution of MIRI LRS, and the high degree of spectral similarity in the mid-infrared between the two brown dwarfs (see Fig. 6.5). While the binary brown dwarf fit yields slightly lower reduced χ^2 compared to the single fit (1.21 v.s. 1.22), the single brown dwarf fit is statistically favored due to its lower number of parameters, with a log Bayes factor of 4.5 (or 3.5σ preference). This means the MIRI LRS data alone would have been insufficient to prove that Gliese 229B is a binary.

The single brown dwarf fit yields $T_{\rm eff} = 840 \pm 20\,K$, which is in between the measured $T_{\rm eff}$ of Ba and Bb from the binary model. The radius from the single brown dwarf fit is inflated to $R = 1.17 \pm 0.02\ R_{\rm Jup}$, which is unusually large for a single object of 71.4 $M_{\rm Jup}$ with a field age and another telltale sign of the binary nature of Gliese 229Bab (see also Howe et al. 2022; Calamari et al. 2022).

6.5 Discussion

Recently, several studies have noted a trend of super-solar C/O ratios for brown dwarfs (both isolated and bound) from retrieval analyses (e.g. Calamari et al., 2022; Zalesky et al., 2022). For brown dwarfs orbiting stars, the stellar abundances are generally similar to the Sun, which has C/O= 0.59 ± 0.08 (Asplund et al., 2021). Nearby field brown dwarfs in the solar neighborhood are also expected to have broadly solar compositions. This makes the inferred atmospheric C/O of the brown dwarfs, which go up to 1.5, anomalously high in these studies. For Gliese 229B, two independent retrieval studies have found atmospheric $C/O \approx 1.1$ even after accounting for missing oxygen sequestered in condensate clouds (Calamari et al., 2022; Howe et al., 2022). These values are approximately 3σ higher than the stellar C/O of 0.68 ± 0.12. Under the assumption that Ba and Bb have the same abundances, our updated measurements of $C/O = 0.65 \pm 0.05$ and $[M/H] = 0.00^{+0.04}_{-0.03}$ for Gliese 229Bab are fully consistent with the abundances of the host star, and unaffected by binarity (§ 6.4). Alternatively, if we fit two distinct sets of C/O and [M/H] for each brown dwarf, we also obtain values consistent with the stellar abundances at

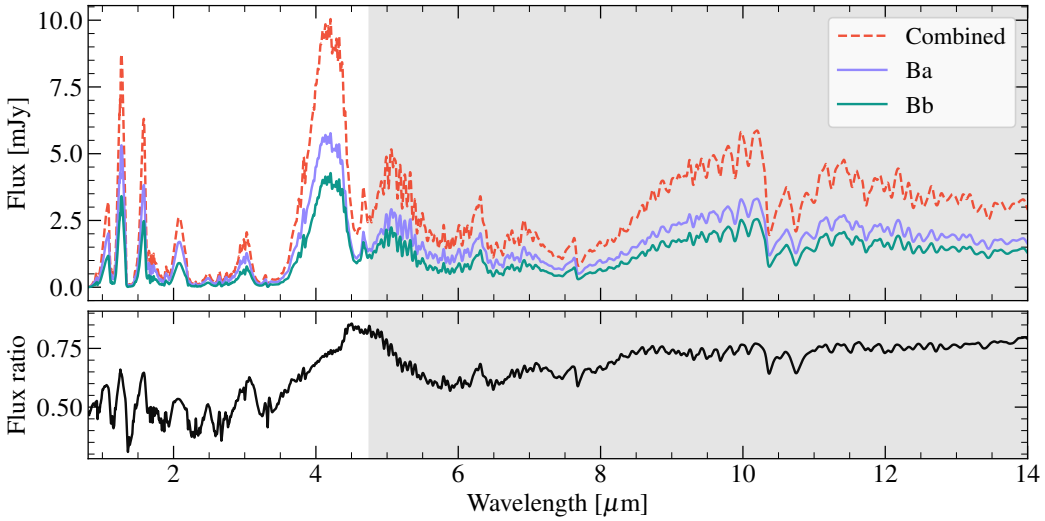

Figure 6.5: Top panel: the best-fit combined (red dashdot) and component models (light purple and teal) from the binary brown dwarf fit. The models are Gaussian-convolved using constant spectral resolution of 200 for illustration purposes. The shaded grey area indicates the wavelength range covered by the MIRI LRS data. Bottom panel: the computed flux ratio (Bb/Ba) from the best-fit models above. In general, the flux ratio in the near-infrared is lower and shows more structure between the two components.

$< 1\sigma$ level (see Table 6.3). From our fits, we predict that near-infrared data is more strongly affected by binarity (see Fig. 6.5), which could potentially bias previous abundance measurements for this particular object. Future work modeling near-infrared spectroscopy of Gliese 229Bab with two-component models will be needed to examine this hypothesis further.

Alternative explanations are still required for other brown dwarfs with high C/O measurements, the vast majority of which are not expected to be unresolved binaries based on the low binary fraction in the substellar regime (Fontanive et al., 2018). These explanations could lie in data systematics, modeling issues, or perhaps both (Calamari et al., 2022). For instance, models could be under-estimating the oxygen abundance. This problem is particularly pertinent for late T dwarfs, which are expected to have silicate clouds below their photospheres. However, quantitatively, Calamari et al. (2024) found that sequestering oxygen in clouds is insufficient in reconciling the large number of observations that find atmospheric C/O$>$ 0.8 for brown dwarfs.

Another potential culprit in the modeling is the use of free chemistry retrievals that assume vertically constant abundances for all species. T dwarfs are known to be

in strong chemical disequilibrium, an effect which is self-consistently accounted for in Sonora Elf Owl with the K_{zz} parameter. In addition to free retrievals, it would be informative to run retrievals using chemical equilibrium models along with quenching (Zahnle et al., 2014) to account for vertically-varying abundances and vertical mixing. This approach has been adopted in many studies of directly imaged planets and brown dwarf companions (e.g. P. Mollière et al., 2020; Y. Zhang et al., 2021b; J. W. Xuan et al., 2022; Inglis et al., 2024), and has generally produced C/O measurements that match the solar or stellar values. Moreover, we demonstrate in this work that the Sonora Elf Owl provides excellent fits to high-quality mid-infrared JWST data for brown dwarfs. This motivates the continued use of forward model fits, in addition to retrievals, in interpreting the atmospheres of brown dwarfs and exoplanets.

There could also be unknown systematics on the data side. It is worth noting that elevated C/O measurements in the literature have almost exclusively come from low-resolution ($R \sim 100$) near-infrared spectroscopy from $\approx 1 - 2.5$ μm. There are known challenges with modeling spectra at these wavelengths, such as theoretical uncertainties in modeling the alkali line wings in the J band (Oreshenko et al., 2020; E. C. Gonzales et al., 2020b), and the increasing impact of cloud opacity at the bluest wavelength. For ground-based observations, it is often necessary to include flux scaling factors between data taken at different epochs and with different instruments. However, because these scaling factors are not known a priori, the results can vary significantly depending on whether scaling factors are included or how priors on these factors are defined (e.g. J. W. Xuan et al., 2022; Z. Zhang et al., 2023).

6.6 Summary

In this work, we present an atmospheric analysis of the nearby brown dwarf binary Gliese 229BaBb using MIRI/LRS spectroscopy ($4.75 - 14$ μm). Using Sonora Elf Owl models, we obtain excellent fits to the data (reduced $\chi^2 \approx 1.2$). We infer the bulk properties of each brown dwarf. Assuming the two brown dwarfs share the same abundances, we find $C/O = 0.65 \pm 0.05$ and $[M/H] = 0.00^{+0.04}_{-0.03}$ (2σ credible intervals), which are fully consistent with the stellar values (Fig. 6.3). We tested an alternative model with different abundances for each brown dwarf, and found this model also yields chemical similarity between the two brown dwarfs and their star.

We find vertical diffusion coefficients of $\log K_{zz} \approx 4.0$ for both brown dwarfs, in line with $\log K_{zz}$ measurements for field brown dwarfs of similar $T_{\rm eff}$ (Mukherjee

et al., 2024). Finally, we provide luminosity measurements for both brown dwarfs, and confirm that the total luminosity of the brown dwarf binary ($\log(L_{\rm bol}/L_\odot) = -5.19 \pm 0.01$) is anomalously high for a single object given the measured dynamical mass.

We discuss our C/O and metallicity measurements in light of previous studies which report anomalously high C/O values for late T dwarfs (e.g. Zalesky et al., 2022), including two retrieval studies on Gliese 229B (Calamari et al., 2022; Howe et al., 2022) before the object was resolved into a binary by VLTI/GRAVITY and VLT/CRIRES+ (J. W. Xuan et al., 2024b). Interestingly, the binarity of Gliese 229Bab does not affect our abundance measurements, as an alternative single brown dwarf model yields the same results. This is potentially due to the very similar $T_{\rm eff}$ ($\approx$ 900 K v.s. $\approx$ 780 K) of two brown dwarfs. Additional work is required to investigate potential issues with modeling archival near-infrared spectra of T dwarfs, which could be affected by data systematics, modeling uncertainties, or both. The exquisite quality and wavelength coverage of JWST spectroscopy is revolutionizing the data quality, allowing us to perform the most stringent tests of atmospheric and evolutionary models.

6.7 Acknowledgments

J.X. thanks Samuel Beiler for discussions about MIRI LRS, Dino Hsu for discussions about the literature of brown dwarf binaries, and Rebecca Oppenheimer for reading an early draft of this paper. J.X. is supported by the NASA Future Investigators in NASA Earth and Space Science and Technology (FINESST) award #80NSSC23K1434 and the NASA JWST grant JWST-GO-03762.003-A. Based on observations with the NASA/ESA/CSA *JWST*, obtained at the Space Telescope Science Institute, which is operated by AURA, Inc., under NASA contract NAS 5-03127. This work benefited from the 2023 Exoplanet Summer Program in the Other Worlds Laboratory (OWL) at the University of California, Santa Cruz, a program funded by the Heising-Simons Foundation and NASA. The data presented in this article were obtained from the Mikulski Archive for Space Telescopes (MAST) at the Space Telescope Science Institute.

6.8 Appendix

Custom subtraction of the stellar PSF from the MIRI LRS data

Here, we describe the subtraction of the stellar PSF from the data. We began with reductions through the pipeline's Detector1 and Image2 stages. Unlike in default

pipeline processing we did not subtract the two nods at this point, deferring that step to later. In other words, this reduction output separate `cal.fits` files for each of the two dither positions, which is needed for the forward modeling process below. We then performed an additional step to identify and mask outlier pixels: the image was first high pass filtered, and then outliers were identified as pixels that were $> 7\sigma$ statistical outliers compared to the estimated uncertainty from the pipeline ERR estimate. The identified pixels were then flagged for exclusion in the data quality array of the original (not high pass filtered) image.

To remove stellar contamination, we use a custom code[3] to forward model the off-axis host star PSF using WebbPSF (Perrin et al., 2012; Perrin et al., 2014) and subtract it from the 2D images. The specific version used in this paper can be found in (J. Xuan et al., 2024b).[4] A starting estimate for the position of the (mostly unseen) host star relative to the slit can be obtained using the World Coordinate System (WCS) metadata. To refine that estimate for the precise geometry as observed, including compensation for residual errors in FITS header coordinates[5], we analyze the target acquisition verification image observed in the F560W filter. We fit that using a forward model consisting of the planet as a point source seen within the slit, the wings of the offset host star outside of the slit, and the diffuse thermal sky background. We use nonlinear least squares to optimize the precise position offsets and flux scale factors for the companion and host star (see Fig. 6.6). The best-fit model parameters yield small corrections ($\lesssim$ 0.25 MIRI pixels) compared to the WCS.

This modeling incidentally yields a flux estimate for Gliese 229B in F560W, including correction for slit losses. The measured value is 1.95 ± 0.2 mJy. This measurement is not the main purpose of the forward model code and has not been rigorously validated, so we conservatively report 10% uncertainties for this. Nonetheless the consistency between this F560W photometry and the LRS spectrum at that wavelength range is reassuring.

We then model the host star's PSF wings seen in the dispersed LRS spectral data using that star's inferred coordinates relative to the slit. Using WebbPSF we generate

[3] `https://github.com/mperrin/miri_lrs_fm`

[4] `https://doi.org/10.5281/zenodo.14032760`

[5] Currently, when target acquisition exposures are used onboard to precisely refine the observatory's pointing, the information about the applied pointing correction is not subsequently used by the ground system and pipeline to improve the astrometric calibration of the science data. In other words, TA exposures improve the *accuracy of the actual achieved pointing* seen in image data, but do not currently improve the *accuracy of the FITS header WCS metadata.*

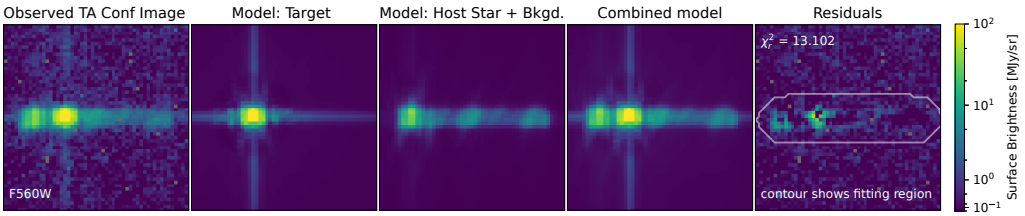

Figure 6.6: Target acquisition confirmation exposure, and forward modeling. Left panel: The observed TA confirmation image, showing the LRS slit with the companion positioned for the first of two nod positions. Second panel: The best-fit PSF model for the science target. Third panel: The best-fit model for the wings of the host star PSF plus the diffuse flat sky background seen through the LRS slit. The host star Gliese 229 itself is out of view, $\sim$ 4.5 arcsec up and to the left from B. For scale, the LRS slit itself is 4.7 arcsec in length. Fourth panel: The combined forward model summing the previous two panels. Right panel: Residuals of the data minus the model. The goodness of fit metric χ^2 is noted, evaluated over the optimization region indicated by the white contour. This is a reasonably good, though imperfect, fit to this complex scene. The geometric parameters refined in this fit were then used for modeling the LRS-dispersed version of this scene.

a series of monochromatic PSFs spanning the LRS spectral range for that offset star. We spatially shifted each monochromatic PSF according to the calibrated spectral dispersion profile of the LRS prism. In other words, we shift each wavelength vertically up or down based on the known wavelength solution of the LRS. We sum those monochromatic PSFs to generate a synthetic 2D spectrum, scaling the flux of each wavelength following a model for the host star's spectral energy distribution. That process yields a 2D forward model of the host star PSF wings as seen through the LRS slit. This process was repeated for the two nod positions in the LRS observation. The resulting models for the dispersed offset stellar PSF in each nod were subtracted from the science data by fitting an overall flux scale factor and a background offset that is allowed to vary linearly with wavelength.

The forward modeling and subtraction of the stellar PSF wings is illustrated in Figure 6.7, which shows that the model provides a clear reduction in the amount of speckle flux in the 2D images. After extracting the 1D spectra (§ 6.2, we find that the two nods agree at the $\approx 2-3\%$ level.

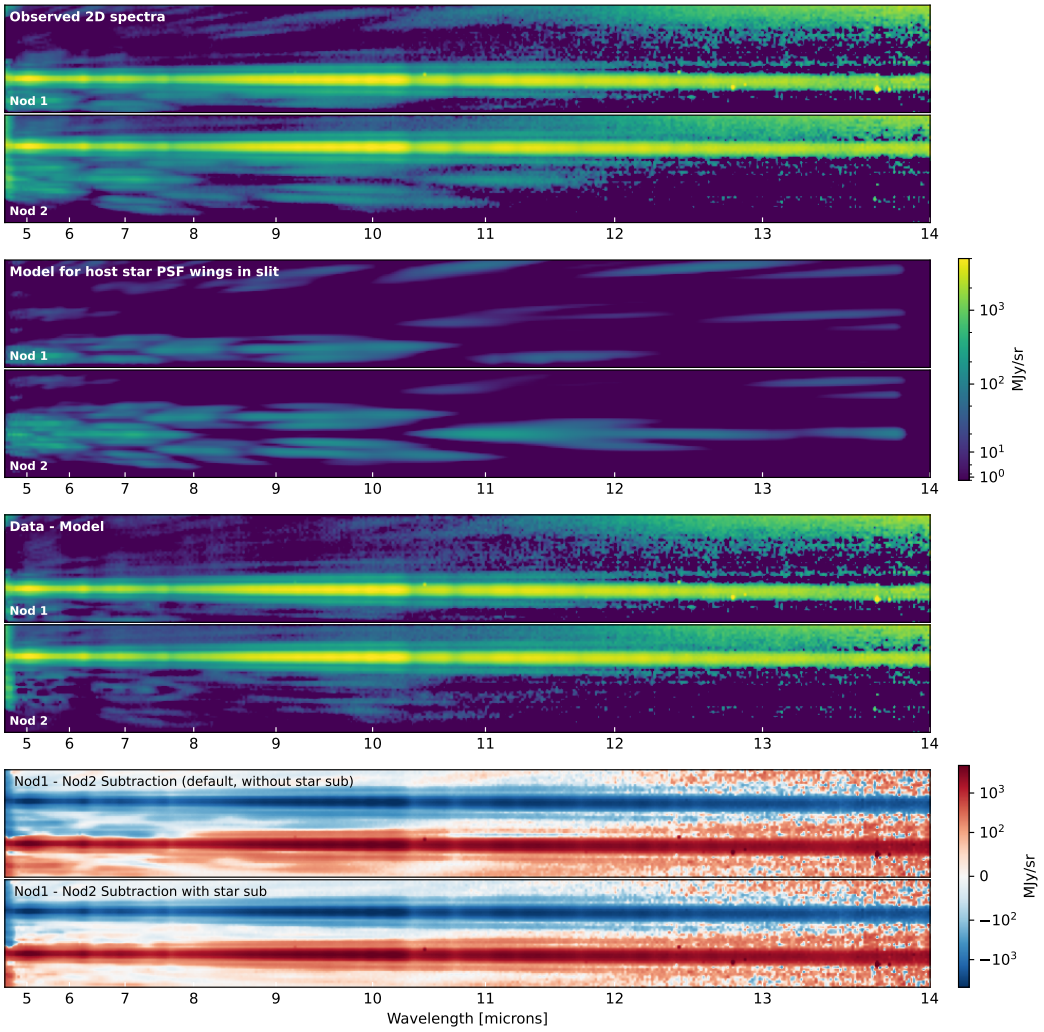

Figure 6.7: Forward modeling of the LRS data to model and subtract the host star light within the slit. *Top 2 panels*: The observed 2D dispersed spectral images for the 2 nod positions, oriented so that the LRS slit direction is vertical and the wavelength dispersion direction is horizontal. These contain both the spectral trace of GJ 229B, and also the dispersed PSF wings of the host star. *Second two panels*: Forward model of the dispersed host star PSF wings for the 2 nod positions, generated using WebbPSF as discussed in the text. *Third two panels*: The observed data minus the PSF models. The contamination from the host star PSF wings is significantly reduced, though there are still smaller residuals due to model imperfections. *Bottom panels*: Comparison of nod subtractions without and with the PSF subtraction. In the default subtraction, residual stellar speckes are visible between the two spectral traces, and indeed contaminating on top of those traces. With the star model subtraction, the clean speckle-free regions between the spectral traces show the reduction in contamination.

Joint posterior distributions from binary model fit

Here, we show the joint posterior distributions of bulk parameters from the binary brown dwarf fit in Fig. 6.8.

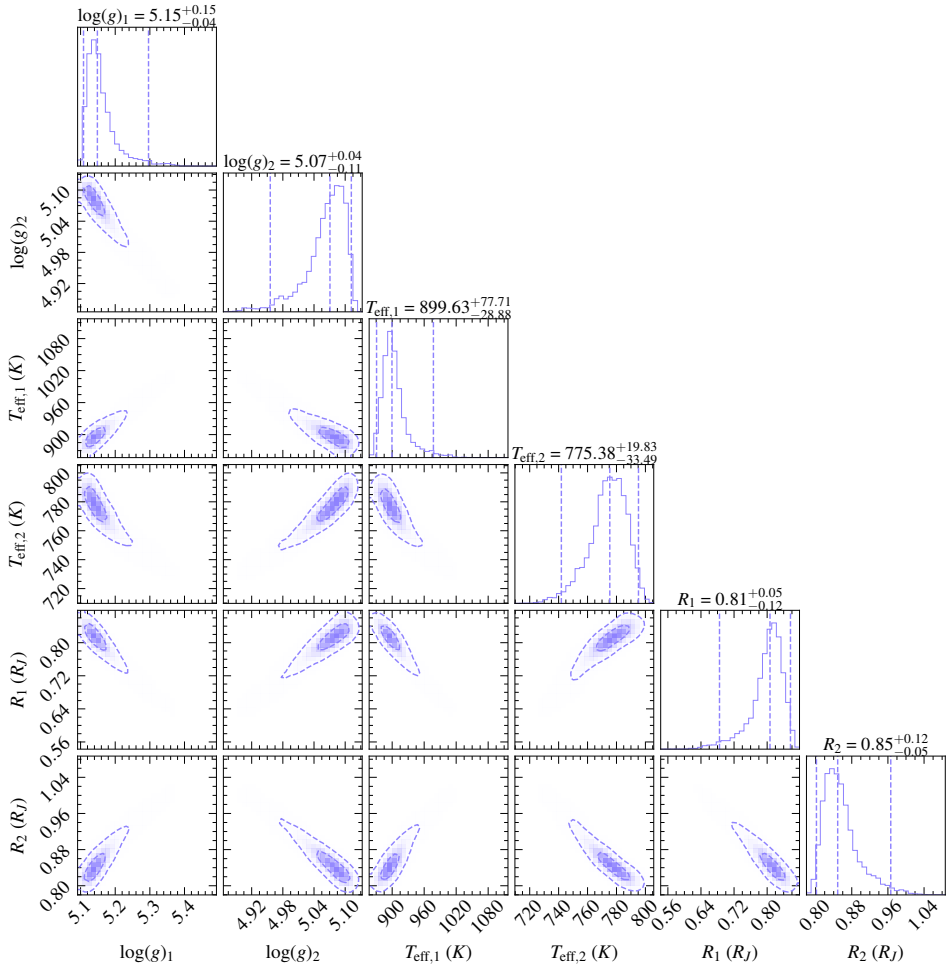

Figure 6.8: Joint posterior distributions for $\log g$, $T_{\rm eff}$, and radius of each brown dwarf from the binary model. The subscript 1 indicates the primary brown dwarf, Gliese 229Ba, and 2 indicates Gliese 229Bb. The dashed lines on the 1D histograms show 95% confidence intervals, while dashed lines on the 2D histograms represent 1σ and 2σ contours.

Retrieved resolving power and wavelength correction

In Fig. 6.9, we show random draws of the inferred R_λ from our single brown dwarf fit. In Fig. 6.10, we compare models and data with and without the wavelength correction of $\lambda' = w_0 + w_1\lambda + w_2\lambda^2$. The best fit parameters are $r = 20.0$ and $r_0 = -73.1$ for the variable resolving power, and $w_0 = -0.0864$, $w_1 = 1.0223$, and $w_2 = -0.0014$ for the wavelength correction. We applied these values in the fits that we report in the paper.

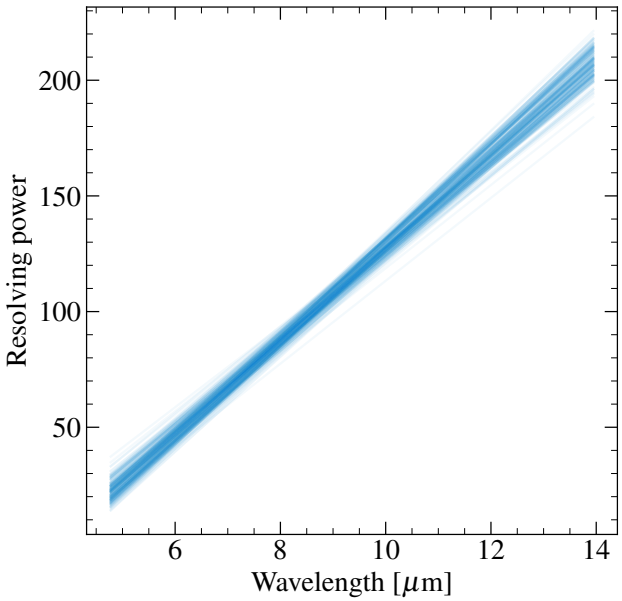

Figure 6.9: 200 random draws of $R\lambda = r_0 + r\lambda$ from an initial single brown dwarf model.

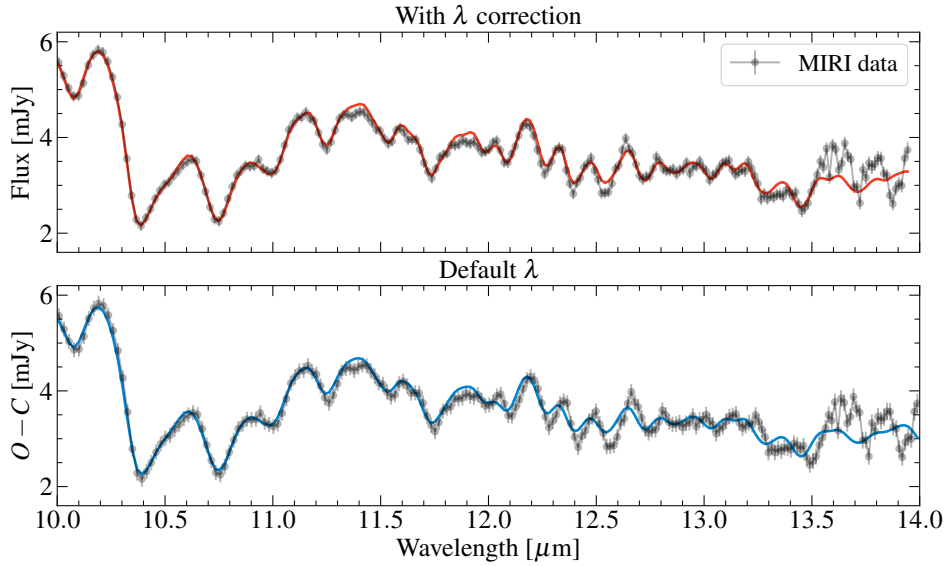

Figure 6.10: Top: the best-fit single brown dwarf model (red) and MIRI data (black) plotted with the corrected wavelength solution, λ'. The error bars are inflated by the best-fit error inflation term b from the model. Bottom: best-fit single model (blue) and MIRI data (black) plotted with the default wavelength values from the pipeline. The effect of the wavelength correction is most significant at wavelengths longward of 10μm, which we show here.

Binary brown dwarf fit with two sets of abundances for Ba and Bb

Here, we provide results of the alternative model, where we fit individual C/O and $[M/H]$ for the two brown dwarfs, along with different $T_{\rm eff}$, $\log g$, radius, and $\log K_{\rm zz}$.

Table 6.3: Results of Elf Owl fit for binary model with different abundances

Parameter	**Value**
Binary brown dwarf model (different abundances)	
$\rm C/O_{Ba}$	$0.54^{+0.23}_{-0.14}$
$\rm C/O_{Bb}$	$0.82^{+0.29}_{-0.31}$
$\rm [M/H]_{Ba}$	$0.07^{+0.35}_{-0.18}$
$\rm [M/H]_{Bb}$	$-0.07^{+0.23}_{-0.26}$
$T_{\rm eff\,1}$ (K)	911^{+65}_{-54}
$T_{\rm eff\,2}$ (K)	765^{+49}_{-32}
$\log g_1$	$5.19^{+0.10}_{-0.07}$
$\log g_2$	$5.03^{+0.06}_{-0.07}$
$\log K_{zz,1}$	3.9 ± 1.5
$\log K_{zz,2}$	$4.1^{+1.9}_{-1.4}$
R_1 ($\rm R_J$)	$0.77^{+0.06}_{-0.08}$
R_2 ($\rm R_J$)	$0.89^{+0.08}_{-0.06}$
$\log(L_{\rm bol}/L_\odot)$	-5.18 ± 0.02
$\log(L_{\rm bol}/L_\odot)_1$	-5.40 ± 0.09
$\log(L_{\rm bol}/L_\odot)_2$	-5.58 ± 0.10

As for Table 6.2, we list 2σ credible intervals with equal probability above and below for median for these parameters.

Chapter 7

CONCLUSIONS

This thesis presents some of the first steps in systematic atmospheric retrievals for directly imaged companions to inform their formation history. The companions studied here have $m > 10\ M_{\rm Jup}$ and $a > 10$ AU (typically dozens to hundreds of AU), and were shown to be chemically homogeneous with their host stars. They likely form as the tail end of star formation processes, including disk instability and cloud fragmentation. In my opinion, a future priority in this field is pushing high- and medium-resolution spectroscopy to lower mass, bona fide planets at smaller orbital distances from their stars. Specifically, we currently have little spectral information for planets with masses and semi-major axes in the intermediate region between transiting hot Jupiters and massive directly imaged companions ($a \sim 1-50$ AU, $m \sim 0.5-10\ M_{\rm Jup}$). This range covers our own Jupiter. It is important to study planets in this intermediate region to quantify how much mixture there might (or might not) be between formation mechanisms. Besides atmospheric compositions, there are also other ways of differentiating between planet-like and star-like formation processes. For example, studies of orbital architectures (e.g. eccentricity, stellar obliquity), and demographics of directly imaged companions have provided useful population-level constraints. All these studies are limited by the small number of directly imaged planets, especially those with masses below $10\ M_{\rm Jup}$, so finding more such planets amenable to orbital and spectral characterization will remain a priority of the field.

Recent technical advances have been and will be improving our ability for direct imaging and spectroscopy of planets between $a \sim 1-50$ AU and $m \sim 0.5-10\ M_{\rm Jup}$. For instance, the transformative sensitivity and stability of *JWST*/NIRSpec at $R \approx 2000-4000$ allows us to spectrally distinguish stellar noise and planet signal at high fidelity and obtain exquisite spectra of faint planets close to their stars (Ruffio et al., 2024). In particular, the $3-5\ \mu$m range of NIRSpec is rich with molecular features from e.g. CO, CO_2, H_2O, CH_4, H_2S, and NH_3, enabling simultaneous measurements of up to four different elemental abundances (C, O, S, and N). Several ongoing JWST programs will start to examine low-mass directly imaged planets at separations $\lesssim 10$ AU.

Several new and upcoming instruments will also significantly benefit our ability to study low-mass planets at high contrast. Keck/HISPEC (Konopacky et al., 2023), an upcoming fiber-fed high-resolution spectrograph ($R \sim 100,000$), will have $\sim 3\times$ higher throughput and spectral resolution than KPIC, enabling the study of the coldest planets such as 51 Eri b ($\sim 2\ M_{\rm Jup}$). The recently commissioned VLTI/GRAVITY+ upgrade is already sensitive to planets as faint as K magnitude of 21, and provides unparalleled power to search for binary brown dwarfs and planets, as demonstrated by Chapter 5. Finally, GRAVITY+ and new high-contrast integral field units including Keck/SCALES (Skemer et al., 2022) and Gemini Planet Imager 2.0 (Chilcote et al., 2022) will search for and characterize upcoming Gaia DR4 planet candidates, yielding a larger sample of imaged planets to study. These planets will be important additions in future studies of orbits, demographics, and atmospheric compositions on a population-level.

Secondly, this thesis provides a breakthrough in the over-massive brown dwarf problem by resolving the first brown dwarf companion, Gliese 229 B, into a pair of brown dwarfs on a 12-day orbit. The combined luminosity of the two brown dwarfs, 34 $M_{\rm Jup}$ and 38 $M_{\rm Jup}$ each, are now fully compatible with substellar evolutionary models. The 12-day period of these two brown dwarfs is remarkably short compared with those of other brown dwarf binaries orbiting stars. The few others that are known have periods of dozens of years. This raises fresh questions about the way in which systems such as Gliese 229 came to be.

The formation process of tight brown dwarf binaries ($a \lesssim 1$ AU) remains highly uncertain, and observations and simulations are both incomplete for binary brown dwarfs with such separations (Burgasser et al., 2007; Fontanive et al., 2018). Because the typical size of initial fragments in a circumstellar disk or molecular cloud can be a few AU or larger, significant dynamical and dissipative processes are required to form tight binary brown dwarf systems like Gliese 229 Bab. The exact processes are unclear, but may involve tidal dissipation from interactions between the accretion disks around the forming objects. For binary brown dwarfs orbiting stars, fragmentation of a massive circumstellar disk is a potential formation route, in which two proto-brown dwarfs fragment in the disk and become bound in a close encounter. However, the frequency and efficiency of such a outcome is unknown, and we would need a larger sample of systems to fully investigate these formation scenarios. In particular, studying the semi-major axis, mass-ratio, eccentricity, and inclination distributions of binary brown dwarfs could provide useful constraints for

various formation models. Binary brown dwarfs in the field show a preference for near-unity mass ratios, which is consistent with the outcome of various hydrodynamical simulations (e.g. Stamatellos et al., 2009; Bate, 2012). However, we may also be missing some of the low mass ratio systems due to instrumental sensitivity limits.

To understand the formation processes of binary brown dwarfs, a closer look at other brown dwarf companions with new instrument capabilities is warranted. This is particularly true for objects such as Gliese 229 B, which exhibit conflicts between observed and theoretically predicted properties. Several other brown dwarf companions show similar discrepancies between dynamical mass and luminosity, smoking guns of binarity. On the other hand, a decent fraction of brown dwarfs are over-luminous for their spectral types (or effective temperatures), or best-fit by two-component blended spectra (e.g. Looper et al., 2008; Bardalez Gagliuffi et al., 2014). These are both indicators of binarity, yet high-resolution imaging has not been able to resolve these into binaries. Future observations with high-resolution spectroscopy and optical interferometry could push the sensitivity towards lower mass ratios and smaller semi-major axes binaries, allowing us to obtain a more complete picture of the population statistics of binary brown dwarfs.

BIBLIOGRAPHY

Ackerman, A. S. and M. S. Marley (Aug. 2001). "Precipitating Condensation Clouds in Substellar Atmospheres". In: *The Astrophysical Journal* 556, pp. 872–884. ISSN: 0004-637X. DOI: 10.1086/321540.

Adams, F. C., S. P. Ruden, and F. H. Shu (Dec. 1989). "Eccentric Gravitational Instabilities in Nearly Keplerian Disks". In: *The Astrophysical Journal* 347, p. 959. DOI: 10.1086/168187.

Agrawal, S. et al. (July 2023). "Detecting Exoplanets Closer to Stars with Moderate Spectral Resolution Integral-field Spectroscopy". In: *The Astronomical Journal* 166.1, 15, p. 15. DOI: 10.3847/1538-3881/acd6a3. arXiv: 2305.10362 [astro-ph.EP].

Alcalá, J. M. et al. (Mar. 2020). "2MASS J15491331-3539118: A new low-mass wide companion of the GQ Lup system". In: *Astronomy and Astrophysics* 635. ISSN: 14320746. DOI: 10.1051/0004-6361/201937309.

Alderson, L. et al. (Feb. 2023). "Early Release Science of the exoplanet WASP-39b with JWST NIRSpec G395H". In: *Nature* 614 (7949), pp. 664–669. ISSN: 14764687. DOI: 10.1038/s41586-022-05591-3.

Allard, F., D. Homeier, and B. Freytag (June 2012). "Models of very-low-mass stars, brown dwarfs and exoplanets". In: *Philosophical Transactions of the Royal Society of London Series A* 370.1968, pp. 2765–2777. DOI: 10.1098/rsta.2011.0269. arXiv: 1112.3591 [astro-ph.SR].

Allard, F. et al. (2001). "The Limiting Effects of Dust in Brown Dwarf Model Atmospheres". In: *The Astrophysical Journal* 556, pp. 357–372. ISSN: 0004-637X. DOI: 10.1086/321547. URL: https://ui.adsabs.harvard.edu/abs/2001ApJ...556..357A%20https://ui.adsabs.harvard.edu/link_gateway/2001ApJ...556..357A/ARTICLE.

Amarsi, A. M., P. E. Nissen, and Á. Skúladóttir (Oct. 2019). "Carbon, Oxygen, and Iron Abundances in Disk and Halo Stars. Implications of 3D Non-LTE Spectral Line Formation". In: *Astronomy and Astrophysics* 630, A104. ISSN: 0004-6361. DOI: 10.1051/0004-6361/201936265.

Anders, F. et al. (Feb. 2022). "Photo-astrometric distances, extinctions, and astrophysical parameters for Gaia EDR3 stars brighter than G = 18.5". In: *Astronomy & Astrophysics* 658, A91, A91. DOI: 10.1051/0004-6361/202142369. arXiv: 2111.01860 [astro-ph.GA].

Apai, D. et al. (May 2013). "HST Spectral Mapping of L/T Transition Brown Dwarfs Reveals Cloud Thickness Variations". In: *The Astrophysical Journal* 768, p. 121. ISSN: 0004-637X. DOI: 10.1088/0004-637X/768/2/121.

Armitage, P. J. and I. A. Bonnell (Feb. 2002). "The brown dwarf desert as a consequence of orbital migration". In: *Monthly Notices of the Royal Astronomical Society* 330.1, pp. L11–L14. DOI: 10.1046/j.1365-8711.2002.05213.x. arXiv: astro-ph/0112001 [astro-ph].

Asplund, M., A. M. Amarsi, and N. Grevesse (Sept. 2021). "The chemical make-up of the Sun: A 2020 vision". In: *Astronomy and Astrophysics* 653. ISSN: 14320746. DOI: 10.1051/0004-6361/202140445.

Asplund, M. et al. (Sept. 2009). "The Chemical Composition of the Sun". en. In: *Annual Review of Astronomy & Astrophysics, vol. 47, Issue 1, pp.481-522* 47.1, p. 481. ISSN: 0066-4146. DOI: 10.1146/annurev.astro.46.060407.145222.

Astropy Collaboration et al. (Aug. 2022). "The Astropy Project: Sustaining and Growing a Community-oriented Open-source Project and the Latest Major Release (v5.0) of the Core Package". In: *The Astrophysical Journal* 935.2, 167, p. 167. DOI: 10.3847/1538-4357/ac7c74. arXiv: 2206.14220 [astro-ph.IM].

August, P. C. et al. (Aug. 2023). "Confirmation of Subsolar Metallicity for WASP-77Ab from JWST Thermal Emission Spectroscopy". In: *The Astrophysical Journal Letters* 953 (2), p. L24. ISSN: 2041-8205. DOI: 10.3847/2041-8213/ace828.

Azzam, A. A. et al. (Aug. 2016). "ExoMol molecular line lists - XVI. The rotation-vibration spectrum of hot H2S". In: *Monthly Notices of the Royal Astronomical Society* 460 (4), pp. 4063–4074. ISSN: 13652966. DOI: 10.1093/mnras/stw1133.

El-Badry, K. (June 2024). "Gaia's binary star renaissance". In: *New Astronomy Reviews* 98, 101694, p. 101694. DOI: 10.1016/j.newar.2024.101694. arXiv: 2403.12146 [astro-ph.SR].

El-Badry, K. et al. (May 2023a). "A red giant orbiting a black hole". In: *Monthly Notices of the Royal Astronomical Society* 521.3, pp. 4323–4348. DOI: 10.1093/mnras/stad799. arXiv: 2302.07880 [astro-ph.SR].

El-Badry, K. et al. (Jan. 2023b). "A Sun-like star orbiting a black hole". In: *Monthly Notices of the Royal Astronomical Society* 518.1, pp. 1057–1085. DOI: 10.1093/mnras/stac3140. arXiv: 2209.06833 [astro-ph.SR].

Balmer, W. O. et al. (Oct. 2023). "VLTI/GRAVITY Observations and Characterization of the Brown Dwarf Companion HD 72946 B". In: *The Astrophysical Journal* 956.2, 99, p. 99. DOI: 10.3847/1538-4357/acf761. arXiv: 2309.04403 [astro-ph.SR].

Balmer, W. O. et al. (Feb. 2024). "VLTI/GRAVITY Provides Evidence the Young, Substellar Companion HD 136164 Ab Formed Like a "Failed Star"". In: *The Astronomical Journal* 167.2, 64, p. 64. DOI: 10.3847/1538-3881/ad1689. arXiv: 2312.08283 [astro-ph.SR].

Baraffe, I. et al. (May 2003). "Evolutionary models for cool brown dwarfs and extrasolar giant planets. The case of HD 209458". en. In: *Astronomy & Astrophysics* 402.2, pp. 701–712. ISSN: 0004-6361, 1432-0746. DOI: 10.1051/0004-6361:20030252. URL: https://www.aanda.org/articles/aa/abs/2003/17/aa3343/aa3343.html (visited on 01/28/2019).

Baraffe, I. et al. (May 2015). "New evolutionary models for pre-main sequence and main sequence low-mass stars down to the hydrogen-burning limit". In: *Astronomy and Astrophysics* 577. ISSN: 14320746. DOI: 10.1051/0004-6361/201425481.

Bardalez Gagliuffi, D. C. et al. (Oct. 2014). "SpeX Spectroscopy of Unresolved Very Low Mass Binaries. II. Identification of 14 Candidate Binaries with Late-M/Early-L and T Dwarf Components". In: *The Astrophysical Journal* 794.2, 143, p. 143. DOI: 10.1088/0004-637X/794/2/143. arXiv: 1408.3089 [astro-ph.SR].

Barman, T. S. et al. (May 2011). "Clouds and Chemistry in the Atmosphere of Extrasolar Planet HR8799b". In: *The Astrophysical Journal* 733.1, 65, p. 65. DOI: 10.1088/0004-637X/733/1/65. arXiv: 1103.3895 [astro-ph.EP].

Barman, T. S. et al. (May 2015). "Simultaneous Detection of Water, Methane, and Carbon Monoxide in the Atmosphere of Exoplanet HR 8799 b". en. In: *The Astrophysical Journal* 804.1, p. 61. ISSN: 0004-637X. DOI: 10.1088/0004-637X/804/1/61. URL: https://doi.org/10.1088%2F0004-637x%2F804%2F1%2F61 (visited on 04/05/2019).

Barrado, D. et al. (Nov. 2023). "15NH3 in the atmosphere of a cool brown dwarf". In: *arXiv e-prints*, arXiv:2311.08054, arXiv:2311.08054. DOI: 10.48550/arXiv.2311.08054. arXiv: 2311.08054 [astro-ph.EP].

Bate, M. R. (Feb. 2012). "Stellar, brown dwarf and multiple star properties from a radiation hydrodynamical simulation of star cluster formation". en. In: *Monthly Notices of the Royal Astronomical Society* 419.4, pp. 3115–3146. ISSN: 0035-8711. DOI: 10.1111/j.1365-2966.2011.19955.x. URL: https://academic.oup.com/mnras/article/419/4/3115/2908052 (visited on 12/26/2018).

Bate, M. R., I. A. Bonnell, and V. Bromm (May 2002). "The formation mechanism of brown dwarfs". en. In: *Monthly Notices of the Royal Astronomical Society* 332.3, pp. L65–L68. ISSN: 0035-8711. DOI: 10.1046/j.1365-8711.2002.05539.x. URL: https://academic.oup.com/mnras/article/332/3/L65/1052962 (visited on 01/06/2019).

Batygin, K. (2018). "On the Terminal Rotation Rates of Giant Planets". en. In: *The Astronomical Journal* 155.4, p. 178. ISSN: 1538-3881. DOI: 10.3847/1538-3881/aab54e. URL: http://stacks.iop.org/1538-3881/155/i=4/a=178 (visited on 12/25/2018).

Batygin, K., P. Bodenheimer, and G. Laughlin (Oct. 2009). "Determination of the Interior Structure of Transiting Planets in Multiple-Planet Systems". In: *The Astrophysical Journal Letters* 704.1, pp. L49–L53. DOI: 10.1088/0004-637X/704/1/L49. arXiv: 0907.5019 [astro-ph.EP].

Bean, J. L. et al. (June 2023). "High atmospheric metal enrichment for a Saturn-mass planet". In: *Nature* 618 (7963), pp. 43–46. ISSN: 14764687. DOI: 10.1038/s41586-023-05984-y.

Beiler, S. A. et al. (July 2023). "The First JWST Spectral Energy Distribution of a Y Dwarf". In: *The Astrophysical Journal Letters* 951.2, L48, p. L48. DOI: 10.3847/2041-8213/ace32c. arXiv: 2306.11807 [astro-ph.SR].

Beiler, S. A. et al. (July 2024). "A Tale of Two Molecules: The Underprediction of CO_2 and Overprediction of PH_3 in Late T and Y Dwarf Atmospheric Models". In: *arXiv e-prints*, arXiv:2407.15950, arXiv:2407.15950. DOI: 10.48550/arXiv.2407.15950. arXiv: 2407.15950 [astro-ph.EP].

Bell, C. P. M., E. E. Mamajek, and T. Naylor (Nov. 2015). "A self-consistent, absolute isochronal age scale for young moving groups in the solar neighbourhood". en. In: *Monthly Notices of the Royal Astronomical Society* 454.1, pp. 593–614. ISSN: 0035-8711. DOI: 10.1093/mnras/stv1981. URL: https://academic.oup.com/mnras/article/454/1/593/1134330 (visited on 07/17/2019).

Bell, T. J. et al. (Nov. 2023). "Methane throughout the atmosphere of the warm exoplanet WASP-80b". In: *Nature* 623.7988, pp. 709–712. DOI: 10.1038/s41586-023-06687-0. arXiv: 2309.04042 [astro-ph.EP].

Benneke, B. and S. Seager (Dec. 2013). "How to Distinguish between Cloudy Mini-Neptunes and Water/Volatile-dominated Super-Earths". In: *The Astrophysical Journal* 778, p. 153. ISSN: 0004-637X. DOI: 10.1088/0004-637X/778/2/153.

Berger, T. A. et al. (June 2020). "The Gaia-Kepler Stellar Properties Catalog. I. Homogeneous Fundamental Properties for 186,301 Kepler Stars". In: *The Astronomical Journal* 159, p. 280. ISSN: 0004-6256. DOI: 10.3847/1538-3881/159/6/280.

Bernath, P. F. (Jan. 2020). "MoLLIST: Molecular Line Lists, Intensities and Spectra". In: *Journal of Quantitative Spectroscopy and Radiative Transfer* 240. ISSN: 00224073. DOI: 10.1016/j.jqsrt.2019.106687.

Best, W. M. J. et al. (July 2017). "The Young L Dwarf 2MASS J11193254-1137466 Is a Planetary-mass Binary". In: *The Astrophysical Journal Letters* 843.1, L4, p. L4. DOI: 10.3847/2041-8213/aa76df. arXiv: 1706.01883 [astro-ph.SR].

Best, W. M. J. et al. (Jan. 2018). "Photometry and Proper Motions of M, L, and T Dwarfs from the Pan-STARRS1 3π Survey". In: *The Astrophysical Journal Supplement Series* 234.1, 1, p. 1. DOI: 10.3847/1538-4365/aa9982. arXiv: 1701.00490 [astro-ph.SR].

Best, W. M. J. et al. (Jan. 2021). "A Volume-limited Sample of Ultracool Dwarfs. I. Construction, Space Density, and a Gap in the L/T Transition". In: *The Astronomical Journal* 161.1, 42, p. 42. DOI: 10.3847/1538-3881/abc893. arXiv: 2010.15853 [astro-ph.SR].

Beuzit, J.-L. et al. (Nov. 2019). "SPHERE: The Exoplanet Imager for the Very Large Telescope". In: *Astronomy and Astrophysics* 631, A155. ISSN: 0004-6361. DOI: 10.1051/0004-6361/201935251.

Biazzo, K. et al. (June 2011). "Elemental abundances of low-mass stars in the young clusters 25 Orionis and λ Orionis". In: *Astronomy & Astrophysics* 530, A19, A19. DOI: 10.1051/0004-6361/201116621. arXiv: 1103.3170 [astro-ph.SR].

Biazzo, K. et al. (Dec. 2012). "Elemental abundances of low-mass stars in nearby young associations: AB Doradus, Carina Near and Ursa Major". In: *Monthly Notices of the Royal Astronomical Society* 427 (4), pp. 2905–2916. ISSN: 13652966. DOI: 10.1111/j.1365-2966.2012.22132.x.

Biazzo, K. et al. (Sept. 2017). "X-shooter spectroscopy of young stellar objects in Lupus: Lithium, iron, and barium elemental abundances". In: *Astronomy & Astrophysics* 605. ISSN: 14320746. DOI: 10.1051/0004-6361/201730850.

Biller, B. A. et al. (Sept. 2010). "The Gemini NICI Planet-finding Campaign: Discovery of a Close Substellar Companion to the Young Debris Disk Star PZ Tel". In: *The Astrophysical Journal Letters* 720.1, pp. L82–L87. DOI: 10.1088/2041-8205/720/1/L82. arXiv: 1007.4808 [astro-ph.SR].

Biller, B. A. et al. (Feb. 2018). "Simultaneous Multiwavelength Variability Characterization of the Free-Floating Planetary-Mass Object PSO J318.5-22". en. In: *The Astronomical Journal* 155.2, p. 95. DOI: 10.3847/1538-3881/aaa5a6.

Biller, B. A. et al. (May 2021). "A High-Contrast Search for Variability in HR 8799bc with VLT-SPHERE". In: *Monthly Notices of the Royal Astronomical Society* 503, pp. 743–767. ISSN: 0035-8711. DOI: 10.1093/mnras/stab202.

Birkby, J. L. (June 2018). "Exoplanet Atmospheres at High Spectral Resolution". In: *arXiv e-prints*, arXiv:1806.04617, arXiv:1806.04617. DOI: 10.48550/arXiv.1806.04617. arXiv: 1806.04617 [astro-ph.EP].

Blackburn, L. et al. (May 2020). "Closure Statistics in Interferometric Data". In: *The Astrophysical Journal* 894.1, 31, p. 31. DOI: 10.3847/1538-4357/ab8469. arXiv: 1910.02062 [astro-ph.IM].

Blake, C. H., D. Charbonneau, and R. J. White (Nov. 2010). "The NIRSPEC Ultracool Dwarf Radial Velocity Survey". In: *The Astrophysical Journal* 723.1, pp. 684–706. DOI: 10.1088/0004-637X/723/1/684. arXiv: 1008.3874 [astro-ph.SR].

Boley, A. C., R. Helled, and M. J. Payne (July 2011). "The heavy-element composition of disk instability planets can range from sub- to super-nebular". In: *Astrophysical Journal* 735 (1). ISSN: 15384357. DOI: 10.1088/0004-637X/735/1/30.

Bonnefoy, M. et al. (Feb. 2014). "A library of near-infrared integral field spectra of young M-L dwarfs". In: *Astronomy & Astrophysics* 562, A127. ISSN: 0004-6361. DOI: 10.1051/0004-6361/201118270. URL: http://adsabs.harvard.edu/abs/2014A%26A...562A.127B (visited on 04/20/2019).

Borucki, W. J., D. Koch, and Kepler Science Team (Oct. 2010). "Kepler Planet Detection Mission: Highlights of the First Results". In: *AAS/Division for Planetary Sciences Meeting Abstracts #42*. AAS/Division for Planetary Sciences Meeting Abstracts, 47.03, p. 47.03.

Boss, A. P. (Jan. 1997). "Giant planet formation by gravitational instability." In: *Science* 276, pp. 1836–1839. DOI: 10.1126/science.276.5320.1836.

Botelho, R. B. et al. (Dec. 2020). "Carbon, isotopic ratio $^{12}C/^{13}C$, and nitrogen in solar twins: constraints for the chemical evolution of the local disc". In: *Monthly Notices of the Royal Astronomical Society* 499.2, pp. 2196–2213. DOI: 10.1093/mnras/staa2917. arXiv: 2009.09003 [astro-ph.SR].

Bouma, L. G., E. K. Palumbo, and L. A. Hillenbrand (Apr. 2023). "The Empirical Limits of Gyrochronology". In: *The Astrophysical Journal Letters* 947 (1), p. L3. ISSN: 2041-8205. DOI: 10.3847/2041-8213/acc589.

Bovy, J. (Jan. 2016). "The Chemical Homogeneity of Open Clusters". In: *The Astrophysical Journal* 817 (1), p. 49. ISSN: 15384357. DOI: 10.3847/0004-637x/817/1/49.

Bowler, B. P. (2016). "Imaging Extrasolar Giant Planets". en. In: *Publications of the Astronomical Society of the Pacific* 128.968, p. 102001. ISSN: 1538-3873. DOI: 10.1088/1538-3873/128/968/102001. URL: http://stacks.iop.org/1538-3873/128/i=968/a=102001 (visited on 09/28/2018).

Bowler, B. P., S. C. Blunt, and E. L. Nielsen (Feb. 2020). "Population-Level Eccentricity Distributions of Imaged Exoplanets and Brown Dwarf Companions: Dynamical Evidence for Distinct Formation Channels". In: *The Astronomical Journal* 159, p. 63. ISSN: 0004-6256. DOI: 10.3847/1538-3881/ab5b11.

Bowler, B. P. and L. A. Hillenbrand (Oct. 2015). "Near-infrared Spectroscopy of 2M0441+2301 AabBab: A Quadruple System Spanning the Stellar to Planetary Mass Regimes". In: *The Astrophysical Journal Letters* 811.2, L30, p. L30. DOI: 10.1088/2041-8205/811/2/L30. arXiv: 1509.01658 [astro-ph.EP].

Bowler, B. P. et al. (Dec. 2011). "A disk around the planetary-mass companion GSC06214-00210b: Clues about the formation of gas giants on wide orbits". In: *Astrophysical Journal* 743 (2). ISSN: 15384357. DOI: 10.1088/0004-637X/743/2/148.

Bowler, B. P. et al. (Aug. 2013). "Planets Around Low-Mass Stars. III. A Young Dusty L Dwarf Companion at the Deuterium-Burning Limit". en. In: *The Astrophysical Journal* 774.1, p. 55. ISSN: 0004-637X. DOI: 10.1088/0004-637X/774/1/55. URL: https://doi.org/10.1088%2F0004-637x%2F774%2F1%2F55 (visited on 07/17/2019).

Bowler, B. P. et al. (Dec. 2014a). "Planets Around Low-Mass Stars (PALMS). IV. The Outer Architecture of M Dwarf Planetary Systems". en. In: *ApJS* 216.1, p. 7. ISSN: 0067-0049. DOI: 10.1088/0067-0049/216/1/7.

Bowler, B. P. et al. (Mar. 2014b). "Spectroscopic Confirmation of Young Planetary-Mass Companions on Wide Orbits". en. In: *The Astrophysical Journal* 784.1, p. 65. ISSN: 0004-637X. DOI: 10.1088/0004-637X/784/1/65. URL: https://doi.org/10.1088%2F0004-637x%2F784%2F1%2F65 (visited on 07/17/2019).

Bowler, B. P. et al. (Oct. 2017). "The Young Substellar Companion ROXs 12 B: Near-infrared Spectrum, System Architecture, and Spin-Orbit Misalignment". In: *The Astronomical Journal* 154, p. 165. ISSN: 0004-6256. DOI: 10.3847/1538-3881/aa88bd. URL: http://adsabs.harvard.edu/abs/2017AJ....154..165B (visited on 10/15/2018).

Bowler, B. P. et al. (June 2021). "The McDonald Accelerating Stars Survey (MASS): Discovery of a Long-period Substellar Companion Orbiting the Old Solar Analog HD 47127". In: *The Astrophysical Journal Letters* 913.2, L26, p. L26. DOI: 10.3847/2041-8213/abfec8. arXiv: 2105.01255 [astro-ph.SR].

Bowler, B. P. et al. (Apr. 2023). "Rotation Periods, Inclinations, and Obliquities of Cool Stars Hosting Directly Imaged Substellar Companions: Spin-Orbit Misalignments Are Common". In: *The Astronomical Journal* 165.4, 164, p. 164. DOI: 10.3847/1538-3881/acbd34. arXiv: 2301.04692 [astro-ph.EP].

Brandt, G. M. et al. (Sept. 2021a). "Htof: A New Open-Source Tool for Analyzing Hipparcos, Gaia, and Future Astrometric Missions". In: *arXiv:2109.06761 [astro-ph]*. arXiv: 2109.06761 [astro-ph].

Brandt, G. M. et al. (Dec. 2021b). "Improved Dynamical Masses for Six Brown Dwarf Companions Using Hipparcos and Gaia EDR3". In: *The Astronomical Journal* 162 (6), p. 301. ISSN: 0004-6256. DOI: 10.3847/1538-3881/ac273e.

Brandt, T. D. (Dec. 2018). "The Hipparcos-Gaia Catalog of Accelerations". en. In: *The Astrophysical Journal Supplement Series* 239.2, p. 31. DOI: 10.3847/1538-4365/aaec06.

– (May 2021a). "The Hipparcos-Gaia Catalog of Accelerations: Gaia EDR3 Edition". In: *arXiv:2105.11662 [astro-ph]*. arXiv: 2105.11662 [astro-ph].

– (May 2021b). "The Hipparcos-Gaia Catalog of Accelerations: Gaia EDR3 Edition". In: *arXiv:2105.11662 [astro-ph]*. arXiv: 2105.11662 [astro-ph].

Brandt, T. D., T. J. Dupuy, and B. P. Bowler (Oct. 2019a). "Precise Dynamical Masses of Directly Imaged Companions from Relative Astrometry, Radial Velocities, and Hipparcos-Gaia DR2 Accelerations". en. In: *The Astronomical Journal* 158.4, p. 140. ISSN: 0004-6256. DOI: 10.3847/1538-3881/ab04a8.

Brandt, T. D. et al. (Oct. 2019b). "A Dynamical Mass of 70 ± 5 Jupiter Masses for Gliese 229B, the First Imaged T Dwarf". In: *arXiv e-prints* 1910. arXiv: 1910.01652.

Brandt, T. D. et al. (May 2021). "Orvara: An Efficient Code to Fit Orbits Using Radial Velocity, Absolute, and/or Relative Astrometry". In: *arXiv:2105.11671 [astro-ph]*. arXiv: 2105.11671 [astro-ph].

Brewer, J. M. et al. (Aug. 2016). "Spectral Properties of Cool Stars: Extended Abundance Analysis of 1,617 Planet-Search Stars". en. In: *ApJS* 225.2, p. 32. ISSN: 0067-0049. DOI: 10.3847/0067-0049/225/2/32.

Brogi, M. and M. R. Line (Mar. 2019). "Retrieving Temperatures and Abundances of Exoplanet Atmospheres with High-resolution Cross-correlation Spectroscopy". In: *The Astronomical Journal* 157.3, 114, p. 114. DOI: 10.3847/1538-3881/aaffd3. arXiv: 1811.01681 [astro-ph.EP].

Brogi, M. et al. (Mar. 2023). "The Roasting Marshmallows Program with IGRINS on Gemini South I: Composition and Climate of the Ultrahot Jupiter WASP-18 b". In: *The Astronomical Journal* 165 (3), p. 91. ISSN: 0004-6256. DOI: 10.3847/1538-3881/acaf5c.

Brooke, J. S. et al. (Jan. 2016). "Line strengths of rovibrational and rotational transitions in the X2 ground state of OH". In: *Journal of Quantitative Spectroscopy and Radiative Transfer* 168, pp. 142–157. ISSN: 00224073. DOI: 10.1016/j.jqsrt.2015.07.021.

Brown, A. G. A. et al. (May 2021). "Gaia Early Data Release 3 - Summary of the Contents and Survey Properties". en. In: *Astronomy & Astrophysics* 649, A1. ISSN: 0004-6361, 1432-0746. DOI: 10.1051/0004-6361/202039657.

Brown-Sevilla, S. B. et al. (May 2023). "Revisiting the atmosphere of the exoplanet 51 Eridani b with VLT/SPHERE". In: *Astronomy & Astrophysics* 673, A98, A98. DOI: 10.1051/0004-6361/202244826. arXiv: 2211.14330 [astro-ph.EP].

Bryan, M. L. et al. (Aug. 2016). "Searching for Scatterers: High-Contrast Imaging of Young Stars Hosting Wide-Separation Planetary-Mass Companions". In: *The Astrophysical Journal* 827, p. 100. ISSN: 0004-637X. DOI: 10.3847/0004-637X/827/2/100. URL: http://adsabs.harvard.edu/abs/2016ApJ...827..100B (visited on 10/15/2018).

Bryan, M. L. et al. (Feb. 2018). "Constraints on the spin evolution of young planetary-mass companions". En. In: *Nature* 2.2, p. 138. ISSN: 2397-3366. DOI: 10.1038/s41550-017-0325-8. URL: https://www.nature.com/articles/s41550-017-0325-8 (visited on 12/26/2018).

Bryan, M. L. et al. (Dec. 2020a). "As the Worlds Turn: Constraining Spin Evolution in the Planetary-mass Regime". In: *The Astrophysical Journal* 905, p. 37. ISSN: 0004-637X. DOI: 10.3847/1538-4357/abc0ef.

Bryan, M. L. et al. (Mar. 2020b). "Obliquity Constraints on an Extrasolar Planetary-mass Companion". In: *The Astronomical Journal* 159 (4), p. 181. ISSN: 00046256. DOI: 10.3847/1538-3881/ab76c6.

Bryan, M. L. et al. (Mar. 2020c). "Obliquity Constraints on an Extrasolar Planetary-mass Companion". In: *The Astronomical Journal* 159 (4), p. 181. ISSN: 00046256. DOI: 10.3847/1538-3881/ab76c6.

Burgasser, A. J. et al. (Jan. 2007). "Not Alone: Tracing the Origins of Very-Low-Mass Stars and Brown Dwarfs Through Multiplicity Studies". In: *Protostars and Planets V*. Ed. by B. Reipurth, D. Jewitt, and K. Keil, p. 427. DOI: 10.48550/arXiv.astro-ph/0602122. arXiv: astro-ph/0602122 [astro-ph].

Burgasser, A. J. (Jan. 2014). "The SpeX Prism Library: 1000+ Low-Resolution, near-Infrared Spectra of Ultracool M, L, T and Y Dwarfs". In: *ASI Conf. Ser.* 11, pp. 7–16. URL: https://ui.adsabs.harvard.edu/abs/2014ASInC..11...7B/abstract.

Burgasser, A. J., J. D. Kirkpatrick, and P. J. Lowrance (June 2005). "Multiplicity among Widely Separated Brown Dwarf Companions to Nearby Stars: Gliese 337CD". In: *The Astronomical Journal* 129.6, pp. 2849–2855. DOI: 10.1086/430218. arXiv: astro-ph/0503379 [astro-ph].

Burgasser, A. J. et al. (Feb. 2006). "A Unified Near-Infrared Spectral Classification Scheme for T Dwarfs". In: *The Astrophysical Journal* 637.2, pp. 1067–1093. DOI: 10.1086/498563. arXiv: astro-ph/0510090 [astro-ph].

Burgasser, A. J. et al. (Oct. 2012). "Discovery of a Very Low Mass Triple with Late-M and T Dwarf Components: LP 704-48/SDSS J0006-0852AB". In: *The Astrophysical Journal* 757.2, 110, p. 110. DOI: 10.1088/0004-637X/757/2/110. arXiv: 1208.0352 [astro-ph.SR].

Burningham, B. et al. (Sept. 2017). "Retrieval of atmospheric properties of cloudy L dwarfs". en. In: *Monthly Notices of the Royal Astronomical Society* 470.1, pp. 1177–1197. ISSN: 0035-8711. DOI: 10.1093/mnras/stx1246. URL: https://academic.oup.com/mnras/article/470/1/1177/3837820 (visited on 12/26/2018).

Burningham, B. et al. (July 2021). "Cloud Busting: Enstatite and Quartz Clouds in the Atmosphere of 2M2224-0158". In: *Monthly Notices of the Royal Astronomical Society* 506.2, pp. 1944–1961. ISSN: 0035-8711, 1365-2966. DOI: 10.1093/mnras/stab1361. arXiv: 2105.04268.

Burrows, A., D. Sudarsky, and I. Hubeny (Apr. 2006). "L and T Dwarf Models and the L to T Transition". In: *The Astrophysical Journal* 640.2, pp. 1063–1077. DOI: 10.1086/500293. arXiv: astro-ph/0509066 [astro-ph].

Butler, R. P. et al. (June 1996). "Attaining Doppler Precision of 3 M s-1". In: *Publications of the Astronomical Society of the Pacific* 108, p. 500. DOI: 10.1086/133755.

Calahan, J. K., E. A. Bergin, and A. D. Bosman (July 2022). "Water UV-shielding in the Terrestrial Planet-forming Zone: Implications for Oxygen-18 Isotope Anomalies in H218O Infrared Emission and Meteorites". In: *The Astrophysical Journal Letters* 934 (1), p. L14. ISSN: 2041-8205. DOI: 10.3847/2041-8213/ac7e55.

Calamari, E. et al. (Dec. 2022). "An Atmospheric Retrieval of the Brown Dwarf Gliese 229B". In: *The Astrophysical Journal* 940, p. 164. ISSN: 0004-637X. DOI: 10.3847/1538-4357/ac9cc9.

Calamari, E. et al. (Jan. 2024). "Predicting Cloud Conditions in Substellar Mass Objects Using Ultracool Dwarf Companions". In: *arXiv e-prints*, arXiv:2401.11038, arXiv:2401.11038. DOI: 10.48550/arXiv.2401.11038. arXiv: 2401.11038 [astro-ph.SR].

Calissendorff, P. et al. (Apr. 2023). "JWST/NIRCam Discovery of the First Y+Y Brown Dwarf Binary: WISE J033605.05-014350.4". In: *The Astrophysical Journal Letters* 947.2, L30, p. L30. DOI: 10.3847/2041-8213/acc86d. arXiv: 2303.16923 [astro-ph.SR].

Carmichael, T. W. et al. (July 2020). "Two Intermediate-mass Transiting Brown Dwarfs from the TESS Mission". In: *The Astronomical Journal* 160.1, p. 53. ISSN: 1538-3881. DOI: 10.3847/1538-3881/ab9b84.

Carson, J. et al. (Feb. 2013). "Direct imaging discovery of a "sUPER-JUPITER" around the late b-type star kap and". In: *Astrophysical Journal Letters* 763 (2). ISSN: 20418205. DOI: 10.1088/2041-8205/763/2/L32.

Carvalho, A. and C. M. Johns-Krull (May 2023). "A Simple Code for Rotational Broadening of Broad Wavelength Range High-Dispersion Spectra". In: *Research Notes of the AAS* 7.5, p. 91. DOI: 10.3847/2515-5172/acd37e. URL: https://dx.doi.org/10.3847/2515-5172/acd37e.

Chabrier, G. et al. (Feb. 2009). "The mass-radius relationship from solar-type stars to terrestrial planets: a review". In: *15th Cambridge Workshop on Cool Stars, Stellar Systems, and the Sun*. Ed. by E. Stempels. Vol. 1094. American Institute of Physics Conference Series, pp. 102–111. DOI: 10.1063/1.3099078.

Chabrier, G. et al. (Mar. 2023). "Impact of a new H/He equation of state on the evolution of massive brown dwarfs". In: *Astronomy & Astrophysics* 671, A119. ISSN: 0004-6361. DOI: 10.1051/0004-6361/202243832.

Chachan, Y. et al. (Feb. 2023). "Breaking Degeneracies in Formation Histories by Measuring Refractory Content in Gas Giants". In: *The Astrophysical Journal* 943.2, 112, p. 112. DOI: 10.3847/1538-4357/aca614. arXiv: 2211.09080.

Charbonneau, D. et al. (Jan. 2000). "Detection of Planetary Transits Across a Sun-like Star". In: *The Astrophysical Journal Letters* 529.1, pp. L45–L48. DOI: 10.1086/312457. arXiv: astro-ph/9911436 [astro-ph].

Charlot, P. et al. (Dec. 2020). "The third realization of the International Celestial Reference Frame by very long baseline interferometry". In: *Astronomy & Astrophysics* 644, A159, A159. DOI: 10.1051/0004-6361/202038368. arXiv: 2010.13625 [astro-ph.GA].

Chauvin, G. et al. (Aug. 2005). "Giant planet companion to 2MASSW J1207334-393254". en. In: *Astronomy & Astrophysics* 438.2, pp. L25–L28. ISSN: 0004-6361, 1432-0746. DOI: 10.1051/0004-6361:200500116. URL: https://www.aanda.org/articles/aa/abs/2005/29/aahd051/aahd051.html (visited on 07/17/2019).

Cheetham, A. et al. (June 2018). "Direct imaging of an ultracool substellar companion to the exoplanet host star HD 4113 A". In: *Astronomy & Astrophysics* 614, A16, A16. DOI: 10.1051/0004-6361/201630136. arXiv: 1712.05217 [astro-ph.EP].

Chen, M. et al. (June 2022). "Precise Dynamical Masses of eps Indi Ba and Bb: Evidence of Slowed Cooling at the L/T Transition". In: *The Astronomical Journal* 163.6, 288, p. 288. DOI: 10.3847/1538-3881/ac66d2. arXiv: 2205.08077 [astro-ph.SR].

Chilcote, J. et al. (Aug. 2022). "GPI 2.0: upgrade status of the Gemini Planet Imager". In: *Ground-based and Airborne Instrumentation for Astronomy IX*. Ed. by C. J. Evans, J. J. Bryant, and K. Motohara. Vol. 12184. Society of Photo-Optical Instrumentation Engineers (SPIE) Conference Series, 121841T, 121841T. DOI: 10.1117/12.2630159.

Christiaens, V. et al. (Jan. 2023). "VIP: A Python package for high-contrast imaging". In: *The Journal of Open Source Software* 8.81, 4774, p. 4774. DOI: 10.21105/joss.04774.

Claudi, R. U. et al. (July 2008). "SPHERE IFS: The Spectro Differential Imager of the VLT for Exoplanets Search". In: *SPIE Astronomical Telescopes + Instrumentation*. Ed. by I. S. McLean and M. M. Casali. Marseille, France, 70143E. DOI: 10.1117/12.788366.

Coles, P. A., S. N. Yurchenko, and J. Tennyson (Dec. 2019). "ExoMol molecular line lists - XXXV. A rotation-vibration line list for hot ammonia". In: *Monthly Notices of the Royal Astronomical Society* 490 (4), pp. 4481–4488. ISSN: 13652966. DOI: 10.1093/mnras/stz2778.

Coria, D. R. et al. (Sept. 2023). "The Missing Link: Testing Galactic Chemical Evolution Models with the First Multi-isotopic Abundances in Solar Twin Stars". In: *The Astrophysical Journal* 954 (2), p. 121. ISSN: 0004-637X. DOI: 10.3847/1538-4357/acea5f. URL: https://iopscience.iop.org/article/10.3847/1538-4357/acea5f.

Costes, J. C. et al. (Apr. 2024). "Fresh view of the hot brown dwarf HD 984 B through high-resolution spectroscopy". In: *arXiv e-prints*, arXiv:2404.11523, arXiv:2404.11523. DOI: 10.48550/arXiv.2404.11523. arXiv: 2404.11523 [astro-ph.SR].

Crepp, J. R. et al. (Dec. 2016). "The TRENDS High-contrast Imaging Survey. VI. Discovery of a Mass, Age, and Metallicity Benchmark Brown Dwarf". In: *The*

Astrophysical Journal 831, p. 136. ISSN: 0004-637X. DOI: 10.3847/0004-637X/831/2/136.

Crepp, J. R. et al. (Feb. 2018). "GPI Spectroscopy of the Mass, Age, and Metallicity Benchmark Brown Dwarf HD 4747 B". In: *The Astrophysical Journal* 853, p. 192. ISSN: 0004-637X. DOI: 10.3847/1538-4357/aaa2fd.

Cridland, A. J. et al. (Oct. 2020). "Connecting planet formation and astrochemistry: C/Os and N/Os of warm giant planets and Jupiter analogues". In: *Astronomy and Astrophysics* 642. ISSN: 14320746. DOI: 10.1051/0004-6361/202038767.

Cristofari, P. I. et al. (Dec. 2023). "Measuring small-scale magnetic fields of 44 M dwarfs from SPIRou spectra with ZeeTurbo". In: *Monthly Notices of the Royal Astronomical Society* 526.4, pp. 5648–5674. DOI: 10.1093/mnras/stad3144. arXiv: 2310.08386 [astro-ph.SR].

Crossfield, I. J. M. et al. (Jan. 2014). "A Global Cloud Map of the Nearest Known Brown Dwarf". In: *Nature* 505, pp. 654–656. ISSN: 0028-0836. DOI: 10.1038/nature12955.

Crossfield, I. J. M. et al. (Jan. 2019). "Unusual Isotopic Abundances in a Fully Convective Stellar Binary". In: *The Astrophysical Journal* 871 (1), p. L3. ISSN: 20418213. DOI: 10.3847/2041-8213/aaf9b6.

Currie, T. et al. (July 2023a). "Direct Imaging and Spectroscopy of Extrasolar Planets". In: *Protostars and Planets VII*. Ed. by S. Inutsuka et al. Vol. 534. Astronomical Society of the Pacific Conference Series, p. 799. DOI: 10.48550/arXiv.2205.05696. arXiv: 2205.05696 [astro-ph.EP].

Currie, T., A. Burrows, and S. Daemgen (June 2014). "A first-look atmospheric modeling study of the young directly imaged planet-mass companion, ROXS 42Bb". In: *Astrophysical Journal* 787 (2). ISSN: 15384357. DOI: 10.1088/0004-637X/787/2/104.

Currie, T. et al. (Dec. 2018). "SCExAO/CHARIS Near-infrared Direct Imaging, Spectroscopy, and Forward-Modeling of κ And b: A Likely Young, Low-gravity Superjovian Companion". In: *The Astronomical Journal* 156, p. 291. ISSN: 0004-6256. DOI: 10.3847/1538-3881/aae9ea.

Currie, T. et al. (Dec. 2020). "SCExAO/CHARIS Direct Imaging Discovery of a 20 au Separation, Low-mass Ratio Brown Dwarf Companion to an Accelerating Sun-like Star". In: *The Astrophysical Journal Letters* 904.2, L25, p. L25. DOI: 10.3847/2041-8213/abc631. arXiv: 2011.08855 [astro-ph.SR].

Currie, T. et al. (Apr. 2023b). "Direct imaging and astrometric detection of a gas giant planet orbiting an accelerating star". In: *Science* 380.6641, pp. 198–203. DOI: 10.1126/science.abo6192. arXiv: 2212.00034 [astro-ph.EP].

Cushing, M. C. et al. (Sept. 2006). "A Spitzer Infrared Spectrograph Spectral Sequence of M, L, and T Dwarfs". en. In: *The Astrophysical Journal* 648.1, p. 614. ISSN: 0004-637X. DOI: 10.1086/505637.

Cutri, R. M. et al. (June 2003). *2MASS All Sky Catalog of Point Sources.* NASA/IPAC Infrared Science Archive.

Cutri, R. M. et al. (Feb. 2021). "VizieR Online Data Catalog: AllWISE Data Release (Cutri+ 2013)". In: *VizieR Online Data Catalog*, II/328, pp. II/328.

Czesla, S. et al. (June 2019). *PyA: Python astronomy-related packages*. ascl: 1906.010.

D'Orazi, V., K. Biazzo, and S. Randich (Feb. 2011). "Chemical composition of the Taurus-Auriga association". In: *Astronomy & Astrophysics* 526 (13). ISSN: 00046361. DOI: 10.1051/0004-6361/201015616.

Daemgen, S. et al. (May 2017). "Mid-infrared characterization of the planetary-mass companion ROXs 42B b". In: *Astronomy and Astrophysics* 601. ISSN: 14320746. DOI: 10.1051/0004-6361/201629949.

De Rosa, R. J., R. Dawson, and E. L. Nielsen (Aug. 2020). "A significant mutual inclination between the planets within the π Mensae system". In: *Astronomy & Astrophysics* 640, A73, A73. DOI: 10.1051/0004-6361/202038496. arXiv: 2007.08549 [astro-ph.EP].

De Rosa, R. J. et al. (June 2016). "Spectroscopic Characterization of HD 95086 b with the Gemini Planet Imager". In: *The Astrophysical Journal* 824, p. 121. ISSN: 0004-637X. DOI: 10.3847/0004-637X/824/2/121.

De Rosa, R. J. et al. (Apr. 2023). "Direct imaging discovery of a super-Jovian around the young Sun-like star AF Leporis". In: *Astronomy & Astrophysics* 672, A94, A94. DOI: 10.1051/0004-6361/202345877. arXiv: 2302.06332 [astro-ph.EP].

De Silva, G. M. et al. (Jan. 2006). "Chemical Homogeneity in the Hyades". In: *The Astronomical Journal* 131.1, pp. 455–460. DOI: 10.1086/497968. arXiv: astro-ph/0509241 [astro-ph].

Deacon, N. R. et al. (Sept. 2014). "Wide Cool and Ultracool Companions to Nearby Stars from Pan-STARRS 1". In: *The Astrophysical Journal* 792.2, 119, p. 119. DOI: 10.1088/0004-637X/792/2/119. arXiv: 1407.2938 [astro-ph.SR].

Delorme, J.-R. et al. (July 2021). "Keck Planet Imager and Characterizer: A Dedicated Single-Mode Fiber Injection Unit for High-Resolution Exoplanet Spectroscopy". In: *Journal of Astronomical Telescopes, Instruments, and Systems* 7, p. 035006. DOI: 10.1117/1.JATIS.7.3.035006.

Demars, D. et al. (Aug. 2023). "Emission line variability of young 10-30 MJup companions: I. The case of GQ Lup b and GSC 06214-00210 b". In: *Astronomy and Astrophysics* 676. ISSN: 14320746. DOI: 10.1051/0004-6361/202346221.

Do Ó, C. R. et al. (Aug. 2023). "The Orbital Eccentricities of Directly Imaged Companions Using Observable-based Priors: Implications for Population-level Distributions". In: *The Astronomical Journal* 166 (2), p. 48. ISSN: 0004-6256. DOI: 10.3847/1538-3881/acdc9a. URL: https://iopscience.iop.org/article/10.3847/1538-3881/acdc9a.

Dodson-Robinson, S. E. et al. (Dec. 2009). "The Formation Mechanism of Gas Giants on Wide Orbits". In: *The Astrophysical Journal* 707, pp. 79–88. DOI: 10.1088/0004-637X/707/1/79. arXiv: 0909.2662 [astro-ph.EP]. URL: http://adsabs.harvard.edu/abs/2009ApJ...707...79D.

Donati, J. F. et al. (Oct. 2012). "Magnetometry of the classical T Tauri star GQ Lup: Non-stationary dynamos and spin evolution of young Suns". In: *Monthly Notices of the Royal Astronomical Society* 425 (4), pp. 2948–2963. ISSN: 13652966. DOI: 10.1111/j.1365-2966.2012.21482.x.

Dorn, R. J. et al. (June 2014). "CRIRES+: Exploring the Cold Universe at High Spectral Resolution". In: *The Messenger* 156, pp. 7–11.

Dorn, R. J. et al. (Mar. 2023). "CRIRES$^+$ on sky at the ESO Very Large Telescope. Observing the Universe at infrared wavelengths and high spectral resolution". In: *Astronomy & Astrophysics* 671, A24, A24. DOI: 10.1051/0004-6361/202245217. arXiv: 2301.08048 [astro-ph.IM].

Duchêne, G. et al. (Feb. 2023). "A low-mass companion desert among intermediate-mass visual binaries: The scaled-up counterpart to the brown dwarf desert". In: *Monthly Notices of the Royal Astronomical Society* 519 (1), pp. 778–798. ISSN: 13652966. DOI: 10.1093/mnras/stac3527.

Dulick, M. et al. (Sept. 2003). "Line Intensities and Molecular Opacities of the FeH F $^4\Delta_i$-X $^4\Delta_i$ Transition". In: *The Astrophysical Journal* 594.1, pp. 651–663. DOI: 10.1086/376791. arXiv: astro-ph/0305162 [astro-ph].

Dupuy, T. J. and A. L. Kraus (Sept. 2013). "Distances, Luminosities, and Temperatures of the Coldest Known Substellar Objects". In: *Science* 341.6153, pp. 1492–1495. DOI: 10.1126/science.1241917. arXiv: 1309.1422 [astro-ph.SR].

Dupuy, T. J. and M. C. Liu (Aug. 2012). "The Hawaii Infrared Parallax Program. I. Ultracool Binaries and the L/T Transition". In: *The Astrophysical Journal Supplement Series* 201.2, 19, p. 19. DOI: 10.1088/0067-0049/201/2/19. arXiv: 1201.2465 [astro-ph.SR].

– (Aug. 2017). "Individual Dynamical Masses of Ultracool Dwarfs". In: *The Astrophysical Journal Supplement Series* 231 (2), p. 15. ISSN: 00670049. DOI: 10.3847/1538-4365/aa5e4c.

Dupuy, T. J., M. C. Liu, and M. J. Ireland (Feb. 2009). "Dynamical Mass of the Substellar Benchmark Binary HD 130948BC". In: *The Astrophysical Journal* 692.1, pp. 729–752. DOI: 10.1088/0004-637X/692/1/729. arXiv: 0807.2450 [astro-ph].

Dupuy, T. J., M. C. Liu, and M. J. Ireland (Aug. 2014). "New Evidence for a Substellar Luminosity Problem: Dynamical Mass for the Brown Dwarf Binary Gl 417BC". In: *The Astrophysical Journal* 790.2, 133, p. 133. DOI: 10.1088/0004-637X/790/2/133. arXiv: 1406.1184 [astro-ph.SR].

Dupuy, T. J. et al. (Oct. 2010). "Studying the physical diversity of late-M dwarfs with dynamical masses". In: *Astrophysical Journal* 721 (2), pp. 1725–1747. ISSN: 15384357. DOI: 10.1088/0004-637X/721/2/1725.

Echeverri, D. et al. (Aug. 2022). "Phase II of the Keck Planet Imager and characterizer: system-level laboratory characterization and preliminary on-sky commissioning". In: *Ground-based and Airborne Instrumentation for Astronomy IX*. Ed. by C. J. Evans, J. J. Bryant, and K. Motohara. Vol. 12184. Society of Photo-Optical Instrumentation Engineers (SPIE) Conference Series, 121841W.

Echeverri, D. et al. (July 2023). "Vortex fiber nulling for exoplanet observations: implementation and first light". In: *Journal of Astronomical Telescopes, Instruments, and Systems* 9, 035002, p. 035002. DOI: 10.1117/1.JATIS.9.3.035002. arXiv: 2309.06514 [astro-ph.IM].

Echeverri, D. et al. (Apr. 2024). "Vortex Fiber Nulling for Exoplanet Observations: First Direct Detection of M Dwarf Companions around HIP 21543, HIP 94666, and HIP 50319". In: *The Astrophysical Journal Letters* 965.2, L15, p. L15. DOI: 10.3847/2041-8213/ad3619. arXiv: 2403.17295 [astro-ph.EP].

Efroimsky, M. and V. V. Makarov (Mar. 2022). "Tidal Quality of the Hot Jupiter WASP-12b". In: *Universe* 8.4, 211, p. 211. DOI: 10.3390/universe8040211. arXiv: 2111.08273 [astro-ph.EP].

Eisenhauer, F. (July 2019). *GRAVITY+: Towards faint science*. DOI: 10.5281/zenodo.3356274. URL: https://doi.org/10.5281/zenodo.3356274.

Eisenhauer, F. et al. (Mar. 2003). "SINFONI - Integral field spectroscopy at 50 milliarcsecond resolution with the ESO VLT". In: *Instrument Design and Performance for Optical/Infrared Ground-based Telescopes*. Ed. by M. Iye and A. F. M. Moorwood. Vol. 4841. Society of Photo-Optical Instrumentation Engineers (SPIE) Conference Series, pp. 1548–1561. DOI: 10.1117/12.459468. arXiv: astro-ph/0306191 [astro-ph].

Faherty, J. K. et al. (Apr. 2024). "Methane emission from a cool brown dwarf". In: *Nature* 628.8008, pp. 511–514. DOI: 10.1038/s41586-024-07190-w. arXiv: 2404.10977 [astro-ph.SR].

Faramaz, V. et al. (June 2021). "A Detailed Characterization of HR 8799's Debris Disk with ALMA in Band 7". In: *The Astronomical Journal* 161 (6), p. 271. ISSN: 0004-6256. DOI: 10.3847/1538-3881/abf4e0.

Feng, F. et al. (Sept. 2022). "3D Selection of 167 Substellar Companions to Nearby Stars". In: *The Astrophysical Journal Supplement Series* 262 (1), p. 21. ISSN: 0067-0049. DOI: 10.3847/1538-4365/ac7e57.

Filippazzo, J. C. et al. (Sept. 2015). "Fundamental Parameters and Spectral Energy Distributions of Young and Field Age Objects with Masses Spanning the Stellar to Planetary Regime". In: *The Astrophysical Journal* 810.2, 158, p. 158. DOI: 10.1088/0004-637X/810/2/158. arXiv: 1508.01767 [astro-ph.SR].

Finnerty, L. et al. (Aug. 2022). "On-sky performance and lessons learned from the phase I KPIC fiber injection unit". In: *Ground-based and Airborne Instrumentation for Astronomy IX*. Ed. by C. J. Evans, J. J. Bryant, and K. Motohara. Vol. 12184. Society of Photo-Optical Instrumentation Engineers (SPIE) Conference Series, 121844Y, 121844Y. DOI: 10.1117/12.2630276.

Finnerty, L. et al. (July 2023). "Keck Planet Imager and Characterizer Emission Spectroscopy of WASP-33b". In: *The Astronomical Journal* 166 (1), p. 31. ISSN: 0004-6256. DOI: 10.3847/1538-3881/acda91.

Finnerty, L. et al. (Jan. 2024). "Atmospheric Metallicity and C/O of HD 189733 b from High-resolution Spectroscopy". In: *The Astronomical Journal* 167.1, 43, p. 43. DOI: 10.3847/1538-3881/ad1180. arXiv: 2312.00141 [astro-ph.EP].

Fischer, D. A. and J. Valenti (Apr. 2005). "The Planet-Metallicity Correlation". en. In: *The Astrophysical Journal* 622.2, p. 1102. DOI: 10.1086/428383. URL: https://ui.adsabs.harvard.edu/abs/2005ApJ...622.1102F/abstract (visited on 08/03/2019).

Fontanive, C. et al. (Sept. 2018). "Constraining the multiplicity statistics of the coolest brown dwarfs: binary fraction continues to decrease with spectral type". In: *Monthly Notices of the Royal Astronomical Society* 479.2, pp. 2702–2727. DOI: 10.1093/mnras/sty1682. arXiv: 1806.08737 [astro-ph.SR].

Foreman-Mackey, D. et al. (Mar. 2013). "emcee: The MCMC Hammer". In: *Publications of the Astronomical Society of the Pacific* 125, p. 306. ISSN: 0004-6280. DOI: 10.1086/670067. URL: http://adsabs.harvard.edu/abs/2013PASP..125..306F (visited on 04/20/2019).

Forgan, D. and K. Rice (2013). "Towards a population synthesis model of objects formed by self-gravitating disc fragmentation and tidal downsizing". In: *Monthly Notices of the Royal Astronomical Society* 432 (4), pp. 3168–3185. ISSN: 13652966. DOI: 10.1093/mnras/stt672.

Fortney, J. J., R. I. Dawson, and T. D. Komacek (2021). "Hot Jupiters: Origins, Structure, Atmospheres". en. In: *Journal of Geophysical Research: Planets* 126.3, e2020JE006629. ISSN: 2169-9100. DOI: 10.1029/2020JE006629.

Fouesneau, M. et al. (June 2022). "Astrophysical parameters from Gaia DR2, 2MASS, and AllWISE". In: *Astronomy & Astrophysics* 662, A125, A125. DOI: 10.1051/0004-6361/202141828. arXiv: 2201.03252 [astro-ph.GA].

Fouqué, P. et al. (Apr. 2018). "SPIRou Input Catalogue: global properties of 440 M dwarfs observed with ESPaDOnS at CFHT". In: *Monthly Notices of the Royal Astronomical Society* 475.2, pp. 1960–1986. DOI: 10.1093/mnras/stx3246. arXiv: 1712.04490 [astro-ph.SR].

Franson, K. and B. P. Bowler (June 2023a). "Dynamical Mass of the Young Brown Dwarf Companion PZ Tel B". In: *The Astronomical Journal* 165.6, 246, p. 246. DOI: 10.3847/1538-3881/acca18. arXiv: 2304.01302 [astro-ph.SR].

Franson, K. et al. (Feb. 2022). "Dynamical Mass of the Young Substellar Companion HD 984 B". In: *The Astronomical Journal* 163.2, 50, p. 50. DOI: 10.3847/1538-3881/ac35e8. arXiv: 2111.01803 [astro-ph.SR].

Franson, K. et al. (June 2023b). "Astrometric Accelerations as Dynamical Beacons: A Giant Planet Imaged inside the Debris Disk of the Young Star AF Lep". In: *The Astrophysical Journal Letters* 950.2, L19, p. L19. DOI: 10.3847/2041-8213/acd6f6. arXiv: 2302.05420 [astro-ph.EP].

Franson, K. et al. (2023c). "Astrometric Accelerations as Dynamical Beacons: Discovery and Characterization of HIP 21152 B, the First T-dwarf Companion in the Hyades". In: *The Astronomical Journal* 165, p. 39. ISSN: 0004-6256. DOI: 10.3847/1538-3881/aca408. URL: https://ui.adsabs.harvard.edu/abs/2023AJ....165...39F%20https://ui.adsabs.harvard.edu/link_gateway/2023AJ....165...39F/ARTICLE.

Fulton, B. J. and E. A. Petigura (Dec. 2018). "The California-Kepler Survey. VII. Precise Planet Radii Leveraging Gaia DR2 Reveal the Stellar Mass Dependence of the Planet Radius Gap". In: *The Astronomical Journal* 156.6, 264, p. 264. DOI: 10.3847/1538-3881/aae828. arXiv: 1805.01453 [astro-ph.EP].

Fulton, B. J. et al. (May 2021). "California Legacy Survey II. Occurrence of Giant Planets Beyond the Ice Line". In: *arXiv:2105.11584 [astro-ph]*. arXiv: 2105.11584 [astro-ph].

Gaarn, J. et al. (June 2023). "The puzzle of the formation of T8 dwarf Ross 458c". In: *Monthly Notices of the Royal Astronomical Society* 521.4, pp. 5761–5775. DOI: 10.1093/mnras/stad753. arXiv: 2303.16863 [astro-ph.SR].

Gaia Collaboration (May 2022). "VizieR Online Data Catalog: Gaia DR3 Part 1. Main source (Gaia Collaboration, 2022)". In: *VizieR Online Data Catalog*, I/355, pp. I/355. DOI: 10.26093/cds/vizier.1355.

Gaia Collaboration et al. (Aug. 2018). "Gaia Data Release 2. Summary of the Contents and Survey Properties". In: *Astronomy & Astrophysics* 616, A1. ISSN: 0004-6361. DOI: 10.1051/0004-6361/201833051.

Gaia Collaboration et al. (June 2023). "Gaia Data Release 3". In: *Astronomy & Astrophysics* 674, A1. ISSN: 0004-6361. DOI: 10.1051/0004-6361/202243940. URL: https://www.aanda.org/10.1051/0004-6361/202243940.

Gaia Collaboration et al. (June 2024). "Discovery of a dormant 33 solar-mass black hole in pre-release Gaia astrometry". In: *Astronomy & Astrophysics* 686, L2, p. L2. DOI: 10.1051/0004-6361/202449763. arXiv: 2404.10486 [astro-ph.GA].

Gaidos, E. and A. W. Mann (Aug. 2014). "M Dwarf Metallicities and Giant Planet Occurrence: Ironing Out Uncertainties and Systematics". In: *The Astrophysical Journal* 791.1, 54, p. 54. DOI: 10.1088/0004-637X/791/1/54. arXiv: 1406.4071 [astro-ph.EP].

Gaidos, E. et al. (July 2013). "An Understanding of the Shoulder of Giants: Jovian Planets around Late K Dwarf Stars and the Trend with Stellar Mass". In: *The Astrophysical Journal* 771.1, 18, p. 18. DOI: 10.1088/0004-637X/771/1/18. arXiv: 1305.3228 [astro-ph.EP].

Gallenne, A. et al. (July 2015). "Robust high-contrast companion detection from interferometric observations. The CANDID algorithm and an application to six binary Cepheids". In: *Astronomy & Astrophysics* 579, A68, A68. DOI: 10.1051/0004-6361/201525917. arXiv: 1505.02715 [astro-ph.SR].

Gallenne, A. et al. (Apr. 2023). "The Araucaria project: High-precision orbital parallaxes and masses of binary stars. I. VLTI/GRAVITY observations of ten double-lined spectroscopic binaries". In: *Astronomy & Astrophysics* 672, A119, A119. DOI: 10.1051/0004-6361/202245712. arXiv: 2302.12960 [astro-ph.SR].

Galli, P. A. et al. (Nov. 2020). "Lupus DANCe: Census of stars and 6D structure with Gaia -DR2 data". In: *Astronomy and Astrophysics* 643. ISSN: 14320746. DOI: 10.1051/0004-6361/202038717.

Gandhi, S., M. Brogi, and R. K. Webb (Oct. 2020). "Seeing above the Clouds with High-Resolution Spectroscopy". In: *Monthly Notices of the Royal Astronomical Society* 498, pp. 194–204. ISSN: 0035-8711. DOI: 10.1093/mnras/staa2424.

Gandhi, S. et al. (Nov. 2023). "JWST Measurements of ^{13}C, ^{18}O, and ^{17}O in the Atmosphere of Super-Jupiter VHS 1256 b". In: *The Astrophysical Journal Letters* 957.2, L36, p. L36. DOI: 10.3847/2041-8213/ad07e2. arXiv: 2311.05349 [astro-ph.EP].

Gao, P., M. S. Marley, and A. S. Ackerman (Mar. 2018). "Sedimentation Efficiency of Condensation Clouds in Substellar Atmospheres". In: *The Astrophysical Journal* 855.2, p. 86. ISSN: 0004-637X. DOI: 10.3847/1538-4357/aab0a1.

Gao, P. et al. (Oct. 2020). "Aerosol Composition of Hot Giant Exoplanets Dominated by Silicates and Hydrocarbon Hazes". en. In: *Nature Astronomy* 4.10, pp. 951–956. ISSN: 2397-3366. DOI: 10.1038/s41550-020-1114-3.

Gao, P. et al. (Feb. 2021). "Aerosols in Exoplanet Atmospheres". In: *arXiv e-prints* 2102, arXiv:2102.03480.

Geballe, T. R. et al. (Aug. 1996). "The Near-Infrared Spectrum of the Brown Dwarf Gliese 229B". In: *The Astrophysical Journal Letters* 467, p. L101. DOI: 10.1086/310203. arXiv: astro-ph/9606056 [astro-ph].

Gierasch, P. J. and B. J. Conrath (1985). "Energy conversion processes in the outer planets." In: *Recent Advances in Planetary Meteorology*. Ed. by G. E. Hunt. Cambridge University Press, pp. 121–146.

Gillon, M. et al. (May 2016). "Temperate Earth-sized planets transiting a nearby ultracool dwarf star". In: *Nature* 533, pp. 221–224. ISSN: 14764687. DOI: 10.1038/nature17448.

Golimowski, D. A. et al. (Oct. 2004). "The Solar Neighborhood. IX. Hubble Space Telescope Detections of Companions to Five M and L Dwarfs within 10 Parsecs of the Sun". In: *The Astronomical Journal* 128.4, pp. 1733–1747. DOI: 10.1086/423911. arXiv: astro-ph/0406664 [astro-ph].

Gomez Gonzalez, C. A. et al. (July 2017). "VIP: Vortex Image Processing Package for High-contrast Direct Imaging". In: *The Astronomical Journal* 154, 7, p. 7. DOI: 10.3847/1538-3881/aa73d7.

Gonzales, E. C. et al. (Dec. 2020a). "Retrieval of the d/sdL7+T7.5p Binary SDSS J1416+1348AB". In: *The Astrophysical Journal* 905, p. 46. ISSN: 0004-637X. DOI: 10.3847/1538-4357/abbee2.

– (Dec. 2020b). "Retrieval of the d/sdL7+T7.5p Binary SDSS J1416+1348AB". In: *The Astrophysical Journal* 905.1, 46, p. 46. DOI: 10.3847/1538-4357/abbee2. arXiv: 2010.01224 [astro-ph.SR].

Gonzales, E. C. et al. (Dec. 2021). "The First Retrieval of a Substellar Subdwarf: A Cloud-free SDSS J125637.13-022452.4". In: *The Astrophysical Journal* 923, p. 19. ISSN: 0004-637X. DOI: 10.3847/1538-4357/ac294e.

Gonzales, E. C. et al. (Oct. 2022). "A Comparative L-dwarf Sample Exploring the Interplay between Atmospheric Assumptions and Data Properties". In: *The Astrophysical Journal* 938 (1), p. 56. ISSN: 0004-637X. DOI: 10.3847/1538-4357/ac8f2a.

Gonzales, E. J. et al. (Apr. 2020). "The TRENDS High-Contrast Imaging Survey. VIII. Compendium of Benchmark Objects". In: *The Astrophysical Journal* 893, p. 27. ISSN: 0004-637X. DOI: 10.3847/1538-4357/ab71fb.

Goodwin, S. P. (Mar. 2013). "Binary mass ratios: system mass not primary mass." In: *Monthly Notices of the Royal Astronomical Society* 430, pp. L6–L9. DOI: 10.1093/mnrasl/sls037. arXiv: 1211.5936 [astro-ph.SR].

Gordon, K. D. et al. (July 2015). "The Mid-Infrared Instrument for the James Webb Space Telescope, X: Operations and Data Reduction". In: *Publications of the Astronomical Society of the Pacific* 127.953, p. 696. DOI: 10.1086/682260. arXiv: 1508.02441 [astro-ph.IM].

GRAVITY Collaboration et al. (June 2017). "First light for GRAVITY: Phase referencing optical interferometry for the Very Large Telescope Interferometer". In: *Astronomy & Astrophysics* 602, A94, A94. DOI: 10.1051/0004-6361/201730838. arXiv: 1705.02345 [astro-ph.IM].

Gravity Collaboration et al. (Jan. 2020). "Peering into the Formation History of β Pictoris b with VLTI/GRAVITY Long-Baseline Interferometry". In: *Astronomy and Astrophysics* 633, A110. ISSN: 0004-6361. DOI: 10.1051/0004-6361/201936898.

GRAVITY+ Collaboration et al. (Sept. 2022). "First light for GRAVITY Wide. Large separation fringe tracking for the Very Large Telescope Interferometer". In: *Astronomy & Astrophysics* 665, A75, A75. DOI: 10.1051/0004-6361/202243941. arXiv: 2206.00684 [astro-ph.IM].

Greco, J. P. and T. D. Brandt (Dec. 2016). "The Measurement, Treatment, and Impact of Spectral Covariance and Bayesian Priors in Integral-field Spectroscopy of Exoplanets". In: *The Astrophysical Journal* 833.2, 134, p. 134. DOI: 10.3847/1538-4357/833/2/134. arXiv: 1602.00691 [astro-ph.EP].

Greenbaum, A. Z. et al. (June 2018). "GPI Spectra of HR 8799 c, d, and e from 1.5 to 2.4 Mm with KLIP Forward Modeling". In: *The Astronomical Journal* 155, p. 226. ISSN: 0004-6256. DOI: 10.3847/1538-3881/aabcb8.

Grether, D. and C. H. Lineweaver (Apr. 2006). "How Dry is the Brown Dwarf Desert? Quantifying the Relative Number of Planets, Brown Dwarfs, and Stellar Companions around Nearby Sun-like Stars". In: *The Astrophysical Journal* 640.2, pp. 1051–1062. DOI: 10.1086/500161. arXiv: astro-ph/0412356 [astro-ph].

Grimm, S. L. and K. Heng (2015). "HELIOS-K: An Ultrafast, Open-source Opacity Calculator for Radiative Transfer". In: *The Astrophysical Journal* 808, p. 182. ISSN: 0004-637X. DOI: 10.1088/0004-637X/808/2/182. URL: https://ui.adsabs.harvard.edu/abs/2015ApJ...808..182G%20https://ui.adsabs.harvard.edu/link_gateway/2015ApJ...808..182G/ARTICLE.

Grimm, S. L. et al. (Mar. 2021). "HELIOS-K 2.0 Opacity Calculator and Open-source Opacity Database for Exoplanetary Atmospheres". In: *The Astrophysical Journal Supplement Series* 253 (1), p. 30. ISSN: 0067-0049. DOI: 10.3847/1538-4365/abd773.

Groff, T. et al. (Sept. 2017). "First light of the CHARIS high-contrast integral-field spectrograph". In: *Society of Photo-Optical Instrumentation Engineers (SPIE) Conference Series*. Ed. by S. Shaklan. Vol. 10400. Society of Photo-Optical Instrumentation Engineers (SPIE) Conference Series, 1040016, p. 1040016. DOI: 10.1117/12.2273525.

Grootel, V. V. et al. (Jan. 2018). "Stellar Parameters for Trappist-1". In: *The Astrophysical Journal* 853 (1), p. 30. ISSN: 15384357. DOI: 10.3847/1538-4357/aaa023.

Guillot, T. (Sept. 2010). "On the Radiative Equilibrium of Irradiated Planetary Atmospheres". In: *Astronomy and Astrophysics* 520, A27. ISSN: 0004-6361. DOI: 10.1051/0004-6361/200913396.

Gurrutxaga, N. et al. (Nov. 2023). "The formation of wide-orbit giant planets in protoplanetary disks with a decreasing pebble flux". In: *arXiv e-prints*, arXiv:2311.04365, arXiv:2311.04365. DOI: 10.48550/arXiv.2311.04365. arXiv: 2311.04365 [astro-ph.EP].

Halbwachs, J. L. et al. (Mar. 2000). "Exploring the brown dwarf desert with Hipparcos". In: *Astronomy & Astrophysics* 355, pp. 581–594.

Hansen, J. E. (Nov. 1971). "Multiple Scattering of Polarized Light in Planetary Atmospheres Part II. Sunlight Reflected by Terrestrial Water Clouds." In: *Journal of the Atmospheric Sciences* 28.8, pp. 1400–1426. DOI: 10.1175/1520-0469(1971)028<1400:MSOPLI>2.0.CO;2.

Hargreaves, R. J. et al. (Apr. 2020). "An Accurate, Extensive, and Practical Line List of Methane for the HITEMP Database". In: *The Astrophysical Journal Supplement Series* 247, p. 55. ISSN: 0067-0049. DOI: 10.3847/1538-4365/ab7a1a.

Hawkins, K. et al. (Feb. 2020). "Identical or Fraternal Twins? The Chemical Homogeneity of Wide Binaries from Gaia DR2". In: *Monthly Notices of the Royal Astronomical Society* 492, pp. 1164–1179. ISSN: 0035-8711. DOI: 10.1093/mnras/stz3132.

Hejazi, N. et al. (June 2023). "Elemental Abundances of the Super-Neptune WASP-107b's Host Star Using High-resolution, Near-infrared Spectroscopy". In: *The Astrophysical Journal* 949 (2), p. 79. ISSN: 0004-637X. DOI: 10.3847/1538-4357/accb97.

Hinkel, N. R. et al. (Sept. 2014). "Stellar Abundances in the Solar Neighborhood: The Hypatia Catalog". In: *The Astronomical Journal* 148.3, 54, p. 54. DOI: 10.1088/0004-6256/148/3/54. arXiv: 1405.6719 [astro-ph.SR].

Hinkley, S. et al. (May 2015). "Early results from VLT sphere: Long-slit spectroscopy of 2MASS 0122-2439 B, A young companion near the deuterium burning limit". In: *Astrophysical Journal Letters* 805 (1). ISSN: 20418213. DOI: 10.1088/2041-8205/805/1/L10.

Hoch, K. K. W. et al. (Nov. 2020). "Moderate-resolution K-band Spectroscopy of Substellar Companion kap Andromedae b". In: *The Astronomical Journal* 160 (5), p. 207. ISSN: 0004-6256. DOI: 10.3847/1538-3881/abb9b1.

Hoch, K. K. W. et al. (Oct. 2022). "Moderate-resolution K-band Spectroscopy of the Substellar Companion VHS 1256 b". In: *The Astronomical Journal* 164.4, 155, p. 155. DOI: 10.3847/1538-3881/ac84d4. arXiv: 2207.03819 [astro-ph.EP].

Hoch, K. K. W. et al. (Sept. 2023). "Assessing the C/O Ratio Formation Diagnostic: A Potential Trend with Companion Mass". In: *The Astronomical Journal* 166.3, 85, p. 85. DOI: 10.3847/1538-3881/ace442. arXiv: 2212.04557 [astro-ph.EP].

Hoeijmakers, H. J. et al. (Oct. 2018). "Medium-Resolution Integral-Field Spectroscopy for High-Contrast Exoplanet Imaging. Molecule Maps of the β Pictoris System with SINFONI". In: *Astronomy and Astrophysics* 617, A144. ISSN: 0004-6361. DOI: 10.1051/0004-6361/201832902.

Hojjatpanah, S. et al. (Sept. 2019). "Catalog for the ESPRESSO blind radial velocity exoplanet survey". In: *Astronomy & Astrophysics* 629, A80, A80. DOI: 10.1051/0004-6361/201834729. arXiv: 1908.04627 [astro-ph.EP].

Hojjatpanah, S. et al. (July 2020). "The correlation between photometric variability and radial velocity jitter. Based on TESS and HARPS observations". In: *Astronomy & Astrophysics* 639, A35, A35. DOI: 10.1051/0004-6361/202038035. arXiv: 2005.10105 [astro-ph.EP].

Holl, B. et al. (May 2022). "Gaia-predicted brown dwarf detection rates around FGK stars in astrometry, radial velocity, and photometric transits". In: *Astronomy & Astrophysics* 661, A151, A151.

Holl, B. et al. (June 2023). "Gaia Data Release 3. Astrometric orbit determination with Markov chain Monte Carlo and genetic algorithms: Systems with stellar, sub-stellar, and planetary mass companions". In: *Astronomy & Astrophysics* 674, A10, A10. DOI: 10.1051/0004-6361/202244161. arXiv: 2206.05439 [astro-ph.EP].

Holstein, R. G. V. et al. (Mar. 2021). "A survey of the linear polarization of directly imaged exoplanets and brown dwarf companions with SPHERE-IRDIS: First polarimetric detections revealing disks around DH Tau B and GSC 6214-210 B". In: *Astronomy and Astrophysics* 647. ISSN: 14320746. DOI: 10.1051/0004-6361/202039290.

Hood, C. E. et al. (Aug. 2023). "Brown Dwarf Retrievals on FIRE!: Atmospheric Constraints and Lessons Learned from High Signal-to-noise Medium-resolution Spectroscopy of a T9 Dwarf". In: *The Astrophysical Journal* 953 (2), p. 170. ISSN: 0004-637X. DOI: 10.3847/1538-4357/ace32e. URL: https://iopscience.iop.org/article/10.3847/1538-4357/ace32e.

Horne, K. (June 1986). "An optimal extraction algorithm for CCD spectroscopy". In: *Publications of the Astronomical Society of the Pacific* 98, pp. 609–617. ISSN: 0004-6280. DOI: 10.1086/131801. URL: http://adsabs.harvard.edu/abs/1986PASP...98..609H (visited on 12/09/2018).

Horstman, K. et al. (Oct. 2024). "RV Measurements of Directly Imaged Brown Dwarf GQ Lup B to Search for Exosatellites". In: *The Astronomical Journal* 168.4, 175, p. 175. DOI: 10.3847/1538-3881/ad73d8. arXiv: 2408.10299 [astro-ph.EP].

Howard, A. W. et al. (Oct. 2010). "The California planet survey. I. four new giant exoplanets". In: *Astrophysical Journal* 721 (2), pp. 1467–1481. ISSN: 15384357. DOI: 10.1088/0004-637X/721/2/1467.

Howe, A. R., A. M. Mandell, and M. W. McElwain (July 2023). "Investigating Possible Binarity for GJ 229B". In: *The Astrophysical Journal Letters* 951.2, L25, p. L25. DOI: 10.3847/2041-8213/acdd76. arXiv: 2306.08450 [astro-ph.SR].

Howe, A. R., M. W. McElwain, and A. M. Mandell (Aug. 2022). "GJ 229B: Solving the Puzzle of the First Known T Dwarf with the APOLLO Retrieval Code". In: *The Astrophysical Journal* 935, p. 107. ISSN: 0004-637X. DOI: 10.3847/1538-4357/ac5590.

Hsu, C.-C., A. J. Burgasser, and C. A. Theissen (Mar. 2023). "Discovery of the Exceptionally Short Period Ultracool Dwarf Binary LP 413-53AB". In: *The Astrophysical Journal Letters* 945.1, L6, p. L6. DOI: 10.3847/2041-8213/acba8c. arXiv: 2301.07039 [astro-ph.SR].

Hsu, C.-C. et al. (Dec. 2021). "The Brown Dwarf Kinematics Project (BDKP). V. Radial and Rotational Velocities of T Dwarfs from Keck/NIRSPEC High-resolution Spectroscopy". In: *The Astrophysical Journal Supplement Series* 257.2, 45, p. 45. DOI: 10.3847/1538-4365/ac1c7d. eprint: 2107.01222 (astro-ph.SR).

Hsu, C.-C. et al. (May 2024a). "Rotation and Abundances of the Benchmark Brown Dwarf HD 33632 Ab from Keck/KPIC High-resolution Spectroscopy". In: *arXiv e-prints*, arXiv:2405.08312, arXiv:2405.08312. DOI: 10.48550/arXiv.2405.08312. arXiv: 2405.08312 [astro-ph.SR].

Hsu, C.-C. et al. (Oct. 2024b). "The Brown Dwarf Kinematics Project (BDKP). VI. Ultracool Dwarf Radial and Rotational Velocities from SDSS/APOGEE High-resolution Spectroscopy". In: *The Astrophysical Journal Supplement Series* 274.2, 40, p. 40. DOI: 10.3847/1538-4365/ad6b27. arXiv: 2403.13760 [astro-ph.SR].

Husser, T.-O. et al. (May 2013). "A new extensive library of PHOENIX stellar atmospheres and synthetic spectra". en. In: *Astronomy & Astrophysics* 553, A6. ISSN: 0004-6361, 1432-0746. DOI: 10.1051/0004-6361/201219058. URL: https://www.aanda.org/articles/aa/abs/2013/05/aa19058-12/aa19058-12.html (visited on 11/07/2018).

Inglis, J. et al. (May 2024). "Atmospheric Retrievals of the Young Giant Planet ROXs 42B b from Low- and High-resolution Spectroscopy". In: *The Astronomical Journal* 167.5, 218, p. 218. DOI: 10.3847/1538-3881/ad2771. arXiv: 2402.09533 [astro-ph.EP].

Ireland, M. J. et al. (Dec. 2010). "Two Wide Planetary-Mass Companions to Solar-Type Stars in Upper Scorpius". en. In: *The Astrophysical Journal* 726.2, p. 113. ISSN: 0004-637X. DOI: 10.1088/0004-637X/726/2/113. URL: https://doi.org/10.1088%2F0004-637x%2F726%2F2%2F113 (visited on 07/17/2019).

Itoh, Y. et al. (2005). "A Young Brown Dwarf Companion to DH Tauri". en. In: *The Astrophysical Journal* 620.2, p. 984. ISSN: 0004-637X. DOI: 10.1086/427086.

URL: http://stacks.iop.org/0004-637X/620/i=2/a=984 (visited on 12/26/2018).

Iyer, A. R. et al. (Feb. 2023). "The SPHINX M-dwarf Spectral Grid. I. Benchmarking New Model Atmospheres to Derive Fundamental M-dwarf Properties". In: *The Astrophysical Journal* 944 (1), p. 41. ISSN: 0004-637X. DOI: 10.3847/1538-4357/acabc2.

Janson, M. et al. (June 2019). "The B-Star Exoplanet Abundance Study: A co-moving 16-25 M Jup companion to the young binary system HIP 79098". In: *Astronomy and Astrophysics* 626. ISSN: 14320746. DOI: 10.1051/0004-6361/201935687.

Jeffreys Harold, S. (1983). *Theory of probability*. Oxford: Clarendon, p. 459. ISBN: 0198531931.

Jennings, R. M. and E. Chiang (Nov. 2021). "Primordial obliquities of brown dwarfs and super-Jupiters from fragmenting gravito-turbulent discs". In: *Monthly Notices of the Royal Astronomical Society* 507 (4), pp. 5187–5194. ISSN: 13652966. DOI: 10.1093/mnras/stab2429.

Jensen, E. L. and R. Akeson (2014). "Misaligned protoplanetary disks in a young binary star system". In: *Nature* 511 (7511), pp. 567–569. ISSN: 14764687. DOI: 10.1038/nature13521.

Johansen, A. and M. Lambrechts (Aug. 2017). "Forming Planets via Pebble Accretion". In: *Annual Review of Earth and Planetary Sciences* 45.1, pp. 359–387. DOI: 10.1146/annurev-earth-063016-020226.

Johnston, V. D., M. C. Cushing, and K. S. Noll (Mar. 2019). "NIRSPEC L-band Spectra of 11 L and T Dwarfs". In: *Research Notes of the AAS* 3.3, p. 52. ISSN: 2515-5172. DOI: 10.3847/2515-5172/ab0e14.

Jones, A. et al. (Dec. 2013). "An advanced scattered moonlight model for Cerro Paranal". In: *Astronomy & Astrophysics* 560, A91, A91. DOI: 10.1051/0004-6361/201322433. arXiv: 1310.7030 [astro-ph.IM].

Jones, J. et al. (Apr. 2016). "The Age of the Directly Imaged Planet Host Star κ Andromedae Determined from Interferometric Observations". In: *The Astrophysical Journal* 822 (1), p. L3. ISSN: 20418213. DOI: 10.3847/2041-8205/822/1/l3.

Juhász, A. et al. (Sept. 2010). "Dust Evolution in Protoplanetary Disks Around Herbig Ae/Be Stars—the Spitzer View". In: *The Astrophysical Journal* 721.1, pp. 431–455. DOI: 10.1088/0004-637X/721/1/431. arXiv: 1008.0083 [astro-ph.SR].

Kaeufl, H.-U. et al. (Sept. 2004). "CRIRES: A high-resolution infrared spectrograph for ESO's VLT". In: *Ground-based Instrumentation for Astronomy*. Ed. by A. F. M. Moorwood and M. Iye. Vol. 5492. Society of Photo-Optical Instrumentation Engineers (SPIE) Conference Series, pp. 1218–1227. DOI: 10.1117/12.551480.

Kammerer, J. et al. (Dec. 2020). "Increasing the achievable contrast of infrared interferometry with an error correlation model". In: *Astronomy & Astrophysics* 644, A110, A110. DOI: 10.1051/0004-6361/202038563. arXiv: 2011.01209 [astro-ph.IM].

Kammerer, J. et al. (Aug. 2021). "GRAVITY K-band spectroscopy of HD 206893 B. Brown dwarf or exoplanet". In: *Astronomy & Astrophysics* 652, A57, A57. DOI: 10.1051/0004-6361/202140749. arXiv: 2106.08249 [astro-ph.EP].

Karalidi, T. et al. (Dec. 2021). "The Sonora Substellar Atmosphere Models. II. Cholla: A Grid of Cloud-free, Solar Metallicity Models in Chemical Disequilibrium for the JWST Era". In: *The Astrophysical Journal* 923, p. 269. ISSN: 0004-637X. DOI: 10.3847/1538-4357/ac3140.

Kaufer, A. et al. (Sept. 1997). "FEROS, the Fiber-Fed Extended Range Optical Spectrograph for the ESO 1.52-m Telescope." In: *The Messenger* 89, pp. 1–4. ISSN: 0722-6691.

Kempton, E. M.-R. and H. A. Knutson (July 2024). "Transiting Exoplanet Atmospheres in the Era of JWST". In: *Reviews in Mineralogy and Geochemistry* 90.1, pp. 411–464. ISSN: 1529-6466. DOI: 10.2138/rmg.2024.90.12. eprint: https://pubs.geoscienceworld.org/msa/rimg/article-pdf/90/1/411/6521125/rmg.2024.90.12.pdf. URL: https://doi.org/10.2138/rmg.2024.90.12.

Kendrew, S. et al. (July 2015). "The Mid-Infrared Instrument for the James Webb Space Telescope, IV: The Low-Resolution Spectrometer". In: *Publications of the Astronomical Society of the Pacific* 127.953, p. 623. DOI: 10.1086/682255. URL: https://dx.doi.org/10.1086/682255.

Kervella, P. et al. (Mar. 2019). "Stellar and Substellar Companions of Nearby Stars from Gaia DR2 - Binarity from Proper Motion Anomaly". en. In: *Astronomy & Astrophysics* 623, A72. ISSN: 0004-6361, 1432-0746. DOI: 10.1051/0004-6361/201834371.

Kitzmann, D. et al. (Feb. 2020). "Helios-R2: A New Bayesian, Open-source Retrieval Model for Brown Dwarfs and Exoplanet Atmospheres". In: *The Astrophysical Journal* 890.2, p. 174. ISSN: 0004-637X. DOI: 10.3847/1538-4357/ab6d71.

Kolecki, J. R. et al. (June 2021). "Searching For Transiting Planets Around Halo Stars. I. Sample Selection and Validation". In: *arXiv e-prints*, arXiv:2106.13251.

Konopacky, Q. M. et al. (May 2012). "Rotational Velocities of Individual Components in Very Low Mass Binaries". In: *The Astrophysical Journal* 750, p. 79. ISSN: 0004-637X. DOI: 10.1088/0004-637X/750/1/79.

Konopacky, Q. M. et al. (Mar. 2013). "Detection of Carbon Monoxide and Water Absorption Lines in an Exoplanet Atmosphere". en. In: *Science* 339.6126, pp. 1398–1401. ISSN: 0036-8075, 1095-9203. DOI: 10.1126/science.1232003. URL: http://science.sciencemag.org/content/339/6126/1398 (visited on 04/05/2019).

Konopacky, Q. M. et al. (Oct. 2023). "The development of HISPEC for Keck and MODHIS for TMT: science cases and predicted sensitivities". In: *Society of Photo-Optical Instrumentation Engineers (SPIE) Conference Series*. Vol. 12680. Society of Photo-Optical Instrumentation Engineers (SPIE) Conference Series, 1268007, p. 1268007. DOI: 10.1117/12.2681522.

Kotani, T. et al. (Dec. 2020). "Extremely High-Contrast, High Spectral Resolution Spectrometer REACH for the Subaru Telescope". In: *Adaptive Optics Systems VII*. Vol. 11448. International Society for Optics and Photonics, p. 1144878. DOI: 10.1117/12.2561755.

Kratter, K. and G. Lodato (Sept. 2016). "Gravitational instabilities in circumstellar disks". In: *Annual Review of Astronomy and Astrophysics* 54, pp. 271–311. ISSN: 00664146. DOI: 10.1146/annurev-astro-081915-023307.

Kratter, K. M., R. A. Murray-Clay, and A. N. Youdin (Feb. 2010a). "The Runts of the Litter: Why Planets Formed Through Gravitational Instability Can Only Be Failed Binary Stars". In: *The Astrophysical Journal* 710.2, pp. 1375–1386. DOI: 10.1088/0004-637X/710/2/1375. arXiv: 0909.2644 [astro-ph.EP].

– (2010b). "The Runts of the Litter: Why Planets Formed Through Gravitational Instability Can Only Be Failed Binary Stars". en. In: *The Astrophysical Journal* 710.2, p. 1375. ISSN: 0004-637X. DOI: 10.1088/0004-637X/710/2/1375. URL: http://stacks.iop.org/0004-637X/710/i=2/a=1375 (visited on 01/22/2019).

Kraus, A. L. and L. A. Hillenbrand (Oct. 2009). "Unusually Wide Binaries: Are They Wide or Unusual?" In: *The Astrophysical Journal* 703.2, pp. 1511–1530. DOI: 10.1088/0004-637X/703/2/1511. arXiv: 0908.1385 [astro-ph.SR]. URL: https://ui.adsabs.harvard.edu/abs/2009ApJ...703.1511K.

Kraus, A. L. et al. (Dec. 2013). "Three Wide Planetary-Mass Companions to FW Tau, ROXs 12, and ROXs 42B". en. In: *The Astrophysical Journal* 781.1, p. 20. ISSN: 0004-637X. DOI: 10.1088/0004-637X/781/1/20. URL: https://doi.org/10.1088%2F0004-637x%2F781%2F1%2F20 (visited on 04/07/2019).

Kreidberg, L. (2018). "Exoplanet Atmosphere Measurements from Transmission Spectroscopy and Other Planet Star Combined Light Observations". In: *Handbook of Exoplanets*. Ed. by H. J. Deeg and J. A. Belmonte, 100, p. 100. DOI: 10.1007/978-3-319-55333-7_100.

Kurucz, R. L. (Apr. 2011). "Including all the lines". In: *Canadian Journal of Physics* 89 (4), pp. 417–428. ISSN: 00084204. DOI: 10.1139/p10-104.

Kuznetsov, M. K. et al. (June 2019). "Characterization of a Sample of Southern M Dwarfs Using Harps and X-shooter Spectra". In: *The Astrophysical Journal* 878.2, 134, p. 134. DOI: 10.3847/1538-4357/ab1fe9.

Kuzuhara, M. et al. (Aug. 2022). "Direct-imaging Discovery and Dynamical Mass of a Substellar Companion Orbiting an Accelerating Hyades Sun-like Star with SCExAO/CHARIS". In: *The Astrophysical Journal Letters* 934.2, L18, p. L18. DOI: 10.3847/2041-8213/ac772f. arXiv: 2205.02729 [astro-ph.SR].

Lachaume, R. et al. (Apr. 2019). "Towards reliable uncertainties in IR interferometry: the bootstrap for correlated statistical and systematic errors". In: *Monthly Notices of the Royal Astronomical Society* 484.2, pp. 2656–2673. DOI: 10.1093/mnras/stz114. arXiv: 1901.02879 [astro-ph.IM].

Lacour, S., Ó. Carrión-González, and M. Nowak (June 2024). "Exoplanets in reflected starlight with dual-field interferometry: A case for shorter wavelengths and a fifth Unit Telescope at VLTI/Paranal". In: *arXiv e-prints*, arXiv:2406.07030, arXiv:2406.07030. DOI: 10.48550/arXiv.2406.07030. arXiv: 2406.07030 [astro-ph.EP].

Lacour, S. et al. (Apr. 2019). "The GRAVITY fringe tracker". In: *Astronomy & Astrophysics* 624, A99, A99. DOI: 10.1051/0004-6361/201834981. arXiv: 1901.03202 [astro-ph.IM].

Lafrenière, D. et al. (Apr. 2009). "HST/NICMOS Detection of HR 8799 b in 1998". In: *The Astrophysical Journal Letters* 694.2, pp. L148–L152. DOI: 10.1088/0004-637X/694/2/L148. arXiv: 0902.3247 [astro-ph.EP].

Lambrechts, M. and A. Johansen (Aug. 2012). "Rapid growth of gas-giant cores by pebble accretion". In: *Astronomy & Astrophysics* 544, A32. ISSN: 0004-6361. DOI: 10.1051/0004-6361/201219127. URL: http://adsabs.harvard.edu/abs/2012A%26A...544A..32L (visited on 04/03/2019).

Landman, R. et al. (July 2023a). "Trade-offs in high-contrast integral field spectroscopy for exoplanet detection and characterisation. Young gas giants in emission". In: *Astronomy & Astrophysics* 675, A157, A157. DOI: 10.1051/0004-6361/202245169. arXiv: 2305.19355 [astro-ph.EP].

Landman, R. et al. (Nov. 2023b). "β Pictoris b through the eyes of the upgraded CRIRES+". In: *arXiv e-prints*. URL: http://arxiv.org/abs/2311.13527.

Langeveld, A. B. et al. (Oct. 2024). "The JWST/NIRISS Deep Spectroscopic Survey for Young Brown Dwarfs and Free-floating Planets". In: *The Astronomical Journal* 168.4, 179, p. 179. DOI: 10.3847/1538-3881/ad6f0c. arXiv: 2408.12639 [astro-ph.EP].

Lapeyrere, V. et al. (July 2014). "GRAVITY data reduction software". In: *Optical and Infrared Interferometry IV*. Ed. by J. K. Rajagopal, M. J. Creech-Eakman, and F. Malbet. Vol. 9146. Society of Photo-Optical Instrumentation Engineers (SPIE) Conference Series, 91462D, p. 91462D. DOI: 10.1117/12.2056850.

Larkin, J. et al. (June 2006). "OSIRIS: a diffraction limited integral field spectrograph for Keck". In: *Ground-based and Airborne Instrumentation for Astronomy*. Ed. by I. S. McLean and M. Iye. Vol. 6269. Society of Photo-Optical Instrumen-

tation Engineers (SPIE) Conference Series, 62691A, 62691A. DOI: 10.1117/12.672061.

Lavie, B. et al. (Sept. 2017). "HELIOS-RETRIEVAL: An Open-source, Nested Sampling Atmospheric Retrieval Code; Application to the HR 8799 Exoplanets and Inferred Constraints for Planet Formation". In: *The Astronomical Journal* 154, p. 91. ISSN: 0004-6256. DOI: 10.3847/1538-3881/aa7ed8.

Lazzoni, C. et al. (Jan. 2024). "Binary planet formation through tides". In: *Monthly Notices of the Royal Astronomical Society* 527.2, pp. 3837–3846. DOI: 10.1093/mnras/stad3443. arXiv: 2311.01618 [astro-ph.EP].

Lee, K. I. et al. (Mar. 2016). "Misalignment of Outflow Axes in the Proto-Multiple Systems in Perseus". In: *The Astrophysical Journal* 820 (1), p. L2. ISSN: 20418213. DOI: 10.3847/2041-8205/820/1/l2.

Leggett, S. K. et al. (May 2002). "Atmospheric analysis of the M/L and M/T dwarf binary systems LHS 102 and Gliese 229". In: *Monthly Notices of the Royal Astronomical Society* 332.1, pp. 78–90. DOI: 10.1046/j.1365-8711.2002.05273.x. arXiv: astro-ph/0112335 [astro-ph].

Leggett, S. K. et al. (2006). "JHK observations of faint standard stars in the Mauna Kea observatories near-infrared photometric system". In: *Monthly Notices of the Royal Astronomical Society* 373 (2), pp. 781–792. ISSN: 13652966. DOI: 10.1111/j.1365-2966.2006.11069.x.

Leggett, S. K. et al. (Sept. 2021). "Measuring and Replicating the 1-20 μm Energy Distributions of the Coldest Brown Dwarfs: Rotating, Turbulent, and Nonadiabatic Atmospheres". In: *The Astrophysical Journal* 918.1, 11, p. 11. DOI: 10.3847/1538-4357/ac0cfe. arXiv: 2107.00696 [astro-ph.SR].

Lei, E. and P. Mollière (Oct. 2024). "easyCHEM: A Python package for calculating chemical equilibrium abundances in exoplanet atmospheres". In: *arXiv e-prints*, arXiv:2410.21364, arXiv:2410.21364. DOI: 10.48550/arXiv.2410.21364. arXiv: 2410.21364 [astro-ph.IM].

Leviton, D. B., B. J. Frey, and T. J. Madison (2007). "Temperature-dependent refractive index of CaF2 and Infrasil 301". In: *SPIE Optical Engineering + Applications*. URL: https://api.semanticscholar.org/CorpusID:67820194.

Li, Y. et al. (July 2023). "Surveying nearby brown dwarfs with HGCA: direct imaging discovery of a faint, high-mass brown dwarf orbiting HD 176535 A". In: *Monthly Notices of the Royal Astronomical Society* 522 (4), pp. 5622–5637. ISSN: 13652966. DOI: 10.1093/mnras/stad1315.

Lightkurve Collaboration et al. (Dec. 2018). *Lightkurve: Kepler and TESS time series analysis in Python*. Astrophysics Source Code Library, record ascl:1812.013. ascl: 1812.013.

Lindegren, L. et al. (July 1997). "Double star data in the HIPPARCOS Catalogue". In: *Astronomy & Astrophysics* 323, pp. L53–L56.

Lindegren, L. et al. (May 2021). "Gaia Early Data Release 3. Parallax bias versus magnitude, colour, and position". In: *Astronomy & Astrophysics* 649, A4, A4. DOI: 10.1051/0004-6361/202039653. arXiv: 2012.01742 [astro-ph.IM].

Line, M. R. et al. (July 2015). "Uniform Atmospheric Retrieval Analysis of Ultracool Dwarfs. I. Characterizing Benchmarks, Gl 570D and HD 3651B". In: *The Astrophysical Journal* 807, p. 183. ISSN: 0004-637X. DOI: 10.1088/0004-637X/807/2/183.

Line, M. R. et al. (Oct. 2017). "Uniform Atmospheric Retrieval Analysis of Ultracool Dwarfs. II. Properties of 11 T dwarfs". In: *The Astrophysical Journal* 848.2, 83, p. 83. DOI: 10.3847/1538-4357/aa7ff0. arXiv: 1612.02809 [astro-ph.SR].

Line, M. R. et al. (Oct. 2021). "A Solar C/O and Sub-Solar Metallicity in a Hot Jupiter Atmosphere". In: *Nature* 598, pp. 580–584. ISSN: 0028-0836. DOI: 10.1038/s41586-021-03912-6.

Liu, M. C. (Sept. 2004). "Substructure in the Circumstellar Disk Around the Young Star AU Microscopii". en. In: *Science* 305.5689, pp. 1442–1444. ISSN: 0036-8075, 1095-9203. DOI: 10.1126/science.1102929.

Liu, M. C., T. J. Dupuy, and K. N. Allers (Dec. 2016). "The Hawaii Infrared Parallax Program. II. Young Ultracool Field Dwarfs". In: *The Astrophysical Journal* 833.1, 96, p. 96. DOI: 10.3847/1538-4357/833/1/96. arXiv: 1612.02426 [astro-ph.SR].

Lodieu, N. et al. (Dec. 2015). "An eclipsing double-line spectroscopic binary at the stellar/substellar boundary in the Upper Scorpius OB association". In: *Astronomy & Astrophysics* 584, A128, A128. DOI: 10.1051/0004-6361/201527464. arXiv: 1511.03083 [astro-ph.SR].

Looper, D. L. et al. (Oct. 2008). "Discovery of a T Dwarf Binary with the Largest Known J-Band Flux Reversal". In: *The Astrophysical Journal* 685.2, pp. 1183–1192. DOI: 10.1086/590382. arXiv: 0803.0544 [astro-ph].

López, R. A. et al. (Dec. 2020). "Characterization and Performance of the Upgraded NIRSPEC on the W. M. Keck Telescope". In: *Ground-Based and Airborne Instrumentation for Astronomy VIII*. Vol. 11447. SPIE, pp. 1436–1450. DOI: 10.1117/12.2563075.

López-Valdivia, R. et al. (Nov. 2021). "The IGRINS YSO Survey. I. Stellar Parameters of Pre-main-sequence Stars in Taurus-Auriga". In: *The Astrophysical Journal* 921.1, 53, p. 53. DOI: 10.3847/1538-4357/ac1a7b. arXiv: 2108.01787 [astro-ph.SR].

Lovis, C. and D. Fischer (2010). "Radial Velocity Techniques for Exoplanets". In: *Exoplanets*. Ed. by S. Seager, pp. 27–53.

Low, C. and D. Lynden-Bell (Aug. 1976). "The minimum Jeans mass or when fragmentation must stop." In: *Monthly Notices of the Royal Astronomical Society* 176, pp. 367–390. DOI: 10.1093/mnras/176.2.367.

Lueber, A. et al. (May 2022). "Retrieval Study of Brown Dwarfs across the L-T Sequence". In: *The Astrophysical Journal* 930 (2), p. 136. ISSN: 0004-637X. DOI: 10.3847/1538-4357/ac63b9.

Lueber, A. et al. (Sept. 2023). "Intercomparison of Brown Dwarf Model Grids and Atmospheric Retrieval Using Machine Learning". In: *The Astrophysical Journal* 954.1, 22, p. 22. DOI: 10.3847/1538-4357/ace530. arXiv: 2305.07719 [astro-ph.SR].

Luhman, K. L. et al. (2006). "Discovery of a Young Substellar Companion in Chamaeleon". In: *The Astrophysical Journal* 649 (2), p. 894. ISSN: 0004-637X. DOI: 10.1086/506517. URL: http://stacks.iop.org/0004-637X/649/i=2/a=894%20http://iopscience.iop.org/article/10.1086/506517/pdf.

Luhman, K. L. (Jan. 2022). "A Census of the Stellar Populations in the Sco-Cen Complex*". In: *The Astronomical Journal* 163 (1), p. 24. ISSN: 0004-6256. DOI: 10.3847/1538-3881/ac35e2.

– (Feb. 2023). "A Census of the Taurus Star-forming Region and Neighboring Associations with Gaia*". In: *The Astronomical Journal* 165 (2), p. 37. ISSN: 0004-6256. DOI: 10.3847/1538-3881/ac9da3.

Luhman, K. L. and T. L. Esplin (June 2020). "Refining the Census of the Upper Scorpius Association with Gaia". In: *The Astronomical Journal* 160 (1), p. 44. ISSN: 00046256. DOI: 10.3847/1538-3881/ab9599.

Luhman, K. L. et al. (Jan. 2024). "A JWST Survey for Planetary Mass Brown Dwarfs in IC 348". In: *The Astronomical Journal* 167.1, 19, p. 19. DOI: 10.3847/1538-3881/ad00b7.

Luna, J. L. and C. V. Morley (Oct. 2021). "Empirically Determining Substellar Cloud Compositions in the Era of the James Webb Space Telescope". In: *The Astrophysical Journal* 920, p. 146. ISSN: 0004-637X. DOI: 10.3847/1538-4357/ac1865.

Lyons, J. R., E. Gharib-Nezhad, and T. R. Ayres (Dec. 2018). "A light carbon isotope composition for the Sun". In: *Nature Communications* 9 (1). ISSN: 20411723. DOI: 10.1038/s41467-018-03093-3.

Ma, B. and J. Ge (Apr. 2014). "Statistical properties of brown dwarf companions: implications for different formation mechanisms". In: *Monthly Notices of the Royal Astronomical Society* 439.3, pp. 2781–2789. DOI: 10.1093/mnras/stu134. arXiv: 1303.6442 [astro-ph.EP].

Macintosh, B. et al. (Sept. 2014). "First light of the Gemini Planet Imager". In: *Proceedings of the National Academy of Science* 111, pp. 12661–12666. DOI: 10.1073/pnas.1304215111. arXiv: 1403.7520 [astro-ph.EP]. URL: http://adsabs.harvard.edu/abs/2014PNAS..11112661M.

Macintosh, B. et al. (Oct. 2015). "Discovery and spectroscopy of the young jovian planet 51 Eri b with the Gemini Planet Imager". In: *Science* 350.6256, pp. 64–67. DOI: 10.1126/science.aac5891. arXiv: 1508.03084 [astro-ph.EP].

Madhusudhan, N. (2012). "C/O Ratio as a Dimension for Characterizing Exoplanetary Atmospheres". en. In: *The Astrophysical Journal* 758.1, p. 36. ISSN: 0004-637X. DOI: 10.1088/0004-637X/758/1/36. URL: http://stacks.iop.org/0004-637X/758/i=1/a=36 (visited on 10/02/2018).

Madhusudhan, N., M. A. Amin, and G. M. Kennedy (Oct. 2014). "Toward Chemical Constraints on Hot Jupiter Migration". In: *The Astrophysical Journal* 794, p. L12. ISSN: 0004-637X. DOI: 10.1088/2041-8205/794/1/L12.

Maire, A. .-. et al. (Mar. 2016). "First light of the VLT planet finder SPHERE. II. The physical properties and the architecture of the young systems PZ Telescopii and HD 1160 revisited". In: *Astronomy & Astrophysics* 587, A56, A56. DOI: 10.1051/0004-6361/201526594. arXiv: 1511.04072 [astro-ph.EP].

Maldonado, J. et al. (Dec. 2020). "HADES RV programme with HARPS-N at TNG. XII. The abundance signature of M dwarf stars with planets". In: *Astronomy & Astrophysics* 644, A68, A68. DOI: 10.1051/0004-6361/202039478. arXiv: 2010.14867 [astro-ph.SR].

Malo, L. et al. (Jan. 2013). "Bayesian Analysis to Identify New Star Candidates in Nearby Young Stellar Kinematic Groups". In: *The Astrophysical Journal* 762.2, 88, p. 88. DOI: 10.1088/0004-637X/762/2/88. arXiv: 1209.2077 [astro-ph.SR].

Mamajek, E. E. and E. D. Feigelson (Jan. 2001). "The Dispersal of Young Stars and the Greater Sco-Cen Association". In: *Young Stars Near Earth: Progress and Prospects*. Ed. by R. Jayawardhana and T. Greene. Vol. 244. Astronomical Society of the Pacific Conference Series, pp. 104–115. DOI: 10.48550/arXiv.astro-ph/0105290. arXiv: astro-ph/0105290 [astro-ph].

Mamajek, E. E. and L. A. Hillenbrand (Nov. 2008). "Improved Age Estimation for Solar-Type Dwarfs Using Activity-Rotation Diagnostics". In: *The Astrophysical Journal* 687, pp. 1264–1293. ISSN: 0004-637X. DOI: 10.1086/591785.

Manjavacas, E. et al. (Nov. 2021). "Revealing the Vertical Cloud Structure of a Young Low-mass Brown Dwarf, an Analog to the β-Pictoris b Directly Imaged Exoplanet, through Keck I/MOSFIRE Spectrophotometric Variability". In: *The Astronomical Journal* 162, p. 179. ISSN: 0004-6256. DOI: 10.3847/1538-3881/ac174c.

Marcussen, M. L. and S. H. Albrecht (June 2023). "Spectroscopic Follow-up of Gaia Exoplanet Candidates: Impostor Binary Stars Invade the Gaia DR3 Astrometric Exoplanet Candidates". In: *The Astronomical Journal* 165.6, 266, p. 266. DOI: 10.3847/1538-3881/acd53d. arXiv: 2305.08623 [astro-ph.EP].

Marfil, E. et al. (Dec. 2021). "The CARMENES search for exoplanets around M dwarfs. Stellar atmospheric parameters of target stars with SteParSyn". In: *Astronomy & Astrophysics* 656, A162, A162. DOI: 10.1051/0004-6361/202141980. arXiv: 2110.07329 [astro-ph.SR].

Marley, M. S. et al. (1996). "Atmospheric, Evolutionary, and Spectral Models of the Brown Dwarf Gliese 229 B". In: *Science* 272.5270, pp. 1919–1921. ISSN: 0036-8075. DOI: 10.1126/science.272.5270.1919. URL: https://science.sciencemag.org/content/272/5270/1919.

Marley, M. and T. Robinson (Aug. 2015). "On the Cool Side: Modeling the Atmospheres of Brown Dwarfs and Giant Planets". In: *Annual Review of Astronomy and Astrophysics* 53.1, pp. 279–323. ISSN: 0066-4146. DOI: 10.1146/annurev-astro-082214-122522.

Marley, M. S. et al. (Oct. 2021). "The Sonora Brown Dwarf Atmosphere and Evolution Models. I. Model Description and Application to Cloudless Atmospheres in Rainout Chemical Equilibrium". In: *The Astrophysical Journal* 920.2, p. 85. ISSN: 0004-637X. DOI: 10.3847/1538-4357/ac141d.

Marois, C. et al. (Apr. 2006). "Angular Differential Imaging: A Powerful High-Contrast Imaging Technique". In: *The Astrophysical Journal* 641, pp. 556–564. DOI: 10.1086/500401.

Martin, E. C. et al. (Aug. 2018). "An overview of the NIRSPEC upgrade for the Keck II telescope". en. In: *SPIE* 10702, 107020A. DOI: 10.1117/12.2312266. URL: https://ui.adsabs.harvard.edu/#abs/arXiv:1808.06024 (visited on 03/29/2019).

Martinez, R. A. and A. L. Kraus (2021). "A Mid-infrared Study of Directly Imaged Planetary-mass Companions Using Archival Spitzer/IRAC Images". In: *The Astronomical Journal* 163 (1), p. 36. ISSN: 1538-3881. DOI: 10.3847/1538-3881/ac3745. URL: https://dx.doi.org/10.3847/1538-3881/ac3745%20https://iopscience.iop.org/article/10.3847/1538-3881/ac3745/pdf.

Mawet, D. et al. (2017). "Observing Exoplanets with High-Dispersion Coronagraphy. II. Demonstration of an Active Single-Mode Fiber Injection Unit". en. In: *The Astrophysical Journal* 838.2, p. 92. ISSN: 0004-637X. DOI: 10.3847/1538-4357/aa647f.

Mayor, M. and D. Queloz (Nov. 1995). "A Jupiter-mass companion to a solar-type star". In: *Nature* 378.6555, pp. 355–359. DOI: 10.1038/378355a0.

McKemmish, L. K., S. N. Yurchenko, and J. Tennyson (Nov. 2016). "ExoMol line lists - XVIII. The high-temperature spectrum of VO". In: *Monthly Notices of the Royal Astronomical Society* 463 (1), pp. 771–793. ISSN: 13652966. DOI: 10.1093/mnras/stw1969.

McKemmish, L. K. et al. (Sept. 2019). "ExoMol molecular line lists – XXXIII. The spectrum of Titanium Oxide". In: *Monthly Notices of the Royal Astronomical Society* 488 (2), pp. 2836–2854. ISSN: 13652966. DOI: 10.1093/mnras/stz1818.

McLean, I. S. et al. (Aug. 1998). "Design and development of NIRSPEC: a near-infrared echelle spectrograph for the Keck II telescope". In: *Infrared Astronomical Instrumentation*. Ed. by A. M. Fowler. Vol. 3354. Society of Photo-Optical Instrumentation Engineers (SPIE) Conference Series, pp. 566–578. DOI: 10.1117/12.317283.

Mérand, A. (Aug. 2022). "Flexible spectro-interferometric modelling of OIFITS data with PMOIRED". In: *Optical and Infrared Interferometry and Imaging VIII*. Ed. by A. Mérand, S. Sallum, and J. Sanchez-Bermudez. Vol. 12183. Society of Photo-Optical Instrumentation Engineers (SPIE) Conference Series, 121831N, 121831N. DOI: 10.1117/12.2626700. arXiv: 2207.11047 [astro-ph.IM].

Metchev, S. A. and L. A. Hillenbrand (Mar. 2009). "The Palomar/Keck Adaptive Optics Survey of Young Solar Analogs: Evidence for a Universal Companion Mass Function". In: *The Astrophysical Journal Supplement Series* 181.1, pp. 62–109. DOI: 10.1088/0067-0049/181/1/62. arXiv: 0808.2982 [astro-ph].

Miles, B. E. et al. (Aug. 2020). "Observations of Disequilibrium CO Chemistry in the Coldest Brown Dwarfs". In: *The Astronomical Journal* 160, p. 63. ISSN: 0004-6256. DOI: 10.3847/1538-3881/ab9114.

Miles, B. E. et al. (Mar. 2023). "The JWST Early-release Science Program for Direct Observations of Exoplanetary Systems II: A 1 to 20 μm Spectrum of the Planetary-mass Companion VHS 1256-1257 b". In: *The Astrophysical Journal Letters* 946.1, L6, p. L6. DOI: 10.3847/2041-8213/acb04a. arXiv: 2209.00620 [astro-ph.EP].

Min, M., J. W. Hovenier, and A. de Koter (Mar. 2005). "Modeling Optical Properties of Cosmic Dust Grains Using a Distribution of Hollow Spheres". In: *Astronomy and Astrophysics* 432.3, p. 909. ISSN: 0004-6361. DOI: 10.1051/0004-6361:20041920.

Miret-Roig, N. et al. (Nov. 2022). "The star formation history of Upper Scorpius and Ophiuchus: A 7D picture: Positions, kinematics, and dynamical traceback ages". In: *Astronomy and Astrophysics* 667. ISSN: 14320746. DOI: 10.1051/0004-6361/202244709.

Mollière, P. and I. A. G. Snellen (Feb. 2019a). "Detecting Isotopologues in Exoplanet Atmospheres Using Ground-Based High-Dispersion Spectroscopy". In: *Astronomy and Astrophysics* 622, A139. ISSN: 0004-6361. DOI: 10.1051/0004-6361/201834169.

Mollière, P. et al. (Apr. 2017). "Observing Transiting Planets with JWST. Prime Targets and Their Synthetic Spectral Observations". In: *Astronomy and Astrophysics* 600, A10. ISSN: 0004-6361. DOI: 10.1051/0004-6361/201629800.

Mollière, P. et al. (July 2019b). "petitRADTRANS. A Python Radiative Transfer Package for Exoplanet Characterization and Retrieval". In: *Astronomy and Astrophysics* 627, A67. ISSN: 0004-6361. DOI: 10.1051/0004-6361/201935470.

Mollière, P. et al. (Aug. 2020). "Retrieving Scattering Clouds and Disequilibrium Chemistry in the Atmosphere of HR 8799e". In: *Astronomy and Astrophysics* 640, A131. ISSN: 0004-6361. DOI: 10.1051/0004-6361/202038325.

Mollière, P. et al. (July 2022). "Interpreting the Atmospheric Composition of Exoplanets: Sensitivity to Planet Formation Assumptions". In: *The Astrophysical Journal* 934, p. 74. ISSN: 0004-637X. DOI: 10.3847/1538-4357/ac6a56.

Mollière, P. M. (2017). *Modeling of Exoplanet Atmospheres*. URL: 10.11588/heidok.00023252.

Mordasini, C. et al. (Nov. 2016). "The Imprint of Exoplanet Formation History on Observable Present-day Spectra of Hot Jupiters". In: *The Astrophysical Journal* 832, p. 41. ISSN: 0004-637X. DOI: 10.3847/0004-637X/832/1/41.

Morley, C. V. et al. (Sept. 2019). "Measuring the D/H Ratios of Exoplanets and Brown Dwarfs". In: *The Astrophysical Journal* 882 (2), p. L29. ISSN: 20418213. DOI: 10.3847/2041-8213/ab3c65.

Morley, C. V. et al. (Nov. 2024). "The Sonora Substellar Atmosphere Models. III. Diamondback: Atmospheric Properties, Spectra, and Evolution for Warm Cloudy Substellar Objects". In: *The Astrophysical Journal* 975.1, 59, p. 59. DOI: 10.3847/1538-4357/ad71d5. arXiv: 2402.00758 [astro-ph.SR].

Morris, E. C. et al. (Oct. 2024). "κ Andromedae b Is a Fast Rotator from KPIC High-resolution Spectroscopy". In: *The Astronomical Journal* 168.4, 144, p. 144. DOI: 10.3847/1538-3881/ad4ecf. arXiv: 2405.13125 [astro-ph.EP].

Moses, J. I. et al. (Jan. 2013). "Chemical Consequences of the C/O Ratio on Hot Jupiters: Examples from WASP-12b, CoRoT-2b, XO-1b, and HD 189733b". In: *The Astrophysical Journal* 763, p. 25. ISSN: 0004-637X. DOI: 10.1088/0004-637X/763/1/25.

Mukherjee, S. et al. (Mar. 2024). "The Sonora Substellar Atmosphere Models. IV. Elf Owl: Atmospheric Mixing and Chemical Disequilibrium with Varying Metallicity and C/O Ratios". In: *The Astrophysical Journal* 963.1, 73, p. 73. DOI: 10.3847/1538-4357/ad18c2. arXiv: 2402.00756 [astro-ph.EP].

Nagpal, V. et al. (Feb. 2023). "The Impact of Bayesian Hyperpriors on the Population-level Eccentricity Distribution of Imaged Planets". In: *The Astronomical Journal* 165.2, 32, p. 32. DOI: 10.3847/1538-3881/ac9fd2. arXiv: 2211.02121 [astro-ph.EP].

Nakajima, T., T. Tsuji, and Y. Takeda (Aug. 2015). "Physical properties of gliese 229B based on newly determined carbon and oxygen abundances of Gliese 229A". In: *Astronomical Journal* 150 (2). ISSN: 00046256. DOI: 10.1088/0004-6256/150/2/53.

Nakajima, T. et al. (Nov. 1995). "Discovery of a cool brown dwarf". In: *Nature* 378.6556, pp. 463–465. DOI: 10.1038/378463a0.

Naoz, S. (Sept. 2016). "The Eccentric Kozai-Lidov Effect and Its Applications". en. In: *Annual Review of Astronomy and Astrophysics* 54, pp. 441–489. ISSN: 0066-4146. DOI: 10.1146/annurev-astro-081915-023315.

Nasedkin, E. et al. (Oct. 2023). "Impacts of high-contrast image processing on atmospheric retrievals". In: *Astronomy & Astrophysics* 678, A41, A41. DOI: 10.1051/0004-6361/202346585. arXiv: 2308.01343 [astro-ph.EP].

Nasedkin, E. et al. (Apr. 2024). "Four-of-a-kind? Comprehensive atmospheric characterisation of the HR 8799 planets with VLTI/GRAVITY". In: *arXiv e-prints*, arXiv:2404.03776, arXiv:2404.03776. DOI: 10.48550/arXiv.2404.03776. arXiv: 2404.03776 [astro-ph.EP].

Neuhäuser, R. et al. (May 2005). "Evidence for a co-moving sub-stellar companion of GQ Lup". In: *Astronomy and Astrophysics* 435 (1). ISSN: 00046361. DOI: 10.1051/0004-6361:200500104.

Neves, V. et al. (Mar. 2013). "Metallicity of M dwarfs. III. Planet-metallicity and planet-stellar mass correlations of the HARPS GTO M dwarf sample". In: *Astronomy & Astrophysics* 551, A36, A36. DOI: 10.1051/0004-6361/201220574. arXiv: 1212.3372 [astro-ph.SR].

Nielsen, E. L. et al. (Oct. 2013). "The Gemini NICI Planet-Finding Campaign: The Frequency of Giant Planets around Young B and A Stars". In: *The Astrophysical Journal* 776.1, 4, p. 4. DOI: 10.1088/0004-637X/776/1/4. arXiv: 1306.1233 [astro-ph.EP].

Nielsen, E. L. et al. (June 2019). "The Gemini Planet Imager Exoplanet Survey: Giant Planet and Brown Dwarf Demographics from 10 to 100 au". In: *The Astronomical Journal* 158.1, p. 13. DOI: 10.3847/1538-3881/ab16e9. URL: https://doi.org/10.3847%2F1538-3881%2Fab16e9.

Nittler, L. R. and E. Gaidos (Dec. 2012). "Galactic chemical evolution and the oxygen isotopic composition of the solar system". In: *Meteoritics & Planetary Science* 47.12, pp. 2031–2048. DOI: 10.1111/j.1945-5100.2012.01410.x. arXiv: 1207.7337 [astro-ph.GA].

Noll, K. S., T. R. Geballe, and M. S. Marley (Nov. 1997). "Detection of Abundant Carbon Monoxide in the Brown Dwarf Gliese 229B". In: *The Astrophysical Journal Letters* 489.1, pp. L87–L90. DOI: 10.1086/310954.

Noll, K. S. et al. (Sept. 2000). "The Onset of Methane in L Dwarfs". In: *The Astrophysical Journal* 541.2, p. L75. ISSN: 0004-637X. DOI: 10.1086/312906.

Noll, S. et al. (July 2012). “An atmospheric radiation model for Cerro Paranal. I. The optical spectral range”. In: *Astronomy & Astrophysics* 543, A92, A92. DOI: 10.1051/0004-6361/201219040. arXiv: 1205.2003 [astro-ph.IM].

Nowak, M. et al. (Apr. 2024). “Upgrading the GRAVITY fringe tracker for GRAVITY+. Tracking the white-light fringe in the non-observable optical path length state-space”. In: *Astronomy & Astrophysics* 684, A184, A184. DOI: 10.1051/0004-6361/202348771. arXiv: 2402.03594 [astro-ph.IM].

Öberg, K. I. and E. A. Bergin (Nov. 2016). “Excess C/O and C/H in Outer Protoplanetary Disk Gas”. In: *The Astrophysical Journal* 831, p. L19. ISSN: 0004-637X. DOI: 10.3847/2041-8205/831/2/L19.

Öberg, K. I., S. Facchini, and D. E. Anderson (2023). “Protoplanetary Disk Chemistry”. In: *Annual Review of Astronomy and Astrophysics* 61.1, pp. 287–328. DOI: 10.1146/annurev-astro-022823-040820. URL: https://doi.org/10.1146/annurev-astro-022823-040820.

Öberg, K. I., R. Murray-Clay, and E. A. Bergin (2011). “The Effects of Snowlines on C/O in Planetary Atmospheres”. en. In: *The Astrophysical Journal Letters* 743.1, p. L16. ISSN: 2041-8205. DOI: 10.1088/2041-8205/743/1/L16. URL: http://stacks.iop.org/2041-8205/743/i=1/a=L16 (visited on 12/25/2018).

Offner, S. S. R. et al. (July 2023). “The Origin and Evolution of Multiple Star Systems”. In: *Protostars and Planets VII*. Ed. by S. Inutsuka et al. Vol. 534. Astronomical Society of the Pacific Conference Series, p. 275. DOI: 10.48550/arXiv.2203.10066. arXiv: 2203.10066 [astro-ph.SR].

Offner, S. S. R. et al. (Dec. 2010). “The Formation of Low-mass Binary Star Systems Via Turbulent Fragmentation”. In: *The Astrophysical Journal* 725, pp. 1485–1494. ISSN: 0004-637X. DOI: 10.1088/0004-637X/725/2/1485.

Offner, S. S. R. et al. (Aug. 2016). “The Turbulent Origin of Outflow and Spin Misalignment in Multiple Star Systems”. In: *The Astrophysical Journal* 827 (1), p. L11. ISSN: 20418213. DOI: 10.3847/2041-8205/827/1/l11.

Ohno, K. and J. J. Fortney (Mar. 2023). “Nitrogen as a Tracer of Giant Planet Formation. I. A Universal Deep Adiabatic Profile and Semianalytical Predictions of Disequilibrium Ammonia Abundances in Warm Exoplanetary Atmospheres”. In: *The Astrophysical Journal* 946 (1), p. 18. ISSN: 0004-637X. DOI: 10.3847/1538-4357/acafed.

Oppenheimer, B. R. et al. (1995). “Infrared Spectrum of the Cool Brown Dwarf Gl 229B”. In: *Science* 270, pp. 1478–1479. ISSN: 0036-8075. DOI: 10.1126/science.270.5241.1478. URL: https://ui.adsabs.harvard.edu/abs/1995Sci...270.1478O.

Oppenheimer, B. R., S. R. Kulkarni, and J. R. Stauffer (May 2000). “Brown Dwarfs”. In: *Protostars and Planets IV*. Ed. by V. Mannings, A. P. Boss, and S. S. Russell, p. 1313.

Oppenheimer, B. R. et al. (Aug. 1998). "The Spectrum of the Brown Dwarf Gliese 229B". In: *The Astrophysical Journal* 502.2, pp. 932–943. DOI: 10.1086/305928. arXiv: astro-ph/9802299 [astro-ph].

Oreshenko, M. et al. (Jan. 2020). "Supervised Machine Learning for Intercomparison of Model Grids of Brown Dwarfs: Application to GJ 570D and the Epsilon Indi B Binary System". In: *The Astronomical Journal* 159.1, 6, p. 6. DOI: 10.3847/1538-3881/ab5955. arXiv: 1910.11795 [astro-ph.SR].

Ortega, V. G. et al. (2002). *The Origin of the β Pictoris Moving Group*.

Osborn, A. and D. Bayliss (2020). "Investigating the planet-metallicity correlation for hot Jupiters". In: *Monthly Notices of the Royal Astronomical Society* 491 (3), pp. 4481–4487. ISSN: 13652966. DOI: 10.1093/MNRAS/STZ3207.

Otten, G. P. P. L. et al. (Feb. 2021). "Direct Characterization of Young Giant Exoplanets at High Spectral Resolution by Coupling SPHERE and CRIRES+". en. In: *Astronomy & Astrophysics, Volume 646, id.A150, <NUMPAGES>19</NUMPAGES> pp.* 646, A150. ISSN: 0004-6361. DOI: 10.1051/0004-6361/202038517.

Padoan, P. and Å. Nordlund (Dec. 2004). "The "Mysterious" Origin of Brown Dwarfs". In: *The Astrophysical Journal* 617, pp. 559–564. ISSN: 0004-637X. DOI: 10.1086/345413.

Palma-Bifani, P. et al. (Feb. 2023). "Peering into the young planetary system AB Pic. Atmosphere, orbit, obliquity, and second planetary candidate". In: *Astronomy & Astrophysics* 670, A90, A90. DOI: 10.1051/0004-6361/202244294. arXiv: 2211.01474 [astro-ph.EP].

Palma-Bifani, P. et al. (Jan. 2024). "Atmospheric properties of AF Lep b with forward modeling". In: *arXiv e-prints*, arXiv:2401.05491, arXiv:2401.05491. DOI: 10.48550/arXiv.2401.05491. arXiv: 2401.05491 [astro-ph.EP].

Peale, S. J. (Jan. 1977). "Rotation Histories of the Natural Satellites". In: *Issue 28 of Colloquium (International Astronomical Union): Planetary Satellites*. Ed. by J. A. Burns, p. 87.

Pearce, L. A. et al. (Jan. 2019). "Orbital Motion of the Wide Planetary-mass Companion GSC 6214-210 b: No Evidence for Dynamical Scattering". In: *The Astronomical Journal* 157.2, p. 71. DOI: 10.3847/1538-3881/aafacb. URL: https://doi.org/10.3847%2F1538-3881%2Faafacb.

Pecaut, M. J. and E. E. Mamajek (Sept. 2016). "The star formation history and accretion-disc fraction among the K-type members of the Scorpius-Centaurus OB association". In: *Monthly Notices of the Royal Astronomical Society* 461 (1), pp. 794–815. ISSN: 13652966. DOI: 10.1093/mnras/stw1300.

Pelletier, S. et al. (May 2021). "Where Is the Water? Jupiter-like C/H Ratio but Strong H$_2$O Depletion Found on τ Boötis b Using SPIRou". en. In: *arXiv e-prints*, arXiv:2105.10513.

Peretti, S. et al. (Nov. 2019). "Orbital and Spectral Analysis of the Benchmark Brown Dwarf HD 4747B". en. In: *Astronomy & Astrophysics* 631, A107. ISSN: 0004-6361, 1432-0746. DOI: 10.1051/0004-6361/201732454.

Perrin, M. D. et al. (Sept. 2012). "Simulating point spread functions for the James Webb Space Telescope with WebbPSF". In: *Space Telescopes and Instrumentation 2012: Optical, Infrared, and Millimeter Wave*. Ed. by M. C. Clampin et al. Vol. 8442. Society of Photo-Optical Instrumentation Engineers (SPIE) Conference Series, 84423D, p. 84423D. DOI: 10.1117/12.925230.

Perrin, M. D. et al. (Aug. 2014). "Updated point spread function simulations for JWST with WebbPSF". In: *Space Telescopes and Instrumentation 2014: Optical, Infrared, and Millimeter Wave*. Ed. by J. Oschmann Jacobus M. et al. Vol. 9143. Society of Photo-Optical Instrumentation Engineers (SPIE) Conference Series, 91433X, p. 91433X. DOI: 10.1117/12.2056689.

Perryman, M. et al. (Dec. 2014). "Astrometric Exoplanet Detection with Gaia". In: *The Astrophysical Journal* 797.1, 14, p. 14. DOI: 10.1088/0004-637X/797/1/14. arXiv: 1411.1173 [astro-ph.EP].

Petigura, E. A. et al. (Feb. 2018). "The California-Kepler Survey. IV. Metal-rich Stars Host a Greater Diversity of Planets". In: *The Astronomical Journal* 155.2, 89, p. 89. DOI: 10.3847/1538-3881/aaa54c. arXiv: 1712.04042 [astro-ph.EP].

Petigura, E. A. (Apr. 2015). "Prevalence of Earth-size Planets Orbiting Sun-like Stars". PhD thesis. University of California, Berkeley.

Petit dit de la Roche, D. J. M., H. J. Hoeijmakers, and I. a. G. Snellen (Aug. 2018). "Molecule Mapping of HR8799b Using OSIRIS on Keck. Strong Detection of Water and Carbon Monoxide, but No Methane". In: *Astronomy and Astrophysics* 616, A146. ISSN: 0004-6361. DOI: 10.1051/0004-6361/201833384.

Petrus, S. et al. (Apr. 2021). "Medium-resolution spectrum of the exoplanet HIP 65426 b". In: *Astronomy & Astrophysics* 648, A59, A59. DOI: 10.1051/0004-6361/202038914. arXiv: 2012.02798 [astro-ph.EP].

Petrus, S. et al. (Feb. 2023). "X-SHYNE: X-shooter spectra of young exoplanet analogs. I. A medium-resolution 0.65-2.5 μm one-shot spectrum of VHS 1256−1257 b". In: *Astronomy & Astrophysics* 670, L9, p. L9. DOI: 10.1051/0004-6361/202244494. arXiv: 2207.06622 [astro-ph.EP].

Petrus, S. et al. (May 2024). "The JWST Early Release Science Program for Direct Observations of Exoplanetary Systems. V. Do Self-consistent Atmospheric Models Represent JWST Spectra? A Showcase with VHS 1256–1257 b". In: *The Astrophysical Journal Letters* 966.1, L11, p. L11. DOI: 10.3847/2041-8213/ad3e7c. arXiv: 2312.03852 [astro-ph.EP].

Phillips, M. W. et al. (May 2020). "A new set of atmosphere and evolution models for cool T-Y brown dwarfs and giant exoplanets". In: *Astronomy and Astrophysics* 637. ISSN: 14320746. DOI: 10.1051/0004-6361/201937381.

Phillips, M. W., M. C. Liu, and Z. Zhang (Feb. 2024). "The Carbon-to-oxygen Ratio in Cool Brown Dwarfs and Giant Exoplanets. I. The Benchmark Late-T Dwarfs GJ 570D, HD 3651B, and Ross 458C". In: *The Astrophysical Journal* 961.2, 210, p. 210. DOI: 10.3847/1538-4357/ad06ba. arXiv: 2312.02001 [astro-ph.SR].

Piette, A. A. A. and N. Madhusudhan (2020). "Considerations for atmospheric retrieval of high-precision brown dwarf spectra". In: *Monthly Notices of the Royal Astronomical Society* 497, pp. 5136–5154. ISSN: 0035-8711. DOI: 10.1093/mnras/staa2289. URL: https://ui.adsabs.harvard.edu/abs/2020MNRAS.497.5136P%20https://arxiv.org/pdf/2007.15004.

Piso, A.-M. A. et al. (Dec. 2015). "C/O and Snowline Locations in Protoplanetary Disks: The Effect of Radial Drift and Viscous Gas Accretion". In: *The Astrophysical Journal* 815, p. 109. ISSN: 0004-637X. DOI: 10.1088/0004-637X/815/2/109.

Pollack, J. B. et al. (Nov. 1996). "Formation of the Giant Planets by Concurrent Accretion of Solids and Gas". In: *Icarus* 124.1, pp. 62–85. ISSN: 0019-1035. DOI: 10.1006/icar.1996.0190. URL: http://www.sciencedirect.com/science/article/pii/S0019103596901906 (visited on 03/26/2019).

Polyansky, O. L. et al. (2017). "ExoMol molecular line lists XIX: high-accuracy computed hot line lists for H218O and H217O". In: *Monthly Notices of the Royal Astronomical Society* 466 (2), pp. 1363–1371. ISSN: 0035-8711. DOI: 10.1093/mnras/stw3125. URL: https://doi.org/10.1093/mnras/stw3125%20https://academic.oup.com/mnras/article-pdf/466/2/1363/10867428/stw3125.pdf%20https://academic.oup.com/mnras/article/466/2/1363/2627209.

Polyansky, O. L. et al. (2018). "ExoMol molecular line lists XXX: a complete high-accuracy line list for water". In: *Monthly Notices of the Royal Astronomical Society* 480 (2), pp. 2597–2608. ISSN: 0035-8711. DOI: 10.1093/mnras/sty1877. URL: https://doi.org/10.1093/mnras/sty1877%20https://academic.oup.com/mnras/article-pdf/480/2/2597/28250193/sty1877.pdf%20https://academic.oup.com/mnras/article/480/2/2597/5054049.

Poovelil, V. J. et al. (Nov. 2020). "Open Cluster Chemical Homogeneity throughout the Milky Way". In: *The Astrophysical Journal* 903 (1), p. 55. ISSN: 0004-637X. DOI: 10.3847/1538-4357/abb93e.

Pueyo, L. (June 2016). "Detection and Characterization of Exoplanets Using Projections on Karhunen–Loève Eigenimages: Forward Modeling". en. In: *The Astrophysical Journal* 824.2, p. 117. ISSN: 0004-637X. DOI: 10.3847/0004-637X/824/2/117.

Qi, C. et al. (Aug. 2013). "Imaging of the CO Snow Line in a Solar Nebula Analog". In: *Science* 341.6146, pp. 630–632. DOI: 10.1126/science.1239560. arXiv: 1307.7439 [astro-ph.SR].

Qi, C. et al. (Nov. 2015). "Chemical Imaging of the CO Snow Line in the HD 163296 Disk". en. In: *The Astrophysical Journal* 813.2. Publisher: The American Astronomical Society, p. 128. ISSN: 0004-637X. DOI: 10.1088/0004-637X/813/2/128. URL: https://dx.doi.org/10.1088/0004-637X/813/2/128 (visited on 09/21/2023).

Qi, C. et al. (Sept. 2019). "Probing CO and N_2 Snow Surfaces in Protoplanetary Disks with N_2H^+ Emission". In: *The Astrophysical Journal* 882.2, 160, p. 160. DOI: 10.3847/1538-4357/ab35d3. arXiv: 1907.10647 [astro-ph.SR].

Radigan, J. et al. (Nov. 2013). "Discovery of a Visual T-dwarf Triple System and Binarity at the L/T Transition". In: *The Astrophysical Journal* 778.1, 36, p. 36. DOI: 10.1088/0004-637X/778/1/36. arXiv: 1308.5702 [astro-ph.SR].

Rafikov, R. R. (Mar. 2005). "Can Giant Planets Form by Direct Gravitational Instability?" In: *The Astrophysical Journal Letters* 621.1, pp. L69–L72. DOI: 10.1086/428899. arXiv: astro-ph/0406469 [astro-ph].

Ratzka, T., R. Köhler, and C. Leinert (July 2005). "A multiplicity survey of the rho Ophiuchi molecular clouds". In: *Astronomy and Astrophysics* 437 (2), pp. 611–626. ISSN: 00046361. DOI: 10.1051/0004-6361:20042107.

Redai, J. I. A. et al. (Feb. 2023). "The Giant Accreting Protoplanet Survey (GAPlanetS): Optimization Techniques for Robust Detections of Protoplanets". In: *The Astronomical Journal* 165 (2), p. 57. ISSN: 0004-6256. DOI: 10.3847/1538-3881/aca60d.

Reggiani, H. et al. (Jan. 2024). "Insight into the Formation of β Pic b through the Composition of Its Parent Protoplanetary Disk as Revealed by the β Pic Moving Group Member HD 181327". In: *The Astronomical Journal* 167.1, 45, p. 45. DOI: 10.3847/1538-3881/ad0f93. arXiv: 2311.12210 [astro-ph.SR].

Rice, M. and J. M. Brewer (Aug. 2020). "Stellar Characterization of Keck HIRES Spectra with The Cannon". In: *The Astrophysical Journal* 898.2, 119, p. 119. DOI: 10.3847/1538-4357/ab9f96. arXiv: 2007.02942 [astro-ph.EP].

Ricker, G. R. et al. (Jan. 2015). "Transiting Exoplanet Survey Satellite (TESS)". In: *Journal of Astronomical Telescopes, Instruments, and Systems* 1, 014003, p. 014003. DOI: 10.1117/1.JATIS.1.1.014003.

Rickman, E. L. et al. (Apr. 2024). "The discovery of two new benchmark brown dwarfs with precise dynamical masses at the stellar-substellar boundary". In: *Astronomy & Astrophysics* 684, A88, A88. DOI: 10.1051/0004-6361/202347906. arXiv: 2401.10058 [astro-ph.SR].

Rieke, G. H. et al. (July 2015). "The Mid-Infrared Instrument for the James Webb Space Telescope, I: Introduction". In: *Publications of the Astronomical Society of the Pacific* 127.953, p. 584. DOI: 10.1086/682252. arXiv: 1508.02294 [astro-ph.IM].

Riello, M. et al. (May 2021). "Gaia Early Data Release 3. Photometric Content and Validation". In: *Astronomy and Astrophysics* 649, A3. ISSN: 0004-6361. DOI: 10.1051/0004-6361/202039587.

Robichaud, J. L. et al. (Aug. 1998). "Cryogenic performance of the NIRSPEC three-mirror anastigmat". In: *Infrared Astronomical Instrumentation*. Ed. by A. M. Fowler. Vol. 3354. Society of Photo-Optical Instrumentation Engineers (SPIE) Conference Series, pp. 1068–1076. DOI: 10.1117/12.317230.

Romano, D. et al. (Sept. 2017). "The evolution of CNO isotopes: A new window on cosmic star formation history and the stellar IMF in the age of ALMA". In: *Monthly Notices of the Royal Astronomical Society* 470 (1), pp. 401–415. ISSN: 13652966. DOI: 10.1093/mnras/stx1197.

Rosenthal, L. J. et al. (May 2021). "The California Legacy Survey I. A Catalog of 177 Planets from Precision Radial Velocity Monitoring of 719 Nearby Stars over Three Decades". In: *arXiv:2105.11583 [astro-ph]*. arXiv: 2105.11583 [astro-ph].

Rothman, L. S. et al. (Oct. 2010). "HITEMP, the high-temperature molecular spectroscopic database". In: *Journal of Quantitative Spectroscopy and Radiative Transfer* 111 (15), pp. 2139–2150. ISSN: 00224073. DOI: 10.1016/j.jqsrt.2010.05.001.

Rowland, M. J., C. V. Morley, and M. R. Line (Apr. 2023). "Toward Robust Atmospheric Retrieval on Cloudy L Dwarfs: the Impact of Thermal and Abundance Profile Assumptions". In: *The Astrophysical Journal* 947 (1), p. 6. ISSN: 0004-637X. DOI: 10.3847/1538-4357/acbb07.

Ruffio, J.-B. (2019). *Direct Detection and Characterization of Exoplanets*. URL: https://purl.stanford.edu/yq071tj0740.

Ruffio, J.-B. et al. (Nov. 2019). "Radial Velocity Measurements of HR 8799 b and c with Medium Resolution Spectroscopy". In: *The Astronomical Journal* 158 (5), p. 200. ISSN: 0004-6256. DOI: 10.3847/1538-3881/ab4594.

Ruffio, J.-B. et al. (Dec. 2021). "Deep Exploration of the Planets HR 8799 b, c, and d with Moderate-resolution Spectroscopy". In: *The Astronomical Journal* 162, p. 290. ISSN: 0004-6256. DOI: 10.3847/1538-3881/ac273a.

Ruffio, J.-B. et al. (Mar. 2023a). "Detecting Exomoons from Radial Velocity Measurements of Self-luminous Planets: Application to Observations of HR 7672 B and Future Prospects". In: *The Astronomical Journal* 165.3, 113, p. 113. DOI: 10.3847/1538-3881/acb34a. arXiv: 2301.04206 [astro-ph.EP].

Ruffio, J.-B. et al. (Oct. 2023b). "JWST-TST High Contrast: Achieving direct spectroscopy of faint substellar companions next to bright stars with the NIRSpec IFU". In: *arXiv e-prints*, arXiv:2310.09902, arXiv:2310.09902. DOI: 10.48550/arXiv.2310.09902. arXiv: 2310.09902 [astro-ph.EP].

Ruffio, J.-B. et al. (Aug. 2024). "JWST-TST High Contrast: Achieving Direct Spectroscopy of Faint Substellar Companions Next to Bright Stars with the NIRSpec Integral Field Unit". In: *The Astronomical Journal* 168.2, 73, p. 73. DOI: 10.3847/1538-3881/ad5281. arXiv: 2310.09902 [astro-ph.EP].

Sahlmann, J. et al. (Jan. 2011). "Search for brown-dwarf companions of stars". In: *Astronomy & Astrophysics* 525, A95, A95. DOI: 10.1051/0004-6361/201015427. arXiv: 1009.5991 [astro-ph.EP].

Samland, M. et al. (July 2017). "Spectral and Atmospheric Characterization of 51 Eridani b Using VLT/SPHERE". In: *Astronomy and Astrophysics* 603, A57. ISSN: 0004-6361. DOI: 10.1051/0004-6361/201629767.

Sanghi, A. et al. (Dec. 2023). "The Hawaii Infrared Parallax Program. VI. The Fundamental Properties of 1000+ Ultracool Dwarfs and Planetary-mass Objects Using Optical to Mid-infrared Spectral Energy Distributions and Comparison to BT-Settl and ATMO 2020 Model Atmospheres". In: *The Astrophysical Journal* 959.1, 63, p. 63. DOI: 10.3847/1538-4357/acff66. arXiv: 2309.03082 [astro-ph.SR].

Santos, N. C. et al. (Mar. 2008). "Chemical abundances in six nearby star-forming regions. Implications for galactic evolution and planet searches around very young stars". In: *Astronomy & Astrophysics* 480.3, pp. 889–897. DOI: 10.1051/0004-6361:20079083. arXiv: 0801.2529 [astro-ph].

Saumon, D. and M. S. Marley (Dec. 2008). "The Evolution of L and T Dwarfs in Color-Magnitude Diagrams". In: *The Astrophysical Journal* 689.2, pp. 1327–1344. DOI: 10.1086/592734. URL: https://doi.org/10.1086%2F592734.

Saumon, D. et al. (Sept. 2000). "Molecular Abundances in the Atmosphere of the T Dwarf GL 229B". In: *The Astrophysical Journal* 541.1, pp. 374–389. DOI: 10.1086/309410. arXiv: astro-ph/0003353 [astro-ph].

Schlaufman, K. C. (Jan. 2018). "Evidence of an Upper Bound on the Masses of Planets and Its Implications for Giant Planet Formation". en. In: *The Astrophysical Journal* 853.1, p. 37. DOI: 10.3847/1538-4357/aa961c. URL: https://ui.adsabs.harvard.edu/abs/2018ApJ...853...37S/abstract (visited on 08/03/2019).

Schneider, A. C. et al. (Sept. 2023). "Astrometry and Photometry for ≈1000 L, T, and Y Dwarfs from the UKIRT Hemisphere Survey". In: *The Astronomical Journal* 166.3, 103, p. 103. DOI: 10.3847/1538-3881/ace9bf. arXiv: 2307.11882 [astro-ph.SR].

Schwarz, H. et al. (2016). "The slow spin of the young substellar companion GQ Lupi b and its orbital configuration". In: *Astronomy and Astrophysics* 593, A74. ISSN: 0004-6361. DOI: 10.1051/0004-6361/201628908. URL: https://ui.adsabs.harvard.edu/abs/2016A&A...593A..74S/abstract%20https://ui.adsabs.harvard.edu/link_gateway/2016A&A...593A..74S/

PUB_PDF%20https://ui.adsabs.harvard.edu/abs/2016A%26A...593A..74S/abstract.

Schweitzer, A. et al. (May 2019). "The CARMENES search for exoplanets around M dwarfs. Different roads to radii and masses of the target stars". In: *Astronomy & Astrophysics* 625, A68, A68. DOI: 10.1051/0004-6361/201834965. arXiv: 1904.03231 [astro-ph.SR].

Sebastian, D. et al. (Jan. 2021). "SPECULOOS: Ultracool dwarf transit survey: Target list and strategy". In: *Astronomy and Astrophysics* 645. ISSN: 14320746. DOI: 10.1051/0004-6361/202038827.

Seifahrt, A., R. Neuhäuser, and P. H. Hauschildt (Feb. 2007). "Near-infrared integral-field spectroscopy of the companion to GQ Lupi". In: *Astronomy and Astrophysics* 463 (1), pp. 309–313. ISSN: 00046361. DOI: 10.1051/0004-6361:20066463.

Service, M. et al. (2016). "A New Distortion Solution for NIRC2 on the Keck II Telescope". In: *Publications of the Astronomical Society of the Pacific* 128, p. 095004. ISSN: 0004-6280. DOI: 10.1088/1538-3873/128/967/095004. URL: http://adsabs.harvard.edu/abs/2016PASP..128i5004S%20http://adsabs.harvard.edu/cgi-bin/nph-data_query?bibcode=2016PASP..128i5004S&link_type=ARTICLE&db_key=AST&high=.

Skemer, A. J. et al. (Sept. 2014). "Directly Imaged L-T Transition Exoplanets in the Mid-infrared". In: *The Astrophysical Journal* 792, p. 17. ISSN: 0004-637X. DOI: 10.1088/0004-637X/792/1/17.

Skemer, A. J. et al. (Aug. 2022). "Design of SCALES: a 2-5 micron coronagraphic integral field spectrograph for Keck Observatory". In: *Proceedings of SPIE*. Vol. 12184. Proceedings of SPIE, 121840I, p. 121840I.

Smette, A. et al. (Apr. 2015). "Molecfit: A general tool for telluric absorption correction - I. Method and application to ESO instruments". en. In: *Astronomy & Astrophysics* 576, A77. ISSN: 0004-6361, 1432-0746. DOI: 10.1051/0004-6361/201423932. URL: https://www.aanda.org/articles/aa/abs/2015/04/aa23932-14/aa23932-14.html (visited on 11/19/2018).

Smith, M. D. (Mar. 1998). "Estimation of a Length Scale to Use with the Quench Level Approximation for Obtaining Chemical Abundances". In: *Icarus* 132.1, pp. 176–184. ISSN: 0019-1035. DOI: 10.1006/icar.1997.5886.

Sneden, C. (Sept. 1973). "The Nitrogen Abundance of the Very Metal-Poor Star HD 122563." In: *The Astrophysical Journal* 184, p. 839. ISSN: 0004-637X. DOI: 10.1086/152374.

Snellen, I. A. G. and A. G. A. Brown (Aug. 2018). "The mass of the young planet Beta Pictoris b through the astrometric motion of its host star". In: *Nature Astronomy* 2, pp. 883–886. DOI: 10.1038/s41550-018-0561-6. arXiv: 1808.06257 [astro-ph.EP].

Snellen, I. A. G. et al. (June 2010). "The orbital motion, absolute mass and high-altitude winds of exoplanet HD209458b". In: *Nature* 465.7301, pp. 1049–1051. DOI: 10.1038/nature09111. arXiv: 1006.4364 [astro-ph.EP].

Snellen, I. A. G. et al. (May 2014). "Fast spin of the young extrasolar planet beta Pictoris b". en. In: *Nature* 509.7498, pp. 63–65. ISSN: 1476-4687. DOI: 10.1038/nature13253. URL: https://www.nature.com/articles/nature13253 (visited on 04/24/2019).

Soummer, R., L. Pueyo, and J. Larkin (Aug. 2012). "Detection and Characterization of Exoplanets and Disks Using Projections on Karhunen-Loève Eigenimages". In: *The Astrophysical Journal* 755, p. L28. ISSN: 0004-637X. DOI: 10.1088/2041-8205/755/2/L28.

Souto, D. et al. (Mar. 2022). "Detailed Chemical Abundances for a Benchmark Sample of M Dwarfs from the APOGEE Survey". In: *The Astrophysical Journal* 927 (1), p. 123. ISSN: 0004-637X. DOI: 10.3847/1538-4357/ac4891.

Sozzetti, A. and S. Desidera (Jan. 2010). "Hipparcos preliminary astrometric masses for the two close-in companions to HD 131664 and HD 43848. A brown dwarf and a low-mass star". In: *Astronomy & Astrophysics* 509, A103, A103. DOI: 10.1051/0004-6361/200912717. arXiv: 0909.4454 [astro-ph.EP].

Speagle, J. S. (Apr. 2020). "DYNESTY: A Dynamic Nested Sampling Package for Estimating Bayesian Posteriors and Evidences". In: *Monthly Notices of the Royal Astronomical Society* 493, pp. 3132–3158. ISSN: 0035-8711. DOI: 10.1093/mnras/staa278.

Speedie, J. et al. (Sept. 2024). "Gravitational instability in a planet-forming disk". In: *Nature* 633.8028, pp. 58–62. DOI: 10.1038/s41586-024-07877-0. arXiv: 2409.02196 [astro-ph.EP].

Spina, L. et al. (Aug. 2014). "The Gaia-ESO Survey: Metallicity of the Chamaeleon I star-forming region". In: *Astronomy & Astrophysics* 568, A2, A2. DOI: 10.1051/0004-6361/201424135. arXiv: 1406.2548 [astro-ph.SR].

Stamatellos, D., D. A. Hubber, and A. P. Whitworth (Nov. 2007). "Brown Dwarf Formation by Gravitational Fragmentation of Massive, Extended Protostellar Discs". In: *Monthly Notices of the Royal Astronomical Society* 382, pp. L30–L34. ISSN: 0035-8711. DOI: 10.1111/j.1745-3933.2007.00383.x.

Stamatellos, D. and A. P. Whitworth (Jan. 2009). "The properties of brown dwarfs and low-mass hydrogen-burning stars formed by disc fragmentation". In: *Monthly Notices of the Royal Astronomical Society* 392, pp. 413–427. ISSN: 0035-8711. DOI: 10.1111/j.1365-2966.2008.14069.x. URL: http://adsabs.harvard.edu/abs/2009MNRAS.392..413S (visited on 04/04/2019).

Stanford-Moore, S. A. et al. (July 2020). "BAFFLES: Bayesian Ages for Field Lower-mass Stars". In: *The Astrophysical Journal* 898 (1), p. 27. ISSN: 15384357. DOI: 10.3847/1538-4357/ab9a35.

Stassun, K. G., R. D. Mathieu, and J. A. Valenti (Mar. 2006). "Discovery of two young brown dwarfs in an eclipsing binary system". In: *Nature* 440.7082, pp. 311–314. DOI: 10.1038/nature04570.

Stassun, K. G. et al. (Sept. 2019). "The Revised TESS Input Catalog and Candidate Target List". In: *The Astronomical Journal* 158 (4), p. 138. ISSN: 00046256. DOI: 10.3847/1538-3881/ab3467.

Stefansson, G. et al. (Oct. 2024). "Gaia-4b and 5b: Radial Velocity Confirmation of Gaia Astrometric Orbital Solutions Reveal a Massive Planet and a Brown Dwarf Orbiting Low-mass Stars". In: *arXiv e-prints*, arXiv:2410.05654, arXiv:2410.05654. DOI: 10.48550/arXiv.2410.05654. arXiv: 2410.05654 [astro-ph.EP].

Stelter, R. D. et al. (Dec. 2020). "Update on the Preliminary Design of SCALES: The Santa Cruz Array of Lenslets for Exoplanet Spectroscopy". In: *Ground-Based and Airborne Instrumentation for Astronomy VIII*. Vol. 11447. SPIE, pp. 1346–1369. DOI: 10.1117/12.2562768.

Stolker, T. et al. (Mar. 2020). "MIRACLES: atmospheric characterization of directly imaged planets and substellar companions at 4-5 μm. I. Photometric analysis of β Pic b, HIP 65426 b, PZ Tel B, and HD 206893 B". In: *Astronomy & Astrophysics* 635, A182, A182. DOI: 10.1051/0004-6361/201937159. arXiv: 1912.13316 [astro-ph.EP].

Stolker, T. et al. (Dec. 2021). "Characterizing the Protolunar Disk of the Accreting Companion GQ Lupi B*". In: *The Astronomical Journal* 162 (6), p. 286. ISSN: 0004-6256. DOI: 10.3847/1538-3881/ac2c7f.

Suárez, G. and S. Metchev (July 2022). "Ultracool dwarfs observed with the Spitzer infrared spectrograph - II. Emergence and sedimentation of silicate clouds in L dwarfs, and analysis of the full M5-T9 field dwarf spectroscopic sample". In: *Monthly Notices of the Royal Astronomical Society* 513.4, pp. 5701–5726. DOI: 10.1093/mnras/stac1205. arXiv: 2205.00168 [astro-ph.SR].

Suárez, G. et al. (Sept. 2023). "Ultracool Dwarfs Observed with the Spitzer Infrared Spectrograph: Equatorial Latitudes in L Dwarf Atmospheres Are Cloudier". In: *The Astrophysical Journal Letters* 954.1, L6, p. L6. DOI: 10.3847/2041-8213/acec4b. arXiv: 2308.02093 [astro-ph.EP].

Surjanovic, N. et al. (2022). "Parallel Tempering With a Variational Reference". In: *Advances in Neural Information Processing Systems*. Ed. by S. Koyejo et al. Vol. 35. Curran Associates, Inc., pp. 565–577. URL: https://proceedings.neurips.cc/paper_files/paper/2022/file/03cd3cf3f74d4f9ce5958de269960884-Paper-Conference.pdf.

Surjanovic, N. et al. (2023). "Pigeons.jl: Distributed sampling from intractable distributions". In: *arXiv:2308.09769*.

Syed, S. et al. (May 2019). "Non-Reversible Parallel Tempering: a Scalable Highly Parallel MCMC Scheme". In: *arXiv e-prints*, arXiv:1905.02939, arXiv:1905.02939. DOI: 10.48550/arXiv.1905.02939. arXiv: 1905.02939 [stat.CO].

Syed, S. et al. (Apr. 2022). “Non-reversible parallel tempering: A scalable highly parallel MCMC scheme”. In: *Journal of the Royal Statistical Society Series B* 84.2, pp. 321–350. DOI: 10.1111/rssb.12464. URL: https://ui.adsabs.harvard.edu/abs/2019arXiv190502939S/abstract.

Tan, X. (Apr. 2022). “Jet Streams and Tracer Mixing in the Atmospheres of Brown Dwarfs and Isolated Young Giant Planets”. In: *Monthly Notices of the Royal Astronomical Society* 511, pp. 4861–4881. ISSN: 0035-8711. DOI: 10.1093/mnras/stac344.

Tan, X. and A. P. Showman (Mar. 2021a). “Atmospheric Circulation of Brown Dwarfs and Directly Imaged Exoplanets Driven by Cloud Radiative Feedback: Effects of Rotation”. In: *Monthly Notices of the Royal Astronomical Society* 502, pp. 678–699. ISSN: 0035-8711. DOI: 10.1093/mnras/stab060.

– (Apr. 2021b). “Atmospheric circulation of brown dwarfs and directly imaged exoplanets driven by cloud radiative feedback: global and equatorial dynamics”. In: *Monthly Notices of the Royal Astronomical Society* 502.2, pp. 2198–2219. DOI: 10.1093/mnras/stab097. arXiv: 2101.04417 [astro-ph.EP].

Tannock, M. E. et al. (May 2021). “Weather on Other Worlds. V. The Three Most Rapidly Rotating Ultra-cool Dwarfs”. In: *The Astronomical Journal* 161.5, 224, p. 224. DOI: 10.3847/1538-3881/abeb67. eprint: 2103.01990 (astro-ph.SR).

Tannock, M. E. et al. (Aug. 2022). “A 1.46-2.48 μm spectroscopic atlas of a T6 dwarf (1060 K) atmosphere with IGRINS: first detections of H_2S and H_2, and verification of H_2O, CH_4, and NH_3 line lists”. In: *Monthly Notices of the Royal Astronomical Society* 514.3, pp. 3160–3178. DOI: 10.1093/mnras/stac1412. arXiv: 2206.03519 [astro-ph.SR].

Theissen, C. A. et al. (May 2020). “WISE J135501.90-825838.9 is a Nearby, Young, Extremely Low-mass Substellar Binary”. In: *Research Notes of the American Astronomical Society* 4.5, 67, p. 67. DOI: 10.3847/2515-5172/ab91c4. arXiv: 2005.07096 [astro-ph.SR].

Thies, I. et al. (July 2010). “Tidally Induced Brown Dwarf and Planet Formation in Circumstellar Disks”. In: *The Astrophysical Journal* 717, pp. 577–585. ISSN: 0004-637X. DOI: 10.1088/0004-637X/717/1/577.

Thompson, W. et al. (Oct. 2023). “Octofitter: Fast, Flexible, and Accurate Orbit Modeling to Detect Exoplanets”. In: *The Astronomical Journal* 166.4, 164, p. 164. DOI: 10.3847/1538-3881/acf5cc. arXiv: 2402.01971 [astro-ph.EP].

Thorngren, D. P. et al. (Oct. 2016). “THE MASS–METALLICITY RELATION FOR GIANT PLANETS”. In: *The Astrophysical Journal* 831 (1), p. 64. ISSN: 15384357. DOI: 10.3847/0004-637x/831/1/64.

Ting, Y. S. et al. (Nov. 2012). “High-resolution elemental abundance analysis of the open cluster IC 4756”. In: *Monthly Notices of the Royal Astronomical Society* 427 (1), pp. 882–892. ISSN: 13652966. DOI: 10.1111/j.1365-2966.2012.22028.x.

Toomre, A. (May 1964). "On the gravitational stability of a disk of stars." In: *The Astrophysical Journal* 139, pp. 1217–1238. DOI: 10.1086/147861.

Toon, O. B. et al. (Aug. 1988). "A Multidimensional Model for Aerosols: Description of Computational Analogs". In: *Journal of the Atmospheric Sciences* 45.15, pp. 2123–2144. ISSN: 0022-4928, 1520-0469. DOI: 10.1175/1520-0469(1988)045<2123:AMMFAD>2.0.CO;2.

Tremblin, P. et al. (May 2015). "Fingering Convection and Cloudless Models for Cool Brown Dwarf Atmospheres". In: *The Astrophysical Journal Letters* 804.1, L17, p. L17. DOI: 10.1088/2041-8205/804/1/L17. arXiv: 1504.03334 [astro-ph.SR].

Tremblin, P. et al. (Feb. 2016). "Cloudless Atmospheres for L/T Dwarfs and Extrasolar Giant Planets". In: *The Astrophysical Journal Letters* 817.2, L19, p. L19. DOI: 10.3847/2041-8205/817/2/L19. arXiv: 1601.03652 [astro-ph.EP].

Triaud, A. H. M. J. et al. (Mar. 2020). "An eclipsing substellar binary in a young triple system discovered by SPECULOOS". In: *Nature Astronomy* 4, pp. 650–657. DOI: 10.1038/s41550-020-1018-2. arXiv: 2001.07175 [astro-ph.SR].

Trotta, R. (Mar. 2008). "Bayes in the sky: Bayesian inference and model selection in cosmology". In: *Contemporary Physics* 49.2, pp. 71–104. DOI: 10.1080/00107510802066753. arXiv: 0803.4089 [astro-ph].

Tsuji, T. (Aug. 2002). "Dust in the Photospheric Environment: Unified Cloudy Models of M, L, and T Dwarfs". In: *The Astrophysical Journal* 575.1, pp. 264–290. DOI: 10.1086/341262. arXiv: astro-ph/0204401 [astro-ph].

Turco, R. P. et al. (Apr. 1979). "A One-Dimensional Model Describing Aerosol Formation and Evolution in the Stratosphere: I. Physical Processes and Mathematical Analogs". In: *Journal of the Atmospheric Sciences* 36.4, pp. 699–717. ISSN: 0022-4928, 1520-0469. DOI: 10.1175/1520-0469(1979)036<0699:AODMDA>2.0.CO;2.

Turrini, D. et al. (Mar. 2021). "Tracing the Formation History of Giant Planets in Protoplanetary Disks with Carbon, Oxygen, Nitrogen, and Sulfur". In: *The Astrophysical Journal* 909 (1), p. 40. ISSN: 0004-637X. DOI: 10.3847/1538-4357/abd6e5.

Venner, A., A. Vanderburg, and L. A. Pearce (July 2021). "True Masses of the Long-period Companions to HD 92987 and HD 221420 from Hipparcos-Gaia Astrometry". In: *The Astronomical Journal* 162.1, 12, p. 12. DOI: 10.3847/1538-3881/abf932. arXiv: 2104.13941 [astro-ph.EP].

Vigan, A. et al. (Feb. 2024). "First light of VLT/HiRISE: High-resolution spectroscopy of young giant exoplanets". In: *Astronomy & Astrophysics* 682, A16, A16. DOI: 10.1051/0004-6361/202348019. arXiv: 2309.12390 [astro-ph.IM].

Vigan, A. (Sept. 2020). "Vlt-Sphere: Automatic VLT/SPHERE Data Reduction and Analysis". In: *Astrophysics Source Code Library*, ascl:2009.002.

Vogt, S. S. et al. (1994). "HIRES: The High-Resolution Echelle Spectrometer on the Keck 10-m Telescope". In: *Proceedings of SPIE* 2198, p. 362. DOI: 10.1117/12.176725.

Vos, J. M., K. N. Allers, and B. A. Biller (June 2017). "The Viewing Geometry of Brown Dwarfs Influences Their Observed Colors and Variability Amplitudes". In: *The Astrophysical Journal* 842.2, 78, p. 78. DOI: 10.3847/1538-4357/aa73cf. arXiv: 1705.06045 [astro-ph.SR].

Vos, J. M. et al. (Jan. 2022). "Let the Great World Spin: Revealing the Stormy, Turbulent Nature of Young Giant Exoplanet Analogs with the Spitzer Space Telescope". In: *The Astrophysical Journal* 924, p. 68. ISSN: 0004-637X. DOI: 10.3847/1538-4357/ac4502.

Vousden, W. D., W. M. Farr, and I. Mandel (Jan. 2016). "Dynamic Temperature Selection for Parallel Tempering in Markov Chain Monte Carlo Simulations". In: *Monthly Notices of the Royal Astronomical Society* 455, pp. 1919–1937. ISSN: 0035-8711. DOI: 10.1093/mnras/stv2422.

Wakeford, H. R. and D. K. Sing (Jan. 2015). "Transmission Spectral Properties of Clouds for Hot Jupiter Exoplanets". In: *Astronomy and Astrophysics* 573, A122. ISSN: 0004-6361. DOI: 10.1051/0004-6361/201424207.

Wang, J. J. et al. (Mar. 2021a). "Constraining the Nature of the PDS 70 Protoplanets with VLTI/GRAVITY". In: *The Astronomical Journal* 161, p. 148. ISSN: 0004-6256. DOI: 10.3847/1538-3881/abdb2d.

Wang, J. J., M. Kulikauskas, and S. Blunt (Jan. 2021b). "Whereistheplanet: Predicting Positions of Directly Imaged Companions". In: *Astrophysics Source Code Library*, ascl:2101.003.

Wang, J. J. et al. (June 2015). "pyKLIP: PSF Subtraction for Exoplanets and Disks". In: *Astrophysics Source Code Library*, ascl:1506.001.

Wang, J. J. et al. (Oct. 2016). "The Orbit and Transit Prospects for β Pictoris b Constrained with One Milliarcsecond Astrometry". In: *The Astronomical Journal* 152.4, 97, p. 97. DOI: 10.3847/0004-6256/152/4/97. arXiv: 1607.05272 [astro-ph.EP].

Wang, J. J. et al. (June 2020). "Keck/NIRC2 L'-Band Imaging of Jovian-mass Accreting Protoplanets around PDS 70". In: *The Astronomical Journal* 159, p. 263. DOI: 10.3847/1538-3881/ab8aef.

Wang, J. J. et al. (Oct. 2021c). "Detection and Bulk Properties of the HR 8799 Planets with High-resolution Spectroscopy". In: *The Astronomical Journal* 162, p. 148. ISSN: 0004-6256. DOI: 10.3847/1538-3881/ac1349.

Wang, J. J. et al. (Oct. 2022). "Atmospheric Monitoring and Precise Spectroscopy of the HR 8799 Planets with SCExAO/CHARIS". In: *The Astronomical Journal* 164.4, 143, p. 143. DOI: 10.3847/1538-3881/ac8984. arXiv: 2208.05594 [astro-ph.EP].

Wang, J. (Sept. 2023a). "Early Accretion of Large Amount of Solids for Directly-Imaged Exoplanets". In: *arXiv e-prints*, arXiv:2310.00088, arXiv:2310.00088. DOI: 10.48550/arXiv.2310.00088. arXiv: 2310.00088 [astro-ph.EP].

– (Nov. 2023b). "Spectral Retrieval with JWST Photometric data: a Case Study for HIP 65426 b". In: *The Astronomical Journal* 166.5, 203, p. 203. DOI: 10.3847/1538-3881/acfca0. arXiv: 2310.00089 [astro-ph.EP].

Wang, J. et al. (Apr. 2017). "Observing Exoplanets with High Dispersion Coronagraphy. I. The Scientific Potential of Current and Next-generation Large Ground and Space Telescopes". In: *The Astronomical Journal* 153, p. 183. ISSN: 0004-6256. DOI: 10.3847/1538-3881/aa6474.

Wang, J. et al. (Sept. 2020). "On the Chemical Abundance of HR 8799 and the Planet c". In: *The Astronomical Journal* 160, p. 150. ISSN: 0004-6256. DOI: 10.3847/1538-3881/ababa7.

Wang, J. et al. (Apr. 2022). "Retrieving the C and O Abundances of HR 7672 AB: A Solar-type Primary Star with a Benchmark Brown Dwarf". In: *The Astronomical Journal* 163, p. 189. ISSN: 0004-6256. DOI: 10.3847/1538-3881/ac56e2.

Wang, J. et al. (2023). "Retrieving C and O Abundance of HR 8799 c by Combining High- and Low-resolution Data". In: *The Astronomical Journal* 165, p. 4. ISSN: 0004-6256. DOI: 10.3847/1538-3881/ac9f19. URL: https://ui.adsabs.harvard.edu/abs/2023AJ....165....4W%20https://ui.adsabs.harvard.edu/link_gateway/2023AJ....165....4W/ARTICLE.

Wang, S.-i. et al. (Mar. 2003). "ARCES: an echelle spectrograph for the Astrophysical Research Consortium (ARC) 3.5m telescope". In: *Instrument Design and Performance for Optical/Infrared Ground-based Telescopes*. Ed. by M. Iye and A. F. M. Moorwood. Vol. 4841. SPIE Conference Series, pp. 1145–1156. DOI: 10.1117/12.461447.

Whitebook, S. et al. (Oct. 2024). "Discovery of the Binarity of Gliese 229B, and Constraints on the System's Properties". In: *The Astrophysical Journal Letters* 974.2, p. L30. DOI: 10.3847/2041-8213/ad7714. URL: https://dx.doi.org/10.3847/2041-8213/ad7714.

Whiteford, N. et al. (Oct. 2023). "Retrieval study of cool directly imaged exoplanet 51 Eri b". In: *Monthly Notices of the Royal Astronomical Society* 525 (1), pp. 1375–1400. ISSN: 13652966. DOI: 10.1093/mnras/stad670.

Wilson, T. L. (1999). "Isotopes in the interstellar medium and circumstellar envelopes". In: *Rep. Prog. Phys* 62, pp. 143–185.

Winn, J. N. (Nov. 2022). "Joint Constraints on Exoplanetary Orbits from Gaia DR3 and Doppler Data". In: *The Astronomical Journal* 164.5, 196, p. 196. DOI: 10.3847/1538-3881/ac9126. arXiv: 2209.05516 [astro-ph.EP].

Winn, J. N. and E. Petigura (Jan. 2024). "Planet Occurrence from Doppler and transit surveys, 2nd ed". In: *arXiv e-prints*, arXiv:2401.16451, arXiv:2401.16451. DOI: 10.48550/arXiv.2401.16451. arXiv: 2401.16451 [astro-ph.EP].

Wright, J. T. et al. (July 2012). "The Frequency of Hot Jupiters Orbiting nearby Solar-type Stars". In: *The Astrophysical Journal* 753.2, 160, p. 160. DOI: 10.1088/0004-637X/753/2/160. arXiv: 1205.2273 [astro-ph.EP].

Xin, Y. et al. (July 2023). "On-sky speckle nulling through a single-mode fiber with the Keck Planet Imager and Characterizer". In: *Journal of Astronomical Telescopes, Instruments, and Systems* 9, 035001, p. 035001. DOI: 10.1117/1.JATIS.9.3.035001. arXiv: 2307.11893 [astro-ph.IM].

Xuan, J. et al. (Sept. 2024a). *GRAVITY and CRIRES+ data for Gliese 229Bab*. Version 1.0. Zenodo. DOI: 10.5281/zenodo.13851639. URL: https://doi.org/10.5281/zenodo.13851639.

Xuan, J. et al. (Nov. 2024b). *JWST/MIRI LRS Forward Modeling*. DOI: 10.5281/zenodo.14032760. URL: https://doi.org/10.5281/zenodo.14032760.

Xuan, J. W. and M. C. Wyatt (July 2020a). "Evidence for a High Mutual Inclination between the Cold Jupiter and Transiting Super Earth Orbiting π Men". In: *Monthly Notices of the Royal Astronomical Society* 497, pp. 2096–2118. DOI: 10.1093/mnras/staa2033.

Xuan, J. W. et al. (Mar. 2020b). "A Rotation Rate for the Planetary-Mass Companion DH Tau b". In: *The Astronomical Journal* 159, p. 97. ISSN: 0004-6256. DOI: 10.3847/1538-3881/ab67c4.

Xuan, J. W. et al. (Oct. 2020c). "Mutual Inclinations between Giant Planets and Their Debris Discs in HD 113337 and HD 38529". In: *Monthly Notices of the Royal Astronomical Society* 499, pp. 5059–5074. ISSN: 0035-8711. DOI: 10.1093/mnras/staa3155.

Xuan, J. W. et al. (Oct. 2022). "A Clear View of a Cloudy Brown Dwarf Companion from High-resolution Spectroscopy". In: *The Astrophysical Journal* 937.2, 54, p. 54. DOI: 10.3847/1538-4357/ac8673.

Xuan, J. W. et al. (July 2024a). "Are These Planets or Brown Dwarfs? Broadly Solar Compositions from High-resolution Atmospheric Retrievals of ~10–30 M_{Jup} Companions". In: *The Astrophysical Journal* 970.1, 71, p. 71. DOI: 10.3847/1538-4357/ad4796.

Xuan, J. W. et al. (Oct. 2024b). "The cool brown dwarf Gliese 229 B is a close binary". In: *Nature* 634.8036, pp. 1070–1074. DOI: 10.1038/s41586-024-08064-x.

Xuan, J. W. et al. (Feb. 2024c). "Validation of Elemental and Isotopic Abundances in Late-M Spectral Types with the Benchmark HIP 55507 AB System". In: *The Astrophysical Journal* 962.1, 10, p. 10. DOI: 10.3847/1538-4357/ad1243.

Xuan, W. J. et al. (Sept. 2018). "Characterizing the Performance of the NIRC2 Vortex Coronagraph at W. M. Keck Observatory". en. In: *The Astronomical Journal* 156.4, p. 156. ISSN: 1538-3881. DOI: 10.3847/1538-3881/aadae6.

Xue, Q. et al. (Mar. 2024). "JWST Transmission Spectroscopy of HD 209458b: A Supersolar Metallicity, a Very Low C/O, and No Evidence of CH_4, HCN, or C_2H_2". In: *The Astrophysical Journal Letters* 963.1, L5, p. L5. DOI: 10.3847/2041-8213/ad2682. arXiv: 2310.03245 [astro-ph.EP].

Yee, S. W., E. A. Petigura, and K. von Braun (Feb. 2017). "Precision Stellar Characterization of FGKM Stars using an Empirical Spectral Library". In: *The Astrophysical Journal* 836.1, 77, p. 77. DOI: 10.3847/1538-4357/836/1/77. arXiv: 1701.00922 [astro-ph.SR].

Yelda, S. et al. (Dec. 2010). "Improving galactic center astrometry by reducing the effects of geometric distortion". In: *Astrophysical Journal* 725 (1), pp. 331–352. ISSN: 15384357. DOI: 10.1088/0004-637X/725/1/331.

Yelverton, B. et al. (Sept. 2019). "A statistically significant lack of debris discs in medium separation binary systems". In: *Monthly Notices of the Royal Astronomical Society* 488.3, pp. 3588–3606. DOI: 10.1093/mnras/stz1927. arXiv: 1907.04800 [astro-ph.EP].

Yu, J. et al. (Feb. 2023). "Revised Extinctions and Radii for 1.5 Million Stars Observed by APOGEE, GALAH, and RAVE". In: *The Astrophysical Journal Supplement Series* 264 (2), p. 41. ISSN: 0067-0049. DOI: 10.3847/1538-4365/acabc8.

Yurchenko, S. N. and J. Tennyson (May 2014). "ExoMol Line Lists - IV. The Rotation-Vibration Spectrum of Methane up to 1500 K". In: *Monthly Notices of the Royal Astronomical Society* 440, pp. 1649–1661. ISSN: 0035-8711. DOI: 10.1093/mnras/stu326.

Yurchenko, S. N. et al. (Sept. 2018). "ExoMol line lists XXVIII: The rovibronic spectrum of AlH". In: *Monthly Notices of the Royal Astronomical Society* 479 (1), pp. 1401–1411. ISSN: 13652966. DOI: 10.1093/MNRAS/STY1524.

Zahnle, K. J. and M. S. Marley (Dec. 2014). "Methane, Carbon Monoxide, and Ammonia in Brown Dwarfs and Self-Luminous Giant Planets". In: *The Astrophysical Journal* 797, p. 41. ISSN: 0004-637X. DOI: 10.1088/0004-637X/797/1/41.

Zalesky, J. A. et al. (May 2019). "A Uniform Retrieval Analysis of Ultra-cool Dwarfs. III. Properties of Y Dwarfs". In: *The Astrophysical Journal* 877.1, 24, p. 24. DOI: 10.3847/1538-4357/ab16db. arXiv: 1903.11658 [astro-ph.SR].

Zalesky, J. A. et al. (Sept. 2022). "A Uniform Retrieval Analysis of Ultra-cool Dwarfs. IV. A Statistical Census from 50 Late-T Dwarfs". In: *The Astrophysical Journal* 936.1, 44, p. 44. DOI: 10.3847/1538-4357/ac786c. arXiv: 2206.01199 [astro-ph.SR].

Zapatero Osorio, M. R. et al. (Nov. 2004). "Dynamical Masses of the Binary Brown Dwarf GJ 569 Bab". In: *The Astrophysical Journal* 615.2, pp. 958–971. DOI: 10.1086/424507. arXiv: astro-ph/0407334 [astro-ph].

Zhang, J. et al. (Aug. 2024). "Discovery of a Jupiter Analog Misaligned to the Inner Planetary System in HD 73344". In: *arXiv e-prints*, arXiv:2408.09614, arXiv:2408.09614. DOI: 10.48550/arXiv.2408.09614. arXiv: 2408.09614 [astro-ph.EP].

Zhang, K. et al. (Sept. 2019). "Systematic Variations of CO Gas Abundance with Radius in Gas-rich Protoplanetary Disks". In: *The Astrophysical Journal* 883 (1), p. 98. ISSN: 15384357. DOI: 10.3847/1538-4357/ab38b9.

Zhang, X. and A. P. Showman (Oct. 2018). "Global-Mean Vertical Tracer Mixing in Planetary Atmospheres. I. Theory and Fast-rotating Planets". In: *The Astrophysical Journal* 866.1, p. 1. ISSN: 0004-637X. DOI: 10.3847/1538-4357/aada85.

Zhang, Y., S. de Regt, and D. González Picos (Sept. 2024). *excalibuhr: a pipeline for VLT/CRIRES+ high- resolution spectral data reduction*. Version v0.1.1. DOI: 10.5281/zenodo.13659358. URL: https://doi.org/10.5281/zenodo.13659358.

Zhang, Y., I. A. G. Snellen, and P. Mollière (Dec. 2021a). "The ^{12}CO/^{13}CO isotopologue ratio of a young, isolated brown dwarf. Possibly distinct formation pathways of super-Jupiters and brown dwarfs". In: *Astronomy & Astrophysics* 656, A76, A76. DOI: 10.1051/0004-6361/202141502. arXiv: 2109.11569 [astro-ph.EP].

Zhang, Y. et al. (July 2021b). "The 13CO-Rich Atmosphere of a Young Accreting Super-Jupiter". In: *Nature* 595.7867, pp. 370–372. ISSN: 1476-4687. DOI: 10.1038/s41586-021-03616-x.

Zhang, Y. et al. (Sept. 2022). "VLT/CRIRES Science Verification Observations: A hint of C18O in the Young Brown Dwarf 2M0355". In: *Research Notes of the AAS* 6 (9), p. 194. DOI: 10.3847/2515-5172/ac9309. URL: https://dx.doi.org/10.3847/2515-5172/ac9309.

Zhang, Z. et al. (Aug. 2021a). "The Second Discovery from the COCONUTS Program: A Cold Wide-orbit Exoplanet around a Young Field M Dwarf at 10.9 pc". In: *The Astrophysical Journal Letters* 916.2, L11, p. L11. DOI: 10.3847/2041-8213/ac1123. arXiv: 2107.02805 [astro-ph.EP].

Zhang, Z. et al. (Nov. 2021b). "Uniform Forward-modeling Analysis of Ultracool Dwarfs. II. Atmospheric Properties of 55 Late-T Dwarfs". In: *The Astrophysical Journal* 921.1, 95, p. 95. DOI: 10.3847/1538-4357/ac0af7. arXiv: 2105.05256 [astro-ph.SR].

Zhang, Z. et al. (Oct. 2023). "ELemental abundances of Planets and brown dwarfs Imaged around Stars (ELPIS). I. Potential Metal Enrichment of the Exoplanet AF Lep b and a Novel Retrieval Approach for Cloudy Self-luminous Atmospheres".

In: *The Astronomical Journal* 166.5, p. 198. DOI: 10.3847/1538-3881/acf768. URL: https://dx.doi.org/10.3847/1538-3881/acf768.

Zhou, Y. et al. (Mar. 2014). "Accretion onto Planetary Mass Companions of Low-mass Young Stars". en. In: *The Astrophysical Journal* 783.1, p. L17. DOI: 10.1088/2041-8205/783/1/L17. URL: https://ui.adsabs.harvard.edu/abs/2014ApJ...783L..17Z/abstract (visited on 04/24/2019).

Zhou, Y. et al. (Feb. 2018). "Cloud Atlas: Rotational Modulations in the L/T Transition Brown Dwarf Companion HN Peg B". In: *The Astronomical Journal* 155.3, p. 132. ISSN: 1538-3881. DOI: 10.3847/1538-3881/aaabbd.

Zhou, Y. et al. (Mar. 2019). "Cloud Atlas: High-contrast Time-resolved Observations of Planetary-mass Companions". en. In: *The Astronomical Journal* 157.3, p. 128. DOI: 10.3847/1538-3881/ab037f. URL: https://ui.adsabs.harvard.edu/abs/2019AJ....157..128Z/abstract (visited on 04/20/2019).

Zhu, Z. et al. (Feb. 2012). "Challenges in forming planets by gravitational instability: Disk irradiation and clump migration, accretion, and tidal destruction". In: *Astrophysical Journal* 746 (1). ISSN: 15384357. DOI: 10.1088/0004-637X/746/1/110.

Zuckerman, B. et al. (May 2011). "The Tucana/Horologium, Columba, AB Doradus, and Argus Associations: New Members and Dusty Debris Disks". In: *The Astrophysical Journal* 732.2, 61, p. 61. DOI: 10.1088/0004-637X/732/2/61. arXiv: 1104.0284 [astro-ph.SR].